Reynolds stresses and enstrophy transport in wall turbulence controlled by streamwise travelling waves

Mohammad Umair

THÈSE

Pour obtenir le grade de

DOCTEUR DE L'UNIVERSITÉ GRENOBLE ALPES

École doctorale : I-MEP2 - Ingénierie - Matériaux, Mécanique, Environnement, Energétique, Procédés, Production
Spécialité : MEP - Mécanique des fluides Energétique, Procédés
Unité de recherche : Laboratoire des Ecoulements Géophysiques et Industriels

Transport des contraintes de Reynolds et de l'enstrophie en turbulence de paroi contrôlée par les ondes progressives longitudinales

Reynolds stresses and enstrophy transport in wall turbulence controlled by streamwise travelling waves

Présentée par :

Mohammad UMAIR

Direction de thèse :

Sedat TARDU MAITRE DE CONFERENCES, Université Grenoble Alpes	Directeur de thèse
Olivier DOCHE Maitre de Conférences, Université Grenoble Alpes	Co-encadrant de thèse

Rapporteurs :

Maurizio QUADRIO
FULL PROFESSOR, Politecnico di Milano
Bettina FROHNAPFEL
FULL PROFESSOR, Karlsruher Institut für Technologie

Thèse soutenue publiquement le **3 novembre 2023**, devant le jury composé de :

Sedat TARDU MAITRE DE CONFERENCES HDR, Université Grenoble Alpes	Directeur de thèse
Maurizio QUADRIO FULL PROFESSOR, Politecnico di Milano	Rapporteur
Bettina FROHNAPFEL FULL PROFESSOR, Karlsruher Institut für Technologie	Rapporteure
Henda DJERIDI PROFESSEURE DES UNIVERSITES, Grenoble INP	Présidente
Davide GATTI SENIOR SCIENTIST, Karlsruher Institut für Technologie	Examinateur

Invités :

Olivier DOCHE
MAITRE DE CONFERENCES, Grenoble INP

UNIVERSITÉ DE GRENOBLE ALPES

ÉCOLE DOCTORALE I-MEP2

Ingénierie - Matériaux, Mécanique, Environnement, Energétique, Procédés, Production.

T H È S E

pour obtenir le titre de

Docteur en sciences

de l'Université Grenoble Alpes

Mention : MEP : MÉCANIQUE DES FLUIDES ENERGÉTIQUE, PROCÉDÉS

Présentée et soutenue par

Mohammad UMAIR

Transport des contraintes de Reynolds et de l'enstrophie en turbulence de paroi contrôlée par les ondes progressives longitudinales

Thèse dirigée par Sedat TARDU et
codirigée par Olivier DOCHE

préparée au laboratoire LEGI

soutenue le 03 Novembre 2023

Jury :

Directeur de thèse :	Sedat TARDU	-	Université Grenoble Alpes
Rapporteur :	Maurizio QUADRIO	-	Politecnico di Milano
Rapporteure :	Bettina FROHNAPFEL	-	Karlsruher Institut für Technologie
Présidente de jury :	Henda DJERIDI	-	Grenoble INP
Examinateur :	Davide GATTI	-	Karlsruher Institut für Technologie
Co-encadrant (Invité) :	Olivier DOCHE	-	Grenoble INP - Phelma

Acknowledgements

At this moment of accomplishment, first and foremost, I would like to express my sincere gratitude to Prof Maurizio Quadrio and Prof Bettina Frohnapfel for taking time out of their busy schedule to review this manuscript and providing their valuable feedback. I would also like to thank Dr Davide Gatti and Prof Henda Djeridi for accepting to be members of the jury on such a short notice.

I would like to extend my heartfelt thanks to the members of my thesis committee, Jan-Bert Flór and Laurent Davoust, for their insightful feedback and constructive criticism that significantly enhanced the quality of this work.

I would like to express my sincere gratitude to my supervisors, Sedat Tardu and Olivier Doche, for giving me the opportunity to carry out my thesis work at LEGI and for providing necessary infrastructure and resources to accomplish this work. I am extremely indebted to Sedat who encouraged and directed me. It is because of his supervision that this work came into existence. They have been extremely supportive since the day I began working on my project. Ever since, Sedat has supported me academically and motivated me through the rough road to finish this work. Despite his hectic schedule, the door to his office was always open whenever I ran into trouble or had a question regarding my work. He consistently steered me in the right direction. His unflinching courage and conviction will always inspire me, and I hope to continue to work with his noble thoughts.

I'm highly indebted to all the members of LEGI for fostering an intellectually stimulating and fun filled environment. My sincere thanks go to Yann, Amélie, Ivan, Benjamin, Mathieu, Karla, Mohammad, Oliver, Sofia, and Achim for many rounds of discussions on many topics be it cooking, travelling, history, culture, or science. I gratefully admire their helping nature. Furthermore, I would like to acknowledge the efforts of LEGI's administration for their timely response whenever I faced any issue.

It's my fortune to gratefully acknowledge the support of some special individuals from Foyer Étudiants Résidence International (4 rue Sainte Ursule) (now closed forever). My special appreciation goes to Mariami, Mariam, Letícia, Pauline, Roberta (Picoletta), Beatriz, Constance, Jean, François, Amine, Adélie, Dušan and Lidiya for their friendship and making my stay in Grenoble a joyful experience. I wish to thank them all for their love, care and moral support. Words fail me to express my appreciation for their support and generous care. They were always beside me during the hard times to push me and motivate me. A journey is easier if you travel together. Interdependence is certainly more valuable than independence. A simple thank doesn't seem sufficient for the support, encouragement, care, understanding and precious friendship.

Last but not least, I would like to pay high regards to my father Mr Saghir Ahmad, mother

(Late) Mrs Razia Shaheen, and brothers Shoeb, Uzair and his wife Neelofer for their sincere encouragement and inspiration throughout my work and lifting me uphill in this phase of life. Besides this, several people have knowingly and unknowingly helped me in the successful completion of this work. I doubt that I will ever be able to convey my appreciation fully, but I owe all of you my external gratitude.

Abstract

Direct numerical simulations of turbulent channel flow subjected to spanwise wall oscillations in the form of streamwise travelling waves (STW) were performed in an effort to elucidate the mechanism responsible for the observed drag reduction. We imposed large amplitudes to identify the proper effects of STW, while keeping the angular frequency and wavenumber fixed at a particular values. We primarily focus on the energy and vorticity transport mechanism, to better understand the influence of STW actuation on the near-wall turbulence. Streamwise travelling waves of large amplitudes were found to block the inter-component energy transfer, resulting in shut off of the near-wall buffer layer dynamics. The analysis presented here suggests that the combined effect of loss of communication between low and high buffer layers with damping in the wall-normal Reynolds stress component is associated to the travelling wave effect, and results in larger drag reduction margins. Furthermore, the analysis of vorticity transport reveals that the primary effect of the STW forcing is to attenuate the spanwise turbulent enstrophy at the wall, which is linked to the fluctuating wall shear stress. To strengthen this point, we performed numerical experiments, where the streamwise fluctuating velocity, and consequently the spanwise vorticity is artificially suppressed next to the wall. The anisotropic invariant maps show striking resemblance for large amplitude STW actuation and artificially forced cases. Detailed analysis of various structural features is provided, which includes the response of the near-wall streaks and shear layers of spanwise fluctuating velocity field. The quasi-streamwise vortices, which play a key role in the production of the near-wall turbulence, are shown to be pushed away from the wall, resulting in their weakened signature at the wall.

Résumé

Des simulations numériques directes ont été réalisées dans un canal pleinement turbulent soumis à des ondes progressives longitudinales (STW) dans le but d'élucider le mécanisme responsable de la réduction de la traînée. De grandes amplitudes ont été imposées pour identifier les effets propres des STW, en maintenant à des valeurs constantes la fréquence angulaire et le nombre d'ondes. Une attention particulière est portée sur le mécanisme de transport de l'énergie et de la vorticité, afin de mieux comprendre l'influence du forçage via les STW sur la turbulence en proche paroi. Les ondes progressives longitudinales de grande amplitude bloquent le transfert d'énergie entre les composantes, ce qui entraîne l'arrêt de la dynamique dans la sous-couche tampon près de la paroi. L'analyse présentée ici suggère que l'effet combiné de la perte de communication entre la haute sous couche tampon et la basse sous couche tampon, combinée avec l'amortissement de la composante verticale des contraintes de Reynolds est associé à l'effet d'ondes progressives et se traduit par des réductions significatives de la traînée. En outre, l'analyse du transport de vorticité révèle que l'effet principal du forçage via les STW est d'atténuer l'enstrophie turbulente transversale, en particulier à la paroi, à travers une diminution importante des fluctuations de la contrainte de cisaillement. Pour renforcer ce dernier point, nous avons réalisé d'autres simulations (des expériences numériques) où les fluctuations de vitesse longitudinale, et par conséquent de la vorticité transversale, ont été artificiellement supprimées en proche paroi. Les invariants de l'anisotropie obtenus à travers le forçage sont fortement similaires à l'écoulement turbulent contrôlé par les STW de grande amplitude. Une analyse détaillée des diverses caractéristiques structurelles est également fournie, notamment la réponse des stries en proche paroi et des couches de cisaillement. Les tourbillons quasi-longitudinaux, qui jouent un rôle clé dans la production de la turbulence pariétale, sont poussés loin de la paroi, ce qui se traduit par un affaiblissement de leur signature dans la sous-couche visqueuse et la basse sous-couche tampon.

Contents

List of Figures

List of Tables

Nomenclature

Acronyms

1C	One component state
2C	Two component state
1D	One dimensional
2D	Two dimensional
3D	Three dimensional
AIM	Anisotropic Invariants Map
BW-STW	Upstream Streamwise travelling waves
FW-STW	Downstream Streamwise travelling waves
CFR	Constant flow rate
CPG	Constant pressure gradient
CS	Compact schemes
DI	Drag increase
DNS	Direct numerical simulations
DR	Drag reduction
EEA	European Environmental Agency
EO	Explicit optimized
FE	Finite element
FD	Finite difference
FV	Finite Volume
HWO	Homogeneous wall oscillations
HSS	High-speed streaks
LSS	Low-speed streaks

LES Large eddy simulations

QSV Quasi-streamwise vortices

RANS Reynolds averaged Navier-Stokes

STW Streamwise travelling waves

Physical quantities

a_n coefficients for the estimation of derivatives using EO schemes

a_{ij} Reynolds stress anisotropy tensor

A Forcing amplitude

$A_{\omega_x\omega_x}, A_{\omega_y\omega_y}, A_{\omega_z\omega_z}$ Advection terms in the transport equations of the streamwise, wall-normal and spanwise enstrophy components

c Wave speed

$\check{c}$ Convection velocity of the near-wall fluctuating field

C_{uv} Correlation coefficient of Reynolds shear stress

C_f Coefficient of friction

C_{f0} Coefficient of friction for uncontrolled flow

C_{Q1}, C_{Q2}, C_{Q3}, C_{Q4} Quadrant events contributions

D_{uu}, D_{vv}, D_{ww}, D_{uv} Viscous diffusion terms in the transport equations of the Reynolds streamwise, wall-normal, spanwise and shear stress components

$D_{\omega_x\omega_x}, D_{\omega_y\omega_y}, D_{\omega_z\omega_z}$ Viscous diffusion terms in the transport equations of the streamwise, wall-normal and spanwise enstrophy components

d_s Distance of QSVs from the wall

Δd_s Drift in QSVs

E Error in the estimation of derivatives

f any arbitrary quantity/function

f_i Forcing term in the momentum equation

$F(y)$ Filter function

L Characteristic length

M, N Number of adjacent nodes from where the derivative of f is estimated

P, p Pressure and its fluctuations, respectively

P, Q, R First, second and third invariants of the velocity gradient tensor

P_{uu}, P_{vv}, P_{ww}, P_{uv} Production terms in the transport equations of the Reynolds streamwise, wall-normal, spanwise and shear stress components

$P_{\omega_x\omega_x}$, $P_{\omega_y\omega_y}$, $P_{\omega_z\omega_z}$ Production terms in the transport equations of the streamwise, wall-normal and spanwise enstrophy components

$Q1$, $Q2$, $Q3$, $Q4$ Quadrant events

$R(y)$ Right-hand side of the Navier-Stokes equations

Re Reynolds number

Re_c Reynolds number based on the centerline velocity

Re_τ Reynolds number based on the friction velocity

S Choi's scaling parameter

S Symetric part of the velocity gradient tensor

S_u, S_v, S_w Skewness factor of the streamwise, wall-normal and spanwise velocity fluctuations

t time

T Forcing period

$T_{uu}, T_{vv}, T_{ww}, T_{uv}$ Transport terms in the transport equations of the Reynolds streamwise, wall-normal, spanwise and shear stress components

$T_{\omega_x\omega_x}, T_{\omega_y\omega_y}, T_{\omega_z\omega_z}$ Transport terms in the transport equations of the streamwise, wall-normal and spanwise enstrophy components

U Characteristic velocity scale

U_b Bulk velocity

U_c Centerline velocity

u_τ Friction velocity

U, V, W Instantaneous streamwise, wall-normal, spanwise velocity

u, v, w Fluctuating streamwise, wall-normal, spanwise velocity

II, III Second and third invariants of the Reynolds stress anisotropy tensor

α parameter to control the steepness of the filter function $F(y)$

β_n coefficients for the estimation of derivatives using EO schemes

γ Empirical coefficient used in the power law scaling of DR

δ Stokes layer thickness

δ Wall-normal distance up to which the filter $F(y)$ acts

ε Dissipation

ε_{uu}, ε_{vv}, ε_{ww}, ε_{uv} Dissipation terms in the transport equations of the Reynolds streamwise, wall-normal, spanwise and shear stress components

$\varepsilon_{\omega_x\omega_x}$, $\varepsilon_{\omega_y\omega_y}$, $\varepsilon_{\omega_z\omega_z}$ Dissipation terms in the transport equations of the streamwise, wall-normal and spanwise enstrophy components

ζ fluctuating field, u, v, w

η Kolmogorov length scale

κ Forcing wavenumber

λ Forcing wavelength

λ_2 Second largest eigen value of the velocity gradient tensor

ν Kinematic viscosity

ξ Instantaneous phase of the wave ($\xi = x - ct$)

π_{uu}, π_{vv}, π_{ww}, π_{uv} Velocity-Pressure gradient terms in the transport equations of the Reynolds streamwise, wall-normal, spanwise and shear stress components

ρ Density

τ_w Wall shear stress

ϕ Phase of the wave

Ψ An instantaneous turbulent signal

Ω Total vorticity

Ω Antisymmetric part of the velocity gradient tensor

ω Forcing angular frequency

Ω_x, Ω_y, Ω_z Instantaneous streamwise, wall-normal, spanwise vorticity

ω_x, ω_y, ω_z Fluctuating streamwise, wall-normal, spanwise vorticity

Spatial Parameters

x, y, z Streamwise, wall-normal, spanwise coordinate

N_x, N_y, N_z Number of grid points in streamwise,wall-normal, spanwise direction

h Channel half-height

$\langle \cdot \rangle$ Phase averaged value

$\tilde{\cdot}$ Periodic fluctuations

$\bar{\cdot}$ Averaged value

$\hat{\cdot}$ Fourier transform

CHAPTER 1

Introduction

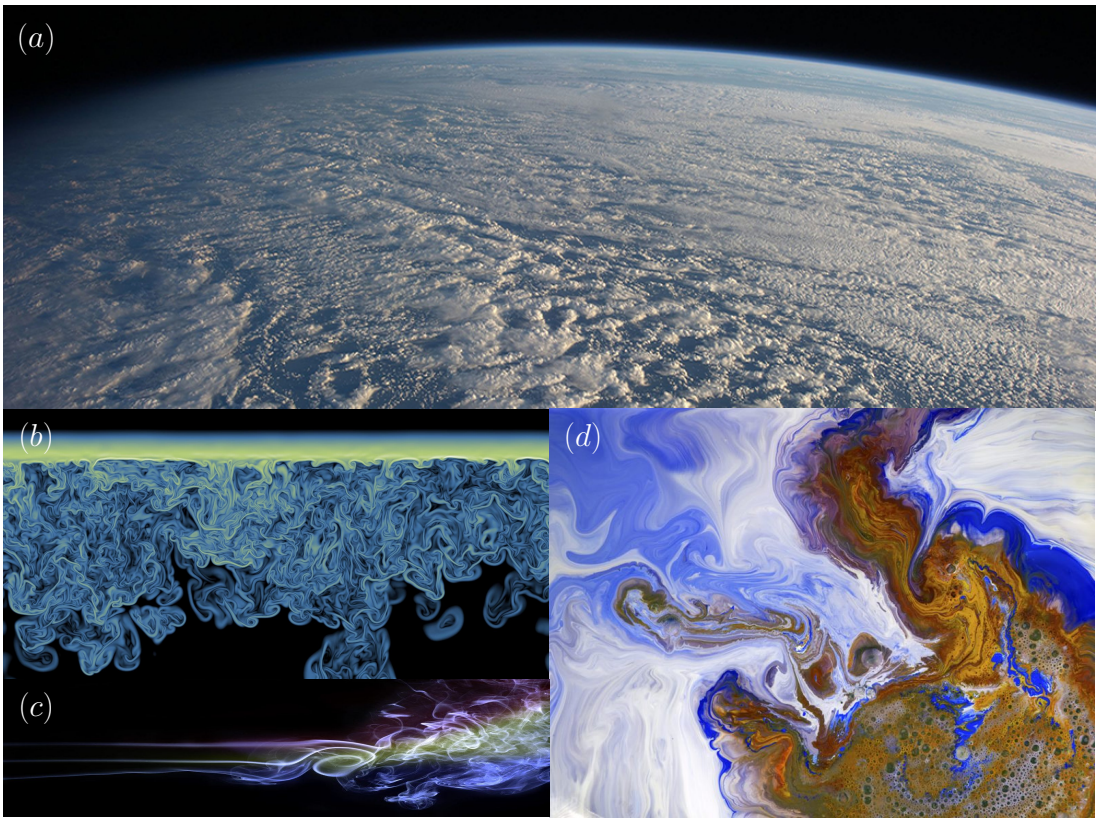

Figure 1.1: Example of turbulent motion: (a) Stratocumulus clouds above the northwestern Pacific Ocean (Credit: NASA) (b) Turbulent structures of the stratocumulus cloud-top inside a vertical plane in terms of the magnitude of the temperature gradient, resolving scales from 4 metres down to about 4 millimetres. The upper horizontal stripe corresponds to the inversion that separates the turbulent cloud below from the warm, clear sky above. The turbulent motion is created by the evaporation of the droplets in a thin region next to that inversion, which cools locally the fluid mixture and leads to finger structures plummeting into the cloud. (Taken from Mellado [1] with permission from Cambridge University Press). (c) A flow visualization image of a fluid flow stream undergoing a transition from a smooth laminar flow to a mixed turbulent flow. Flow is from left to right. (d) Patterns formed on a soap film.

Turbulent flows are of extreme interest due to their prevalence in nature and many industrial applications: common examples include the rise of cigarette smoke, waterfalls, blood flow in arteries, and most of the terrestrial atmospheric recirculation. Some other examples are illustrated in figure 1.1. Turbulence can either be desirable in some physical systems that require efficient mixing, for example, heat exchangers, or can have a drastic consequence.

Climate change is a global issue that is rapidly intensifying, impacting regions worldwide. Rare extreme events, such as droughts in South Asia, forest fires, floods, etc are becoming increasingly common. A recent example include the deadly floods that have engulfed the northern Italian region of *Emilia Romagna*, killing at least 14 people and displacing thousands, are another sign of the accelerating climate crisis. The floods come after years of severe drought in the region, which has compacted the soil, reducing its ability to absorb rainfall. Rising temperatures intensify drought episodes, drying up the soil and changing its permeability in different ways.

The melting of ice caps in the Arctic and the closure of skiing stations in Grenoble due to insufficient snow are some of the well-known manifestations of climate change. These events have profound consequences, affecting both economies and the lives of people directly impacted by them.

The aviation industry, in particular, plays a role in exacerbating climate change. In 2018, flights departing from EU27+EFTA countries accounted for approximately 16% of global aviation's CO2 emissions. Furthermore, in 2019, departing flights from Europe contributed to 5.2% of the total greenhouse gas emissions of EU27+EFTA countries (a significant increase from 1.8% in 1990) and 18.3% of emissions from the transportation sector. Aviation ranks as the second-largest source of emissions in the transport sector, following road transport, according to the latest report by the European Environment Agency (EEA).

Skin friction drag is a significant component of the resistance experienced by various transportation systems. It accounts for approximately 50% of the total resistance for aeroplanes, 90% for underwater vehicles, and nearly 100% for internal flows through pipes and channels. A considerable amount of skin friction is generated in the near-wall turbulent flow region. This not only impacts the performance of these systems, but also has detrimental environmental effects. The energy required to overcome skin friction leads to increased fuel consumption and elevated greenhouse gas emissions.

While completely eliminating air travel is not a realistic solution, given its integral role in our economic system, efforts must be made to minimize emissions from the aviation industry. Current aircraft designs allow for the reduction of transition delay on wings and appendages, but the longer fuselage, where half of the skin friction drag occurs, presents a challenge. Therefore, there is widespread interest in researching methods specifically aimed at reducing turbulent skin friction drag. Even a few percent reductions in frictional losses in turbulent flows holds significant engineering and practical value, as it has the potential to yield substantial economic and

environmental benefits.

1.1 Turbulence control

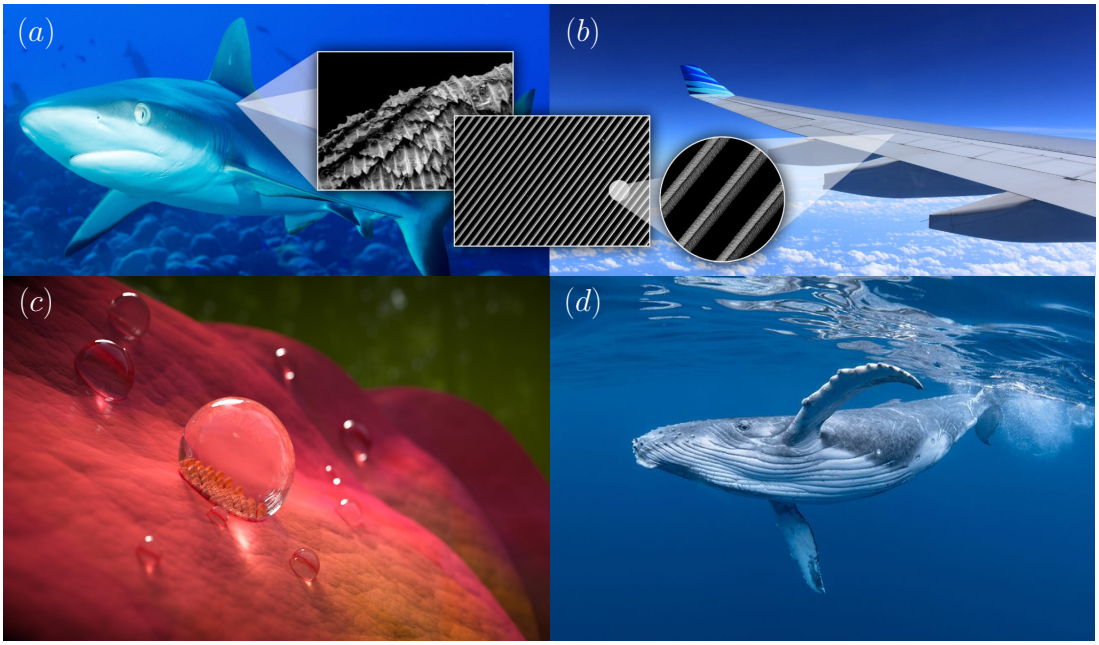

Figure 1.2: (a) Scale patterns on fast-swimming sharks, (b) Wing partly covered with riblet film. There have also been a few tests on full-size aircraft by both Boeing and Airbus. Airbus started riblet film tests on an A320 aircraft that provided the expected results. Later, a long-range A340 airliner, partly covered (30%) with 3M riblet film, was flown for several years in commercial service by Cathay Pacific Airways. (c) Droplets on a rose petal (Source: ©Anna Tanczos/Sci Comm Studios). (d) A blue whale swimming in the ocean.

Numerous turbulence control techniques, some practically feasible and others more conceptual, have been devised over the course of the last several decades in an attempt to mitigate the skin friction at the wall. Turbulence control techniques specifically targeted at reducing the skin friction are broadly classified into two categories: passive and active. Passive techniques do not require energy and tend to be far more practically feasible as compared to active techniques, which by definition require energy for their actuation. It is not surprising to see that the nature has already provided us the essential means to tackle these challenges. Aquatic animals, for example, have evolved a diversity of propulsive methods to traverse effectively through water. This is the result of a long evolutionary process during which natural selection has generated an array of novel anatomical and physiological responses to the problem of moving efficiently through water [2]. Fishes, whales, seals, penguins, etc., for example, use the movement of their body to

produce thrust, while simultaneously reducing the resistance to their motion through morphological design, phased kinematics, and behaviours. These are one of the many ways how evolution over the past millions of years have enabled many creatures to adapt to the environment and 'creatively' face its challenges (figure 1.2). Biologically inspired design, adaptation, or derivation from nature referred to as 'biomimetics' paved the way for the design and development of many passive drag reduction techniques.

Riblets, for example, have been inspired from the dermal denticles present on the sharks' skins (figure 1.2*a*). These micro groove patters help them to manoeuvre seamlessly under the water. Riblets, similarly to shark skin, have tiny grooves arranged longitudinally along the flow direction and are known to reduce the skin friction drag up to 8%. Amongst many other passive drag control techniques, riblets are the one that have been studied most extensively. The results emanating from these studies have been so promising and encouraging that the concept has been evaluated in actual flight tests.

Another passive technique that finds its root in the nature is the use of super hydrophobic surfaces. This technique has been inspired from the extreme water repellence and self-cleaning performance of the Sacred Lotus (*Nelumbo nucifera*) (figure 1.2*c*). Compared to other natural plant leaves, lotus leaf is the most super hydrophobic, with a water contact angle as high as 160° and sliding angle as low as 5°, hence it always remains clean in muddy and dirty ponds and therefore, undoubtedly served as a symbol of purity in Asian culture for over 2,000 years. Numerous studies have consistently shown that super hydrophobic surfaces can dramatically reduce the skin friction drag in both laminar and turbulent flows.

Although the passive control techniques are technically more feasible than their active counterpart, the robustness and scalability of such techniques at high Reynolds number constitute recurrent problems. The use of riblets, for example, although being mostly successful, cannot produce drag reduction larger than 10%. Moreover, their capability to reduce skin friction drag is constrained to within a small range of the riblets spacing and heights, and is therefore quite sensitive to changes in the external flow conditions. The use of super hydrophobic surfaces, on the other hand, is by definition limited by the fact that it can only be used in liquid flows. Not to mention the fact that maintaining the designed solid-liquid interface poses its own additional challenges and requires extra energy input in practice. Additionally, many factors, such as interface width, impact velocities, vibrations, contamination effects, etc. influence the characteristics of air pockets which makes it even more difficult to maintain a flat solid-liquid interface. Moreover, super hydrophobic surfaces are severely vulnerable to high pressure and high shear rate. These are a few of the several reasons why they have not yet evolved into a practical means.

Active control techniques, despite requiring energy input to operate, produce significantly large drag reduction margins. In contrast to passive techniques, they can be applied in more common conditions and operate at a much wider range of spatio-temporal scales. Active control can either be applied in an open-loop manner independent of the flow state or in an adaptive

closed-loop manner where the actuation parameters are dynamically modified using a feedback control loop. Opposition control [3], is perhaps one of the post popular control strategies that lie under this category. It relies on sensing the wall-normal velocity at a detection plane above the wall, then applying blowing and suction at the wall exactly opposite to the detected wall-normal velocity. The opposition control can effectively reduce the skin friction drag by opposing the motion of the near-wall turbulent structures. In general, closed-loop control techniques make use of actuators and sensors network, and their performance relies heavily on the response time of the control system. Although, the power and reliability of the actuators and sensors have dramatically increased, thanks to the advancement in micro-electro-mechanical systems (MEMs) fabrication technologies, it is extremely difficult to install many small-scale sensors and actuators over a wide range of wall area in real experiments. For the open-loop techniques, on the hand, the control law is predetermined, and the control is applied irrespective of the instantaneous state of the system, thus obviating the need of such a complex network of actuation and sensing. For this reason, the open-loop techniques have received a significant attention over the last several decades and is still a subject of ongoing research interest.

This thesis focuses on one of the most celebrated open loop technique, called spanwise wall oscillations. Since, its inception, it has gained wide popularity among the drag reduction community due to its capability of producing significantly large drag reduction margin of up to 60%. Even though wall oscillations based techniques still haven't yet evolved to be applied for commercial purposes, nevertheless they paved the way for the design of many other complex techniques, such as wavy-wall deformation, sinusoidal riblets, rotating discs, etc.

1.2 Research goals and expected outcomes

The central focus of the present work is kept on the travelling wave-like wall oscillations techniques intended for turbulent drag reduction in internal and external flows. To render the analyses as easy as possible, the channel flow configuration was used to avoid additional complexities in the flow arising due to geometrical features. Moreover, the channel flow configuration has been widely used to elucidate various captivating features of the turbulent flow field both with and without control. Inasmuch as the capability of wall oscillations drag control techniques are by now well-established, however the fundamental explanation of the control mechanism still remains unclear. This is perhaps unsurprising, given the formidable complexity of the phenomenon of turbulence itself, a challenge further exacerbated by the non-linear interaction between oscillating wall and near-wall flow structures. This study puts forward an effort towards understanding the underlying mechanism of drag reduction, and highlights various captivating features and modifications of the near wall turbulent flow field altered by streamwise travelling waves of spanwise velocity that has never been observed before. To this end, numerical experiments were performed to evaluate the drag reduction performance of wall oscillation techniques

under turbulent flow conditions at low Reynolds number. The principal objectives of the research presented in this thesis can be broadly summarized as follows:

- Investigation of the effect of control on the main flow statistics,
- Investigation of the Reynolds stress transport mechanism to identify key interactions within individual budgets and among budgets for different components of the Reynolds stress tensor,
- Investigation of the vorticity transport mechanism to pinpoint the cause of suppression of fluctuating wall shear stress,
- Identification of the major changes in the near-wall flow structures.

Hopefully, the outcomes of this study will help address some current challenges facing the widespread adoption of drag reduction strategies in practical flow systems, and contribute meaningfully to the ongoing scientific effort to gain deeper insight into the physics of wall oscillations induced drag reduction phenomena.

1.3 Organisation of thesis contents

Chapter 1 provides a contextual overview of the background and motivation for this study, and outlines the key goals and expected research outcomes of the thesis.

Chapter 2 reviews extant literature on the two well-known drag reduction methods that form the central focus of this thesis — simple homogeneous wall oscillations and travelling wave wall oscillations. The chapter begins with a brief historical perspective of wall oscillations control, followed by a summary of experimental phenomenology and classical mechanistic descriptions of the drag reduction mechanism. Recent developments in the field, including key physical insights gained from numerical investigations, are mentioned briefly highlighted.

Chapter 3 describes the governing equations and numerical techniques and procedure employed for the direct numerical simulations.

Chapter 4 explores the Reynolds stresses transport mechanism in the flows controlled by the streamwise travelling waves, and gives new insights in the changes in the flow field.

Chapter 5 explores the vorticity transport mechanism in the flows controlled by the streamwise travelling waves, and gives new insights in the changes in the flow field.

Chapter 6 presents the effect of streamwise travelling waves on the near-wall structures.

Chapter 7 concludes the thesis with a summary of the overall study, its outcomes and anticipated impact, and ends with a brief outlook on potential avenues for future exploration and research.

Appendix A presents the full derivation of the phase-averaged and mean vorticity transport equations.

Image Credits and Attribution are provided for all externally sourced plots and photographs reproduced in this thesis.

References are numbered sequentially in the order of their first appearance and are listed at the end of the text.

CHAPTER 2

Literature review

Amongst many open-loop drag control techniques, transverse wall oscillations has proven to be one of the most promising candidates, due to their capability to produce significantly large drag reduction with net power savings. In its simplest form, the transverse wall oscillations are imposed homogeneously throughout the streamwise direction according to:

$$W(x, y = 0, z, t) = A \sin(\omega t), \tag{2.1}$$

where W is the instantaneous spanwise velocity, A is its amplitude, $\omega = 2\pi/T$ is the angular frequency, and T is the period of the oscillations. Here, x, y, z represents the streamwise, wall-normal, spanwise direction, respectively, and t is time. The spanwise wall oscillation forcing results in a Stokes layer which interacts with the background turbulence to yield either turbulence suppression (drag reduction: DR) or turbulence enhancement (drag increase: DI), depending on the control parameters. Even though the precise reason behind the turbulence suppression is still unclear, nevertheless, considerable advances have been made towards unravelling the key interactions occurring in the turbulent flow field controlled by spanwise wall oscillations. At near optimal conditions, the Stokes layer thickness (δ) is confined to the low buffer layer, and is of the order of a few wall units. As the turbulence intensities are low in the viscous sublayer, the spanwise flow induced by the oscillating wall can be decoupled from the mean flow, and an analytical expression can be derived relating the DR margin to the actuation parameter. These laminar solutions have been useful for the prediction of relevant quantities, such as the spanwise velocity profile during the initial phase of the oscillation [4], and the power spent for oscillating the wall against the frictional resistance of the fluid [5–7].

Although there is an extensive body of literature on turbulence control using wall oscillations, we will specifically focus on those that have made notable advancements in this field. This selective approach is not meant to undermine the value of other studies, but rather to provide a concise overview without deviating from the primary focus of this work. By highlighting a few key studies that serve as important milestones in our current understanding of the subject, we aim to offer readers a comprehensive grasp of the topic. However, for a very detailed review on the subject, the reader is directed to a recent review by Ricco *et al.* [8] that provides a wide-ranging overview of the numerous experimental, computational, and modelling studies that deal with the effects of temporally and/or spatially varying spanwise wall motion on turbulent wall-bounded flows. It includes a variety of forcing scenarios, oscillatory as well as unidirectional in

transient conditions, in which the baseline wall-bounded turbulent flows are either statistically streamwise-homogeneous, as in a fully-developed channel or pipe flows, or spatially developing, as in free-stream boundary layers.

Motivated by the earlier experiments conducted by Bradshaw & Pontikos [9] and Driver & Hebbar [10], which demonstrated transient reductions in Reynolds shear stress and turbulent kinetic energy when a 2D turbulent boundary layer was subjected to a sudden spanwise pressure gradient, Jung *et al.*'s [11] and Akhavan *et al.* [12] conducted a study to investigate the response of wall turbulence to spanwise oscillations induced by either spanwise oscillatory flow or wall oscillations. To conduct this study, direct numerical simulations were employed in a turbulent channel flow, marking the first time such an approach was utilized.

They reported a drag reduction of approximately 40% when wall oscillations were imposed at a period of about 100 wall units. They attributed the observed reductions in various turbulence quantities to a decrease in the number and intensity of turbulent bursts in the controlled flow compared to the unperturbed flow. Additionally, Akhavan *et al.* [12] stated that the suppression of turbulence is due to a continual shift of the near-wall streamwise vortices relative to the near-wall streaks, which resulted in their widening, merging, and weakening, ultimately leading to a reduction in turbulence production.

Subsequently, a wind tunnel experiment was conducted by Laadhari *et al.* [13] to verify the numerical findings of Jung *et al.*'s [11]. The experiment involved an oscillating flat plate, driven at frequencies ranging from 2 to 10 Hz (0.0033 to 0.0166 in wall units) and a displacement amplitude of 2.5 cm (160 wall units), in a turbulent boundary layer setup. The results revealed a reduction in the mean streamwise velocity near the wall, as well as a decrease in turbulence intensities, with a significant reduction of about 50% in the Reynolds shear stress at high frequencies. They demonstrated a relative increase in the contribution of sweep events.

In order to understand the underlying mechanism by which spanwise wall oscillations reduce turbulent drag, Baron & Quadrio [14] conducted numerical simulations of a turbulent channel flow. Their aim was to assess the potential of oscillating walls for practical applications by varying the amplitude of oscillation at a fixed period of 100 wall units, as initially proposed by Jung and his colleagues. The authors conducted several simulations at four different amplitudes, ranging from 0.25 to 1.0 in outer units. In addition to the drag reduction, they also examined the power consumption required to sustain the oscillation of the wall. The results of their investigation support the earlier findings of Jung *et al.* [11], indicating that a maximum reduction in drag of approximately 40% can be achieved for amplitudes greater than 0.75. For a lower amplitude of 0.25, the authors reported an overall net positive benefit. However, they also discovered that the reduction in drag did not follow a linear trend with the amplitude. For a lower amplitude of 0.25, the authors reported an overall net positive benefit. Overall, their results were inline with the earlier studies of Jung *et al.* [11] and Laadhari *et al.* [13], showing a significant reduction in the turbulence intensities and Reynolds shear stress.

In addition, their analysis includes the third-order (skewness) and fourth-order (flatness) moments of the fluctuating velocity components. They reported an increase in the skewness factor near the wall for the streamwise component of the velocity fluctuations, with a maxima at about 5-10 wall units above the wall. Due to reflectional symmetry, the skewness factor for the spanwise component was zero for both the unperturbed and oscillating case. However, the wall-normal velocity component showed a distinct negative peak at about 15 wall units, confirming the findings of Laadhari *et al.* [13] that demonstrate a relative increase in sweep events. Similar response was observed for the flatness factor of the streamwise component, exhibiting a local maximum and slightly higher value at the wall. The profile for the wall-normal component, however, assumed very high values at the wall, superior to those of the fixed wall case. Furthermore, their instantaneous visualizations of the near-wall streaks show a drastic weakening of the streaky structure, confirming again the previous findings. Their analysis also includes a brief discussion on the response of the turbulent kinetic energy budget, showing a significant reduction in all the quantities.

Interestingly, Orlandi & Fatica [15] also drew similar conclusions about the widening of the wall streaks in their simulations of rotating pipe flow. Similar to the earlier experimental results [16–21], their simulations demonstrated drag reduction and a tendency towards a parabolic laminar Poiseuille profile at high rotation rates. The earlier experiments by Nishibori *et al.* [19] and Reich & Beer [21] had suggested that the centrifugal force of the swirling flow component was responsible for the drag reduction and turbulence suppression. However, the simulations of Orlandi & Fatica [15] added a new contribution by linking the drag reduction to modifications in the near-wall vortical structures.

During a similar time frame, Choi and Graham [22] conducted the first experimental verification of turbulent drag reduction through circumferential oscillations of a pipe wall. The findings indicated that active manipulation of near-wall turbulence structure via circular-wall oscillation can reduce the friction factor of the pipe by up to 25%. The observed drag reduction was lower compared to the earlier studies of Jung *et al.* [11] in channel flow and the experimental study by Choi *et al.* [23] on turbulent boundary layers, which show a drag reduction of about 40-45%. This is not surprising because the Reynolds numbers in each investigation were quite different; the DNS of Jung *et al.* [11] study was carried out at a low Reynolds number of about one order of magnitude smaller than that of the experimental studies. Additionally, their experiment showed a clear increase in bulk velocity, further supporting the measured drag reduction. The percentage reduction in pipe friction was found to be better scaled with the non-dimensional velocity of the oscillating wall, rather than its non-dimensional period, which confirms the suggestion that drag reduction is the result of realigning longitudinal vortices into a circumferential direction via wall oscillation. Overall, this study provides valuable insights into the potential for reducing friction drag in turbulent pipe flows through active manipulation of near-wall turbulence structure.

Miyake *et al.* [24] examined the generation of quasi-streamwise vortices to investigate the mechanism of drag reduction in a channel flow subjected to spanwise wall oscillations. They

found that the vorticity production rate fluctuates with the phase of wall oscillation and is enhanced at specific favourable phases, but suppressed overall in one oscillation period. They showed that the wall oscillations mainly affects the strong vortices by reducing the production term of the streamwise vorticity related to stretching. The suppression of vorticity generation by stretching was associated to the decrease in the inclination angles of the buffer layer vortices.

In a series of studies by Choi and co-workers [23, 25, 26], experimental investigation were carried out in turbulent boundary layers controlled by wall oscillations in a wind tunnel to better understand the mechanism of turbulent drag reduction. They observed a drag reduction of about 45% at high oscillation frequencies. A range of statistical information is included, confirming the earlier observations of Jung *et al.* [11], Laadhari *et al.* [13], and Baron & Quadrio [14]. They argued that the mechanism of drag reduction by spanwise-wall oscillation is strongly related to the spanwise vorticity generated at the edge of the viscous sublayer by the periodic Stokes layer. Choi *et al.* [23] demonstrated that the spanwise motion of the wall generates a positive spanwise vorticity (figure 2.1) that reduces the mean velocity gradient near the wall, and at the same time reducing the stretching of the longitudinal vortices in the viscous sublayer to reduce their streamwise vorticity. This results in a remarkable decrease in the intensity and duration of bursting events in the near-wall region, associated with the downwash of high-momentum fluid near the wall sweeps, thus leading to a reduction in turbulent skin-friction drag.

In pursuit of a possible active feedback turbulence control method utilizing a flexible wall, Mito & Kasagi [27] conducted direct numerical simulation of turbulent channel flow with an oscillatory deformed wall. In the range of parameters they considered, the spanwise wavelength of the wall deformation was found to be more effective in the turbulent drag reduction than the time period, while imposing the temporal parameter on the wall deformation which is essential to the skin friction reduction. The time evolution of the skin friction coefficient showed a short-period fluctuations based on the wall deformation and long-period fluctuations based on the alteration of the turbulent structures. Their instantaneous visualization illustrated that the scales of turbulent structures are largely dependent on the spatial scales of the wall deformation, and that the turbulence becomes highly intermittent. They also observed an intrusion of high-momentum fluid near the wall at the initial period of increase in the long-period fluctuations of the skin friction coefficient.

Orlandi & Jiménez [28] studied the formation of near-wall streaks in turbulent boundary layers using a simplified 2D computational model and showed that the redistribution of the longitudinal velocity by streamwise vortices produces features very similar to those observed in the experiments, and that compact streamwise vortices form naturally from more general vorticity distributions. They also showed the effects of streaks formation is to increase the average wall friction, and suggested it to be the cause for the higher friction in turbulent boundary layers, as opposed to laminar ones.

Using the model proposed by Orlandi & Jiménez [28], Dhanak & Si [29] studied the effect on

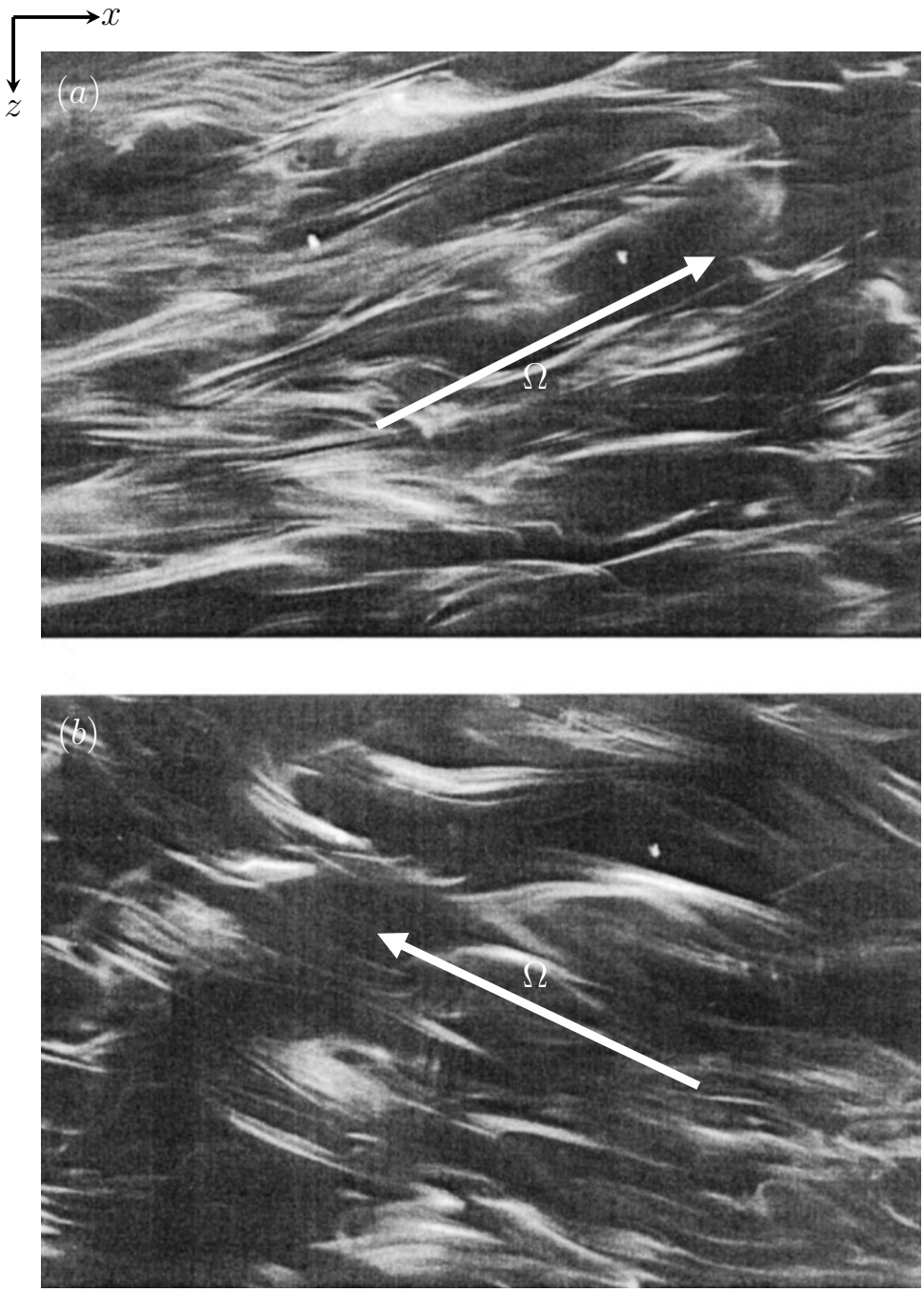

Figure 2.1: Smoke flow visualization of the near-wall turbulent structures by Choi [25] (a) when the longitudinal vortices are tilted upwards, and (b) when the longitudinal vortices are tilted downwards. The flow is from left to right. The arrow indicates the vorticity vector (Ω) tilted in the spanwise direction. A negative spanwise vorticity is created in the turbulent boundary layer during both negative (upward) and positive (downward) movement of the spanwise-wall oscillation. Taken from Choi *et al.* [25], under the terms and conditions provided by AIP Publishing and Copyright Clearance Center.

the skin friction of oscillating the surface beneath the boundary layer in the spanwise direction. They showed that when a periodic spanwise oscillatory flow is established over the surface, the coherent structures are deformed in a way which promotes their interaction with the rigid surface beneath, leading to their rapid annihilation. The severity of the process depends on the phase of the oscillation relative to the appearance of such structures near the wall and the rate of axial strain. The low-speed streaks are significantly distorted owing to mixing, by the oscillatory motion, of momentum associated with the low-speed ejection regions and that associated with the high-speed 'sweep' regions, resulting in a reduction in the rate of momentum convection normal to the wall. This in turn has a direct impact on the Reynolds stress and the skin friction.

Quadrio & Sibilla [30] performed DNS of turbulent flow in a pipe oscillating around its longitudinal axis. They reported a maximum drag reduction of about 40% and showed that a net energetic benefit of about 5-7% can be obtained at low amplitude of wall oscillations. Their analysis revealed that the Stokes layer induces a skewing of the near-wall portion of the elongated low- and high-speed streaks, and results in their lateral displacement with respect to the quasi-streamwise vortical structures in the buffer layer which is responsible for reducing the contribution of the ejection events to the Reynolds stresses in the flow, and eventually the skin-friction drag. Quadrio & Sibilla [30] propose a crude model to explaining how the spanwise Stokes layer displaces the near-wall streaks. Figure 2.2 illustrates the proposed model:

(i) Assuming a scenario where the quasi-streamwise vortex have streamwise vorticity of the same sign as the vorticity induced by the oscillating wall, at the beginning of the accelerating phase, the turbulent structures in the buffer layer are supposed to show a pattern similar to that of the reference flow (figure 2.2*a*) where the low-momentum fluid is ejected away from the wall ($Q2$-event: dashed line) and high-momentum fluid is swept towards the wall ($Q4$-event: solid line).

(ii) At a phase angle of $\pi/2$ when the tangential velocity reaches its maximum value, the Stokes layer causes a skewing of the near-wall low- and high-speed streaks in the direction of the mean tangential flow resulting in a stacking of high-speed fluid under the low-speed fluid and vice versa (figure 2.2*b*). This stacking generates regions of steep streamwise velocity gradients in the wall-normal direction, and thus high shear.

(iii) During the decelerating phase (figure 2.2*c*), as the wall is still moving in the same tangential direction, the skewing and stacking of streaks is further enhanced. The advection induced by the quasi-streamwise vortex moves high-speed fluid away from the wall, thus generating counter-gradient Reynolds stresses (Q1 events). Owing to the effect of these shear layers, the local radial gradients of axial velocity in the Stokes layer are *smoothed*.

(iv) At a phase angle of π (figure 2.2*d*), the intensity of axial velocity fluctuations is therefore reduced in both low- and high-speed regions.

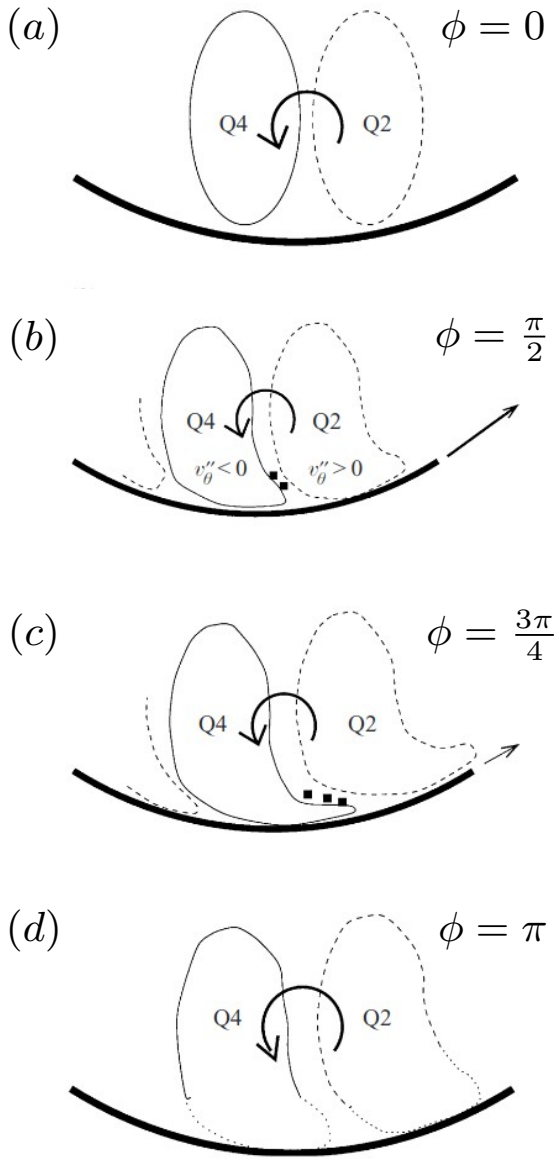

Figure 2.2: Conceptual model of the coherent structure dynamics during one half of the oscillation cycle. Adapted from Quadrio & Sibilla [30] with permission from Cambridge University Press.

The above description, though very crude, provides a good insight into how wall oscillations modifies the near-wall structures to produce drag reduction.

While the model of Quadrio & Sibilla [30] assumed that the near-wall QSVs are not affected by the wall oscillations, Coxe *et al.* [31] proposed another simple model based on the hypothesis that quasi-streamwise buffer layer vortices are sheared by wall oscillations. They showed that the oscillating wall affects the near-wall counter-rotating vortex pairs unequally. This is illustrated in figure 2.3. Starting from the beginning of the wall oscillation cycle when the flow has just experienced half a period of negative cycle, which acts to strengthen the clockwise vortices. As the wall oscillations progress, somewhere in the first quarter phase, the counter-rotating streamwise vortex pair return to equal strength. However, as the wall continues to move, the counterclockwise vortical structures are enhanced, skewing ejection and sweep events, thus reducing momentum transfer between the bulk and the wall region. The second half the of the wall oscillation is simply a mirror image of the first half, where induced velocities are skewed in opposite directions.

Their qualitative model, although very simple, is corroborated by the phasewise statistics of the vorticity components, which show that the skewness of vorticity dependent upon the wall phase angle and oscillations have the effect of increasing the likelihood of occurrence of large streamwise vortices in the region below the buffer layer.

Unsatisfied from the explanations given by earlier studies that show distortion of the relative arrangement of the vortices and streaks to be the cause of observed drag reduction, Nikitin [32] argued that the longitudinal vortices and streaks should not be treated as freestanding independent entities, and a spanwise displacement of the vortices should be accompanied by a similar displacement of the streaks without distorting their relative arrangement. Applying the theory of excitation of longitudinal vortices in near-wall turbulent flows [33] to the case of an oscillating wall, Nikitin [32] suggested that the mechanism of turbulence suppression by spanwise wall oscillations maybe due to the transverse oscillatory motion of the fluid preventing the excitation of longitudinal vortices which are weakened due to a mismatch between the slope of the equiphase lines of the vortices in a plane perpendicular to the flow and the velocity gradient of the oscillatory motion.

By employing a similar methodology to that of Jiménez & Moin [35], Hamilton *et al.*[36] studied the dynamics of the near-wall structures found in turbulent flows and describe a regeneration cycle which consists of three sequential sub-processes that includes streak formation, streak breakdown and vortex regeneration (figure 2.5). The streaks' formation was found to be the result of simple advection of momentum by streamwise vortices, and breakdown is due to an instability of the streaks. During streak breakdown, a somewhat complicated set of interactions re-energizes the streamwise vortices, leading to formation of a new set of streaks, and completing the regeneration cycle.

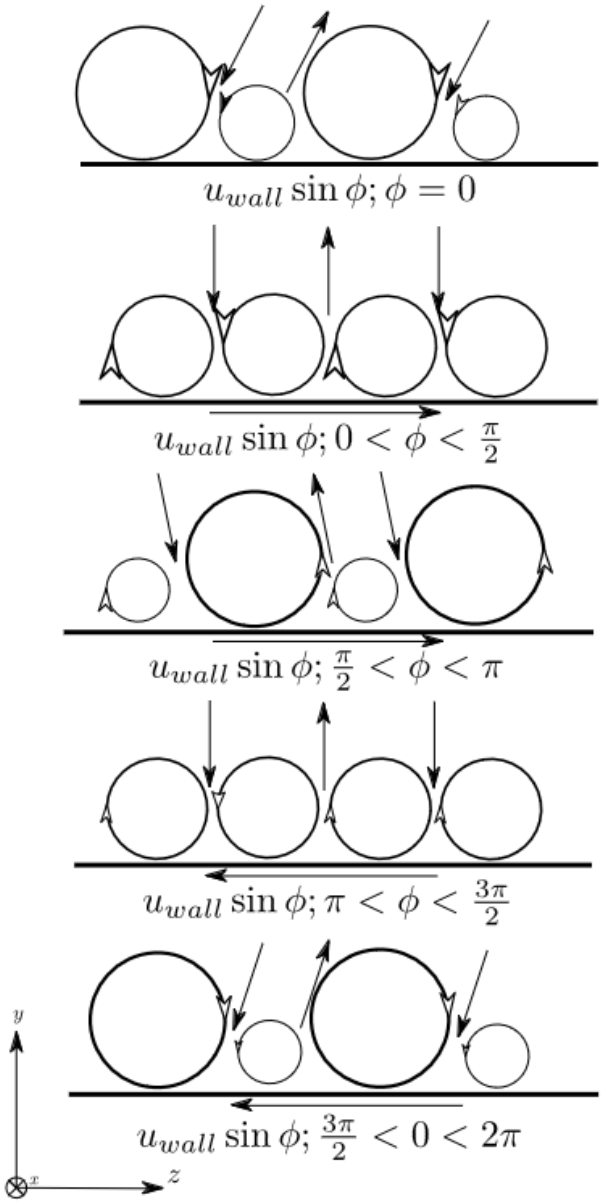

Figure 2.3: Model proposed by Coxe *et al.* [31]. Circles with hollow arrows indicate vorticity and its direction (clockwise positive, counter-clockwise negative looking from upstream down) and the black filled arrows indicate in-plane velocity fluctuations.

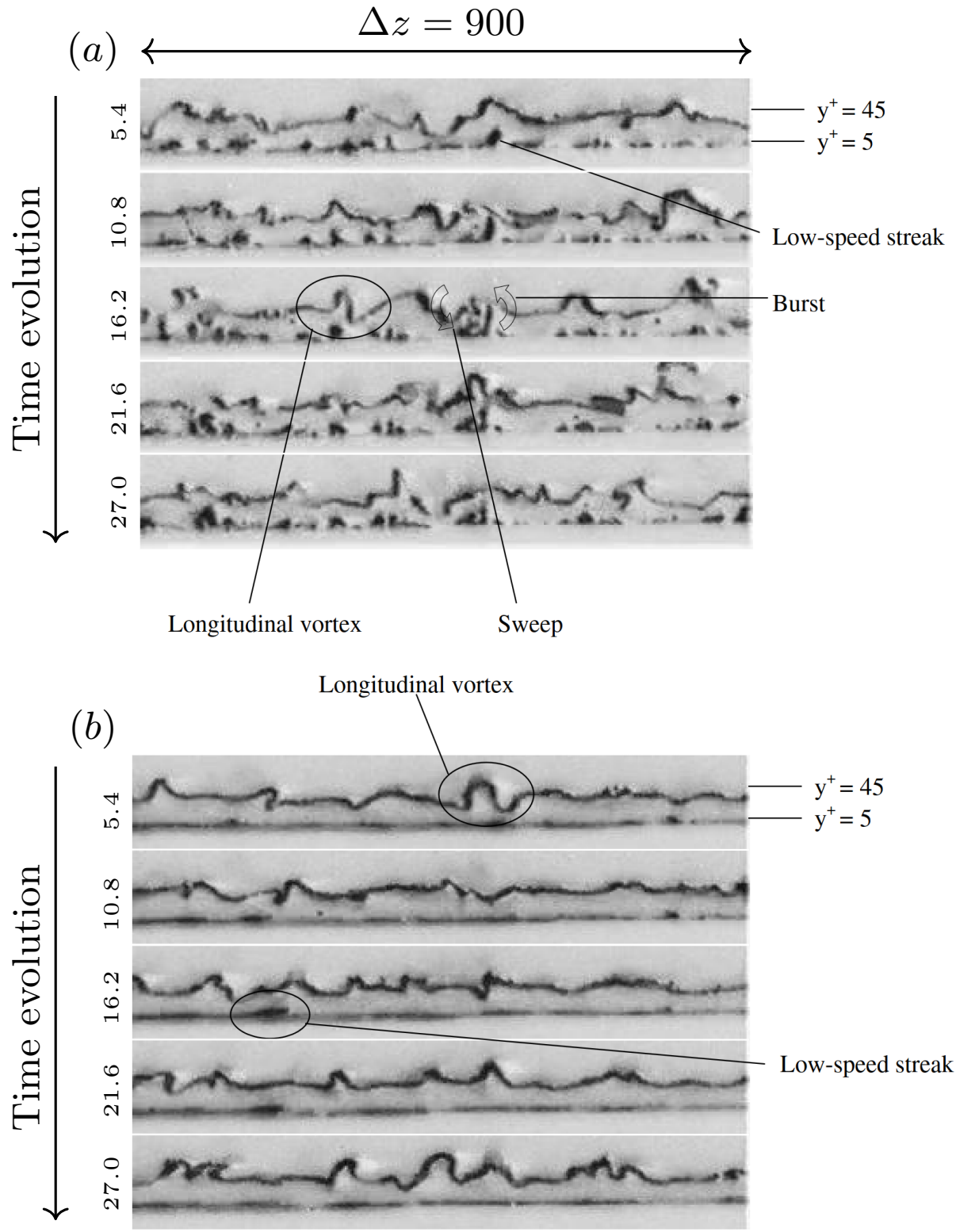

Figure 2.4: Flow visualization of the near-wall turbulent structures by hydrogen bubbles generated by platinum wires at wall-normal locations of 5 and 45 wall units: (a) stationary wall case, and (b) moving wall case. Adapted from Ricco [34] with permission from Taylor & Francis.

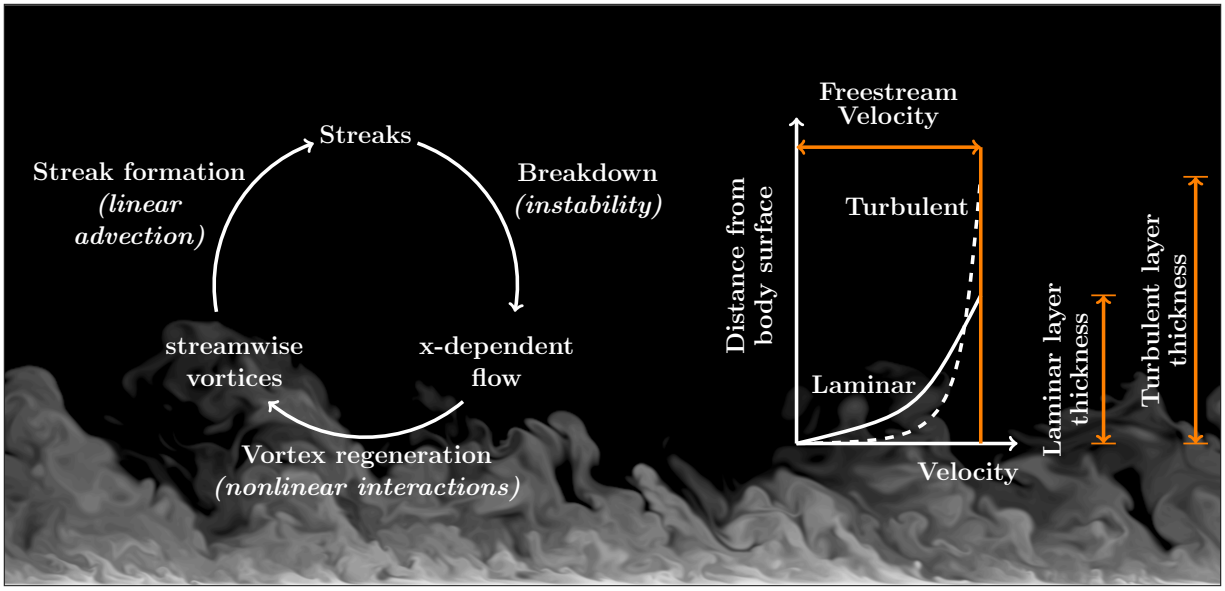

Figure 2.5: Regeneration cycle of near-wall turbulence proposed by Hamilton *et al.* [36]. The snapshot of the scalar field in the background image illustrates the development of Kelvin-Helmholtz rollers within a turbulent boundary, as the wall moves towards the right. Taken from Kozul *et al.* [37] with permission from Cambridge University Press.

The arguments put forward by Nikitin [32] sounds physical in view of the regeneration cycle of near-wall structures described by Hamilton *et al.*[36], however, the measurements of Choi [25] and the visualizations coming from the study of Ricco [34] seem to be in line with the model described by Quadrio & Sibilla [30], supporting the idea of decorrelation of the streamwise vortices and the near-wall streaks due to imposed spanwise shear. Visualizations of Ricco [34], reproduced in figure 2.4, show time evolutions of near-wall structures at two different wall-normal locations, both in the stationary wall (figure 2.4*a*) and the oscillating wall (figure 2.4*b*) case, respectively. Their study showed that the cyclic tilting of streaks and the reduced length of streaks occur for the entire range of drag-reduction values. Furthermore, they show that the sweeping motions of high-speed fluid from near-wall regions towards the wall are strongly reduced as a result of a *shielding* effect created by the transversal Stokes layer that largely impedes high-speed fluid to arrive at the wall surface, thus resulting in reduced wall drag. As highlighted by Touber & Leschziner [38], even though, Choi [25] and Ricco [34] conclude that the drag-reduction process is driven primarily by a strong decrease in the intensity and duration of sweep events, probability density functions of the streamwise fluctuations in Choi [25] indicate, on the contrary, an increasing predominance of high-intensity sweeps and large high-speed streamwise fluctuations near the wall in the presence of wall oscillations which is more in line with the view of Laadhari *et al.* [13], thus contradicting the concept of *shielding* effect.

Katasonov & Kozlov [39] carried out an experimental investigation in a low-speed wind tun-

nel to study the behaviour of streaky structures over a flat plate with spanwise wall oscillations. A group of longitudinal structures were generated using suction/injection technique through several cross slots, which modelled the boundary layer streaky structures at high free stream turbulence, observable in natural conditions. They observed a strong decrease in intensity of these localized structures with spanwise wall oscillations. They conclude that the amplitude of spanwise wall oscillations should be of the same order of that of the transverse scale of the longitudinal structures. This is consistent with Choi *et al.* [23] who argued that to obtain drag reduction the wall should move at least about a distance larger than the typical spacing of the streaks in the spanwise direction to disrupt the spatial coherence of the near-wall structures. Furthermore, Katasonov & Kozlov [39] hypothesized that the spanwise motion influenced the velocity gradient in the spanwise direction and thereby the secondary instability which result in breakdown of longitudinal structure.

Howard & Sandham [40] explored the behaviour of a channel flow subjected to a sudden imposed unidirectional spanwise wall motion. Even though the drag reduction was sustained only temporarily after the onset of forcing, their study showed that the drag reduction is linked to the damping of turbulence energy and its production near the wall. They also showed that the skewing motion of the wall results in a weakening and flattening of the quasi-streamwise vortices.

Similar to earlier studies, the experiments of Di Cicca *et al.* [41] using Particle Image Velocimetry (PIV) also show that wall oscillations provoke a significant reduction in the streamwise and wall-normal turbulence intensities that are associated with a reduction in turbulent kinetic-energy production. In agreement with Laadhari *et al.* [13], they show that the major contributor to the drag reduction is the preferential weakening of the low-speed streaks, leading to a disruption of the regeneration process.

Duggleby *et al.* [42] examined the effect of spanwise wall oscillations on the dynamics of the near-wall turbulent structures in a turbulent pipe flow using Karhunen-Loève (KL) decomposition. They argued that the main effect of the Stokes layer generated by spanwise wall oscillations is to push the structures away from the wall into the region of higher mean velocity by creating a zone where turbulent structures cannot form. As a consequence, the structures are advected faster with less time to interact with the roll modes to transfer energy, resulting in their shorter lifetime, and hence damping of the Reynolds shear stress generating bursting events.

Other routes have also been taken in the past to understand how the forcing derives the flow towards a drag reduced state. One such route involves the study of the transients following a sudden imposition of spanwise wall oscillations. Studies, for example Quadrio & Ricco [4] and Xu & Huang [43], showed that the turbulence intensities tend to reduce monotonically with the drag, with the production term showing some overshoots at the onset of oscillations. Xu & Huang [43] includes the complete transport terms and found that the attenuation of pressure-strain correlations resulting in the hindrance of inter-component transfer of turbulent

kinetic energy is responsible for drag reduction. The final reduced-drag quasi-steady state was shown to attained within three to five oscillation periods. Quadrio & Ricco [4] reported that the duration of the transient for the longitudinal wall shear-stress was found to be significantly longer, independent of the oscillation period, but to be related to the maximum wall velocity. In the present work, it is noted that the transient time strongly depends on the maximum wall velocity, and can last longer, up to 15 cycles, especially for the large amplitudes.

Delving into the details to illuminate the various mechanisms at play, Touber & Leschziner [38] analysed the Reynolds stress budgets in the flows controlled by the homogeneous wall oscillations. They concluded that the primary cause of the suppression of the near-wall turbulence is the reduction in the wall-normal component of the Reynolds stress tensor. They also investigated the response of the near-wall streaks to the spanwise wall oscillations, and showed that the low-speed streaks align themselves at an angle depending on the ratio between the streamwise and spanwise strain. They showed that at the optimum forcing period the organization of the near-wall is severely disrupted owing to the rapid change in the Stokes strain, resulting in their suppression, and hence a significant reduction in skin-friction. However, the low-speed streaks tend to re-establish themselves when the Stokes strain varied rather slowly. These observations point to a major mechanism at play that the streak-generation mechanism is hugely affected by the rate of change of the Stokes strain.

Motivating the connection between the global enstrophy and the turbulent kinetic energy dissipation, Ricco *et al.* [44] studied the transient response of the global turbulent enstrophy in a turbulent channel flow subjected to homogeneous to the wall oscillation. They found that after a sudden implementation of spanwise oscillations, the turbulent enstrophy shows a transient increase, which directly enhances the turbulent dissipation. As a consequence, the turbulent activity is suppressed by the transient increase of the turbulent enstrophy in the initial phase, which drifts the flow towards the low-drag state. Later, Ge & Jin [45] conducted a similar study, focusing more on the response of the various production terms appearing in the transport equations of turbulent enstrophy in each direction.

In contrast to transient analysis, Agostini *et al.* [46, 47] adopted a different approach where they intentionally impose homogeneous wall oscillations at suboptimal period to allow the flow field to oscillate about a mean low-drag state. This approach is convenient in the sense that, firstly, it avoids uncertainties arising from using a single instantaneous field, which generally results in non-converged results, especially for higher order moments and their budgets, and secondly, it allows the separation of the stochastic turbulence field from the imposed fluctuating field, which is crucial especially if the focus in on studying the near-wall behaviour of the actuated flow field. In their studies, the focus was mainly kept on the phase-averaged properties. The showed that the drag reduction phases extend over a longer proportion of the cycle than the subsequent drag increase phases, and hence display a hysteresis. Agostini *et al.* [47] studied the modification in the enstrophy field provoked by the Stokes strain. They observed a strong increase in the spanwise turbulent enstrophy during the drag reduction phase, and identified the

Stokes strain driven production terms related to vortex tilting and stretching in the regions of high skewness being responsible for the observed effect. They showed that the spanwise tilting of wall-normal turbulent vorticity (that are primarily linked to the near-wall streaks) provoke a strong increase in the skewness near the wall, resulting in reduction in the shear stress. However, a closer look at their plots reveal that the spanwise turbulent enstrophy is annihilated at the drag reduction phases next to the wall – an observation very similar to what we will show in the present study in the case of STW actuation.

Yakeno *et al.* [48] evaluated the quantitative contributions from four quadrants of the Reynolds shear stress on the wall skin friction based on the Fukagata-Iwamoto-Kasagi (FIK) identity [49]. They found that the drag reduction effect is mostly caused by the suppression of the ejection events when the oscillation period is below the optimal value of $T = 75$ wall units, whereas the drastic enhancement of the sweep events diminishes the drag reduction effect at larger oscillation periods. Using conditional sampling around QSVs, they showed that suppression of ejection events occur at phases where the spanwise shear induced by the oscillating wall counteracts the rotation of the QSV at around $y = 10$ wall units.

Other form of control techniques based on a similar approach have been proposed in the past. For example, Du & Karniadakis [50] and Du *et al.* [51], induced exponentially decaying travelling waves by a spanwise force, confined within the viscous sublayer. They compared their results with the spanwise oscillations excited using a similar force. Both types of forcing found to produce large drag reductions, but the near-wall structures appeared to be different. In their spanwise oscillatory excitation case there observed a clear presence of wall-streaks, whereas in the travelling wave excitation case the streaks disappeared. They concluded that the appropriate enhancement of the streamwise vortices leads to weakening of the streak intensity, and correspondingly substantial suppression of turbulence production.

Even though the homogeneous (streamwise uniform) spanwise wall forcing is capable of producing large drag reduction margins, the applicability of such type of control renders it impractical to use as a passive device. Addressing this issue, Viotti *et al.* [52] converted the purely temporal forcing to its spatial counterpart. The transformed forcing is given by

$$W(x, y = 0, z, t) = A \sin(\kappa x), \tag{2.2}$$

where $\kappa = 2\pi/\lambda$ is the wavenumber of the standing wave and λ is its wavelength. Remarkably, this type of forcing, was found to yield even larger drag reduction margins of about 50%, with an improved net energy savings of about 20% (at $Re_\tau = 200$). The forcing wavelength that yields the maximum drag reduction obtained was found to correspond to the optimal period of the oscillating wall converted in length through $\lambda = \check{c}T$ ($\check{c}$ being the convection velocity of the near-wall fluctuations), validating the applicability of the applied transformation. Yakeno *et al.* [53] also confirmed the striking similarity between these two types of forcing, and showed that the phase wise variations of the Reynolds shear stress is larger compared to the purely temporal case. Later, Skote [54] conducted direct numerical simulations to study the effect of a stationary

spanwise wall forcing in a turbulent boundary layer, and obtained a drag reduction of about 50%, similar to Viotti *et al.* [52].

Quadrio et al. [6] introduced even a more complicated form of transverse wall forcing involving streamwise travelling waves (STW) given by

$$W(x, y = 0, z, t) = A \sin(\kappa x - \omega t). \tag{2.3}$$

This type of forcing was shown to perform far better in comparison to the merely temporal or spatial variant, and producing a drag reduction margins of up to 60%. The STW essentially combines both the purely temporal wall oscillations and their spatial variant. The drag reduction margin was shown to depend strongly on the operating parameters. Depending on the wave speed $c = \omega/\kappa$, both backward (BW) and forward (FW) waves travelling along the streamwise direction can be imposed. While the BW-STW always yield drag reduction, the response of the flow to FW-STW is rather complex. An increase in drag is observed when the waves travel with a phase speed comparable to the convection velocity of near-wall turbulent fluctuations.

Auteri *et al.* [55] conducted experiments in a turbulent pipe flow with the wall subdivided into thin independently rotating slabs. Designing an experiment where such a complicated wave form can be imposed is in itself a complicated challenge. A compromise has to be reached on the width of the thin sections to form a discrete wave that can essentially mimic the travelling wave behaviour. Their experiments confirmed the DNS results of Quadrio *et al.* [6], and demonstrated the possibility of achieving large reductions of friction in the turbulent regime, thus providing the first experimental verification of the drag reducing capability of STW. They obtained a drag reduction of up to 33% for slow FW-STW, while the BW-STW invariably produced drag reduction. Interestingly, they found a substantial degradation of drag reduction when the phase speed of FW-STW matches with the convection velocity of the near-wall structures.

Later, Bird *et al.* [56] carried out experiments in a turbulent boundary layer on a flat plate at $Re_\tau = 1125$. The travelling wave was generated using a pneumatically actuated compliant structure based on the kagome lattice geometry, supporting a pre-tensioned membrane skin. Carefully designed of the structure enabled them to generate waves of variable wavelength, frequencies and amplitudes known to produce drag reduction. They reported a drag reduction of about 21.5% for BW-STW, similar to the DNS results of Quadrio *et al.* [6].

Quadrio & Ricco [7] derived an analytical expression for the spanwise boundary layer induced by the STW. Under the assumption that the thickness of the Stokes layer is much smaller than the channel half-height, the laminar solution was found to agree well with the turbulent space-averaged spanwise flow and to possess good predictive capabilities for DR margin at low Re. However, most of the scaling laws introduced so far fail at large Re.

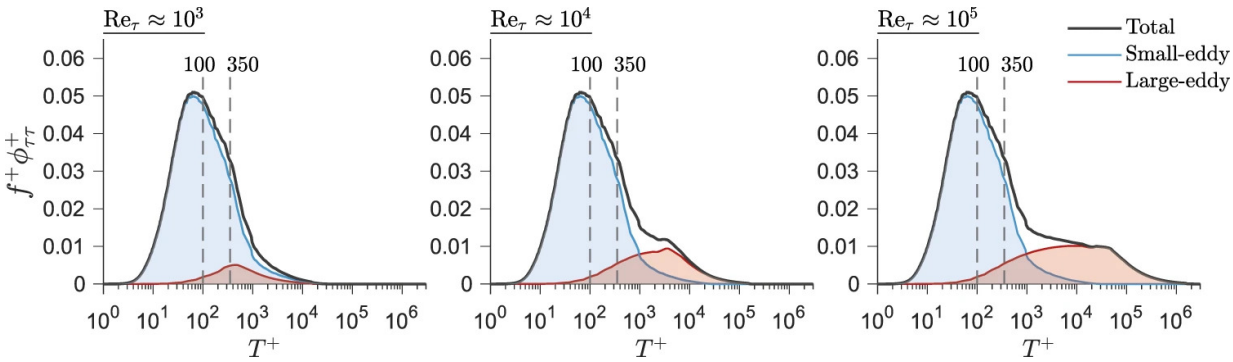

Figure 2.6: Wall stress spectrum dependence on Reynolds number. Taken from Marusic *et al.* [59] under Creative Commons license.

Scaling of DR with different forcing parameters

To address the scaling of drag reduction with various operating parameters, Choi *et al.* [57] introduced two parameters for assessing the drag reduction margin. The first parameter is related to the thickness of the Stokes layer, while the second parameter focuses on the acceleration of the Stokes layer. The concept of the acceleration parameter originated from the findings of Quadrio & Sibilla [30], who observed that drag reduction margins were lower in cases of steady pipe rotation. By incorporating these parameters, Choi *et al.* [57] provided a framework for understanding and predicting the drag reduction performance under different conditions. The DR margin demonstrated a correlation with both parameters, and the correlation increased when the two quantities were combined in a unique factor.

Later, Quadrio *et al.* [58] performed a detailed analysis of the dependence of drag reduction over a wide range of wall velocity and actuation periods, for a channel flow at $Re_\tau = 200$. The results were conveyed through drag-reduction maps (also famously known as *Quadrio maps*). They found that the for oscillation half-period shorter than a typical lifetime of the turbulent near-wall structures ($T \approx 150$ wall units), drag reduction margins collapse on a line in a plot that relates the drag-reduction level to the scaling parameter (S) of Choi *et al.* [57]. For longer periods of oscillation, the scaling parameter found to predict a slower drop in drag reduction margins to that obtained from their numerical data. Ricco & Quadrio [5] later recast the data available in the literature in the form of the drag reduction DR vs S, confirming the applicability of the scaling for low-Reynolds-number values when $T < 150$ wall units.

Behaviour at large Reynolds number

Despite decades of research, the behaviour of wall oscillations control at large Re has always been a subject of active debate. With many studies suggesting degrading performance of the control with increasing Re [5, 38, 60–63] and others suggesting little to no Re effect [22, 64], the overall behaviour appears to be rather complex and remains poorly understood. Designing a control strategy which can produce sustained drag reduction at Re of practical significance is of great importance. The root cause of Re dependence of skin-friction drag is still a subject of active research. Some rare experimental and numerical studies at Re_τ up to 32000 in experiments [65–69] and 8000 in direct numerical simulations (DNS) [70, 71], hint towards the presence of large-scale energetic structures based on the appearance of a secondary peak in streamwise turbulent kinetic energy component at higher wall-normal location. These large-scale passive structures, that reside in the outer layer of the turbulent flow field, modulates the near-wall small-scale active structures, the foot-print of which is evident in the increase in the wall-shear stress. To highlight the increasing importance of this foot-printing process, Marusic *et al.* [59] plot the pre-multiplied spectra of fluctuating wall-shear stress reproduced in figure 2.6 for three different Re_τ from 10^3 to 10^3. As seen in figure 2.6, the contribution of the large-scale structures to the fluctuating wall shear-stress grows with increasing Re_τ.

Previous studies have often suggested a power law decay for the drag reduction margin, characterized as $DR \propto Re^{-\gamma}$, where γ being an empirical exponent. Various DNS-based investigations have indicated that the exponent γ typically falls within the range of 0.1 to 0.5 [5, 6, 38, 60, 61]. Gatti & Quadrio [61] conducted a comprehensive parametric study encompassing a wide range of control parameters at Re_τ up to 2000. However, their utilization of small computational domains may have led to an overestimation of the achieved drag reduction. Nevertheless, one significant finding from their investigation is that the parameter γ exhibits a strong dependence on both the forcing parameters and the Reynolds number itself. This observation was subsequently validated by Hurst *et al.* [60], who performed simulations using sufficiently large computational domains at Re_τ from 200 to 1600.

Subsequently, Gatti & Quadrio [62] highlighted the limitation of using γ to describe the effect of Re_τ on drag reduction, as it lacks specific physical significance. Building upon the concept of roughness and riblets, they introduced a more physically meaningful approach to quantifying drag reduction by considering the vertical shift of the mean velocity profile. Using this approach, they predicted a slower deterioration in drag reduction with increasing Reynolds number, in contrast to the conventional power-law relation.

Achieving high drag reduction margin doesn't necessarily imply a positive net power savings. The associated cost of imposing the control needs to be taken into account. The energy required to impose wall oscillation grows exponentially with increasing Re. Hence, targeting the near-wall small-scale structures is not a feasible strategy to achieve net power savings at high Re.

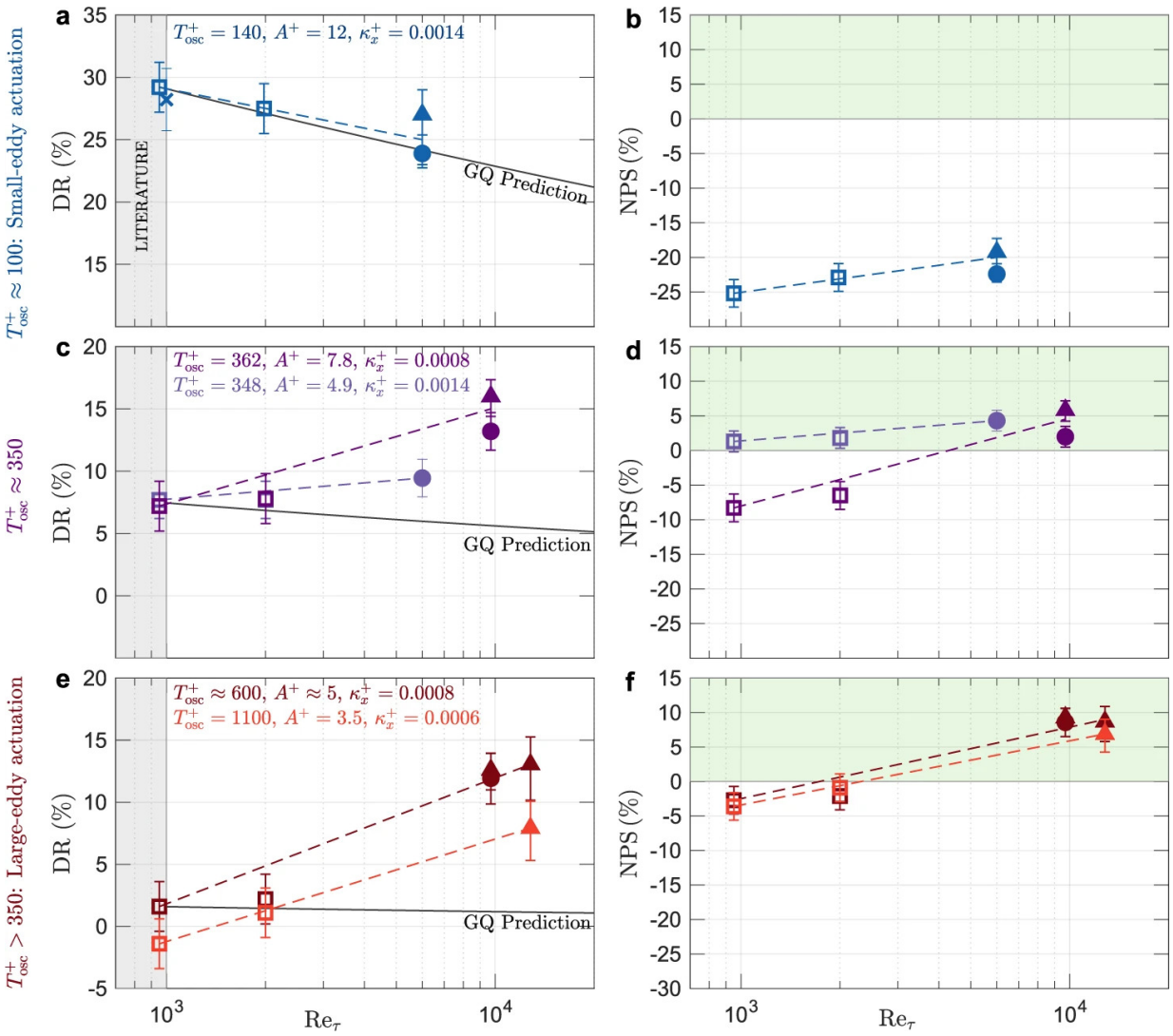

Figure 2.7: Drag reduction and net power savings at different Reynolds number for different actuation schemes. Note here that the superscript '+' indicates quantities scaled in wall units. Taken from Marusic *et al.* [59] under Creative Commons license.

Considering the increasing contribution of the large-scales to the wall shear stress, Marusic *et al.* [59] suggested a new pathway that involves low frequency actuation comparable to that of the large-scale passive structures. This actuation scheme that couples to the large-scales was shown to achieve substantial DR margins at large Re while also maintaining positive net power savings.

Figure 2.7 presents the DR margin and net power savings obtained by Marusic *et al.* [59] for three different actuation scenarios. The first scenario refers to the actuation frequencies comparable to the time scales of near-wall small-scale structures. Only a modest decrease in DR margin from 30% at $Re_\tau = 951$ to 25% at $Re_\tau = 6000$ was observed at nearly optimum control settings. This trend of decreasing effectiveness of control at large Re is consistent with many previous studies, a broad review of which is presented in Ricco *et al.* [8].

The second scenario refers to the actuation frequencies where the oscillation period is comparable to the large-scale cut-off, which was set to 350 following Mathis *et al.* [72]. For this actuation scenario, only two different sets of actuation parameters were tested, $A = 7.8$, $k = 0.0008$ and $A = 4.9$, $k = 0.0014$ (wall units). For the first set, with larger amplitude of oscillation, the DR increased from 13% to 16% as Re was increased to 9700. While these actuation parameters incur a net power loss of 8% at $Re_\tau < 2000$, they were able to generate $2-6\%$ net power savings at $Re_\tau = 9700$ (figures 2.7c,d). Similarly, the second set of actuation parameters was able to generate DR of 9.5% at $Re_\tau = 6000$ while maintaining up to $1-5\%$ net power savings for Re_τ in the range $950-6000$.

The third and the most promising scenario refers to the actuation with frequencies comparable to those of large-scale outer motions. For this scenario with even lower amplitude and longer oscillation period of about 1100, the drag reduction margin found to increase about ten folds from 1.6% to approximately 13% when Re_τ was increased from 951 to 12800. Most importantly, the net power savings was estimated to grow from -4% at $Re_\tau = 951$ up to 10% at friction $Re_\tau = 9700$ (figure 2.7f), which is quite promising especially for practical applications.

Even though the evidence points to a possibility of obtaining significant net power savings at large Re by targeting the large-scale motions, a clear conclusion cannot be drawn as the actuation parameters were varied simultaneously owing to the challenges posed by the experimental setup, where it is difficult to isolate the effect of Re without affecting the actuation parameters. Therefore, a detailed DNS based parametric study is needed to further explore this new pathway for a wider range of actuation parameters at Re close to practical significance.

Aim of present work

Based on the review of the current state of research, it is evident that a comprehensive and definitive explanation of the drag reduction mechanism is still lacking. Most of the progress in

understanding the underlying physical processes has been made through studies involving homogeneous wall oscillation forcing. However, there is limited research specifically focused on streamwise travelling waves (STW). The primary focus of most of the earlier investigations [6, 59–62] has been to explore the parametric space to find the optimal set of parameters that leads to DR at different Reynolds numbers and/or to develop scaling laws that predict DR for different actuation scenarios. Studies that primarily target on elucidating the mechanism behind the observed DR are quite rare. In this study, we aim to provide a detailed investigation into the modifications induced by streamwise travelling waves in turbulent channel flow. Our analysis encompasses a wide range of drag reduction levels, ranging from approximately 20% to 60%, with particular attention given to cases involving large amplitude streamwise travelling waves that result in significantly large drag reduction margins. The main objective is to identify the key terms present in the transport equations of turbulent kinetic energy and turbulent enstrophy that have a substantial impact on the near-wall turbulence. Additionally, through numerical experiments, we show a striking resemblance in the trajectory of the anisotropy invariants of the large amplitude STW and artificial suppression of turbulent activity. We also examine the influence of STW on near-wall quasi-streamwise vortical structures and estimate the drag reduction margin based on their displacement.

CHAPTER 3

Computational Methods

In the present work, we only consider incompressible fluids with constant material properties, which can be treated as a continuum. This implies that the smallest scales of the flow are large in comparison to the (average) distance between individual molecules, the so-called mean-free path length. Applying the basic principles of conservation of mass and momentum results in the most celebrated set of the following Navier-Stokes equations

$$\frac{\partial u_i}{\partial x_i} = 0, \text{ and} \tag{3.1a}$$

$$\frac{\partial u_i}{\partial t} + \frac{\partial u_i u_j}{\partial x_j} = -\frac{\partial p}{\partial x_i} + \frac{1}{Re}\frac{\partial^2 u_i}{\partial x_j^2} \quad (+f_i), \tag{3.1b}$$

where u_i are the components of the instantaneous velocity field, p is the pressure, t is time and $Re = LU/\nu$ is the Reynolds number based on characteristic length (L) and velocity (U), respectively, and (ν) is the kinematic viscosity of the fluid. Physically, equation 3.1a implies that the rate of change of the dilatation along particle paths in the flow vanishes, i.e., that any infinitesimal material element keeps its volume while being moved and distorted by the flow, and is famously called as the continuity equation. Note that, the Einstein's summation convention is used here, i.e., a summation is implied for any repeated index. The term f_i in the momentum equation 3.1b includes all the additional forces, for example, body forces due to varying density field (buoyancy), and/or forces stemming from a large-scale forcing scheme in the form of Lorentz force, travelling waves, etc. It is widely accepted that, these equations, together with appropriate initial and boundary conditions, describe the evolution of incompressible turbulent flows once the Reynolds number reaches *large enough* values ($Re \gg 1$). Typical values of Reynolds number in geophysical and engineering flows are usually very large. For example, the Reynolds number of the flow over a wing of an aeroplane is about $O(10^7)$, and a typical Reynolds number of flow in an atmospheric boundary layer is about $O(10^9)$. A large Reynolds number allows disturbances to develop large velocity gradients locally in the flow before viscous diffusion will have time to smear them out. Hence, turbulence can be defined as a state of a physical system with many interacting degrees of freedom deviated far from equilibrium. This state is irregular both in time and in space and is accompanied by dissipation.

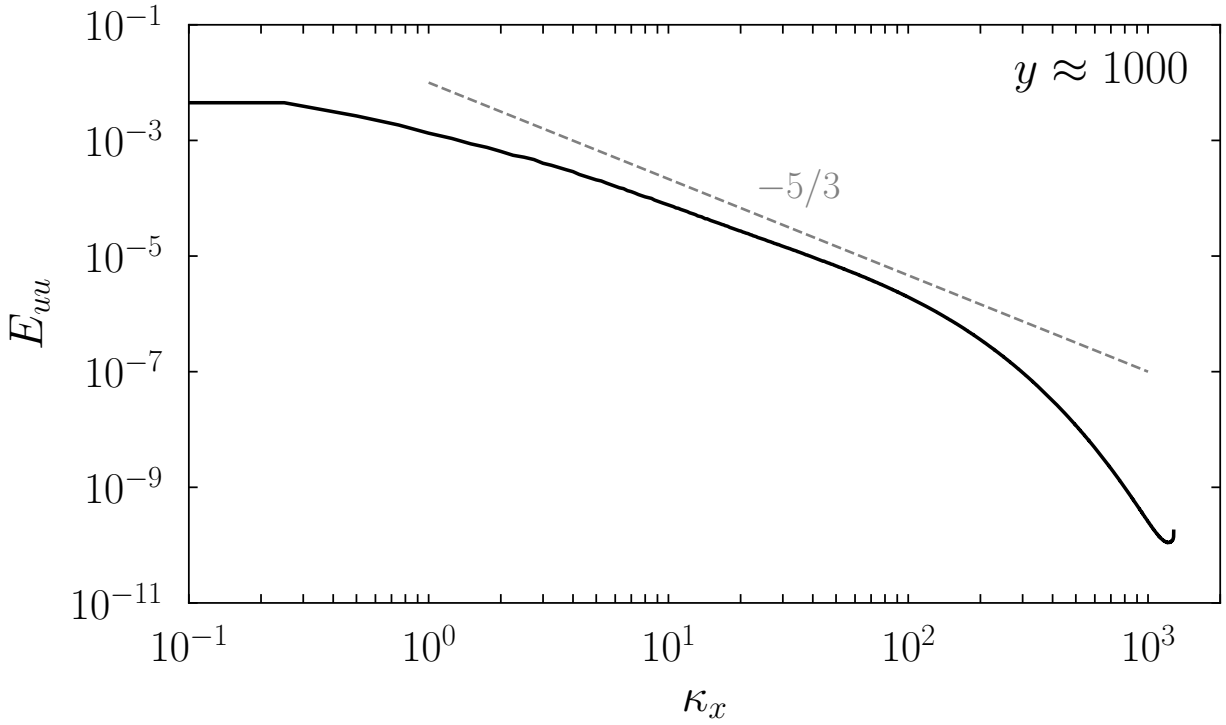

Figure 3.1: Energy spectrum (E_{uu}) for a turbulent channel flow at $Re_\tau \approx 5200$ at a homogeneous plane located within the logarithmic layer at about $y = 1000$. (The figure was produced from the data of Lee & Moser [73])

3.1 Energy cascade

Turbulence is typically characterized by the excitation of a multitude of spatial and temporal scales, which involves a large number of degrees of freedom interacting non-linearly in space and time. The basic physics of turbulence is largely dictated by the way energy is transferred across scales. The classical conceptual framework that dictates this process is the self-similar Richardson cascade [74] (figure 3.1). It assumes that the energy transfer is local in scale, with no significant interactions between scales of very different sizes. The largest scales, with length scale comparable to the flow dimensions, extract energy from the mean flow and transfer it to small scales where it is finally dissipated. The production process is highly anisotropic and is mostly not influenced by viscosity, whereas the small scales tend to be isotropic and have universal characteristics. From energy conservation arguments, Kolmogorov [75] derived how energy is distributed among the eddies of the inertial range of isotropic flows and estimated the viscous length scale at which energy is finally dissipated, $\eta = (\nu^3/\varepsilon)^{1/4}$, where ε is the rate of energy transfer and ν is the kinematic viscosity.

Such a complex behaviour is inherent to rather the simple set of Navier-Stokes equations.

Analytical solutions describing the complete behaviour of turbulent flows even in the simplest form of flow configurations do not exist. Attempts to overcome this issue have been carried out through a statistical theory of turbulence. However, very often for the designing purposes of engineering equipments, the full detailed instantaneous features of the flow field is not required. Instead, the evolution of the mean flow field variables are sought, primarily the single point statistical quantities such as mean flow velocity and turbulent kinetic energy. Approaches such as Reynolds Averaged Navier Stokes equations (RANS) relies on this approach. However, this approach faces a new problem that relies on the closure of its formulation. The closure problem arises from the coupling of successive moments of the distribution function that originates from the Reynolds stresses encompassing the nonlinear terms. Most often, the models to close the set of equations are derived from rather simple and idealistic flow configurations. Applications of these models to complex problems still pose a challenge, and a huge amount of research effort is still going on to improve and design models that are robust. There is another approach called Large Eddy Simulation (LES) where the large the scales of motions are resolved while the small *sub-grid scales* are modelled. This approach relies on the idea that the small scales are not influenced by the boundary conditions and tend to be more homogeneous, in a sense that there is some universality in their behaviour. Hence, the LES models are simpler and require fewer adjustments when applied to different flows than similar models for the RANS equations.

3.2 Direct Numerical Simulations

Although the statistical approaches such as RANS and LES allow modelling turbulence phenomena, they may not represent the actual picture. Therefore, a complete description of a turbulent flow can only be obtained by numerically solving the Navier-Stokes equations. Such solutions are termed as Direct Numerical Simulations (DNS). This approach provides the most accurate numerical description of turbulent flows without introducing any bias related to numerical modelling. However, one of the issues when using this computational approach resides in the fact that the range of scales in turbulent flows increases dramatically with the Reynolds number. Therefore, a wide range of scales on the spatial domain needs to be resolved at every time step. More precisely, the underlying physics dictates that scales on the order of the Kolmogorov length scales have to be consistently resolved.

3.2.1 Spatial discretization

Numerical methods for the DNS of turbulent flows are required to accurately reproduce its evolution over a wide range of length and time scales that are dictated by the physics [76]. This requires for the continuous space to be divided into a set of discrete points which leads to a set of ordinary differential equations for each point. As the Navier-Stokes equations are elliptic in

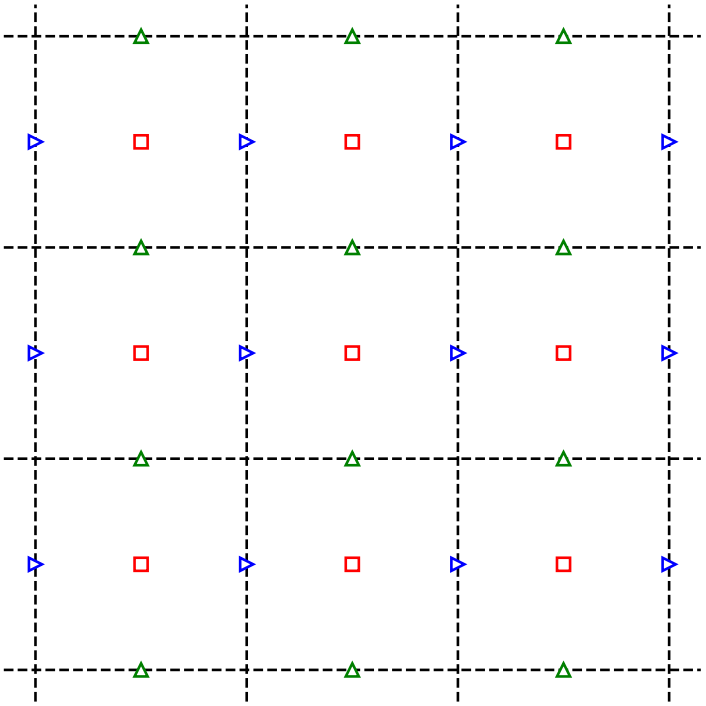

Figure 3.2: A typical staggered 2D grid configuration. The blue triangles represent the location of the streamwise component of velocity, the green arrows represent the locations of the vertical component of velocity, and the red squares represent the locations of pressure.

space, all the domain should be resolved simultaneously. Grid generation consists in dividing the physical flow domain into smaller domains called control volumes or cells. The arrangement of variables in the grid can also have a strong impact on the accuracy of the solution. Unlike in a collocated grid where all variables are stored at the same grid points, the present study employs a staggered grid configuration where a variable is shifted by half of a grid spacing with respect to each other (figure 3.2). For most DNS simulations, the staggered method is preferred to avoid *gibbs* oscillations in the solution.

The grid determines the scales that are represented, while the accuracy with which these scales are represented is determined by the numerical method. Along statistically inhomogeneous directions, physical parameters such as channel width, boundary layer thickness, or mixing layer thickness determine the largest scales. Along homogeneous directions, where the periodic boundary conditions are imposed, two-point correlations of the solution are required to decay nearly to zero within half of the domain, to ensure proper statistical representation of the large scales. The Kolmogorov scales, $\eta = (\nu^3/\varepsilon)^{1/4}$, is commonly quoted as the smallest scale that needs to be resolved. However, this requirement is probably too stringent. The resolution requirements are of course influenced by the numerical method used, but the smallest resolved length scale is required to be of $O(\eta)$, not equal to η.

The most commonly used discretization methods are finite difference (FD), spectral, finite element (FE), and finite volume (FV) methods. Of course, there are also methods of mixed type, such as the spectral element method or the finite element method with control volume. But, due to their ease of implementation, suitability for parallelization, and potential high-order accuracy, finite difference (FD) methods are becoming increasingly popular for DNS. A wide range of options is available. However, the conventional explicit FD method exhibits serious numerical artefacts in the presence of high frequency components and/or coarse grids. This problem would drastically increase both memory requirements and computational costs, especially for large models, since a fine grid should be properly designed and a high-order FD operator applied. A common method to avoid this problem is to manually reduce the dominant frequency. This method could result in acceptable runtime, but would result in very limited spatial resolution since high frequency components are required to improve the final resolution. Another option is to use advanced methods that have lower numerical dispersion, such as optimized explicit FD methods and implicit FD methods (either conventional or optimized). Compared to implicit FD methods, explicit FD methods are usually much less computationally intensive. Therefore, we prefer to develop an optimized scheme for explicit FD methods to further reduce the numerical dispersion while reducing the computational cost.

Optimized FD schemes have been widely used to reduce numerical dispersions in many practical applications, e.g. in acoustics, seismology and electromagnetics. The basic idea is to increase the accurate wavenumber coverage of the FD operator within a tolerable error range by modifying the constant coefficients. The main advantages of the optimized explicit FD methods are that we can significantly improve the numerical results without changing the algorithm

structure, the source code and the computational efficiency. In addition, we can use a relatively coarser grid as well as a larger time step, which would further decrease the memory requirement and the total running time.

3.2.1.1 Dispersion Relation Preserving (DRP) schemes

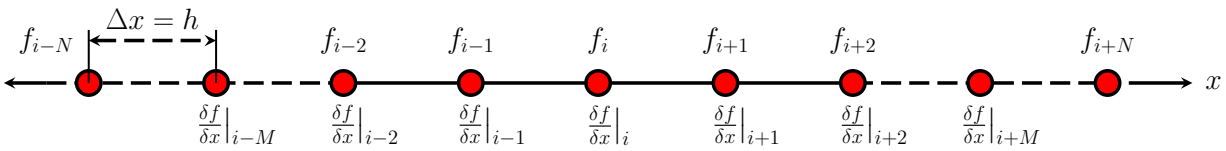

Figure 3.3: One-dimensional stencil showing the arrangement of a quantity f at different grid points.

First derivatives can be estimated from the function value at N nodes in the neighbourhood of the node i and from the estimate at M adjacent nodes (figure 3.3)

$$\left.\frac{\delta f}{\delta x}\right|_i + \sum_{m=1}^{M} \alpha_m \left(\left.\frac{\delta f}{\delta x}\right|_{i+m} + \left.\frac{\delta f}{\delta x}\right|_{i-m} \right) = \sum_{n=1}^{N} a_n \frac{(f_{i+n} - f_{i-n})}{h}, \tag{3.2}$$

where α_m and a_n are real coefficients. This system of equations can also be represented in the matrix form as,

$$Af' = Bf, \tag{3.3}$$

where A is the $(2M+1)$ banded matrix associated to the first derivative approximation f' and B is the $(2N+1)$ banded matrix associated with the function values f. Depending on whether $M = 0$ or not, one can group finite difference schemes in two categories: explicit $(M = 0)$ and implicit $(M > 0)$. For explicit schemes, the matrix A is one-banded and hence, the approximation can be straightforwardly obtained from the function values. While implicit schemes require a systematic matrix inversion procedure.

The usual approach to derive the coefficients a_n and α_m is to substitute the function and its derivative around the considered node through the Taylor expansion. Tam & Webb [77] used a different approach based on spectral analysis of the error to determine these coefficients. The idea is to minimize the error committed on the Fourier modes. The Fourier transform of f is defined as

$$\hat{f} = \frac{1}{2\pi} \int_{-\infty}^{\infty} f e^{j\kappa x}, \tag{3.4}$$

where κ is the wavenumber. Hence, the equation 3.2, for the case of $M = 0$, can be written as

$$j\kappa \hat{f} = \left[\frac{1}{h} \sum_{n=1}^{N} a_n (e^{j\kappa nh} - e^{-j\kappa nh}) \right] \hat{f}. \tag{3.5}$$

On comparing the two sides of the equation 3.5, we have

$$\kappa_{\text{eq}} = \frac{-j}{h}\sum_{n=1}^{N} a_n(e^{j\kappa nh} - e^{-j\kappa nh}) = \frac{2}{h}\sum_{n=1}^{N} a_n sin(n\kappa h), \tag{3.6}$$

where κ_{eq} is the equivalent wavenumber. Consider a single Fourier mode in one dimension, namely $f = e^{j\kappa x}$ (where $j = \sqrt{-1}$). The exact first derivative of f at node i is $df/dx = j\kappa e^{j\kappa x_i}$; the numerically computed derivative will be of the form $\delta f/\delta x = i\kappa_{eq} e^{j\kappa x_i}$. Hence,

$$\left.\frac{\delta f}{\delta x}\right|_i = \frac{\kappa_{\text{eq}}}{\kappa}\left.\frac{df}{dx}\right|_i \tag{3.7}$$

The error (ε) induced by the discretization is given as

$$\varepsilon = \left(\left.\frac{df}{dx}\right|_i - \left.\frac{\delta f}{\delta x}\right|_i\right) = \left(1 - \frac{\kappa_{\text{eq}}}{\kappa}\right)\left.\frac{df}{dx}\right|_i. \tag{3.8}$$

EO schemes are designed to reach maximum spectral resolution with the considered stencil. A classical choice of a_n is to give as accurate as possible a derivative in the limit $h \to 0$. This choice would give $f_0' = f_0 + O(h^{2N})$. Another approach would be to use a limited number of degrees of freedom (L): $f_0' = f_0 + O(h^{2L})$, and to use the remaining $N - L$ degrees of freedom to optimize the derivative such that κ_{eq} is as close to κ as possible under some suitable metric.

Two different approaches can be followed to minimize the error. The first method is based on the *global* minimization, in which scheme coefficients are evaluated in order to minimize the overall error E on a selected range of wavenumber, defined by κ_{max}:

$$E = \int_0^{\kappa_{\text{max}}} \left|1 - \frac{\kappa_{\text{eq}}}{\kappa}\right|^2 d\kappa; \quad \frac{\partial E}{\partial a_n} = 0, \ \forall\, n \in \{1,2,3,..,N\} \tag{3.9}$$

Tam & Webb [77], for example, used $N = 3$ and $L = 2$ with $\kappa_{\text{max}} = \pi/2$. The second method utilizes the *local* minimization approach [78] to derive the compact FD schemes, which consists of ensuring a perfect accuracy $(\kappa_{\text{eq}}/\kappa = 1)$ for a set of modes distributed in the range wherein a good accuracy is required. The coefficients can then be obtained by solving the following set of constraints

$$\frac{\kappa_{\text{eq}}(\kappa_n h)}{\kappa_n} = 1 \ \ \forall\, n \in \{1,2,3,..,N\}. \tag{3.10}$$

In practice, both Taylor and Fourier minimization approaches can be combined to obtain the coefficients based on different constraints. The in house code MULTIFAST used in the present study utilizes the second approach to derive an explicit optimized scheme using $N = 6$ for the first derivative. A similar methodology is adopted to derive coefficients to approximate the second derivative. The detailed methodology and the coefficients can be found in Bauer *et al.* [79].

The reasons for choosing the code based on EO schemes lie in its performance and ease of implementation. The EO schemes developed by Bauer *et al.* [79] are more efficient in terms

of computational costs compared to the compact schemes. EO and CS are different not only in their implementation strategy, but also in their compatibility with the numerical framework. This is particularly important in the code parallelization where the explicit nature of EO makes the domain decomposition easier while the implicit nature of the compact schemes imposes the use of a 2D domain decomposition or even more sophisticated strategies.

3.2.2 Temporal integration

Considering the temporal integration, the solution at the next time (sub)iteration $k+1$ is explicitly obtained by integrating equation 3.1b. The time interval $[t,\ t+\Delta t]$ is divided into n_k sub-steps ($t_1 = t, t_2, t_3, ..., t_{n_k} = t+\Delta t$). By applying the fractional step method, the velocity is corrected to become solenoidal at each time iteration. Making use of the conventional Einstein notation for spatial coordinate and velocity components (for which subscripts $1,2,3$ refer, respectively, to the spanwise (x), wall-normal (y), and streamwise (z) component), the temporal advancement of equation 3.1b can be expressed as

$$u^{k+1} = u^k + R_{\text{pmean}} + R_{\text{pfluc}} + R_{\text{adv}} + R_{\text{diff}}, \tag{3.11}$$

where,

$$R_{\text{pmean}} = -\int_{t_k}^{t_{k+1}} \left(\overline{\frac{\partial p}{\partial x_i}}\right) dt,\ R_{\text{pfluc}} = -\int_{t_k}^{t_{k+1}} \left(\frac{\partial p'}{\partial x_i}\right) dt, \tag{3.12}$$

$$R_{\text{adv}} = -\int_{t_k}^{t_{k+1}} \left(\frac{\partial u_i u_j}{\partial x_j}\right) dt,\ R_{\text{diff}} = \frac{1}{\text{Re}} \int_{t_k}^{t_{k+1}} \left(\frac{\partial^2 u_i}{\partial x_j^2}\right) dt, \tag{3.13}$$

$(\partial \overline{p}/\partial x_i)$ and $(\partial p'/\partial x_i)$ stand for the mean and the fluctuating pressure gradient, respectively. R_{pmean} is evaluated through the global flow rate conservation. The advection (R_{adv}) and diffusion (R_{diff}) terms are estimated explicitly from the previous $(k-1)$ and the current (k) fields as

$$\begin{aligned} R_{\text{adv}} + R_{\text{diff}} = \alpha_k \Delta t \left(-\widehat{\frac{\partial u_i u_j}{\partial x_j}} + \frac{1}{\text{Re}} \widehat{\frac{\partial^2 u_i}{\partial x_j^2}} \right)_k \\ + \beta_k \Delta t \left(-\widehat{\frac{\partial u_i u_j}{\partial x_j}} + \frac{1}{\text{Re}} \widehat{\frac{\partial^2 u_i}{\partial x_j^2}} \right)_{k-1}, \end{aligned} \tag{3.14}$$

where $\widehat{(.)}$ denotes spatially discretized operators.

The time advancement is performed by a Runge-Kutta third-order (RK3) scheme, in which the coefficients involved in the three iteration steps are $\alpha_{1,2,3} = [8/15, 5/12, 3/4]$ and $\beta_{1,2,3} = [0, -17/60, -5/12]$. The quantity R_{pfluc} is evaluated from the pressure at $k+1$. The equation 3.14 can be reformulated as

$$u^{k+1} = \widetilde{u^{k+1}} - (\alpha_k + \beta_k)\Delta t \widehat{\nabla p'^{(k+1)}}, \tag{3.15}$$

where $\widetilde{u^{k+1}} = u^k + R_{\text{pmean}} + R_{\text{adv}} + R_{\text{diff}}$ is the first estimation of the velocity field based on the terms known at the current time iteration. The quantity $p'^{(k+1)}$ is then calculated by applying the divergence free operator to equation 3.15, and solving the resulting Poisson equation:

$$\widehat{\nabla^2 p'^{(k+1)}} = \frac{1}{\Delta t(\alpha_k + \beta_k)} \widehat{\nabla \widetilde{u^{k+1}}}. \tag{3.16}$$

The Poisson equation for the pressure is solved in the Fourier domain (through FFT decomposition) at each xz plane.

3.2.3 Near wall refinement

As mentioned above, this derivative discretization is valid only if the grid is homogeneous. While it is the case for the streamwise (x) and spanwise (z) direction, however, it is not the case for the wall-normal direction, as there is a refinement near the wall and thus the spacings between two consecutive nodes is not the same. The refinement near the wall is necessary to obliterate the numerical instabilities arising due to grid resolution and also to resolve the near wall flow features. The near wall refinement is performed using a simple hyperbolic tangent distribution on a regular grid $s(j) = (j-1)/N_y$ (N_y being the number of grid points in the y direction)

$$y(j) = 1 + \frac{\tanh(\alpha[s(j) - 0.5])}{\tanh(\alpha/2)}, \tag{3.17}$$

where the parameter α simply controls the degree of refinement. Here, we chose $a = 3.8$.

Hence, in this particular case, a Jacobian approach is used, where first the derivatives along the wall-normal direction are calculated on the regular grid $s(j)$, and then are later transformed on the refined grid $y(j)$ using the following relations for the first and second order derivatives along the y-direction

$$\frac{\partial f}{\partial y} = \frac{\partial s}{\partial y} * \frac{\partial f}{\partial s}, \qquad \frac{\partial^2 f}{\partial y^2} = \frac{\partial^2 s}{\partial y^2} * \frac{\partial f}{\partial s} + \left(\frac{\partial s}{\partial y}\right)^2 * \frac{\partial^2 f}{\partial s^2}. \tag{3.18}$$

3.3 Computational domain

The computational domain used in the present work is a plane channel of size $L_x \times L_y \times L_z$ in the streamwise (x), wall-normal (y) and spanwise direction (z), respectively. The turbulent channel flow was the first wall-bounded turbulent flow studied through DNS [80]. Since then, the turbulent channel flow has been a standard benchmark to study the physics of turbulent wall-bounded flows. The configuration schematically sketched in figure 3.4 consists of two parallel

$L_x \times L_y \times L_z$	$N_x \times N_y \times N_z$	Δx_0	Δy_0	Δz_0	Re	Re_τ
$6\pi h \times 2h \times 3\pi h$	$401 \times 129 \times 335$	8.5	0.5-5.5	5	4200	180

Table 3.1: Details of the computational domain and grid resolution used in the present study. The subscript '0' represents wall units based on the friction velocity of the uncontrolled flow.

plates of infinite span. The flow between the two plates can either be driven by a constant pressure gradient (CPG) or at a constant flow rate (CFR) or a certain combination involving both. In the present study, the flow was driven at CFR. Computationally speaking, it would be impossible to simulate an infinite system, hence in practice the simulations are conducted in boxes of finite sizes. The wall-normal direction (y) is bounded by the two walls with distance $2h$, where h is the channel half-height. Periodicity is assumed in the other two directions, i.e. the streamwise (x) and spanwise (z) directions. It is important to note that the restricting the domain to a finite size can have drastic consequence on the resulting statistics. Jiménez & Moin [35] investigated the minimal box required to sustain the turbulence. They found that it is not possible to sustain turbulence in boxes with a spanwise length of less than 100 wall units. The wall units are to be explained later in this section. This simplified model, commonly celebrated as the *minimal flow unit*, has been widely used since then to unravel various aspects of the near wall turbulence regeneration cycle. In this configuration, the small scales of wall turbulence are well resolved, but the limited streamwise extent presents non-physical constraints on the largest flow scales that often result in under-resolved higher-order statistics.

In the present study, we present the near wall dynamics of the turbulent channel flow subjected to transverse wall oscillations in the form of streamwise travelling waves. As the imposition of the wall-forcing adds additional complexity to the dynamics of the near wall flow field, we chose relatively larger computational boxes to avoid any uncertainties arising in the statistics related to the extent of the domain. All simulations were performed over the same computational box of size $L_x = 6\pi h$, $L_y = 2h$, $L_z = 3\pi h$ in the streamwise, wall-normal and spanwise direction, respectively. The box was covered by $N_x \times N_y \times N_z = 401 \times 129 \times 335$ (≈ 17.3 million) nodes which were distributed uniformly along the streamwise and spanwise directions, while were clustered in the wall-normal direction near the wall through a hyperbolic tangent distribution. The size of the computational domain along with the grid resolution are given in table 3.1.

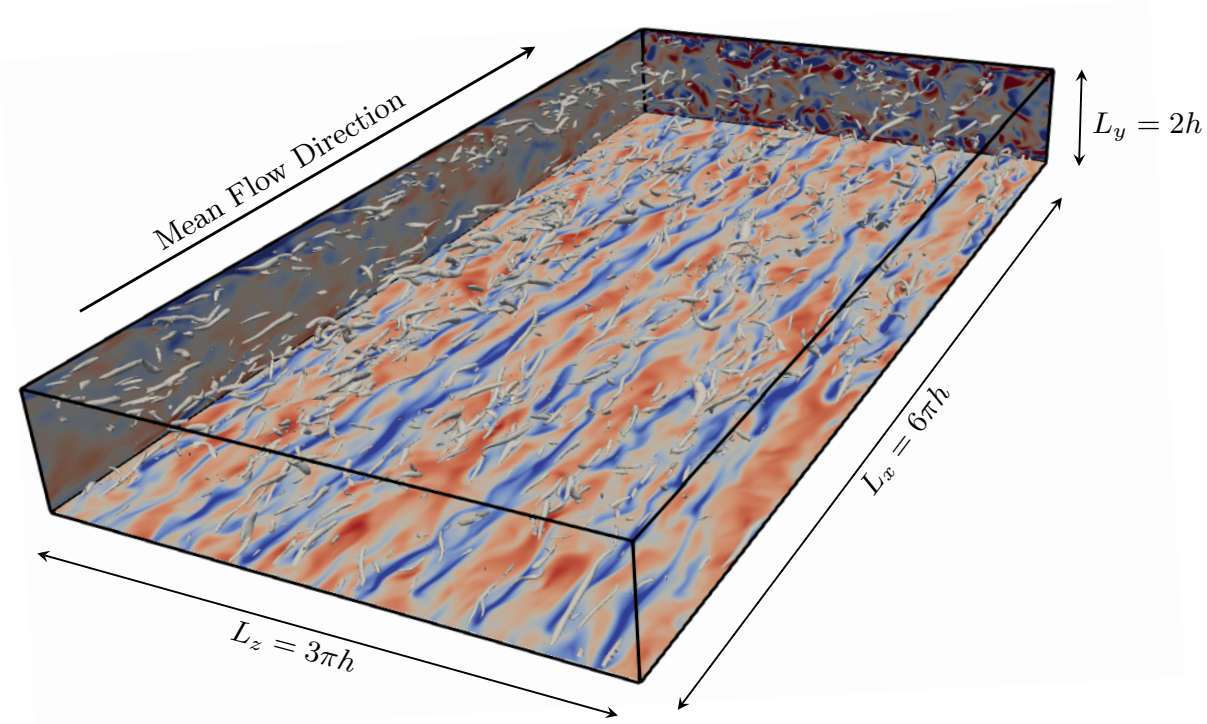

Figure 3.4: Schematic diagram of the rectangular channel of size $L_x \times L_y \times L_z = 6\pi h \times 2h \times 3\pi h$ in the streamwise, wall-normal, and spanwise direction, respectively.

3.3.1 Boundary conditions for transverse wall oscillations cases

The transverse wall oscillation in the form of streamwise travelling waves are imposed on the parallel walls using

$$W = A\ \sin(\kappa\ x - \omega\ t), \tag{3.19}$$

where W represents the instantaneous velocity in the spanwise direction, and A, κ and ω are the three actuation parameters, namely, amplitude, wavenumber and angular frequency of the travelling wave, respectively. In present study, the range of actuation parameters have been narrowed down to the optimal forcing scenarios to investigate the proper effect of travelling waves control on the near-wall turbulence dynamics. The values of κ and ω were kept fixed at 1.66 and 0.16, respectively. Both of these values arise upon the use of outer units based on h and U_c. Table 3.2 gives the details of the cases considered in the present work. The naming of the cases is based on the forcing amplitude in outer units.

One of the aims of the present work is to investigate the direct effects of the STW with respect to the simple homogeneous wall oscillations (HWO). Transverse wall oscillations in the form of STW result in larger DR margin compared to HWO. We will show and discuss in detail later that some terms appearing in the Reynolds stresses and turbulent enstrophy transport equations are a direct consequence of the STW. The response of the flow to the STW is rather complex when examined as a function of ω and κ. Depending on the value of κ, drag can be either increased or decreased for a fixed value of ω. Therefore, it is difficult to compare both types of forcing on the basis of actuation parameters. Yet, a clear base has to be defined for comparison; hence, we opted to compare the travelling wave effects with the HWO in their optimal configuration with $A_0 = 12$ and $T_0 = 100$ for the Re investigated here [38, 58]. Note that the optimal configuration is a function of Re [60, 62]. Here, the subscript '0' represents quantities scaled by the friction velocity (u_τ) of the uncontrolled flow, and ν.

3.4 Post-processing methodology

Fluid flows described by the Navier-Stokes equations are completely deterministic in the sense that the temporal evolution is fully described by the initial condition, unless a probabilistic external forcing is applied. There is no need for a statistical description up to this point, taking a glimpse at a turbulent signal immediately reveals the stochastic nature of the problem. The strong fluctuations suggest a certain degree of randomness. The reason for randomness entering the turbulence phenomenon is that the Navier-Stokes equations represent a set of nonlinear, non-local partial differential equations with solutions exhibiting spatio-temporal complexity, which makes it intractable to methods from pattern formation, as the system is too unstructured to be described by a few degrees of freedom. At the same time turbulent fields do not appear as purely random, the coherent structures indicate a certain degree of spatial organization, yet being a

case	A (U_C)	A $(u_{\tau 0})$	A (u_τ)	ω (u_τ^2/ν)	κ (u_τ/ν)	Re_τ (hu_τ/ν)	%DR	$\%P_{\text{net}}$
HWO	0.51	12.0	14.9	0.098	-	144.2	36	-44
*A*0.15	0.15	3.5	4.0	0.027	0.248	156.9	26	23
*A*0.30	0.30	7.0	9.0	0.035	0.360	139.0	42	30
*A*0.50	0.50	11.7	16.1	0.039	0.408	130.7	48	15
*A*0.75	0.75	17.5	25.3	0.043	0.450	124.5	52	-19
*A*0.95	0.95	22.2	32.7	0.045	0.470	121.9	54	-50
*A*1.25	1.25	29.2	44.3	0.048	0.498	118.4	58	-130

Table 3.2: %DR margins and the net power savings ($\%P_{\text{net}}$) for different oscillatory conditions. The values of angular frequency (ω) and wavenumber (κ) of STW were kept fixed at 0.16 and 1.66 (outer units). Their corresponding values in local units are also provided to facilitate comparison with the available literature.

rather complicated one. As a consequence, a simple stochastic modelling will be inappropriate. Together with the chaotic behaviour in time, the whole system displays a sensitive dependence on initial conditions. Small changes in the experiments or numerical environment will eventually lead to a completely different time evolution of the system. These considerations show that the nature of turbulence is intrinsically stochastic and therefore requires a statistical description.

3.4.1 Reynolds decomposition

When the flow is turbulent, it is preferable to decompose the instantaneous variables (for example the velocity components and pressure) into a mean and a fluctuating component (figure 3.5). Let ψ denotes an instantaneous quantity, then employing Reynolds decomposition, we can write

$$\psi = \overline{\psi} + \psi', \tag{3.20}$$

where ψ' denotes the fluctuating component and $\overline{\psi}$ denotes the time averaged value (the mean component), defined as

$$\overline{\psi}(\mathbf{X}, t_0) = \frac{1}{T}\int_{t_0}^{t_0+T} \psi(\mathbf{X}, t)\, dt \tag{3.21}$$

where T is sufficiently large. The measurement is carried out at a specified location denoted by $\mathbf{X}$. In some situations, the average $\overline{\psi}$ could depend on the time t_0 at which the measure-

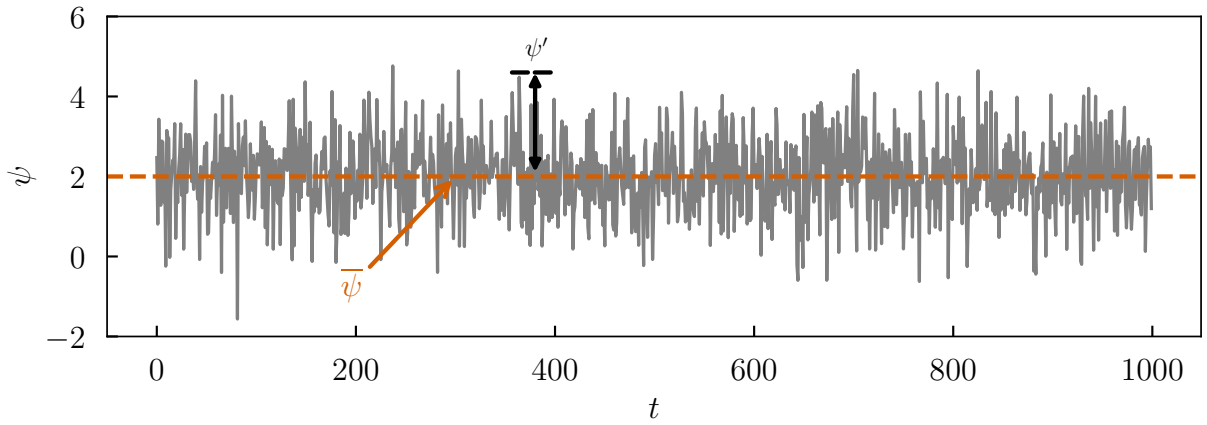

Figure 3.5: A typical turbulent signal.

ment is started. However, in most of the situations, the mean flow variables are stationary, i.e. independent of t_0. In this case, the above expression can simply be reduced to

$$\overline{\psi}(\mathbf{X}) = \frac{1}{T}\int_0^T \psi(\mathbf{X},t)\,dt. \tag{3.22}$$

In this case, it does not matter when the measurement is started at a given point, however, one has to be sure that the flow has already acquired a quasi-stationary state. In the present study, for example, for the reference uncontrolled channel flow case, the solution was integrated for about 37000 wall units, after the flow attained the stationary state. The statistical calculations were performed using 50 statistically independent full 3D instantaneous flow fields (snapshots) separated by 770 wall units.

In the flow configuration considered here, the streamwise (x) and the spanwise (z) directions are homogeneous, hence it is preferable to perform spatial averaging over the homogeneous plane xz at different wall-normal locations (y). Let $\langle\psi\rangle_{xz}$ denote the spatial averaging for any quantity ψ over the homogeneous plane. Then, the spatial mean of the quantity ψ at any time t_0 in the plane y is defined as

$$\langle\psi(y,t_0)\rangle_{xz} = \frac{1}{N_x N_z}\sum\sum\psi(x,y,z,t_0) \tag{3.23}$$

where N_x and N_z are the number of grid points in the streamwise (x) and spanwise (z) directions, respectively. This is done for all the homogeneous planes in wall-normal direction. In the present, both spatial and time averaging are performed. Throughout the thesis, a temporally and spatially averaged quantity will be denoted by an overbar $\overline{\psi}$. Thus, the time and space averaged profile of the flow variable of interest $\psi(x,y,z,t)$ is given by

$$\overline{\psi}(y) = \frac{1}{T}\int_0^T \frac{1}{N_x N_z}\sum\sum\psi(x,y,z,t)\,dt \tag{3.24}$$

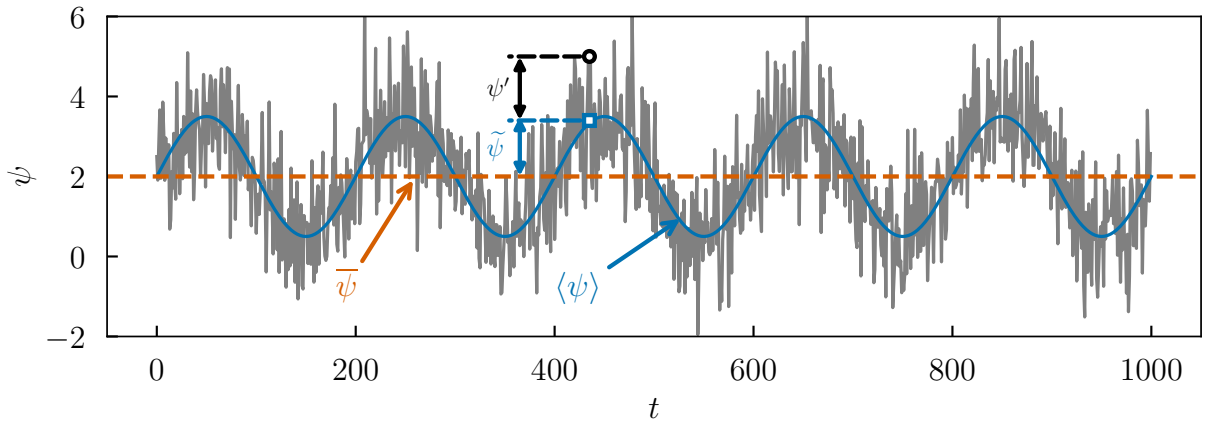

Figure 3.6: Schematic of a turbulent signal with an imposed background wave.

Besides the mean and fluctuating flow field, it is also important to look at the correlations, for example, the Reynolds stresses $\overline{u_i u_j}$. The Reynolds stresses play a crucial role in the wall turbulence. They are the components of the second-order tensor $\overline{\mathbf{uu}}$ described as

$$\overline{\mathbf{uu}} = \begin{bmatrix} \overline{uu} & \overline{uv} & \overline{uw} \\ \overline{uv} & \overline{vv} & \overline{vw} \\ \overline{uw} & \overline{vw} & \overline{ww} \end{bmatrix}. \tag{3.25}$$

The diagonal components $\overline{uu}$, $\overline{vv}$ and $\overline{ww}$ are normal stresses, while the off-diagonal components $\overline{uv}$, $\overline{uw}$ and $\overline{vw}$ are shear stresses. They result from the turbulent transport of momentum. In internal flow configurations, for example channel and pipe flows, the flow is symmetrical with respect to the planes normal to the transverse direction (in our case it is the spanwise direction z). Consequently, all the correlations containing w (the spanwise fluctuating velocity) are zero. The components of Reynolds stress tensor are obtained using the following relation for any two flow field variables ψ and ϕ

$$\overline{\phi'\psi'} = \overline{\phi\psi} - \overline{\phi}\,\overline{\psi}. \tag{3.26}$$

A similar approach can be used to calculate other higher-order moments.

3.4.2 Phase averaging

In the present study, we impose transverse wall oscillations in the form of travelling waves. Hence, besides the stochastic fluctuating component, a low frequency periodic component is also present in the flow field quantities (figure 3.6). In this section, we introduce the decomposition technique that is used to extract different components from a flow field in such cases.

To extract the stochastic fluctuations from the instantaneous field, we adopt the famous triple

decomposition introduced by Hussain & Reynolds [81], described as follows

$$\begin{aligned}\Psi(x,y,z,t) &= \langle\Psi\rangle(y,\xi) + \psi(x,y,z,t) \\ &= \overline{\Psi}(y) + \widetilde{\Psi}(y,\xi) + \psi(x,y,z,t),\end{aligned} \tag{3.27}$$

where $\langle\Psi\rangle(y,\xi)$ is the phase averaged field, $\overline{\Psi}(y)$ is the ensemble average, $\widetilde{\Psi}(y,\xi)$ is the fluctuating component due to periodic forcing, and $\psi(x,y,z,t)$ is the stochastic fluctuations characterizing turbulence. Throughout the manuscript, the turbulent quantities are represented by the lower case letters. The phase average of a field variable is defined as

$$\langle\Psi\rangle(y,\xi) = \frac{1}{N_\xi} \sum_{x,t\,\in\,\xi} \left[\frac{1}{L_z}\int_0^{L_z} \psi(x,y,z,t)\, dz\right], \tag{3.28}$$

where $\langle\Psi\rangle$ is the phase averaged field, $\xi = \xi^* - (n-1)\lambda$ is the phase of the travelling wave centred between 0 and λ, N_ξ is the total number of values of Φ corresponding to ξ, and n is the number of the cycle, $n = \lfloor \xi^*/\lambda \rfloor + 1 \;\forall\; n > 0$ and $n = \lfloor \xi/\lambda \rfloor \;\forall\; n < 0$ ($\lfloor . \rfloor$ represents the greatest integer value). The time-averaged value ($\overline{\Psi}$) of the flow variable at a particular wall-normal location can be easily recovered from the phase averaged field, $\langle\Psi\rangle$, either by averaging it over the phases of the travelling wave or by deconstructing $\langle\Psi\rangle$ into its constituent Fourier modes and extracting the fundamental mode. Here, we adopt the former method which is quite straightforward to implement,

$$\overline{\Psi}(y) = \frac{1}{\lambda}\int_0^{\lambda} \langle\Psi\rangle(y,\xi)\, d\xi \tag{3.29}$$

The stochastic fluctuations ($\overline{\phi\psi}$) can be obtained using $\overline{\phi\psi} = \overline{\langle\Phi\Psi\rangle} - \overline{\langle\Phi\rangle\langle\Psi\rangle}$. Figure 3.7($a$,$b$) show the phase-wise variations of the phase-averaged spanwise velocity at different wall-normal locations for $A0.50$ case.

3.4.3 Validation and statistical convergence

There are mainly three particularities of the present DNS: First, the resolution is very fine, with the mesh size in the wall-normal direction Δy being 1/3 of the Kolmogorov scale (η) near the wall while $\Delta y \approx 1.4\eta$ at the centreline. The resolution in the near wall region compares with previous DNS, but it is much finer in the core region here. The mesh size in the streamwise direction is as small as twice the Kolmogorov length at the centreline. The mesh size in the spanwise direction is about η at the centreline. The grid employed in the present study is sufficiently fine to resolve the relevant scales present in the turbulent flow field, and is even finer in the streamwise and spanwise directions compared with many other published DNS studies on channel flows. The second particularity of these DNS is the use of particularly large computational domains:

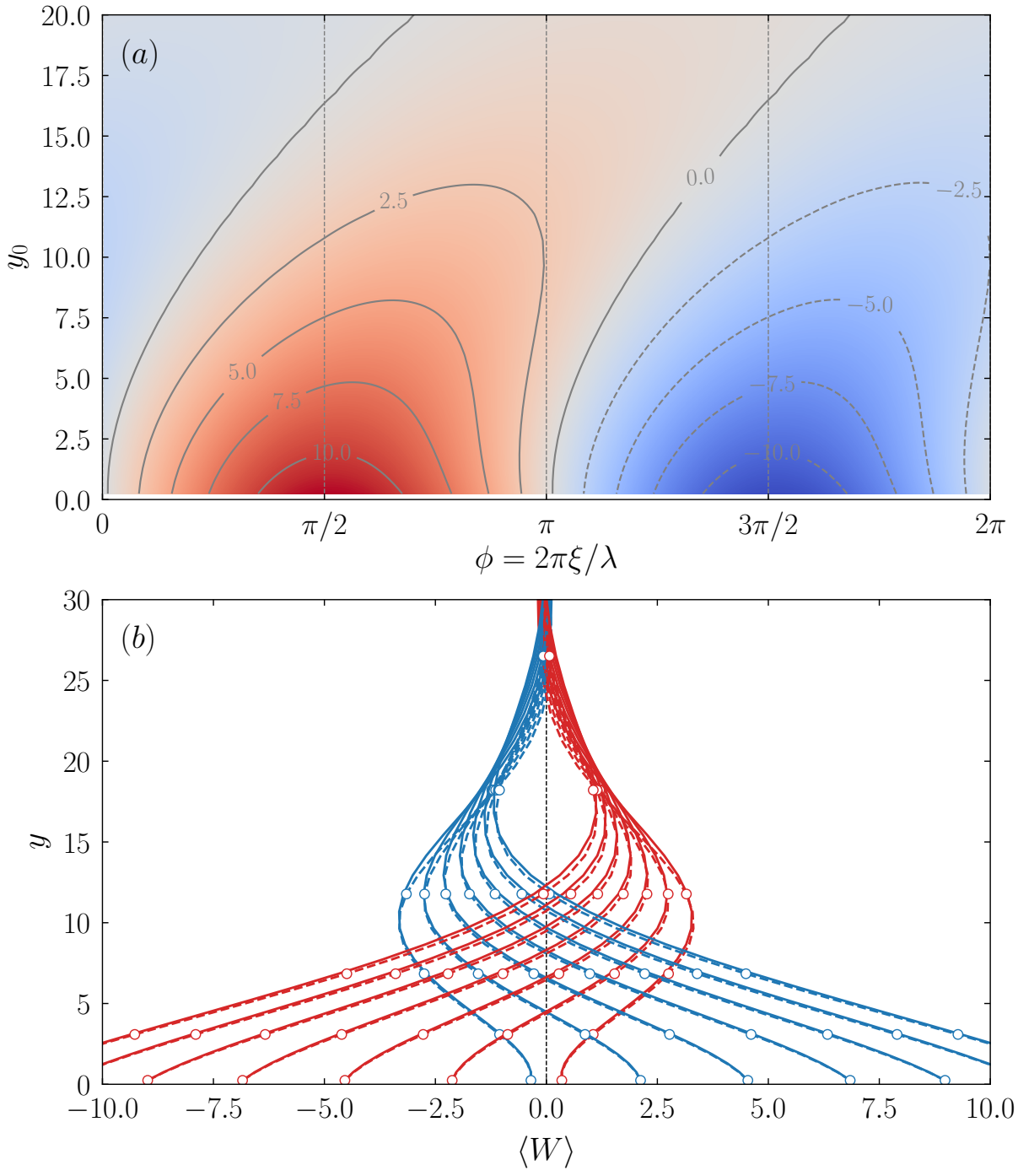

Figure 3.7: Phase wise variations of phase-averaged spanwise velocity $\langle W \rangle$ at different wall-normal locations y for $A0.50$ case: (a) normalized in inner units using friction velocity of the uncontrolled flow, and (b) normalized in inner units using friction velocity of the controlled flow. The red contours in figure (a) correspond to positive values, while the blue contours correspond to negative values. The phase-averaged profiles collapse well with the laminar solution (represented by dots) of Quadrio & Ricco [7].

the streamwise and spanwise lengths of the computational domain are $6\pi h$ and $3\pi h$. They are taken particularly large to accommodate multiple wavelengths. The third is the use of 6th order explicit optimized (EO) finite differences scheme, which resulted in near spectral resolution. The adequacy of the resolution was examined by comparing the profiles of the root-mean-square velocity and vorticity components with the data of Moser and Kim [82] at $Re_\tau = 180$ in Figure 3.8. As seen in Figure 3.8, the profiles of root-mean-square velocity and vorticity components match perfectly with the data of Moser and Kim [82].

In the controlled flow, however, the determination of the stochastic field requires the introduction of the triple decomposition, defined as:

$$F = \langle F \rangle + f, \tag{3.30}$$

where, F is the instantaneous field, $\langle F \rangle$ is the phase-averaged field, and f is the purely stochastic field. The computation of phase-averaged field requires division of the wave cycle into bins of equal widths. We typically chose 200-500 bins, depending on the amplitude of the forcing. To improve the convergence, we further decreased the time-step to increase the number of variables collected per bin. We tested the convergence of the phase-averaged statistics by computing the ensemble average of the quantities such as Reynolds stresses over 5, 10, 15, 20, etc cycles. In view of the very high associated costs involved in running the simulation for very long durations, we decided to perform averages over 40 temporal cycles, which is yet very long compared to other studies at even larger Reynolds number. The conclusion that the errors are small is strengthened by the fact that tests with averaging over 20 cycles gave fields very close to those with averaging over all 40 cycles. Despite the fair smoothness observed for all the quantities, the phase-averaged quantities cannot be fully converged because of the presence of the large-scale oscillations in C_f. However, the error is small (less than 1.5%), as illustrated by Fig. 3.9. In order to avoid cluttering, only the error margins for the $A1.25$ case are shown for the Reynolds stresses.

3.4.4 Detection of near wall quasi streamwise vortices: λ_2 criterion

Turbulent flows are typically characterized by the excitation of a multitude of spatial and temporal scales, which involves numerous degrees of freedom interacting non-linearly in space and time. It is known that a large amount of turbulent kinetic energy is generated in a thin, highly viscous region very close to the solid boundary. This thin near-wall region is known to be dominated by a set of organized motions commonly called as “eddies”, “coherent structures” or “vortical structures”. These structures can be thought of as individual entities possessing spatio-temporal coherence. Advancement in the flow visualizations techniques and the rise of high performance computational facilities enabled the structural features of the turbulent flow field to be observed in unprecedented detail. An extensive literature is devoted to the identification and kinematics of these structures from both numerical and experimental studies, details of which

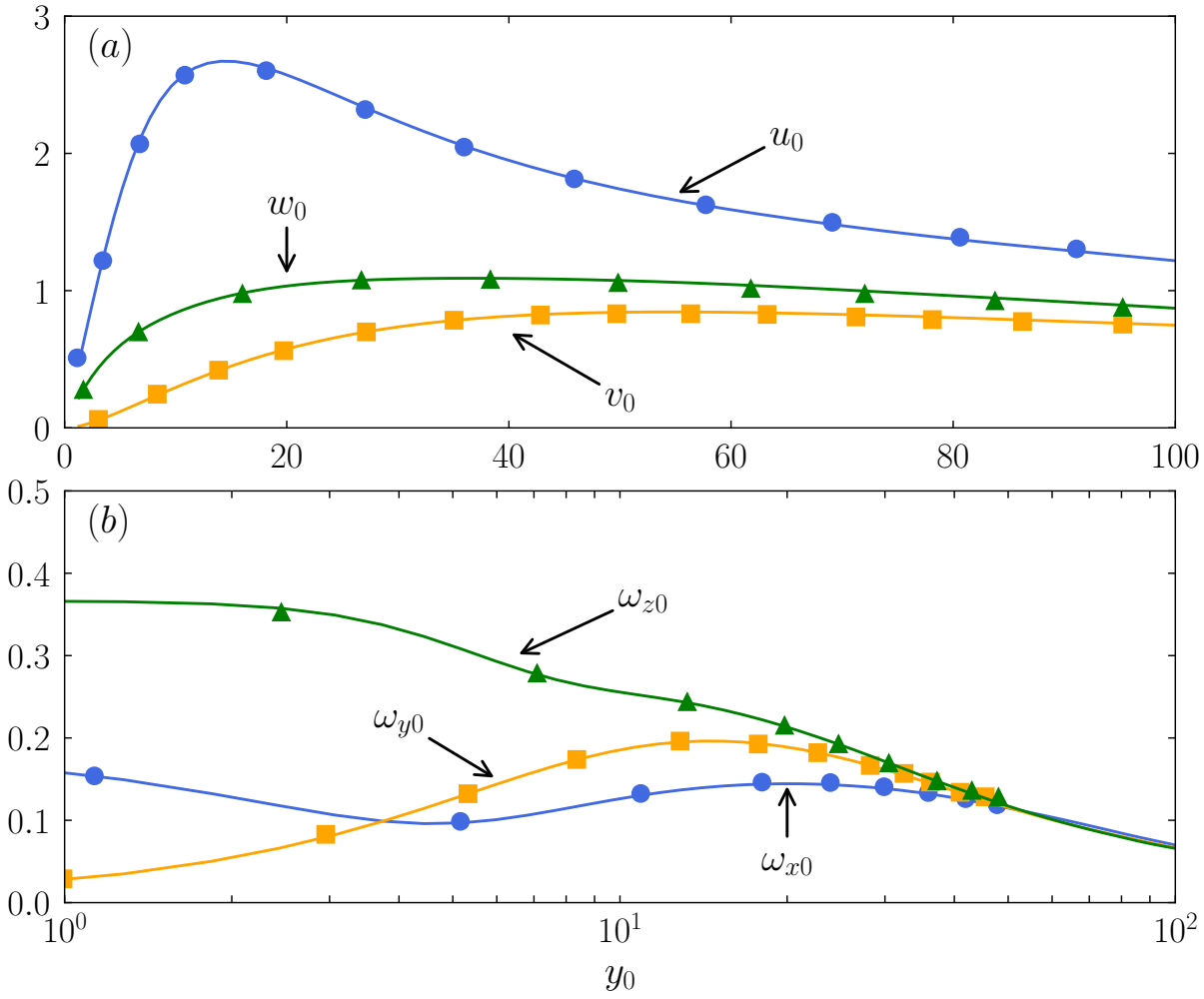

Figure 3.8: Comparison of (a) root-mean-square velocity, and (b) root-mean-square vorticity components in the streamwise, spanwise and wall-normal directions with the data of Moser & Kim [82] (in markers).

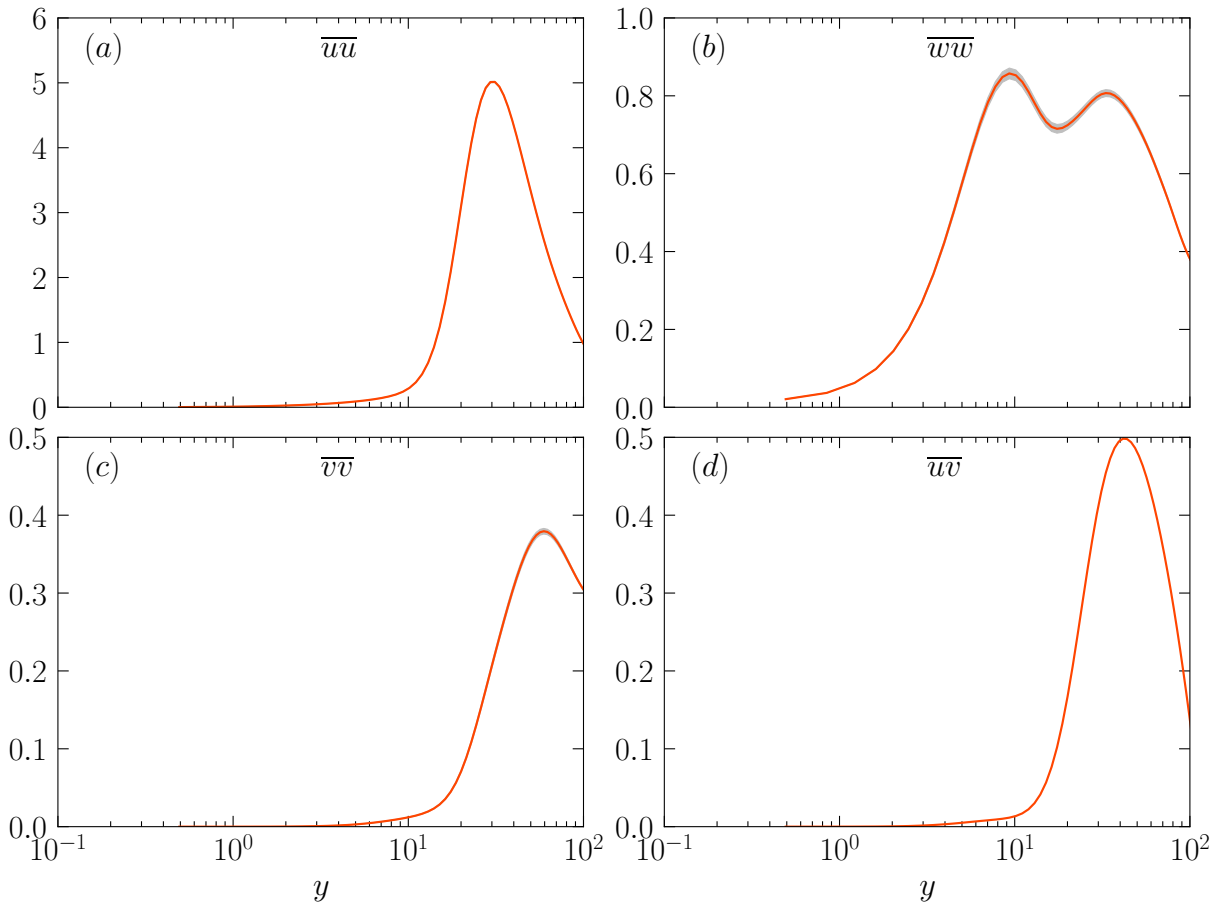

Figure 3.9: Reynolds stresses profiles for the $A1.25$ case scaled with the local friction velocity, with the corresponding error margins. (a) streamwise component $\overline{uu}$, (b) spanwise component $\overline{ww}$, (c) wall-normal component $\overline{vv}$, and (d) shear stress $-\overline{uv}$.

are not of primary importance for the present study. The kinematic and dynamical properties of these structures are of considerable importance not only for the development of closure models for turbulence, but also for the development of feasible control strategies to mitigate the skin friction.

Coherent structures play a fundamental role in the transport of momentum and scalar quantities in turbulent flows. The generation of skin friction is closely related to the coherent structures present in the turbulent flow field. The dominant structures in the near-wall turbulent flow field are the high- and low-speed streamwise velocity streaks (HSS and LSS, respectively), and the quasi-streamwise vortices (QSVs). The HSS and LSS were one of the earliest discovered features of a turbulent flow field next to boundaries. They consist of long connected regions of high- and low-momentum fluid that extend to over $O(10^3)$ viscous lengths in the streamwise direction, with an average spanwise spacing of about $O(10^2)$ viscous lengths (figure 3.10). Closely asso-

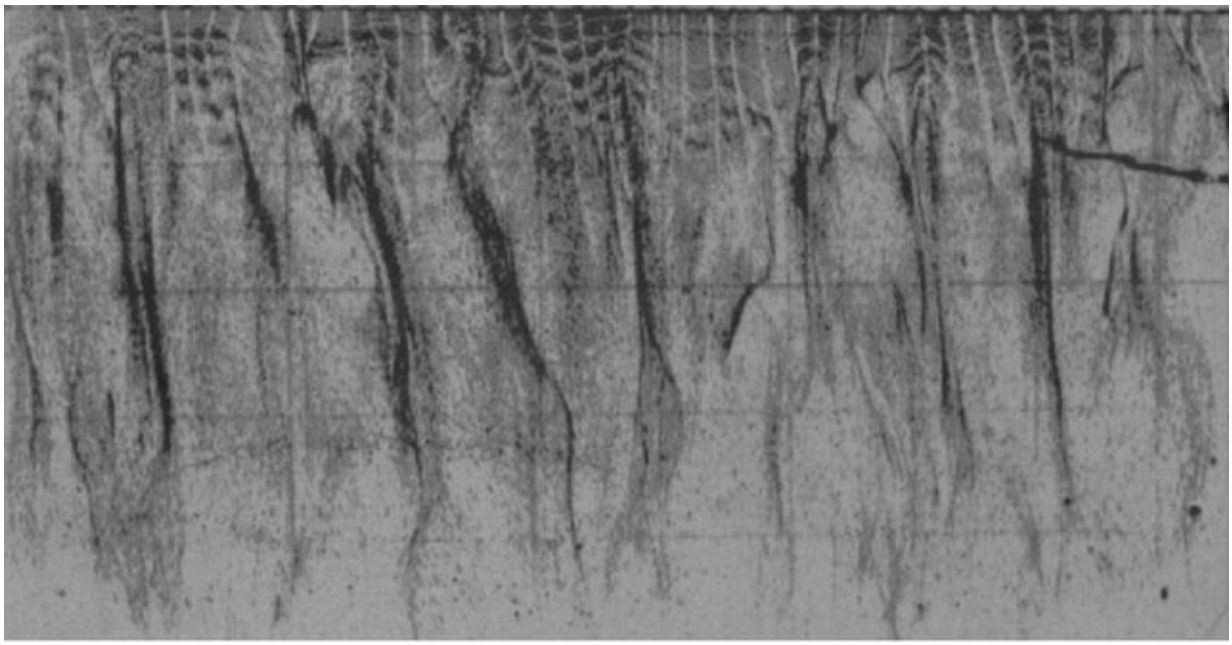

Figure 3.10: Near-wall streaks visualized using hydrogen bubbles by Kline *et al.* [83].

ciated with the near-wall velocity streaks are the quasi-streamwise vortices (QSVs) which make a predominant contribution to the production of the near-wall Reynolds shear stress and hence deserve a special attention. The QSVs are inclined in the wall-normal and spanwise directions, and are centred roughly at $10-50$ wall units from the wall in the buffer region, with their typical diameter of the order of $20-50$ wall units. Conventional paradigm focus mainly on QSVs as being the primary dynamical structures responsible for streaks formation and turbulence generation. These structures are responsible for inducing relatively high- and low-speed streaks via the sweep and ejection events, respectively, which act to enhance the momentum transport in the near-wall region. The high-speed streaks near the wall account largely for a significant increase in the skin friction drag. Several conceptual models describe a 'regeneration' or 'autonomous' cycle wherein new vortical structures are generated by low-speed streaks instability, nonlinear amplification and breakdown, with new vortical structures regenerating new streaks [36]. However, until now, there is no complete agreement on the precise mechanism responsible for generation and sustenance of the near-wall coherent structures. The study of flow topology is of broad interest, particularly in the field of turbulence. Researchers are interested in identifying coherent structures to aid turbulence modelling, to guide flow control, to expose mechanisms of turbulence production and dissipation, and to understand the passage of coherent structures and engineering quantities of interest [84].

Now we move our attention to the identification of QSVs. Here, we only focus our attention on the velocity-gradient based vortex identification criteria that utilize the concept of critical points to characterize the topology of turbulence. Many vortex visualization methods have been

proposed based on the velocity gradient tensor, for example, Q criterion, λ_2, λ_c, etc.

The eigenvalues (λ) of the velocity gradient tensor (∇u) satisfy the following equation:

$$\lambda^3 + P\lambda^2 + Q\lambda + R = 0, \tag{3.31}$$

where, P, Q and R are three invariants of the velocity gradient tensor given by

$$P = -\mathrm{Tr}(\nabla u), \tag{3.32}$$

$$Q = \frac{1}{2}(P^2 - \mathrm{Tr}(\nabla u^2)), \text{ and} \tag{3.33}$$

$$R = \frac{1}{2}(-P^3 + 3PQ - \mathrm{Tr}(\nabla u^3)), \tag{3.34}$$

where 'Tr' represents the trace of the matrix. In the case of incompressible flows $P = 0$ due to continuity. The velocity gradient tensor can be decomposed into two parts as follows:

$$\nabla u = \left(\frac{\nabla u + \nabla u^T}{2}\right) + \left(\frac{\nabla u - \nabla u^T}{2}\right) = S + \Omega, \tag{3.35}$$

where S is the symmetric part known as the rate of strain tensor and Ω is the antisymmetric part known as the rate of strain tensor and vorticity tensor, respectively. The Q criterion can be directly derived using $Q = (||\Omega||^2 - ||S||^2)/2$. The Q criterion $(Q > 0)$ identifies the connected regions in the flow field where the vorticity magnitude is greater than the magnitude of the rate of strain. Jeong *et al.* [85] showed that the definitions based on the discriminant $\Delta = (Q/3)^3 + (R/2)^2 > 0$ and $Q > 0$ are not helpful in certain situations. In the present work, we used λ_2 criterion proposed by Jeong *et al.* [85] to identify the QSVs. λ_2 is defined as the second-largest eigenvalue of the gradient tensor $S^2 + \Omega^2$. If the unsteady and viscous terms in the incompressible Navier-Stokes equation are ignored, then $S^2 + \Omega^2 = -\nabla p/\rho$. When there are two negative eigenvalues, the pressure is a minimum in the plane formed by the corresponding eigenvectors of these two negative eigenvalues.

Figure 3.11 shows a snapshot of the near-wall QSVs identified by $\lambda_2 = -0.02$ in a channel flow at $Re_\tau = 180$. Based on their sense of rotation, QSVs can either be classified as positive $(\omega_x > 0)$ or negative $(\omega_x < 0)$. The whole region is populated with a number of vortices with varied sizes and orientations. A "vortex" has to be a "developed compact object" of sufficient length to exist and be dynamically significant (*mature*). To extract the shapes of these dynamically significant structures, an ensemble average method is adopted, which includes the identification of vortex cores and conditional averaging of the relevant structures with the same sense of rotation.

To detect the near-wall QSVs, first, we detect the vortex cores where the value of $\lambda_2 \leq -0.02$ directly from the 3D instantaneous velocity fields. Then we identify and count only the structures that have streamwise extent greater than or equal to 150 wall units with inclination and titling

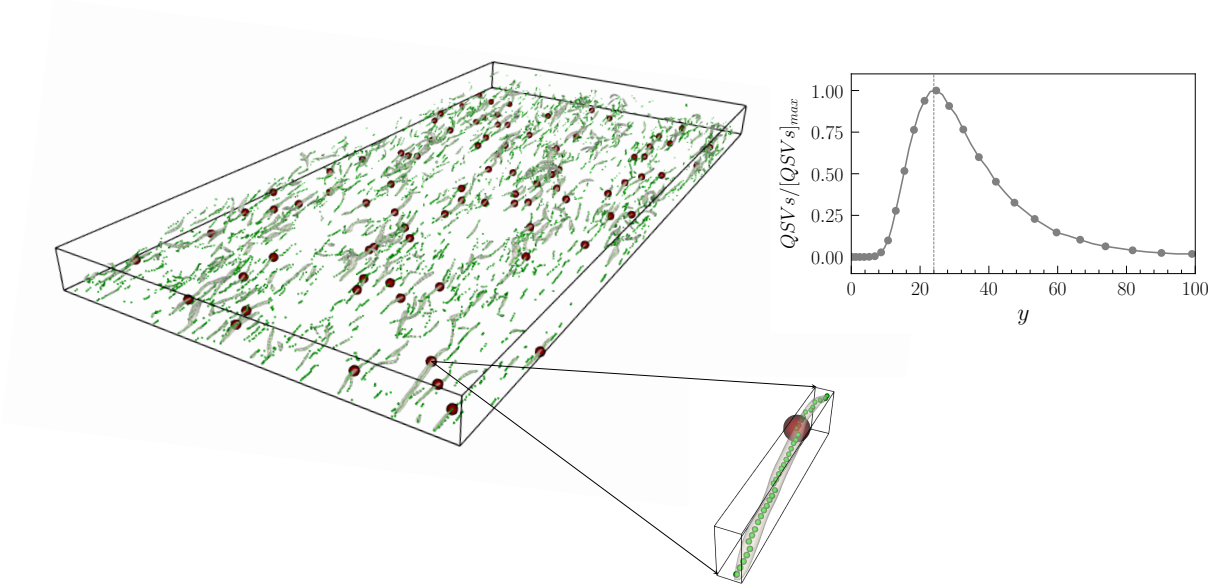

Figure 3.11: λ_2 structures and their distribution. The green dot shows the detected vortex cores, and the red dot shows the centres of the vortices.

angles in the range -30° to $+30^\circ$, respectively. The centre of each individual structure is obtained by locating the point where λ_2 attains its local minimum value within the structure. For all the cases studied here, we analysed an ensemble of at least 50 independent full 3D instantaneous fields separated by roughly one full-through time unit $(20h/U_c)$. Since the criteria we chose to select the relevant QSVs is quite strict, as a consequence only few structures qualify to be considered as relevant candidates. For example, in the uncontrolled case, only about 90 structures met the imposed criteria in one snapshot of the instantaneous 3D field. Figure 3.11 show that, for the canonical turbulent channel flow, the majority of the mature QSVs are located at $y \approx 24$, which is in agreement with Jeong *et al.* [85]. A conditional averaged vortex with positive sense of rotation is shown in figure 3.12. As we will see in later in chapter 6, the control in the form of STW results in a significant drift of QSVs away from the wall, thus reducing their signature at the wall and hence, skin-friction.

3.4.5 A brief note on scaling

As the flow is driven at constant flow rate (CFR), two different inner scaling options are available for the controlled cases, one based on the inner variables derived using the friction velocity of the uncontrolled flow $(u_{\tau 0})$ and the other based on the inner variables derived using the respective local (actual) friction velocities of the controlled cases (u_τ). As the flow is still in turbulent regime even at the largest imposed amplitude, the use of actual friction velocity of the controlled

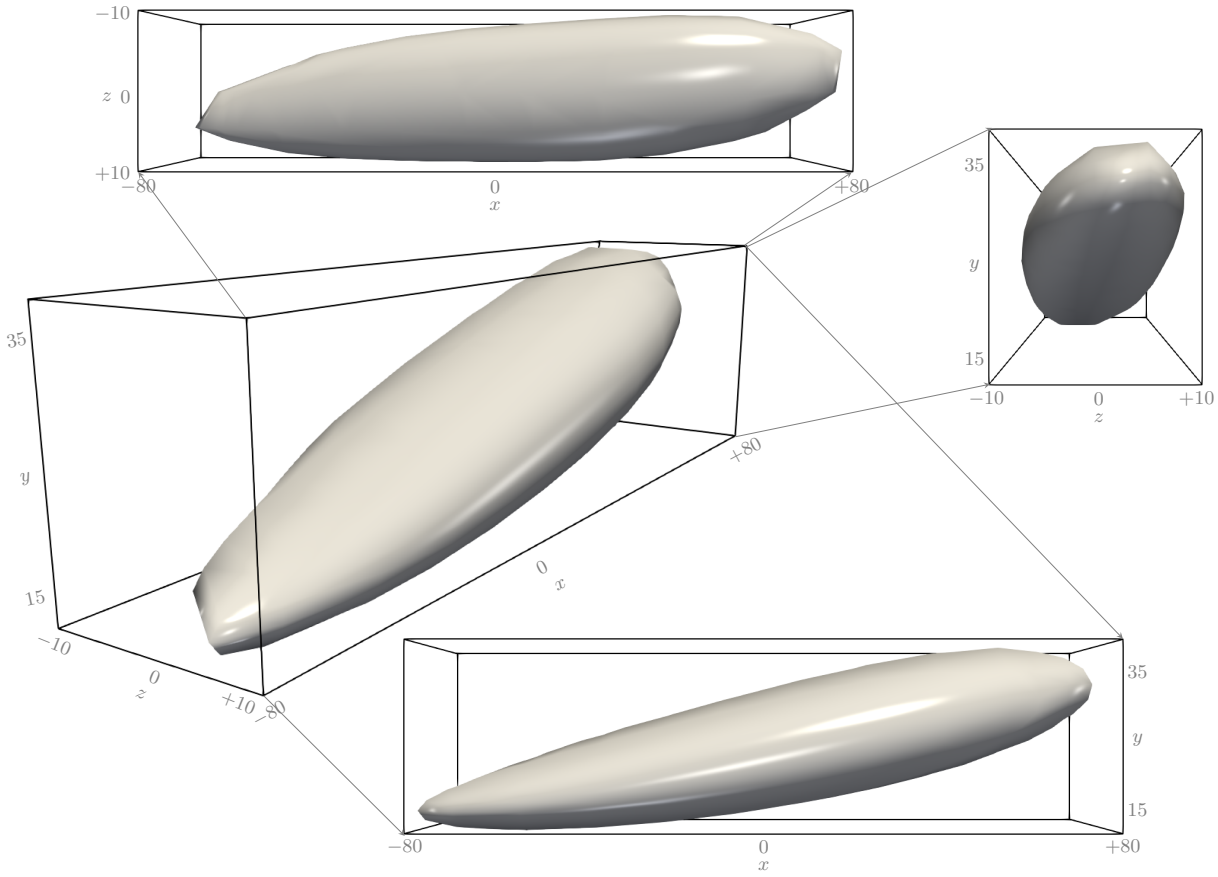

Figure 3.12: A typical conditional λ_2 structure ($\lambda = -0.02$) with positive sense of rotation (i.e. $\omega_x > 0$) for the uncontrolled flow.

flow is physically correct, especially near the wall. Moreover, since the imposed control is based on the wall and its influence is limited to the near-wall region, the use of actual friction velocity would bring about the important structural changes in the flow field. Scaling with the inner variables based on $u_{\tau 0}$ brings about the absolute changes of the quantities, while scaling with the local inner variables based on u_τ leads to the direct "in-situ" non-dimensionalization of the mean flow near the wall, and thus allows for a comparison between the near-wall drag-reduced statistics and the statistics of the uncontrolled flow at the same friction Reynolds number (Re_τ) [38, 44]. Real structural changes can only be analysed through local units; this point will be further illustrated in the later sections.

Throughout the manuscript, the quantities with subscript '0' are normalized using the inner variables based on $u_{\tau 0}$; absence of this qualifier implies scaling with inner variables based on u_τ of the controlled cases.

CHAPTER 4

Reynolds Stress Transport

In this chapter, we first start with presenting the results concerning the mean flow statistics such as the drag reduction margins, and effect on the mean velocity profiles. Later, we move on to detail the effect of forcing on the various Reynolds stresses components. We will see further that the spanwise Reynolds stress component show some peculiar behaviour that is specific to the streamwise travelling waves control. Hence, to gain a better understanding, we present detailed analyses on the Reynolds stresses budgets. Some results presented in this chapter appeared in *Physical Review Fluids, Vol. 7, Issue 5 – May 2022* (https://doi.org/10.1103/PhysRevFluids.7.054601).

4.1 Response of skin-friction coefficient

As the flow is driven at constant flow rate, the drag reduction (DR) margin is simply characterized by the change in the wall-shear stress (τ_w) as

$$DR = -\frac{\Delta\tau_w}{\tau_{w0}} = -\frac{\Delta C_f}{C_{f0}} = \left(1 - \frac{C_f}{C_{f0}}\right), \tag{4.1}$$

where C_f is the skin-friction coefficient for the controlled flow and C_{f0} is the skin-friction coefficient for the uncontrolled flow. The skin-friction coefficient is defined as $C_f = 2\overline{\tau_w}/\rho U_b^2$, where $\overline{\tau_w}$ is the wall shear-stress averaged over homogeneous directions x and z, ρ is the density of the fluid, and $U_b(= 2U_c/3)$ is the bulk flow velocity. Figure 4.1 shows the initial response of C_f (normalized by C_{f0}) after the actuation of control. C_f begins to decrease sharply, and the rate of the initial decay is similar for all forcing amplitudes, except for $A0.15$ case. The responses of the large amplitude cases are quite interesting, for instance, the flow is not far from the relaminarization limit near $t_0 = 2000$ for the $A1.25$ case, but returns back to the turbulent state at $t_0 = 3000$. Such complex responses of skin-friction coefficients are also observed in optimal wall turbulence control at moderate optimization horizons [86].

The time of initial decay varies with the amplitude of forcing and is about 5-6 cycles ($t_0 \approx 1600$) for $A0.15$ case, and 13–14 cycles ($t_0 \approx 4000$) for $A1.25$ case. After the elapsed of the initial transient phase, the flow acquires a new quasi-stationary state, and C_f begins to oscillate

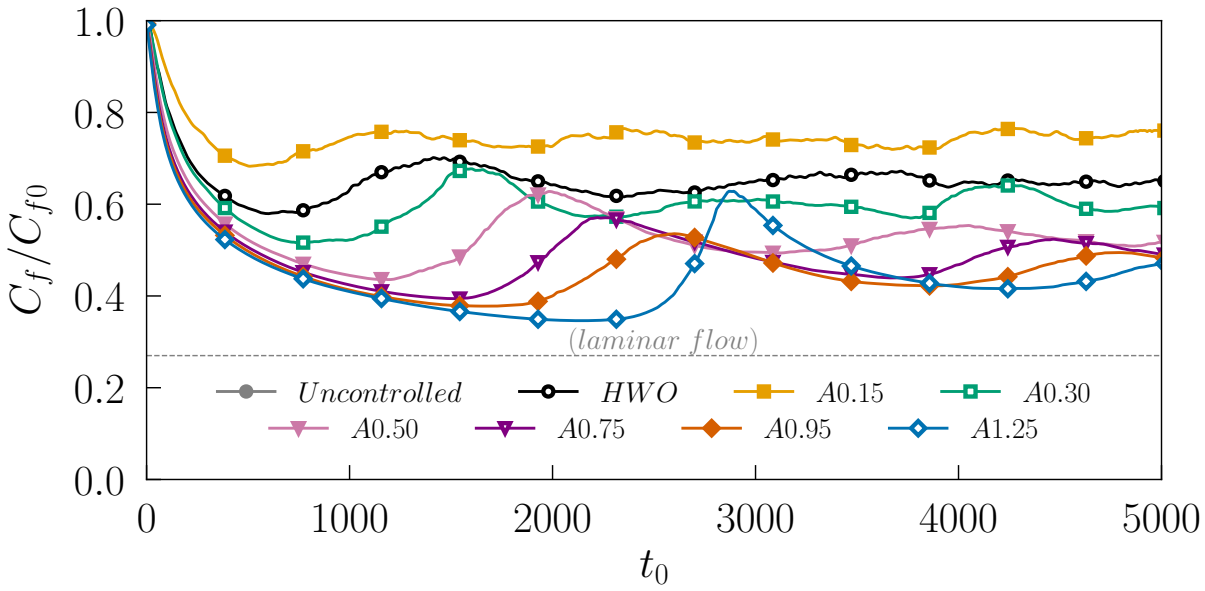

Figure 4.1: Initial response of the normalized skin-friction coefficient (C_f/C_{f0}) after the actuation of control for different forcing amplitudes. The long time averaged skin-friction coefficient for the uncontrolled case is $C_{f0} = 8.02 \times 10^{-3}$.

about a mean level. The period of oscillation of C_f differs with the amplitude of forcing, but in general it is about one order of magnitude longer than the period of forcing.

Figure 4.2 presents the level of drag reduction margins obtained for different amplitudes of forcing. The drag reduction margin obtained in the present study compares well with those of Quadrio *et al.* [6] for the travelling wave cases, showing an increasing trend with increasing amplitude of the travelling wave at fixed ω and κ (in outer units). The corresponding drag reduction margin for the simple homogeneous wall oscillation case is also included in the figure 4.2 and compared with that obtained by Quadrio *et al.* [4] and Hurst *et al.* [60] for similar forcing parameters at $\mathrm{Re}_\tau = 200$. The results included illustrate that the present simulation for the simple homogeneous wall oscillation case at close-to-optimum forcing parameters yields a drag reduction margin that is entirely compatible with those of Quadrio *et al.* [4] and Hurst *et al.* [60].

4.2 Response of the mean flow velocity

Figure 4.3 conveys the effect of forcing on the mean flow velocity profile, scaled with the local as well as reference friction velocity. Consistent with the previous studies, the mean velocity profiles show an upward shift in the logarithmic portion and thickening of the viscous sublayer when scaled with the respective friction velocities of the drag reduced flows. This behaviour is

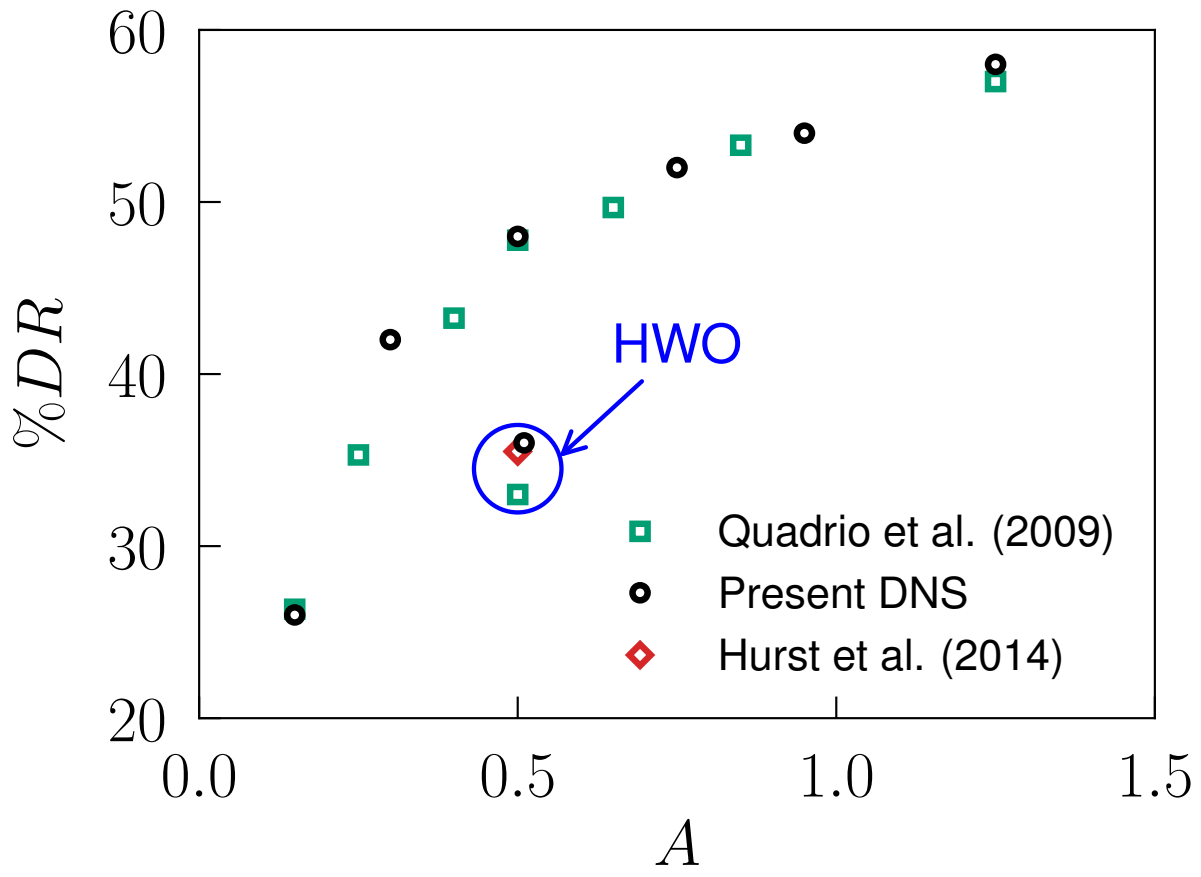

Figure 4.2: Drag reduction margin for different forcing amplitudes compared with the data of Quadrio *et al.* [6] at $\mathrm{Re}_\tau = 200$ for streamwise travelling wave forcing. The drag reduction margin for HWO case is also included and compared with the data of Quadrio *et al.* [4] and Hurst *et al.* [60].

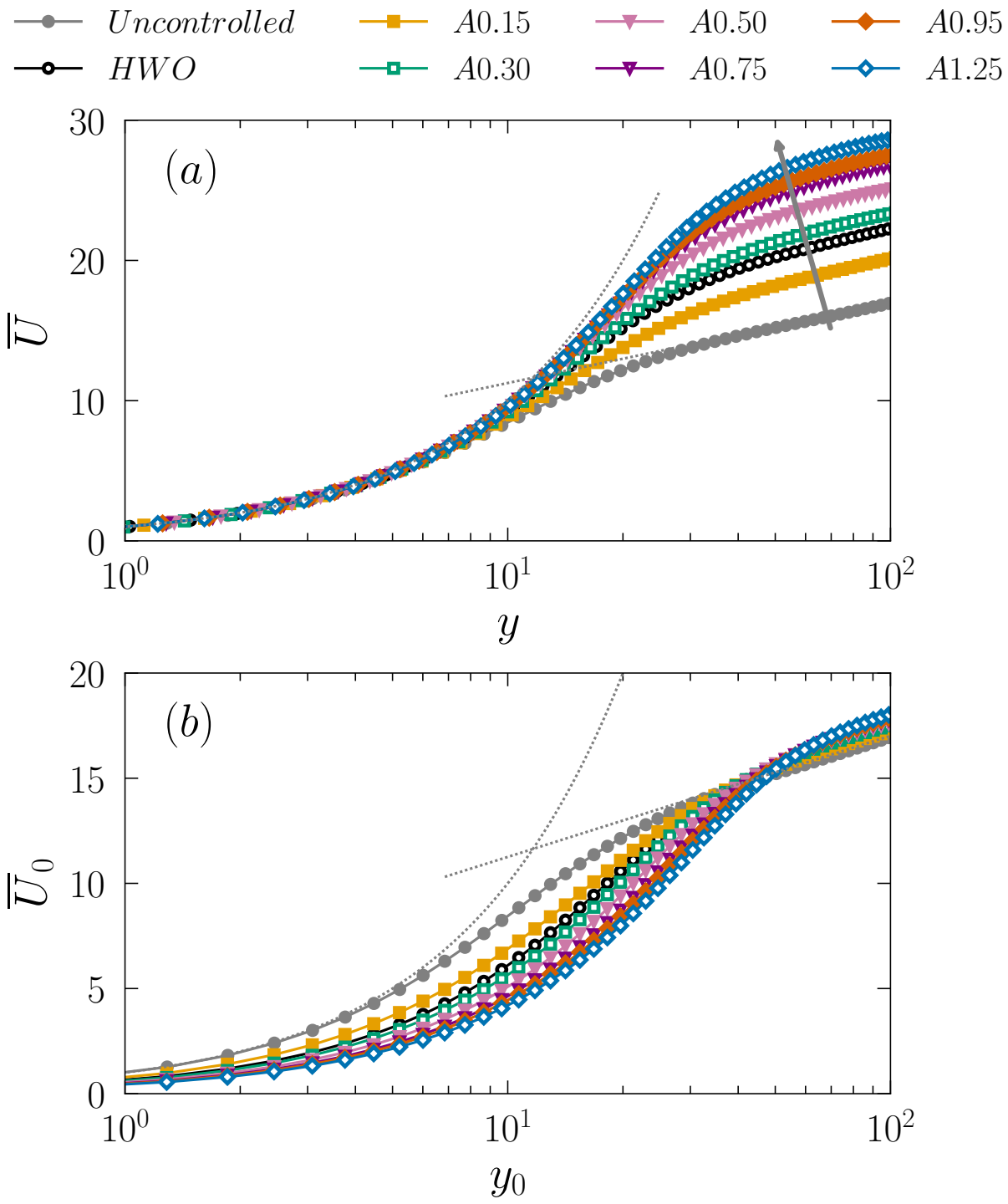

Figure 4.3: Mean flow velocity profiles for the uncontrolled and controlled cases: scaled with the (a) actual (local) friction velocities of the controlled cases; (b) friction velocity of the (reference) uncontrolled flow.

typical to drag reduction scenarios regardless of the control type — except for super-hydrophobic surfaces, where drag reduction results in thinning of the buffer layer along with a downward shift in the logarithmic region. The magnitude of the upward shift in the logarithmic portion is proportional to the DR margin [62]. Scaling with respect to the reference friction velocity brings out the fact that the major effect of forcing is to significantly lower the velocity in the near wall viscous sublayer, while the effect in the log region is a slight elevation.

4.3 Response of Reynolds stresses components

Figures 4.4-4.7 show the effect of forcing on the mean Reynolds stresses components $\overline{uu}$, $\overline{vv}$, $\overline{ww}$ and $\overline{uv}$, respectively, for the uncontrolled and controlled cases. Forcing results in a substantial decline in the streamwise component $\overline{uu}$ (figure 4.4a), especially close to the wall, reflecting a strong reduction in the near-wall streaks strength. The peak value of $\overline{uu}$ is shifted away from the wall and reflects the lifting of the quasi streamwise vortices (QSVs) [87]. An interesting feature worth noticing is that the profiles of $\overline{uu}$ approximately collapse at wall-normal locations $y > 30$, reflecting that the structural changes brought up by the control are limited to the region close to the wall. The peak value of the wall-normal component $\overline{vv}$ (figure 4.5a) progressively declines as the amplitude of the forcing is increased. Contrary to $\overline{uu}$, the location of its peak remains unaffected. It is important to stress that $\overline{vv}$ plays the primary role in the production of Reynolds shear stress $\overline{uv}$. Attenuation of $\overline{vv}$ indicates damping of sweep and ejection events that are primarily responsible for most of the turbulent kinetic energy production. Likewise, the magnitude of $\overline{uv}$ (figure 4.7a) also shows a substantial decline at all wall-normal locations, with a significant reduction close to the wall.

The response of the spanwise component $\overline{ww}$ is strikingly different, with the emergence of a second peak at $y \approx 8$ near the edge of the viscous sublayer at the largest imposed amplitude $A = 1.25$ investigated here (figure 4.6a). Despite the appearance of two production terms arising in its transport equation due to forcing (4.6), $\overline{ww}$ progressively declines at wall-normal locations $y > 20$. It is important to note that these peculiar behaviours can hardly be detected if the quantities were scaled with the friction velocity of the uncontrolled flow. To stress this point, we have also presented in figures 4.4(b), 4.5(b), 4.6(b) and 4.7(b) the profiles of Reynolds stresses, where the scaling is now with respect to the friction velocity of the uncontrolled flow $(u_{\tau 0})$. It is clearly seen that the peculiar structural modifications are hardly discernible in figure 4.6(b) in comparison to figure 4.6(a). Scaling with local inner variables results in correct non-dimensionalization and allows sorting out the structural changes of the response of the near-wall turbulence.

To summarize, globally, the profiles of Reynolds stresses components approximately collapse for $A \geq 0.75$ when scaled with the local friction velocity, except the spanwise component $\overline{ww}$. The streamwise component $\overline{uu}$ is significantly damped close to the wall, reflecting a strong

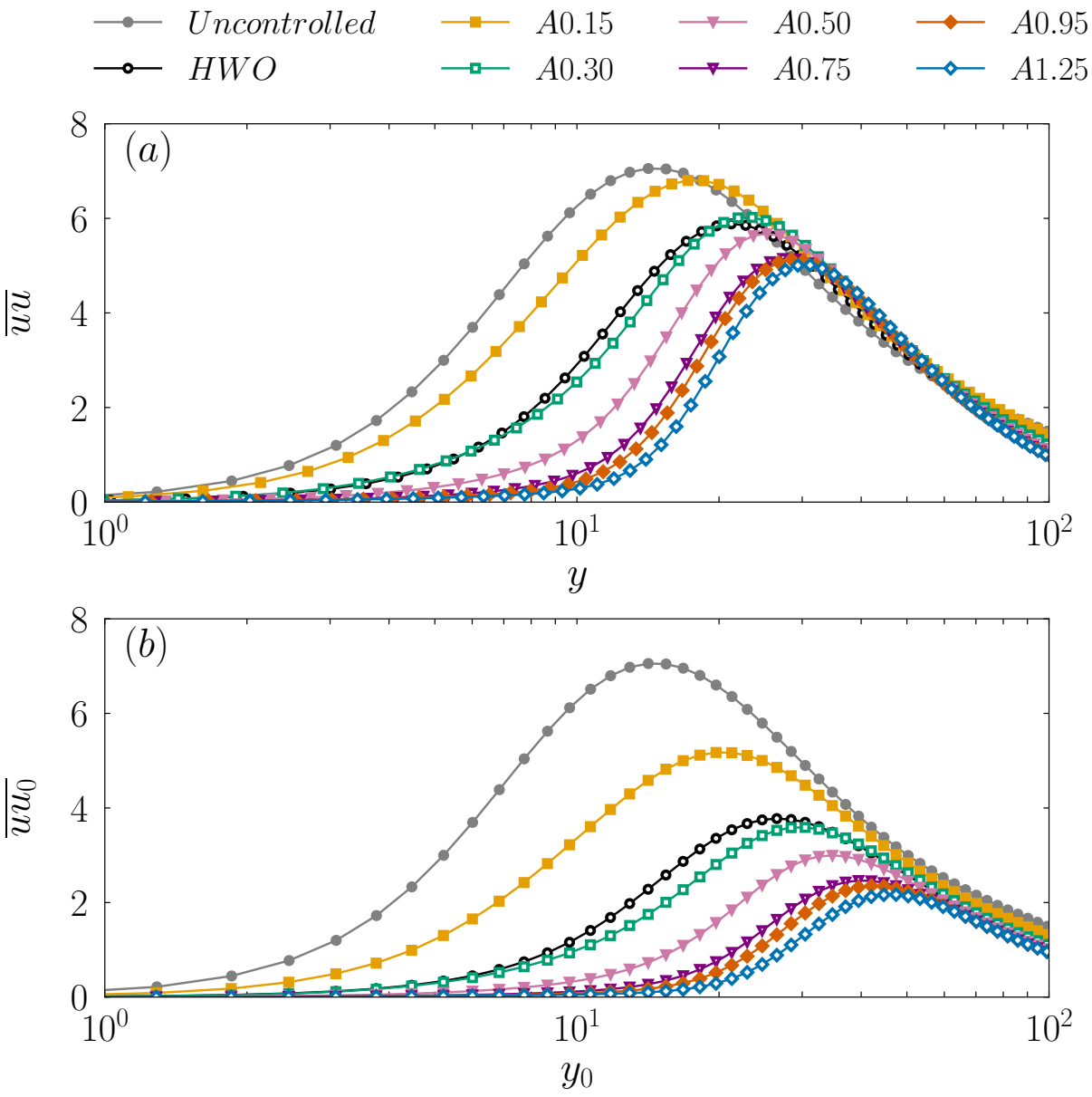

Figure 4.4: Profiles of the streamwise normal component ($\overline{uu}$) of Reynolds stress tensor, scaled with the friction velocity of (a) controlled and (b) uncontrolled flow.

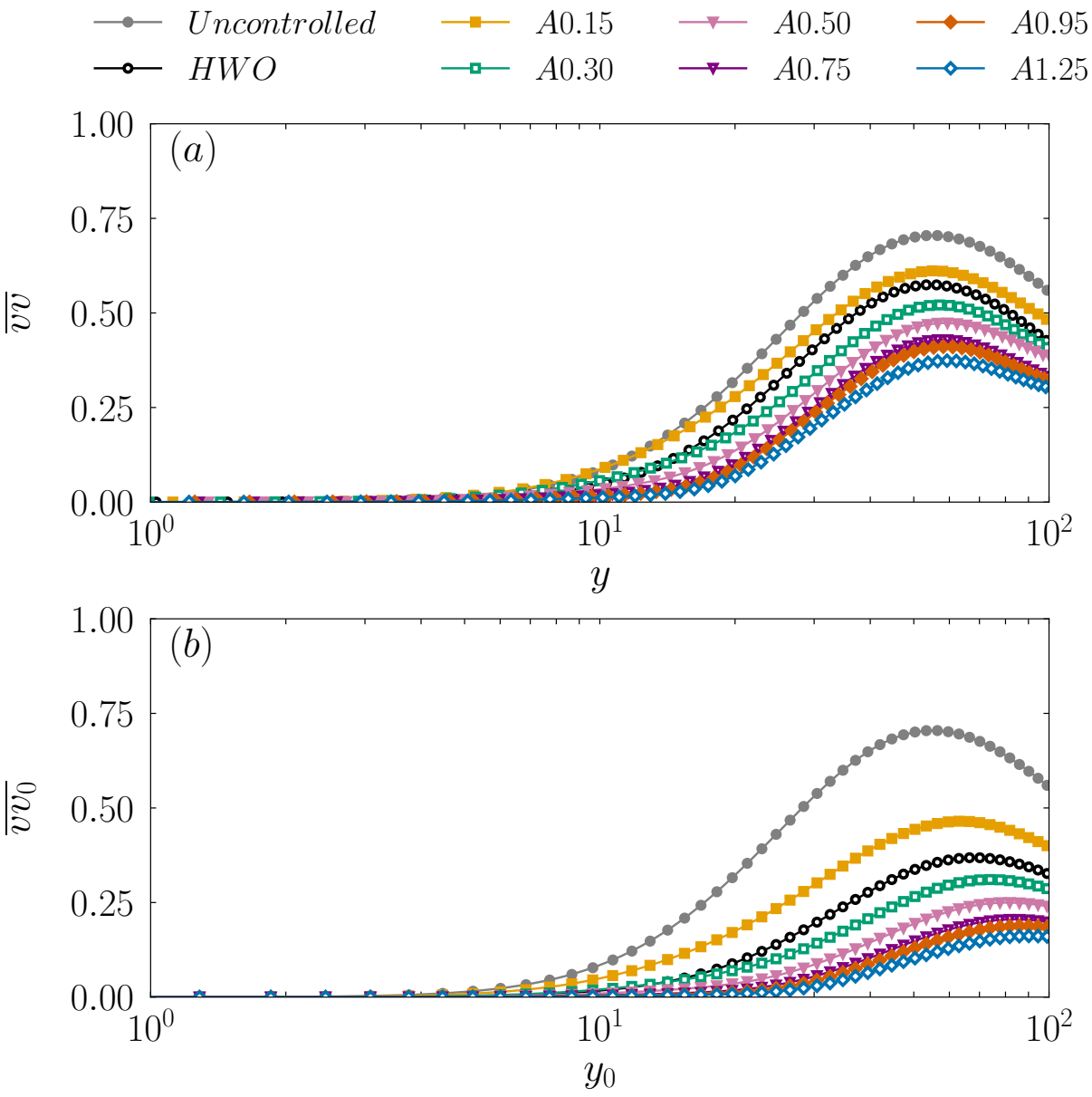

Figure 4.5: Profiles of the wall-normal normal component ($\overline{vv}$) of Reynolds stress tensor, scaled with the friction velocity of (a) controlled and (b) uncontrolled flow.

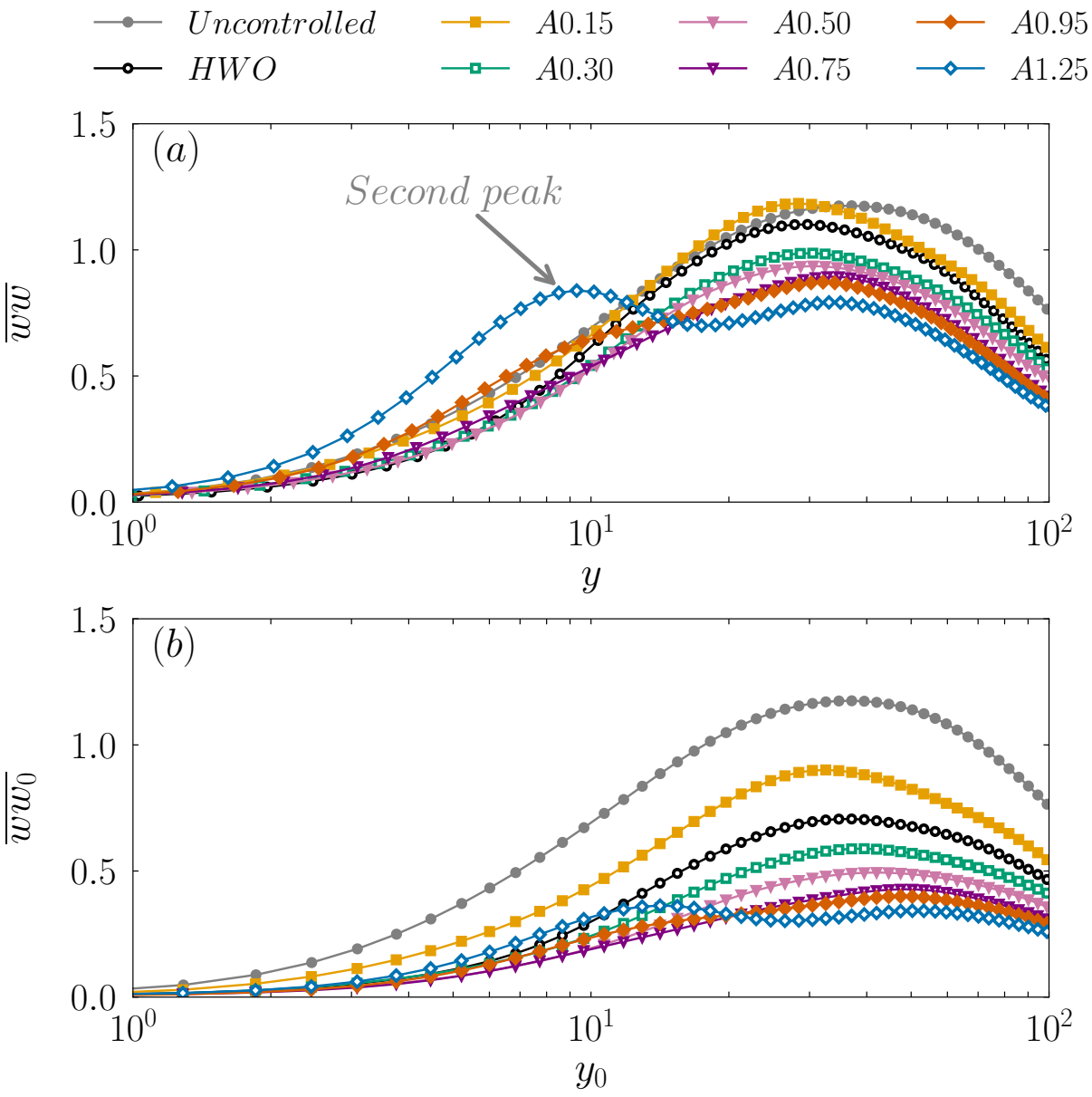

Figure 4.6: Profiles of the spanwise normal component ($\overline{ww}$) of Reynolds stress tensor, scaled with the friction velocity of (a) controlled and (b) uncontrolled flow.

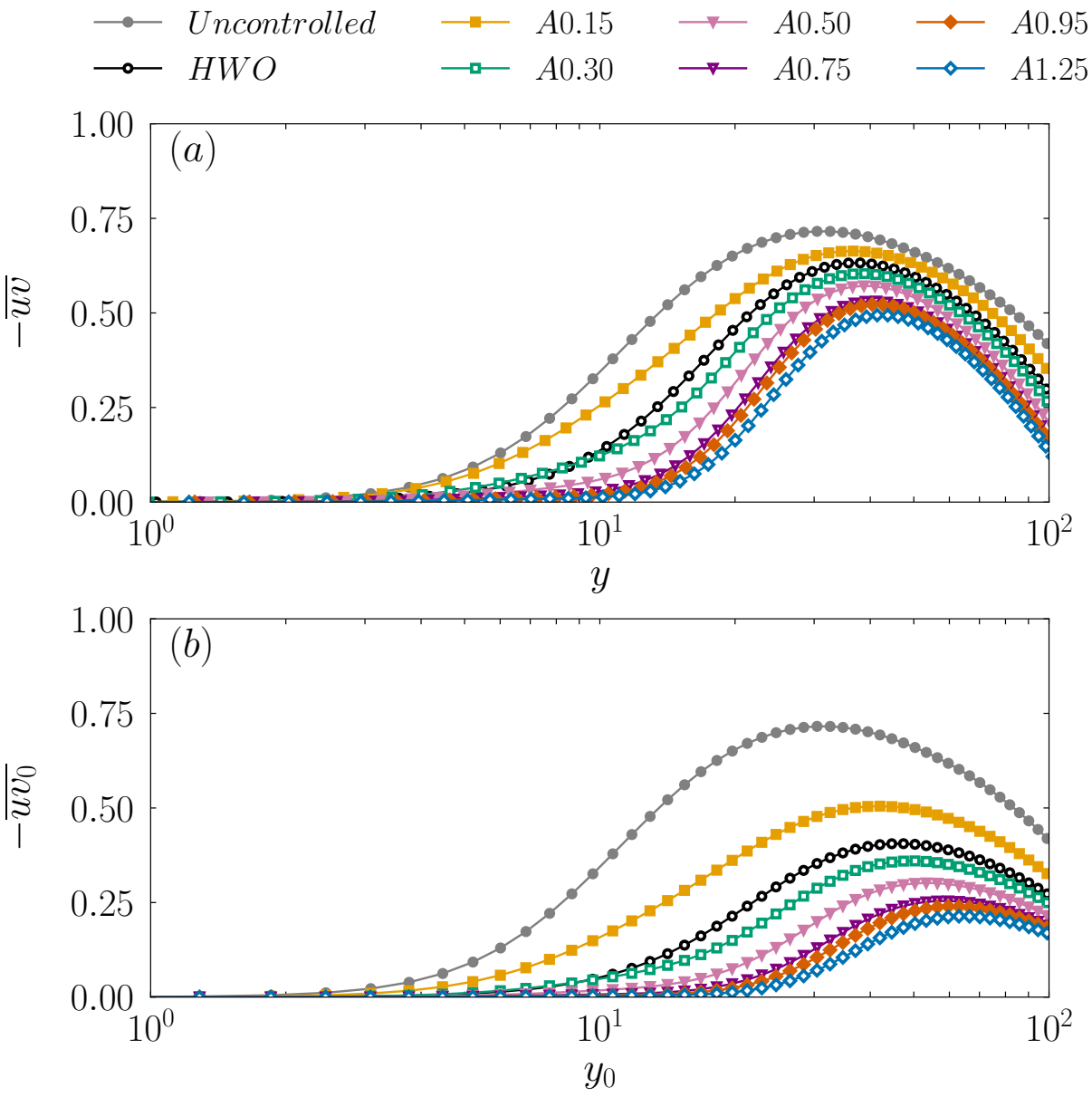

Figure 4.7: Profiles of the Reynolds shear stress ($\overline{uv}$), scaled with the friction velocity of (a) controlled and (b) uncontrolled flow.

reduction in the near-wall streaks strength. The peak of $\overline{uu}$ and $\overline{uv}$ shifts towards the edge of the buffer layer at $y \approx 30$ (figures 4.4*a* and 4.7*a*). The profile of spanwise component $\overline{ww}$ for the $A1.25$ case exhibits a second peak close to the wall at $y \approx 8$; this unique feature is explained in the following section. Discarding the appearance of the second peak in $\overline{ww}$ at $A = 1.25$, the wall-normal locations of the peak values of $\overline{vv}$ and $\overline{ww}$ are not altered by the STW. Again, all these quantities were scaled using the local friction velocity. When scaled with the friction velocity of the uncontrolled flow, all the peak values are shifted away from the wall in proportion to $u_{\tau 0}/u_\tau = \sqrt{1/(1-DR)}$.

4.4 Mean Reynolds stresses budgets

The transport equation for the streamwise component ($\overline{uu}$) reads

$$\underbrace{\overbrace{-2\overline{\langle uu\rangle\frac{\partial\widetilde{U}}{\partial x}}}^{\overline{P^1_{uu}}}\overbrace{-2\overline{\langle uv\rangle\frac{\partial\widetilde{U}}{\partial y}}}^{\overline{P^2_{uu}}}\overbrace{-2\overline{uv}\frac{d\overline{U}}{dy}}^{\overline{P^3_{uu}}}}_{\overline{P_{uu}}}-\underbrace{\left(\overbrace{\frac{d\overline{\langle uu\rangle\widetilde{V}}}{dy}}^{\overline{T^1_{uu}}}+\overbrace{\frac{d\overline{uuv}}{dy}}^{\overline{T^2_{uu}}}\right)}_{\overline{T_{uu}}}\underbrace{-2u\overline{\frac{\partial p}{\partial x}}}_{\overline{\Pi_{uu}}}+\underbrace{\frac{d^2\overline{uu}}{dy^2}}_{\overline{D_{uu}}}\underbrace{-2\left(\overline{\frac{\partial u}{\partial x}\frac{\partial u}{\partial x}}+\overline{\frac{\partial u}{\partial y}\frac{\partial u}{\partial y}}+\overline{\frac{\partial u}{\partial z}\frac{\partial u}{\partial z}}\right)}_{\overline{\varepsilon_{uu}}}=0. \tag{4.2}$$

The transport equation for the wall-normal component ($\overline{vv}$) reads

$$\underbrace{\overbrace{-2\overline{\langle uv\rangle\frac{\partial\widetilde{V}}{\partial x}}}^{\overline{P^1_{vv}}}\overbrace{-2\overline{\langle vv\rangle\frac{\partial\widetilde{V}}{\partial y}}}^{\overline{P^2_{vv}}}}_{\overline{P_{vv}}}-\underbrace{\left(\overbrace{\frac{d\overline{\langle vv\rangle\widetilde{V}}}{dy}}^{\overline{T^1_{vv}}}+\overbrace{\frac{d\overline{vvv}}{dy}}^{\overline{T^2_{vv}}}\right)}_{\overline{T_{vv}}}\underbrace{-2v\overline{\frac{\partial p}{\partial y}}}_{\overline{\Pi_{vv}}}+\underbrace{\frac{d^2\overline{vv}}{dy^2}}_{\overline{D_{vv}}}\underbrace{-2\left(\overline{\frac{\partial v}{\partial x}\frac{\partial v}{\partial x}}+\overline{\frac{\partial v}{\partial y}\frac{\partial v}{\partial y}}+\overline{\frac{\partial v}{\partial z}\frac{\partial v}{\partial z}}\right)}_{\overline{\varepsilon_{vv}}}=0. \tag{4.3}$$

The transport equation for the spanwise component ($\overline{ww}$) reads

$$\underbrace{\overbrace{-2\overline{\langle uw\rangle\frac{\partial\widetilde{W}}{\partial x}}}^{\overline{P^1_{ww}}}\overbrace{-2\overline{\langle vw\rangle\frac{\partial\widetilde{W}}{\partial y}}}^{\overline{P^2_{ww}}}}_{\overline{P_{ww}}}-\underbrace{\left(\overbrace{\frac{d\overline{\langle ww\rangle}\widetilde{V}}{dy}}^{\overline{T^1_{ww}}}+\overbrace{\frac{d\overline{wwv}}{dy}}^{\overline{T^2_{ww}}}\right)}_{\overline{T_{ww}}}\underbrace{-2w\overline{\frac{\partial p}{\partial z}}}_{\overline{\Pi_{ww}}}$$
$$+\underbrace{\frac{d^2\overline{ww}}{dy^2}}_{\overline{D_{ww}}}\underbrace{-2\left(\overline{\frac{\partial w}{\partial x}\frac{\partial w}{\partial x}}+\overline{\frac{\partial w}{\partial y}\frac{\partial w}{\partial y}}+\overline{\frac{\partial w}{\partial z}\frac{\partial w}{\partial z}}\right)}_{\overline{\varepsilon_{ww}}}=0. \tag{4.4}$$

Finally, the transport equation for the Reynolds shear stress ($\overline{uv}$) reads

$$\underbrace{\overbrace{-\langle uv\rangle\frac{\partial\widetilde{U}}{\partial x}}^{\overline{P^1_{uv}}}\overbrace{-\langle vv\rangle\frac{\partial\widetilde{U}}{\partial y}}^{\overline{P^2_{uv}}}\overbrace{-\langle uu\rangle\frac{\partial\widetilde{V}}{\partial x}}^{\overline{P^3_{uv}}}\overbrace{-\langle vv\rangle\frac{\partial\widetilde{V}}{\partial y}}^{\overline{P^4_{uv}}}\overbrace{-\overline{vv}\frac{d\overline{U}}{dy}}^{\overline{P^5_{uv}}}}_{\overline{P_{uv}}}\underbrace{-\left(\overbrace{\frac{d\overline{\langle uv\rangle}\widetilde{V}}{dy}}^{\overline{T^1_{uv}}}+\overbrace{\frac{d\overline{uvv}}{dy}}^{\overline{T^2_{uv}}}\right)}_{\overline{T_{uv}}}$$
$$\underbrace{-\left(\overline{u\frac{\partial p}{\partial y}}+\overline{v\frac{\partial p}{\partial x}}\right)}_{\overline{\Pi_{uv}}}+\underbrace{\frac{d^2\overline{uv}}{dy^2}}_{\overline{D_{uv}}}\underbrace{-2\left(\overline{\frac{\partial u}{\partial x}\frac{\partial v}{\partial x}}+\overline{\frac{\partial u}{\partial y}\frac{\partial v}{\partial y}}+\overline{\frac{\partial u}{\partial z}\frac{\partial v}{\partial z}}\right)}_{\overline{\varepsilon_{uv}}}=0. \tag{4.5}$$

Besides the classical terms, quantities directly related to the STW emerge in the transport equations. These extra terms account for the interaction between the phase-averaged Reynolds stresses and the gradients of the periodic fluctuations due to forcing. All the extra terms emerging from the wall-normal and streamwise gradients of $\langle U_i\rangle$ (where $i=1,2,3$ denote streamwise, wall-normal and spanwise direction, respectively) are negligible compared to the other terms in the overall budget of Reynolds stresses components, except for those intervening in the spanwise component $\overline{ww}$ induced by $\partial\widetilde{W}/\partial x$ and $\partial\widetilde{W}/\partial y$, as shown in figure 4.8. Recall that, the production term in the transport equation of $\overline{ww}$ is zero for the canonical (uncontrolled) channel flow. Hence, the level of $\overline{ww}$ is maintained solely by the velocity-pressure gradient term $\overline{\Pi_{ww}}=\overline{-2w\partial p/\partial z}$, the role of which is to extract energy from $\overline{uu}$ and transfer it to $\overline{ww}$. However, under the presence of STW, two production terms coming from the streamwise and wall-normal gradients of $\widetilde{W}$ emerge in the transport equation of $\overline{ww}$, and the total production term for the spanwise component reads

$$\overline{P_{ww}}=\underbrace{\overline{-2\langle wu\rangle\frac{\partial\widetilde{W}}{\partial x}}}_{\overline{P^1_{ww}}}\underbrace{\overline{-2\langle wv\rangle\frac{\partial\widetilde{W}}{\partial y}}}_{\overline{P^2_{ww}}}. \tag{4.6}$$

These terms are denoted by $\overline{P^1_{ww}}$ and $\overline{P^2_{ww}}$, respectively, in the above equation 4.6. Curiously enough, the total production $\overline{P_{ww}}$ increases in the low buffer layer, with a maximum at $y\approx 8$ for

cases with amplitudes $A > 0.50$, as seen in figure $4.8(c)$. This explains the emergence of the second peak in $\overline{ww}$ observed in figure $4.6(a)$ at the same wall-normal location.

The production term $\overline{P^1_{ww}}$ is negative for small imposed amplitudes $A \leq 0.50$ (see figure $4.8a$), but $\overline{P^2_{ww}}$, which is strictly positive at all wall-normal locations (figure $4.8b$), largely overcomes the total mean production $\overline{P_{ww}}$ in the viscous and low buffer layers. Both, $\langle P^1_{ww} \rangle$ and $\langle P^2_{ww} \rangle$ are strongly modulated and reach very large values during the phase-cycle. These peculiar behaviours will be further elucidated in the section 4.5, where we discuss the phase-wise variations of transport quantities. At this stage, it is important to point out, in particular, the response of the velocity-pressure gradient correlations $\overline{\Pi_{uu}}$ and $\overline{\Pi_{ww}}$, shown in figure $4.10(c)$ and $4.9(c)$, respectively. It is seen that the increase in $\overline{P_{ww}}$ (figure $4.9a$) is accompanied by a strong decrease in the velocity-pressure gradient term $\overline{\Pi_{ww}}$. The latter is entirely annihilated within the low buffer and viscous sublayers $y < 8$ when the imposed amplitude is beyond $A > 0.5$ (figure $4.9c$). Remark that, in the uncontrolled channel flow $\overline{\Pi_{ww}}$ is large in the buffer layer with a maximum at $y \approx 10$, as the velocity-pressure gradient term is the main source term in the transport equation of $\overline{ww}$. In canonical wall-bounded turbulent flows, the inter-component transfer $\overline{uu} \rightarrow \overline{ww}$ is established through the velocity-pressure gradient correlations $\overline{\Pi_{uu}} \rightarrow \overline{\Pi_{ww}}$. This process fades away next to the wall up to the top of the low buffer layer in the presence of STW of large enough amplitudes $A > 0.5$. Indeed, $\overline{\Pi_{uu}}$ progressively goes to zero as amplitude increases in concordance with $\overline{\Pi_{ww}}$ (figures $4.10c$ and $4.9e$). Thus, interestingly enough, the communication between $\overline{uu}$ and $\overline{ww}$ is cut-off at $y < 8$, and as a consequence the spanwise turbulent intensity $\overline{ww}$ evolves somewhat freely, with a local equilibrium between the production and dissipation $\overline{P_{ww}} \approx -\overline{\varepsilon_{ww}}$, in a rough sense (figure 4.9), with the slight differences being compensated by the turbulent transport $\overline{T_{ww}}$ and viscous diffusion $\overline{D_{ww}}$, shown in figures $4.9(d)$ and $4.9(e)$, respectively.

Unlike $\overline{ww}$, the net production term $\overline{P_{vv}}$ in the transport equation of the wall-normal component $\overline{vv}$ is zero in the flows altered by STW (figure $4.11a$). Hence, it is fair to state that the mechanism responsible for maintaining the level of $\overline{vv}$ is similar to that for the uncontrolled case, i.e., inter-component energy transfer $\overline{uu} \rightarrow \overline{vv}$ through $\overline{\Pi_{uu}} \rightarrow \overline{\Pi_{vv}}$. Similar to what observed for $\overline{ww}$ transport, the communication $\overline{uu} \rightarrow \overline{vv}$ fades away in the low buffer layer as $\overline{\Pi_{vv}} \sim \overline{\Pi_{uu}} \approx 0$ for large imposed amplitudes of STW, resulting in a strong decline in $\overline{vv}$ close to the wall, as seen in figure 4.5. Overall, as seen in figure 4.11, the budget of $\overline{vv}$ is dominated by the velocity-pressure gradient $\overline{\Pi_{vv}}$ and dissipation $\overline{\varepsilon_{vv}}$. Globally, the profiles of $\overline{\Pi_{vv}}$ and $\overline{\varepsilon_{vv}}$ approximately collapse for large imposed amplitudes $A > 0.50$ of the STW. As the production of shear stress $\overline{P_{uv}}$ is directly linked to $\overline{vv}$, such a collapse is expected. It is pertinent to stress here again that these peculiar behaviours arise upon scaling with the local inner variables. The response of the $\overline{vv}$ transport to STW is quite similar to that observed in the simple homogeneous wall oscillations control [38].

The transport of Reynolds shear stress $\overline{uv}$ is dominated by the production $\overline{P_{uv}}$ and the velocity-pressure gradient $\overline{\Pi_{uv}}$ terms (figure 4.12). The role of $\overline{\Pi_{uv}}$ is to reduce the magnitude of $\overline{uv}$. As forcing results in a strong decline in $\overline{vv}$, consequently, $\overline{P_{uv}}$ drops drastically at large imposed

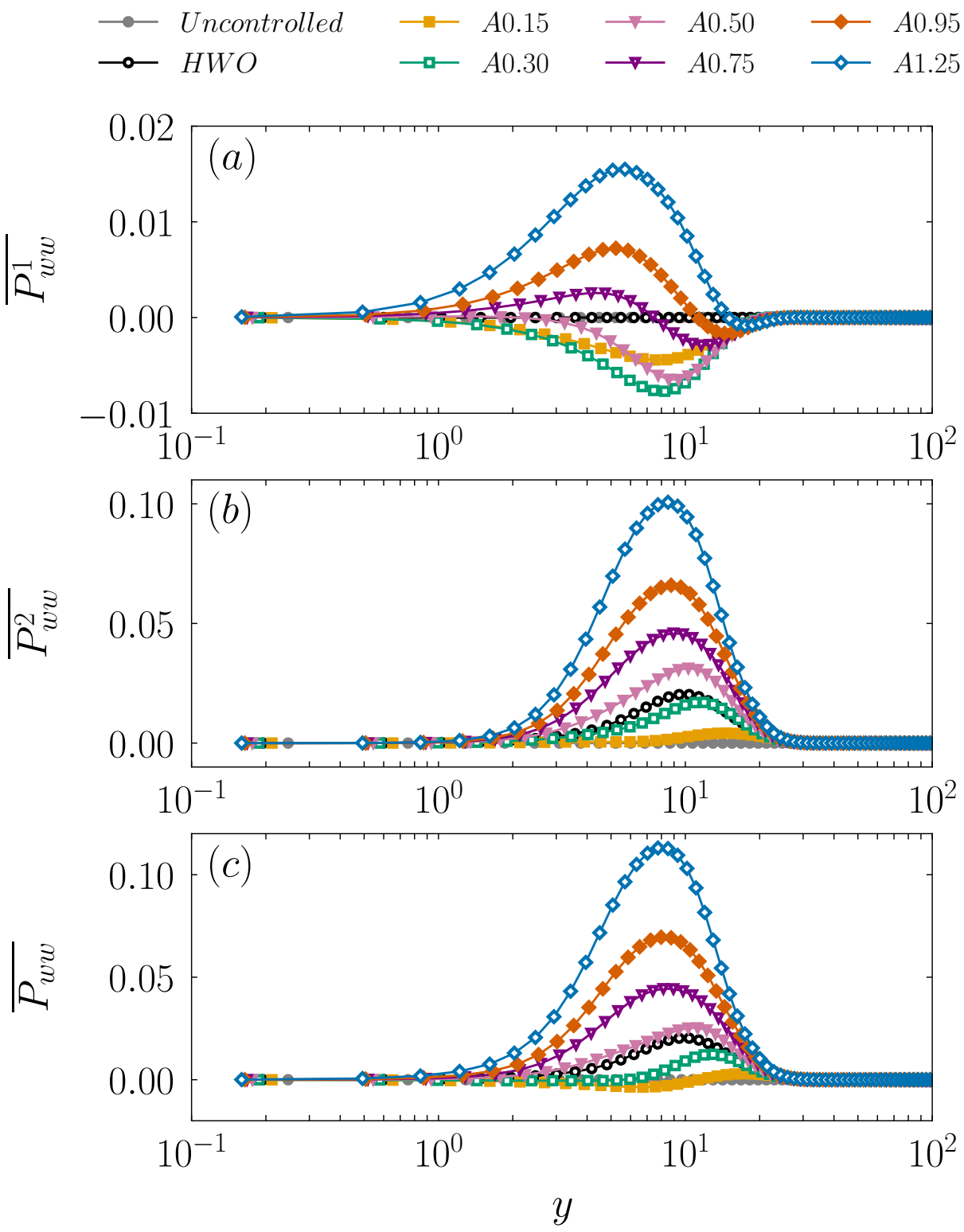

Figure 4.8: Production terms: (a) $\overline{P^1_{ww}} = -2\overline{\langle wu\rangle \partial \widetilde{W}/\partial x}$, (b) $\overline{P^2_{ww}} = -2\overline{\langle wv\rangle \partial \widetilde{W}/\partial y}$, and (c) the total production term $\overline{P_{ww}}$ appearing in the transport equation of spanwise Reynolds stress component $\overline{ww}$.

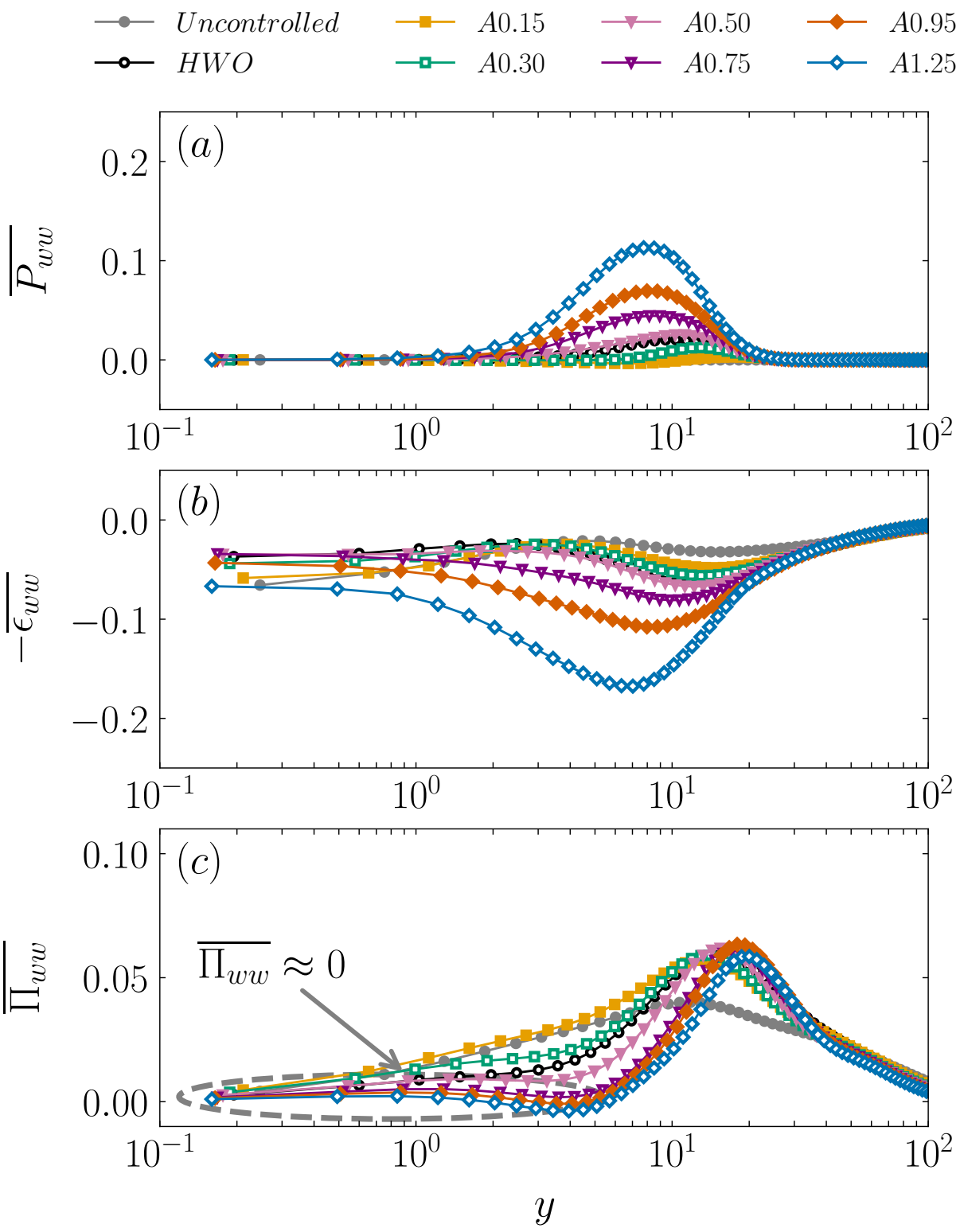

Figure 4.9: Wall-normal distributions of terms appearing in the transport equations of the spanwise Reynolds stress component $\overline{ww}$: (a) Production $\overline{P_{ww}}$, (b) dissipation $\overline{\varepsilon_{ww}}$, (c) velocity-pressure gradient $\overline{\Pi_{ww}}$, (*cont.*)

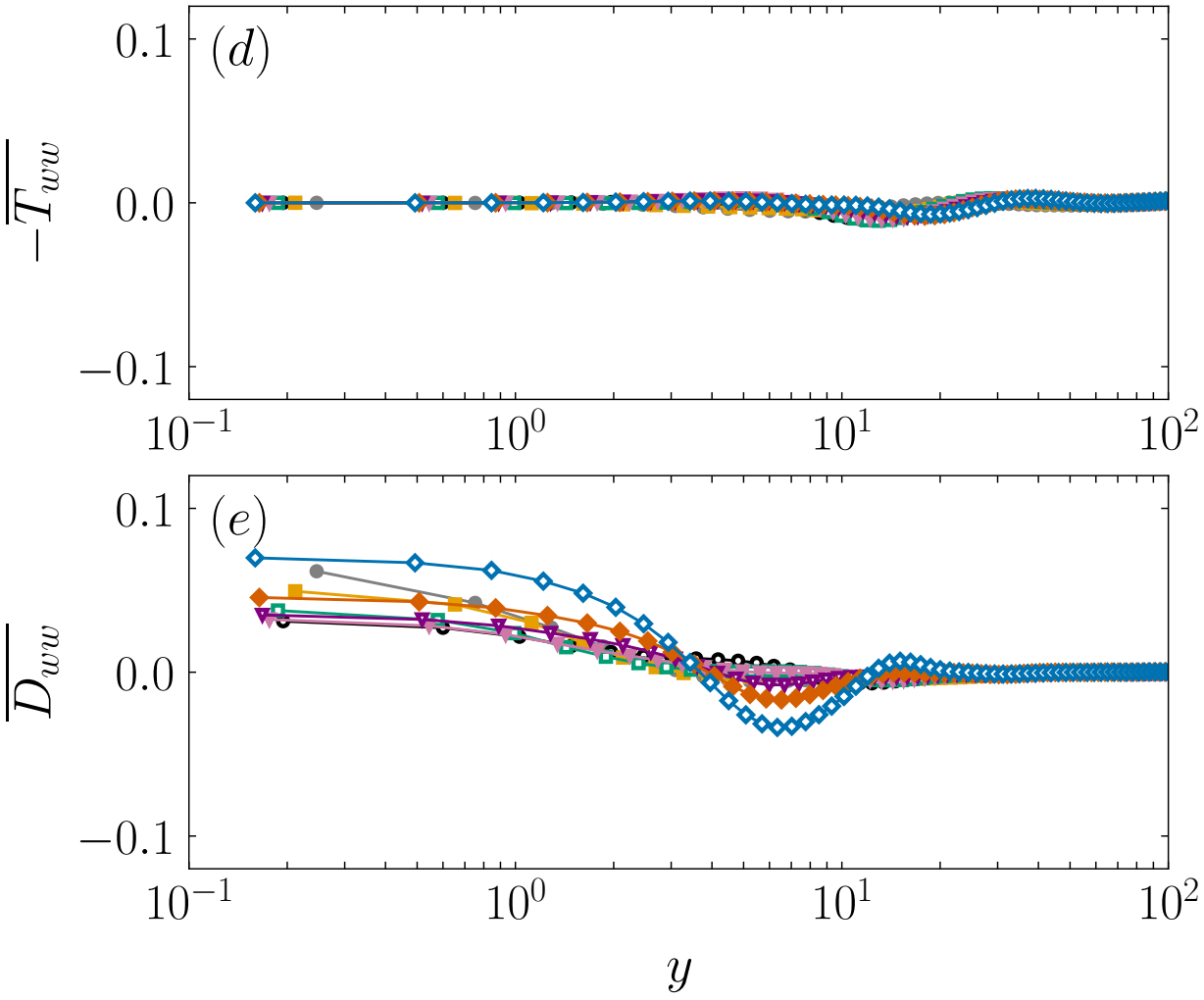

Figure 4.9: (d) turbulent diffusion $\overline{T_{ww}}$, and (e) diffusion term $\overline{D_{ww}}$.

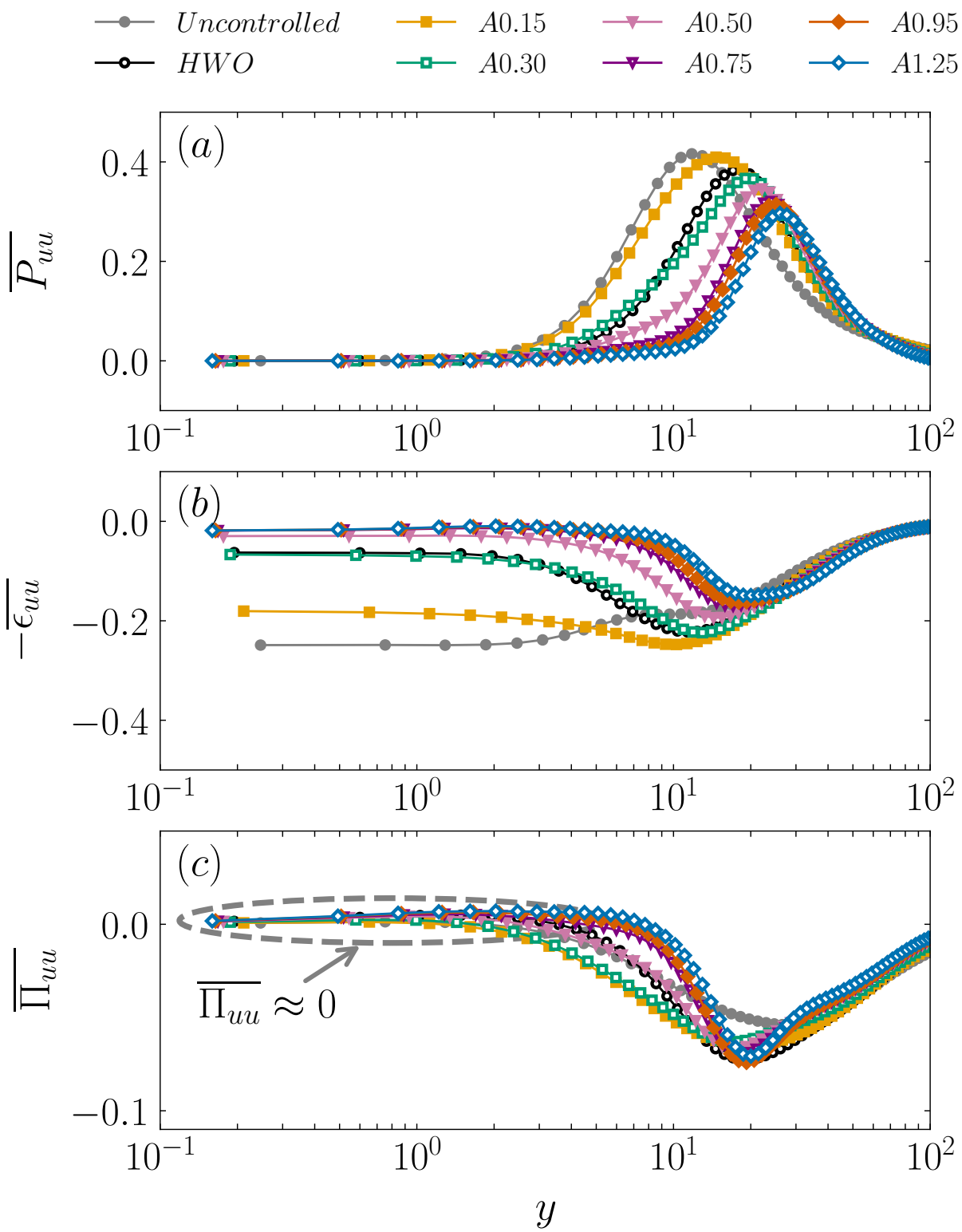

Figure 4.10: Wall-normal distributions of terms appearing in the transport equations of the streamwise Reynolds stress component $\overline{uu}$: (a) Production $\overline{P_{uu}}$, (b) dissipation $\overline{\varepsilon_{uu}}$, (c) velocity-pressure gradient $\overline{\Pi_{uu}}$, (*cont.*)

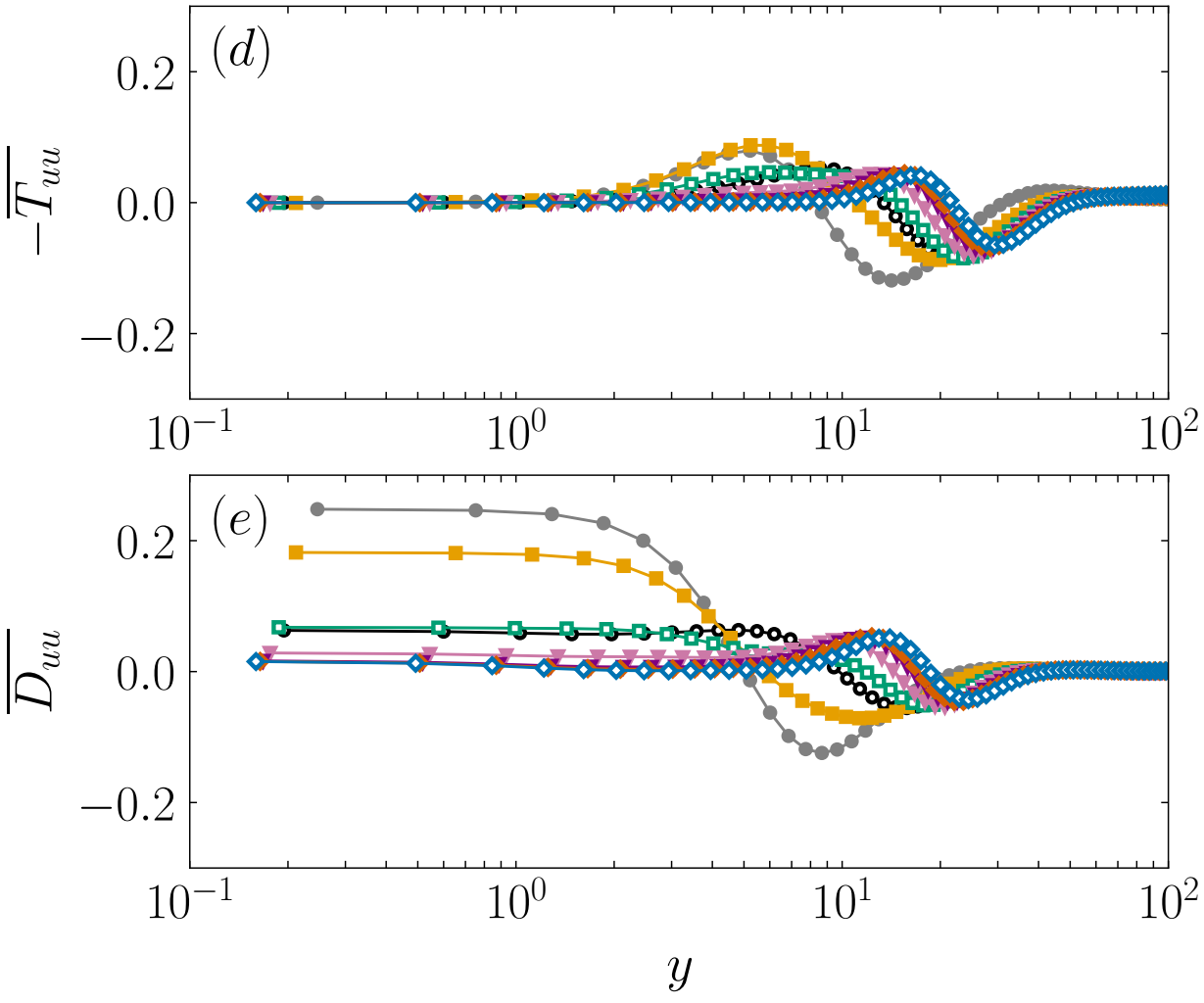

Figure 4.10: (d) turbulent diffusion $\overline{T_{uu}}$, and (e) diffusion term $\overline{D_{uu}}$.

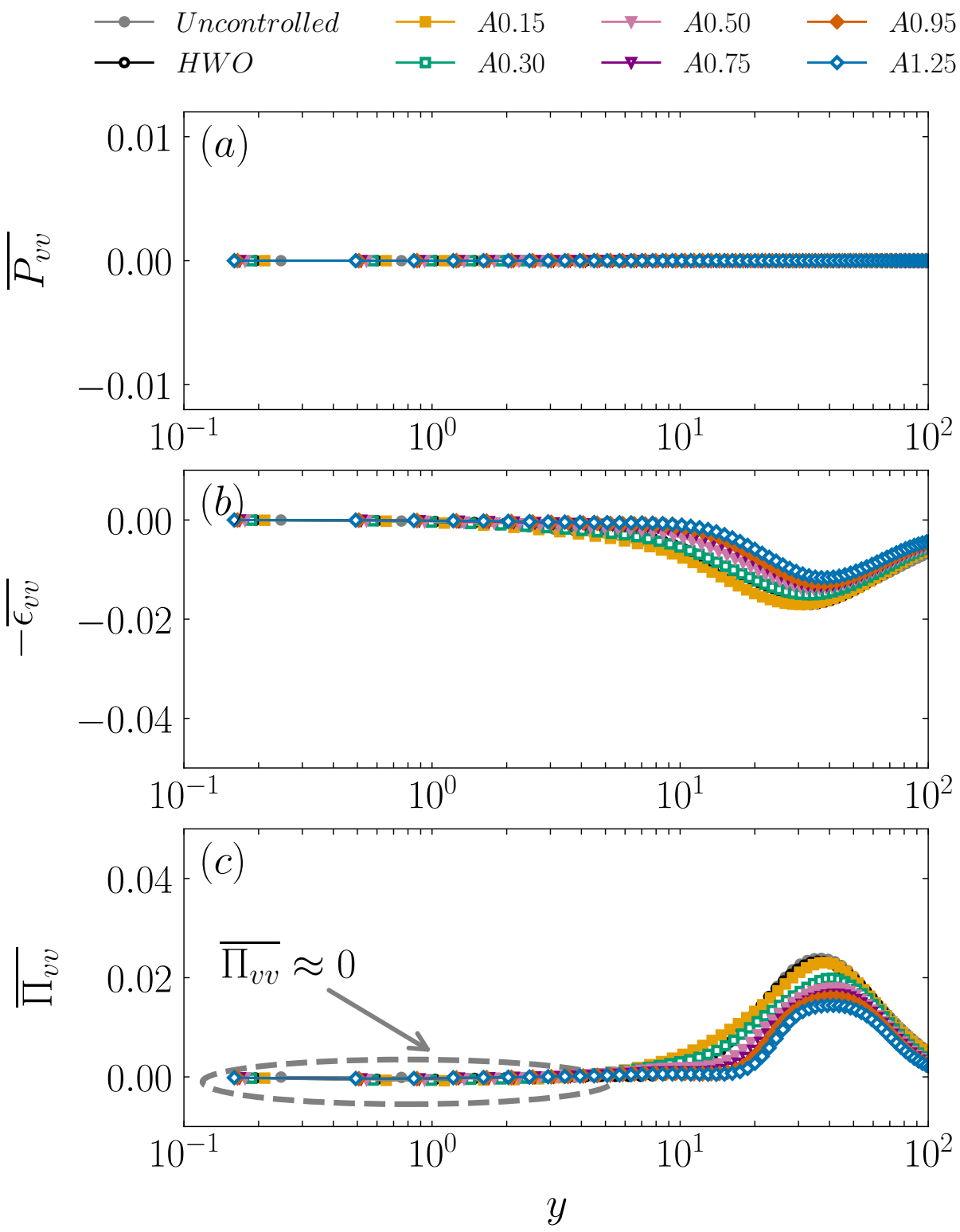

Figure 4.11: Wall-normal distributions of terms appearing in the transport equations of the wall-normal Reynolds stress component $\overline{vv}$: (a) Production $\overline{P_{vv}}$, (b) dissipation $\overline{\varepsilon_{vv}}$, (c) velocity-pressure gradient $\overline{\Pi_{vv}}$, (*cont.*)

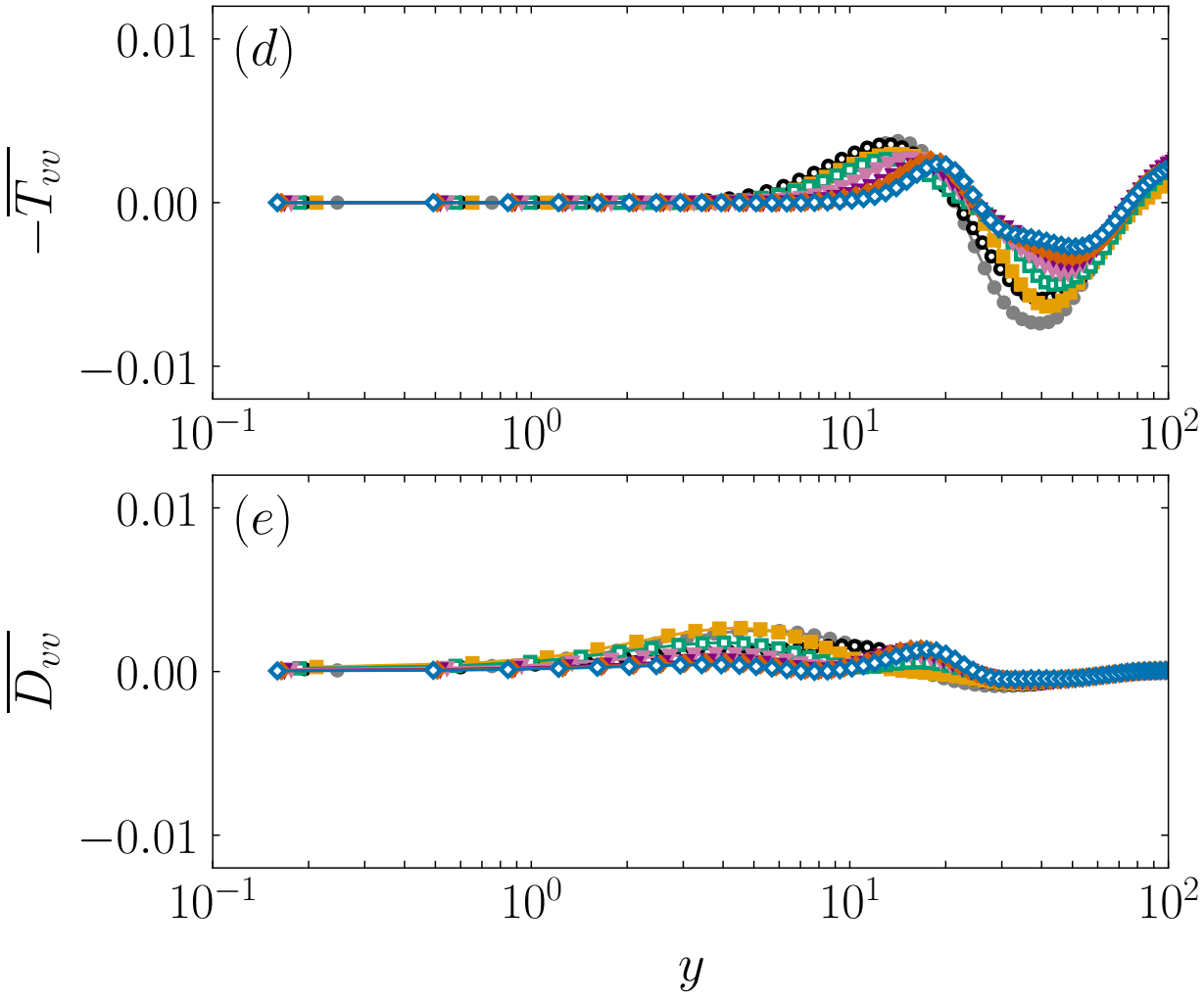

Figure 4.11: (d) turbulent diffusion $\overline{T_{vv}}$, and (e) diffusion term $\overline{D_{vv}}$.

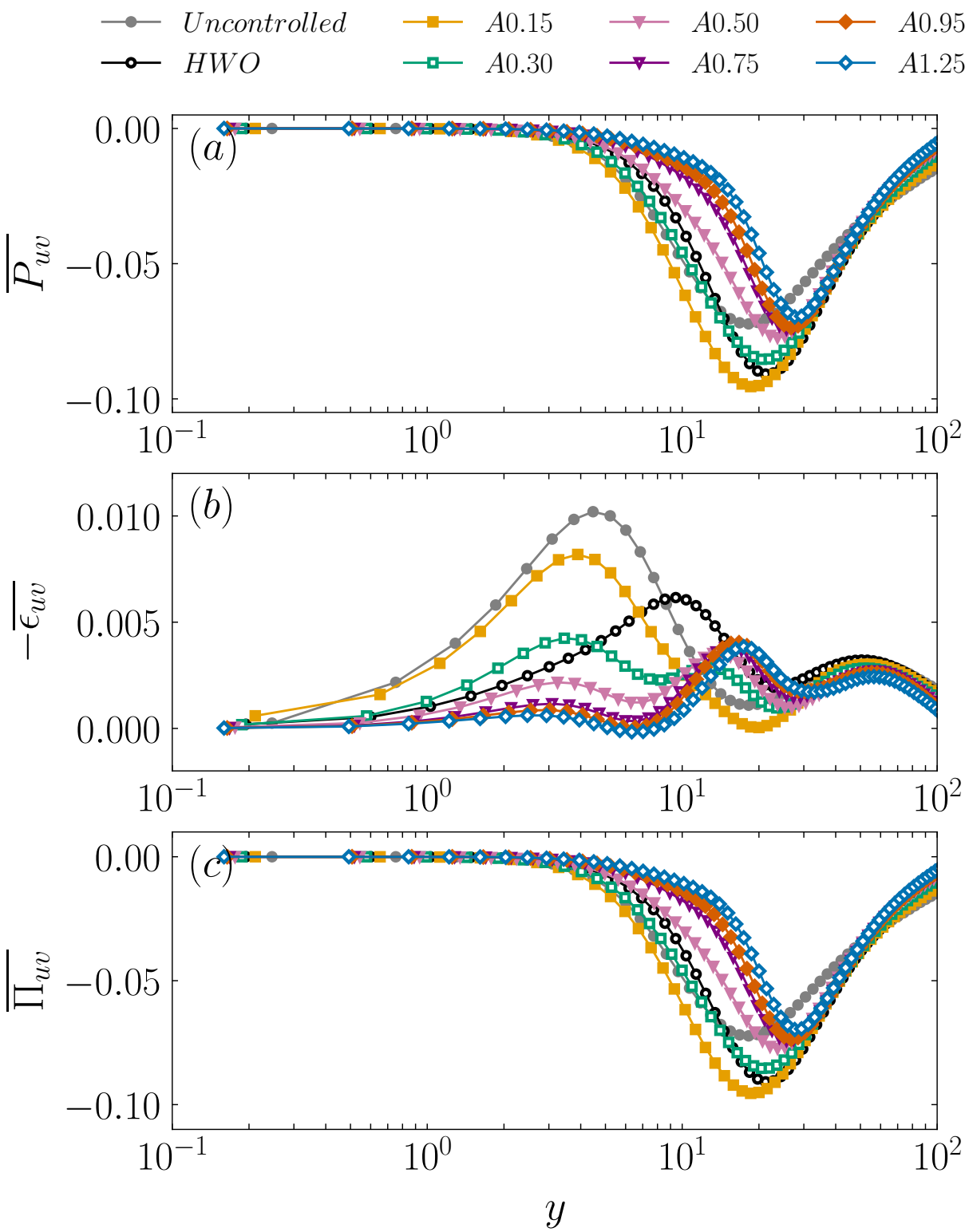

Figure 4.12: Wall-normal distributions of terms appearing in the transport equations of the Reynolds shear stress $\overline{uv}$: (a) Production $\overline{P_{uv}}$, (b) dissipation $\overline{\varepsilon_{uv}}$, (c) velocity-pressure gradient $\overline{\Pi_{uv}}$, (*cont.*)

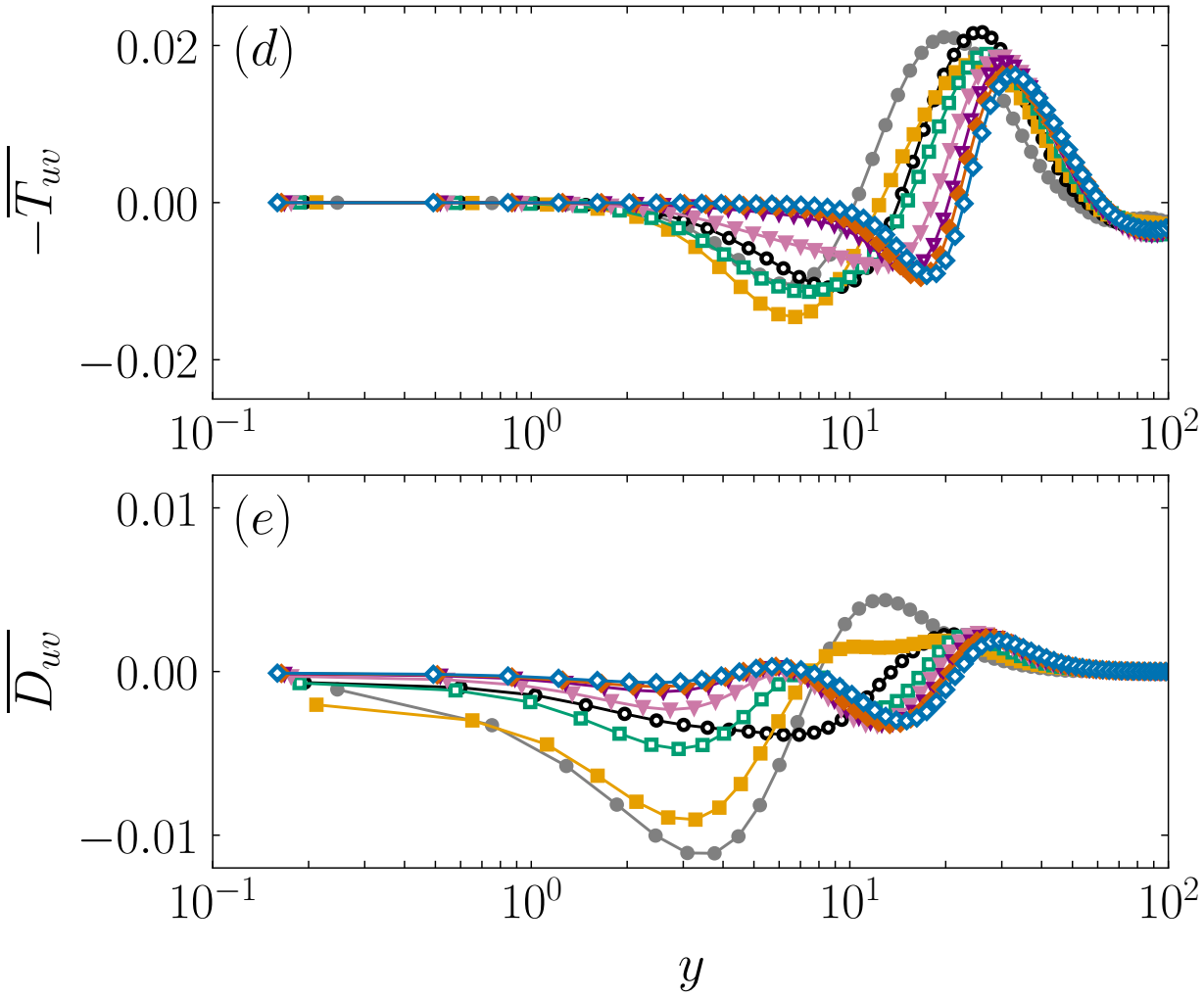

Figure 4.12: (d) turbulent diffusion $\overline{T_{uv}}$, and (e) diffusion term $\overline{D_{uv}}$.

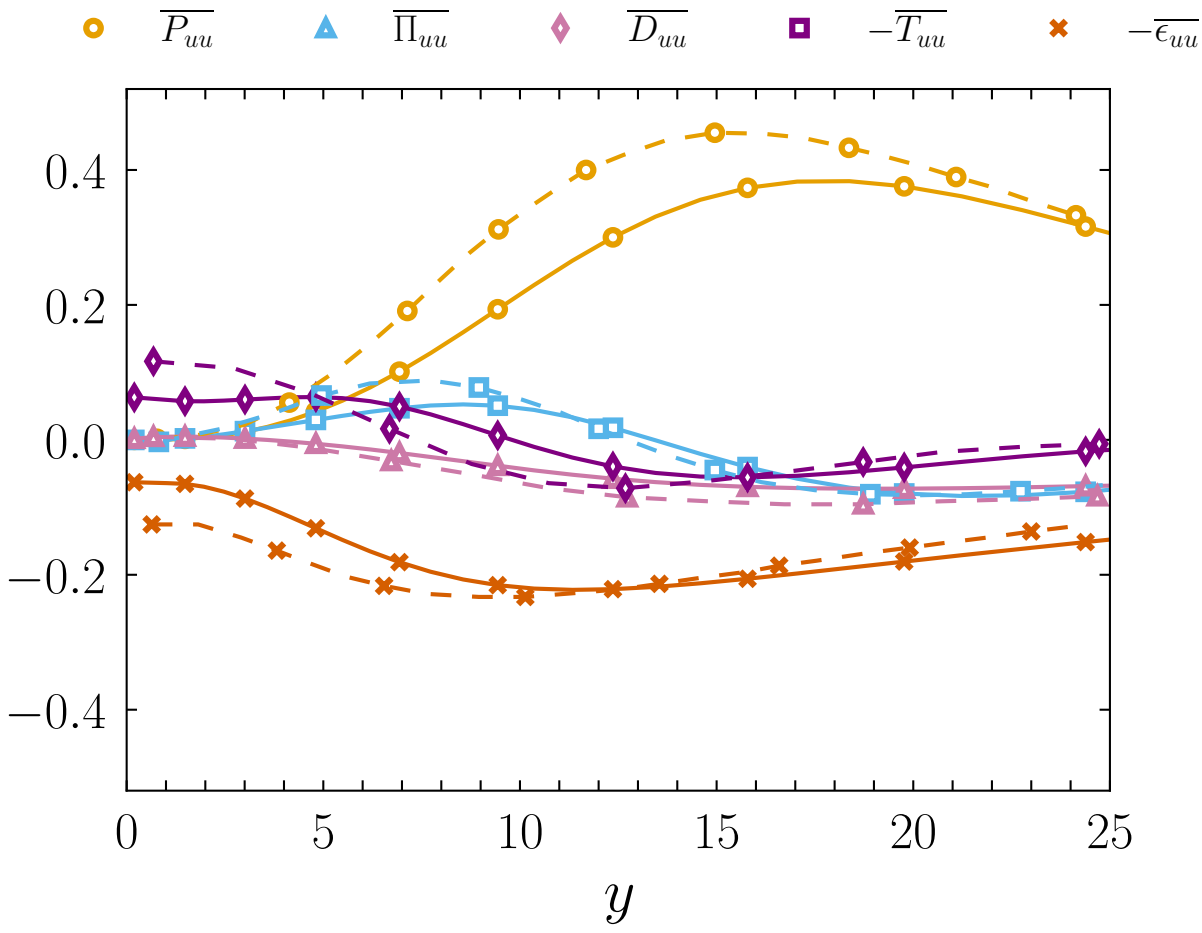

Figure 4.13: Comparison of transport terms in the $\overline{uu}$ budget for HWO case (solid lines) with Touber and Leschziner [38] data (broken lines) at $\mathrm{Re}_\tau = 500$ at same control parameters.

amplitudes of STW. Correspondingly, $\overline{\Pi_{uv}}$ declines, and the slight difference is absorbed by a relatively low turbulent diffusion $\overline{T_{uv}}$ and viscous diffusion $\overline{D_{uv}}$. The profiles of $\overline{P_{uv}}$ and $\overline{\Pi_{uv}}$ collapse very well for the cases with amplitudes $A \geq 0.75$.

One of the aims of this investigation is to sort out the proper effects of the imposed STW that result in larger DR margins compared to HWO. The interpretation would be straightforward if we could detect direct effects arising from $\partial\langle U_i\rangle/\partial x$ in the transport terms, but unfortunately that was not the case. Consequently, we decided to compare the travelling wave effects with the HWO in their optimal configuration with $A_0 = 12$ ($A = 0.51$) and $T_0 = 100$, for reasons stated earlier. Globally, the ensemble of the transport terms corresponding to HWO fall between $A = 0.15$ and $A = 0.50$ cases of the STW. There is some noticeable decrease of $\overline{\Pi_{ww}}$ in the buffer layer in the HWO case too (figure 4.9*c*). This particular point has already been nicely discussed in Touber and Leschinizer [38]. However, in the entire low buffer layer $\overline{\Pi_{ww}}$ annihilation is clearly a real effect of large amplitude STW and this is quite uncommon in wall turbulence control. Note,

by the way that, the suppression of $\overline{\Pi_{ww}}$ points at the entire decorrelation between the pressure and spanwise local gradient $\partial w/\partial z$, since $\overline{\Pi_{ww}} = -2\overline{p\partial w/\partial z}$ by spanwise homogeneity. Furthermore, the transport terms in the HWO case compare globally well with the distributions of Touber and Leschziner [38], at the same oscillation parameters but larger Re_τ. Figure 4.13 compares the $\overline{uu}$ transport terms in HWO obtained here and those of Touber and Leschziner [38] at $\mathrm{Re}_\tau = 500$, next to the wall. It is seen that the distributions collapse qualitatively well. In the absence of more objective criteria, it would be, therefore, fair to attribute the structural modifications observed here at $A > 0.50$ to the effect of STW itself. The structural modification brought up by the STW are discussed later in chapter 6. Here, we briefly discuss the response of turbulent streamwise vorticity ω_x to highlight the structural modifications. Detailed results on the vorticity transport mechanism under STW are reported in the next chapter.

The velocity-pressure gradient term Π_{ww} next to the wall can be related to the flux of ω_x. This has not been noticed before to our best knowledge. Indeed, in the region very close to the wall in the viscous sublayer, the spanwise turbulent intensity can be related to the streamwise turbulent vorticity by $w \approx y\omega_{x,0}$. Here, the subscript ',0' refers to the wall. Furthermore, the pressure gradient $\partial p/\partial z$ at the wall is equal to the flux of ω_x, i.e., $\partial p/\partial z_{,0} = \partial \omega_x/\partial y_{,0}$. Combining both gives the near-wall asymptotic behaviour,

$$\overline{\Pi_{ww}} = -2\overline{\left\langle w\frac{\partial p}{\partial z}\right\rangle} \approx -y\frac{\partial\overline{\langle\omega_x^2\rangle}}{\partial y}\bigg|_{y=0}. \tag{4.7}$$

Figure 4.14(a) shows the wall-normal distribution of $\overline{\omega_x^2}$. Equation 4.7 predicts excellently the near-wall behaviour of $\overline{\Pi_{ww}}$ in the canonical flow (figure 4.9c). The wall gradient $\partial\overline{\Pi_{ww}}/\partial y_{,0}$ is 0.01 in figure 4.9(c) and coincides perfectly with $-\partial\overline{\langle\omega_x^2\rangle}/\partial y_{,0}$ in figure 4.14(a) for the uncontrolled case. The lack of correlation $\overline{\Pi_{ww}} \approx 0$ in the flows altered by STW of large amplitudes would imply $\overline{\langle\omega_x^2\rangle} \approx$ constant next to the wall according to equation 4.7. There is indeed a significant undermining of $\overline{\omega_x^2}$ variations in the viscous sublayer once $A > 0.50$. For instance, at $A = 1.25$, $\overline{\omega_x^2}$ varies only by 20% from the wall to its local minimum at $y = 3.5$. This variation is an order of magnitude smaller than that in the uncontrolled flow, in which $\overline{\omega_x^2}$ decreases by 400% from the wall to its local minimum at $y = 5$.

The occurrence of a local minimum and maximum in $\overline{\omega_x^2}$ is attributed to the QSVs [88]. The local maxima $\overline{\omega_x^2}_{\max}$ is the intensity of the QSVs, and the local minima is the consequence of the non-slip boundary condition. The Rankine vortex model introduced by Kim et al. [88] estimate acceptably well the streamwise turbulent vorticity at the wall induced by QSVs through $\overline{\omega_x^2}_{,0} = (9/4)\overline{\omega_x^2}_{\max}$ in the canonical wall-bounded flows. This crude model predicts acceptably well $\overline{\omega_x^2}_{,0}$ for the smallest amplitude $A = 0.15$, but fails at larger amplitudes. This is either because the model is too crude, and/or there are important structural changes in the flow field because of the presence of STW. Note in figure 4.14(a) that the local maxima and minima emanating

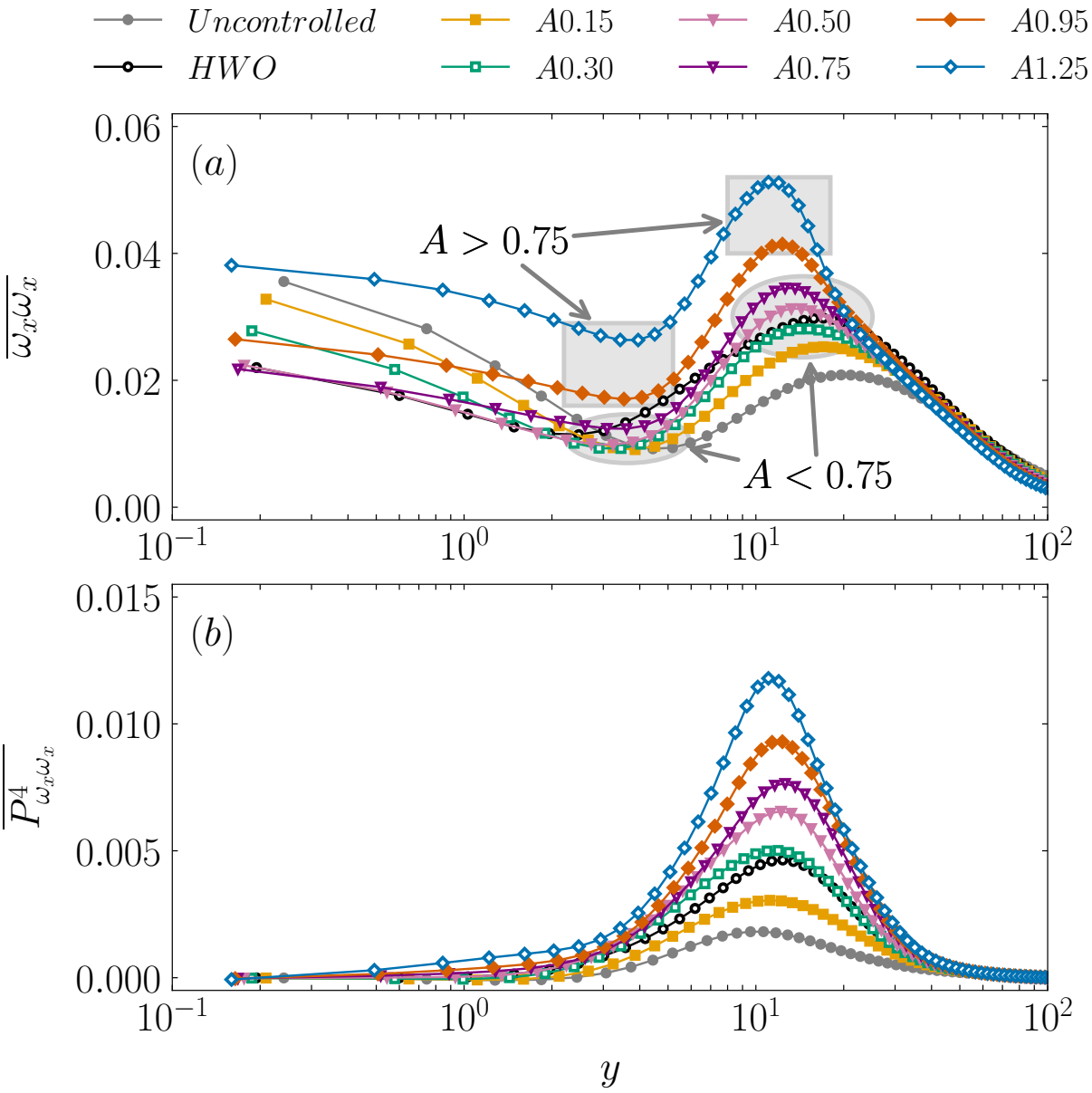

Figure 4.14: Wall-normal distribution of (a) the streamwise component of turbulent enstrophy $\overline{\omega_x\omega_x}$ and (b) its main production term. Note in the above figure that the local maxima and minima emanating from different cases are relatively well regrouped for $A < 0.75$ including HWO. The profiles gradually deviate once $A > 0.75$, pointing at severe alterations of the near-wall coherent eddies regeneration process.

from different cases are relatively well regrouped for $A < 0.75$ including HWO. However, once $A > 0.75$ the profiles gradually deviate, pointing at severe alterations of the near-wall coherent eddies regeneration process.

To summarize, the communication in the inter-component transfer is cut-off by the travelling waves of $A > 0.50$ in the low buffer layer, in which $\overline{\Pi_{uu}} \sim \overline{\Pi_{ww}} \approx 0$. The low and high buffer layers are disconnected. The consequence is the push-up of the peak of the shear stress production $\overline{P_{uv}}$ from $y = 15$ in the uncontrolled flow to $y = 30$ at $A > 0.50$ (figure 4.12*a*). The shift in the peak of $\overline{uv}$ to $y = 30$ results in the shift of the $\overline{uu}$ production $\overline{P_{uu}}$ to the same wall-normal location (figure 4.10*a*). The buffer layer dynamics which is capital in canonical wall-bounded turbulence is shut off. It is seen in figure 4.5 that there is a strong damping of the wall-normal turbulent activity, in agreement with earlier investigations [38]. The local maximum of $\overline{\Pi_{vv}}$ and $\overline{\varepsilon_{vv}}$ decrease systematically with the increasing amplitudes, and the decrease is as large as 40%. The weakening in $\overline{\Pi_{vv0}}$ and $\overline{\varepsilon_{vv0}}$, scaled by the inner variables based on the friction velocity of the uncontrolled flow, is as large as 70% at $A = 1.25$. Thus, the damping of the wall-normal activity still remains a key phenomenon under the presence of travelling waves. However, it is important to note that $\overline{\Pi_{vv}}$ and $\overline{\varepsilon_{vv}}$ are well regrouped for all the cases investigated here, once they are properly scaled by the local inner variables. Since, the results related to HWO fall again within $0.15 < A < 0.50$, the combined effect of the loose of communication between the low and high buffer layers with the $\overline{vv}$ damping is related to the travelling waves effect.

4.5 Phase-wise variations of transport quantities

The phase averages of different terms emerging in the Reynolds stresses transport equations have been carefully determined and analysed in detail. Globally, the cyclic variations of turbulent quantities are constrained at $y < 15$ where $\partial\langle W\rangle/\partial y$ is significant. The most salient effects are found in the terms related to $D\langle ww\rangle/Dt$ and will shortly be discussed hereafter.

The mean correlations $\overline{uw}$ and $\overline{vw}$ are zero, as in the case of uncontrolled flow (not shown). However, both of them, especially, $\langle uw\rangle$ reaches large cyclic variations up to the edge of the Stokes layer induced by the STW. Figure 4.15(*a*) shows $\langle uw\rangle$ and $\langle vw\rangle$ at $y = 15$ for $A1.25$ case. It can be seen that the cyclic variations in $\langle vw\rangle$ are smaller compared to $\langle uw\rangle$. Yet, the shear $\partial\langle W\rangle/\partial y$, which is proportional to A (for fixed ω and κ in outer units), reaches large cyclic values close to the wall at large imposed amplitudes. The consequence are the large cyclic modulations in $\langle P^1_{ww}\rangle$ and $\langle P^2_{ww}\rangle$. Figure 4.15(*b*) shows the cyclic variations of terms that significantly contributes to $\langle ww\rangle$ transport at $y = 5$ for $A1.25$ case. Note first that $\langle P^1_{ww}\rangle$ reaches negative values at some phases, thus becomes locally an annihilation term. Yet, $\langle P^2_{ww}\rangle$, which is larger and positive, overcomes $\langle P^1_{ww}\rangle$ so that $\langle P_{ww}\rangle > 0$. Second, the dissipation is not locally in equilibrium with the production, pointing to truly unsteady effects due to STW actuation.

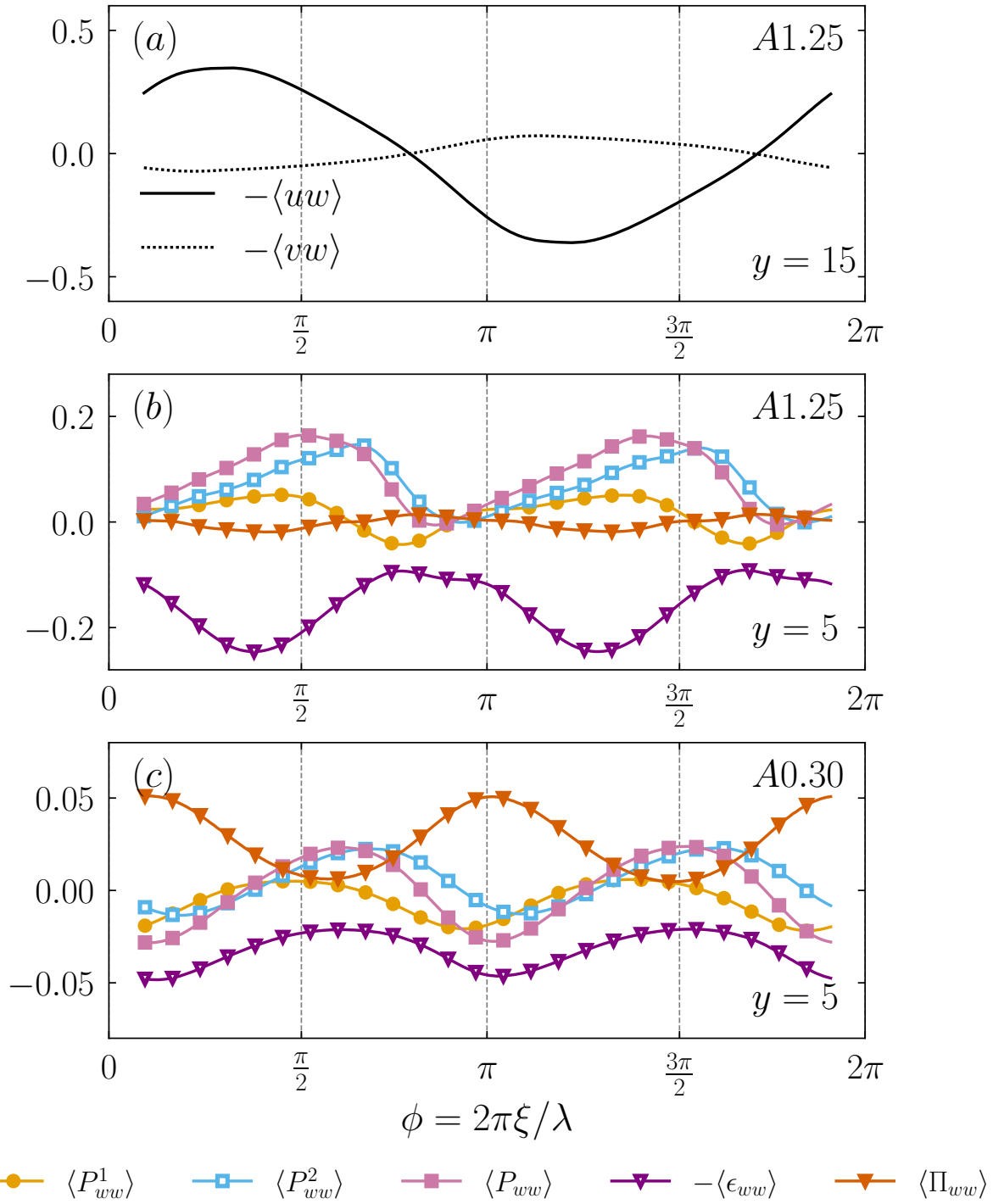

Figure 4.15: (a) Phase-wise variations of $-\langle uw\rangle$ and $-\langle vw\rangle$ at $y = 15$ for $A1.25$ case. Phase-wise variations of $\langle P^1_{ww}\rangle$, $\langle P^2_{ww}\rangle$, $\langle P_{ww}\rangle$, $-\langle \varepsilon_{ww}\rangle$, and $\langle \Pi_{ww}\rangle$ at $y = 5$ for (b) $A1.25$ and (c) $A0.30$ cases, respectively. Note how $\langle \Pi_{ww}\rangle$ for $A1.25$ case is entirely frozen compared to $A0.30$ case where there are large modulations.

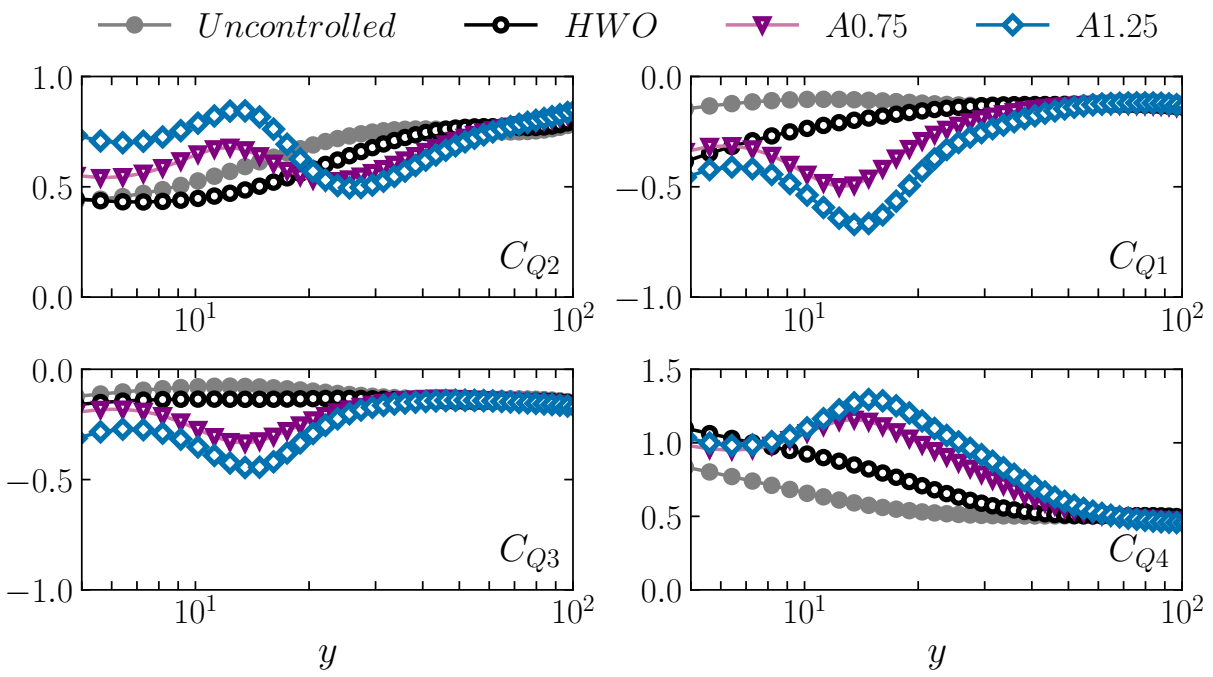

Figure 4.16: Reynolds shear stress from each quadrant normalized by the local mean Reynolds shear stress.

Finally, note in figure 4.15(b) that the velocity-pressure gradient correlation is entirely frozen during the whole cycle, i.e., $\langle \Pi_{ww} \rangle \approx 0$. The fact that the large amplitude travelling waves aborts the $uu \rightarrow ww$ communication can be better appreciated once figure 4.15(b) is compared with figure 4.15(c). The latter shows the phase averages of $\langle ww \rangle$ transport terms at the same wall-normal location $y = 5$, but at a lower imposed amplitude $A = 0.30$. It is clearly seen that the velocity-pressure gradient term $\langle \Pi_{ww} \rangle$ responds to the unsteady wave, and that its modulation amplitude is comparable to that of $\langle P_{ww} \rangle$. Note also in figure 4.15(c) that $\langle P^{1}_{ww} \rangle$ is negative almost throughout the whole cycle and destroys production $\langle P_{ww} \rangle$. The latter is even negative during half of the cycle. The response of $\langle ww \rangle$ changes strongly at large imposed amplitudes, wherein the DR is larger than HWO. Thus, it is reasonable to directly attribute the behavioural changes of the near-wall turbulence at $A > 0.50$ to the travelling waves.

4.6 Quadrant contributions to the Reynolds shear stress and Skewness of fluctuating velocity fields

In this section, we present the contribution of the quadrant events to the total Reynolds shear stress. Following Wallace *et al.* [89] and Lu & Willmarth [90], the total Reynolds shear stress

can be divided into four different categories depending on the signs of u and v. The first quadrant (Q_1) event, characterized by $u > 0$ and $v > 0$, represents the outward motion of the high-speed fluid; the second quadrant (Q_2) event, characterized by $u < 0$ and $v > 0$, represents the ejection of low-speed fluid away from the wall; the third quadrant (Q_3) event, characterized by $u < 0$ and $v < 0$, represents the interaction occurring due to the wall-ward motion of the low-speed fluid; finally, the fourth quadrant (Q_4) event, characterized by $u > 0$ and $v < 0$, represents the wall-ward motion (sweeps) of the high-speed fluid. The second (Q_2) and fourth (Q_4) quadrant events contribute positively to the production of the Reynolds shear stress and are associated with the organized (coherent) structures in the near-wall turbulence, while the first (Q_1) and third (Q_3) quadrant events contribute negatively to the production of Reynolds shear stress. The contribution to the Reynolds shear stress from each quadrant as a function of wall-normal distance y is shown in figure 4.16. In the canonical as well as controlled cases, the main contribution to the total Reynolds shear stress clearly comes from the ejection and sweep events throughout the generation region. The relative importance of ejections and sweeps varies on the distance from the wall. In the canonical case, below roughly $y \approx 15$ the contribution of sweep events is larger while ejections dominates above $y \approx 15$. In the large amplitude case, the contribution of sweeps increases up to 130% and the region where sweep dominates extends up to $y = 40$. This can also be observed by looking at the skewness profiles S_u and S_v (figure 4.17), that show a large negative peak in S_v and positive peak in S_u at about $y \approx 18$. Quite interestingly, the contributions of Q_1 and Q_3 events, that amount to about 20% in total in the canonical case, increased to about 80% up to the edge of the buffer layer. An increase in the contribution of these events that act to destroy the production of Reynolds shear stress can be attributed to the increased incoherence of the near-wall flow field. This can also be clearly observed by looking at the correlation coefficient of Reynolds shear stress $C_{uv} = -\overline{uv}/u'v'$ (here, prime indicates the root-mean-square values), shown in figure 4.18, that shows a significant decline in the same region for the large amplitude STW cases. The ensemble of these results are in agreement with the drift of the near-wall quasi-streamwise vortices that is presented in chapter 6.

4.7 Summary

Direct numerical simulations were performed to investigate the effect of transverse wall oscillations in the form of streamwise travelling waves on the Reynolds stresses transport, for the first time to our best knowledge. The angular frequency and the wavelength of the STW were fixed at $\omega = 0.16$ and $\kappa = 1.66$ (in outer units), and the imposed amplitude was varied nearly by one decade from $A = 0.15$ to $A = 1.25$. The drag reduction at the largest amplitude reaches 58%. The results were compared with homogeneous spanwise wall oscillations case with imposed period $T_0 = 100$ and amplitude $A_0 = 12$, to identify the proper impact of the STW on the near-wall turbulence.

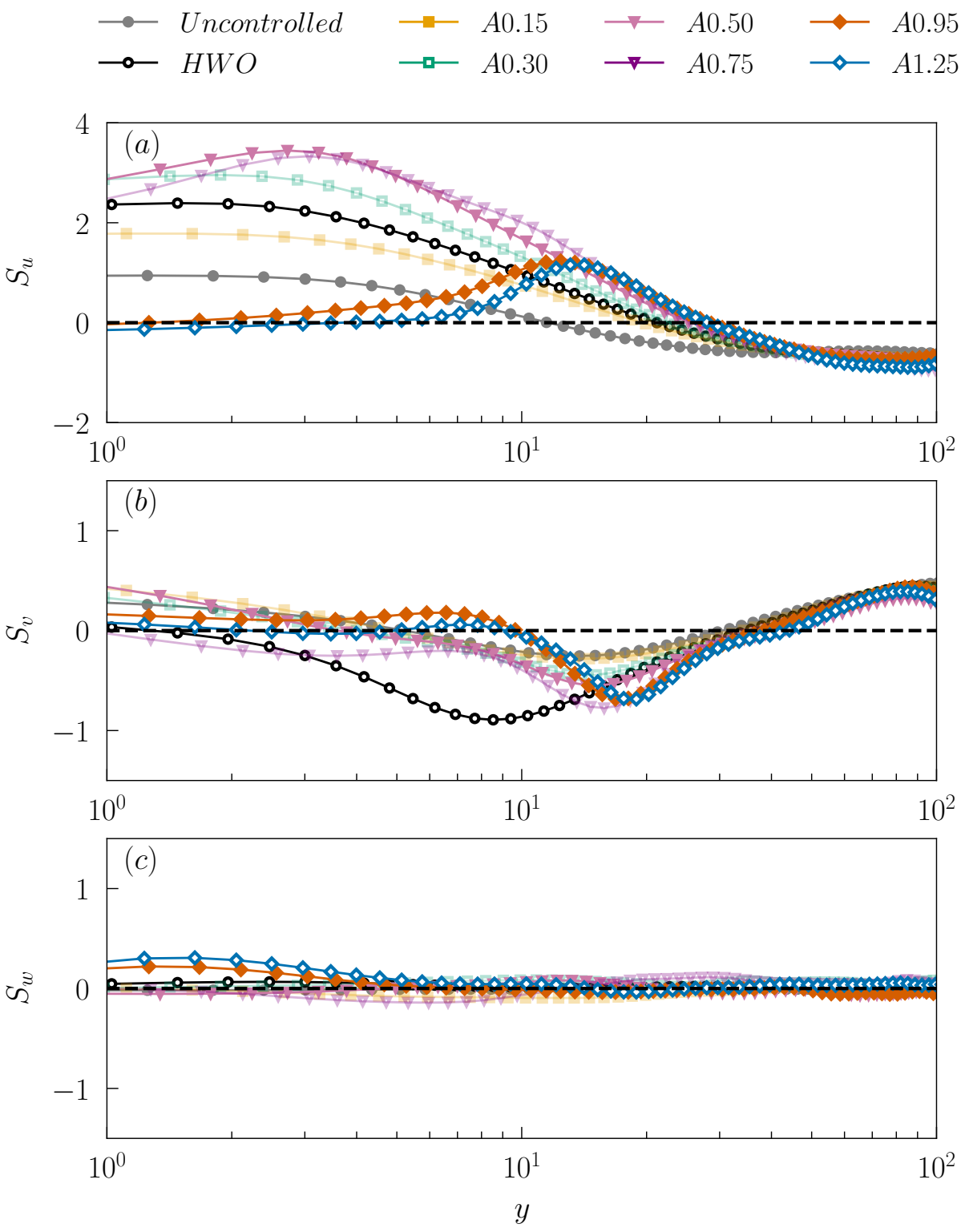

Figure 4.17: Skewness factor for the fluctuating velocity components in the uncontrolled and controlled flows.

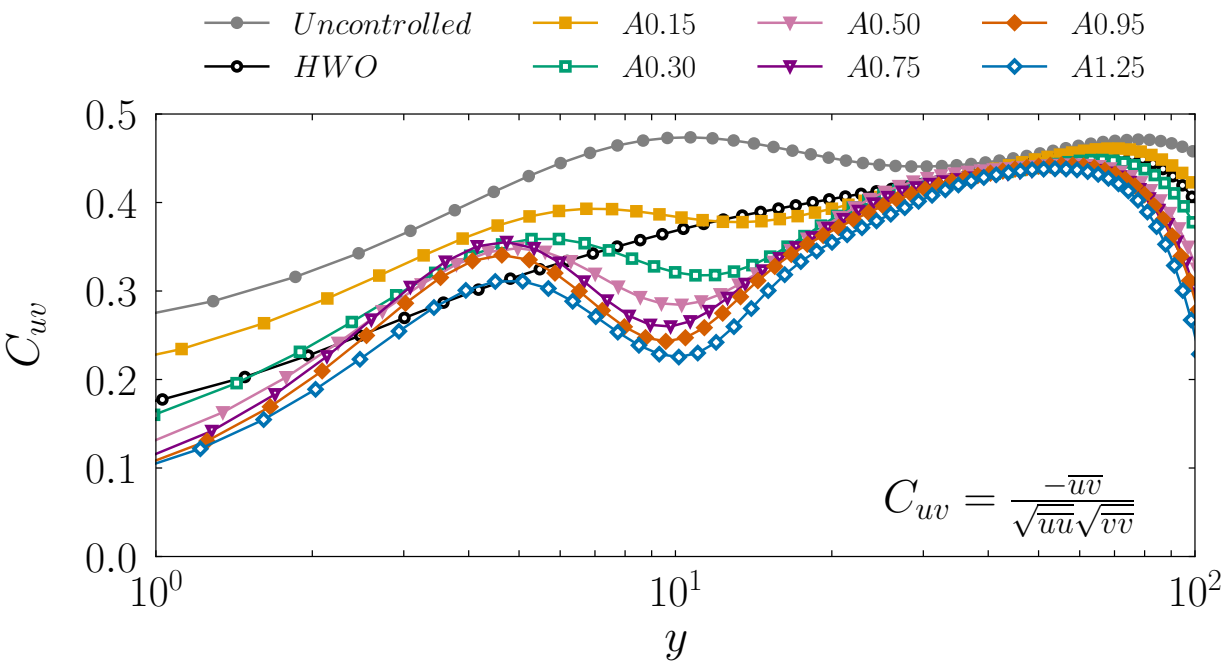

Figure 4.18: Correlation coefficient of uv.

Forcing in the form of the STW results in substantial decline of all the Reynolds stresses components. The transport terms are in close similarity with HWO when the imposed amplitude of the STW are within the intermediate range $0.30 < A < 0.50$. This regime is marked by a strong damping of the wall normal velocity fluctuations on one hand, and some noticeable decline in the velocity-pressure gradient correlations, on the other. The present investigation globally confirms previously published results on HWO.

The situation changes drastically in the large amplitude STW cases when $A > 0.50$. The inter-component transfer between the Reynolds stresses fades away in the low buffer layer, wherein it is found that $\overline{\Pi_{uu}} \sim \overline{\Pi_{vv}} \sim \overline{\Pi_{ww}} \approx 0$. The annihilation of $\overline{\Pi_{ww}}$ at $y < 10$ is particularly spectacular. It is shown that $\overline{\Pi_{ww}} \approx 0$ in the low buffer layer results in the flattening of the streamwise vorticity intensity near the wall and points to a strong alteration of the active eddies regeneration process. The spanwise component $\overline{ww}$ is autonomously produced by the Stokes strain related terms $\overline{P^1_{ww}} = -2\overline{\langle wu \rangle \partial \widetilde{W}/\partial x}$ and $\overline{P^2_{ww}} = -2\overline{\langle wv \rangle \partial \widetilde{W}/\partial y}$ in the low buffer layer, and the production simply dissipates. Unexpectedly large values of the phase averages $\langle wu \rangle$ are observed at $A > 0.75$, but $\overline{P^2_{ww}}$ dominates the $\overline{ww}$ production in the low buffer layer as $\partial \widetilde{W}/\partial y \gg \partial \widetilde{W}/\partial x$.

The low and high buffer layer get disconnected at large forcing amplitudes. Forcing also results in the cut-off of inter-component energy transfer between different Reynolds stresses components. The low buffer layer becomes autonomous, self-sustained by pure Stokes strain effects. The capital role of the low buffer layer in the uncontrolled flow is by-passed by forcing, resulting in a disconnection with the high buffer layer. This situation is rather uncommon in the

near-wall turbulence control.

CHAPTER 5

Enstrophy Transport

This chapter delves into the analysis of vorticity transport mechanisms in flows controlled by streamwise travelling waves. Specifically, our focus is directed towards the spanwise turbulent enstrophy, as it is the primary component influenced by the large amplitude streamwise travelling waves. Additionally, we conducted several numerical experiments to artificially suppress near-wall velocity fluctuations, revealing remarkable similarities in the anisotropy invariant maps between cases involving large amplitude streamwise travelling wave actuation and artificially forced scenarios. Some results presented in this chapter appeared in *Journal of Fluid Mechanics, Vol. 967, A9 – 25 July 2023* (https://doi.org/10.1017/jfm.2023.478).

5.1 Response of turbulent enstrophy

In the previous chapter, we analysed in detail the Reynolds stresses transport in flows controlled using STW. However, it is pertinent to highlight some of its peculiar aspects before moving further with the discussion on the vorticity transport. Figures 4.4-4.7 show the mean Reynolds stresses profiles for all the cases listed in table 3.2. The profiles of the mean streamwise component $\overline{uu}$ (figure 4.4) collapse nicely into a single distribution for STW with $A > 0.75$. Moreover, in the entire low buffer layer (up to $y \approx 10$) $\overline{uu}$ clearly vanishes. This is readily attributed to the shift of the production term of $\overline{uu}$ to a higher wall-normal location at $y \approx 20$, as discussed in detail in the last chapter. The spanwise component $\overline{ww}$ (figure 4.6) shows an increase in the low buffer layer, and exhibits a second peak at $y \approx 8$ for the largest amplitude case $A1.25$ investigated in the present study. This is linked to the emergence of the production term in the transport equation of $\overline{ww}$. Like $\overline{uu}$, the wall-normal component $\overline{vv}$ and the Reynolds shear stress $\overline{uv}$ also show a steep decline in the low buffer layer up to $y \approx 10$ (figures 4.5-4.7).

Figure 5.1 shows the component-wise contribution to the turbulent vorticity components for all the cases listed in table 3.2. As $\sqrt{\overline{(\partial v/\partial x)^2}}$ is an order of magnitude smaller than $\sqrt{\overline{(\partial u/\partial y)^2}}$ up to $y \approx 10$ (figure 5.1*c*), the local spanwise turbulent vorticity (ω_z) near the wall can be approximated as $\omega_z \sim -\partial u/\partial y$ up to $y \approx 3$ (and approximately in the entire viscous sublayer). Strong damping of $\overline{uu}$ up to the low buffer layer would consequently imply that one should have $\omega_z \approx 0$ in the large amplitude STW controlled cases, at least up to $y \approx 5$. This is indeed what is observed

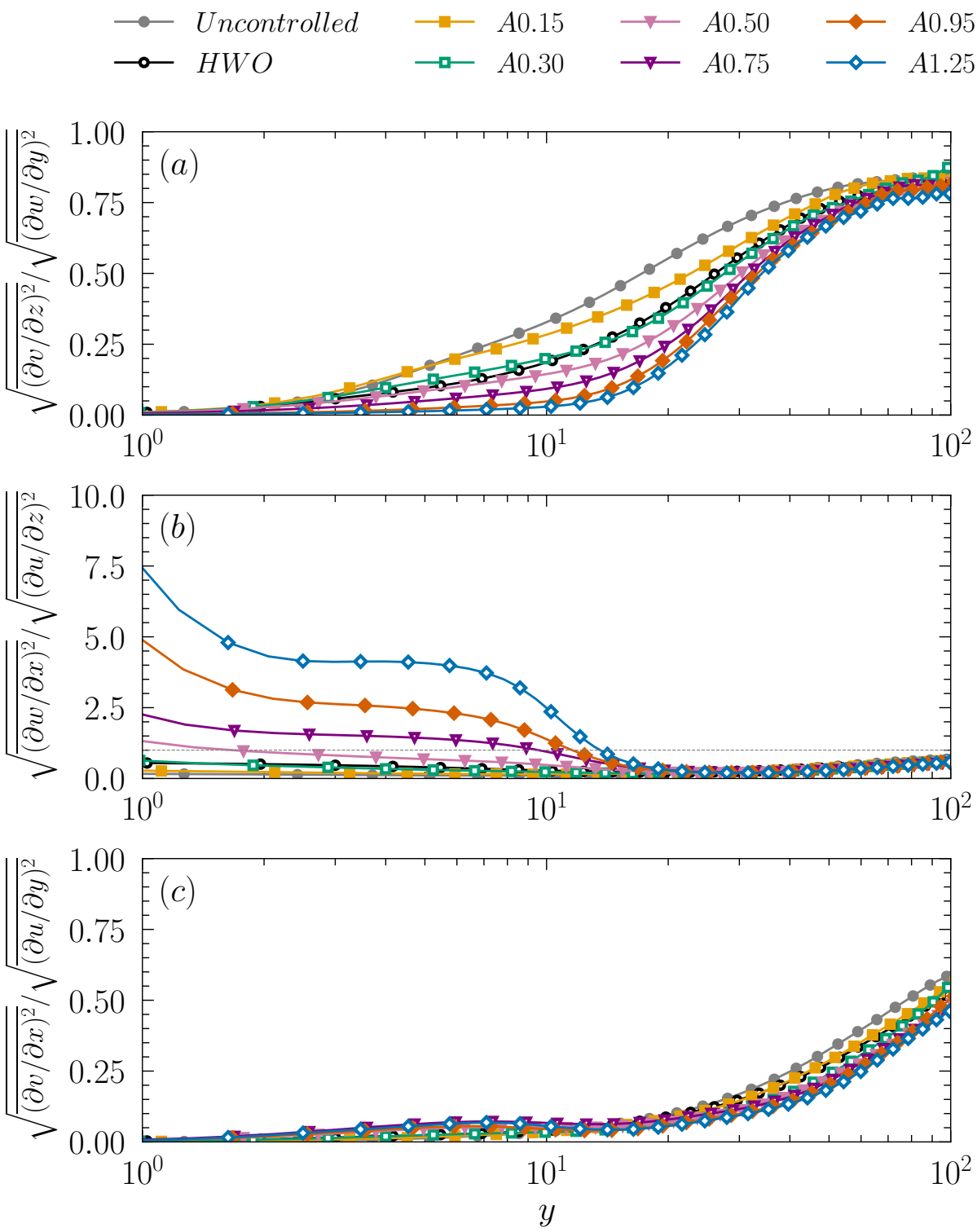

Figure 5.1: Ratio of component-wise contribution to the vorticity components for uncontrolled and controlled cases for (a) streamwise turbulent enstrophy ($\overline{\omega_x\omega_x}$), (b) wall-normal turbulent enstrophy ($\overline{\omega_y\omega_y}$), and (c) spanwise turbulent enstrophy ($\overline{\omega_z\omega_z}$).

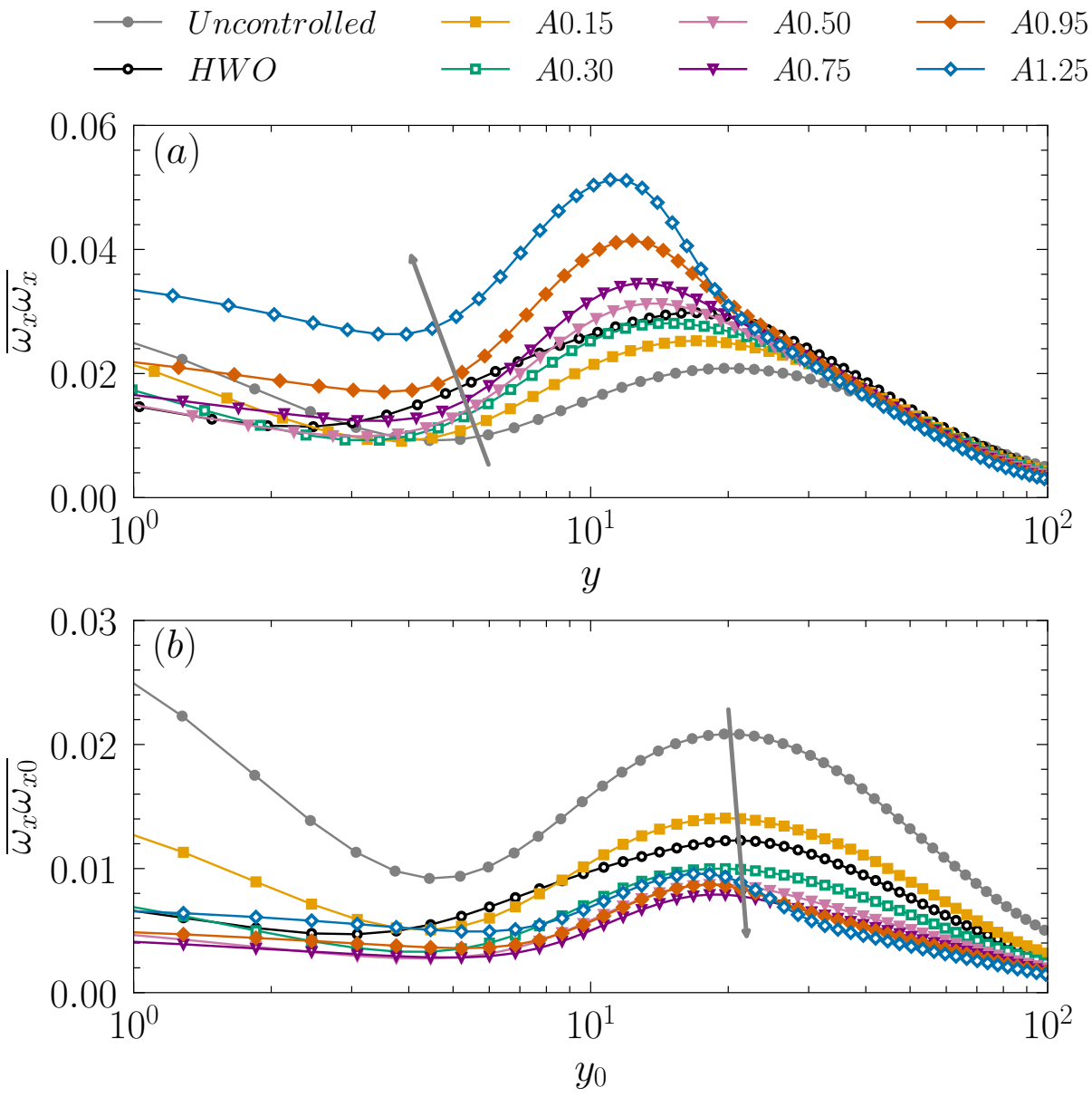

Figure 5.2: Mean streamwise turbulent enstrophy for uncontrolled and controlled cases scaled with the friction velocity of the: (a) controlled and (b) uncontrolled flow.

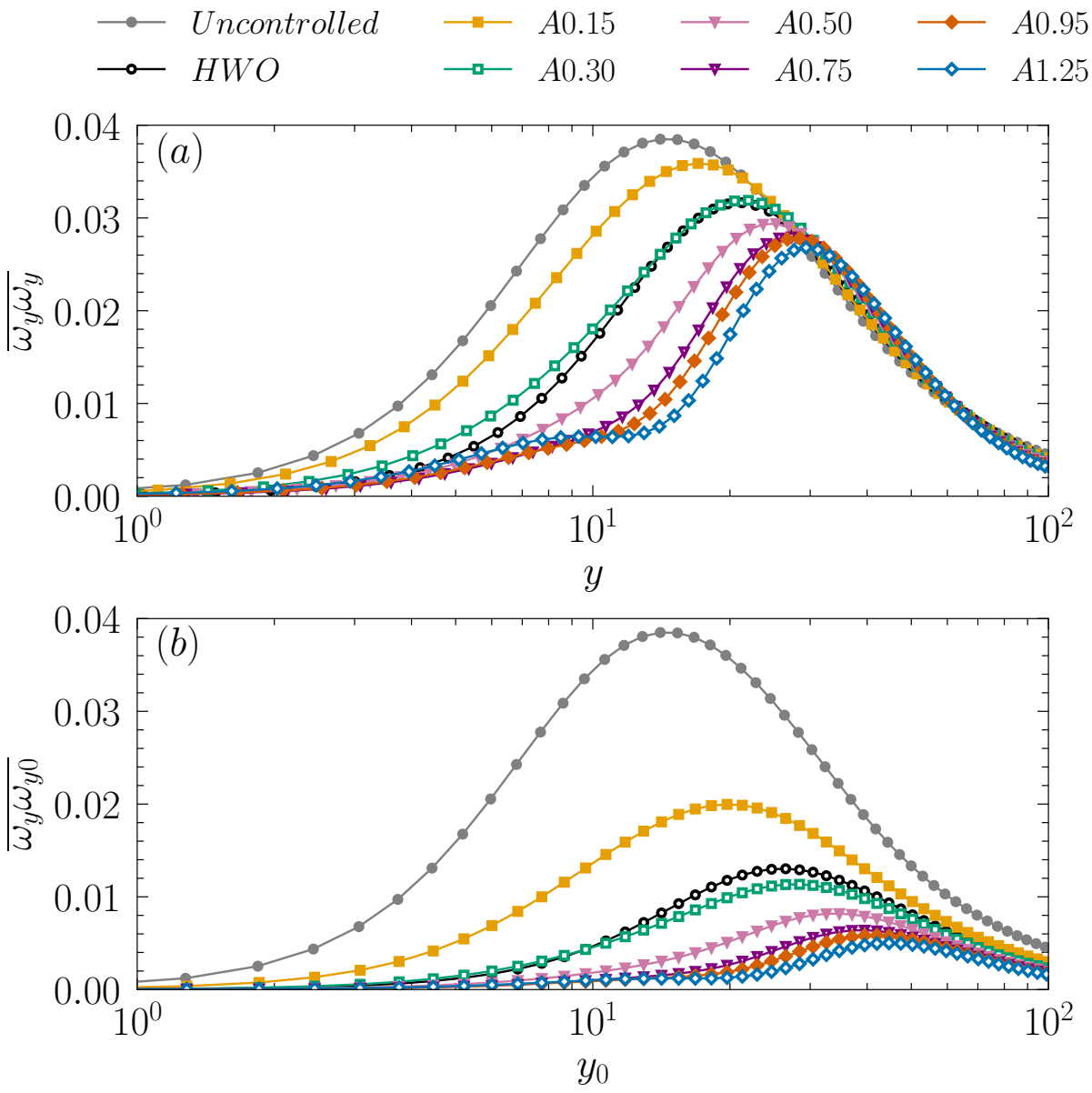

Figure 5.3: Mean wall-normal turbulent enstrophy for uncontrolled and controlled cases scaled with the friction velocity of the: (a) controlled and (b) uncontrolled flow.

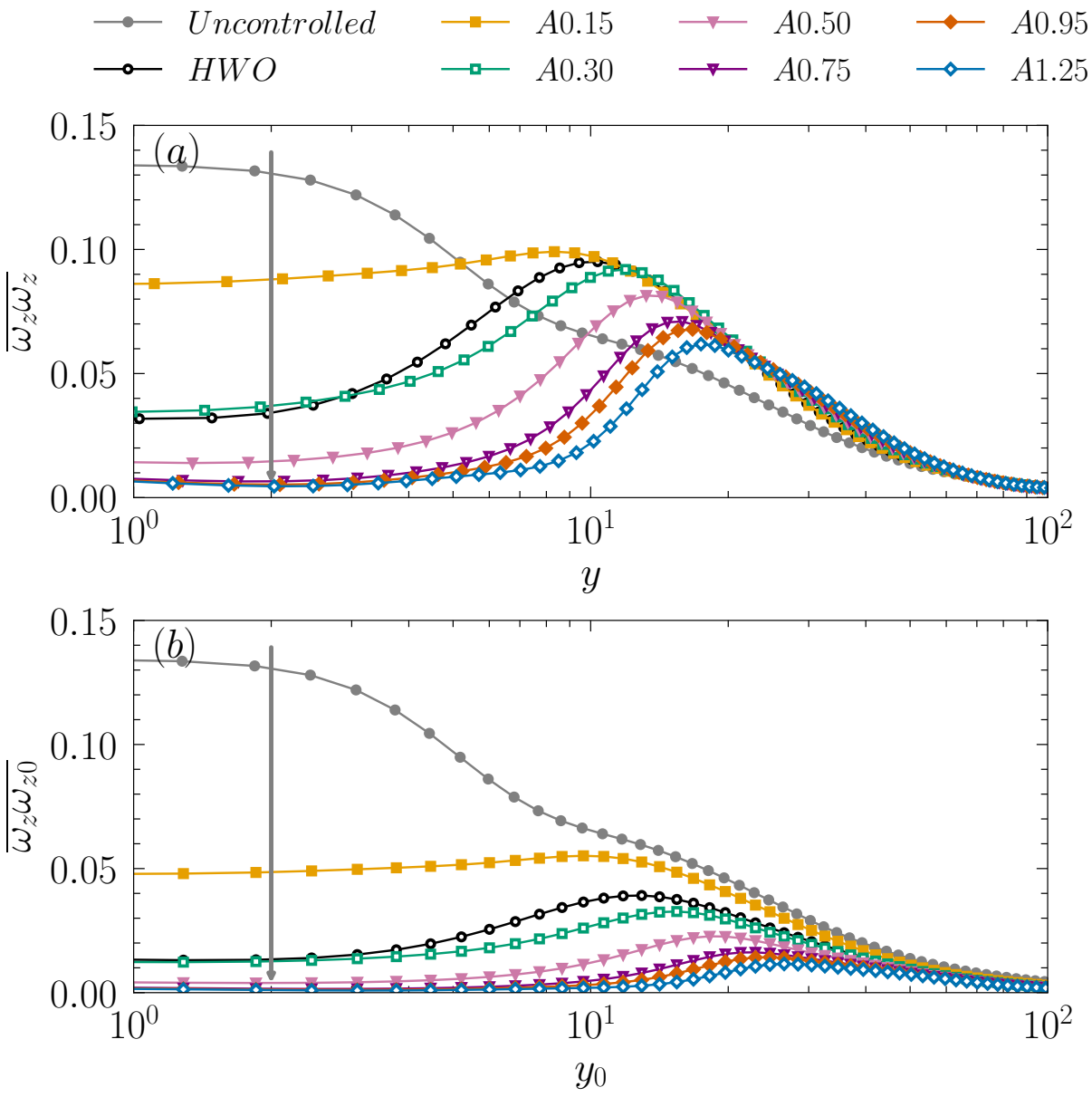

Figure 5.4: Mean spanwise turbulent enstrophy for uncontrolled and controlled cases scaled with the friction velocity of the: (a) controlled and (b) uncontrolled flow.

in figure 5.4, where we can clearly see how the spanwise turbulent enstrophy component ($\overline{\omega_z\omega_z}$) is significantly damped in the viscous and low buffer layer by the STW of large amplitudes.

In the canonical wall-bounded turbulent flows, the production term of $\overline{\omega_z\omega_z}$ reaches its maximum in the viscous sublayer at $y \approx 3$. The spanwise turbulent vorticity (ω_z) diffuses to the wall to generate the streamwise fluctuating wall shear stress (τ'), which is the capital quantity in wall-bounded turbulence – at least in the context of the present study. The spanwise turbulent enstrophy component ($\overline{\omega_z\omega_z}$) is asymptotically equal to $\overline{\tau'\tau'}$ next to the wall up to $y \approx 2$. In the large amplitude STW controlled cases, $\overline{\omega_z\omega_z}$ is spectacularly annihilated up to $y \approx 8$, with entirely negligible turbulent activity ($\overline{\tau'\tau'}$) at the wall. This is one of the outstanding effects of STW control compared to the simple homogeneous wall oscillation control – the $\overline{\omega_z\omega_z}$ profile of which collapse rather with the small amplitude STW case $A0.30$ (figure 5.4). In the case of HWO $\overline{\omega_z\omega_z}$ is damped in the viscous sublayer with a maximum at $y \approx 10$, while the peak of $\overline{\omega_z\omega_z}$ in the case of large amplitude STW is pushed towards the high buffer layer at $y \approx 20$.

5.2 Turbulent enstrophy transport

5.2.1 Spanwise enstrophy transport

The complete individual transport equations for the turbulent enstrophy in each direction can be found in the appendix 9.2, here we list only the terms that are relevant for the forthcoming discussion. The production term for the mean spanwise turbulent enstrophy $\overline{\omega_z\omega_z}$ reads

$$\begin{aligned}\overline{P_{\omega_z\omega_z}} = &\underbrace{\overline{2\widetilde{\Omega_x}\left\langle\omega_z\frac{\partial w}{\partial x}\right\rangle}}_{\overline{P^1_{\omega_z\omega_z}}} + \underbrace{\overline{2\widetilde{\Omega_y}\left\langle\omega_z\frac{\partial w}{\partial y}\right\rangle}}_{\overline{P^2_{\omega_z\omega_z}}} + \underbrace{\overline{2\widetilde{\Omega_z}\left\langle\omega_z\frac{\partial w}{\partial z}\right\rangle}}_{\overline{P^3_{\omega_z\omega_z}}} + \underbrace{2\overline{\Omega_z}\,\overline{\omega_z\frac{\partial w}{\partial z}}}_{\overline{P^4_{\omega_z\omega_z}}} + \underbrace{2\overline{\omega_x\omega_z\frac{\partial w}{\partial x}}}_{\overline{P^5_{\omega_z\omega_z}}} \\ &+ \underbrace{2\overline{\omega_y\omega_z\frac{\partial w}{\partial y}}}_{\overline{P^6_{\omega_z\omega_z}}} + \underbrace{2\overline{\omega_z\omega_z\frac{\partial w}{\partial z}}}_{\overline{P^7_{\omega_z\omega_z}}} + \underbrace{2\overline{\langle\omega_x\omega_z\rangle\frac{\partial\widetilde{W}}{\partial x}}}_{\overline{P^8_{\omega_z\omega_z}}} + \underbrace{2\overline{\langle\omega_y\omega_z\rangle\frac{\partial\widetilde{W}}{\partial y}}}_{\overline{P^9_{\omega_z\omega_z}}}\end{aligned} \tag{5.1}$$

The terms with '$\sim$' are purely a consequence of the periodic forcing in the form of spanwise wall oscillations.

In the canonical turbulent channel flows, the mean production term $\overline{P_{\omega_z\omega_z}}$ peaks at $y \approx 4$ within the viscous sublayer, and is roughly in equilibrium with the dissipation, as shown by the profiles in broken lines in figure 5.5(a). The viscous and turbulent diffusion terms are negligible except next to the wall at which they equilibrate mutually as expected. In the controlled cases, all the transport terms are shifted away from the viscous sublayer. In the case of HWO and STW

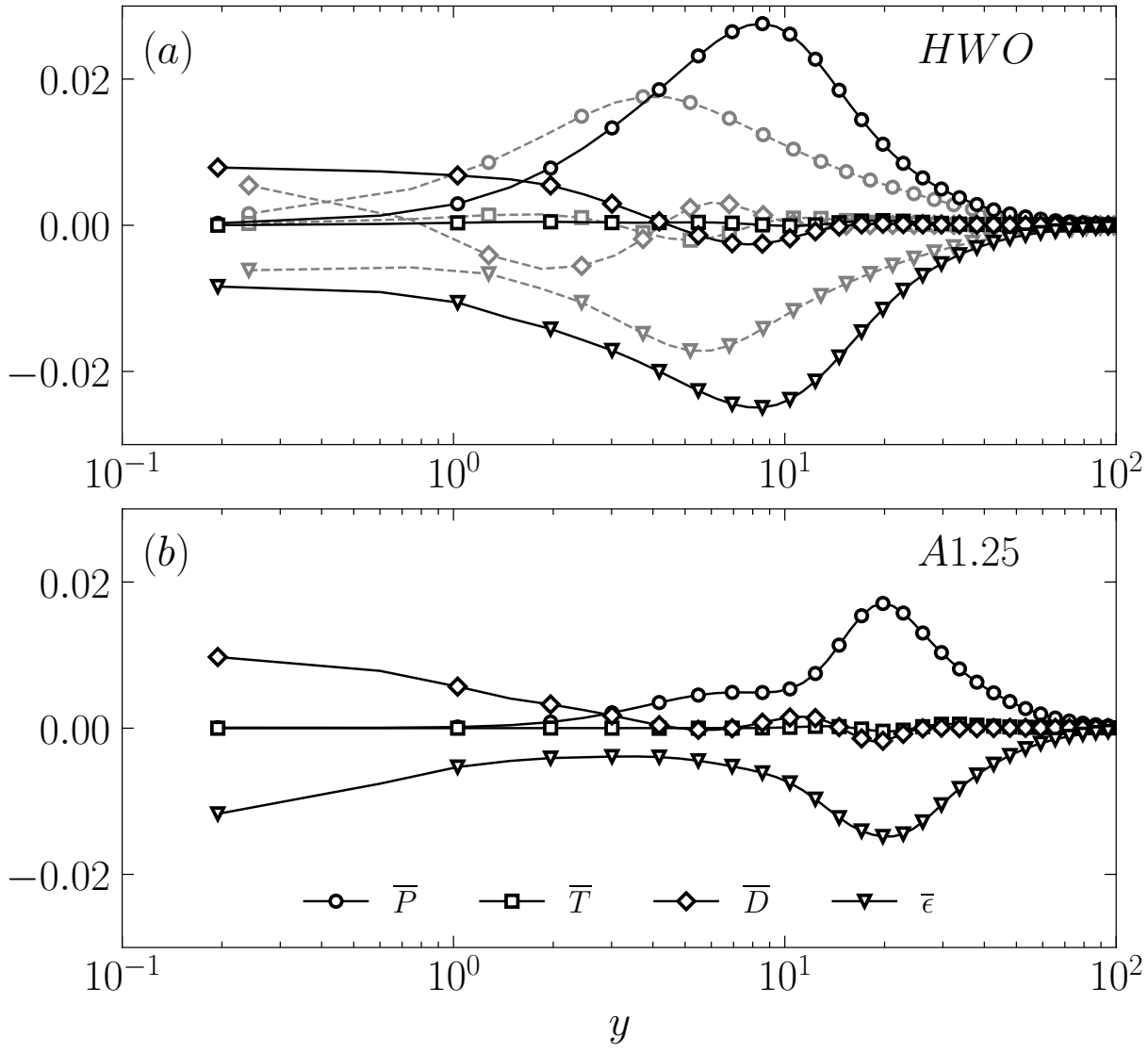

Figure 5.5: Budget of spanwise turbulent enstrophy transport for (a) HWO and (b) $A1.25$ cases. The budget for the reference (uncontrolled) canonical case is also included in figure (a) in grey broken lines for comparison. The mean advection term $\overline{A_{\omega_z\omega_z}}$ is negligible, and hence not displayed in the figures to avoid cluttering.

cases with $A < 0.50$, the mean production $\overline{P_{\omega_z\omega_z}}$ peaks at $y \approx 9$. The maximum is even further shifted towards the middle of the buffer layer at $y \approx 20$ for the large amplitude STW (figure 5.5*b*).

In the case of canonical turbulent channel flow, the main production for the spanwise turbulent enstrophy ($\overline{\omega_z\omega_z}$) is $\overline{P^4_{\omega_z\omega_z}} = 2\overline{\Omega_z}\overline{\omega_z\frac{\partial w}{\partial z}}$, which peaks at the edge of the viscous sublayer roughly at $y = 5$ (figure 5.6*c*). This term emanates from the stretching of the spanwise vorticity $\overline{\omega_z\frac{\partial w}{\partial z}}$ interacting with the mean shear $\overline{\Omega_z}$. In all the controlled cases, including HWO, the peak of $\overline{P^4_{\omega_z\omega_z}}$ is shifted towards the buffer layer, but there is a further shift of about $\Delta y \sim 10$ towards the middle of the buffer layer in large amplitude STW controlled cases. The maximum $\overline{P^4_{\omega_z\omega_z}}$ slightly decreases for STW cases with $A > 0.50$, with a difference of about 20% for $A1.25$ case compared to HWO case.

The transport of phase averaged spanwise turbulent enstrophy $\langle\omega_z\omega_z\rangle$ in the low buffer and viscous sublayers has striking characteristics, and deserves a detailed discussion. The direct effect of STW appears in the term $\langle P^2_{\omega_z\omega_z}\rangle = -2\frac{\partial\widetilde{W}}{\partial x}\langle\omega_z\frac{\partial w}{\partial y}\rangle$, where the Stokes straining term $\partial\widetilde{W}/\partial x$ is correlated with $\langle\omega_z\frac{\partial w}{\partial y}\rangle$. It originates from the tilting of the imposed wall-normal vorticity $\widetilde{\Omega_y}$ by the local $\partial w/\partial y$ gradient. Figure 5.6(b) shows that the term $\overline{P^2_{\omega_z\omega_z}}$ acts as a sink, i.e., there is a destruction of the spanwise vorticity by the direct straining through $\partial\widetilde{W}/\partial x$, especially next to the wall. This particular effect is obviously absent in the case of HWO.

There is a second Stokes straining production term originating from the twisting of the deterministic streamwise vorticity $\widetilde{\Omega_x}$ by the local $\partial W/\partial y$ gradient, denoted by $\langle P^1_{\omega_z\omega_z}\rangle = 2\frac{\partial\widetilde{w}}{\partial x}\langle\omega_z\frac{\partial w}{\partial x}\rangle$. This term also acts as a sink, annihilating the $\langle\omega_z\omega_z\rangle$ intensity, as seen in figure 5.7(a) that shows $\overline{P^1_{\omega_z\omega_z}} < 0$ from the edge of the viscous sublayer up to $y = 10$. Furthermore, in the case of HWO $\overline{P^1_{\omega_z\omega_z}} \sim 0$, suggesting that both Stokes straining production terms, $\overline{P^1_{\omega_z\omega_z}}$ and $\overline{P^2_{\omega_z\omega_z}}$, are a result of particular effects of streamwise travelling waves.

The third significant Stokes straining term is $\overline{P^9_{\omega_z\omega_z}} = 2\overline{\langle\omega_y\omega_z\rangle\frac{\partial\widetilde{W}}{\partial y}}$ which results from the tilting of (this time) the local wall-normal vorticity ω_y by the Stokes strain $\partial\widetilde{W}/\partial y$. The term $\overline{P^9_{\omega_z\omega_z}}$ is significant in both the HWO and STW control cases, and is large next to the edge of the viscous sublayer (figure 5.7*b*). Conveniently, the terms $\overline{P^1_{\omega_z\omega_z}}$ and $\overline{P^9_{\omega_z\omega_z}}$ can be combined to give

$$\overline{P^{1*}_{\omega_z\omega_z}} = \overline{P^1_{\omega_z\omega_z}} + \overline{P^9_{\omega_z\omega_z}} = 2\overline{\frac{\partial\widetilde{W}}{\partial y}\left\langle\omega_z\frac{\partial u}{\partial z}\right\rangle}. \tag{5.2}$$

The resulting term $\overline{P^{1*}_{\omega_z\omega_z}}$ now has a different physical meaning. As $\langle\omega_z\frac{\partial u}{\partial z}\rangle$ is the twisting term of the local ω_x transport equation, $\overline{P^{1*}_{\omega_z\omega_z}}$ is therefore the Stokes straining of $\langle\omega_z\frac{\partial u}{\partial z}\rangle$ by the deterministic streamwise vorticity $\widetilde{\Omega_x}$. Figure 5.6(a) clearly shows that $\overline{P^{1*}_{\omega_z\omega_z}}$ is strongly attenuated in the STW cases of large amplitudes ($A > 0.5$), and its peak is further shifted away towards the buffer layer compared to HWO. This shift is as large as twice the thickness of the viscous sublayer, for

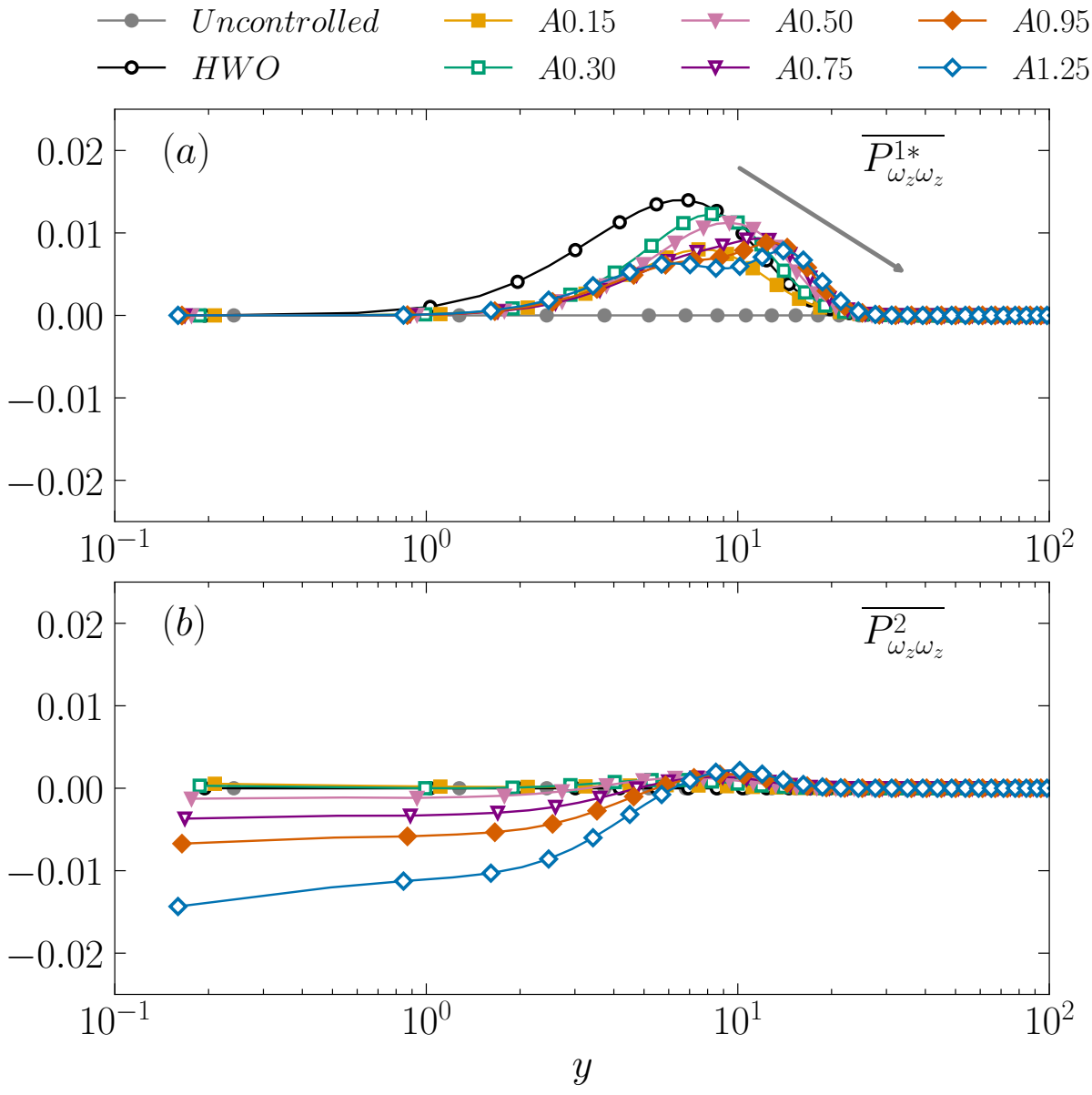

Figure 5.6: Production terms (a) $\overline{P^{1*}_{\omega_z\omega_z}}$ and (b) $\overline{P^{2}_{\omega_z\omega_z}}$ *(contd.)*.

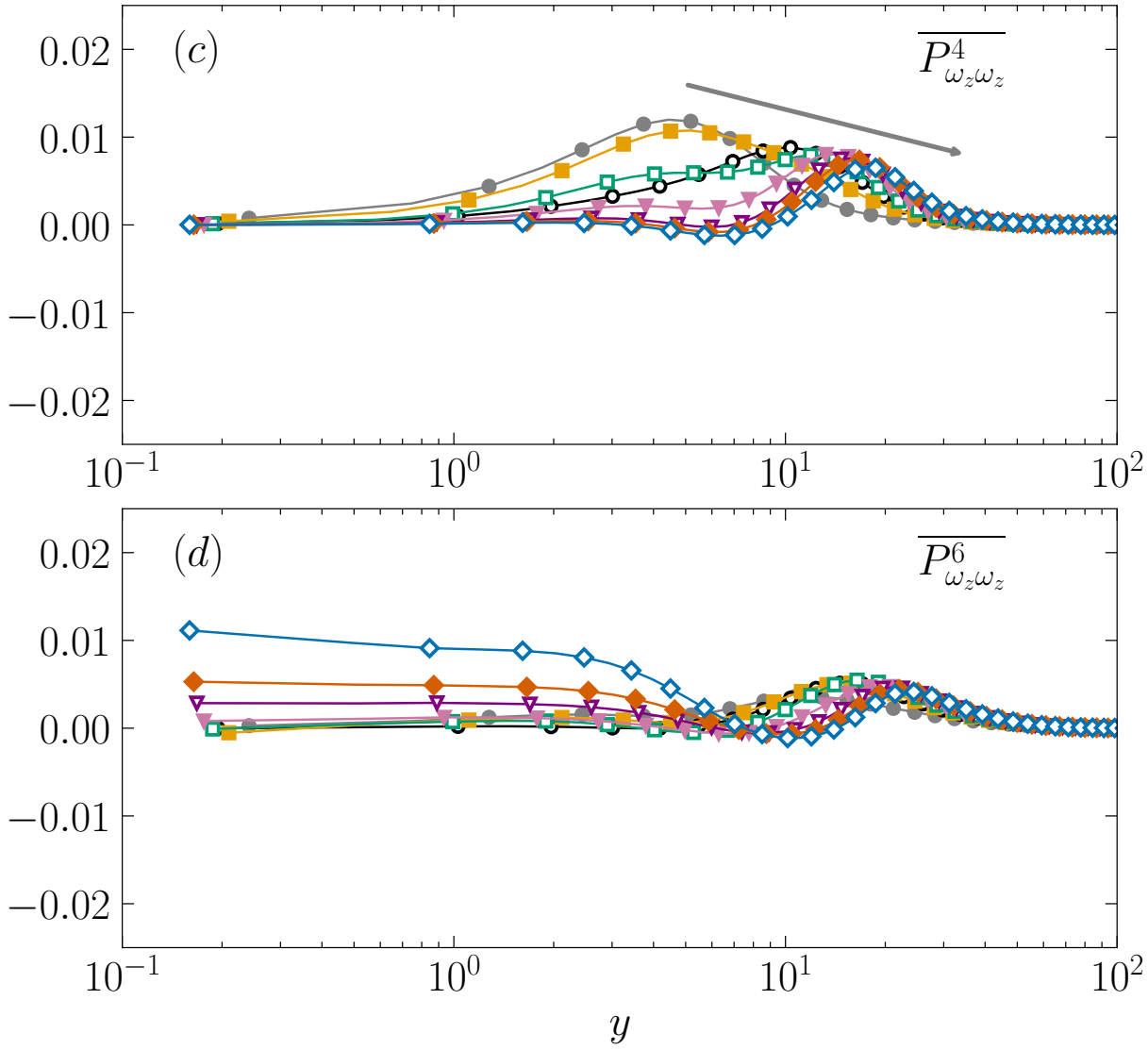

Figure 5.6: (c) $\overline{P^4_{\omega_z\omega_z}}$ and (d) $\overline{P^6_{\omega_z\omega_z}}$.

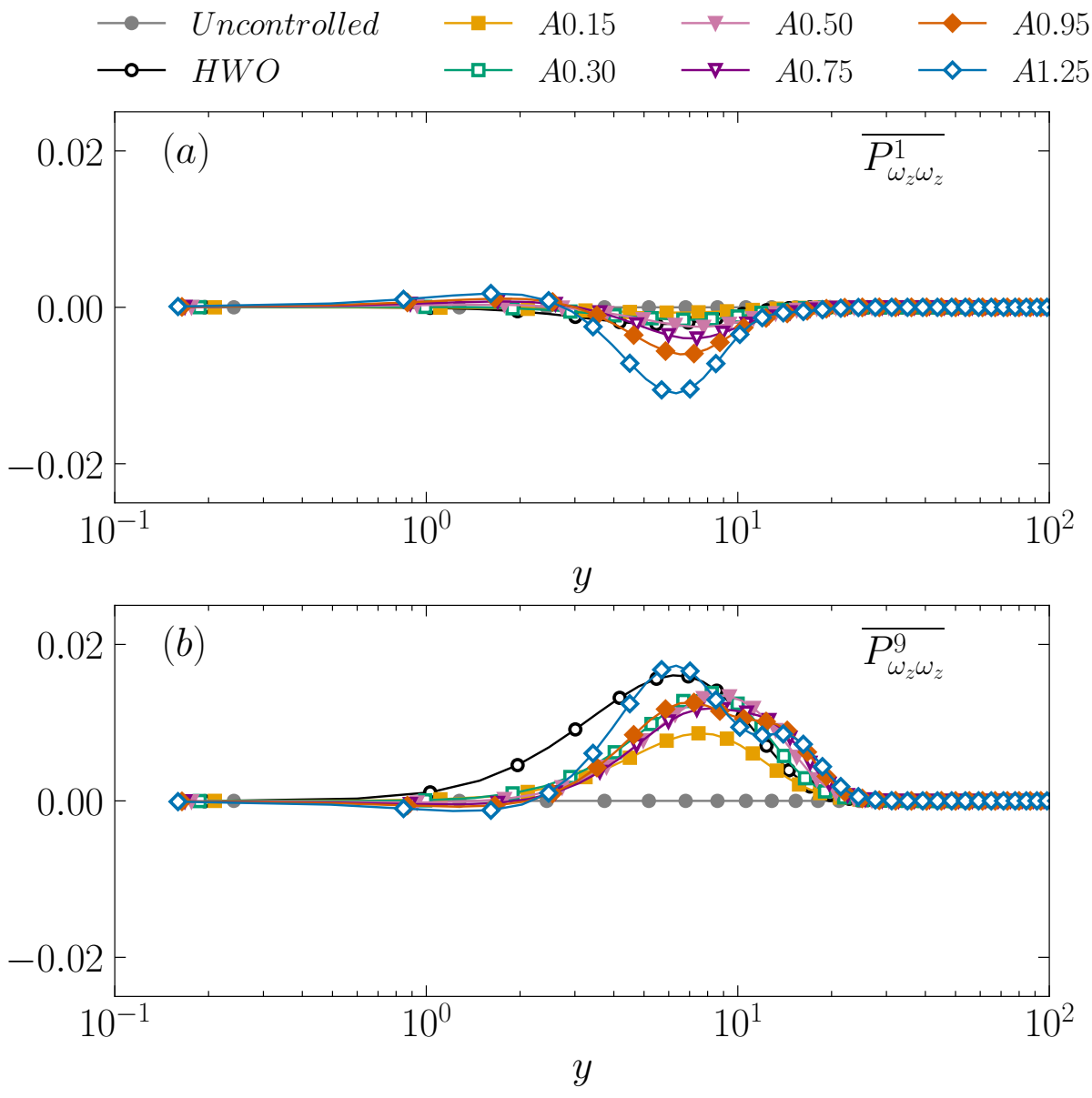

Figure 5.7: Production terms (a) $\overline{P^1_{\omega_z\omega_z}}$ and (b) $\overline{P^9_{\omega_z\omega_z}}$.

$A1.25$ case.

A closer look at figure 5.8 reveals another peculiar behaviour of $\overline{\omega_z\omega_z}$ production mechanism next to the wall. The production terms $\overline{P^2_{\omega_z\omega_z}}$ and $\overline{P^6_{\omega_z\omega_z}}$ cancel each other in the viscous sublayer and low buffer layer up to $y \approx 10$. Figure 5.8(c) shows how well the phase averages $\langle P^2_{\omega_z\omega_z}\rangle$ and $-\langle P^6_{\omega_z\omega_z}\rangle$ coincide in a somewhat unexpected way at $y = 2$. There is indeed no direct link between $\overline{P^2_{\omega_z\omega_z}}$ and $\overline{P^6_{\omega_z\omega_z}}$. Recall that $\overline{P^2_{\omega_z\omega_z}} = -2\overline{\frac{\partial\widetilde{W}}{\partial x}\langle\omega_z\frac{\partial w}{\partial y}\rangle}$ results from Stokes straining, while $\overline{P^6_{\omega_z\omega_z}} = 2\overline{\langle\omega_z\omega_z\frac{\partial w}{\partial y}\rangle}$ comes from the local tilting term $\langle\omega_y\frac{\partial w}{\partial y}\rangle$. Next to the wall, $\overline{P^6_{\omega_z\omega_z}}$ reduces to the triple correlation $\overline{P^6_{\omega_z\omega_z}} \approx \overline{\omega_x\omega_y\omega_z}$ and can hardly be connected to $\overline{P^2_{\omega_z\omega_z}}$. As seen in figure 5.9, the deterministic $\partial\langle W\rangle/\partial x$ reaches very large values at large imposed amplitudes next to the wall, and correlates almost perfectly with $\langle\omega_z\partial w/\partial y\rangle$.

To summarize, figures 5.6 recapitulates the major production terms of the $\overline{\omega_z\omega_z}$ transport equations, namely, $\overline{P^{1*}_{\omega_z\omega_z}}$, $\overline{P^2_{\omega_z\omega_z}}$, $\overline{P^4_{\omega_z\omega_z}}$ and $\overline{P^6_{\omega_z\omega_z}}$, and figure 5.10 summarizes the main characteristics of the $\overline{\omega_z\omega_z}$ production process. All these terms are the consequences of different mechanisms. Basically, the proper (direct) effect of STW is to reduce the intensity of the production terms by Stokes straining (i.e., $\overline{P^1_{\omega_z\omega_z}}$ and $\overline{P^2_{\omega_z\omega_z}}$), consequently the peak of the total production $\overline{P_{\omega_z\omega_z}}$ is shifted away from the wall to the buffer layer. The shift with respect to HWO is as large as 10 wall-units (figure 5.5). There are finally two terms, namely, $\overline{P^4_{\omega_z\omega_z}}$ which is the major term in the uncontrolled flow and $\overline{P^{1*}_{\omega_z\omega_z}}$ which is specific to HWO and STW. A similar attenuation and shift can also be observed in the dissipation $\overline{\varepsilon_{\omega_z\omega_z}}$ profiles (figure 5.11).

5.2.2 Streamwise enstrophy transport

The production term for the streamwise turbulent enstrophy component is given as

$$\begin{aligned}\overline{P_{\omega_x\omega_x}} = &\underbrace{\overline{2\widetilde{\Omega_x}\langle\omega_x\frac{\partial u}{\partial x}\rangle}}_{\overline{P^1_{\omega_x\omega_x}}} + \underbrace{\overline{2\widetilde{\Omega_y}\langle\omega_x\frac{\partial u}{\partial y}\rangle}}_{\overline{P^2_{\omega_x\omega_x}}} + \underbrace{\overline{2\widetilde{\Omega_z}\langle\omega_x\frac{\partial u}{\partial z}\rangle}}_{\overline{P^3_{\omega_x\omega_x}}} - \underbrace{2\overline{\omega_x\frac{\partial w}{\partial x}\frac{d\overline{U}}{dy}}}_{\overline{P^4_{\omega_x\omega_x}}} \\ &+ \underbrace{\overline{2\omega_x\omega_x\frac{\partial u}{\partial x}}}_{\overline{P^5_{\omega_x\omega_x}}} + \underbrace{\overline{2\omega_x\omega_y\frac{\partial u}{\partial y}}}_{\overline{P^6_{\omega_x\omega_x}}} + \underbrace{\overline{2\omega_x\omega_z\frac{\partial u}{\partial z}}}_{\overline{P^7_{\omega_x\omega_x}}} + \underbrace{\overline{2\langle\omega_x\omega_x\rangle\frac{\partial\widetilde{U}}{\partial x}}}_{\overline{P^8_{\omega_x\omega_x}}} + \underbrace{\overline{2\langle\omega_x\omega_y\rangle\frac{\partial\widetilde{U}}{\partial y}}}_{\overline{P^9_{\omega_x\omega_x}}}.\end{aligned} \tag{5.3}$$

The first three and the last two terms, namely, $\overline{P^1_{\omega_x\omega_x}}$, $\overline{P^2_{\omega_x\omega_x}}$, $\overline{P^3_{\omega_x\omega_x}}$, $\overline{P^8_{\omega_x\omega_x}}$ and $\overline{P^9_{\omega_x\omega_x}}$ represent the contribution arising directly from the forcing. A careful analysis reveals that most of the terms in equation 5.3 are either negligible or cancel each other. For example, the term $\overline{P^6_{\omega_x\omega_x}}$ which comes from the tilting of the wall-normal fluctuating vorticity ω_y by the fluctuating shear $\partial u/\partial y$, and the term $\overline{P^7_{\omega_x\omega_x}}$ which represents the turning of the spanwise turbulent vorticity ω_z due to $\partial u/\partial z$,

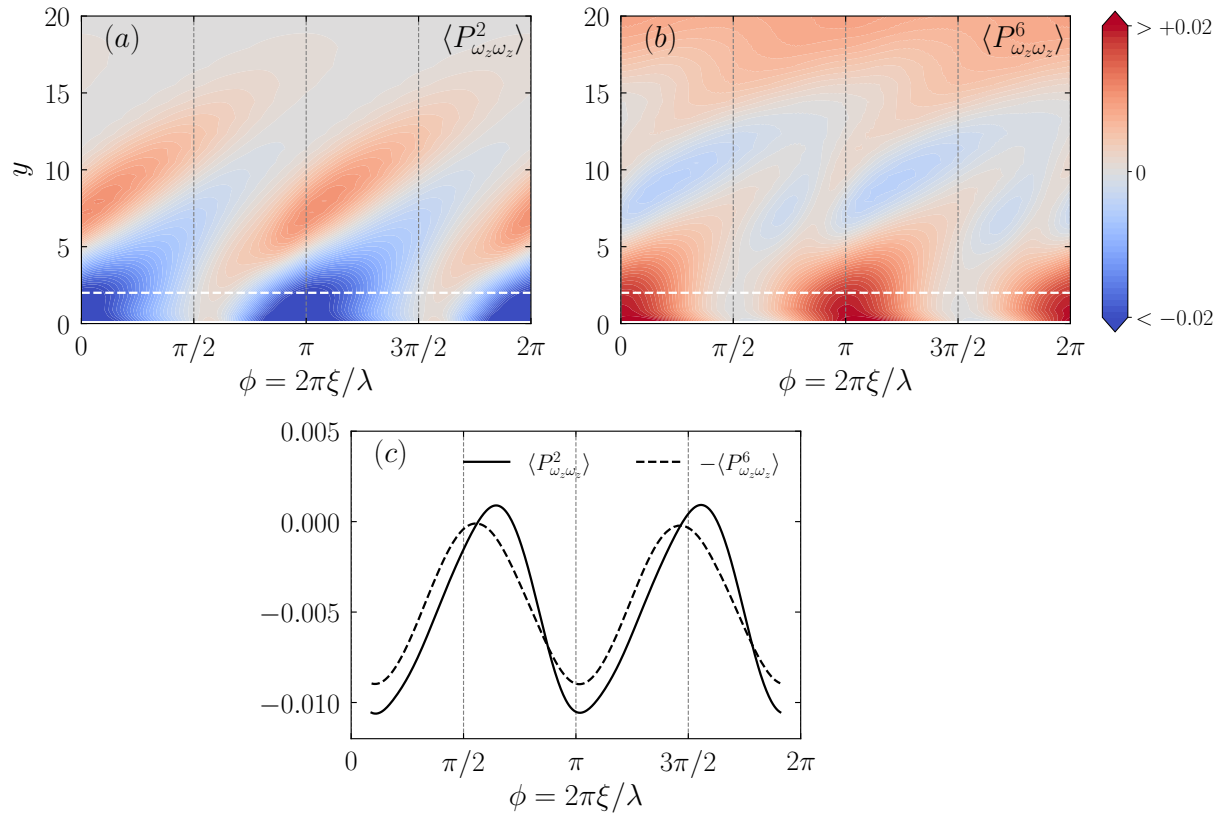

Figure 5.8: Phase wise variations of (a) $\langle P^2_{\omega_z\omega_z}\rangle$ and (b) $\langle P^6_{\omega_z\omega_z}\rangle$ for $A0.95$ case, respectively. The white dotted horizontal lines correspond to $y = 2$. (c) The phase wise variation of $\langle P^2_{\omega_z\omega_z}\rangle$ and $\langle P^6_{\omega_z\omega_z}\rangle$ at $y = 2$.

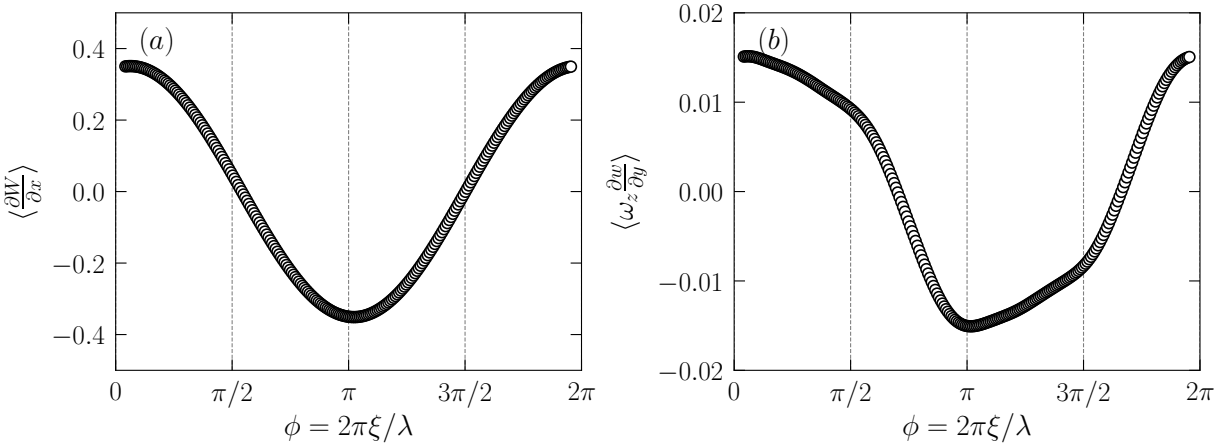

Figure 5.9: Phase wise variations of (a) $\partial\langle W\rangle/\partial x$ and (b) $\langle\omega_z\partial w/\partial y\rangle$ for $A0.95$ case at $y = 2$, respectively.

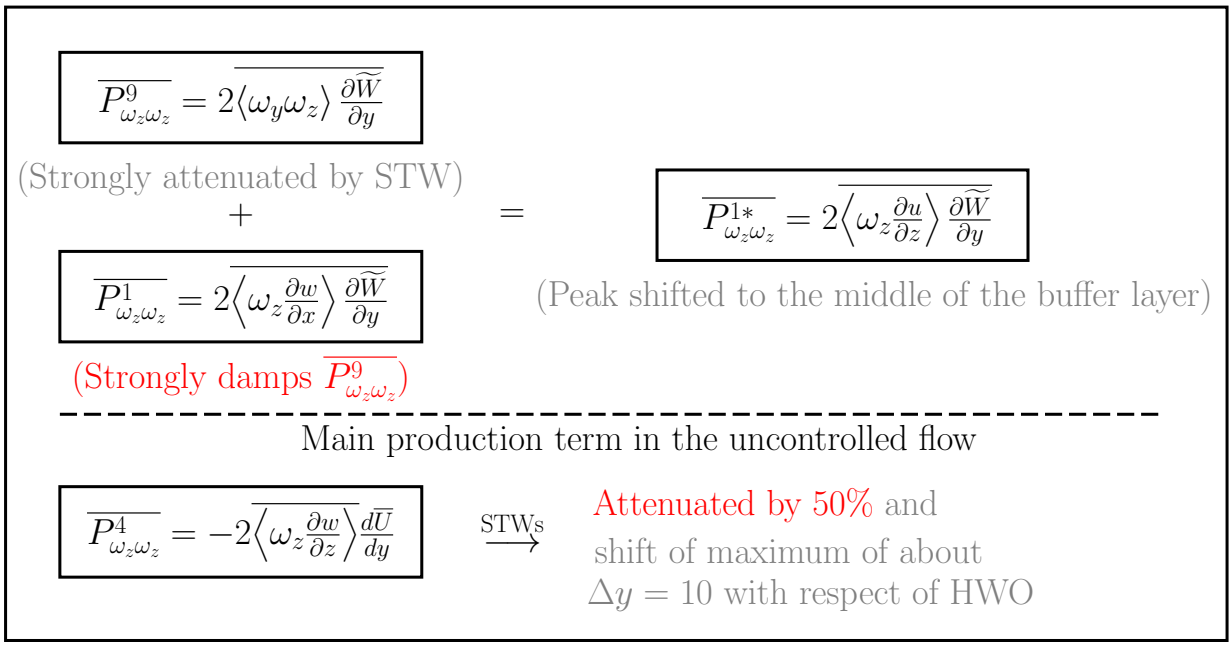

Figure 5.10: Summary of main characteristics of the effect of control on the spanwise turbulent enstrophy production process.

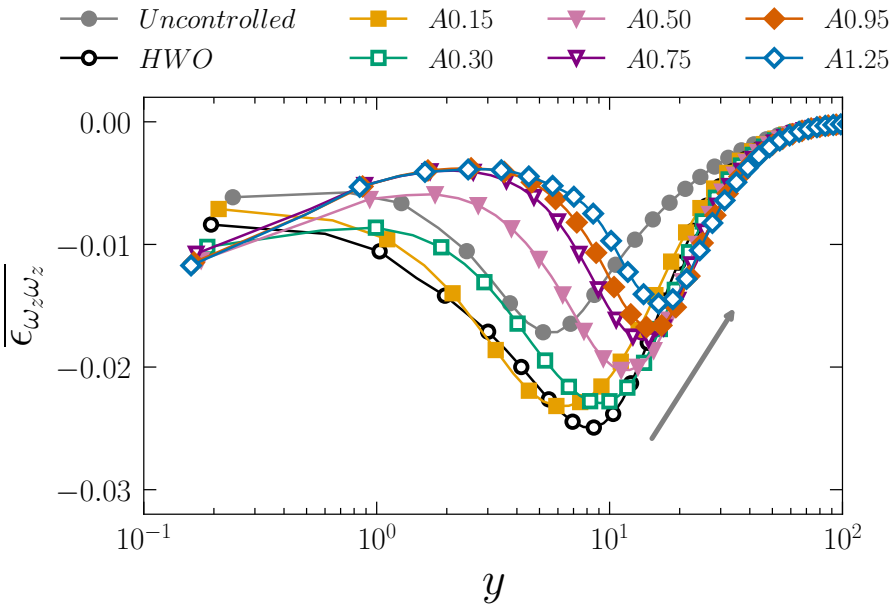

Figure 5.11: Dissipation term ($\overline{\varepsilon_{\omega_z\omega_z}}$) for the spanwise turbulent enstrophy component.

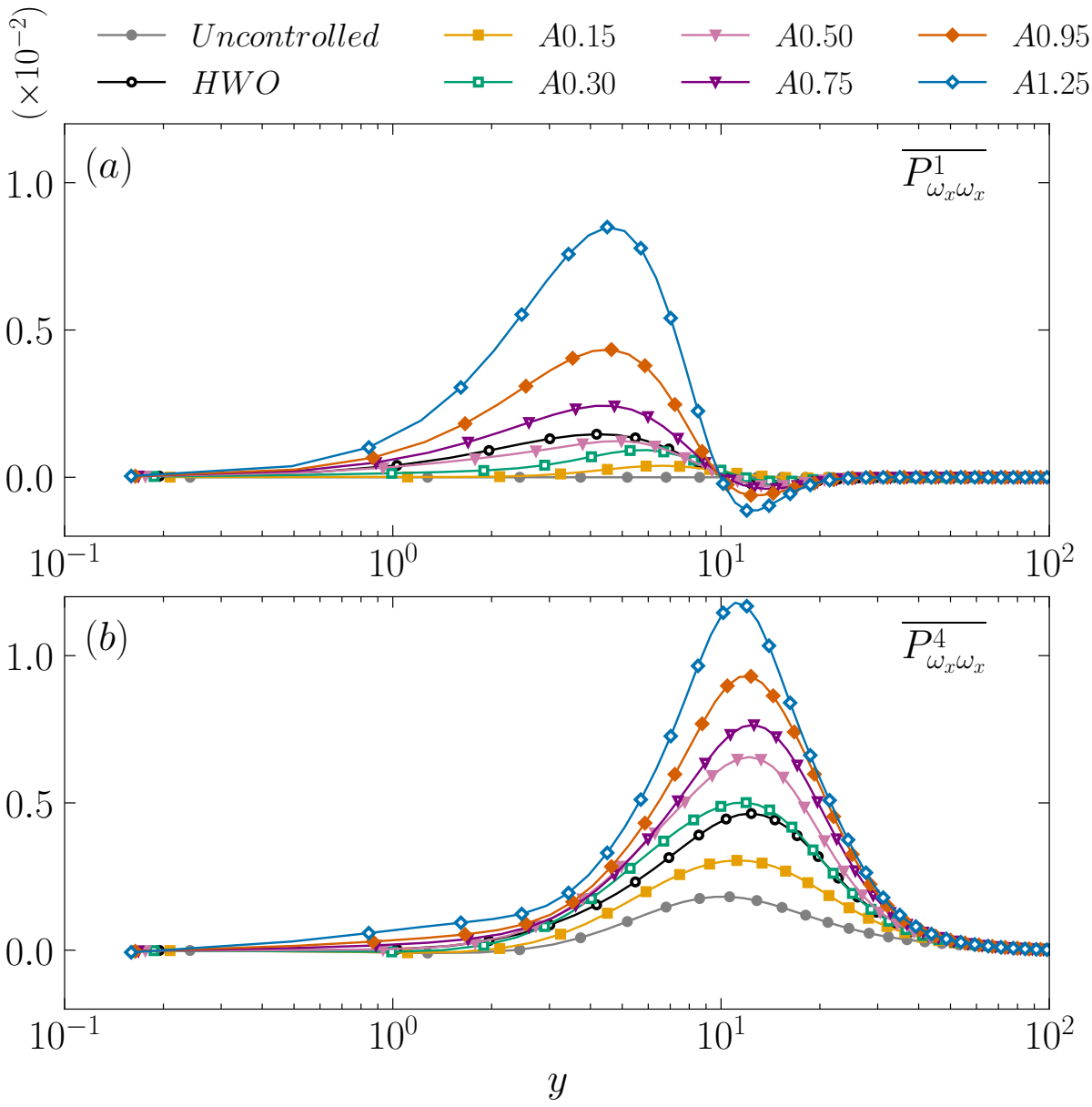

Figure 5.12: Production terms (a) $\overline{P^1_{\omega_x\omega_x}}$ and (b) $\overline{P^4_{\omega_x\omega_x}}$.

almost cancel each other, both in the case of uncontrolled and controlled flows. Thus, the total production term $\overline{P_{\omega_x\omega_x}}$ effectively reduces to just two terms

$$\overline{P_{\omega_x\omega_x}} \approx \underbrace{2\overline{\widetilde{\Omega}_x\left\langle \omega_x \frac{\partial u}{\partial x}\right\rangle}}_{\overline{P^1_{\omega_x\omega_x}}} \underbrace{-2\overline{\omega_x \frac{\partial w}{\partial x}\frac{d\overline{U}}{dy}}}_{\overline{P^4_{\omega_x\omega_x}}}. \tag{5.4}$$

The production term $\overline{P^1_{\omega_x\omega_x}}$ represents the interaction of the Stokes shear $\widetilde{\Omega}_x = \partial\widetilde{W}/\partial y$ with the stretching of the streamwise vorticity $\langle\omega_x \partial u/\partial x\rangle$. This term is a direct consequence of forcing, and hence is absent in the canonical uncontrolled case. It increases with the amplitude of the STW, reaching large values for $A1.25$ case, and peaks within the viscous sublayer at $y = 5$ (figure 5.12*a*). It is also present in the HWO case, but is negligible compared to that in the large amplitude STW cases.

The response of the streamwise turbulent enstrophy $\overline{\omega_x\omega_x}$ to the STW forcing is shown in figure 5.2. The local minimum and maximum in the profiles of $\overline{\omega_x\omega_x}$ are attributed to the streamwise vortices in the near-wall region [88]. The local minimum of $\overline{\omega_x\omega_x}$ increases with the amplitude of the STW, under the effect of Stokes shear $\partial\widetilde{W}/\partial y$ induced production $\overline{P^1_{\omega_x\omega_x}}$. The local minima in $\overline{\omega_x\omega_x}$ is related to the presence of buffer layer QSV's [88]. $\overline{P^1_{\omega_x\omega_x}}$ weakens the signature of the QSVs near the wall under large amplitude STW. Note that there is also a significant undermining of $\overline{\omega_x\omega_x}$ variation in the viscous sublayer when $A > 0.50$. For the STW $A1.25$ case, $\overline{\omega_x\omega_x}$ varies only slightly between the local minimum and the wall, compared to 400% increase from the local minimum to $\overline{\omega_x\omega_x}$ at the wall in the uncontrolled case. This point, discussed in detail in the previous chapter, is related to the lack of velocity-pressure gradient correlation in the spanwise velocity transport equation in the near-wall region.

The main production term for $\overline{\omega_x\omega_x}$ in the uncontrolled flow comes from the tilting of the wall-normal turbulent vorticity ω_y by the mean shear $d\overline{U}/dy$, i.e., $\overline{P^4_{\omega_x\omega_x}} = -2\overline{\omega_x\frac{\partial w}{\partial x}}\frac{d\overline{U}}{dy}$. This is also the major production term in the controlled flows, as shown in figure 5.12(b). It peaks roughly at $y \approx 10-12.5$ for all the cases. Note that the profile of $\overline{P^4_{\omega_x\omega_x}}$ in HWO case collapse almost perfectly with the STW case $A0.30$. This strengthens again the observation made in the previous chapter that the direct effects of STW mainly appear at $A > 0.30$.

The turbulent transport (or turbulent diffusion) term in the uncontrolled flow is $\overline{T_{\omega_x\omega_x}} = -d\overline{\omega_x\omega_x v}/dy$, and is globally, negligible compared to the other terms appearing in the transport equation of $\overline{\omega_x\omega_x}$. However, two additional transport terms emerge directly from the imposed unsteadiness in the STW cases. They are, respectively, given as $\overline{T^1_{\omega_x\omega_x}} = -2\overline{\langle\omega_x u\rangle\partial\widetilde{\Omega}_x/\partial x}$ and $\overline{T^2_{\omega_x\omega_x}} = -2\overline{\langle\omega_x v\rangle\partial\widetilde{\Omega}_x/\partial y}$ (see, appendix 9.2). Figure 5.13(b) shows that $\overline{T^2_{\omega_x\omega_x}}$ attains large values in the large amplitude STW cases. Recall that the turbulent transport terms correspond to the spatial redistribution of ω_x. These nonlinear terms do not create or destroy enstrophy, but they act to simply redistribute it in space. Instantaneous visualizations reveal that the production and

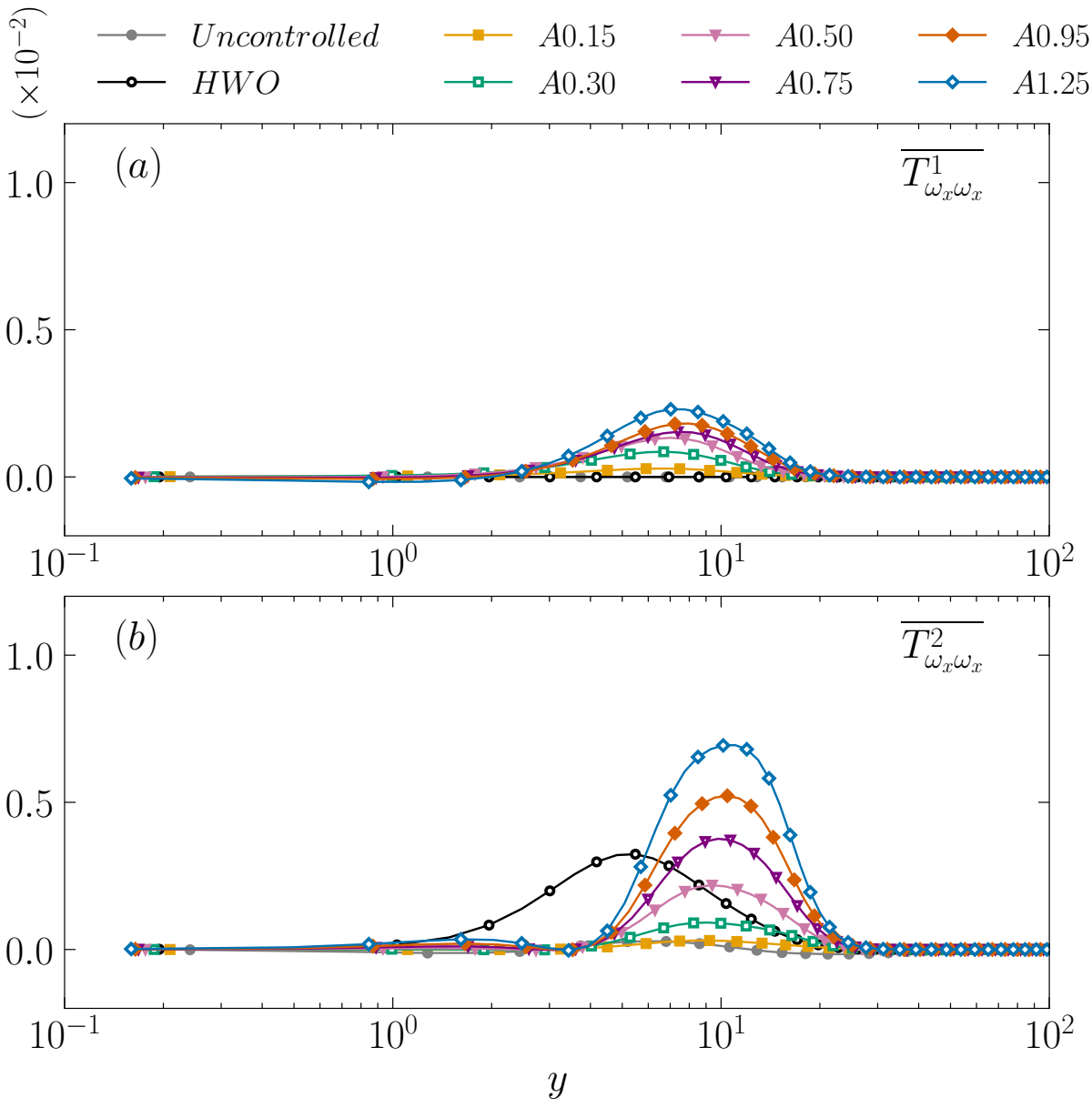

Figure 5.13: Turbulent transport (or turbulent diffusion) terms (a) $\overline{T^1_{\omega_x\omega_x}}$ and (b) $\overline{T^2_{\omega_x\omega_x}}$.

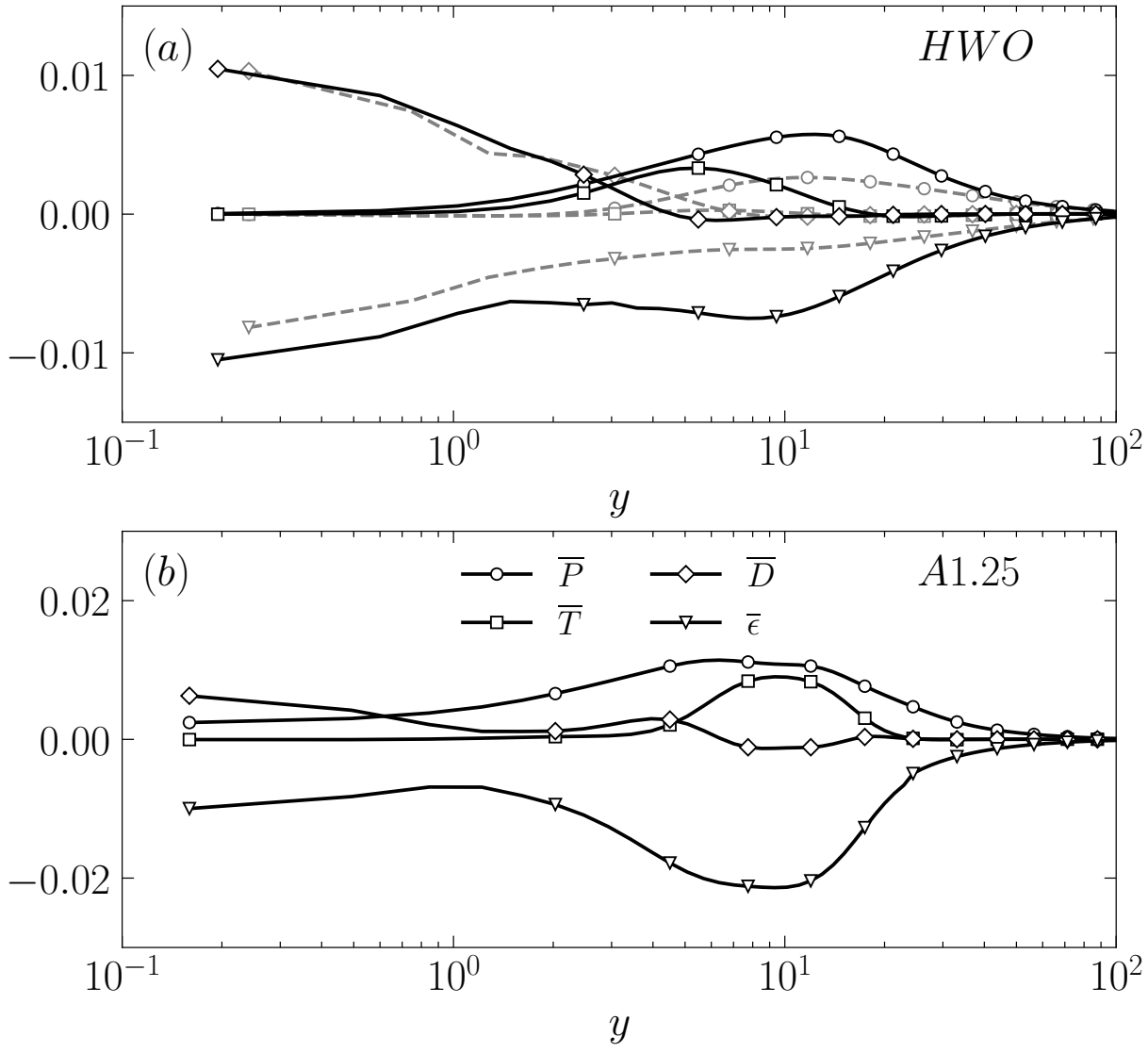

Figure 5.14: Budget of streamwise turbulent enstrophy transport for (a) HWO and (b) $A1.25$ cases. The budget for the reference (uncontrolled) canonical case is also included in figure (a) in grey broken lines for comparison. The mean advection term $\overline{A_{\omega_x\omega_x}}$ is negligible, and hence not displayed in the figures to avoid cluttering.

transport are closely associated next to the wall at $y \approx 10$. The important point here is that the turbulent transport reaches large values comparable to the production $\overline{P_{\omega_x\omega_x}}$ (figure 5.14*b*). The direct consequence is the setup of excessive dissipation $\overline{\varepsilon_{\omega_x\omega_x}}$ which is twice the production $\overline{P_{\omega_x\omega_x}}$ near $y = 10$. As mentioned before, $\overline{T_{\omega_x\omega_x}}$ is negligible for the uncontrolled case (represented by broken lines in figure 5.14*a*). In the HWO case, the turbulent transport is comparably smaller, and it is restricted to $y < 10$ (figure 5.14*a*).

To partially resume, $\overline{\omega_x\omega_x}$ attains large values close to the wall compared to the uncontrolled case. For large amplitude STW, the near-wall variation from the location of local minima and the wall is almost flattened as a consequence of lack of velocity-pressure gradient term in the transport equation of spanwise turbulent intensity $\overline{ww}$. The streamwise vorticity layers in the STW cases with large amplitudes are simultaneously produced and transported in space by the turbulent diffusion, but they at the same time dissipate quickly and hence do not contribute actively to the formation of the near-wall QSVs.

5.2.3 Wall-normal enstrophy transport

The peculiar behaviour of the $\partial w/\partial x$ and $\partial u/\partial z$ shear layers, constituting ω_y at large amplitude STW, will be discussed in the next chapter in detail. In section 5.3, we will show that the suppression of ω_z also leads to the suppression of ω_y. The maximum of $\overline{\omega_y\omega_y}$ is at $y \approx 10$ in the uncontrolled flow, and is shifted towards $y \approx 20$ in the large amplitude STW cases (figure 5.3). Globally, all the transport terms in transport equation of $\overline{\omega_y\omega_y}$ are weakened and shifted towards the middle of the buffer layer. This is clearly seen in the dissipation ($\overline{\varepsilon_{\omega_y\omega_y}}$) profiles shown in figure 5.15(c). It shows also the suppression of ω_y activity in the viscous sublayer with $\overline{\varepsilon_{\omega_y\omega_y}} \approx 0$ at the wall.

The production terms for the $\overline{\omega_y\omega_y}$ component is given as

$$\begin{aligned}\overline{P_{\omega_y\omega_y}} = &\underbrace{\overline{2\widetilde{\Omega_x}\left\langle\omega_y\frac{\partial v}{\partial x}\right\rangle}}_{\overline{P^1_{\omega_y\omega_y}}} + \underbrace{\overline{2\widetilde{\Omega_y}\left\langle\omega_y\frac{\partial v}{\partial y}\right\rangle}}_{\overline{P^2_{\omega_y\omega_y}}} + \underbrace{\overline{2\widetilde{\Omega_z}\left\langle\omega_y\frac{\partial v}{\partial z}\right\rangle}}_{\overline{P^3_{\omega_y\omega_y}}} + \underbrace{\overline{2\Omega_z}\,\overline{\omega_y\frac{\partial v}{\partial z}}}_{\overline{P^4_{\omega_y\omega_y}}} + \underbrace{\overline{2\omega_x\omega_y\frac{\partial v}{\partial x}}}_{\overline{P^5_{\omega_y\omega_y}}} \\ &+ \underbrace{\overline{2\omega_y\omega_y\frac{\partial v}{\partial y}}}_{\overline{P^6_{\omega_y\omega_y}}} + \underbrace{\overline{2\omega_z\omega_y\frac{\partial v}{\partial z}}}_{\overline{P^7_{\omega_y\omega_y}}} + \underbrace{\overline{2\langle\omega_x\omega_y\rangle\frac{\partial\widetilde{V}}{\partial x}}}_{\overline{P^8_{\omega_y\omega_y}}} + \underbrace{\overline{2\langle\omega_y\omega_y\rangle\frac{\partial\widetilde{V}}{\partial y}}}_{\overline{P^9_{\omega_y\omega_y}}}.\end{aligned} \tag{5.5}$$

Most of the terms appearing in the production term 5.5 either vanish or are negligible. Among the first three terms involving the Stokes strain, the only term which differs from zero is $\overline{P^1_{\omega_y\omega_y}}$, but it is also found to be negligible (not shown). The major production of $\overline{\omega_y\omega_y}$ for the controlled cases still comes from the tilting of the wall-normal turbulent vorticity ω_y by the mean shear

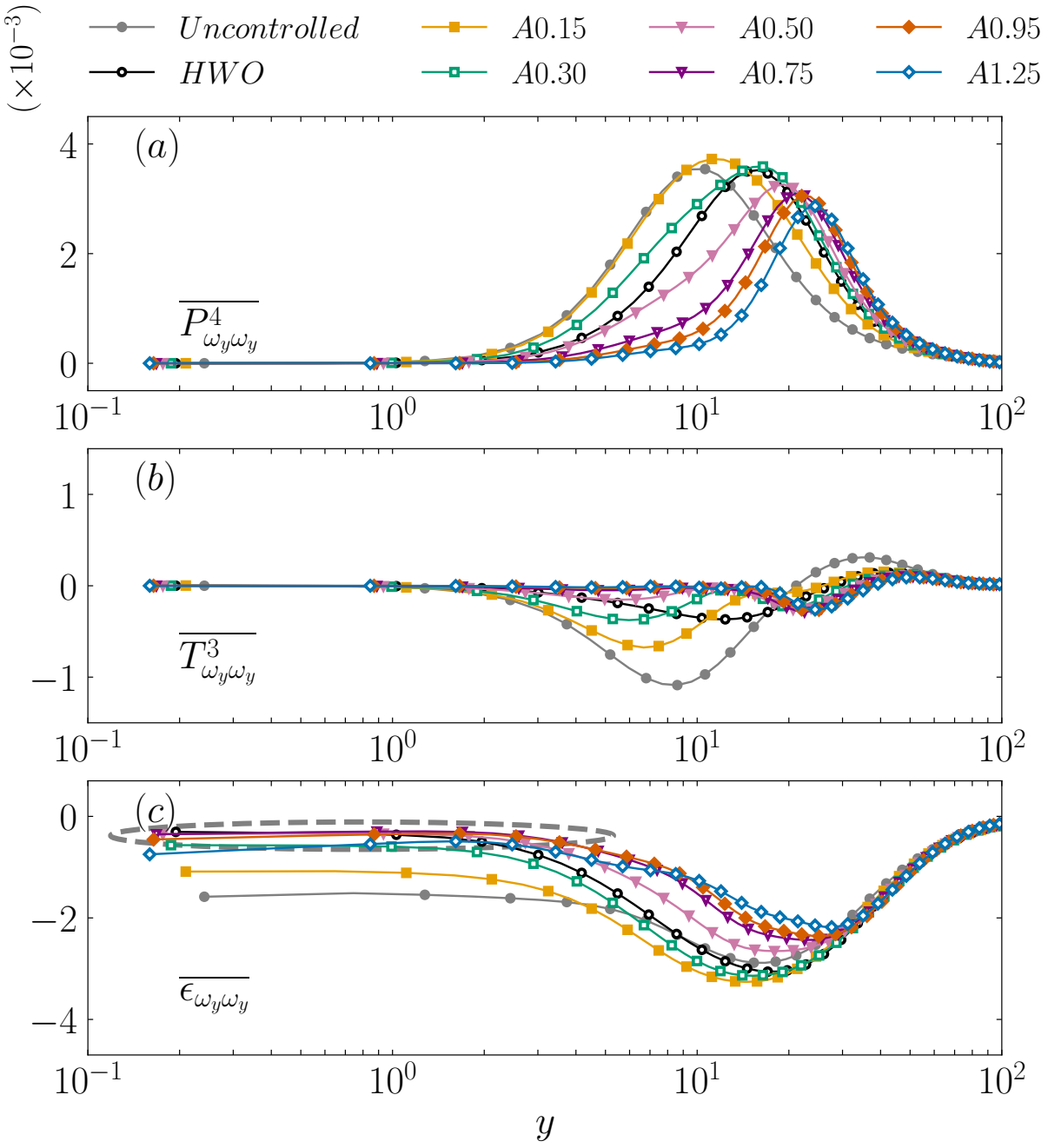

Figure 5.15: The main transport terms appearing in the budget equation of wall-normal turbulent enstrophy component $\overline{\omega_y\omega_y}$: (a) the production term $\overline{P^4_{\omega_y\omega_y}}$, (b) the turbulent diffusion term $\overline{T^3_{\omega_y\omega_y}}$, and (c) the dissipation term $\overline{\varepsilon_{\omega_y\omega_y}}$.

($\overline{P^4_{\omega_y\omega_y}}$), as in the case of the uncontrolled flow. The maximum of the production term $\overline{P^4_{\omega_y\omega_y}}$ is shifted towards $y \approx 20$ in the large amplitude STW cases (figure 5.15*a*), which explains the shift in the maximum of $\overline{\omega_y\omega_y}$ in figure 5.3. The Stokes straining turbulent transport terms $\overline{T^1_{\omega_y\omega_y}} = -2\overline{\langle\omega_y u\rangle\frac{\partial\widetilde{\Omega_y}}{\partial x}}$ and $\overline{T^2_{\omega_y\omega_y}} = -2\overline{\langle\omega_y v\rangle\frac{\partial\widetilde{\Omega_y}}{\partial y}}$ are both nearly zero (not shown). The third turbulent transport term $\overline{T^3_{\omega_y\omega_y}} = -2d\overline{\omega_y\omega_y v}/dy$ has some importance at $y < 20$ in the uncontrolled flow, but becomes insignificant in the STW cases (figure 5.15*b*).

5.3 Artificial suppression of the near-wall turbulent activity

It is seen in figures 4.4-4.5 that both the streamwise and wall-normal turbulent intensities are strongly damped in the large amplitude STW cases. The response of the spanwise turbulent intensity (figure 4.6) is peculiar for the reasons mentioned in the previous chapter. Moreover, in section 5.2 we highlighted the role of production terms appearing directly as a consequence of STW in the spanwise turbulent enstrophy transport in suppressing $\overline{\omega_z\omega_z}$ close to the wall when the imposed amplitude is large enough. Hence, the capital role of the large amplitude STW is to suppress the spanwise vorticity (and therefore streamwise velocity fluctuations) in the near-wall region. To assert this point, we conducted few numerical experiments where the near-wall streamwise, wall-normal and spanwise velocity fluctuations, u, v, w, respectively, were explicitly damped up to a given wall-normal distance δ. The main idea is to see which case collapse to the large amplitude STW cases on the anisotropy invariant maps. The effect of suppressing the turbulent activity in the viscous sublayer on the near-wall turbulence regeneration mechanism and drag reduction has already been investigated by Lee & Kim [91].

The generic algorithm is similar to Jiménez & Pinelli [92], and can be written as

$$\zeta(y,t+dt) = [\zeta(y,t) + dt\ R(y)]F(y), \tag{5.6}$$

where ζ is either u, v or w, R is the appropriate right-hand side, and F is the filter function given as

$$F(y) = 0.5\ \{1 + \tanh\ [\alpha(y-\delta)]\}, \tag{5.7}$$

such that $F(y) \ll 1$ for $y \ll \delta$. Here, the parameter α controls the steepness of the filter function. For all the numerical experiments, the values of α and δ were kept fixed at 0.25 and 10, respectively, to suppress the fluctuations in the viscous sublayer and low buffer layer effectively up to $y \approx 8$. This was done deliberately to avoid strong damping of the fluctuations near the wall. All the simulations were started from an initial turbulent flow field at $\mathrm{Re}_\tau = 180$, and the flow was left to develop for at least 3000 wall units before collecting the data to compute statistics to avoid biases in the statistical calculations related to the transient interval. Statistical data were obtained by averaging 25 full 3D snapshots of instantaneous velocities and pressure fields, covering a time window of approximately 5000 wall units separated by approximately 200 reference wall units.

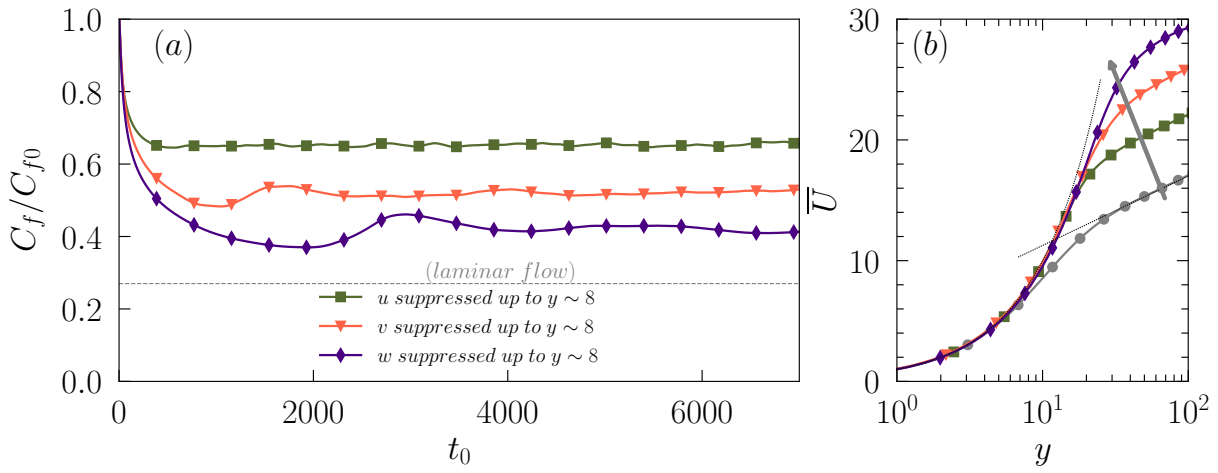

Figure 5.16: (a) Initial response of the skin friction coefficient C_f (normalized by the skin-friction coefficient of the reference uncontrolled flow C_{f0}) and (b) mean velocity profiles for the uncontrolled reference case and the artificially forced cases, respectively.

The initial response of the skin-friction coefficient and the resulting mean velocity profile are shown in figure 5.16. In agreement with Lee & Kim [91], some moderate 30% of drag reduction was achieved by suppressing u up to $y \approx 8$, while suppressing w up to the same wall-normal distance resulted in significantly larger drag reduction margin of about 60%. The near-wall mean velocity profile shown in figure 5.16(b) agrees reasonably well with that of the typical drag reduction scenarios, exhibiting a linear behaviour in the viscous sublayer and an upward shift in the region beyond.

Figures 5.17,5.18 & 5.19 shows response of the turbulent enstrophy profiles resulting from u (or ω_z), v, and w suppression, respectively, in the low buffer layer. Near the wall, ω_z can be approximated as $\omega_z \approx -\partial u/\partial y$, and can be rewritten as $u \approx -y\omega_z(y=0)$. Therefore, suppressing u is effectively similar to suppressing ω_z near the wall. This is indeed clear by looking at the profile of $\overline{\omega_z\omega_z}$ in figure 5.17, where $\overline{\omega_z\omega_z}$ is completely suppressed up to $y \approx 8$. A striking correspondence in the near-wall profile of $\overline{\omega_z\omega_z}$ can be seen with those of the STW controlled cases of $A \geq 0.75$ shown in figure 5.4, suggesting that the major effect of the STW is similar to the artificial suppression of the near-wall streaks up to the low buffer layer. Note that unlike STW control, artificial suppression of u close to the wall also leads to the annihilation of $\overline{\omega_y\omega_y}$ up to $y \approx 8$, as in the case of canonical turbulent channel flows ω_y is dominated by $\partial u/\partial z$. In contrast, we will show in the next chapter that in the large amplitude STW controlled cases, triangular wavy patterns of $\partial w/\partial x$ shear layers start to emerge. The contribution of $\partial w/\partial x$ to ω_y thus becomes increasingly significant, reaching approximately ten times that of $\partial u/\partial z$ very close to the wall (figure 5.1b). This is one of the strong signatures of large amplitude STW that are essentially absent in both the HWO control and the canonical turbulent channel flows, and hence point towards a strong structural alteration in the near-wall turbulence. These aspects

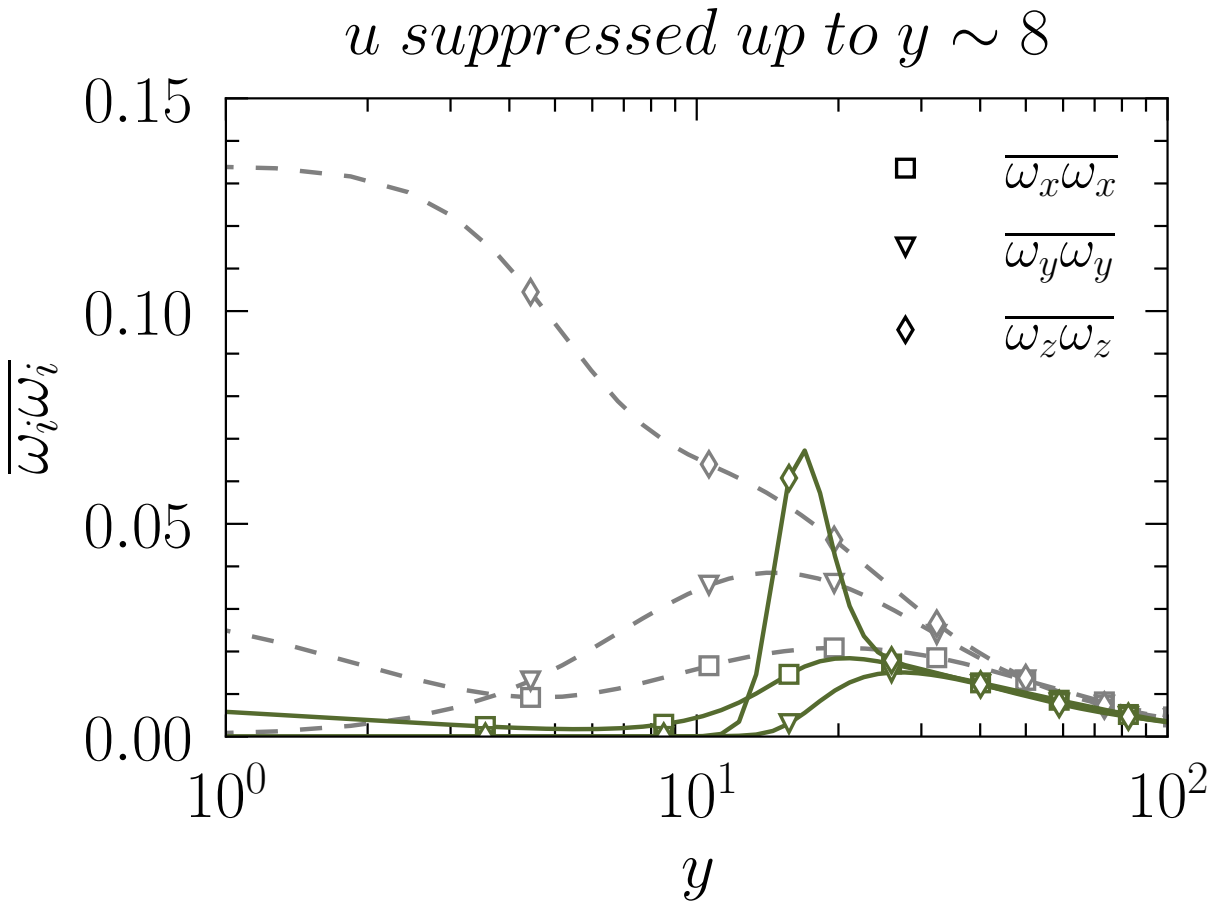

Figure 5.17: Mean profiles of turbulent enstrophies for the streamwise fluctuating field (u) suppression case. Note that all the profiles are scaled with the local friction velocities of the forced cases.

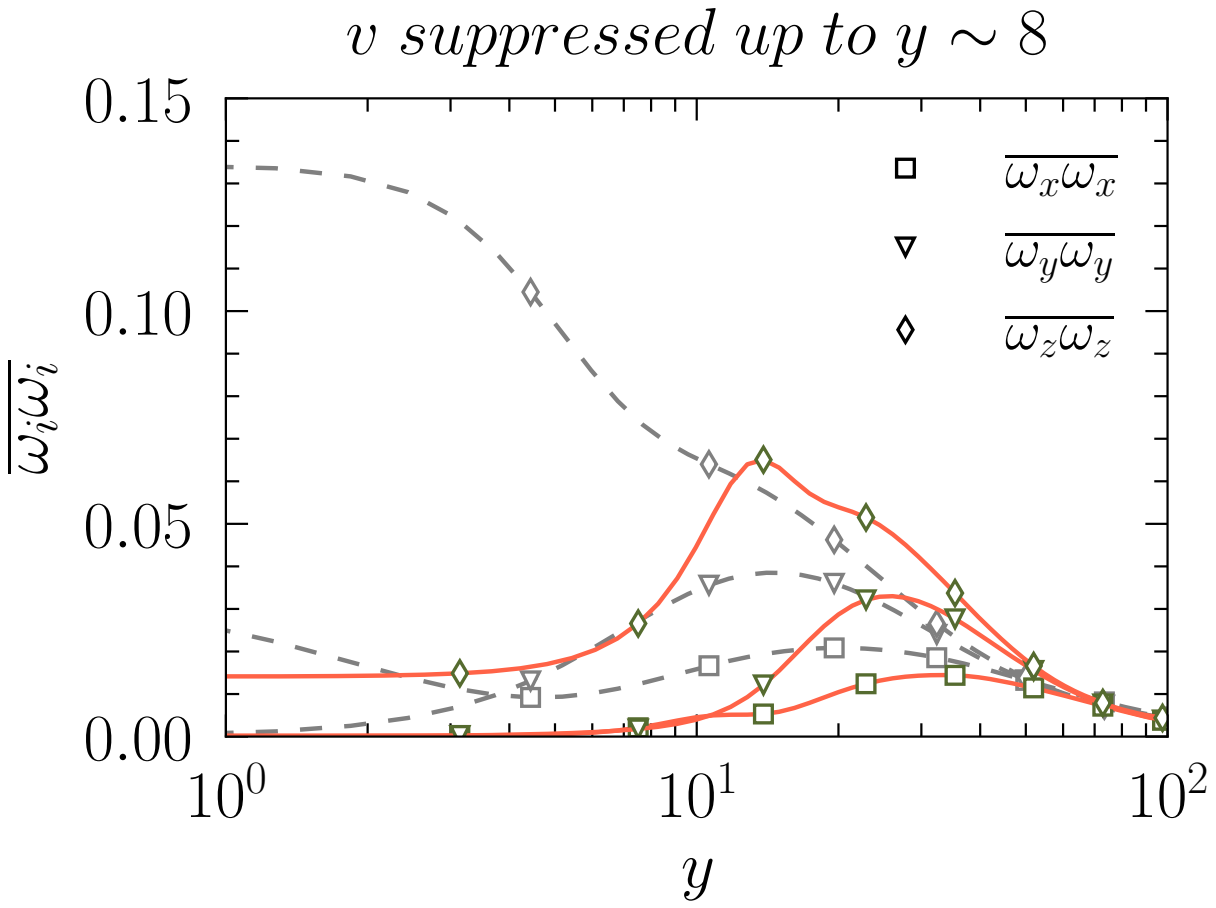

Figure 5.18: Mean profiles of turbulent enstrophies for the wall-normal fluctuating field (v) suppression case. Note that all the profiles are scaled with the local friction velocities of the forced cases.

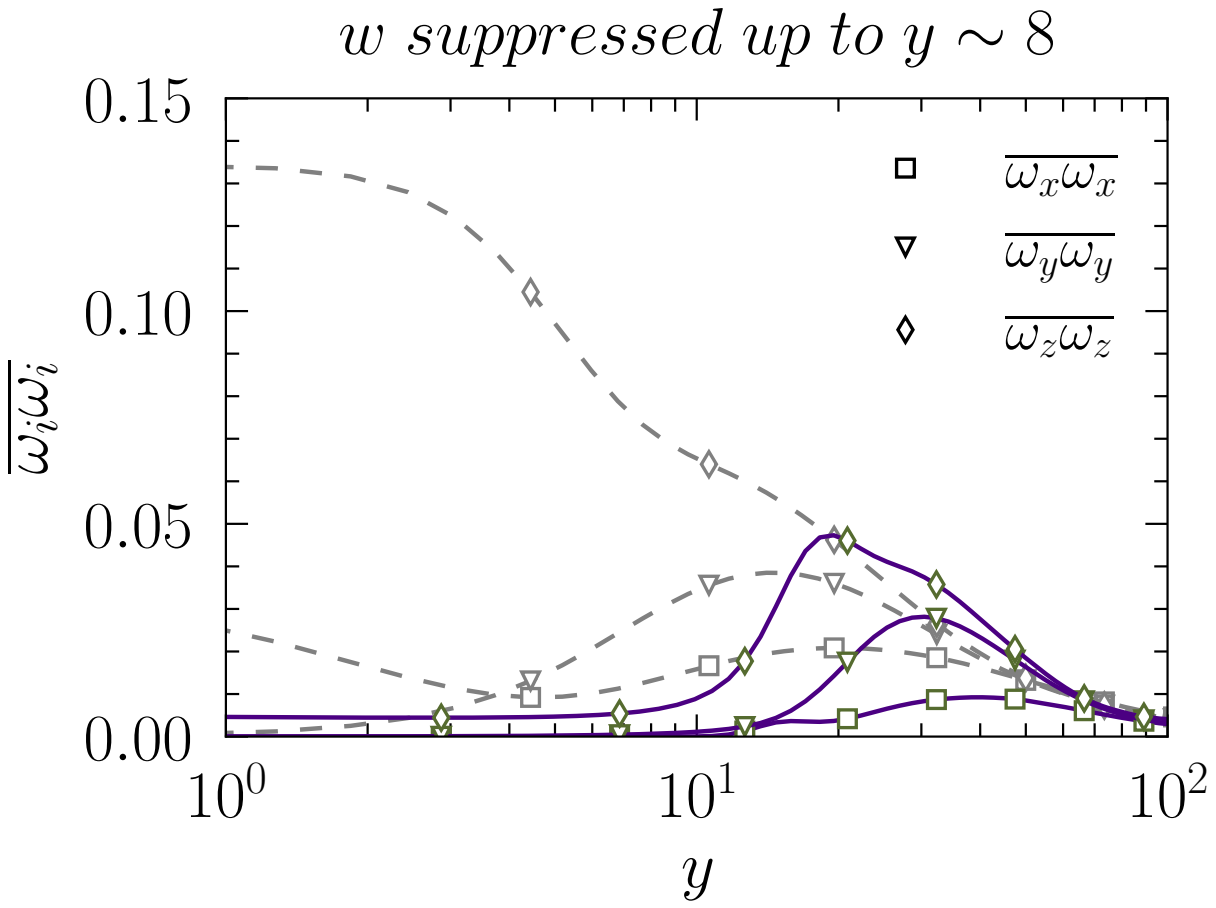

Figure 5.19: Mean profiles of turbulent enstrophies for the spanwise fluctuating field (w) suppression case. Note that all the profiles are scaled with the local friction velocities of the forced cases.

will be discussed in more detail in the next chapter. Note by the way that, the removal of the spanwise vorticity in the viscous and low buffer layers do not modify the intensity and the peak location of the streamwise vorticity (figure 5.17). However, the response of the $\overline{\omega_x\omega_x}$ intensity (figure 5.2) under large amplitude STW is entirely different. The maximum of $\overline{\omega_x\omega_x}$ increases with the imposed amplitude, and there is curiously a negative drift of the streamwise vorticity layers. This is a consequence of the specific response of the near-wall turbulence to the large amplitude STW, and will also be discussed in the next chapter.

We now return to the next main point of our concern, namely the anisotropy invariants. The wall-bounded turbulent flows are characterized by the presence of organized motions, which reflects a high degree of turbulence anisotropy in the near-wall region. The anisotropy invariant map (AIM) introduced by Lumley & Newman [93] provides a convenient way to visualize the anisotropy of the turbulent velocity fluctuations through the Reynolds stress anisotropy tensor

$$a_{ij} = \frac{\overline{u_i u_j}}{\overline{u_i u_i}} - \frac{1}{3}\delta_{ij}, \tag{5.8}$$

where, $\overline{u_i u_i}$ is twice the turbulent kinetic energy, and δ_{ij} represents the Kronecker delta'[94, 95]. A plot of the second and third scalar invariants of the tensor a_{ij}, defined as $II = a_{ij}a_{ji}$, and $III = a_{ij}a_{jk}a_{ki}$ [96], constitutes the well celebrated Lumley triangle or AIM within which all the realizable turbulent states must lie. The II invariant characterizes the degree of anisotropy, while the III invariant identifies its type. The left and right curve corresponds to the axisymmetric disc-like (straining) and axisymmetric rod-like (expansion) states, and are defined by $II = \pm 3/2(4|III|/3)^{2/3}$. The two-component (2C) state is defined by the straight line $II = 2/9 + 2III$. The three corners of the Lumley triangle or AIM correspond to three different limiting states. The left corner corresponds to the isotropic two-component state, the corner on the right-hand side corresponds to the one-component (1C) axisymmetric state, while the bottom most corner of the triangle at $II = III = 0$ corresponds to the isotropic turbulence state.

In the canonical turbulent channel flows, the trajectory of II and III invariants, shown in figures 5.20-5.25 with broken grey lines, lie close to the $2C$ state next to the wall, as $\overline{vv}$ is much weaker in comparison to $\overline{uu}$ and $\overline{ww}$. Away from the wall, in the viscous sublayer, the anisotropy increases reaching a maximum at $y \approx 8$ with $\overline{uu}$ larger than $\overline{vv}$ and $\overline{ww}$, pushing the trajectory towards the rod-like axisymmetric expansion state, in agreement with Moser *et al.* [82]. Further away from this region with increasing distance from the wall, the turbulence becomes more and more isotropic, ultimately acquiring the isotropic state at the centreline.

Figure 5.20 shows the AIM for the case where ω_z (or u) is artificially suppressed. The AIMs of STW cases of large amplitudes $(A > 0.5)$ are surprisingly similar. Figure 5.25 shows for instance the AIM for $A0.75$ case. Similar results are obtained for $A0.95$ and $A1.25$ cases, hence not shown. The AIM trajectories are closely similar in both the large amplitude STW cases and ω_z (or u) suppressed case. In both cases, the trajectories are pushed rapidly from 2C state near the wall towards the disk-like axisymmetric contraction state in the buffer layer. This is mainly due to the

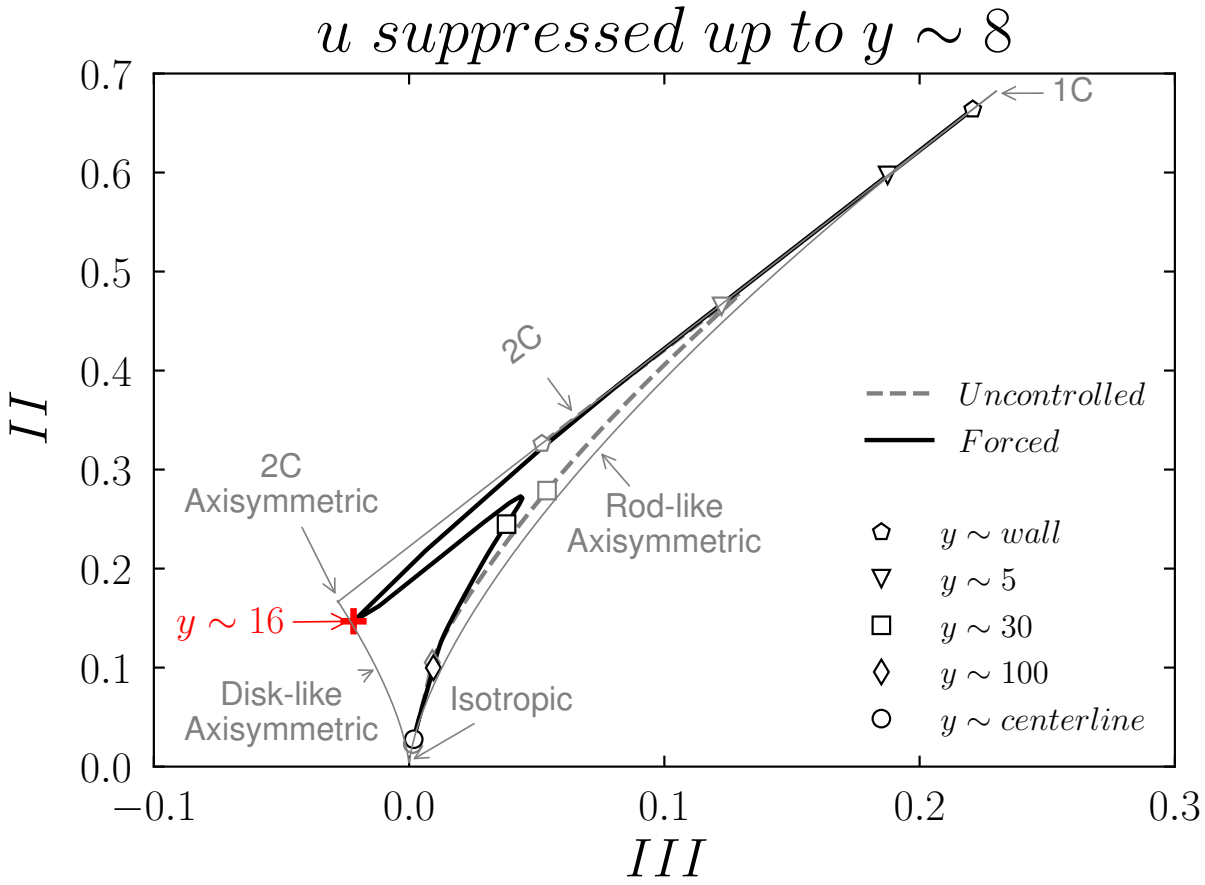

Figure 5.20: Invariant maps for u suppressed case.

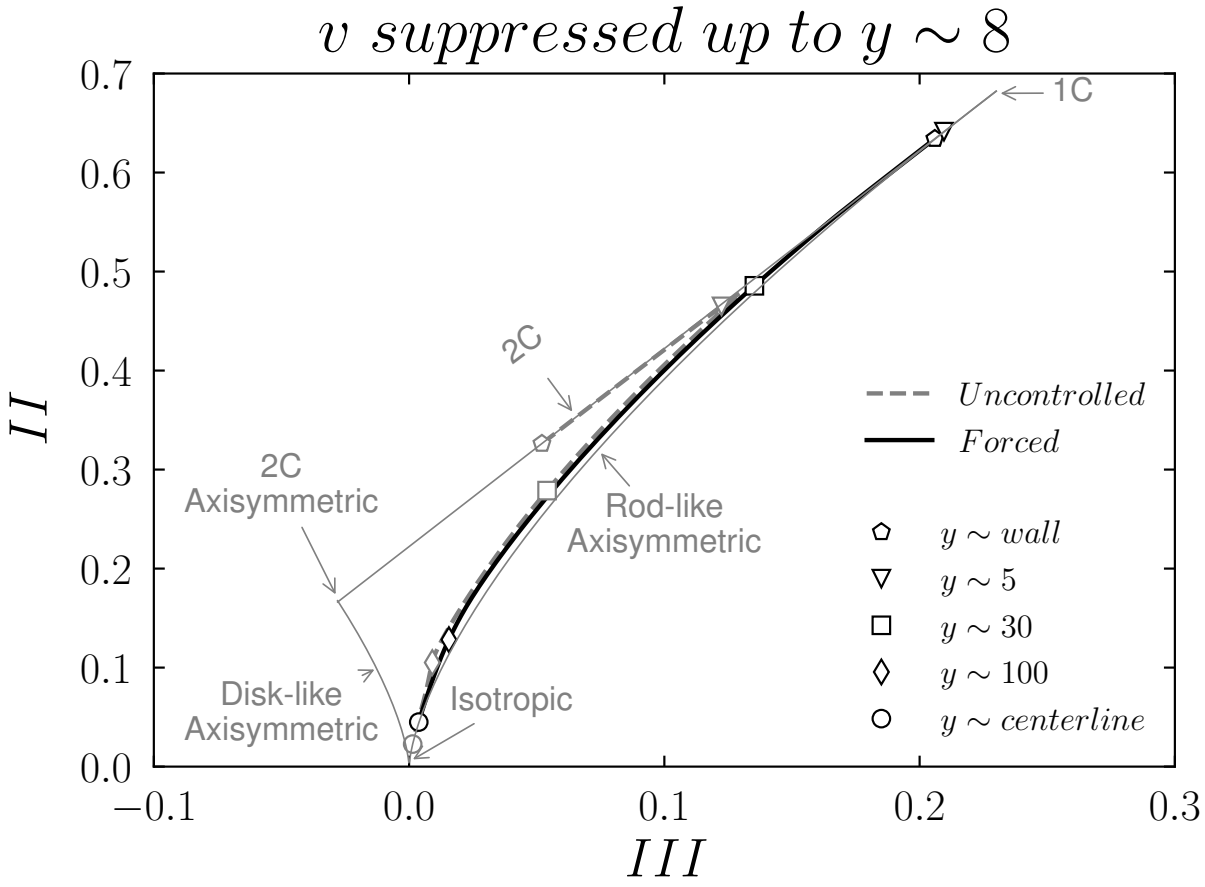

Figure 5.21: Invariant maps for *v* suppressed case.

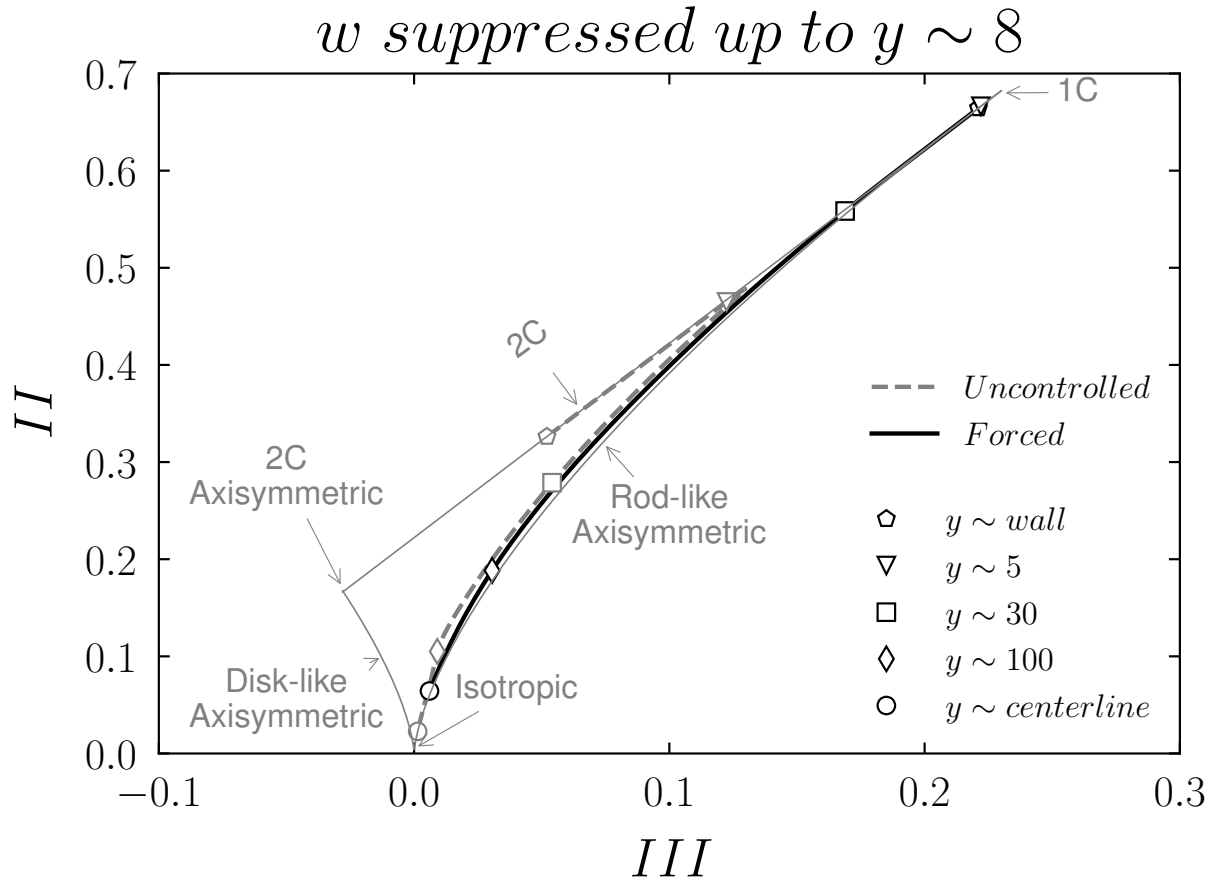

Figure 5.22: Invariant maps for *w* suppressed case.

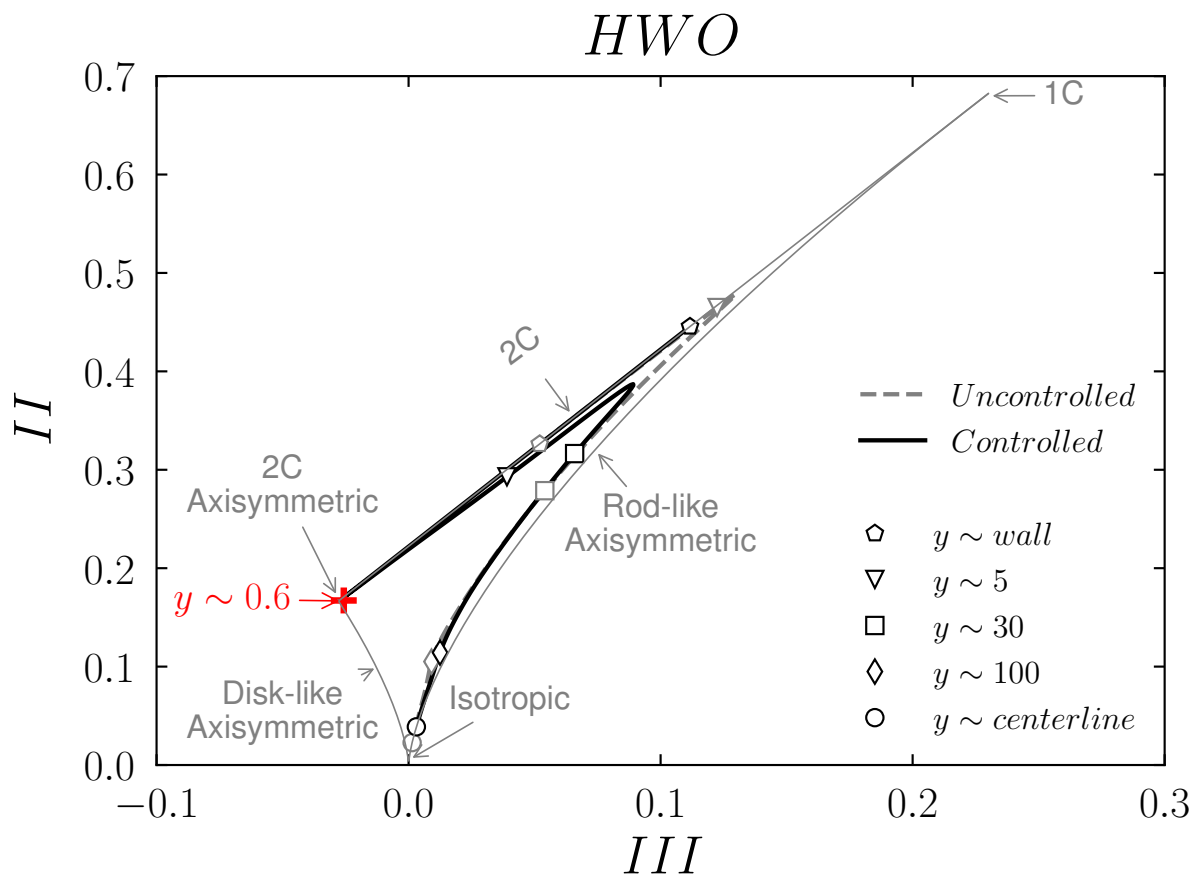

Figure 5.23: Invariants maps for HWO case.

annihilation of the near-wall streamwise turbulent intensity ($\overline{uu}$), which is the largest component in canonical turbulent channel flows. It is pertinent to mention that this terminology is strictly related to the shape of the Reynolds stress tensor, which in no way should be confused with the shapes of the turbulent eddies. This point is clarified in detail by Simonsen & Krogstad [97]. The stress tensor has two equal positive and one negative eigen values in the disk-like axisymmetric state, which is opposite to the rod-like axisymmetric state. The AIM trajectory approaches the isotropic state transiting through the disk-like axisymmetry from a reduced anisotropy state and catches the trajectory of the canonical turbulent channel flow at $y > 30$.

Figures 5.23 & 5.24 show the AIMs of STW case HWO and $A0.50$, respectively. Both AIMs are quite similar and differ from $A0.75$ case (figure 5.25). The trajectory changes rapidly from $2C$ state at the wall to the $2C$ axisymmetric state, but stay then relatively away from the isotropic state without touching the disk-like axisymmetric curve.

Frohnapfel *et al.* [96] considered the drag reduced flow from an anisotropy invariants point of view. Their analyses include the effects of additives, riblets, strong acceleration of boundary

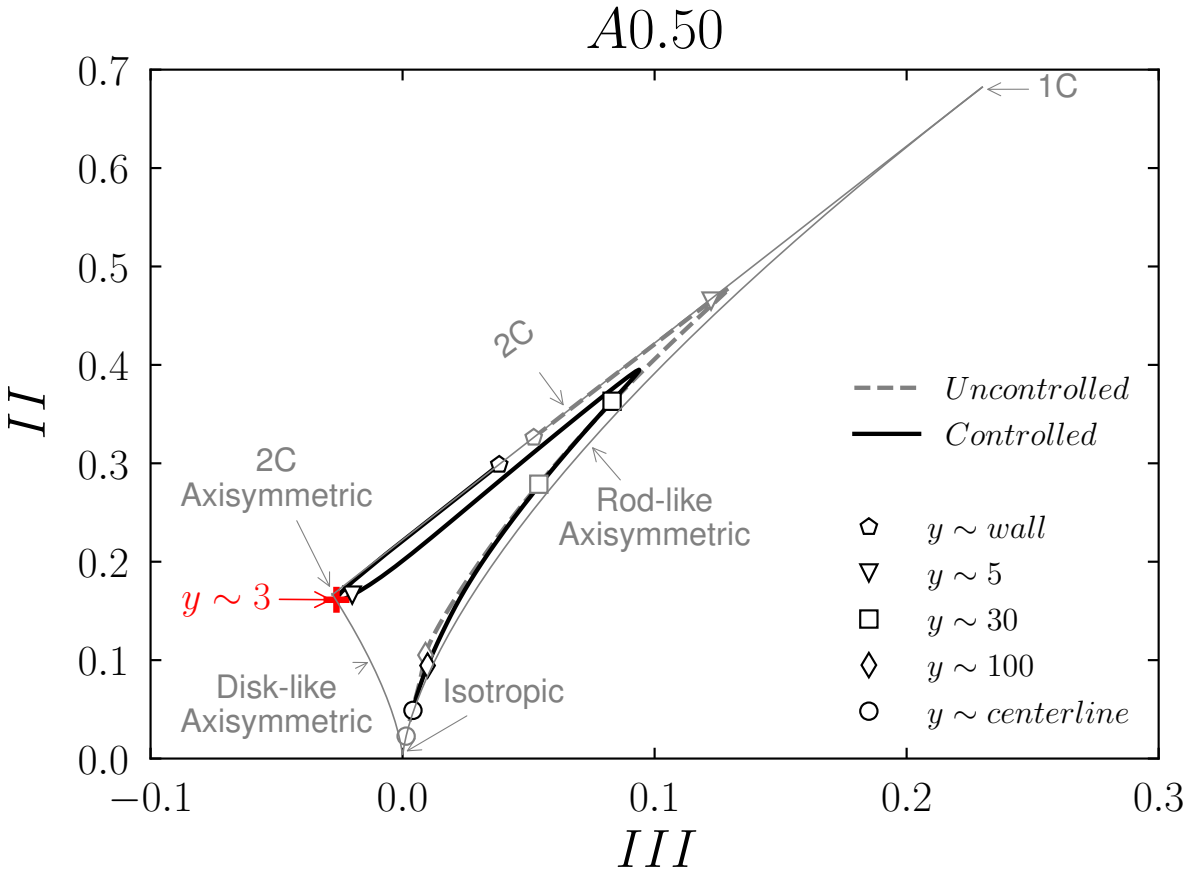

Figure 5.24: Invariants maps for STW case *A*0.50.

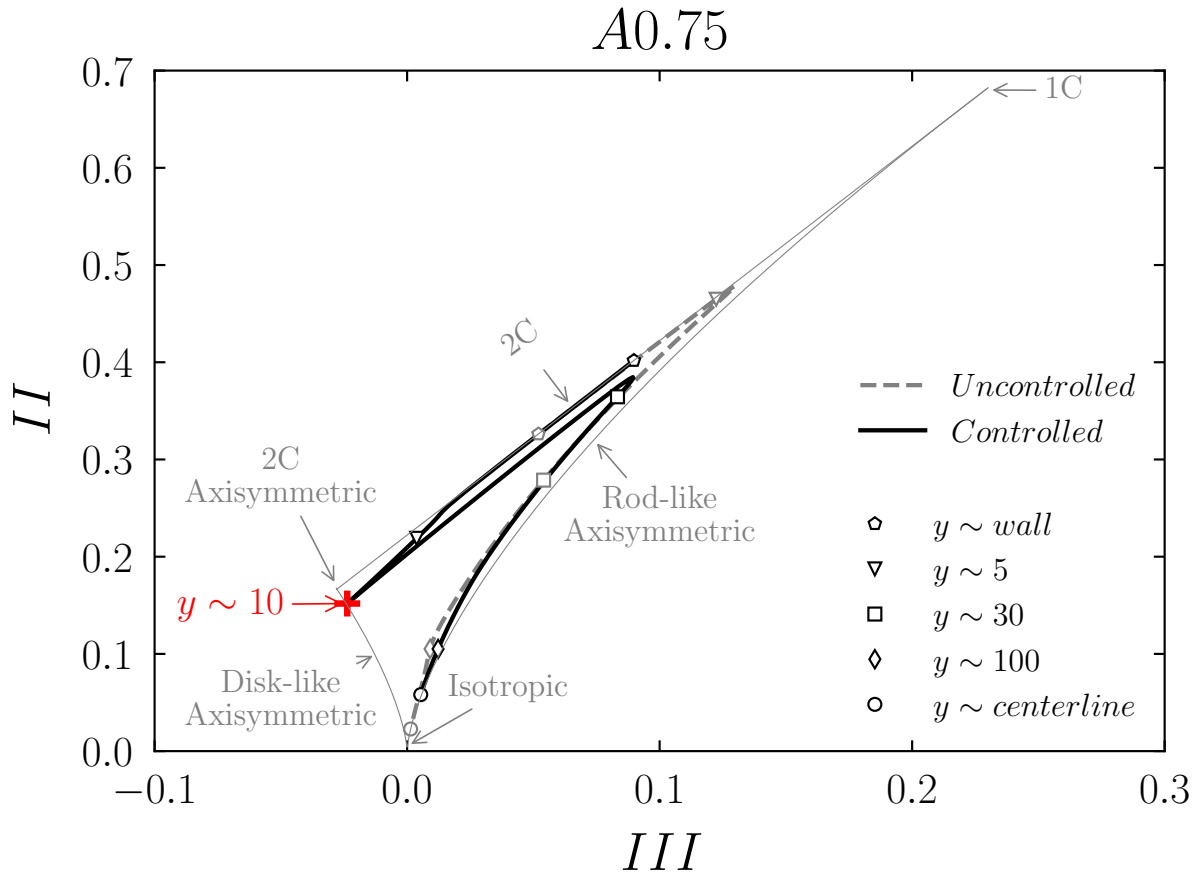

Figure 5.25: Invariants maps for STW case *A*0.75.

layers, and some forced boundary conditions. In their forced cases, they modify the boundary conditions to force near-wall turbulence to tend towards an axisymmetric state by imposing the spanwise fluctuating velocity to follow the wall-normal fluctuations. They obtain a DR of about 32%, and conclude that the anisotropy of the turbulence increases towards the 1C limit in the near-wall region. Curiously, a closer look at their figure $9(b)$ reveals that their forcing also results in a significant suppression of the spanwise fluctuations. Artificial suppression of the wall-normal and spanwise fluctuating velocity field in the viscous and low buffer layers lead indeed to a scenario similar to their suggestion. This is clearly seen in figure 5.22 that shows the AIM when w is suppressed up to $y \approx 8$, resulting in DR margin of about 60% in agreement with Lee & Kim [91]. However, in the HWO and STW cases the trend in the AIM trajectory is entirely opposite, with a tendency towards isotropy, especially in STW of amplitude $A > 0.50$. This shows that DR doesn't necessarily lead to increased anisotropy.

5.4 Summary

In this chapter, we examined the effect of spanwise wall oscillations in the form of STW on the vorticity transport mechanism. The wall-normal and spanwise turbulent enstrophy show a significant reduction in their intensity, the latter almost vanishes in the viscous sublayer for large amplitudes STW. The contribution of the $\partial w/\partial x$ with respect to $\partial u/\partial z$ becomes increasingly important next to the wall for large amplitude STW. The streamwise turbulent enstrophy show a moderate increase in its intensity, and its near-wall variation is almost flattened as a consequence of lack of velocity-pressure gradient term in the transport equation of spanwise turbulent intensity, as explained in chapter 4.

The main production term for the spanwise turbulent enstrophy is shifted in the middle of the buffer layer in large amplitude STW cases. The phasewise plots of the production terms, originating due to forcing, reveal that there is a destruction of the spanwise vorticity by the direct straining through $\partial\widetilde{W}/\partial x$, especially next to the wall. This particular effect is obviously absent in the case of HWO. Globally, STW of large amplitudes attenuates the production by Stokes straining effects and push the profiles towards the buffer layer.

For the streamwise turbulent enstrophy, the main production still originates from the tilting of the wall-normal vorticity by the mean shear, as in the case of uncontrolled flow. The location of the peak remains roughly at the same wall-normal location between $y = 10 - 12.5$ for all the cases. Two additional turbulent diffusion terms emerge in the transport equation of the streamwise turbulent enstrophy that are directly related to the forcing. The second term attains large values comparable to the total production term in the large amplitude STW cases. However, these terms do not essentially create or destroy the enstrophy, but act to redistribute it in space. Consequently, the level of dissipation get enhanced almost twice of production at roughly $y = 10$.

Hence, the streamwise vorticity layers in the large amplitude STW cases are produced and transported in the space simultaneously, but also get dissipated quickly. As a consequence, these near-wall streamwise vorticity layers do not actively contribute in the regeneration mechanism of near-wall QSVs.

The artificial suppression of the near-wall streamwise fluctuating velocity field results in a significantly large drag reduction margin. A striking correspondence in the near-wall profile of the spanwise turbulent enstrophy can be seen with those of the STW controlled cases of large amplitudes, suggesting that the major effect of the STW is similar to the artificial suppression of the near-wall streaks up to the low buffer layer. This is clearly represented in the AIMs which show a striking resemblance to the large amplitude STW cases. In both cases, the trajectories are pushed rapidly from $2C$ state near the wall towards the disk-like axisymmetric contraction state in the buffer layer.

CHAPTER 6

Near-wall Structures

In this chapter, we delve into a comprehensive analysis of the effect of STW control on the structural features prevalent in near-wall turbulent flows. Our focus extends to examining the response of the near-wall streaks and shear layers of spanwise fluctuating velocity field. Moreover, we emphasize the crucial role of the quasi-streamwise vortices in the regeneration mechanism and their significant influence on the flow dynamics. Notably, we demonstrate that these vortices are displaced away from the wall as a result of control, leading to their weakened impact at the wall. Some results presented in this chapter appeared in *Physical Review Fluids, Vol. 7, Issue 5 – May 2022* (https://doi.org/10.1103/PhysRevFluids.7.054601) and *Journal of Fluid Mechanics, Vol. 967, A9 – 25 July 2023* (https://doi.org/10.1017/jfm.2023.478).

6.1 Effects on the near-wall streaks

The spanwise fluctuating velocity field plays a prominent role in the near-wall turbulence. The low- and high-speed streaks of spanwise velocity are the signatures of the QSVs in the early periods of their regeneration process [98]. Even though they do not implicitly contribute to the production of turbulent kinetic energy, they are, however, linked to the Reynolds shear stress producing events, and hence intrinsically linked to the characteristics of the near-wall coherent structures [99]. The connection between the spanwise fluctuating velocity field and the intense Reynolds shear stress generating events become clear if one considers the classical hairpin and horseshoe vortex paradigm. The spanwise fluctuating velocity field is nearly zero between the legs of the hairpin vortices, where the intense sweep or ejection events occur. The w-streaks spacing is roughly 100 wall-units in the buffer layer, similar to the spanwise spacing of low- and high-speed streaks of streamwise velocity. Figures 6.1 show the w-streaks in the uncontrolled and controlled flows at different wall-normal locations. The structural modification brought up by the STW of large amplitudes are clearly visible in figure 6.1. It can be seen that the longitudinal w-streaks are tilted in the spanwise direction and are now organized in $\Lambda-$shaped patterns. This peculiar spanwise reorganization appears at amplitudes $A > 0.50$. A similar reorganization of the $u-$streaks is also observed in figure $6.2(h)$, even though the communication between u and w is cut-off in the low buffer layer for the reasons stated earlier in chapter 4. The usual characteristics of the $u-$ and $w-$streaky structures are recovered only at $y > 20$.

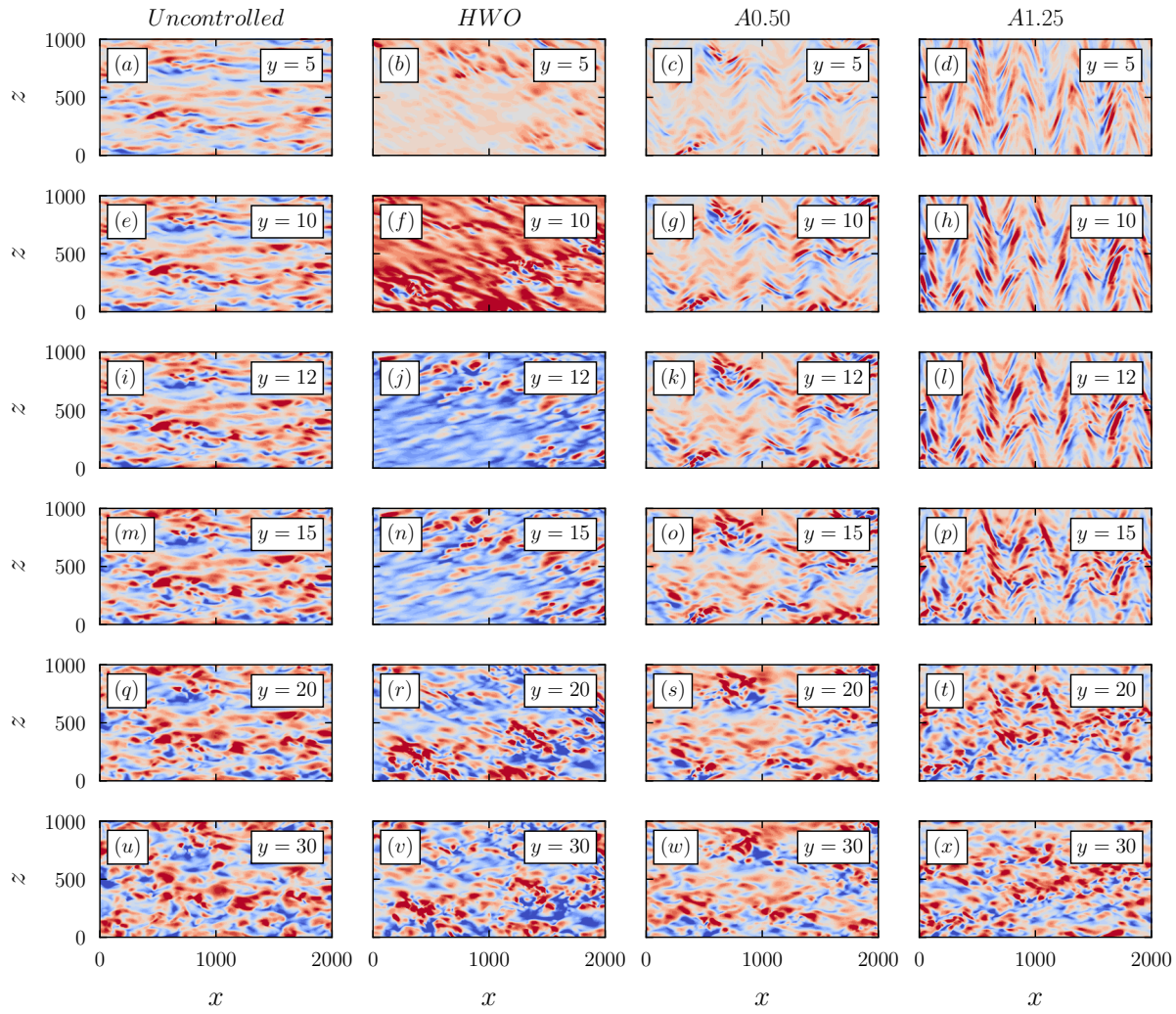

Figure 6.1: Spanwise velocity fluctuations (w) at $y = 5,\ 10,\ 12,\ 15,\ 20,$ and 30 for (a,e,i,m,q,u) uncontrolled, (b,f,j,n,r,v) HWO, (c,g,k,o,s,w) $A0.50$, and (d,h,l,p,t,x) $A1.25$ case, respectively. The blue color represents the low-speed $w-$streaks $(w < 0)$, while the red color represents the high-speed $w-$streaks $(w > 0)$. The contours are in the range -2 to $+2$. Note that w was scaled by the local friction velocity.

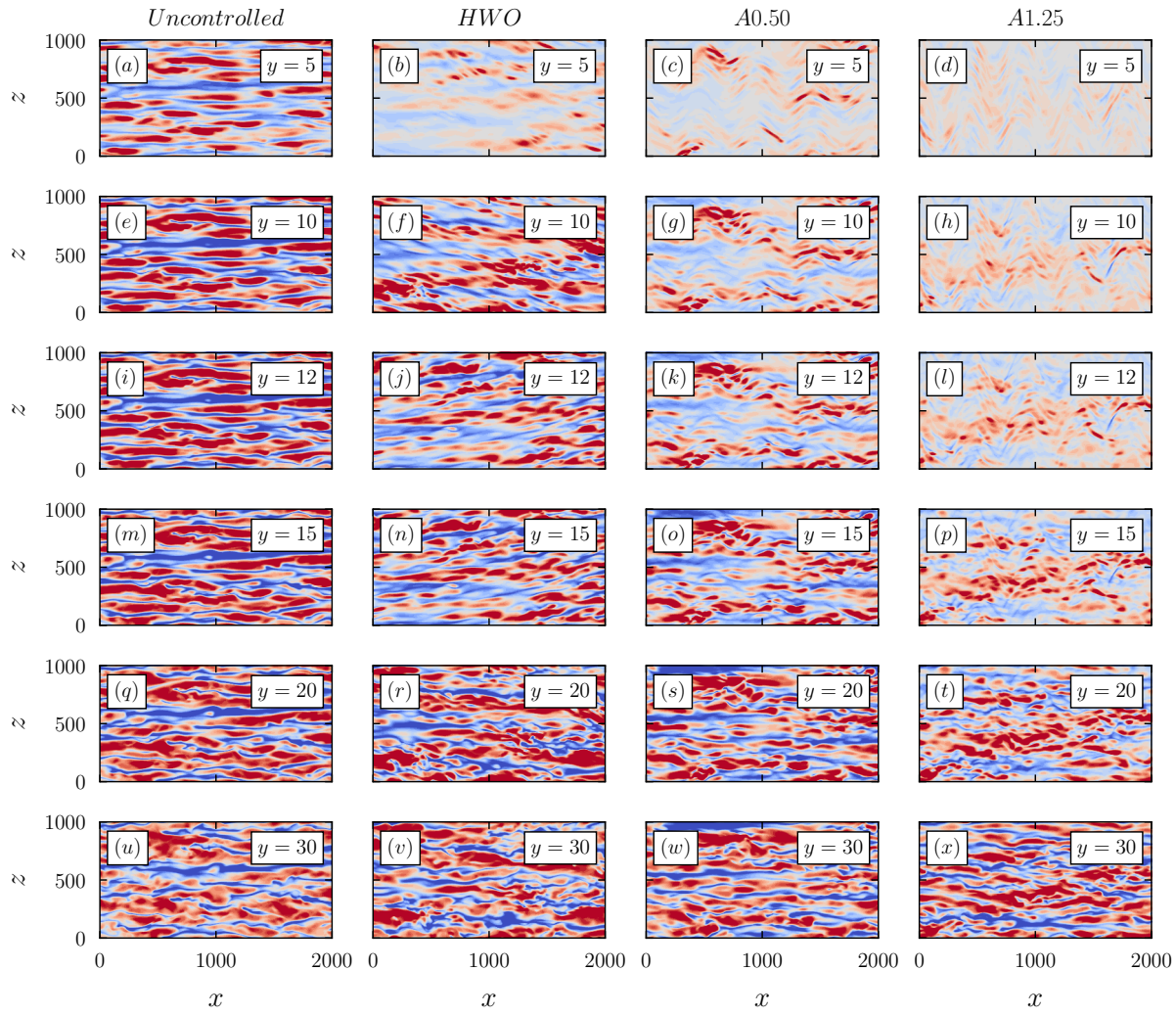

Figure 6.2: Streamwise velocity fluctuations (u) at $y = 5$, 10, 12, 15, 20, and 30 for (a,e,i,m,q,u) uncontrolled, (b,f,j,n,r,v) HWO, (c,g,k,o,s,w) $A0.50$, and (d,h,l,p,t,x) $A1.25$ case, respectively. The blue color represents the low-speed $u-$streaks $(u<0)$, while the red color represents the high-speed $u-$streaks $(u>0)$. The contours are in the range -3 to $+3$. Note that u was scaled by the local friction velocity; had it been scaled by the friction velocity of the uncontrolled flow, the streaky structures would have disappeared, especially for the large DR cases.

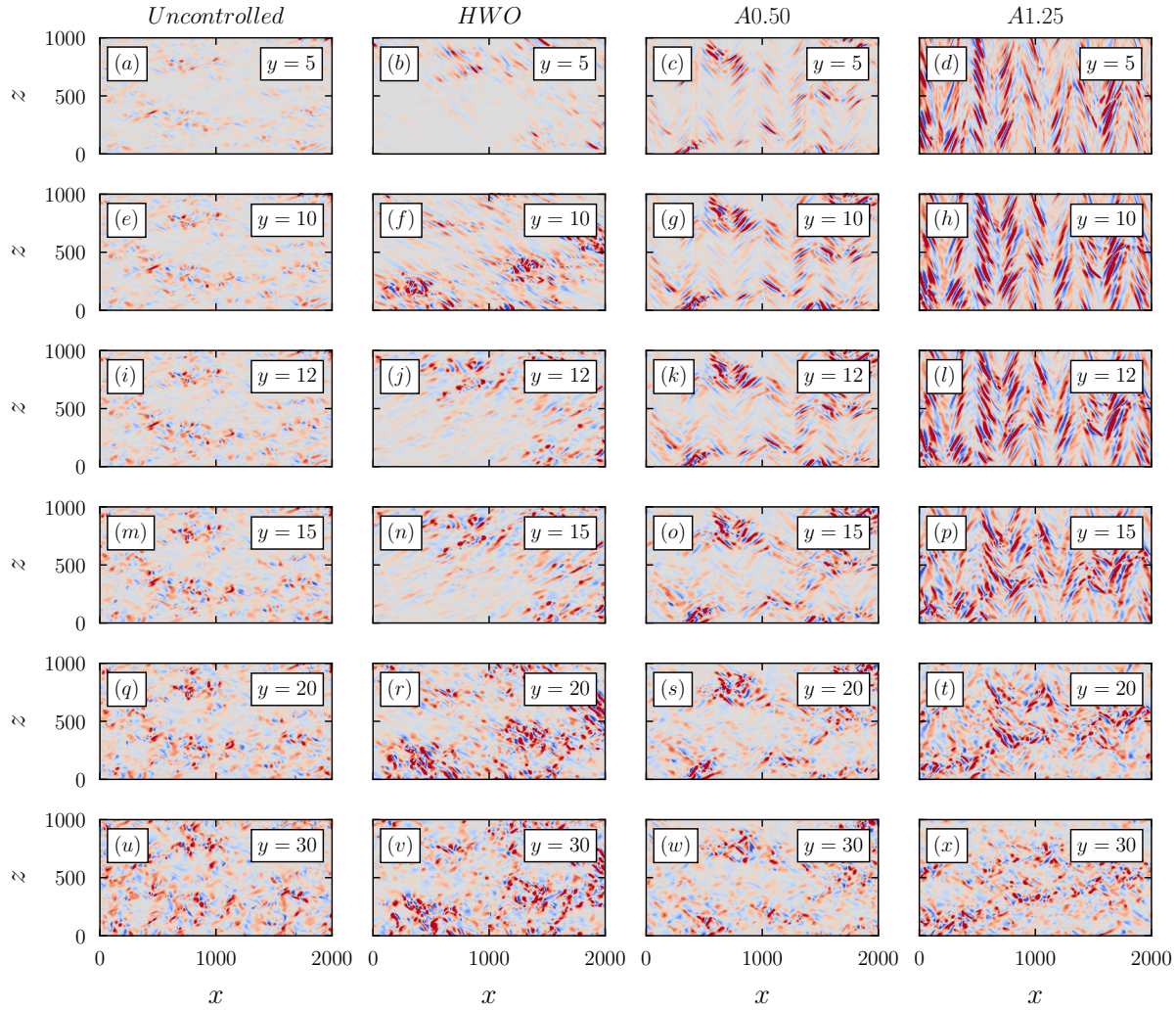

Figure 6.3: $\partial w/\partial x$ shear layers at $y = 5,\ 10,\ 12,\ 15,\ 20,$ and 30 for (a,e,i,m,q,u) uncontrolled, (b,f,j,n,r,v) HWO, (c,g,k,o,s,w) $A0.50$, and (d,h,l,p,t,x) $A1.25$ case, respectively. The blue color represents the negative, while the red color represents the positive values. The contours are in the range -0.1 to $+0.1$. Here also $\partial w/\partial x$ was scaled by the local friction velocity. Note that the heavily modulated $\Lambda-$shaped structures of $\partial w/\partial x$ start to appear for cases with large imposed amplitudes of STW. These structures are absent for both the uncontrolled and HWO cases.

Both $u-$ and $w-$streaky structures are the footprints of the QSVs that are mainly responsible for the production of Reynolds shear stress in the buffer layer in the canonical wall-bounded flows. The individual self-organization of the spanwise velocity streaks (w) in the low buffer layer has a direct consequence on the regeneration of the near-wall active QSVs. In the canonical wall layer, the main regeneration term of the local streamwise turbulent vorticity ω_x in the low buffer layer comes from the titling of the wall-normal turbulent vorticity ω_y and reduces to $-\frac{\partial w}{\partial x}\frac{d\overline{U}}{dy}$. Hence, the $\partial w/\partial x$ shear layers play a crucial role in the generation of ω_x prior to their roll up into QSVs [84, 99–101]. Therefore, as we saw earlier in chapter 5, the suppression of the spanwise velocity fluctuations in the viscous sublayer results in significantly larger drag reduction compared to the suppression of the streamwise or wall-normal velocity fluctuations. Brooke & Hanratty [100] had shown that the tilting term overcomes twisting and stretching at $y < 10$ and peaks at $y = 8$. Like $u-$ and $w-$streaks, the structures of the $\partial w/\partial x$ shear layers are strongly altered by the STW of large amplitudes. These shear layers, shown in figure 6.3, are also organized in similar $\Lambda-$shaped patterns as observed for w-streaks in figure 6.1 for the STW $A1.25$ case.

The main production term of the enstrophy transport $D\overline{\omega_x\omega_x}/Dt$ is still the term related to the tilting of the $\partial w/\partial x$ shear layers in the controlled flow. Figure 5.12(b) shows the production term $\overline{P_{\omega_x\omega_x}} = -2\overline{\langle\omega_x\partial w/\partial x\rangle}d\overline{U}/dy$. It is seen that $\overline{P_{\omega_x\omega_x}}$ peaks at $y \approx 10$ and increases with the imposed amplitude A of the STW. Note in figure 5.12(b) that $\overline{P_{\omega_x\omega_x}}$ is an order of magnitude larger for the $A1.25$ case than that in the uncontrolled flow. The HWO case coincides well with the STW $A0.30$ case, strengthening again, that $A = 0.30$ is the lower limit above which the direct effect of STW are felt in the wall turbulence.

In the canonical turbulent channel flow, the $\partial w/\partial x$ shear layers are spotty and slightly stretched in the spanwise direction, as shown in figure 6.4(a). Using the multiscale approach, Tardu [102] showed that some of the $\partial w/\partial x$ shear layers may appear as spanwise streaks. As seen in figure 6.4(e), the tilting of these shear layers into identifiable elongated ω_x layers already set up at $y = 10$. The morphology of $\partial w/\partial x$ shear layers under the large amplitude STW is strikingly different. The $\partial w/\partial x > 0$ and $\partial w/\partial x < 0$ are organized into Λ-shaped Christmas-tree like structures resulting from a direct effect of STW (figure 6.4d). Their legs are inclined along the spanwise direction by roughly $\pm\pi/4$ and they are tilted by the shear $d\overline{U}/dy \approx 1$ near $y = 10$ (not shown). The titled ω_x layers are consequently also Λ-shaped, and they are far being elongated into streamwise structures (figure 6.4h). It is necessary to go further away from the wall towards $y \approx 30$ to identify the elongated streamwise vorticity layers (figures 6.5a,b). It is also roughly at this position that the contours of $\omega_x\partial w/\partial x$, related to the major production term $P^4_{\omega_x\omega_x}$, appears as long coherent streaky like structures (figures 6.5c). The ω_x layers at $y = 10$ for $A0.50$ case are organized more clearly into streamwise elongated structures compared to $A1.25$ case. They achieve their conventional morphology at $y = 20$, earlier than the $A1.25$ case.

The flow under STW control at large amplitudes develop its own structures in the low buffer

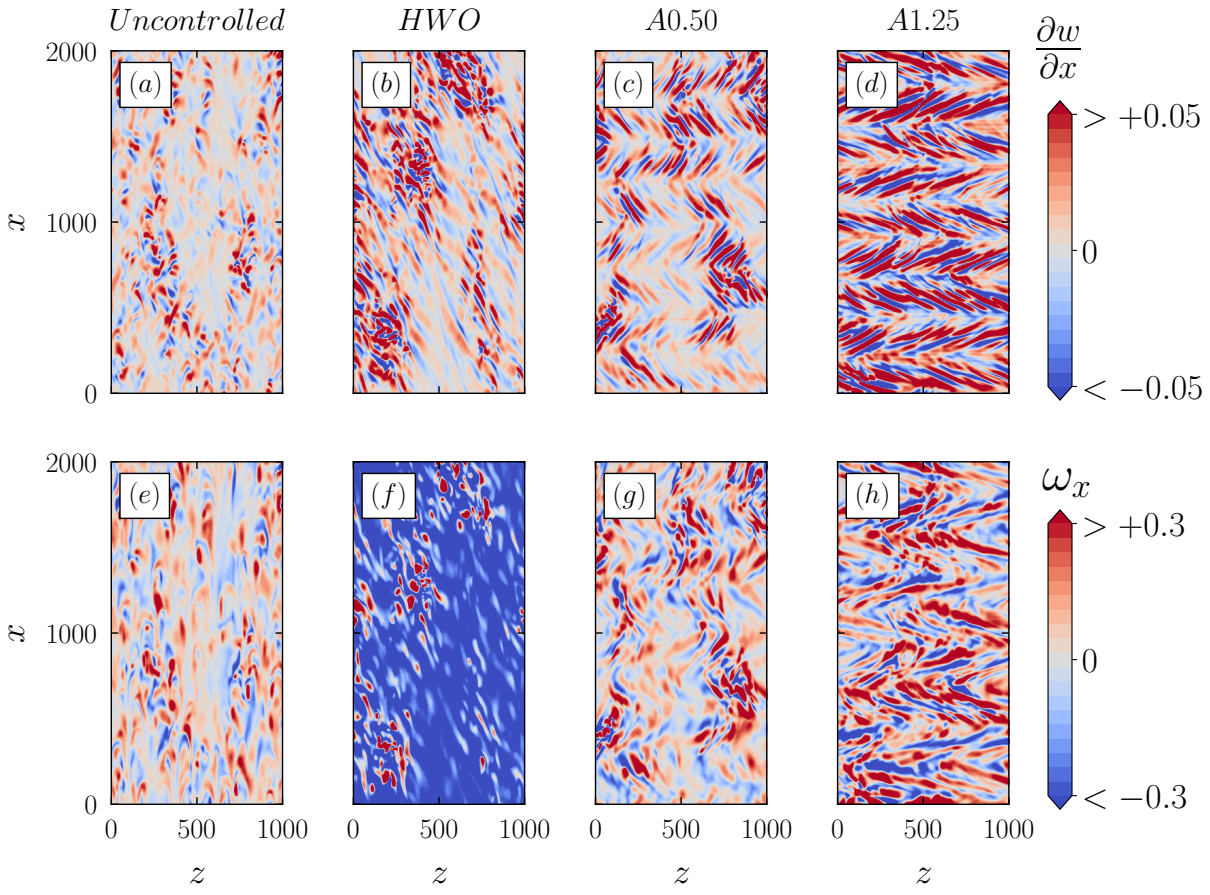

Figure 6.4: Instantaneous field of $\partial w/\partial x$ shear layers and ω_x layers at $y = 10$ for the uncontrolled, HWO, $A0.50$, and $A1.25$ case, respectively.

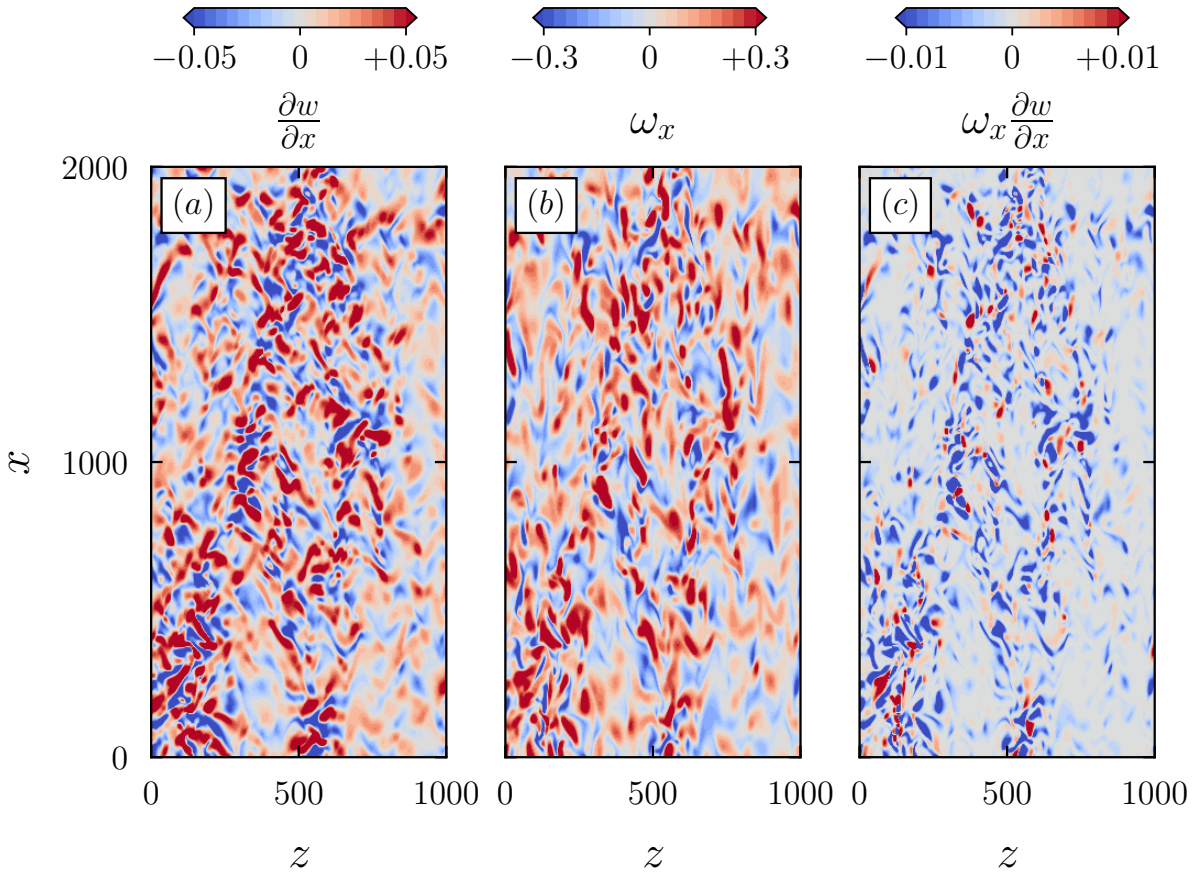

Figure 6.5: Instantaneous field of (a) $\partial w/\partial x$ shear layers, (b) ω_x layers, and (c) $\omega_x \partial w/\partial x$ layers at $y = 30$ for $A1.25$ case.

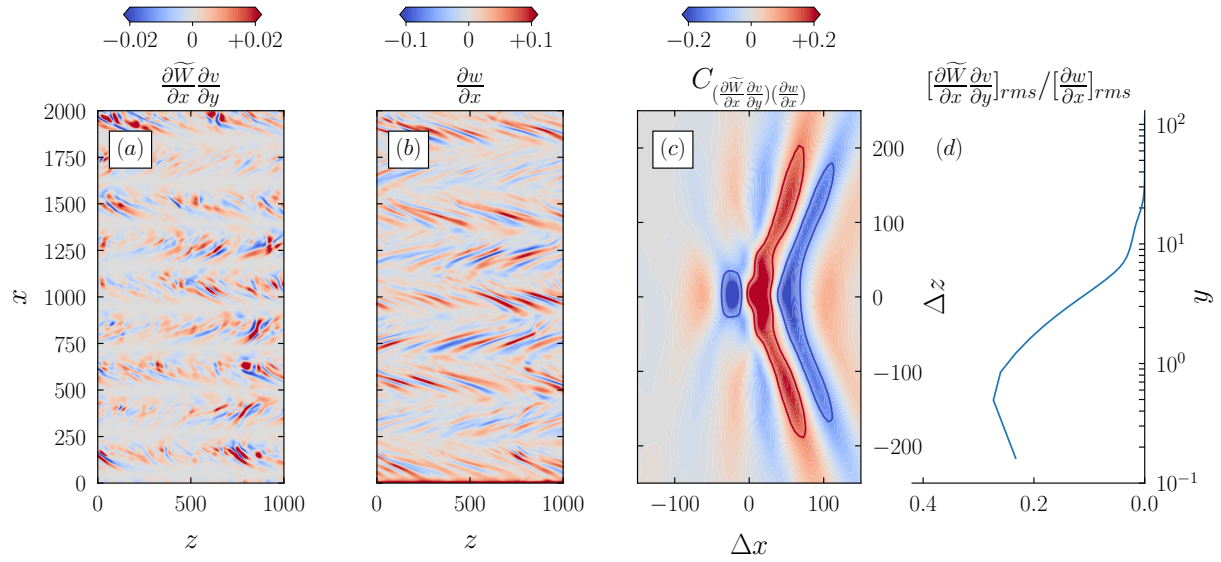

Figure 6.6: Instantaneous field of (a) $\frac{\partial \widetilde{W}}{\partial x}\frac{\partial v}{\partial y}$ shear layers, (b) $\partial w/\partial x$ layers, (c) their cross-correlation coefficient at $y = 2.5$, and (d) the wall-normal distribution of the ratio of their root-mean-square (rms) values for $A1.25$ case.

layer. In the case of HWO, the $\partial w/\partial x$ shear layers are inclined in the streamwise direction, but do not exhibit Λ-shaped structures that are specific to the STW control. The origin of these structures is delicate to understand. The $\partial w/\partial x$ patterns next to the wall, in the large amplitude STW case, are too regular to be considered as induced by the random turbulence phenomenon. They are indeed related to the large $\partial \widetilde{W}/\partial x$ modulation occurring at the wall. Consider the instantaneous transport equation for the streamwise gradient of the instantaneous spanwise velocity field $(\partial W/\partial x)$ given as

$$\frac{D}{Dt}\frac{\partial W}{\partial x} = \frac{\partial W}{\partial x}\frac{\partial V}{\partial y} - \frac{\partial V}{\partial x}\frac{\partial W}{\partial y} - \frac{\partial^2 P}{\partial x \partial z} + \nu\nabla^2\frac{\partial W}{\partial x}. \tag{6.1}$$

The complete analysis of $\frac{D}{Dt}\frac{\partial w}{\partial x}\frac{\partial w}{\partial x}$, which contains 10 terms at the right-hand side (not shown), is complex, especially, because of the local pressure term appearing on the right-hand side of equation 6.1, and hence, is out of scope of the present investigation. There are several terms on the right-hand side of equation 6.1, among which the term $\frac{\partial \widetilde{W}}{\partial x}\frac{\partial v}{\partial y}$, which represents the stretching of the Stokes shear $\partial \widetilde{W}/\partial x$ by the local $\partial v/\partial y$, is negligible at $y > 5$, but reaches large values near the wall at $y \approx 0$. Figures 6.6(a,b) compare the $\frac{\partial \widetilde{W}}{\partial x}\frac{\partial v}{\partial y}$ contours with those of $\partial w/\partial x$ layers at $y = 2.5$, respectively. A striking similarity emerges from these two figures. The Stokes shear $\partial \widetilde{W}/\partial x$ induces Λ-shaped $\partial w/\partial x$ next to the wall. The latter are further stretched, intensified and extended to the viscous sublayer. One quick way to estimate the quantitative importance of $\frac{\partial \widetilde{W}}{\partial x}\frac{\partial v}{\partial y}$ is to compare its root-mean-square value (rms) with the rms of $\partial w/\partial x$. A similar procedure has been conducted, for instance, by Brooke &Hanratty [100] in the local transport

equation $D\omega_x/Dt$. Figure 6.6(d) shows that the rms value of $\frac{\partial \widetilde{W}}{\partial x}\frac{\partial v}{\partial y}$ is as large as 30% of the rms of $\partial w/\partial x$ at $y \approx 1$, and progressively disappears towards the edge of the viscous sublayer. Figure 6.6(c) shows the normalized cross-correlation coefficient C between $\frac{\partial \widetilde{W}}{\partial x}\frac{\partial v}{\partial y}$ and $\partial w/\partial x$ at $y = 2.5$. We observe specific cross-correlation patterns that are somewhat similar to the patterns observed in the autocorrelations of $\frac{\partial \widetilde{W}}{\partial x}\frac{\partial v}{\partial y}$ and $\partial w/\partial x$ (not shown). The cross-correlations reach values as large as 0.2, which is far from being neglectable.

The key question here is to determine whether these shear layers roll-up into coherent vortices or not. This is important since the coherent active eddies lead to the generation of the Reynolds shear stress uv and the drag. In case of roll-up, the resulting topological structure of the coherent structures near the wall would be seriously altered at large imposed amplitudes, by the apparition of contra-rotating vortices strongly inclined along the spanwise direction coming from the unfamiliar topological nature of $\partial w/\partial x$. We carefully analysed the λ_2 structures using tens of snapshots, in particular for the STW cases with $0.75 < A < 1.25$. The symmetric and antisymmetric parts of the velocity gradient tensor from which the second-largest eigenvalue is determined are conveniently scaled by the local inner variables. A movie is available for $A1.25$ case as a supplementary material online. Figure 6.7 shows the top and side views of an instantaneous snapshot of λ_2 structures for the $A1.25$ case. The structures with $\omega_x > 0$ are coloured in red and $\omega_x < 0$ in blue. One finds the classical topological features of the QSVs observed in the uncontrolled flow. Thus, the peculiar $\partial w/\partial x$ layers titled by the mean shear in figure 6.3(c) and figure 6.3(d) clearly do not roll-up into coherent vortices. The vast majority of the coherent structures reach their maturity well above $y = 20$ (figure 6.7b). Therefore, there is a drift of the active ω_x layers that lead to Reynolds shear-stress producing eddies at large amplitude STW. In Sec. 4.4, we discussed in detail the disconnection at large amplitudes of the Reynolds stresses transport between low and high buffer layers. The only remaining possibility of communication that remained was the generation of the coherent active eddies emanating from the roll-up of the atypical shear layers of figure 6.3(c) and 6.3(d). This possibility by now is also discarded.

Last but not least, it is noticeable that the QSVs are systematically organized as packets at $A^* > 0.75$ and have similarities with the transitional-turbulent spots [103]. Packets of vortices, or large-scale motions, containing typically three individual structures, exist in the uncontrolled flow, including at moderate Re [104, 105]. At $A^* > 0.75$, on the one hand, the packets are comparatively more common, and on the other hand, they contain a much larger number of individual structures similar to turbulent spots.

6.2 Drifts of the near-wall QSVs

Quasi-streamwise vortices (QSVs) are a prominent feature of the near-wall turbulent flow field. The QSVs have been recognized to play a significant role in the regeneration cycle of

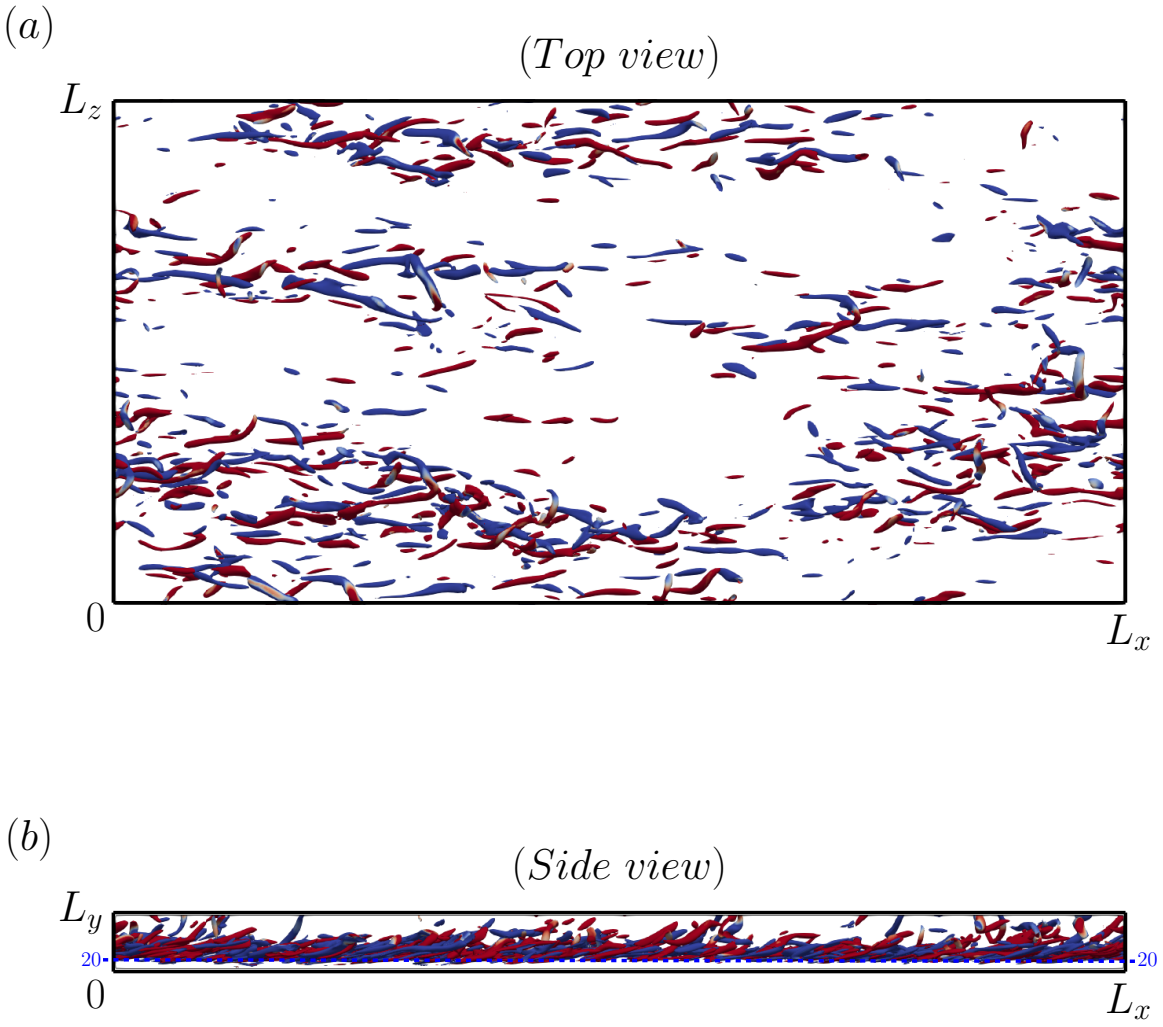

Figure 6.7: Instantaneous near-wall vortical structures ($\lambda_2 = -0.02$) scaled by the local inner variables for the $A1.25$ case. (a) Top and (b) side view. The regions where $\omega_x > 0$ are colored in red and where $\omega_x < 0$ are colored in blue.

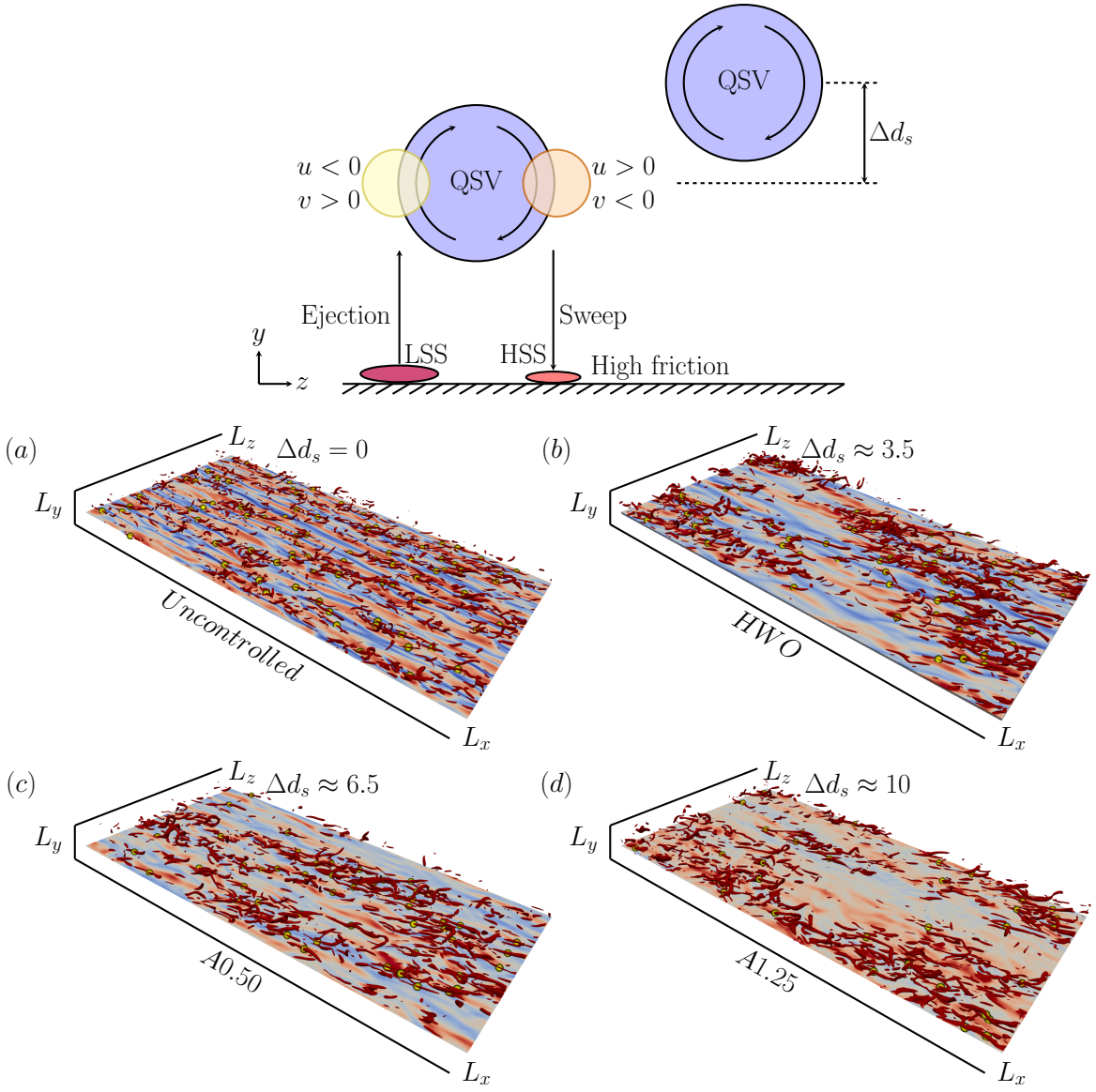

Figure 6.8: Quasi-streamwise vortical (QSVs) structures identified using $\lambda_2 = -0.02$ along with the instantaneous field of streamwise velocity fluctuations u (red: $u > 0$; blue: $u < 0$) on a wall-parallel plane at $y = 15$ for (a) Uncontrolled, (b) HWO, (c) $A0.50$, and (d) $A1.25$ case, respectively. The centres of the active QSVs educed using the criteria mentioned in section 6.2 are marked with yellow dots. The schematic diagram on the top shows the drift (Δd_s) in the QSVs with respect to the canonical uncontrolled case.

near-wall turbulence [36]. They facilitate the exchange of momentum and energy in the near-wall region, and contribute significantly to the generation of Reynolds shear-stress by inducing ejection and sweep events. During an ejection event, the low-momentum fluid is transported away from the wall on one side of the QSV, while on the other side, the high-momentum fluid is transported towards the wall. These ejection and sweep events are the major contributors to the production of turbulent kinetic energy [85].

Earlier studies have reported a drastic suppression of the near-wall quasi-streamwise vortices due to the spanwise wall oscillations control. For example, Yakeno *et al.* [48] studied the effect of homogeneous spanwise wall oscillations on the structural modifications of QSVs. They found that the wall-normal location of the peak population density of QSVs is not affected by the presence of control. Extending the analysis of Yakeno *et al.* [48] to the STW control, Gallorini *et al.* [106] also report little to no shift in the position of QSVs. However, their analysis includes only one STW case that produce a DR margin of about 36%. In the last section, on the other hand, we pointed out that the QSVs reach their full maturity well above $y \approx 20$ for the large amplitude STW. This point, indeed, needs to be clarified whether the STW control affect the position of the near-wall QSVs.

To clarify this point, we examine the effect of STW actuation on the near-wall QSVs, focusing on detecting the drift (Δd_s) in QSVs because of the control, if any. We employ the classical eduction scheme proposed by Jeong *et al.* [85] to detect the near-wall QSVs. First, we detect the vortex cores where the value of $\lambda_2 \leq -0.02$ directly from the 3D instantaneous velocity fields, where λ_2 being the second-largest eigenvalue of the symmetric and antisymmetric parts of the velocity gradient tensor. Then we identify and count only the structures that have streamwise extent greater than or equal to 150 wall units with inclination and titling angles in the range -30° to $+30^\circ$, respectively. The centre of each individual structure is obtained by locating the point where λ_2 attains its local minimum value within the structure. For all the cases studied here, we analysed an ensemble of at least 50 independent full 3D instantaneous fields separated by roughly one full-through time unit $(20h/U_c)$. Since the criteria we chose to select the relevant QSVs is quite strict, as a consequence only few structures qualify to be considered as relevant candidates. For example, in the uncontrolled case, only about 90 structures met the imposed criteria in one snapshot of the instantaneous 3D field. Figure 6.8 shows the λ_2 structures for a few of the cases studied here, and figure 6.9 shows their respective wall-normal distribution of the number of vortices, normalized by the maximum number of vortices.

For the canonical turbulent channel flow, the majority of the mature QSVs are located at $y \approx 24$, which is in agreement with Jeong *et al.* [85]. For the STW cases, however, we observe a systematic drift of QSVs away from the wall (figure 6.9). The drift is about 6 wall units for the $A0.50$ case, and 10 wall units for the $A1.25$ case. This is in disagreement with Gallorini *et al.* [106]. These authors consider a single DR case with control parameters different from us. The closest case we have to them in terms of DR is $A0.30$ for which we observe a drift of about 4.5 wall units, while they report little to no drift. This discrepancy is plausibly coming from

the criteria used to select the vortices. There are two points to consider: first, a "vortex" has to be a "developed compact object" of sufficient length to exist and be dynamically significant (*mature*). In the present work, we exclude vortices with streamwise extents shorter than 150 wall units in the same way as in Jeong *et al.* [85], whereas Gallorini *et al.* [106] use rather a lower threshold length of 50 wall units, which means in their case a significant number of the detected vortices are *immature* low buffer layer structures. That indeed results in a twice smaller tilt angle of the structures they detect compared to Jeong *et al.* [85]. Second, in their controlled case they "opted to discard the same percentage of candidate vortices considered in the reference case, to avoid the assumption that control does not affect the length of QSV", but forcing may affect the related probability density functions, and rejecting the same percentage as in the reference case may induce some bias. Whereas, in the present work, the criteria used to select the mature vortices is unique and consistent for all the cases. The capacity of near-wall QSVs to regenerate new structures is proportional to their intensity and inversely proportional to the square of their distances (d_s) from the wall, as will be discussed in the subsection below. In the drag reduction scenarios, one would expect an increase in d_s, as observed in the present study. It may, however, happen that d_s remains unaffected, but the intensity of the structures or their population density decreases.

In the next section, we estimate the drift directly from the instantaneous visualizations of the near-wall velocity streaks, and show that the drifts estimated from these two independent methods are in close agreement. Moreover, we show that the drift we observe combined with the rest of the results give us a reasonable estimate of the DR margin, thus increasing the quality of these results.

6.3 Estimation of DR using the drift in QSVs

The drift Δd_s of the active streamwise ω_x vorticity layers decreases the drag according to the conceptual model of Jiménez [107] and also discussed in some detail by Tardu [108]. By active ω_x layers, we mean those layers from which the Reynolds shear stress producing QSVs emerge. Given the complexity of the wall response to the large amplitude STW discussed before, it is difficult to directly determine the drift. One somewhat qualitative, yet objective, way is to investigate the near-wall streaks in order to estimate the drift. The near-wall streaks in the canonical turbulent wall flows are the footprints of the QSVs, and are at best detected by the $\partial u/\partial z$ shear layers near the wall [102]. The $\partial u/\partial z$ shear layers are the thin wall-normal turbulent vorticity ω_y layers separating the low- and high-speed streaks. Figure 6.10 shows a snapshot of $\partial u/\partial z$ in the uncontrolled, HWO and STW $A1.25$ case, respectively. The near-wall long streaks in the canonical flow are already detectable at the edge of the viscous sublayer with a streak spacing of about 80 wall units, in agreement with previously published results [84]. The footprints of QSVs are weak at $y = 5$ under HWO, and they are clearly discernable only at $y \approx 12$,

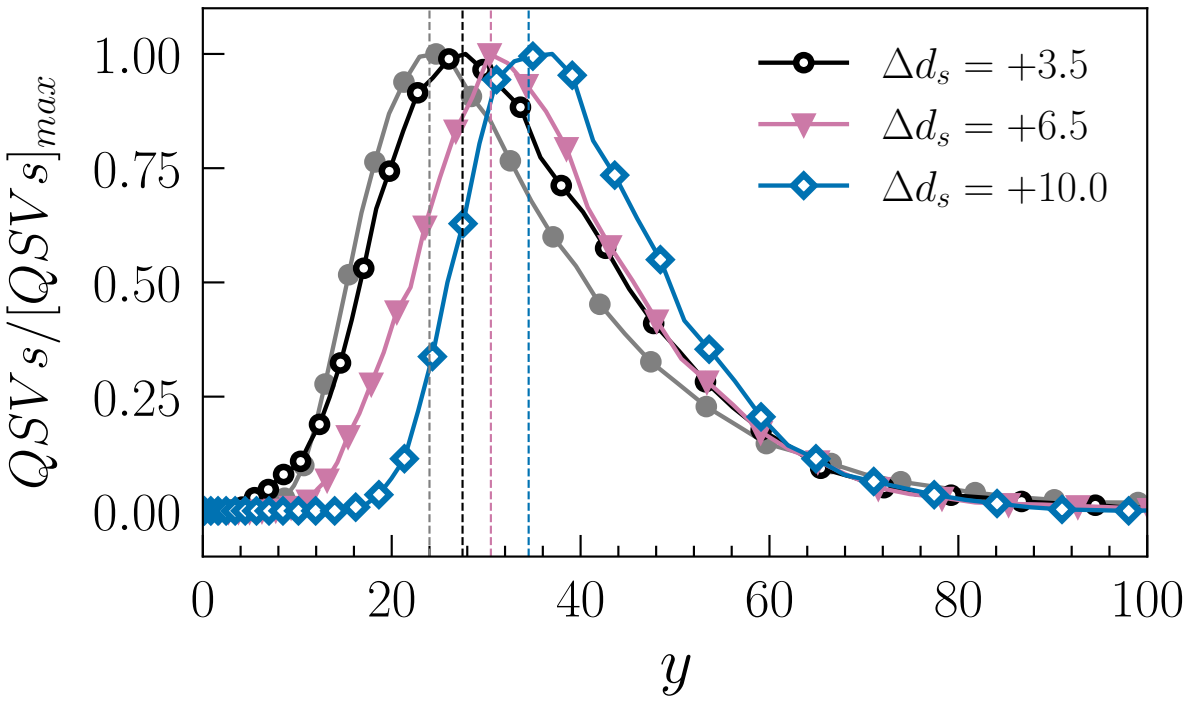

Figure 6.9: QSVs distribution for the uncontrolled, HWO, $A0.50$, and $A1.25$ case, respectively. The colours and markers in the plot correspond to those presented in figure 4.1.

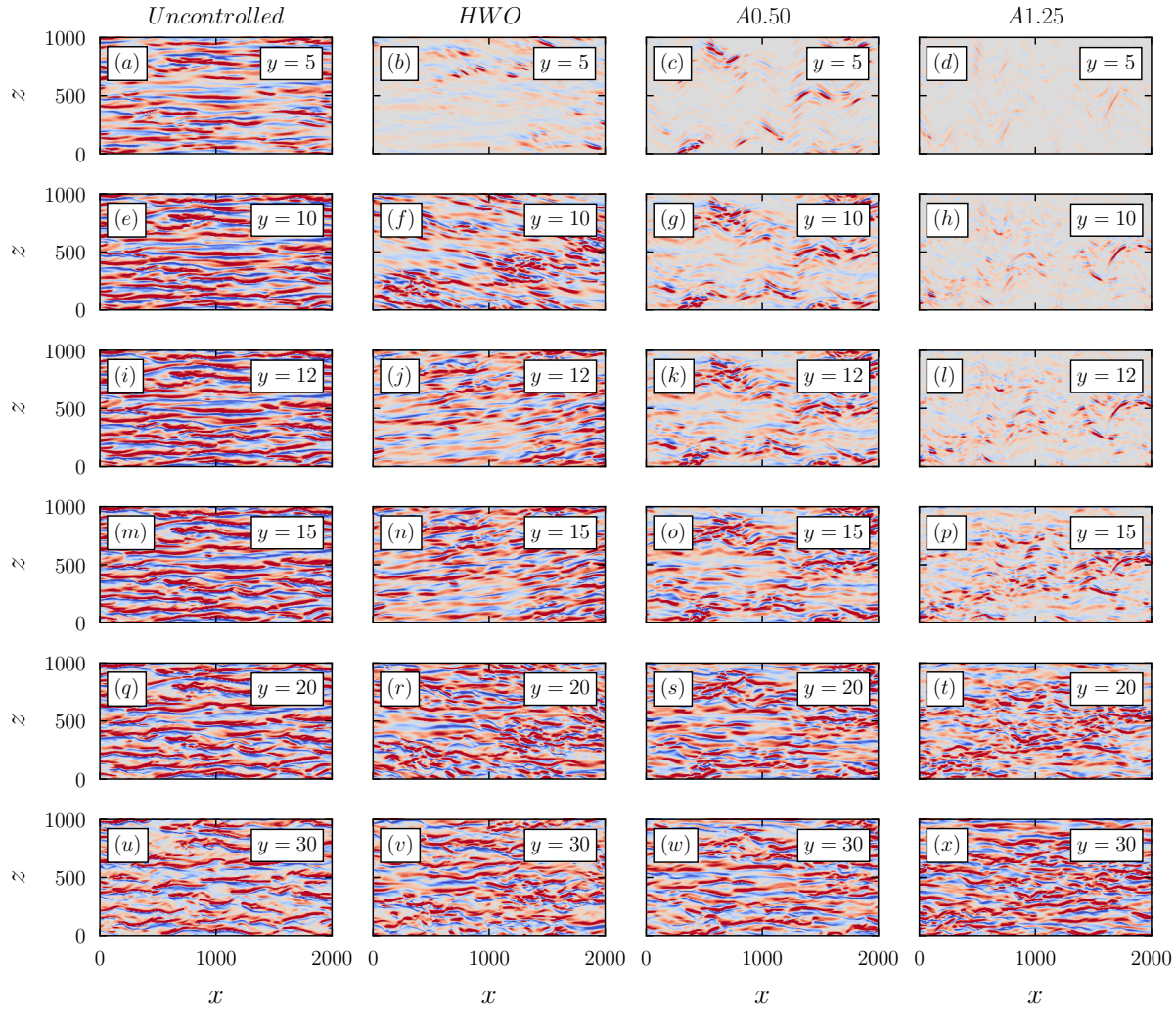

Figure 6.10: Instantaneous fields of $\partial u/\partial z$ shear layers at $y = 5,\ 10,\ 12,\ 15,\ 20,$ and 30 for (a,e,i,m,q,u) uncontrolled, (b,f,j,n,r,v) HWO, (c,g,k,o,s,w) $A0.50$, and (d,h,l,p,t,x) $A1.25$ case, respectively. The blue colour represents the region where $\partial u/\partial z < 0$, while the red colour represents the region where $\partial u/\partial z > 0$. The contours are in the range -0.2 to $+0.2$.

with slightly larger spacing of about 100 wall units.

On comparing figure 6.10(o,k), we see that in the case of large amplitude STW $(A1.25)$, we have to go even further in the buffer layer, towards $y \approx 20$, to detect the near-wall streaks of reasonable coherence. Let us suppose that the drift Δd_s in coherent $\partial u/\partial z$ layers can be related to the drift Δd_s of the active streamwise vorticity layers from which Reynolds shear stress producing eddies emanate. Then figure 6.10 suggests that $\Delta d_s \approx 7$ in the HWO case, because the distribution of $\partial u/\partial z$ shear layers at $y \approx 12$ under HWO becomes comparable to that of the uncontrolled flow at $y = 5$. Similarly, comparing figure 6.10(l,a) suggests that $\Delta d_s \approx 10$ for STW $A1.25$ case. These observations are in agreement with the previous discussion based on figure 6.9.

The flow is turbulent in all the controlled cases here, even though the laminar limit is closely approached for $A1.25$ case. Thus, we have on purpose chosen to use the local wall units to scale the turbulent quantities, the main aim being here is to determine the proper structural modifications. All the quantities scaled by the local inner variables can easily be transformed to the quantities scaled with respect to those based on the friction velocity of the uncontrolled case. Figure 6.11(a) shows the wall-normal distribution of the streamwise turbulent enstrophy $\overline{\omega_x\omega_{x0}}$ and its main production term, $\overline{P^4_{\omega_x\omega_{x0}}}$ in figure 6.11(b), both scaled with the wall units based on the friction velocity of the uncontrolled flow. It is seen that $\overline{\omega_x\omega_{x0}}$ decreases systematically in the controlled cases, while the peak location y_0 is not significantly altered and is at about 20 wall units.

Orlandi & Jiménez [28] relates the location d_s and intensity of the QSVs to the wall shear by

$$\tau_w^* \propto \left(\frac{\Gamma^*}{\nu d_s^{*2}}\right)^{1/2}, \tag{6.2}$$

in dimensional units. In this relation $\Gamma^* = \pi R^{*2}\omega_x^*$ is the mean circulation of the QSVs, d_s^* is the distance to the wall and R is their radius. The qualifier '$*$' here represents quantities in physical dimensional units. This approximate relationship is obtained through a physical argument based on the stagnation flow induced by the QSVs. It gives only a qualitative description of the effect of QSVs on the wall shear, but has the merit to relate intensity and the stand-off distance of the coherent eddies on τ_w. According to equation 6.2, the rate of change of $\Delta\tau_{w0}$ can be related to

$$\frac{\Delta\tau_{w0}}{\tau_{w0}} = \frac{1}{2}\frac{\Delta\Gamma_0}{\Gamma_0} - \frac{\Delta d_{s0}}{d_{s0}}, \tag{6.3}$$

when adequately scaled with the wall units based on the friction velocity of the uncontrolled flow.

One of the observations emerging from figure 6.10 and the λ_2 structures, shown before in figure 6.8, is that the radius of the QSVs (scaled in local wall units) is, in a rough sense, remains unaffected in all the controlled cases. Using $R =$ constant and $\overline{\omega_x\omega_{x0}}$ profiles (figure 6.11a), we

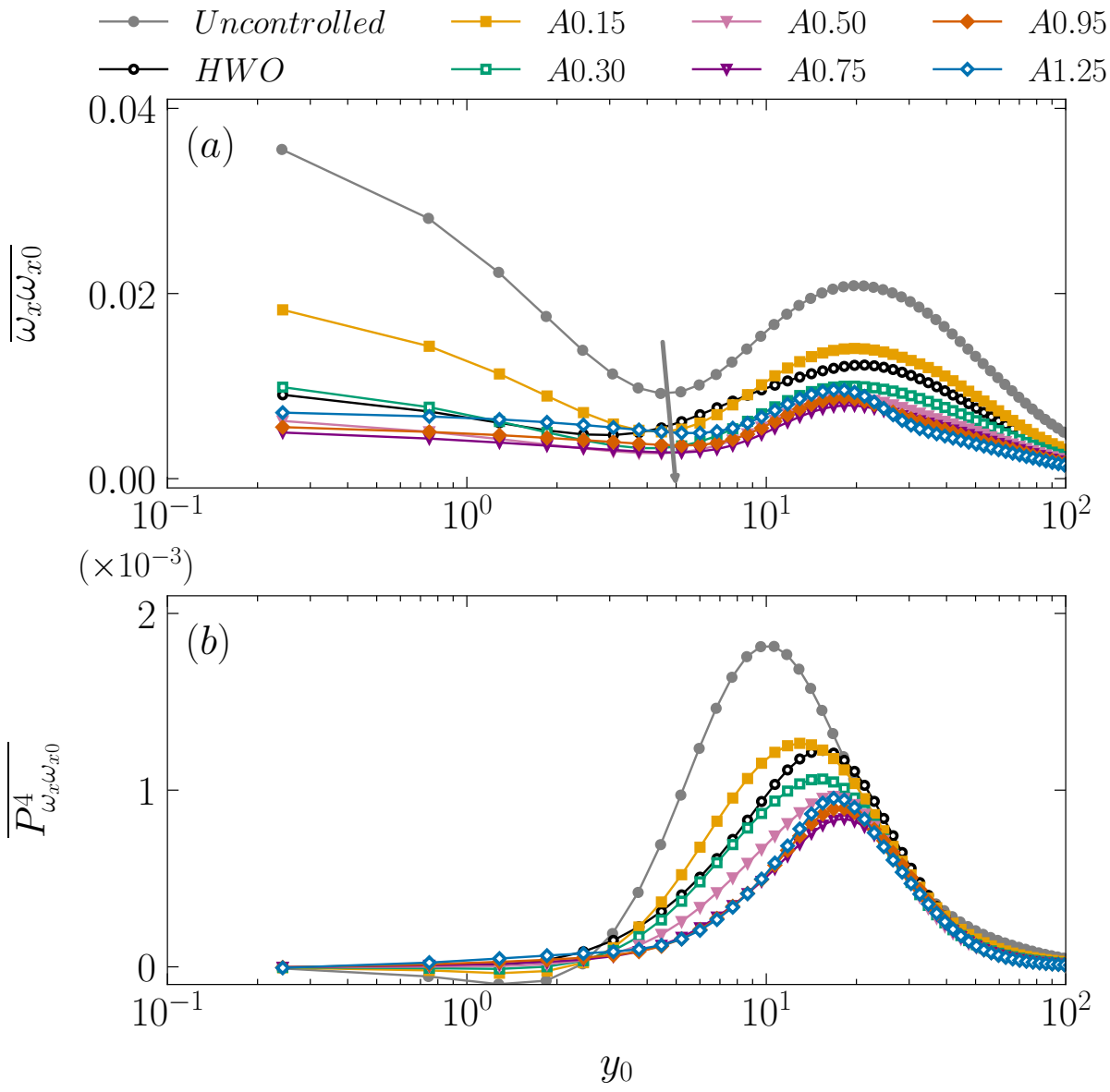

Figure 6.11: Wall-normal distribution of the (a) streamwise turbulent enstrophy $\overline{\omega_x\omega_{x0}}$, and (b) its main production term $\overline{P^4_{\omega_x\omega_{x0}}}$, scaled with the wall units based on the friction velocity of the uncontrolled flow.

estimated 42% of DR for $A0.50$ case from equation 6.3, which is in close agreement with the value reported in table 3.2. However, the equation 6.3 gives 80% of drag reduction at the largest imposed amplitude $A1.25$ case, which is about 30% overestimated. In any case, $\Delta\Gamma_0/\Gamma_0$ term is found to contribute only 20% to the DR. Consequently, the drift $\Delta d_{s0}/d_{s0}$ plays a critical role in the drag reduction mechanism investigated here.

Duggleby *et al.* [42] examined the effect of spanwise wall oscillations on the dynamics of the near-wall turbulent structures in a turbulent pipe flow using Karhunen-Loève (KL) decomposition. They argued that the main effect of the Stokes layer generated by spanwise wall oscillations is to push the structures away from the wall into the region of higher mean velocity by creating a zone where turbulent structures cannot form. As a consequence, the structures are advected faster with less time to interact with the roll modes to transfer energy, resulting in their shorter lifetime, and hence damping of the Reynolds shear stress generating bursting events. Our finding strengthen the arguments presented by them and is in full concordance with their interpretation that although drag reduction results in the decorrelation of the near-wall streaks and the QSVs, but it is the lifting of the turbulent structures away from the wall by the Stokes layer induced by the spanwise wall oscillations that result in drag reduction.

6.4 Summary

In this chapter, we presented the changes in the near-wall structures of the turbulent flow instigated by the imposed streamwise travelling waves. The structural modification brought up by the STW of large amplitudes were clearly visible in spanwise streaks. It was observed that the longitudinal w-streaks are tilted in the spanwise direction and were organized in $\Lambda-$shaped patterns. This peculiar spanwise reorganization appears at amplitudes $A > 0.50$. A similar reorganization of the $u-$streaks was also observed, even though the communication between u and w is cut-off in the low buffer layer for the reasons stated earlier in chapter 4. The usual characteristics of the $u-$ and $w-$streaky structures are recovered only at $y > 20$.

The $\partial w/\partial x$ shear layers were also observed to undergo a similar transformation and form coherent Λ-shaped patterns. Interestingly, these patterns exhibit a regularity that distinguishes them from the random turbulence phenomenon typically observed. Upon analysing the instantaneous transport equation of the $\partial W/\partial x$ shear layers, it becomes evident that these patterns are directly influenced by the Stokes strain $\partial\widetilde{W}/\partial x$. It is important to note that although these shear layers are present, they do not actively contribute to the generation of near-wall QSVs, which is a unique scenario rarely observed in wall-bounded turbulence.

The near-wall quasi-streamwise vortices (QSVs) were shown to drift away from the wall. This drift was determined through two distinct approaches: firstly, by identifying the region where QSVs are predominantly concentrated, and secondly, by examining instantaneous visual-

izations of the near-wall streaks. Remarkably, both methods yielded similar results regarding the drift of the QSVs. By considering this observed drift in conjunction with the other findings, a reasonable estimation of the drag reduction (DR) margin was derived.

CHAPTER 7

Conclusion and perspectives

In this study, direct numerical simulations were performed to investigate the effect of spanwise wall oscillations in the form of STW on the streamwise travelling waves on the Reynolds stresses and vorticity transport mechanism in a turbulent channel flow at Reynolds number $Re_\tau = 180$. The frequency and wavelength of the imposed travelling wave were kept fixed at $\omega = 0.16$ and $\kappa = 1.66$ (in outer units), and only the imposed amplitude was varied nearly by one decade from $A = 0.15$ to $A = 1.25$ (based on U_c) to examine the direct effect arising because of travelling wave like wall oscillations. The results were compared with homogeneous spanwise wall oscillations control at its optimal setting with imposed period $T_0 = 100$ and amplitude $A_0 = 12$. At the largest amplitude studied here, the flow almost reached the relaminarization limit. Such a significant level of drag reduction cannot be achieved in case of homogeneous wall oscillation.

Forcing in the form of the STW results in substantial decline of all the Reynolds stresses components. The transport terms are in close similarity with HWO case when the imposed amplitude of the STW are within the intermediate range $0.30 < A < 0.50$. This regime is marked by a strong damping of the wall normal velocity fluctuations on one hand, and some noticeable decline in the velocity-pressure gradient correlations, on the other. The present investigation globally confirms previously published results on HWO.

The situation changes drastically in the large amplitude STW cases when $A > 0.50$. The intercomponent transfer between the Reynolds stresses fade away in the low buffer layer, wherein it is found that $\overline{\Pi_{uu}} \sim \overline{\Pi_{vv}} \sim \overline{\Pi_{ww}} \approx 0$. The annihilation of $\overline{\Pi_{ww}}$ at $y < 10$ is particularly spectacular. It is shown that $\overline{\Pi_{ww}} \approx 0$ in the low buffer layer results in the flattening of the streamwise vorticity intensity near the wall and points at a strong alteration of the active eddies regeneration process. The spanwise component $\overline{ww}$ is autonomously produced by the Stokes strain related terms $\overline{P^1_{ww}} = -2\overline{\langle wu\rangle \partial\widetilde{W}/\partial x}$ and $\overline{P^2_{ww}} = -2\overline{\langle wv\rangle \partial\widetilde{W}/\partial y}$ in the low buffer layer, and the production simply dissipates. Unexpectedly large values of the phase averages $\langle wu\rangle$ are observed at $A > 0.75$, but $\overline{P^2_{ww}}$ dominates the $\overline{ww}$ production in the low buffer layer as $\partial\widetilde{W}/\partial y \gg \partial\widetilde{W}/\partial x$.

The low and high buffer layer get disconnected at large forcing amplitudes. Forcing also results in the cut-off of inter-component energy transfer between different Reynolds stresses components. The low buffer layer becomes autonomous, self-sustained by pure Stokes strain effects. The capital role of the low buffer layer in the uncontrolled flow is by-passed by forcing,

resulting in a disconnection with the high buffer layer.

The wall-normal and spanwise turbulent enstrophy also show a significant reduction in their intensity, the latter almost vanishes in the viscous sublayer for large amplitudes STW. The contribution of the $\partial w/\partial x$ with respect to $\partial u/\partial z$ becomes increasingly important next to the wall for large amplitude STW. However, the attenuation of the wall-normal turbulent enstrophy is of subordinate importance compared to the spanwise turbulent enstrophy. This is also evident from the numerical experiments conducted in section 5.3, which demonstrates that suppressing the spanwise vorticity near the wall results also in a significant attenuation of ω_y. The streamwise turbulent enstrophy show a moderate increase in its intensity, and its near-wall variation is almost flattened as a consequence of lack of velocity-pressure gradient term in the transport equation of spanwise turbulent intensity, as explained in chapter 4.

The main production term for the spanwise turbulent enstrophy is shifted in the middle of the buffer layer in large amplitude STW cases. The phasewise plots of the production terms, originating due to forcing, reveal that there is a destruction of the spanwise vorticity by the direct straining through $\partial\widetilde{W}/\partial x$, especially next to the wall. This particular effect is obviously absent in the case of HWO. Globally, STW of large amplitudes attenuates the production by Stokes straining effects and push the profiles towards the buffer layer.

For the streamwise turbulent enstrophy, the main production still originates from the tilting of the wall-normal vorticity by the mean shear, as in the case of uncontrolled flow. The location of the peak remains roughly at the same wall-normal location between $y = 10 - 12.5$ for all the cases. Two additional turbulent diffusion terms emerge in the transport equation of the streamwise turbulent enstrophy that are directly related to the forcing. The second term attains large values comparable to the total production term in the large amplitude STW cases. However, these terms do not essentially create or destroy the enstrophy, but act to redistribute it in space. This is clearly evident in the movie attached as a supplementary material. Consequently, the level of dissipation get enhanced almost twice of production at roughly $y = 10$. Hence, the streamwise vorticity layers in the large amplitude STW cases are produced and transported in the space simultaneously, but also get dissipated quickly. As a consequence, these near-wall streamwise vorticity layers do not actively contribute in the regeneration mechanism of near-wall QSVs.

The artificial suppression of the near-wall streamwise fluctuating velocity field results in a significantly large drag reduction margin. A striking correspondence in the near-wall profile of the spanwise turbulent enstrophy can be seen with those of the STW controlled cases of large amplitudes, suggesting that the major effect of the STW is similar to the artificial suppression of the near-wall streaks up to the low buffer layer. This is clearly represented in the AIMs which show a striking resemblance to the large amplitude STW cases. In both cases, the trajectories are pushed rapidly from 2C state near the wall towards the disk-like axisymmetric contraction state in the buffer layer.

The near-wall QSVs show a systematic drift away from the wall. It was calculated using two procedures: by identifying the location where QSVs are mostly populated, and also by looking at the instantaneous visualizations of the near-wall streaks. Both procedure give roughly the same drift. The observed drift combined with the rest of the results gives a reasonable estimate of the DR margin.

The spanwise fluctuating velocity field which plays a prominent role in the near-wall turbulence shows interesting features. The flow is nearly transitional at the largest imposed amplitude STW, wherein the buffer layer develops its own structures induced by the stokes straining $\partial\widetilde{W}/\partial x$ and thus becomes entirely uncoupled with the rest of the flow. The $\partial w/\partial x$ shear layers, which are spotty and slightly stretched in the spanwise direction in the case of uncontrolled flow, begin to form coherent Λ-shaped patterns. However, these structures are too regular to be considered induced by the random turbulence phenomenon. The analysis of the instantaneous transport equation of $\partial W/\partial x$ shear layers show that these patterns are directly connected to the Stokes strain $\partial\widetilde{W}/\partial x$. These shear layers, however, do not play any active role in the generation of near-wall QSVs. Such a scenario is rarely observed in wall-bounded turbulence.

Although the work presented here contributes to our understanding of drag reduction by streamwise travelling waves, further efforts are required to gain deeper insights into the underlying mechanism. It is evident from our discussion that most of our knowledge about flows controlled using streamwise travelling waves is derived from numerical studies, with limited experimental investigations conducted thus far. Notably, recent experimental work by Marusic *et al.* [59] and colleagues has shown promising results, suggesting the potential for achieving net positive gain even at high Reynolds numbers. This highlights the complexity of the physics involved in the control mechanism. Investigating this parameter space at very high Reynolds numbers is crucial to unravel the intricacies of the process. Additionally, we observed that the performance of drag control methods diminishes at large Reynolds numbers, emphasizing the need for a comprehensive investigation to understand the Reynolds number dependence of the control. As noted by Ricco *et al.* [8], a particularly challenging goal is to establish a mathematical relationship between wall-shear stress and actuation parameters based on the transport equations. By establishing a quantitative relationship, it would enable researchers and engineers to design and optimize control strategies with greater accuracy and efficiency. Future research should also focus on studying flows in more realistic geometries beyond canonical configurations. At large Reynolds numbers, the contribution of outer scales becomes significant, warranting further investigations to develop control strategies that specifically target these larger scales.

Another challenge that needs to be address is to find ways to implement control techniques based on wall oscillations. Indeed, the implementation of a control device for drag reduction based on streamwise travelling waves would typically involve the use of active actuation systems or perhaps smart materials. However, it would be highly intriguing to explore the possibility of designing a passive technique that can mimic the behaviour of streamwise travelling waves without the need for any external power input. Such a passive technique would offer advantages in

terms of simplicity, cost-effectiveness, and potentially long-term durability. The development of such passive methods would require innovative engineering solutions and a deep understanding of the underlying fluid dynamics. It presents an exciting avenue for future research and could open up new possibilities for practical applications in various industries involving turbulence control.

CHAPTER 8

Appendix A: Reynolds shear stress transport equations

The Reynolds shear stress transport equations are shortly discussed here. The production, turbulent transport, pressure-velocity gradient, dissipation, and diffusion terms are denoted by $\overline{P_{u_iu_j}}$, $\overline{T_{u_iu_j}}$, $\overline{\Pi_{u_iu_j}}$, $\overline{\varepsilon_{u_iu_j}}$ and $\overline{D_{u_iu_j}}$, respectively. There are terms that directly come from the presence of the travelling waves and induced by streamwise gradients of the velocity field U_i. These are discussed in the main text in detail.

The transport equation for the streamwise turbulent intensity $\overline{uu}$ is given by:

$$\frac{D\overline{uu}}{Dt} = \overline{P_{uu}} - \overline{T_{uu}} + \overline{\Pi_{uu}} - \overline{\varepsilon_{uu}} + \overline{D_{uu}} = 0, \tag{8.1}$$

where:

$$\overline{P_{uu}} = \underbrace{-2\overline{\langle uu\rangle\frac{\partial\widetilde{U}}{\partial x}}}_{\overline{P^1_{uu}}} \underbrace{-2\overline{\langle uv\rangle\frac{\partial\widetilde{U}}{\partial y}}}_{\overline{P^2_{uu}}} \underbrace{-2\overline{\langle uv\rangle}\frac{d\overline{U}}{dy}}_{\overline{P^3_{uu}}}, \tag{8.1a}$$

$$\overline{T_{uu}} = \underbrace{\frac{d\overline{\langle uu\rangle}\widetilde{V}}{dy}}_{\overline{T^1_{uu}}} + \underbrace{\frac{d\overline{\langle uuv\rangle}}{dy}}_{\overline{T^2_{uu}}}, \tag{8.1b}$$

$$\overline{\Pi_{uu}} = -2\overline{\left\langle u\frac{\partial p}{\partial x}\right\rangle}, \tag{8.1c}$$

$$\overline{\varepsilon_{uu}} = 2\left(\overline{\left\langle\frac{\partial u}{\partial x}\frac{\partial u}{\partial x}\right\rangle} + \overline{\left\langle\frac{\partial u}{\partial y}\frac{\partial u}{\partial y}\right\rangle} + \overline{\left\langle\frac{\partial u}{\partial z}\frac{\partial u}{\partial z}\right\rangle}\right), \tag{8.1d}$$

and

$$\overline{D_{uu}} = \frac{d^2\overline{\langle uu\rangle}}{dy^2}. \tag{8.1e}$$

The transport equation for the wall normal turbulent velocity intensity $\overline{vv}$ is given by:

$$\frac{D\overline{vv}}{Dt} = \overline{P_{vv}} - \overline{T_{vv}} + \overline{\Pi_{vv}} - \overline{\varepsilon_{vv}} + \overline{D_{vv}} = 0, \tag{8.2}$$

where:

$$\overline{P_{vv}} = \underbrace{-2\overline{\langle vu\rangle \frac{\partial \widetilde{V}}{\partial x}}}_{\overline{P^1_{vv}}} \underbrace{-2\overline{\langle vv\rangle \frac{\partial \widetilde{V}}{\partial y}}}_{\overline{P^2_{vv}}}, \tag{8.2a}$$

$$\overline{T_{vv}} = \underbrace{\frac{d\overline{\langle vv\rangle \widetilde{V}}}{dy}}_{\overline{T^1_{vv}}} + \underbrace{\frac{d\overline{\langle vvv\rangle}}{dy}}_{\overline{T^2_{vv}}}, \tag{8.2b}$$

$$\overline{\Pi_{vv}} = -2\overline{\left\langle v\frac{\partial p}{\partial y}\right\rangle}, \tag{8.2c}$$

$$\overline{\varepsilon_{vv}} = 2\left(\overline{\left\langle \frac{\partial v}{\partial x}\frac{\partial v}{\partial x}\right\rangle} + \overline{\left\langle \frac{\partial v}{\partial y}\frac{\partial v}{\partial y}\right\rangle} + \overline{\left\langle \frac{\partial v}{\partial z}\frac{\partial v}{\partial z}\right\rangle}\right), \tag{8.2d}$$

and

$$\overline{D_{vv}} = \frac{d^2\overline{\langle vv\rangle}}{dy^2}. \tag{8.2e}$$

The transport equation for the spanwise turbulent velocity $\overline{ww}$ intensity is:

$$\frac{D\overline{ww}}{Dt} = \overline{P_{ww}} - \overline{T_{ww}} + \overline{\Pi_{ww}} - \overline{\varepsilon_{ww}} + \overline{D_{ww}} = 0, \tag{8.3}$$

where:

$$\overline{P_{ww}} = \underbrace{-2\overline{\langle wu\rangle \frac{\partial \widetilde{W}}{\partial x}}}_{\overline{P^1_{ww}}} \underbrace{-2\overline{\langle wv\rangle \frac{\partial \widetilde{W}}{\partial y}}}_{\overline{P^2_{ww}}}, \tag{8.3a}$$

$$\overline{T_{ww}} = \underbrace{\frac{d\overline{\langle ww\rangle \widetilde{V}}}{dy}}_{\overline{T^1_{ww}}} + \underbrace{\frac{d\overline{\langle wwv\rangle}}{dy}}_{\overline{T^2_{ww}}}, \tag{8.3b}$$

$$\overline{\Pi_{ww}} = -2\overline{\left\langle w\frac{\partial p}{\partial z}\right\rangle}, \tag{8.3c}$$

$$\overline{\varepsilon_{ww}} = 2\left(\overline{\left\langle \frac{\partial w}{\partial x}\frac{\partial w}{\partial x}\right\rangle} + \overline{\left\langle \frac{\partial w}{\partial y}\frac{\partial w}{\partial y}\right\rangle} + \overline{\left\langle \frac{\partial w}{\partial z}\frac{\partial w}{\partial z}\right\rangle}\right), \tag{8.3d}$$

and

$$\overline{D_{ww}} = \frac{d^2\overline{\langle ww\rangle}}{dy^2}. \tag{8.3e}$$

Finally, the transport equation for the Reynolds shear stress $\overline{uv} < 0$ (not $-\overline{uv} > 0$) is:

$$\frac{D\overline{uv}}{Dt} = \overline{P_{uv}} - \overline{T_{uv}} + \overline{\Pi_{uv}} - \overline{\varepsilon_{uv}} + \overline{D_{uv}} = 0, \tag{8.4}$$

where:

$$\overline{P_{uv}} = \underbrace{-\overline{\langle uv\rangle \frac{\partial \widetilde{U}}{\partial x}}}_{\overline{P^1_{uv}}} \underbrace{-\overline{\langle vv\rangle \frac{\partial \widetilde{U}}{\partial y}}}_{\overline{P^2_{uv}}} \underbrace{-\overline{\langle uu\rangle \frac{\partial \widetilde{V}}{\partial x}}}_{\overline{P^3_{uv}}} \underbrace{-\overline{\langle uv\rangle \frac{\partial \widetilde{V}}{\partial y}}}_{\overline{P^4_{uv}}} \underbrace{-\overline{\langle vv\rangle} \frac{d\overline{U}}{dy}}_{\overline{P^5_{uv}}}, \tag{8.4a}$$

$$\overline{T_{uv}} = \underbrace{\frac{d\overline{\langle uv\rangle \widetilde{V}}}{dy}}_{\overline{T^1_{uv}}} + \underbrace{\frac{d\overline{\langle uvv\rangle}}{dy}}_{\overline{T^2_{uv}}}, \tag{8.4b}$$

$$\overline{\Pi_{uv}} = -\overline{\left\langle u\frac{\partial p}{\partial y}\right\rangle} - \overline{\left\langle v\frac{\partial p}{\partial x}\right\rangle}, \tag{8.4c}$$

$$\overline{\varepsilon_{uv}} = 2\left(\overline{\left\langle \frac{\partial u}{\partial x}\frac{\partial v}{\partial x}\right\rangle} + \overline{\left\langle \frac{\partial u}{\partial y}\frac{\partial v}{\partial y}\right\rangle} + \overline{\left\langle \frac{\partial u}{\partial z}\frac{\partial v}{\partial z}\right\rangle}\right), \tag{8.4d}$$

and

$$\overline{D_{uv}} = \frac{d^2\overline{\langle uv\rangle}}{dy^2}. \tag{8.4e}$$

CHAPTER 9

Appendix B: Transport equations for turbulent enstrophy components

9.1 Derivations of the transport equations of turbulent enstrophy field

9.1.1 Transport equations of phase averaged turbulent enstrophy field

The instantaneous vorticity transport equation for incompressible flows reads

$$\frac{\partial \Omega_i}{\partial t} + U_k \frac{\partial \Omega_i}{\partial x_k} = \Omega_k \frac{\partial U_i}{\partial x_k} + \nu \frac{\partial^2 \Omega_i}{\partial x_k \partial x_k}. \tag{9.1}$$

Putting $\Omega_i = \langle \Omega_i \rangle + \omega_i$, $\Omega_k = \langle \Omega_k \rangle + \omega_k$, $U_i = \langle U_i \rangle + u_i$ and $U_k = \langle U_k \rangle + u_k$ in the above equation gives

$$\begin{aligned} \frac{\partial \langle \Omega_i \rangle}{\partial t} + \frac{\partial \omega_i}{\partial t} + \langle U_k \rangle \frac{\partial \langle \Omega_i \rangle}{\partial x_k} + u_k \frac{\partial \langle \Omega_i \rangle}{\partial x_k} + \langle U_k \rangle \frac{\partial \omega_i}{\partial x_k} + u_k \frac{\partial \omega_i}{\partial x_k} = \langle \Omega_k \rangle \frac{\partial \langle U_i \rangle}{\partial x_k} + \\ \langle \Omega_k \rangle \frac{\partial u_i}{\partial x_k} + \omega_k \frac{\partial \langle U_i \rangle}{\partial x_k} + \omega_k \frac{\partial u_i}{\partial x_k} + \nu \frac{\partial^2 \langle \Omega_i \rangle}{\partial x_k \partial x_k} + \nu \frac{\partial^2 \omega_i}{\partial x_k \partial x_k}. \end{aligned} \tag{9.2}$$

After phase averaging we have,

$$\frac{\partial \langle \Omega_i \rangle}{\partial t} + \langle U_k \rangle \frac{\partial \langle \Omega_i \rangle}{\partial x_k} + \Big\langle u_k \frac{\partial \omega_i}{\partial x_k} \Big\rangle = \langle \Omega_k \rangle \frac{\partial \langle U_i \rangle}{\partial x_k} + \Big\langle \omega_k \frac{\partial u_i}{\partial x_k} \Big\rangle + \nu \frac{\partial^2 \langle \Omega_i \rangle}{\partial x_k \partial x_k}, \tag{9.3}$$

as $\langle \omega_i \rangle = 0$, $\langle \omega_k \rangle = 0$, $\langle u_i \rangle = 0$, and $\langle u_k \rangle = 0$. Subtracting equation 9.3 from equation 9.2 yields the following equation for the transport of the instantaneous fluctuating vorticity field

$$\begin{aligned} \frac{\partial \omega_i}{\partial t} + u_k \frac{\partial \langle \Omega_i \rangle}{\partial x_k} + \langle U_k \rangle \frac{\partial \omega_i}{\partial x_k} + u_k \frac{\partial \omega_i}{\partial x_k} - \Big\langle u_k \frac{\partial \omega_i}{\partial x_k} \Big\rangle = \langle \Omega_k \rangle \frac{\partial u_i}{\partial x_k} + \omega_k \frac{\partial \langle U_i \rangle}{\partial x_k} + \\ \omega_k \frac{\partial u_i}{\partial x_k} - \Big\langle \omega_k \frac{\partial u_i}{\partial x_k} \Big\rangle + \nu \frac{\partial^2 \omega_i}{\partial x_k \partial x_k}. \end{aligned} \tag{9.4}$$

Multiplying both sides of equation 9.4 by ω_j and adding to the corresponding equation with exchanged i and j gives

$$\begin{aligned}
&\frac{\partial \omega_i\omega_j}{\partial t} + \omega_j\left(u_k\frac{\partial\langle\Omega_i\rangle}{\partial x_k} + \langle U_k\rangle\frac{\partial\omega_i}{\partial x_k} + u_k\frac{\partial\omega_i}{\partial x_k} - \Big\langle u_k\frac{\partial\omega_i}{\partial x_k}\Big\rangle\right)\\
&\quad+\omega_i\left(u_k\frac{\partial\langle\Omega_j\rangle}{\partial x_k} + \langle U_k\rangle\frac{\partial\omega_j}{\partial x_k} + u_k\frac{\partial\omega_j}{\partial x_k} - \Big\langle u_k\frac{\partial\omega_j}{\partial x_k}\Big\rangle\right)\\
&\quad=\omega_j\left(\langle\Omega_k\rangle\frac{\partial u_i}{\partial x_k} + \omega_k\frac{\partial\langle U_i\rangle}{\partial x_k} + \omega_k\frac{\partial u_i}{\partial x_k} - \Big\langle\omega_k\frac{\partial u_i}{\partial x_k}\Big\rangle + \nu\frac{\partial^2\omega_i}{\partial x_k\partial x_k}\right)\\
&\quad+\omega_i\left(\langle\Omega_k\rangle\frac{\partial u_j}{\partial x_k} + \omega_k\frac{\partial\langle U_j\rangle}{\partial x_k} + \omega_k\frac{\partial u_j}{\partial x_k} - \Big\langle\omega_k\frac{\partial u_j}{\partial x_k}\Big\rangle + \nu\frac{\partial^2\omega_j}{\partial x_k\partial x_k}\right).
\end{aligned} \tag{9.5}$$

After phase averaging and rearranging, we get

$$\begin{aligned}
&\frac{\partial\langle\omega_i\omega_j\rangle}{\partial t} + \langle\omega_j u_k\rangle\frac{\partial\langle\Omega_i\rangle}{\partial x_k} + \langle\omega_i u_k\rangle\frac{\partial\langle\Omega_j\rangle}{\partial x_k} + \langle U_k\rangle\frac{\partial\langle\omega_i\omega_j\rangle}{\partial x_k} + \frac{\partial\langle\omega_i\omega_j u_k\rangle}{\partial x_k}\\
&\quad=\langle\Omega_k\rangle\Big\langle\omega_j\frac{\partial u_i}{\partial x_k} + \omega_i\frac{\partial u_j}{\partial x_k}\Big\rangle + \Big\langle\omega_j\omega_k\frac{\partial u_i}{\partial x_k}\Big\rangle + \Big\langle\omega_i\omega_k\frac{\partial u_j}{\partial x_k}\Big\rangle\\
&\quad+\langle\omega_j\omega_k\rangle\frac{\partial\langle U_i\rangle}{\partial x_k} + \langle\omega_i\omega_k\rangle\frac{\partial\langle U_j\rangle}{\partial x_k} + \nu\frac{\partial^2\langle\omega_i\omega_j\rangle}{\partial x_k\partial x_k} - 2\nu\Big\langle\frac{\partial\omega_i}{\partial x_k}\frac{\partial\omega_j}{\partial x_k}\Big\rangle.
\end{aligned} \tag{9.6}$$

Setting $i = j$ yields the following transport equation for the phase averaged turbulent enstrophy field

$$\begin{aligned}
&\frac{\partial\langle\omega_i\omega_i\rangle}{\partial t} + 2\langle\omega_i u_k\rangle\frac{\partial\langle\Omega_i\rangle}{\partial x_k} + \langle U_k\rangle\frac{\partial\langle\omega_i\omega_i\rangle}{\partial x_k} + \frac{\partial\langle\omega_i\omega_i u_k\rangle}{\partial x_k} = 2\langle\Omega_k\rangle\Big\langle\omega_i\frac{\partial u_i}{\partial x_k}\Big\rangle\\
&\quad+2\Big\langle\omega_i\omega_k\frac{\partial u_i}{\partial x_k}\Big\rangle + 2\langle\omega_i\omega_k\rangle\frac{\partial\langle U_i\rangle}{\partial x_k} + \nu\frac{\partial^2\langle\omega_i\omega_i\rangle}{\partial x_k\partial x_k} - 2\nu\Big\langle\frac{\partial\omega_i}{\partial x_k}\frac{\partial\omega_i}{\partial x_k}\Big\rangle.
\end{aligned} \tag{9.7}$$

The equation 9.7 can be rewritten in the form

$$\frac{\partial\langle\omega_i\omega_i\rangle}{\partial t} = \langle P_{\omega_i\omega_i}\rangle - \langle A_{\omega_i\omega_i}\rangle - \langle T_{\omega_i\omega_i}\rangle - \langle\varepsilon_{\omega_i\omega_i}\rangle + \langle D_{\omega_i\omega_i}\rangle, \tag{9.8}$$

where $\langle P_{\omega_i\omega_i}\rangle$, $\langle A_{\omega_i\omega_i}\rangle$, $\langle T_{\omega_i\omega_i}\rangle$, $\langle\varepsilon_{\omega_i\omega_i}\rangle$ and $\langle D_{\omega_i\omega_i}\rangle$ represents the phase averaged production, advection, turbulent transport, dissipation, and diffusion, respectively, and are given by

$$\begin{aligned}
\langle P_{\omega_i\omega_i}\rangle &= 2\langle\Omega_k\rangle\Big\langle\omega_i\frac{\partial u_i}{\partial x_k}\Big\rangle + 2\Big\langle\omega_i\omega_k\frac{\partial u_i}{\partial x_k}\Big\rangle + 2\langle\omega_i\omega_k\rangle\frac{\partial\langle U_i\rangle}{\partial x_k},\\
\langle A_{\omega_i\omega_i}\rangle &= \langle U_k\rangle\frac{\partial\langle\omega_i\omega_i\rangle}{\partial x_k},\\
\langle T_{\omega_i\omega_i}\rangle &= 2\langle\omega_i u_k\rangle\frac{\partial\langle\Omega_i\rangle}{\partial x_k} + \frac{\partial\langle\omega_i\omega_i u_k\rangle}{\partial x_k},\\
\langle\varepsilon_{\omega_i\omega_i}\rangle &= 2\nu\Big\langle\frac{\partial\omega_i}{\partial x_k}\frac{\partial\omega_i}{\partial x_k}\Big\rangle, \text{and}\\
\langle D_{\omega_i\omega_i}\rangle &= \nu\frac{\partial^2\langle\omega_i\omega_i\rangle}{\partial x_k\partial x_k}.
\end{aligned} \tag{9.8a}$$

The transport equation for the phase averaged streamwise component $\langle \omega_x \omega_x \rangle$ is given as

$$\frac{\partial \langle \omega_x \omega_x \rangle}{\partial t} = \langle P_{\omega_x \omega_x} \rangle - \langle A_{\omega_x \omega_x} \rangle - \langle T_{\omega_x \omega_x} \rangle - \langle \varepsilon_{\omega_x \omega_x} \rangle + \langle D_{\omega_x \omega_x} \rangle, \tag{9.9}$$

where

$$\begin{aligned}
\langle P_{\omega_x \omega_x} \rangle &= \underbrace{2\widetilde{\Omega_x}\Big\langle \omega_x \frac{\partial u}{\partial x} \Big\rangle}_{\langle P^1_{\omega_x \omega_x} \rangle} + \underbrace{2\widetilde{\Omega_y}\Big\langle \omega_x \frac{\partial u}{\partial y} \Big\rangle}_{\langle P^2_{\omega_x \omega_x} \rangle} + \underbrace{2\widetilde{\Omega_z}\Big\langle \omega_x \frac{\partial u}{\partial z} \Big\rangle}_{\langle P^3_{\omega_x \omega_x} \rangle} + \underbrace{2\overline{\Omega_z}\Big\langle \omega_x \frac{\partial u}{\partial z} \Big\rangle}_{\langle P^4_{\omega_x \omega_x} \rangle} \\
&\quad + \underbrace{2\Big\langle \omega_x \omega_x \frac{\partial u}{\partial x} \Big\rangle}_{\langle P^5_{\omega_x \omega_x} \rangle} + \underbrace{2\Big\langle \omega_x \omega_y \frac{\partial u}{\partial y} \Big\rangle}_{\langle P^6_{\omega_x \omega_x} \rangle} + \underbrace{2\Big\langle \omega_x \omega_z \frac{\partial u}{\partial z} \Big\rangle}_{\langle P^7_{\omega_x \omega_x} \rangle} \\
&\quad + \underbrace{2\langle \omega_x \omega_x \rangle \frac{\partial \widetilde{U}}{\partial x}}_{\langle P^8_{\omega_x \omega_x} \rangle} + \underbrace{2\langle \omega_x \omega_y \rangle \frac{\partial \widetilde{U}}{\partial y}}_{\langle P^9_{\omega_x \omega_x} \rangle} + \underbrace{2\langle \omega_x \omega_y \rangle \frac{d\overline{U}}{dy}}_{\langle P^{10}_{\omega_x \omega_x} \rangle}, \\
\langle A_{\omega_x \omega_x} \rangle &= \underbrace{\widetilde{U} \frac{\partial \langle \omega_x \omega_x \rangle}{\partial x}}_{\langle A^1_{\omega_x \omega_x} \rangle} + \underbrace{\widetilde{V} \frac{\partial \langle \omega_x \omega_x \rangle}{\partial y}}_{\langle A^2_{\omega_x \omega_x} \rangle} + \underbrace{\overline{U} \frac{\partial \langle \omega_x \omega_x \rangle}{\partial x}}_{\langle A^3_{\omega_x \omega_x} \rangle}, \\
\langle T_{\omega_x \omega_x} \rangle &= \underbrace{2\langle \omega_x u \rangle \frac{\partial \widetilde{\Omega_x}}{\partial x}}_{\langle T^1_{\omega_x \omega_x} \rangle} + \underbrace{2\langle \omega_x v \rangle \frac{\partial \widetilde{\Omega_x}}{\partial y}}_{\langle T^2_{\omega_x \omega_x} \rangle} + \underbrace{\frac{\partial \langle \omega_x \omega_x v \rangle}{\partial y}}_{\langle T^3_{\omega_x \omega_x} \rangle} \\
&\quad + \underbrace{\frac{\partial \widetilde{\omega_x \omega_x} u}{\partial x}}_{\langle T^4_{\omega_x \omega_x} \rangle} + \underbrace{\frac{\partial \widetilde{\omega_x \omega_x} v}{\partial y}}_{\langle T^5_{\omega_x \omega_x} \rangle}, \\
\langle \varepsilon_{\omega_x \omega_x} \rangle &= 2\nu \left(\Big\langle \frac{\partial \omega_x}{\partial x} \frac{\partial \omega_x}{\partial x} \Big\rangle + \Big\langle \frac{\partial \omega_x}{\partial y} \frac{\partial \omega_x}{\partial y} \Big\rangle + \Big\langle \frac{\partial \omega_x}{\partial z} \frac{\partial \omega_x}{\partial z} \Big\rangle \right), \text{and} \\
\langle D_{\omega_x \omega_x} \rangle &= \nu \frac{\partial^2 \langle \omega_x \omega_x \rangle}{\partial x \partial x} + \nu \frac{\partial^2 \langle \omega_x \omega_x \rangle}{\partial y \partial y}.
\end{aligned} \tag{9.9a}$$

The transport equation for the phase averaged wall-normal component $\langle \omega_y \omega_y \rangle$ is given as

$$\frac{\partial \langle \omega_y \omega_y \rangle}{\partial t} = \langle P_{\omega_y \omega_y} \rangle - \langle A_{\omega_y \omega_y} \rangle - \langle T_{\omega_y \omega_y} \rangle - \langle \varepsilon_{\omega_y \omega_y} \rangle + \langle D_{\omega_y \omega_y} \rangle, \tag{9.10}$$

where

$$
\begin{aligned}
\langle P_{\omega_y\omega_y}\rangle &= \underbrace{2\widetilde{\Omega_x}\big\langle \omega_y \frac{\partial v}{\partial x}\big\rangle}_{\langle P^1_{\omega_y\omega_y}\rangle} + \underbrace{2\widetilde{\Omega_y}\big\langle \omega_y \frac{\partial v}{\partial y}\big\rangle}_{\langle P^2_{\omega_y\omega_y}\rangle} + \underbrace{2\widetilde{\Omega_z}\big\langle \omega_y \frac{\partial v}{\partial z}\big\rangle}_{\langle P^3_{\omega_y\omega_y}\rangle} + \underbrace{2\overline{\Omega_z}\big\langle \omega_y \frac{\partial v}{\partial z}\big\rangle}_{\langle P^4_{\omega_y\omega_y}\rangle} \\
&\quad + \underbrace{2\big\langle \omega_x\omega_y \frac{\partial v}{\partial x}\big\rangle}_{\langle P^5_{\omega_y\omega_y}\rangle} + \underbrace{2\big\langle \omega_y\omega_y \frac{\partial v}{\partial y}\big\rangle}_{\langle P^6_{\omega_y\omega_y}\rangle} + \underbrace{2\big\langle \omega_z\omega_y \frac{\partial v}{\partial z}\big\rangle}_{\langle P^7_{\omega_y\omega_y}\rangle} \\
&\quad + \underbrace{2\langle \omega_x\omega_y\rangle \frac{\partial \widetilde{V}}{\partial x}}_{\langle P^8_{\omega_y\omega_y}\rangle} + \underbrace{2\langle \omega_y\omega_y\rangle \frac{\partial \widetilde{V}}{\partial y}}_{\langle P^9_{\omega_y\omega_y}\rangle}, \\
\langle A_{\omega_y\omega_y}\rangle &= \underbrace{\widetilde{U}\frac{\partial\langle \omega_y\omega_y\rangle}{\partial x}}_{\langle A^1_{\omega_y\omega_y}\rangle} + \underbrace{\widetilde{V}\frac{\partial\langle \omega_y\omega_y\rangle}{\partial y}}_{\langle A^2_{\omega_y\omega_y}\rangle} + \underbrace{\overline{U}\frac{\partial\langle \omega_y\omega_y\rangle}{\partial x}}_{\langle A^3_{\omega_y\omega_y}\rangle}, \\
\langle T_{\omega_y\omega_y}\rangle &= \underbrace{2\langle \omega_y u\rangle \frac{\partial \widetilde{\Omega_y}}{\partial x}}_{\langle T^1_{\omega_y\omega_y}\rangle} + \underbrace{2\langle \omega_y v\rangle \frac{\partial \widetilde{\Omega_y}}{\partial y}}_{\langle T^2_{\omega_y\omega_y}\rangle} + \underbrace{\frac{\partial\langle \omega_y\omega_y v\rangle}{\partial y}}_{\langle T^3_{\omega_y\omega_y}\rangle} \\
&\quad + \underbrace{\frac{\partial \widetilde{\omega_y\omega_y u}}{\partial x}}_{\langle T^4_{\omega_y\omega_y}\rangle} + \underbrace{\frac{\partial \widetilde{\omega_y\omega_y v}}{\partial y}}_{\langle T^5_{\omega_y\omega_y}\rangle}, \\
\langle \varepsilon_{\omega_y\omega_y}\rangle &= 2\nu\left(\big\langle \frac{\partial\omega_y}{\partial x}\frac{\partial\omega_y}{\partial x}\big\rangle + \big\langle \frac{\partial\omega_y}{\partial y}\frac{\partial\omega_y}{\partial y}\big\rangle + \big\langle \frac{\partial\omega_y}{\partial z}\frac{\partial\omega_y}{\partial z}\big\rangle\right), \text{and} \\
\langle D_{\omega_y\omega_y}\rangle &= \nu\frac{\partial^2\langle \omega_y\omega_y\rangle}{\partial x\partial x} + \nu\frac{\partial^2\langle \omega_y\omega_y\rangle}{\partial y\partial y}.
\end{aligned}
\tag{9.10a}
$$

The transport equation for the phase averaged spanwise component $\langle \omega_z\omega_z\rangle$ is given as

$$
\frac{\partial\langle \omega_z\omega_z\rangle}{\partial t} = \langle P_{\omega_z\omega_z}\rangle - \langle A_{\omega_z\omega_z}\rangle - \langle T_{\omega_z\omega_z}\rangle - \langle \varepsilon_{\omega_z\omega_z}\rangle + \langle D_{\omega_z\omega_z}\rangle, \tag{9.11}
$$

where

$$
\begin{aligned}
\langle P_{\omega_z\omega_z}\rangle &= \underbrace{2\widetilde{\Omega_x}\Big\langle\omega_z\frac{\partial w}{\partial x}\Big\rangle}_{\langle P^1_{\omega_z\omega_z}\rangle}+\underbrace{2\widetilde{\Omega_y}\Big\langle\omega_z\frac{\partial w}{\partial y}\Big\rangle}_{\langle P^2_{\omega_z\omega_z}\rangle}+\underbrace{2\widetilde{\Omega_z}\Big\langle\omega_z\frac{\partial w}{\partial z}\Big\rangle}_{\langle P^3_{\omega_z\omega_z}\rangle}+\underbrace{2\overline{\Omega_z}\Big\langle\omega_z\frac{\partial w}{\partial z}\Big\rangle}_{\langle P^4_{\omega_z\omega_z}\rangle}\\
&+\underbrace{2\Big\langle\omega_x\omega_z\frac{\partial w}{\partial x}\Big\rangle}_{\langle P^5_{\omega_z\omega_z}\rangle}+\underbrace{2\Big\langle\omega_y\omega_z\frac{\partial w}{\partial y}\Big\rangle}_{\langle P^6_{\omega_z\omega_z}\rangle}+\underbrace{2\Big\langle\omega_z\omega_z\frac{\partial w}{\partial z}\Big\rangle}_{\langle P^7_{\omega_z\omega_z}\rangle}\\
&+\underbrace{2\langle\omega_x\omega_z\rangle\frac{\partial\widetilde{W}}{\partial x}}_{\langle P^8_{\omega_z\omega_z}\rangle}+\underbrace{2\langle\omega_y\omega_z\rangle\frac{\partial\widetilde{W}}{\partial y}}_{\langle P^9_{\omega_z\omega_z}\rangle},\\
\langle A_{\omega_z\omega_z}\rangle &= \underbrace{\widetilde{U}\frac{\partial\langle\omega_z\omega_z\rangle}{\partial x}}_{\langle A^1_{\omega_z\omega_z}\rangle}+\underbrace{\widetilde{V}\frac{\partial\langle\omega_z\omega_z\rangle}{\partial y}}_{\langle A^2_{\omega_z\omega_z}\rangle}+\underbrace{\overline{U}\frac{\partial\langle\omega_z\omega_z\rangle}{\partial x}}_{\langle A^3_{\omega_z\omega_z}\rangle},\\
\langle T_{\omega_z\omega_z}\rangle &= \underbrace{2\langle\omega_z u\rangle\frac{\partial\widetilde{\Omega_z}}{\partial x}}_{\langle T^1_{\omega_z\omega_z}\rangle}+\underbrace{2\langle\omega_z v\rangle\frac{\partial\widetilde{\Omega_z}}{\partial y}}_{\langle T^2_{\omega_z\omega_z}\rangle}+\underbrace{2\langle\omega_z v\rangle\frac{d\overline{\Omega_z}}{dy}}_{\langle T^3_{\omega_z\omega_z}\rangle}+\underbrace{\frac{\partial\langle\omega_z\omega_z v\rangle}{\partial y}}_{\langle T^4_{\omega_z\omega_z}\rangle}\\
&+\underbrace{\frac{\partial\widetilde{\omega_z\omega_z u}}{\partial x}}_{\langle T^5_{\omega_z\omega_z}\rangle}+\underbrace{\frac{\partial\widetilde{\omega_z\omega_z v}}{\partial y}}_{\langle T^6_{\omega_z\omega_z}\rangle},\\
\langle\varepsilon_{\omega_z\omega_z}\rangle &= 2\nu\left(\Big\langle\frac{\partial\omega_z}{\partial x}\frac{\partial\omega_z}{\partial x}\Big\rangle+\Big\langle\frac{\partial\omega_z}{\partial y}\frac{\partial\omega_z}{\partial y}\Big\rangle+\Big\langle\frac{\partial\omega_z}{\partial z}\frac{\partial\omega_z}{\partial z}\Big\rangle\right),\text{and}\\
\langle D_{\omega_z\omega_z}\rangle &= \nu\frac{\partial^2\langle\omega_z\omega_z\rangle}{\partial x\partial x}+\nu\frac{\partial^2\langle\omega_z\omega_z\rangle}{\partial y\partial y}.
\end{aligned}
\tag{9.11a}
$$

Because of spanwise homogeneity, the terms involving spanwise derivative of phase averaged quantities are zero.

9.2 Transport equations of mean turbulent enstrophy field

Averaging equation 9.8 over all the phases results in the evolution equation for the mean turbulent enstrophy which can be written as follows

$$
\begin{aligned}
\frac{\partial\overline{\omega_i\omega_i}}{\partial t}+2\overline{\omega_i u_k\frac{\partial\langle\Omega_i\rangle}{\partial x_k}}+2\frac{\partial\overline{\omega_i\omega_i u_k}}{\partial x_k} &= 2\overline{\langle\Omega_k\rangle\Big\langle\omega_i\frac{\partial u_i}{\partial x_k}\Big\rangle}+2\overline{\omega_i\omega_k\frac{\partial u_i}{\partial x_k}}\\
&+2\overline{\langle\omega_i\omega_k\rangle\frac{\partial\langle U_i\rangle}{\partial x_k}}+\nu\frac{\partial^2\overline{\omega_i\omega_i}}{\partial x_k\partial x_k}-2\nu\overline{\frac{\partial\omega_i}{\partial x_k}\frac{\partial\omega_i}{\partial x_k}}.
\end{aligned}
\tag{9.12}
$$

The above equation can be re-written as

$$\begin{aligned}\frac{\partial\overline{\omega_i\omega_i}}{\partial t}+2\overline{\omega_i u_k\frac{\partial\widetilde{\Omega_i}}{\partial x_k}}+2\overline{\omega_i u_k}\frac{\partial\overline{\Omega_i}}{\partial x_k}+2\frac{\partial\overline{\omega_i\omega_i u_k}}{\partial x_k}=2\overline{\widetilde{\Omega_k}\left\langle\omega_i\frac{\partial u_i}{\partial x_k}\right\rangle}+2\overline{\Omega_k}\,\overline{\omega_i\frac{\partial u_i}{\partial x_k}}\\+2\overline{\omega_i\omega_k\frac{\partial u_i}{\partial x_k}}+2\overline{\langle\omega_i\omega_k\rangle\frac{\partial\widetilde{U_i}}{\partial x_k}}+2\overline{\omega_i\omega_k}\frac{\partial\overline{U_i}}{\partial x_k}+\nu\frac{\partial^2\overline{\omega_i\omega_i}}{\partial x_k\partial x_k}-2\nu\overline{\frac{\partial\omega_i}{\partial x_k}\frac{\partial\omega_i}{\partial x_k}}.\end{aligned}\tag{9.13}$$

The terms marked with $\sim$ are purely a result of periodic forcing in the form of transverse wall oscillations. By setting these terms to zero, one could recover the transport equations for turbulent enstrophy for the canonical turbulent channel flow as follows:

$$\begin{aligned}\frac{\partial\overline{\omega_i\omega_i}}{\partial t}+2\overline{\omega_i u_k}\frac{\partial\overline{\Omega_i}}{\partial x_k}+2\frac{\partial\overline{\omega_i\omega_i u_k}}{\partial x_k}=2\overline{\Omega_k}\,\overline{\omega_i\frac{\partial u_i}{\partial x_k}}\\+2\overline{\omega_i\omega_k\frac{\partial u_i}{\partial x_k}}+2\overline{\omega_i\omega_k}\frac{\partial\overline{U_i}}{\partial x_k}+\nu\frac{\partial^2\overline{\omega_i\omega_i}}{\partial x_k\partial x_k}-2\nu\overline{\frac{\partial\omega_i}{\partial x_k}\frac{\partial\omega_i}{\partial x_k}}.\end{aligned}\tag{9.14}$$

The equation 9.13 can be written in the form

$$\frac{\partial\overline{\omega_i\omega_i}}{\partial t}=\overline{P_{\omega_i\omega_i}}-\overline{A_{\omega_i\omega_i}}-\overline{T_{\omega_i\omega_i}}-\overline{\varepsilon_{\omega_i\omega_i}}+\overline{D_{\omega_i\omega_i}}=0,\tag{9.15}$$

where $\overline{P_{\omega_i\omega_i}}$, $\overline{A_{\omega_i\omega_i}}$, $\overline{T_{\omega_i\omega_i}}$, $\overline{\varepsilon_{\omega_i\omega_i}}$ and $\overline{D_{\omega_i\omega_i}}$ represents the mean production, advection, turbulent transport, dissipation, and diffusion, respectively.

The transport equation for the mean streamwise turbulent enstrophy component $\overline{\omega_x\omega_x}$ is given as

$$\frac{\partial\overline{\omega_x\omega_x}}{\partial t}=\overline{P_{\omega_x\omega_x}}-\overline{A_{\omega_x\omega_x}}-\overline{T_{\omega_x\omega_x}}-\overline{\varepsilon_{\omega_x\omega_x}}+\overline{D_{\omega_x\omega_x}},\tag{9.16}$$

where

$$
\begin{aligned}
\overline{P_{\omega_x\omega_x}} &= \underbrace{\overline{2\widetilde{\Omega_x}\left\langle\omega_x\frac{\partial u}{\partial x}\right\rangle}}_{\overline{P^1_{\omega_x\omega_x}}} + \underbrace{\overline{2\widetilde{\Omega_y}\left\langle\omega_x\frac{\partial u}{\partial y}\right\rangle}}_{\overline{P^2_{\omega_x\omega_x}}} + \underbrace{\overline{2\widetilde{\Omega_z}\left\langle\omega_x\frac{\partial u}{\partial z}\right\rangle}}_{\overline{P^3_{\omega_x\omega_x}}} - \underbrace{2\frac{d\overline{U}}{dy}\overline{\omega_x\frac{\partial w}{\partial x}}}_{\overline{P^4_{\omega_x\omega_x}}} \\
&\quad + \underbrace{\overline{2\omega_x\omega_x\frac{\partial u}{\partial x}}}_{\overline{P^5_{\omega_x\omega_x}}} + \underbrace{\overline{2\omega_x\omega_y\frac{\partial u}{\partial y}}}_{\overline{P^6_{\omega_x\omega_x}}} + \underbrace{\overline{2\omega_x\omega_z\frac{\partial u}{\partial z}}}_{\overline{P^7_{\omega_x\omega_x}}} + \underbrace{\overline{2\langle\omega_x\omega_x\rangle\frac{\partial\widetilde{U}}{\partial x}}}_{\overline{P^8_{\omega_x\omega_x}}} + \underbrace{\overline{2\langle\omega_x\omega_y\rangle\frac{\partial\widetilde{U}}{\partial y}}}_{\overline{P^9_{\omega_x\omega_x}}}, \\
\overline{A_{\omega_x\omega_x}} &= \underbrace{\overline{\widetilde{U}\frac{\partial\langle\omega_x\omega_x\rangle}{\partial x}}}_{\overline{A^1_{\omega_x\omega_x}}} + \underbrace{\overline{\widetilde{V}\frac{\partial\langle\omega_x\omega_x\rangle}{\partial y}}}_{\overline{A^2_{\omega_x\omega_x}}}, \\
\overline{T_{\omega_x\omega_x}} &= \underbrace{\overline{2\langle\omega_x u\rangle\frac{\partial\widetilde{\Omega_x}}{\partial x}}}_{\overline{T^1_{\omega_x\omega_x}}} + \underbrace{\overline{2\langle\omega_x v\rangle\frac{\partial\widetilde{\Omega_x}}{\partial y}}}_{\overline{T^2_{\omega_x\omega_x}}} + \underbrace{\frac{d\overline{\omega_x\omega_x v}}{dy}}_{\overline{T^3_{\omega_x\omega_x}}}, \\
\overline{\varepsilon_{\omega_x\omega_x}} &= 2\left(\overline{\frac{\partial\omega_x}{\partial x}\frac{\partial\omega_x}{\partial x}} + \overline{\frac{\partial\omega_x}{\partial y}\frac{\partial\omega_x}{\partial y}} + \overline{\frac{\partial\omega_x}{\partial z}\frac{\partial\omega_x}{\partial z}}\right), \text{and} \\
\overline{D_{\omega_x\omega_x}} &= \frac{d^2\overline{\omega_x\omega_x}}{dy^2}.
\end{aligned}
\tag{9.16a}
$$

The transport equation for the mean wall-normal turbulent enstrophy component $\overline{\omega_y\omega_y}$ is given as

$$
\frac{\partial\overline{\omega_y\omega_y}}{\partial t} = \overline{P_{\omega_y\omega_y}} - \overline{A_{\omega_y\omega_y}} - \overline{T_{\omega_y\omega_y}} - \overline{\varepsilon_{\omega_y\omega_y}} + \overline{D_{\omega_y\omega_y}} = 0, \tag{9.17}
$$

where

$$
\begin{aligned}
\overline{P_{\omega_y\omega_y}} &= \underbrace{\overline{2\widetilde{\Omega_x}\left\langle\omega_y\frac{\partial v}{\partial x}\right\rangle}}_{\overline{P^1_{\omega_y\omega_y}}} + \underbrace{\overline{2\widetilde{\Omega_y}\left\langle\omega_y\frac{\partial v}{\partial y}\right\rangle}}_{\overline{P^2_{\omega_y\omega_y}}} + \underbrace{\overline{2\widetilde{\Omega_z}\left\langle\omega_y\frac{\partial v}{\partial z}\right\rangle}}_{\overline{P^3_{\omega_y\omega_y}}} + \underbrace{2\overline{\Omega_z}\,\overline{\omega_y\frac{\partial v}{\partial z}}}_{\overline{P^4_{\omega_y\omega_y}}} \\
&\quad + \underbrace{\overline{2\omega_x\omega_y\frac{\partial v}{\partial x}}}_{\overline{P^5_{\omega_y\omega_y}}} + \underbrace{\overline{2\omega_y\omega_y\frac{\partial v}{\partial y}}}_{\overline{P^6_{\omega_y\omega_y}}} + \underbrace{\overline{2\omega_z\omega_y\frac{\partial v}{\partial z}}}_{\overline{P^7_{\omega_y\omega_y}}} \\
&\quad + \underbrace{\overline{2\langle\omega_x\omega_y\rangle\frac{\partial\widetilde{V}}{\partial x}}}_{\overline{P^8_{\omega_y\omega_y}}} + \underbrace{\overline{2\langle\omega_y\omega_y\rangle\frac{\partial\widetilde{V}}{\partial y}}}_{\overline{P^9_{\omega_y\omega_y}}}, \\
\overline{A_{\omega_y\omega_y}} &= \underbrace{\overline{\widetilde{U}\frac{\partial\langle\omega_y\omega_y\rangle}{\partial x}}}_{\overline{A^1_{\omega_y\omega_y}}} + \underbrace{\overline{\widetilde{V}\frac{\partial\langle\omega_y\omega_y\rangle}{\partial y}}}_{\overline{A^2_{\omega_y\omega_y}}}, \\
\overline{T_{\omega_y\omega_y}} &= \underbrace{\overline{2\langle\omega_y u\rangle\frac{\partial\widetilde{\Omega_y}}{\partial x}}}_{\overline{T^1_{\omega_y\omega_y}}} + \underbrace{\overline{2\langle\omega_y v\rangle\frac{\partial\widetilde{\Omega_y}}{\partial y}}}_{\overline{T^2_{\omega_y\omega_y}}} + \underbrace{\frac{d\overline{\omega_y\omega_y v}}{dy}}_{\overline{T^3_{\omega_y\omega_y}}}, \\
\overline{\varepsilon_{\omega_y\omega_y}} &= 2\left(\overline{\frac{\partial\omega_y}{\partial x}\frac{\partial\omega_y}{\partial x}} + \overline{\frac{\partial\omega_y}{\partial y}\frac{\partial\omega_y}{\partial y}} + \overline{\frac{\partial\omega_y}{\partial z}\frac{\partial\omega_y}{\partial z}}\right), \text{and} \\
\overline{D_{\omega_y\omega_y}} &= \frac{d^2\overline{\omega_y\omega_y}}{dy^2}.
\end{aligned}
\tag{9.17a}
$$

The transport equation for the mean spanwise component $\langle\omega_z\omega_z\rangle$ is given as

$$
\frac{\partial\overline{\omega_z\omega_z}}{\partial t} = \overline{P_{\omega_z\omega_z}} - \overline{A_{\omega_z\omega_z}} - \overline{T_{\omega_z\omega_z}} - \overline{\varepsilon_{\omega_z\omega_z}} + \overline{D_{\omega_z\omega_z}} = 0, \tag{9.18}
$$

where

$$
\begin{aligned}
\overline{P_{\omega_z\omega_z}} &= \underbrace{\overline{2\widetilde{\Omega_x}\left\langle\omega_z\frac{\partial w}{\partial x}\right\rangle}}_{\overline{P^1_{\omega_z\omega_z}}} + \underbrace{\overline{2\widetilde{\Omega_y}\left\langle\omega_z\frac{\partial w}{\partial y}\right\rangle}}_{\overline{P^2_{\omega_z\omega_z}}} + \underbrace{\overline{2\widetilde{\Omega_z}\left\langle\omega_z\frac{\partial w}{\partial z}\right\rangle}}_{\overline{P^3_{\omega_z\omega_z}}} + \underbrace{2\overline{\Omega_z}\overline{\omega_z\frac{\partial w}{\partial z}}}_{\overline{P^4_{\omega_z\omega_z}}} \\
&\quad + \underbrace{2\overline{\omega_x\omega_z\frac{\partial w}{\partial x}}}_{\overline{P^5_{\omega_z\omega_z}}} + \underbrace{2\overline{\omega_y\omega_z\frac{\partial w}{\partial y}}}_{\overline{P^6_{\omega_z\omega_z}}} + \underbrace{2\overline{\omega_z\omega_z\frac{\partial w}{\partial z}}}_{\overline{P^7_{\omega_z\omega_z}}} \\
&\quad + \underbrace{2\overline{\langle\omega_x\omega_z\rangle\frac{\partial\widetilde{W}}{\partial x}}}_{\overline{P^8_{\omega_z\omega_z}}} + \underbrace{2\overline{\langle\omega_y\omega_z\rangle\frac{\partial\widetilde{W}}{\partial y}}}_{\overline{P^9_{\omega_z\omega_z}}}, \\
\overline{A_{\omega_z\omega_z}} &= \underbrace{\overline{\widetilde{U}\frac{\partial\langle\omega_z\omega_z\rangle}{\partial x}}}_{\overline{A^1_{\omega_z\omega_z}}} + \underbrace{\overline{\widetilde{V}\frac{\partial\langle\omega_z\omega_z\rangle}{\partial y}}}_{\overline{A^2_{\omega_z\omega_z}}}, \\
\overline{T_{\omega_z\omega_z}} &= \underbrace{2\overline{\langle\omega_z u\rangle\frac{\partial\widetilde{\Omega_z}}{\partial x}}}_{\overline{T^1_{\omega_z\omega_z}}} + \underbrace{2\overline{\langle\omega_z v\rangle\frac{\partial\widetilde{\Omega_z}}{\partial y}}}_{\overline{T^2_{\omega_z\omega_z}}} + \underbrace{2\overline{\omega_z v}\frac{d\overline{\Omega_z}}{dy}}_{\overline{T^3_{\omega_z\omega_z}}} + \underbrace{\frac{d\overline{\omega_z\omega_z v}}{dy}}_{\overline{T^4_{\omega_z\omega_z}}}, \\
\overline{\varepsilon_{\omega_z\omega_z}} &= 2\left(\overline{\frac{\partial\omega_z}{\partial x}\frac{\partial\omega_z}{\partial x}} + \overline{\frac{\partial\omega_z}{\partial y}\frac{\partial\omega_z}{\partial y}} + \overline{\frac{\partial\omega_z}{\partial z}\frac{\partial\omega_z}{\partial z}}\right), \text{and} \\
\overline{D_{\omega_z\omega_z}} &= \frac{d^2\overline{\omega_z\omega_z}}{dy^2}.
\end{aligned}
\tag{9.18a}
$$

The transport equations of turbulent enstrophy components are shortly discussed here. The production, turbulent transport, pressure-velocity gradient, dissipation, and diffusion terms are denoted by $\overline{P_{\omega_i\omega_j}}$, $\overline{T_{\omega_i\omega_j}}$, $\overline{\varepsilon_{\omega_i\omega_j}}$ and $\overline{D_{\omega_i\omega_j}}$, respectively. There are terms that directly come from the presence of the travelling waves and induced by streamwise gradients of the velocity field U_i. These are discussed in the main text in detail.

The transport equation for the streamwise enstrophy component $\overline{\omega_x\omega_x}$ is given by:

$$
\frac{D\overline{\omega_x\omega_x}}{Dt} = \overline{P_{\omega_x\omega_x}} - \overline{T_{\omega_x\omega_x}} - \overline{\varepsilon_{\omega_x\omega_x}} + \overline{D_{\omega_x\omega_x}} = 0, \tag{9.19}
$$

where:

$$\begin{aligned}\overline{P_{\omega_x\omega_x}} = &\underbrace{2\overline{\widetilde{\Omega_x}\left\langle \omega_x\frac{\partial u}{\partial x}\right\rangle}}_{\overline{P^1_{\omega_x\omega_x}}} + \underbrace{2\overline{\widetilde{\Omega_y}\left\langle \omega_x\frac{\partial u}{\partial y}\right\rangle}}_{\overline{P^2_{\omega_x\omega_x}}} + \underbrace{2\overline{\widetilde{\Omega_z}\left\langle \omega_x\frac{\partial u}{\partial z}\right\rangle}}_{\overline{P^3_{\omega_x\omega_x}}} + \underbrace{2\overline{\Omega_z}\overline{\left\langle \omega_x\frac{\partial u}{\partial z}\right\rangle}}_{\overline{P^{4*}_{\omega_x\omega_x}}} \\ &+ \underbrace{2\overline{\left\langle \omega_x\omega_x\frac{\partial u}{\partial x}\right\rangle}}_{\overline{P^5_{\omega_x\omega_x}}} + \underbrace{2\overline{\left\langle \omega_x\omega_y\frac{\partial u}{\partial y}\right\rangle}}_{\overline{P^6_{\omega_x\omega_x}}} + \underbrace{2\overline{\left\langle \omega_x\omega_z\frac{\partial u}{\partial z}\right\rangle}}_{\overline{P^7_{\omega_x\omega_x}}} \\ &+ \underbrace{2\overline{\langle\omega_x\omega_x\rangle\frac{\partial \widetilde{U}}{\partial x}}}_{\overline{P^8_{\omega_x\omega_x}}} + \underbrace{2\overline{\langle\omega_x\omega_y\rangle\frac{\partial \widetilde{U}}{\partial y}}}_{\overline{P^9_{\omega_x\omega_x}}} + \underbrace{2\overline{\langle\omega_x\omega_y\rangle}\frac{d\overline{U}}{dy}}_{\overline{P^{10}_{\omega_x\omega_x}}}.\end{aligned} \tag{9.19a}$$

For clarity, $\overline{P^{4*}_{\omega_x\omega_x}}$ and $\overline{P^{10}_{\omega_x\omega_x}}$ are usually combined to give $\overline{P^4_{\omega_x\omega_x}}$:

$$\overline{P^4_{\omega_x\omega_x}} = \overline{P^{4*}_{\omega_x\omega_x}} + \overline{P^{10}_{\omega_x\omega_x}} = 2\overline{\Omega_z}\overline{\left\langle \omega_x\frac{\partial u}{\partial z}\right\rangle} + 2\overline{\langle\omega_x\omega_y\rangle}\frac{d\overline{U}}{dy} = -2\overline{\left\langle \omega_x\frac{\partial w}{\partial x}\right\rangle}\frac{d\overline{U}}{dy}, \tag{9.19b}$$

$$\overline{T_{\omega_x\omega_x}} = \underbrace{2\overline{\langle\omega_x u\rangle\frac{\partial\widetilde{\Omega_x}}{\partial x}}}_{\overline{T^1_{\omega_x\omega_x}}} + \underbrace{2\overline{\langle\omega_x v\rangle\frac{\partial\widetilde{\Omega_x}}{\partial y}}}_{\overline{T^2_{\omega_x\omega_x}}} + \underbrace{\frac{d\overline{\langle\omega_x\omega_x v\rangle}}{dy}}_{\overline{T^3_{\omega_x\omega_x}}}, \tag{9.19c}$$

$$\overline{\varepsilon_{\omega_x\omega_x}} = \frac{2}{Re}\left(\overline{\left\langle\frac{\partial\omega_x}{\partial x}\frac{\partial\omega_x}{\partial x}\right\rangle} + \overline{\left\langle\frac{\partial\omega_x}{\partial y}\frac{\partial\omega_x}{\partial y}\right\rangle} + \overline{\left\langle\frac{\partial\omega_x}{\partial z}\frac{\partial\omega_x}{\partial z}\right\rangle}\right), \tag{9.19d}$$

and

$$\overline{D_{\omega_x\omega_x}} = \frac{1}{Re}\frac{d^2\overline{\langle\omega_x\omega_x\rangle}}{dy^2}. \tag{9.19e}$$

The transport equation for the wall-normal turbulent enstrophy component $\overline{\omega_y\omega_y}$ is given by:

$$\frac{D\overline{\omega_y\omega_y}}{Dt} = \overline{P_{\omega_y\omega_y}} - \overline{T_{\omega_y\omega_y}} - \overline{\varepsilon_{\omega_y\omega_y}} + \overline{D_{\omega_y\omega_y}} = 0, \tag{9.20}$$

where:

$$\begin{aligned}\overline{P_{\omega_y\omega_y}} = &\underbrace{2\overline{\widetilde{\Omega}_x\left\langle \omega_y\frac{\partial v}{\partial x}\right\rangle}}_{\overline{P^1_{\omega_y\omega_y}}} + \underbrace{2\overline{\widetilde{\Omega}_y\left\langle \omega_y\frac{\partial v}{\partial y}\right\rangle}}_{\overline{P^2_{\omega_y\omega_y}}} + \underbrace{2\overline{\widetilde{\Omega}_z\left\langle \omega_y\frac{\partial v}{\partial z}\right\rangle}}_{\overline{P^3_{\omega_y\omega_y}}} + \underbrace{2\overline{\Omega_z}\overline{\left\langle \omega_y\frac{\partial v}{\partial z}\right\rangle}}_{\overline{P^4_{\omega_y\omega_y}}} \\ &+ \underbrace{2\overline{\left\langle \omega_x\omega_y\frac{\partial v}{\partial x}\right\rangle}}_{\overline{P^5_{\omega_y\omega_y}}} + \underbrace{2\overline{\left\langle \omega_y\omega_y\frac{\partial v}{\partial y}\right\rangle}}_{\overline{P^6_{\omega_y\omega_y}}} + \underbrace{2\overline{\left\langle \omega_y\omega_z\frac{\partial v}{\partial z}\right\rangle}}_{\overline{P^7_{\omega_y\omega_y}}} \\ &+ \underbrace{2\overline{\langle\omega_x\omega_y\rangle\frac{\partial \widetilde{V}}{\partial x}}}_{\overline{P^8_{\omega_y\omega_y}}} + \underbrace{2\overline{\langle\omega_y\omega_y\rangle\frac{\partial \widetilde{V}}{\partial y}}}_{\overline{P^9_{\omega_y\omega_y}}},\end{aligned} \tag{9.20a}$$

$$\overline{T_{\omega_y\omega_y}} = \underbrace{2\overline{\langle\omega_y u\rangle\frac{\partial\widetilde{\Omega_y}}{\partial x}}}_{\overline{T^1_{\omega_y\omega_y}}} + \underbrace{2\overline{\langle\omega_y v\rangle\frac{\partial\widetilde{\Omega_y}}{\partial y}}}_{\overline{T^2_{\omega_y\omega_y}}} + \underbrace{\frac{d\overline{\langle\omega_y\omega_y v\rangle}}{dy}}_{\overline{T^3_{\omega_y\omega_y}}}, \tag{9.20b}$$

$$\overline{\varepsilon_{\omega_y\omega_y}} = \frac{2}{Re}\left(\overline{\left\langle\frac{\partial\omega_y}{\partial x}\frac{\partial\omega_y}{\partial x}\right\rangle} + \overline{\left\langle\frac{\partial\omega_y}{\partial y}\frac{\partial\omega_y}{\partial y}\right\rangle} + \overline{\left\langle\frac{\partial\omega_y}{\partial z}\frac{\partial\omega_y}{\partial z}\right\rangle}\right), \tag{9.20c}$$

and

$$\overline{D_{\omega_y\omega_y}} = \frac{1}{Re}\frac{d^2\overline{\langle\omega_y\omega_y\rangle}}{dy^2}. \tag{9.20d}$$

Finally, the transport equation for the spanwise enstrophy component $\overline{\omega_z\omega_z}$ is given by:

$$\frac{D\overline{\omega_z\omega_z}}{Dt} = \overline{P_{\omega_z\omega_z}} - \overline{T_{\omega_z\omega_z}} - \overline{\varepsilon_{\omega_z\omega_z}} + \overline{D_{\omega_z\omega_z}} = 0, \tag{9.21}$$

where:

$$\begin{aligned}\overline{P_{\omega_z\omega_z}} = &\underbrace{2\overline{\widetilde{\Omega}_x\left\langle \omega_z\frac{\partial w}{\partial x}\right\rangle}}_{\overline{P^1_{\omega_z\omega_z}}} + \underbrace{2\overline{\widetilde{\Omega}_y\left\langle \omega_z\frac{\partial w}{\partial y}\right\rangle}}_{\overline{P^2_{\omega_z\omega_z}}} + \underbrace{2\overline{\widetilde{\Omega}_z\left\langle \omega_z\frac{\partial w}{\partial z}\right\rangle}}_{\overline{P^3_{\omega_z\omega_z}}} + \underbrace{2\overline{\Omega_z}\overline{\left\langle \omega_z\frac{\partial w}{\partial z}\right\rangle}}_{\overline{P^4_{\omega_z\omega_z}}} \\ &+ \underbrace{2\overline{\left\langle \omega_x\omega_z\frac{\partial w}{\partial x}\right\rangle}}_{\overline{P^5_{\omega_z\omega_z}}} + \underbrace{2\overline{\left\langle \omega_y\omega_z\frac{\partial w}{\partial y}\right\rangle}}_{\overline{P^6_{\omega_z\omega_z}}} + \underbrace{2\overline{\left\langle \omega_z\omega_z\frac{\partial w}{\partial z}\right\rangle}}_{\overline{P^7_{\omega_z\omega_z}}} \\ &+ \underbrace{2\overline{\langle\omega_x\omega_z\rangle\frac{\partial\widetilde{W}}{\partial x}}}_{\overline{P^8_{\omega_z\omega_z}}} + \underbrace{2\overline{\langle\omega_y\omega_z\rangle\frac{\partial\widetilde{W}}{\partial y}}}_{\overline{P^9_{\omega_z\omega_z}}},\end{aligned} \tag{9.21a}$$

The terms $\overline{P^1_{\omega_z\omega_z}}$ and $\overline{P^9_{\omega_z\omega_z}}$ can be combined to give:

$$\overline{P^1_{\omega_z\omega_z}} + \overline{P^9_{\omega_z\omega_z}} = 2\overline{\widetilde{\Omega}_x\left\langle \omega_z\frac{\partial w}{\partial x}\right\rangle} + 2\overline{\langle\omega_y\omega_z\rangle\frac{\partial\widetilde{W}}{\partial y}} = 2\overline{\frac{\partial\widetilde{W}}{\partial y}\left\langle \omega_z\frac{\partial u}{\partial z}\right\rangle}. \tag{9.21b}$$

The terms $\overline{P^2_{\omega_z\omega_z}}$ and $\overline{P^8_{\omega_z\omega_z}}$ can be combined to give:

$$\overline{P^2_{\omega_z\omega_z}} + \overline{P^8_{\omega_z\omega_z}} = -2\overline{\widetilde{\Omega}_y\left\langle \omega_z\frac{\partial w}{\partial y}\right\rangle} + 2\overline{\langle\omega_x\omega_z\rangle\frac{\partial\widetilde{W}}{\partial x}} = -2\overline{\frac{\partial\widetilde{W}}{\partial x}\left\langle \omega_z\frac{\partial v}{\partial z}\right\rangle}. \tag{9.21c}$$

$$\overline{T_{\omega_z\omega_z}} = \underbrace{2\overline{\langle\omega_z u\rangle\frac{\partial\widetilde{\Omega_z}}{\partial x}}}_{\overline{T^1_{\omega_z\omega_z}}} + \underbrace{2\overline{\langle\omega_z v\rangle\frac{\partial\widetilde{\Omega_z}}{\partial y}}}_{\overline{T^2_{\omega_z\omega_z}}} + \underbrace{2\overline{\langle\omega_z v\rangle}\frac{d\overline{\Omega_z}}{dy}}_{\overline{T^3_{\omega_z\omega_z}}} + \underbrace{\frac{d\overline{\langle\omega_z\omega_z v\rangle}}{dy}}_{\overline{T^4_{\omega_z\omega_z}}}, \tag{9.21d}$$

$$\overline{\varepsilon_{\omega_z\omega_z}} = \frac{2}{Re}\left(\overline{\left\langle\frac{\partial\omega_z}{\partial x}\frac{\partial\omega_z}{\partial x}\right\rangle} + \overline{\left\langle\frac{\partial\omega_z}{\partial y}\frac{\partial\omega_z}{\partial y}\right\rangle} + \overline{\left\langle\frac{\partial\omega_z}{\partial z}\frac{\partial\omega_z}{\partial z}\right\rangle}\right), \tag{9.21e}$$

and

$$\overline{D_{\omega_z\omega_z}} = \frac{1}{Re}\frac{d^2\overline{\langle\omega_z\omega_z\rangle}}{dy^2}. \tag{9.21f}$$

Bibliography

1. Mellado, J. P. The evaporatively driven cloud-top mixing layer. *Journal of Fluid Mechanics* **660,** 5–36 (2010) (cit. on p. 1).
2. Fish, F. & Lauder, G. Passive and active flow control by swimming fishes and mammals. *Annual Review of Fluid Mechanics* **38,** 193–224 (2006) (cit. on p. 3).
3. Choi, H., Moin, P. & Kim, J. Active turbulence control for drag reduction in wall-bounded flows. *Journal of Fluid Mechanics* **262,** 75–110 (1994) (cit. on p. 5).
4. Quadrio, M. & Ricco, P. Initial response of a turbulent channel flow to spanwise oscillation of the walls. *Journal of Turbulence* **4,** N7 (2003) (cit. on pp. 9, 20, 21, 56, 57).
5. Ricco, P. & Quadrio, M. Wall-oscillation conditions for drag reduction in turbulent channel flow. *International Journal of Heat and Fluid Flow* **29,** 891–902 (2008) (cit. on pp. 9, 24, 25).
6. Quadrio, M., Ricco, P. & Viotti, C. Streamwise-travelling waves of spanwise wall velocity for turbulent drag reduction. *J. Fluid Mech.* **627,** 161–178 (2009) (cit. on pp. 9, 23, 25, 28, 56, 57).
7. Quadrio, M. & Ricco, P. The laminar generalized Stokes layer and turbulent drag reduction. *J. Fluid Mech.* **667,** 135–157 (2011) (cit. on pp. 9, 23, 45).
8. Ricco, P., Skotes, M. & Leschziner, M. A review of turbulent skin-friction drag reduction by near-wall transverse forcing. *Progress in Aerospace Sciences* **123** (2021) (cit. on pp. 9, 27, 143).
9. Brooke, P. & Pontikos, N. Measurements in a turbulent boundary layer on 'infinite' swept-wing. *J. Fluid Mech.* **159,** 105 (1985) (cit. on p. 10).
10. Driver, D. & Hebbar, S. Experimental study on a three-dimensional, shear-driven, turbulent boundary layer. *AIAA* **25,** 35 (1987) (cit. on p. 10).
11. Jung, W., Mangiavacchi, N. & Akhavan, R. Suppression of turbulence in wall-bounded flows by high-frequency spanwise wall oscillations. *Phys. Fluids A 4(8),* 1605–1607 (1992) (cit. on pp. 10–12).
12. Akhavan, R., Jung, W. & Mangiavacchi, N. Turbulence control in wall-bounded flows by spanwise ocillations. *Appl. Sci. Res.* **51,** 299–303 (1993) (cit. on p. 10).
13. Laadhari, F, Skandaji, L & Morel, R. Turbulence reduction in a boundary layer by a local spanwise oscillating surface. *Phys. Fluids* **6** (1994) (cit. on pp. 10–12, 19, 20).
14. Baron, A. & Quadrio, M. Turbulent drag reduction by spanwise wall ocillations. *Appl. Sci. Res.* **55,** 311–326 (1996) (cit. on pp. 10, 12).

15. Orlandi, P. & Fatica, M. Direct simulations of turbulent flow in a pipe rotating about its axis. *Journal of Fluid Mechanics* **343,** 43–72 (1997) (cit. on p. 11).

16. Murakami, M. & Kikuyama, K. Turbulent flow in axially rotating pipes. *Transactions of the ASME Journal of Fluids Engineering* **102,** 97–103 (1980) (cit. on p. 11).

17. Kikuyama, K., Murakami, M. & Nishibori, K. Development of three dimensional turbulent boundary layer in an axially rotating pipe. *Transactions of the ASME Journal of Fluids Engineering* **105,** 154–160 (1983) (cit. on p. 11).

18. Kikuyama, K., Murakami, M., Nishibori, K. & Maeda, K. Flow in an axially rotating pipe (a calculation of flow in the saturated region). *Bulletin of the JSME* **26,** 506–513 (1983) (cit. on p. 11).

19. Nishibori, K., Kikuyama, K. & Murakami, M. Laminarization of turbulent flow in the inlet region of an axially rotating pipe. *JSME International Journal* **30,** 255–262 (1987) (cit. on p. 11).

20. Hirai, S., Takagi, T. & Matsumoto, M. Prediction of the laminarization phenomena in an axially rotating pipe flow. *Transactions of the ASME Journal of Fluids Engineering* **110,** 424–430 (1988) (cit. on p. 11).

21. Reich, G. & Beer, H. Fluid flow and heat transfer in axially rotating pipe 1. Effect of rotation on turbulent pipe flow. *International Journal of Heat and Mass Transfer* **32,** 551–561 (1989) (cit. on p. 11).

22. Choi, K.-S. & Graham, M. Drag reduction of turbulent pipe flows by circular-wall oscillation. *Physics of Fluids* **10,** 7–9 (1998) (cit. on pp. 11, 25).

23. Choi, K.-S., DeBisschop, J.-R. & Clayton, B. R. Turbulent Boundary-Layer Control by Means of Spanwise-Wall Oscillation. *AIAA Journal* **36,** 1157–1163 (1998) (cit. on pp. 11, 12, 20).

24. Miyake, Y., Tsujimoto, K. & Takahashi, M. On the Mechanism of Drag Reduction of Near-Wall Turbulence by Wall Oscillation. *JSME International Journal Series B* **40,** 558–566 (1997) (cit. on p. 11).

25. Choi, K.-S. Near-wall structure of turbulent boundary layer with spanwise oscillation. *Phys. Fluids* **14,** 2530–2542 (2002) (cit. on pp. 12, 13, 19).

26. Choi, K.-S. & Clayton, B. R. The mechanism of turbulent drag reduction with wall oscillation. *International Journal of Heat and Fluid Flow* **22,** 1–9 (2001) (cit. on p. 12).

27. Mito, Y. & Kasagi, N. DNS study of turbulence modification with streamwise-uniform sinusoidal wall-oscillation. *International Journal of Heat and Fluid Flow* **19,** 470–481 (1998) (cit. on p. 12).

28. Orlandi, P. & Jiménez, J. On the generation of turbulent wall friction. *Physics of Fluids* **6,** 634–641 (1994) (cit. on pp. 12, 136).

29. Dhanak, M. & Si, C. On reduction of turbulent wall friction through spanwise wall oscillations. *J. Fluid Mech.* **383,** 175–195 (1999) (cit. on p. 12).

30. Quadrio, M. & Sibilla, S. Numerical simulation of turbulent flow in a pipe oscillating around its axis. *Journal of Fluid Mechanics* **424,** 217–241 (2000) (cit. on pp. 14–16, 19, 24).

31. Coxe, D., Peet, Y. & Adrian, R. J. *Vorticity statistics and distributions in drag reduced turbulent pipe flow with transverse wall oscillations* in *11th International Symposium on Turbulence and Shear Flow Phenomena (TSFP11)* (Southampton, UK, 2019), 1–6 (cit. on pp. 16, 17).

32. Nikitin, N. On the Mechanism of Turbulence Suppression by Spanwise Surface Oscillations. *Fluid Dynamics* **35,** 185–190 (2000) (cit. on pp. 16, 19).

33. Nikitin, N. B. & Chernyshenko, S. I. On the nature of the organized structures in turbulent near-wall flows. *Fluid Dynamics* **32,** 18–23 (1997) (cit. on p. 16).

34. Ricco, P. Modification of near-wall turbulence due to spanwise oscillations. *J. Turbul. 5,* N24 (2004) (cit. on pp. 18, 19).

35. Jiménez, J. & Moin, P. The minimal flow unit in near-wall turbulence. *Journal of Fluid Mechanics* **225,** 213–240 (1991) (cit. on pp. 16, 38).

36. Hamilton, J. M., Kim, J. & Waleffe, F. Regeneration mechanisms of near-wall turbulence structures. *J. Fluid Mech.* **287,** 317–348 (1995) (cit. on pp. 16, 19, 49, 132).

37. Kozul, M., Chung, D. & Monty, J. P. Direct numerical simulation of the incompressible temporally developing turbulent boundary layer. *Journal of Fluid Mechanics* **796,** 437–472 (2016) (cit. on p. 19).

38. Touber, E. & Leschziner, M. A. Near-wall streak modification by spanwise oscillatory wall motion and drag-reduction mechanisms. *J. Fluid Mech.* **693,** 150–200 (Feb. 2012) (cit. on pp. 19, 21, 25, 40, 53, 66, 76, 77, 79).

39. Katasonov, M. M. & Kozlov, V. V. *Boundary Layer Longitudinal Localized Structures Control by Means of Spanwisewall Oscillations* in *Laminar-Turbulent Transition* (eds Fasel, H. F. & Saric, W. S.) (Springer Berlin Heidelberg, Berlin, Heidelberg, 2000), 143–148 (cit. on pp. 19, 20).

40. Howard, R. & Sandham, N. Simulation and modelling of a skewed turbulent channel flow. *Flow Turbulence and Combustion* **65,** 83–109 (2000) (cit. on p. 20).

41. Di Cicca, G. M., Iuso, G., Spazzini, P. G. & Onorato, M. Particle image velocimetry investigation of a turbulent boundary layer manipulated by spanwise wall oscillations. *Journal of Fluid Mechanics* **467,** 41–56 (2002) (cit. on p. 20).

42. Duggleby, A., Ball, K. S. & Paul, M. R. The effect of spanwise wall oscillation on turbulent pipe flow structures resulting in drag reduction. *Physics of Fluids* **19,** 125107. eprint: https://doi.org/10.1063/1.2825428 (2007) (cit. on pp. 20, 138).

43. Xu, C. X. & Huang, W. X. Transient response of Reynolds stress transport to spanwise wall oscillation in a turbulent channel flow. *Phys. Fluids* **17** (1 2005) (cit. on p. 20).

44. Ricco, P., Ottonelli, C., Hasegawa, Y. & Quadrio, M. Changes in turbulent dissipation in a channel flow with oscillating walls. *J. Fluid Mech.* **700,** 77–104 (2012) (cit. on pp. 21, 53).

45. Ge, M. & Jin, G. Response of turbulent enstrophy to sudden implementation of spanwise wall oscillation in channel flow. *Appl. Math. Mech.-Engl* **38,** 1159–1170 (2017) (cit. on p. 21).

46. Agostini, L., Touber, E. & Leschziner, M. A. Spanwise oscillatory wall motion in channel flow: Drag-reduction mechanisms inferred from DNS-predicted phase-wise property variations at $Re_\tau = 1000$. *J. Fluid Mech.* **743,** 606–635 (2014) (cit. on p. 21).

47. Agostini, L., Touber, E. & Leschziner, M. A. The turbulence vorticity as a window to the physics of friction-drag reduction by oscillatory wall motion. *Int. J. Heat and Fluid Flow* **51,** 3–15 (2015) (cit. on p. 21).

48. Yakeno, A., Hasegawa, Y. & Kasagi, N. Modification of quasi-streamwise vortical structure in a drag-reduced turbulent channel flow with spanwise wall oscillation. *Phys. Fluids* **26** (2014) (cit. on pp. 22, 132).

49. Fukagata, K., Iwamoto, K. & Kasagi, N. Contribution of Reynolds stress distribution to the skin friction in wall-bounded flows. *Physics of Fluids* **14,** L73–L76 (2002) (cit. on p. 22).

50. Du, Y. & Karniadakis, G. Suppressing Wall Turbulence by Means of a Transverse Traveling Wave. *Science* **288,** 1230–1234 (2000) (cit. on p. 22).

51. Du, Y., Symeonidis, V. & Karniadakis, G. Drag reduction in wall-bounded turbulence via a transverse travelling wave. *Journal of Fluid Mechanics* **457,** 1–34 (2002) (cit. on p. 22).

52. Viotti, C., Quadrio, M. & Luchini, P. Streamwise oscillation of spanwise velocity at the wall of a channelfor turbulent drag reduction. *Phys. Fluids* **21** (2009) (cit. on pp. 22, 23).

53. Yakeno, A., Hasegawa, Y. & Kasagi, N. *Spatio-Temporally Periodic Control for Turbulent Friction Drag Reduction* in *Sixth International Symposium on Turbulence and Shear Flow Phenomena* (Seoul, Korea, 2009), 598–603 (cit. on p. 22).

54. Skote, M. Turbulent boundary layer flow subject to streamwise oscillation of spanwise wall-velocity. *Physics of Fluids* **23,** 081703 (2011) (cit. on p. 22).

55. Auteri, F., Baron, A., Belan, M., Campanardi, G. & Quadrio., M. Experimental assessment of turbulent drag reduction by traveling waves in a turbulent pipe flow. *Phys. Fluids* **22** (2010) (cit. on p. 23).

56. Bird, J., Santer, M. & Morrison, J. F. Experimental Control of Turbulent Boundary Layers with In-plane Travelling Waves. *Flow Turbulence and Combustion* **100,** 1015–1035 (2018) (cit. on p. 23).

57. Choi, J.-I., Xu, C.-X. & Sung, H. J. Drag Reduction by Spanwise Wall Oscillation in Wall-Bounded Turbulent Flows. *AIAA Journal* **40,** 842–850 (2002) (cit. on p. 24).

58. Quadrio, M. & Ricco, P. Critical assessment of turbulent drag reduction through spanwise wall oscillations. *J. Fluid Mech.* **521,** 251–271 (2004) (cit. on pp. 24, 40).

59. Marusic, I. *et al.* An energy-efficient pathway to turbulent drag reduction. *Nature Communications* **12** (2021) (cit. on pp. 24–28, 143).

60. Hurst, E., Yang, Q. & Chung, Y. M. The effect of Reynolds number on turbulent drag reduction by streamwise travelling waves. *J. Fluid Mech.* **759,** 28–55 (2014) (cit. on pp. 25, 28, 40, 56, 57).

61. Gatti, D. & Quadrio, M. Performance losses of drag-reducing spanwise forcing at moderate values of the Reynolds number. *Phys. Fluids* **25** (12 2013) (cit. on pp. 25, 28).

62. Gatti, D. & Quadrio, M. Reynolds-number dependence of turbulent skin-friction drag reduction induced by spanwise forcing. *J. Fluid Mech.* **802,** 553–582 (2016) (cit. on pp. 25, 28, 40, 59).

63. Yao, J., Chen, X. & Hussain, F. Reynolds number effect on drag control via spanwise wall oscillation in turbulent channel flows. *Phys. Fluids* **31** (8 2019) (cit. on p. 25).

64. Ricco, P. & Quadrio, M. Wall-oscillation conditions for drag reduction in turbulent channel flow. *International Journal of Heat and Fluid Flow* **29,** 601–612 (2008) (cit. on p. 25).

65. Marusic, I. On the role of large-scale structures in wall turbulence. *Phys. Fluids* **13** (2001) (cit. on p. 25).

66. Hutchins, N. & Marusic, I. Large-scale influences in near-wall turbulence. *Phil. Trans. Roy. Soc. Lond.* **365,** 647–664 (2007) (cit. on p. 25).

67. Rosenberg, B., Hultmark, M., Vallikivi, M., Baily, S. & Smits, A. Turbulence spectra in smooth-and rough-wall pipe flow at extreme Reynolds number. *J. Fluid Mech.* **731,** 46–63 (2013) (cit. on p. 25).

68. Vallikivi, M., Hultmark, M. & Smits, A. Turbulent boundary layer statistics at very high Reynolds number. *J. Fluid Mech.* **779,** 371–389 (2015) (cit. on p. 25).

69. Baars, W. & Marusic, I. Data-driven decomposition of the streamwise turbulence kinetic energy in boundary layer. *J. Fluid Mech.* **882** (2020) (cit. on p. 25).

70. Lee, J., Lee, J. H., Choi, J.-I. & Sung, H. J. Spatial organization of large- and very-large-scale motions in a turbulent channel flow. *Journal of Fluid Mechanics* **749,** 818–840 (2014) (cit. on p. 25).

71. Yamamoto, Y. & Tsuji, Y. Numerical evidence of logarithmic regions in channel flow at $\mathrm{Re}_\tau = 8000$. *Phys. Rev. Fluids* **3,** 012602 (1 2018) (cit. on p. 25).

72. Mathis, R., Marusic, I., Chernyshenko, S. I. & Hutchins, N. Estimating wall-shear-stress fluctuations given an outer region input. *Journal of Fluid Mechanics* **715,** 163 (2013) (cit. on p. 27).

73. Lee, M. & Moser, R. D. Direct numerical simulation of turbulent channel flow up to $Re_\tau \approx 5200$. *Journal of Fluid Mechanics* **774,** 395–415 (2015) (cit. on p. 30).

74. Richardson, L. F. & Walker, G. T. Atmospheric diffusion shown on a distance-neighbour graph. *Proceedings of the Royal Society of London. Series A, Containing Papers of a Mathematical and Physical Character* **110,** 709–737 (1926) (cit. on p. 30).

75. Kolmogorov, A. N. The local structure of turbulence in incompressible viscous fluid for very large Reynolds numbers. *Doklady Akademii Nauk SSSR* **30,** 301–305 (1941) (cit. on p. 30).

76. Moin, P. & Mahesh, K. DIRECT NUMERICAL SIMULATION: A Tool in Turbulence Research. *Annual Review of Fluid Mechanics* **30,** 539–578 (1998) (cit. on p. 31).

77. Tam, C. K. & Webb, J. C. Dispersion-Relation-Preserving Finite Difference Schemes for Computational Acoustics. *Journal of Computational Physics* **107,** 262–281 (1993) (cit. on pp. 34, 35).

78. Lele, S. K. Compact finite difference schemes with spectral-like resolution. *Journal of Computational Physics* **103,** 16–42 (1992) (cit. on p. 35).

79. Bauer, F., Tardu, S. & Doche, O. Efficiency of high accuracy DRP schemes in direct numerical simulations of incompressible turbulent flows. *Computers and Fluids* **107,** 123–140 (2015) (cit. on p. 35).

80. Moin, P. & Kim, J. Numerical investigation of turbulent channel flow. *Journal of Fluid Mechanics* **118,** 341–377 (1982) (cit. on p. 37).

81. Hussain, A. K. & Reynolds, W. C. The mechanics of an organized wave in turbulent shear flow. *J. Fluid Mech.* **41,** 241–258 (2 Apr. 1970) (cit. on p. 44).

82. Moser, R. D., Kim, J. & Mansour, N. N. Direct numerical simulation of turbulent channel flow up to $Re_\tau = 590$. *Phys. Fluids* **11,** 943–945 (4 1999) (cit. on pp. 46, 47, 112).

83. Kline, S., Reynolds, W., Schraub, F. & Runstadler, P. The structure of turbulent boundary layers. *Journal of Fluid Mechanics* **30,** 741–773 (1967) (cit. on p. 49).

84. Tardu, S. *Transport and Coherent Structures in Wall Turbulence* (Wiley-ISTE, 2014) (cit. on pp. 49, 125, 133).

85. Jeong, J., Hussain, F., Schoppa, W. & Kim, J. Coherent structures near the wall in a turbulent channel flow. *Journal of Fluid Mechanics* **332,** 185–214 (1997) (cit. on pp. 50, 51, 132, 133).

86. Bewley, T. R., Moin, P. & Temam, R. DNS-based predictive control of turbulence: an optimal benchmark for feedback algorithms. *J. Fluid Mech.* **447,** 179–225 (2001) (cit. on p. 55).

87. Tardu, S. Active control of near-wall turbulence by local oscillating blowing. *J. Fluid Mech.* **439,** 217–253 (July 2001) (cit. on p. 59).

88. Kim, J., Moin, P. & Moser, R. Turbulence statistics in fully developed channel flow at low Reynolds number. *J. Fluid Mech.* **177,** 133–166 (1987) (cit. on pp. 77, 102).

89. Wallace, J. M., Eckelmann, H. & Brodkey, R. S. The Wall Region in Turbulent Shear Flow. *Journal of Fluid Mechanics* **54,** 39–48 (1972) (cit. on p. 81).

90. Lu, S. & Willmarth, W. Measurements of the Structure of the Reynolds Stress in a Turbulent Boundary Layer. *Journal of Fluid Mechanics* **60,** 481–511 (1973) (cit. on p. 81).

91. Lee, C. & Kim, J. Control of the viscous sublayer for drag reduction. *Physics of Fluids* **14,** 2523–2529 (2002) (cit. on pp. 107, 108, 119).

92. Jiménez, J. & Pinelli, A. The autonomous cycle of near-wall turbulence. *Journal of Fluid Mechanics* **389,** 335–359 (1999) (cit. on p. 107).

93. Lumley, J. L. & Newman, G. R. The return to isotropy of homogeneous turbulence. *Journal of Fluid Mechanics* **82,** 161–178 (1977) (cit. on p. 112).

94. Pope, S. B. *Turbulent Flows* (Cambridge University Press, 2000) (cit. on p. 112).

95. Busse, A. & Sandham, N. D. Parametric forcing approach to rough-wall turbulent channel flow. *Journal of Fluid Mechanics* **712,** 169–202 (2012) (cit. on p. 112).

96. Frohnapfel, B., Lammers, P., Jovanović, J. & Durst, F. Interpretation of the mechanism associated with turbulent drag reduction in terms of anisotropy invariants. *Journal of Fluid Mechanics* **577,** 457–466 (2007) (cit. on pp. 112, 116).

97. Simonsen, A. J. & Krogstad, P.-r. Turbulent stress invariant analysis: Clarification of existing terminology. *Physics of Fluids* **17,** 088103 (2005) (cit. on p. 116).

98. Tardu, S. & Doche, O. Communication between the buffer layer and the wall in a turbulent channel flow. *Int. J. Heat and Fluid Flow* **82** (2020) (cit. on p. 121).

99. Tardu, S. Concomitance of the local spanwise velocity and production in wall turbulence. *Phys. Fluids* **28** (2016) (cit. on pp. 121, 125).

100. Brooke, J. W. & Hanratty, T. Origin of turbulence-producing eddies in a channel flow. *Phys. Fluids A* **5,** 1011–1022 (1993) (cit. on pp. 125, 128).

101. Tardu, S. F. *Stochastic synchronization of the near wall turbulence* in. **20** (2008) (cit. on p. 125).

102. Tardu, S. Multiscale analysis of some shear layers in a fully developed turbulent channel flow. *Computers & Fluids* **240,** 105459 (2022) (cit. on pp. 125, 133).

103. Wu, X. *et al.* Transitional–turbulent spots and turbulent–turbulent spots in boundary layers. *Proceedings of the National Academy of Sciences* **114,** E5292–E5299 (2017) (cit. on p. 129).

104. Tardu, S. Characteristics of single and clusters of bursting events. *Exp. in Fluids* **33,** 640–652 (2002) (cit. on p. 129).

105. Adrian, R. J. Hairpin vortex organization in wall turbulence a). *Phys. Fluids* **19,** 041301 (2007) (cit. on p. 129).

106. Gallorini, E., Quadrio, M. & Gatti, D. Coherent near-wall structures and drag reduction by spanwise forcing. *Phys. Rev. Fluids* **7,** 114602 (11 2022) (cit. on pp. 132, 133).

107. Jiménez, J. On the structure and control of near wall turbulence. *Physics of Fluids* **6,** 944–953. eprint: https://doi.org/10.1063/1.868327 (1994) (cit. on p. 133).

108. Tardu, S. Coherent structures and riblets. *Appl. Sci. Res.* **54,** 349–385 (1995) (cit. on p. 133).

Reynolds stresses transport in a turbulent channel flow subjected to streamwise traveling waves

Mohammad Umair* and Sedat Tardu
University of Grenoble Alpes, CNRS, Grenoble-INP, LEGI, F-38000 Grenoble, France

Olivier Doche
University of Grenoble Alpes, CNRS, Grenoble-INP, SIMAP, F-38000 Grenoble, France

(Received 17 January 2022; accepted 18 April 2022; published 6 May 2022)

Reynolds stresses transport in a turbulent channel flow under streamwise traveling waves is analyzed in detail using direct numerical simulations to gain physical insights into the mechanism of drag reduction. Streamwise traveling waves are known to produce larger drag reduction margins compared to simple homogeneous wall oscillations. The aim of the current investigation is to identify and analyze the direct effects arising from streamwise traveling waves that leads to larger drag reduction margins compared to simple homogeneous wall oscillations. Several cases were considered, with amplitudes ranging from 0.15 to 1.25 (in outer units) at fixed angular frequency and wave number of 0.16 and 1.66 (in outer units), respectively, to yield drag reduction margins ranging from 26% to 58%, respectively. Streamwise traveling waves of large amplitudes were found to block the intercomponent energy transfer, resulting in shut off of the near-wall buffer layer dynamics. The analyses here suggest that the combined effect of loss of communication between low and high buffer layers with damping in the wall-normal Reynolds stress component is associated to the traveling wave effect and results in larger drag reduction margins.

DOI: 10.1103/PhysRevFluids.7.054601

I. INTRODUCTION

The demand to reduce energy consumption and control pollutants emissions has led researchers to devise various flow control techniques directed at reducing skin-friction drag. In a flow field, most of the skin-friction is generated in a thin highly viscous region close to the wall where the flow is highly turbulent. Skin-friction contributes to about 50% of the total drag in flow over a commercial aircraft [1] and almost 100% in internal flows (for example, parallel pipe and channel flows). It means that most of the energy used to drive the flow is dissipated by the wall due to skin-friction. Hence, a small reduction in skin-friction drag would result in substantial fuel savings.

Over several decades, various drag reduction (DR) techniques have been proposed. Based on whether the energy is fed into the system, DR techniques are classified as passive and active. Many passive DR techniques have been investigated in the past and shown to bring about sustained DR. However, due to their limited performance, active DR techniques have attracted considerable attention. Examples of passive DR techniques include the use of super-hydrophobic surfaces [2,3], riblets [4], etc. Compared to passive DR techniques, active DR techniques achieve larger DR margins under a wider range of flow conditions and operate at much larger spatio-temporal scales. Examples of active DR techniques include transverse wall oscillations [5], wall blowing and suction [6], rotating discs [7], plasma actuation [8], spanwise wall jet forcing [9], etc. Active DR

*mohammad.umair@legi.grenoble-inp.fr

techniques can be further classified into two categories, closed-loop techniques which require a feedback control law and open-loop techniques for which the control law is predetermined, and the control is applied independent of the instantaneous turbulent flow field, thus obviating the need for complex sensing and actuating systems.

Among many open-loop active DR techniques, one of the most promising candidates for reducing skin-friction drag is the transverse wall oscillations. Since introduced by Jung *et al.* [10], there have been a plethora of investigations, both experimental and numerical, devoted to quantify DR margins for a wide range of actuation parameters at low to moderate Reynolds number (Re). Numerous investigations, both numerical and experimental, have shown that the transverse wall oscillations in the form of streamwise traveling waves (STW) can produce significant DR margins as large as 60% and a net power savings of up to 26% can be achieved upon a careful selection of actuation parameters [11–15].

While considerable attention has been devoted in the past to the parametric studies, investigations that primarily aim at elucidating the mechanism behind drag reduction are rare. A few studies [10,16–26] exist that attempt to shed a light on the mechanism for a limiting case of a control where the spanwise wall oscillations are imposed homogeneously throughout the streamwise direction. Studies, for example of Jung *et al.* [10], Laadhari *et al.* [16], Choi *et al.* [17], Ricco [19], Touber and Leschznier [21], etc., suggest that the forcing in the form of homogeneous wall oscillations results in the damping of the near-wall streaks strength, thickening of viscous sublayer, an upward shift in the logarithmic portion of the mean flow profile, a significant reduction in the sweep and ejection events associated with huge damping in the wall-normal turbulence intensity, etc. Xu and Huang [20] examined the transient response of a turbulent channel flow subjected to homogeneous spanwise wall oscillations for the first two oscillation periods. They found that the attenuation of pressure-strain correlations resulting in the hindrance of intercomponent transfer of turbulent kinetic energy is responsible for drag reduction. Touber and Leschziner [21] showed that the cross-flow straining due to wall oscillations cause major distortions in the near-wall streaks strength which leads to a significant damping of wall-normal momentum exchange in the viscous sublayer and hence results in the suppression of wall-shear stress production. Yakeno *et al.* [23] studied the impact of wall oscillations on the structures of quasi streamwise vortices (QSVs) and found that the damping of ejection events governs the DR at relatively small oscillation periods. Ricco *et al.* [22], using direct numerical simulations at constant pressure gradient, carried out energy and enstrophy balances to emphasize the role of the oscillating spanwise shear layer and showed that drag reduction is associated with the increased dissipation rate of turbulent kinetic energy. Agostini *et al.* [24], on the other hand, found that the forcing in the form of wall oscillations results in a decrease in the turbulent dissipation rate at constant flow rate conditions.

While considerable advances have been made to unravel the physics of DR for simple homogeneous wall oscillations control, however, to this date, no advancement has been made to reveal the physical insights in the flows controlled by STW. The focus of most of the previous investigations, both experimental [15,27,28] and numerical [11–14], on STW control has been to find a scaling parameter that dictates DR margin. Some studies report at least some statistical information, for example, of Quadrio *et al.* [11] and Quadrio and Ricco [29], but the analyses are limited to the response of Reynolds stresses for very limited actuation scenarios. The objective of the present work is, therefore, to gain further insight into the physical mechanism behind STW control by analyzing and identifying the important interactions occurring within the budgets of Reynolds stresses. As we will see later in the discussions, some extra terms that are directly linked to the forcing appear in the transport equations of Reynolds stresses. These terms account for the interaction between the Reynolds stresses and the gradients of the periodic fluctuations due to forcing, and play a fundamental role in modifying the response of the Reynolds stresses, especially of the spanwise component. The approach is to identify the key terms appearing in the Reynolds stresses transport equations that are directly linked to the forcing. One of the secondary aims is also to investigate why STW control perform better than simple homogeneous wall oscillations.

TABLE I. %DR margins and the net power savings ($\%P_{\text{net}}$) for different oscillatory conditions. The values of angular frequency (ω^*) and wave number (κ^*) of STW were kept fixed at 0.16 and 1.66 (outer units). Their corresponding values in local units are also provided to facilitate comparison with the available literature.

Case	A^* (U_C)	A_0 ($u_{\tau 0}$)	A (u_τ)	ω (u_τ^2/ν)	κ (u_τ/ν)	Re_τ (hu_τ/ν)	%DR	$\%P_{\text{net}}$
HWO	0.51	12.0	14.9	0.098	—	144.2	36	−44
*A*0.15	0.15	3.5	4.0	0.027	0.248	156.9	26	23
*A*0.30	0.30	7.0	9.0	0.035	0.360	139.0	42	30
*A*0.50	0.50	11.7	16.1	0.039	0.408	130.7	48	15
*A*0.75	0.75	17.5	25.3	0.043	0.450	124.5	52	−19
*A*0.95	0.95	22.2	32.7	0.045	0.470	121.9	54	−50
*A*1.25	1.25	29.2	44.3	0.048	0.498	118.4	58	−130

The paper is divided into two main parts. Section II is devoted to the flow configuration and short details on the direct numerical simulations we used. The results (Sec. III) contains the Reynolds stress transport phenomena under STW, wherein the structural modifications observed in the near-wall turbulence are discussed in some details. Finally, the concluding remarks are provided in Sec. IV.

II. DETAILS OF FLOW CONFIGURATION AND NUMERICAL PROCEDURES

The configuration selected here is a fully developed incompressible channel flow. The Reynolds number $\text{Re} = hU_c/\nu$ was fixed at 4200, where U_c is the centerline velocity of the Poiseuille flow, h is the channel half-width, and ν is the kinematic viscosity. For the uncontrolled case, it corresponds to friction Reynolds number $\text{Re}_{\tau 0} = hu_{\tau 0}/\nu = 180$, where $u_{\tau 0}$ is the friction velocity of the uncontrolled flow. The flow is subjected to spanwise wall oscillations in the form of STW, which is prescribed by

$$W^*(x^*, y^* = 0, z^*) = A^* \sin(\kappa^* x^* - \omega^* t^*), \tag{1}$$

where W^* is the instantaneous spanwise velocity, A^* is its amplitude at the wall, κ^* is the wave number in the streamwise direction, and ω^* is the angular frequency of the traveling wave. Here x^*, y^*, z^* represent the streamwise, wall-normal, spanwise directions, respectively, and t^* is time. The superscript $*$ denotes quantities normalized using outer units; absence of this qualifier implies scaling in inner units. The values of ω^* and κ^* were kept fixed at 0.16 and 1.66, respectively, while the amplitude was varied from $A^* = 0.15$ to 1.25. The corresponding %DR margins are listed in Table I. The chosen set of ω^* and κ^* corresponds to the optimal settings at $A^* = 0.50$ and leads to $DR = 48\%$, which is in good agreement with Quadrio *et al.* [11]. Concerning the net power savings ($\%P_{\text{net}}$), it is well known that there is a penalty in imposing wall actuation control. The net power saving is computed in the same manner as described in Quadrio *et al.* [11] and are provided in Table I. The estimated $\%P_{\text{net}}$ compare well with these authors. It is important to note that the large imposed amplitude A0.95 case results in roughly the same net power saving as the simple homogeneous wall oscillations (HWO) case; however, the drag reduction margin is significantly larger. This strengthens the main aim of this investigation, namely, looking for the physical process that makes the STWs more efficient. The range of actuation parameters considered here has been narrowed down to the optimum case scenario to investigate the direct effect of STW on the near-wall turbulence dynamics. The naming of the cases is based on the forcing amplitude in outer units, for example, the case *A*1.25 refers to the STW controlled case of imposed amplitude $A^* = 1.25$. One of the aims here is to investigate the direct effects of the STW with respect to the simple homogeneous wall oscillations (HWO). Transverse wall oscillations in the form of STW result in larger DR margin compared to HWO. We will show and discuss in detail later that some terms

appearing in the Reynolds stresses transport equations are a direct consequence of the STW. The response of the flow to the STW is rather complex when examined as a function of ω^* and κ^*. Depending on the value of κ^*, drag can be either increased or decreased for a fixed value of ω^*. Therefore, it is difficult to compare both types of forcing on the basis of actuation parameters. Yet, a clear base has to be defined for comparison; hence, we opted to compare the traveling wave effects with the HWO in their optimal configuration with $A_0 = 12$ ($A^* = 0.51$) and $T_0 = 100$ for the Re investigated here [21,30]. Note that the optimal configuration is a function of Re [13,14]. Here, the subscript '0' represents quantities scaled by the friction velocity of the uncontrolled flow.

Direct numerical simulations (DNS) were performed using MULTIFAST, a highly parallel code developed by our team that solves incompressible Navier-Stokes equations using explicit optimized (EO) finite difference schemes for spatial discretization and low-storage third-order Runge-Kutta method to advance the solution in time. MULTIFAST has been used previously in many studies [31–34]. Further details about the numerical scheme is provided in Appendix A.

All simulations were performed over the same computational box of size $L_x = 6\pi h$, $L_y = 2h$, $L_z = 3\pi h$ in the streamwise, wall-normal, and spanwise direction, respectively. The box was covered by $N_x \times N_y \times N_z = 401 \times 129 \times 335$ ($\approx$17.3 million) nodes, which were distributed uniformly along the streamwise and spanwise directions, while they were clustered in the wall-normal direction near the wall through a hyperbolic tangent distribution. The corresponding cell dimensions were Δx_0, Δy_0, $\Delta z_0 = 8.5$, 0.5–5.5, 5. The simulation for the uncontrolled flow was performed at a constant time-step $dt_0 = 0.04$, which is well below that used in previous studies at larger Re [12,14,21,24,35]. The statistics for the uncontrolled flow were obtained using a total of 50 snapshots covering a time window of $t_0 \approx 37\,000$, separated by $\Delta t_0 \approx 770$.

Two different inner scaling options are available in the constant flow rate (CFR) conditions for the controlled cases, one based on the inner variables derived using the friction velocity of the uncontrolled flow ($u_{\tau 0}$) and the other based on the inner variables derived using the respective local (actual) friction velocities of the controlled cases (u_τ). As the flow is still in turbulent regime even at the largest imposed amplitude, the use of actual friction velocity of the controlled flow is physically correct, especially near the wall. Moreover, since the imposed control is based on the wall and its influence is limited to the near-wall region, the use of actual friction velocity would bring about the important structural changes in the flow field. Scaling with the inner variables based on $u_{\tau 0}$ brings about the absolute changes of the quantities, while scaling with the local inner variables based on u_τ leads to the direct *in situ* nondimensionalization of the mean flow near the wall, and thus allows for a comparison between the near-wall drag-reduced statistics and the statistics of the uncontrolled flow at the same friction Reynolds number (Re_τ) [21,22]. Real structural changes can only be analyzed through local units; this point will be further illustrated in the later sections.

Throughout the manuscript, the quantities with subscript "0" are normalized using the inner variables based on $u_{\tau 0}$; absence of this qualifier implies scaling with inner variables based on u_τ of the controlled cases.

Considering the periodic nature of the imposed control, the fluctuations associated with the wall forcing must be removed to obtain the purely stochastic fluctuations. Hence, for statistical analyses we adopt the classical triple decomposition introduced by Hussain and Reynolds [36] to decompose an instantaneous flow field variable (F) into a time-invariant mean component ($\overline{F}$), a periodic fluctuating component ($\widetilde{F}$), arising due to the periodic forcing, and a purely stochastic component (f), characterizing the turbulent fluctuations. The decomposition can be expressed as

$$F = \overline{F} + \widetilde{F} + f = \langle F \rangle + f, \tag{2}$$

where $\langle F \rangle$ is the phase-averaged value of F. This convention is followed throughout the manuscript. The flow field variables were phase-averaged over the phase $\xi = x - ct$ of the traveling wave, where $c = \omega/\kappa$ is the speed of the traveling wave. Figures 1(a) and 1(b) show the phasewise variations of the phase-averaged spanwise velocity at different wall-normal locations for $A0.50$ case.

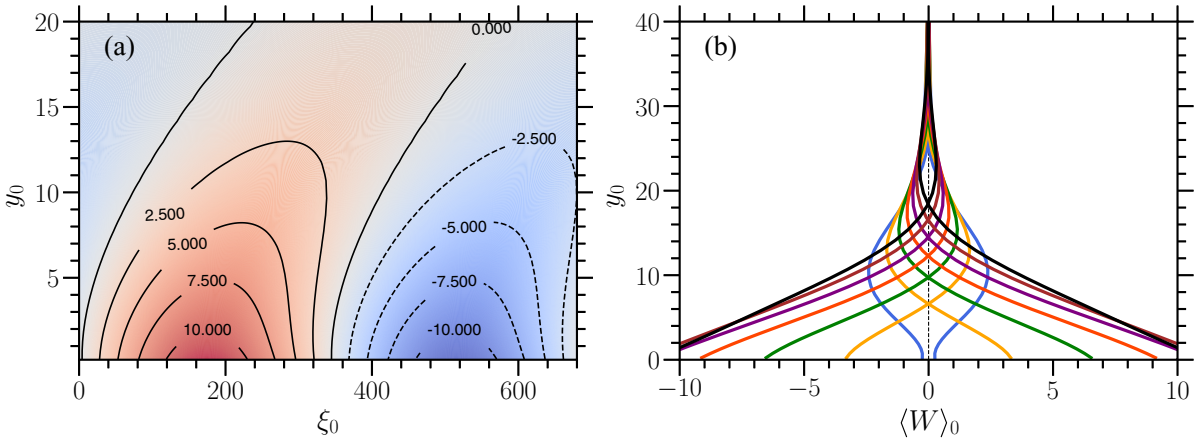

FIG. 1. Phasewise variations of phase-averaged spanwise velocity $\langle W_0 \rangle$ at different wall-normal locations y_0 for $A0.50$ case. The red contours in the left figure correspond to positive values, while the blue contours correspond to negative values.

For the controlled cases, the uncontrolled flow was used as the initial condition, and the time-step was reduced to $dt_0 = 0.008$ to converge the phase-averaged statistics. At least 20 initial cycles were discarded to ensure that the time window over which the data was collected to perform statistics doesn't overlap with the transient phase over which the control leads the flow towards the drag reduced state. To ensure the convergence of the phase-averaged statistics, the data was collected for at least 40 cycles corresponding to a time window of $t_0 \approx 12\,000$. The details about the convergence of the phase-averaged statistics is provided in Appendix B. All the simulations were performed on the computational clusters of GRICAD, University of Grenoble-Alpes. Even at such a low Re, each simulation for the controlled case typically required CPU-time of about 90 000 core-hours, distributed across 128 processors.

III. RESULTS AND DISCUSSIONS

A. Skin-friction coefficient and the mean flow

The skin-friction coefficient (C_f) is defined as

$$C_f = \frac{2\tau_w}{\rho U_b^2}, \tag{3}$$

where U_b is the bulk flow velocity, ρ is the density of the fluid, and τ_w is the shear stress at the wall. The %DR margin is quantified in terms of relative change in C_f,

$$\%DR = (1 - C_f/C_{f0}) \times 100, \tag{4}$$

where C_{f0} is the skin-friction coefficient of the uncontrolled flow.

Figure 2(a) shows the initial response of C_f (normalized by C_{f0}) after the actuation of control. C_f began to decrease sharply, and the rate of the initial decay is similar for all forcing amplitudes, except for $A0.15$ case. The response of the large amplitude cases are quite interesting, for instance, the flow is not far from the relaminarization limit at $A^* = 1.25$ near $t_0 = 2000$ but returns back to a turbulent state at $t_0 = 3000$. Such complex responses of skin-friction are also observed in optimal wall turbulence control at moderate optimization horizons (see Fig. 11 of Bewley *et al.* [37]).

The time of initial decay varies with the amplitude of forcing and is about 5–6 cycles ($t_0 \approx 1600$) for $A0.15$ case, and 13–14 cycles ($t_0 \approx 4000$) for $A1.25$ case. After the elapsed of the initial transient phase, the flow acquires a new quasistationary state, and C_f begins to oscillate about a mean level. The period of oscillation of C_f differs with the amplitude of forcing, but in general it is about one order of magnitude longer than the period of forcing.

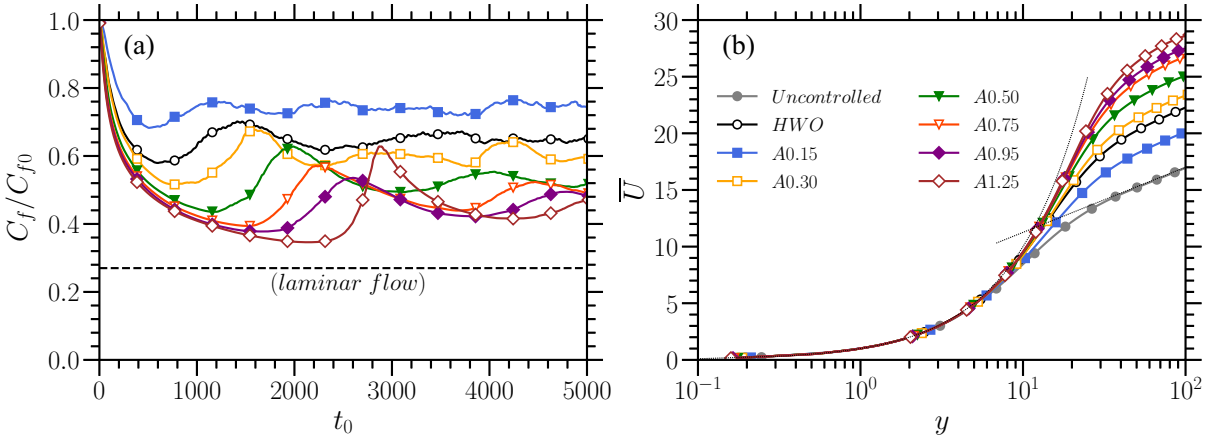

FIG. 2. (a) Initial response of the normalized skin friction coefficient (C_f/C_{f0}) after the actuation of control for different forcing amplitudes. (b) Mean velocity profiles for the uncontrolled and controlled cases.

Figure 2(b) conveys the effect of forcing on the mean velocity profile. Consistent with the previous studies, the mean velocity profiles show an upward shift in the logarithmic portion and thickening of the viscous sublayer when scaled with the respective friction velocities of the drag reduced flows. This behavior is typical to drag reduction scenarios regardless of the control type—except for superhydrophobic surfaces, where drag reduction results in thinning of the buffer layer along with a downward shift in the logarithmic region. The magnitude of the upward shift in the logarithmic portion is proportional to the DR margin [14].

B. Reynolds stresses components

Figure 3 shows the effect of forcing on the Reynolds stresses components for the uncontrolled and controlled cases. Forcing results in a substantial decline in the streamwise component $\overline{uu}$ [Fig. 3(a)], especially close to the wall, reflecting a strong reduction in the near-wall streaks strength. The peak value of $\overline{uu}$ is shifted away from the wall and reflects the lifting of the quasistreamwise vortices (QSVs) [38]. An interesting feature worth noticing is that the profiles of $\overline{uu}$ approximately collapse for $y > 30$, reflecting that the structural changes brought up by the control are limited to the region close to the wall. The peak value of the wall-normal component $\overline{vv}$ progressively declines as the amplitude of the forcing is increased [see Fig. 3(c)]. Contrary to $\overline{uu}$, the location of its peak remains unaffected. It is important to stress that $\overline{vv}$ plays the primary role in the production of Reynolds shear stress $\overline{uv}$. Attenuation of $\overline{vv}$ indicates damping of sweep and ejection events that are primarily responsible for most of the turbulent kinetic energy production. Likewise, the magnitude of $\overline{uv}$ also shows a substantial decline at all wall-normal locations [Fig. 3(c)] with a significant reduction close to the wall.

The response of the spanwise component $\overline{ww}$ is strikingly different, with the emergence of a second peak at $y \approx 8$ near the edge of the viscous sublayer at the largest imposed amplitude $A^* = 1.25$ investigated here [see Fig. 3(b)]. Despite the appearance of two production terms arising in its transport equation due to forcing (see Appendix C), $\overline{ww}$ progressively declines at wall-normal locations $y > 20$. It is important to note that these peculiar behaviors can hardly be detected if the quantities were scaled with the friction velocity of the uncontrolled flow. To stress this point, we show in Fig. 3(d) the profiles of $\overline{ww}_0$, where the scaling is now with respect to the friction velocity of the uncontrolled flow ($u_{\tau 0}$). It is clearly seen that the peculiar structural modifications are hardly discernible in Fig. 3(d) in comparison to Fig. 3(b). Scaling with local inner variables results in correct nondimensionalization and allows sorting out the structural changes of the response of the near-wall turbulence.

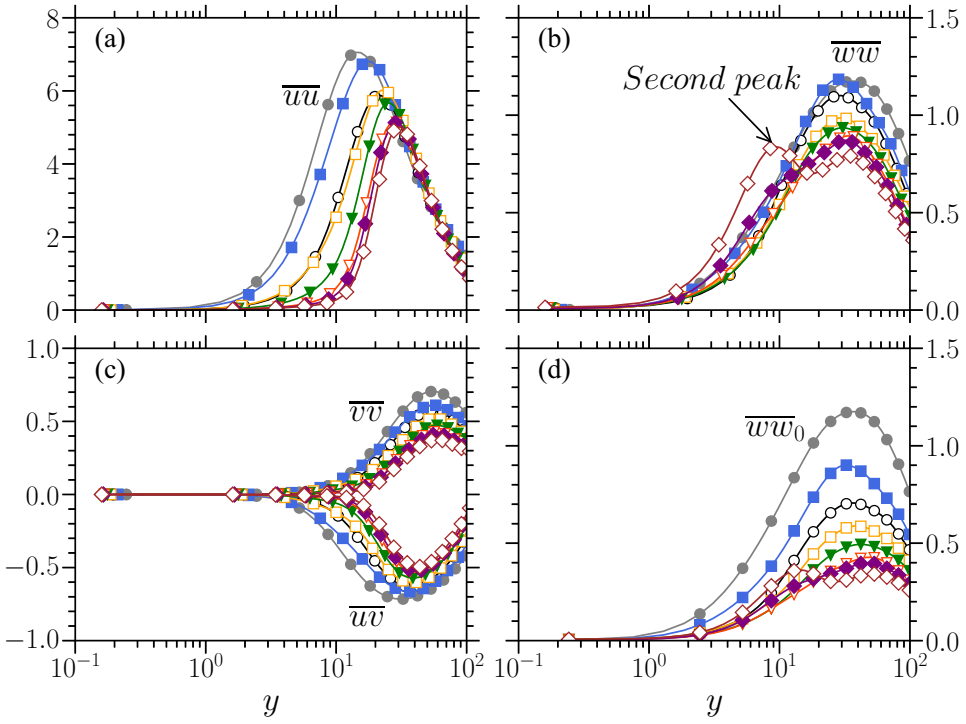

FIG. 3. Reynolds stresses profiles for uncontrolled and controlled cases. (a) streamwise component $\overline{uu}$, (b) spanwise component $\overline{ww}$ (scaled with local friction velocity), (c) wall-normal component $\overline{vv}$ and Reynolds shear stress $\overline{uv}$, and (d) spanwise component $\overline{ww}_0$ (scaled with the friction velocity of the uncontrolled flow). The profiles in panels (a), (b), and (c) were scaled with the local friction velocity, while the profiles in panel (d) were scaled with the friction velocity of the uncontrolled flow. Refer to Fig. 2 for markers corresponding to different cases.

To summarize, globally, the profiles of Reynolds stresses components approximately collapse for $A^* \geqslant 0.75$ when scaled with the local friction velocity, except the spanwise component $\overline{ww}$. The streamwise component $\overline{uu}$ is significantly damped close to the wall, reflecting a strong reduction in the near-wall streaks strength. The peaks of $\overline{uu}$ and $\overline{uv}$ shifts toward the edge of the buffer layer at $y \approx 30$ [see Figs. 3(a) and 3(c)]. The profile of spanwise component $\overline{ww}$ for the $A1.25$ case exhibits a second peak close to the wall at $y \approx 8$; this unique feature is explained in the following section. Discarding the appearance of the second peak in $\overline{ww}$ at $A^* = 1.25$, the wall-normal locations of the peak values of $\overline{vv}$ and $\overline{ww}$ are not altered by the STW. Again, all these quantities were scaled using the local friction velocity. When scaled with the friction velocity of the uncontrolled flow, all the peak values are shifted away from the wall in proportion to $u_{\tau 0}/u_\tau = \sqrt{1/(1-DR)}$.

C. Mean Reynolds stresses budgets

The Reynolds stresses transport equations for the streamwise component $\overline{uu}$, wall-normal component $\overline{vv}$, spanwise component $\overline{ww}$, and shear stress $\overline{uv}$ are provided in Appendix C. Besides the classical terms, quantities directly related to the STW emerge in the transport equations. These extra terms account for the interaction between the phase-averaged Reynolds stresses and the gradients of the periodic fluctuations due to forcing. All the extra terms emerging from the wall-normal and streamwise gradients of $\langle U_i \rangle$ (where $i = 1, 2, 3$ denote streamwise, wall-normal, and spanwise direction, respectively) are negligible compared to the other terms in the overall budget of Reynolds stresses components, except for those intervening in the spanwise component $\overline{ww}$ induced by $\partial\langle W\rangle/\partial x$ and $\partial\langle W\rangle/\partial y$, as shown in Fig. 4. Recall that, the production term in the transport equation of $\overline{ww}$ is zero for the canonical (uncontrolled) channel flow. Hence, the level of $\overline{ww}$ is maintained solely by the velocity-pressure gradient term $\overline{\Pi_{ww}} = -\overline{2w\partial p/\partial z}$, the role of which is to

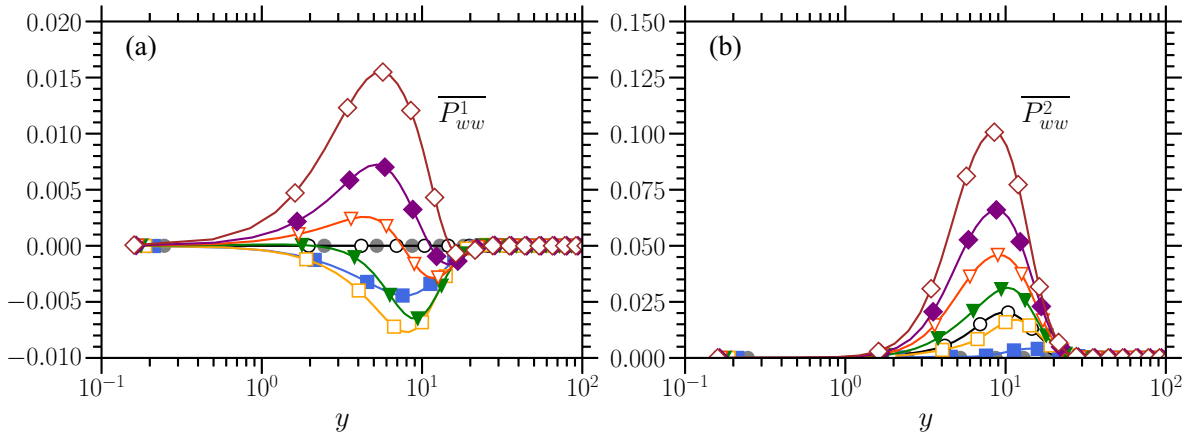

FIG. 4. Extra production terms (a) $\overline{P^1_{ww}} = -2\overline{\langle wu\rangle \partial\widetilde{W}/\partial x}$ and (b) $\overline{P^2_{ww}} = -2\overline{\langle wv\rangle \partial\widetilde{W}/\partial y}$ appearing in the transport equation of spanwise Reynolds shear stress component $\overline{ww}$. Refer to Fig. 2 for markers corresponding to different cases.

extract energy from $\overline{uu}$ and transfer it to $\overline{ww}$. However, under the presence of STW, two production terms coming from the streamwise and wall-normal gradients of $\langle W\rangle$ emerge in the transport equation of $\overline{ww}$. These terms are denoted by $\overline{P^1_{ww}} = -2\overline{\langle wu\rangle \partial\widetilde{W}/\partial x}$ and $\overline{P^2_{ww}} = -2\overline{\langle wv\rangle \partial\widetilde{W}/\partial y}$, respectively, in Appendix C. Curiously enough, the total production $\overline{P_{ww}} = \overline{P^1_{ww}} + \overline{P^2_{ww}}$ increases in the low buffer layer, with a maximum at $y \approx 8$ for cases with amplitudes $A^* > 0.50$, as seen in Fig. 5(e). This explains the emergence of the second peak in $\overline{ww}$ observed in Fig. 3(b) at the same wall-normal location.

The production term $\overline{P^1_{ww}}$ is negative for small imposed amplitudes $A^* \leqslant 0.50$ [see Fig. 4(a)], but $\overline{P^2_{ww}}$, which is strictly positive at all wall-normal locations [see Fig. 4(b)], largely overcomes the total mean production $\overline{P_{ww}}$ in the viscous and low buffer layers. Both, $\langle P^1_{ww}\rangle$ and $\langle P^2_{ww}\rangle$ are strongly modulated and reach very large values during the ξ-cycle. These peculiar behaviors will be further elucidated in the Sec. III D, where we discuss the phasewise variations of transport quantities. At this stage, it is important to point out, in particular, the response of the velocity-pressure gradient correlations $\overline{\Pi_{uu}}$ and $\overline{\Pi_{ww}}$, shown in Figs. 5(b) and 5(f), respectively. It is seen that the increase in $\overline{P_{ww}}$ [see Fig. 5(e)] is accompanied by a strong decrease in the velocity-pressure gradient term $\overline{\Pi_{ww}}$. The latter is entirely annihilated within the low buffer and viscous sublayers $y < 8$ when the imposed amplitude is beyond $A^* > 0.5$ [see Fig. 5(f)]. Remark that, in the uncontrolled channel flow $\overline{\Pi_{ww}}$ is large in the buffer layer with a maximum at $y \approx 10$, as the velocity-pressure gradient term is the main source term in the transport equation of $\overline{ww}$. In canonical wall-bounded turbulent flows, the intercomponent transfer $\overline{uu} \rightarrow \overline{ww}$ is established through the velocity-pressure gradient correlations $\overline{\Pi_{uu}} \rightarrow \overline{\Pi_{ww}}$. This process fades away next to the wall up to the top of the low buffer layer in the presence of STW of large enough amplitudes $A^* > 0.5$. Indeed, $\overline{\Pi_{uu}}$ progressively goes to zero as amplitude increases in concordance with $\overline{\Pi_{ww}}$ [see Figs. 5(b) and 5(f)]. Thus, interestingly enough, the communication between $\overline{uu}$ and $\overline{ww}$ is cut off at $y < 8$, and as a consequence the spanwise turbulent intensity $\overline{ww}$ evolves somewhat freely, with a local equilibrium between the production and dissipation $\overline{P_{ww}} \approx -\overline{\epsilon_{ww}}$, in a rough sense [see Fig. 5(e)], with the slight differences being compensated by the turbulent transport $\overline{T_{ww}}$ and viscous diffusion $\overline{D_{ww}}$ (not shown).

Unlike $\overline{ww}$, the net production term $\overline{P_{vv}}$ in the transport equation of the wall-normal component $\overline{vv}$ is zero in the flows altered by STW. Hence, it is fair to state that the mechanism responsible for maintaining the level of $\overline{vv}$ is similar to that for the uncontrolled case, i.e., intercomponent energy transfer $\overline{uu} \rightarrow \overline{vv}$ through $\overline{\Pi_{uu}} \rightarrow \overline{\Pi_{vv}}$. Similar to what was observed for $\overline{ww}$ transport, the communication $\overline{uu} \rightarrow \overline{vv}$ fades away in the low buffer layer as $\overline{\Pi_{vv}} \sim \overline{\Pi_{uu}} \approx 0$ for large imposed amplitudes of STW, resulting in a strong decline in $\overline{vv}$ close to the wall, as seen in Fig. 3(c).

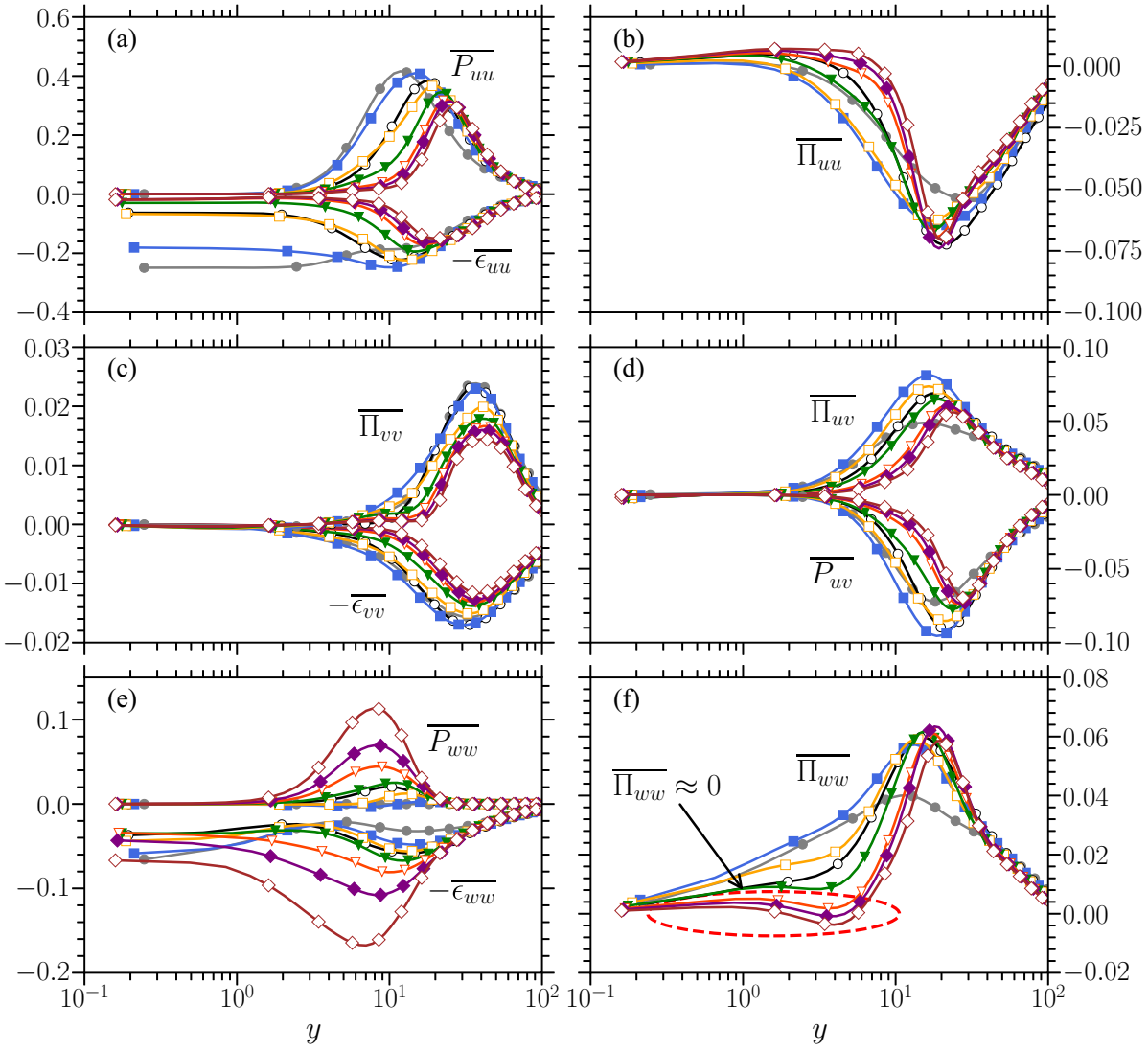

FIG. 5. Wall-normal distributions of terms appearing in the transport equations of Reynolds stresses components. (a) Production $\overline{P_{uu}}$, dissipation $-\overline{\epsilon_{uu}}$; (b) velocity-pressure gradient $\overline{\Pi_{uu}}$ term for streamwise component $\overline{uu}$; (c) velocity-pressure gradient $\overline{\Pi_{vv}}$, dissipation $-\overline{\epsilon_{vv}}$ term for wall-normal component $\overline{vv}$; (d) velocity-pressure gradient $\overline{\Pi_{uv}}$, production $\overline{P_{uv}}$ term for shear stress component $\overline{uv}$; (e) production $\overline{P_{ww}}$, dissipation $-\overline{\epsilon_{ww}}$; and (f) velocity-pressure gradient $\overline{\Pi_{ww}}$ term for spanwise component $\overline{ww}$. Refer to Fig. 2 for markers corresponding to different cases.

Overall, as seen in Fig. 5(c), the budget of $\overline{vv}$ is dominated by the velocity-pressure gradient $\overline{\Pi_{vv}}$ and dissipation $\overline{\epsilon_{vv}}$. Globally, the profiles of $\overline{\Pi_{vv}}$ and $\overline{\epsilon_{vv}}$ approximately collapse for large imposed amplitudes $A^* > 0.50$ of the STW. As the production of shear stress $\overline{P_{uv}}$ is directly linked to $\overline{vv}$, such a collapse is expected. It is pertinent to stress here again that these peculiar behaviors arise upon scaling with the local inner variables. The response of the $\overline{vv}$ transport to STW is quite similar to that observed in the simple homogeneous wall oscillations control [21].

The transport of Reynolds shear stress $\overline{uv}$ is dominated by the production $\overline{P_{uv}}$ and the velocity-pressure gradient $\overline{\Pi_{uv}}$ terms [see Fig. 5(d)]. The role of $\overline{\Pi_{uv}}$ is to reduce the magnitude of $\overline{uv}$. As forcing results in a strong decline in $\overline{vv}$, consequently, $\overline{P_{uv}}$ drops drastically at large imposed amplitudes of STW. Correspondingly, $\overline{\Pi_{uv}}$ declines, and the slight difference is absorbed by a relatively low turbulent diffusion $\overline{T_{uv}}$ and viscous diffusion $\overline{D_{uv}}$ (not shown). The profiles of $\overline{P_{uv}}$ and $\overline{\Pi_{uv}}$ collapse very well for the cases with amplitudes $A^* \geqslant 0.75$.

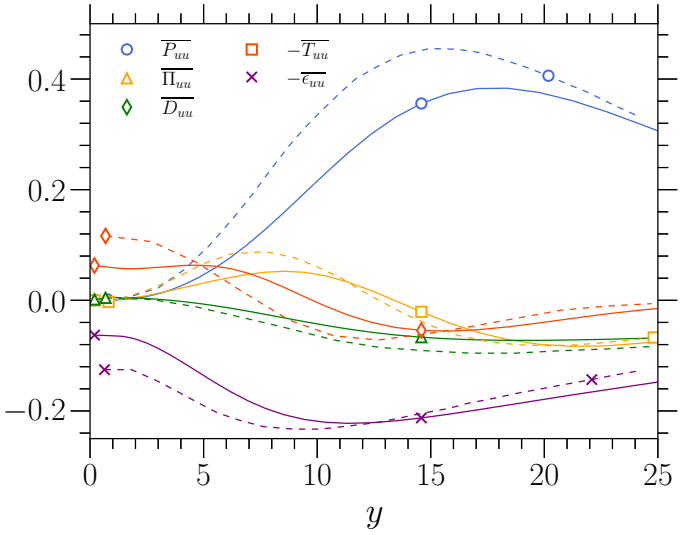

FIG. 6. Comparsion of transport terms in the $\overline{uu}$ budget for HWO case (solid lines) with Touber and Leschziner [21] data (broken lines) at $\mathrm{Re}_\tau = 500$ at same control parameters.

One of the aims of this investigation is to sort out the proper effects of the imposed STW that result in larger DR margins compared to HWO. The interpretation would be straightforward if we could detect direct effects arising from $\partial\langle U_i\rangle/\partial x$ in the transport terms, but unfortunately that was not the case. Consequently, we decided to compare the traveling wave effects with the HWO in their optimal configuration with $A_0 = 12$ ($A^* = 0.51$) and $T_0 = 100$, for reasons stated earlier. Globally, the ensemble of the transport terms corresponding to HWO fall between $A^* = 0.15$ and $A^* = 0.50$ cases of the STW. There is some noticeable decrease of $\overline{\Pi_{ww}}$ in the buffer layer in the HWO case too [Fig. 5(b)]. This particular point has already been nicely discussed in Touber and Leschinizer [21]. However, in the entire low buffer layer $\overline{\Pi_{ww}}$ annihilation is clearly a real effect of large amplitude STW and this is quite uncommon in wall turbulence control. Note, by the way that, the suppression of $\overline{\Pi_{ww}}$ points at the entire decorrelation between the pressure and spanwise local gradient $\partial w/\partial z$, since $\overline{\Pi_{ww}} = -2\overline{p\partial w/\partial z}$ by spanwise homogeneity. Furthermore, the transport terms in the HWO case compare globally well with the distributions of Touber and Leschziner [21], at the same oscillation parameters but larger Re_τ. Figure 6 compares the $\overline{uu}$ transport terms in HWO obtained here and those of Touber and Leschziner [21] at $\mathrm{Re}_\tau = 500$, next to the wall. It is seen that the distributions collapse qualitatively well. In the absence of more objective criteria, it would be, therefore, fair to attribute the structural modifications observed here at $A^* > 0.50$ to the effect of STW itself. The structural modification brought up by the STW are discussed later in Sec. III E. Here, we briefly discuss the response of turbulent streamwise vorticity ω_x to highlight the structural modifications. Detailed results on the vorticity transport mechanism under STW will be reported separately.

The velocity-pressure gradient term Π_{ww} next to the wall can be related to the flux of ω_x. This has not been noticed before to our best knowledge. Indeed, in the region very close to the wall in the viscous sublayer, the spanwise turbulent intensity can be related to the streamwise turbulent vorticity by $w \approx y\omega_{x,0}$. Here, the subscript ",0" refers to the wall. Furthermore, the pressure gradient $\partial p/\partial z$ at the wall is equal to the flux of ω_x, i.e., $\partial p/\partial z_{,0} = \partial\omega_x/\partial y_{,0}$. Combining gives the near-wall asymptotic behavior,

$$\overline{\Pi_{ww}} = -2\overline{\left\langle w\frac{\partial p}{\partial z}\right\rangle} \approx -y\frac{\partial\overline{\langle\omega_x^2\rangle}}{\partial y}\bigg|_{y=0}. \tag{5}$$

Figure 7(a) shows the wall-normal distribution of $\overline{\omega_x^2}$. Equation (5) predicts in an excellent manner the near-wall behavior of $\overline{\Pi_{ww}}$ in the canonical flow [Fig. 5(f)]. The wall gradient $\partial\overline{\Pi_{ww}}/\partial y_{,0}$

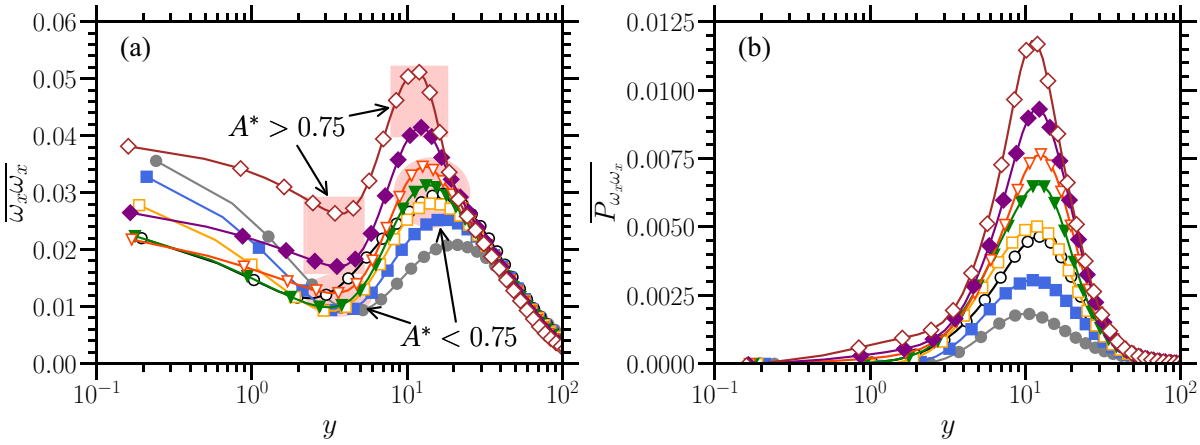

FIG. 7. Wall-normal distribution of (a) the streamwise component of turbulent enstrophy $\overline{\omega_x\omega_x}$ and (b) its production term. Note in the above figure that the local maxima and minima emanating from different cases are relatively well regrouped for $A^* < 0.75$ including HWO. The profiles gradually deviate once $A^* > 0.75$, pointing at severe alterations of the near-wall coherent eddies regeneration process. Refer to Fig. 2 for markers corresponding to different cases.

is 0.01 in Fig. 5(f) and coincides perfectly with $-\partial\overline{\langle\omega_x^2\rangle}/\partial y_{,0}$ in Fig. 7(a) for the uncontrolled case. The lack of correlation $\overline{\Pi_{ww}} \approx 0$ in the flows altered by STW of large amplitudes would imply $\overline{\langle\omega_x^2\rangle} \approx$ constant next to the wall according to Eq. (5). There is indeed a significant undermining of $\overline{\omega_x^2}$ variations in the viscous sublayer once $A^* > 0.50$. For instance, at $A^* = 1.25$, $\overline{\omega_x^2}$ varies only by 20% from the wall to its local minimum at $y = 3.5$. This variation is an order of magnitude smaller than that in the uncontrolled flow, in which $\overline{\omega_x^2}$ decreases by 400% from the wall to its local minimum at $y = 5$.

The occurrence of a local minimum and maximum in $\overline{\omega_x^2}$ is attributed to the QSVs [39]. The local maxima $\overline{\omega_{x\max}^2}$ is the intensity of the QSVs, and the local minima is the consequence of the no-slip boundary condition. The Rankine vortex model introduced by Kim *et al.* [39] estimate acceptably well the streamwise turbulent vorticity at the wall induced by QSVs through $\overline{\omega_{x,0}^2} = (9/4)\overline{\omega_{x\max}^2}$ in the canonical wall-bounded flows. This crude model predicts acceptably well $\overline{\omega_{x,0}^2}$ for the smallest amplitude $A^* = 0.15$, but fails at larger amplitudes. This is either because the model is too crude, and/or there are important structural changes in the flow field because of the presence of STW. Note in Fig. 7 that the local maxima and minima emanating from different cases are relatively well regrouped for $A^* < 0.75$ including HWO. However, once $A^* > 0.75$ the profiles gradually deviate, pointing at severe alterations of the near-wall coherent eddies regeneration process.

To summarize, the communication in the intercomponent transfer is cut off by the traveling waves of $A^* > 0.50$ in the low buffer layer, in which $\overline{\Pi_{uu}} \sim \overline{\Pi_{ww}} \approx 0$. The low and high buffer layers are disconnected. The consequence is the push-up of the peak of the shear stress production $\overline{P_{uv}}$ from $y = 15$ in the uncontrolled flow to $y = 30$ at $A^* > 0.50$ [see Fig. 5(d)]. The shift in the peak of $\overline{uv}$ to $y = 30$ results in the shift of the $\overline{uu}$ production $\overline{P_{uu}}$ to the same wall-normal location Fig. 3(a). The buffer layer dynamics which is capital in canonical wall-bounded turbulence is shut off. It is seen in Fig. 3(c) that there is a strong damping of the wall-normal turbulent activity, in agreement with earlier investigations [21]. The local maximum of $\overline{\Pi_{vv}}$ and $\overline{\epsilon_{vv}}$ decrease systematically with the increasing amplitudes, and the decrease is as large as 40%. The weakening in $\overline{\Pi_{vv0}}$ and $\overline{\epsilon_{vv0}}$, scaled by the inner variables based on the friction velocity of the uncontrolled flow, is as large as 70% at $A^* = 1.25$. Thus, the damping of the wall-normal activity still remains a key phenomenon under the presence of traveling waves. However, it is important to note that $\overline{\Pi_{vv}}$ and $\overline{\epsilon_{vv}}$ are well regrouped for all the cases investigated here, once they are properly scaled by the local inner variables. Since,

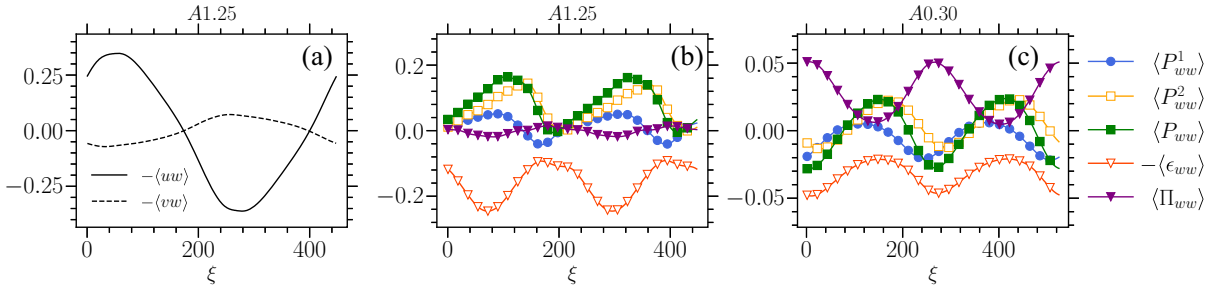

FIG. 8. (a) Phasewise variations of $-\langle uw\rangle$ and $-\langle vw\rangle$ at $y = 15$ for $A1.25$ case. Phasewise variations of $\langle P^1_{ww}\rangle$, $\langle P^2_{ww}\rangle$, $\langle P_{ww}\rangle$, $-\langle \epsilon_{ww}\rangle$, and $\langle \Pi_{ww}\rangle$ at $y = 5$ for (b) $A1.25$ and (c) $A0.30$ cases, respectively. Note how $\langle \Pi_{ww}\rangle$ for $A1.25$ case is entirely frozen compared to $A0.30$ case where there are large modulations.

the results related to HWO fall again within $0.15 < A^* < 0.50$, the combined effect of the loose of communication between the low and high buffer layers with the $\overline{vv}$ damping is related to the traveling waves effect.

D. Phasewise variations of transport quantities

The phase averages of different terms emerging in the Reynolds stresses transport equations have been carefully determined and analyzed in detail. Globally, the cyclic variations of turbulent quantities are constrained at $y < 15$ where $\partial\langle W\rangle/\partial y$ is significant. The most salient effects are found in the terms related to $D\langle ww\rangle/Dt$ and will shortly be discussed hereafter.

The mean correlations $\overline{uw}$ and $\overline{vw}$ are zero, as in the case of uncontrolled flow (not shown). However, both of them, especially, $\langle uw\rangle$ reaches large cyclic variations up to the edge of the Stokes layer induced by the STW. Figure 8(a) shows $\langle uw\rangle$ and $\langle vw\rangle$ at $y = 15$ for $A1.25$ case. It can be seen that the cyclic variations in $\langle vw\rangle$ are smaller compared to $\langle uw\rangle$. Yet, the shear $\partial\langle W\rangle/\partial y$, which is proportional to A^* (for fixed ω^* and κ^*), reaches large cyclic values close to the wall at large imposed amplitudes. The consequence are the large cyclic modulations in $\langle P^1_{ww}\rangle$ and $\langle P^2_{ww}\rangle$. Figure 8(b) shows the cyclic variations of terms that significantly contributes to $\langle ww\rangle$ transport at $y = 5$ for $A1.25$ case. Note first that $\langle P^1_{ww}\rangle$ reaches negative values at some phases, thus becomes locally an annihilation term. Yet, $\langle P^2_{ww}\rangle$, which is larger and positive, overcomes $\langle P^1_{ww}\rangle$ so that $\langle P_{ww}\rangle > 0$. Second, the dissipation is not locally in equilibrium with the production, pointing to truly unsteady effects due to STW actuation. Finally, note in Fig. 8(b) that the velocity-pressure gradient correlation is entirely frozen during the whole cycle, i.e., $\langle \Pi_{ww}\rangle \approx 0$. The fact that the large amplitude traveling waves aborts the $uu \rightarrow ww$ communication can be better appreciated once Fig. 8(c) is compared with Fig. 8(b). The latter shows the phase averages of $\langle ww\rangle$ transport terms at the same wall-normal location $y = 5$, but at a lower imposed amplitude $A^* = 0.30$. It is clearly seen that the velocity-pressure gradient term $\langle \Pi_{ww}\rangle$ responds to the unsteady wave, and that its modulation amplitude is comparable to that of $\langle P_{ww}\rangle$. Note also in Fig. 8(c) that $\langle P^1_{ww}\rangle$ is negative almost throughout the whole cycle and destroys production $\langle P_{ww}\rangle$. The latter is even negative during half of the cycle. The response of $\langle ww\rangle$ changes strongly at large imposed amplitudes, wherein the DR is larger than HWO. Thus, it is reasonable to directly attribute the behavioral changes of the near-wall turbulence at $A^* > 0.50$ to the traveling waves.

E. Effects on streaks and shear layers

The low- and high-speed streaks of spanwise velocity are the signatures of the QSVs in the early periods of their regeneration process [40]. The w-streaks spacing is roughly 100 wall-units in the buffer layer, similar to the spanwise spacing of low- and high-speed streaks of streamwise velocity. Figure 9(b) shows the w-streaks in the uncontrolled flow at $y = 10$. The structural modification brought up by the STW of large amplitudes are clearly visible in Fig. 9(k). It can be seen that

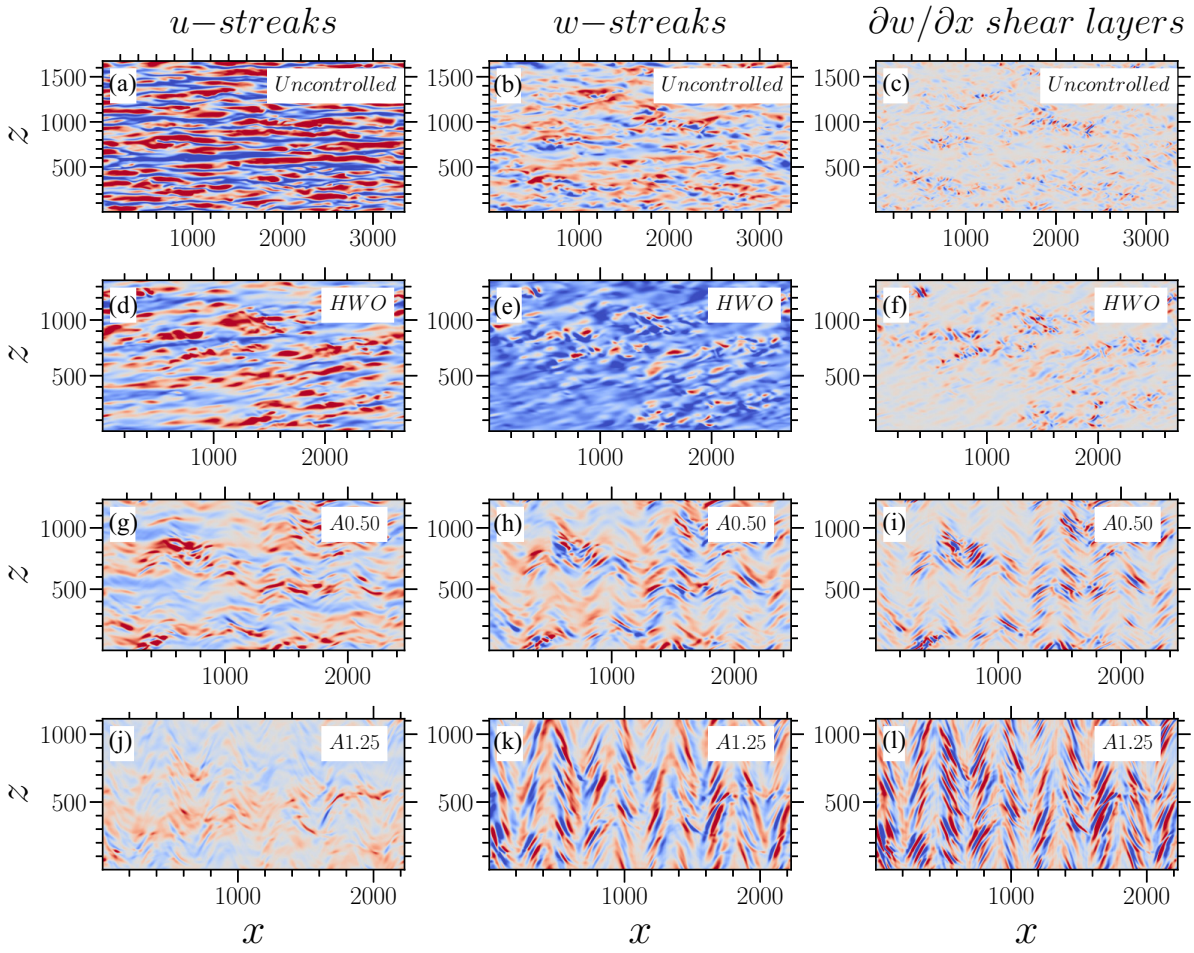

FIG. 9. Streamwise velocity fluctuations (u) at $y = 10$ for (a) uncontrolled, (d) HWO, (g) $A0.50$, and (j) $A1.25$ cases, respectively. The blue color represents the low-speed u-streaks ($u < 0$), while the red color represents the high-speed u-streaks ($u > 0$). The contours are in the range -3 to $+3$. Note that u was scaled by the local friction velocity; had it been scaled by the friction velocity of the uncontrolled flow, the streaky structures would have disappeared, especially for the large DR cases. Spanwise velocity fluctuations (w) at $y = 10$ for (b) uncontrolled, (e) HWO, (h) $A0.50$, and (k) $A1.25$ cases, respectively. The blue color represents the low-speed w-streaks ($w < 0$), while the red color represents the high-speed w-streaks ($w > 0$). The contours are in the range -2 to $+2$. Note that w was scaled by the local friction velocity. The instantaneous visualizations of the $\partial w/\partial x$ shear layers at $y = 10$ for (c) uncontrolled, (f) HWO, (i) $A0.50$, and (l) $A1.25$ cases, respectively. The blue color represents the negative, while the red color represents the positive values. The contours are in the range -0.1 to $+0.1$. Here also $\partial w/\partial x$ was scaled by the local friction velocity. Note that the heavily modulated Λ-shaped structures of $\partial w/\partial x$ start to appear for cases with large imposed amplitudes of STW. These structures are absent for both the uncontrolled and HWO cases.

the longitudinal w-streaks are tilted in the spanwise direction and are now organized in Λ-shaped patterns. This peculiar spanwise reorganization appears at amplitudes $A^* > 0.50$. A similar reorganization of the u-streaks [Fig. 9(j)] is also observed, even though the communication between u and w is cut off in the low buffer layer for the reasons stated earlier. The usual characteristics of the u- and w-streaky structures are recovered only at $y > 20$.

Both u- and w-streaky structures are the footprints of the QSVs that are mainly responsible for the production of Reynolds shear stress in the buffer layer in canonical wall-bounded flows. The individual self-organization of w in the low buffer layer has a direct consequence on the regeneration of the active QSVs. In the canonical wall layer, the main regeneration term of the local streamwise turbulent vorticity ω_x in the low buffer layer comes from the titling of the wall-normal

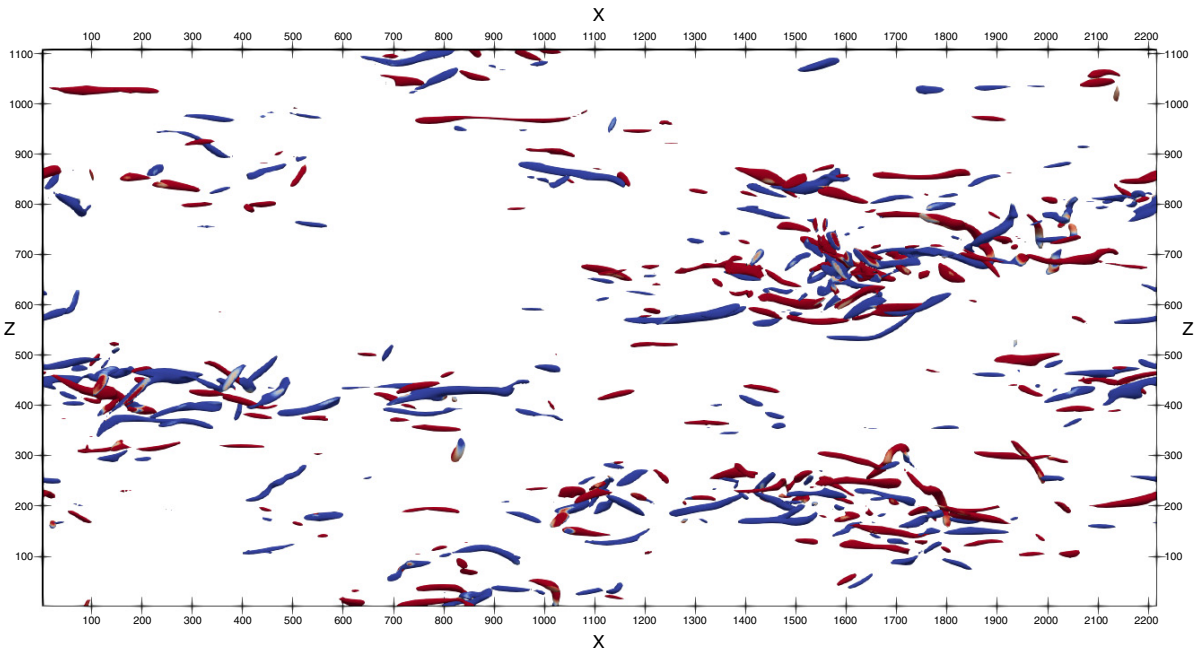

FIG. 10. (Top View) Instantaneous near-wall vortical structures ($\lambda_2 = -0.02$) scaled by the local inner variables for the $A1.25$ case. The regions where $\omega_x > 0$ are colored in red and where $\omega_x < 0$ are colored in blue.

turbulent vorticity ω_y and reduces to $-\frac{\partial w}{\partial x}\frac{\partial \overline{U}}{\partial y}$. Brooke and Hanratty [41] had shown that the tilting term overcomes twisting and stretching at $y < 10$ and peaks at $y = 8$. Like u- and w-streaks, the structures of the $\partial w/\partial x$ shear layers are strongly altered by the STW of large amplitudes. These shear layers [in Fig. 9(l)] are also organized in similar Λ-shaped patterns as observed for w-streaks in Fig. 9(k).

The main production term of the enstrophy transport $D\overline{\omega_x\omega_x}/Dt$ is still the term related to the tilting of the $\partial w/\partial x$ shear layers in the controlled flow. Figure 7(b) shows the production term $\overline{P_{\omega_x\omega_x}} = -2\overline{\langle\omega_x\partial w/\partial x\rangle}d\overline{U}/dy$. It is seen that $\overline{P_{\omega_x\omega_x}}$ peaks at $y \approx 10$ and increases with the imposed amplitude A of the STW. Note in Fig. 7(b) that $\overline{P_{\omega_x\omega_x}}$ is an order of magnitude larger at $A^* = 1.25$ than that in the uncontrolled flow. The HWO case coincides well with $A^* = 0.30$, strengthening again, that $A^* = 0.30$ is the lower limit above which the direct effect of STW are felt in the wall turbulence.

The Λ-shaped shear layers are organized as alternating positive $\partial w/\partial x > 0$ and $\partial w/\partial x < 0$ structures in Figs. 9(i) and 9(l). Their legs are inclined along the spanwise direction by roughly $\pm\pi/4$. They are tilted by the shear $d\overline{U}/dy \approx 1$ near $y = 10$ (not shown). The key question here is to determine whether these shear layers roll-up into coherent vortices or not. This is important since the coherent active eddies lead to the generation of the Reynolds shear stress uv and the drag. In case of roll-up, the resulting topological structure of the coherent structures near the wall would be seriously altered at large imposed amplitudes, by the apparition of contrarotating vortices strongly inclined along the spanwise direction coming from the unfamiliar topological nature of $\partial w/\partial x$. We carefully analyzed the λ_2 structures using tens of snapshots, in particular for the $0.75 < A^* < 1.25$ cases. The symmetric and antisymmetric parts of the velocity gradient tensor from which the second-largest eigenvalue is determined are conveniently scaled by the local inner variables. A movie is available for $A1.25$ case as a supplementary material online [42]. Figures 10 and 11 show the top and side views of an instantaneous snapshot of λ_2 structures for the $A1.25$ case. The structures with $\omega_x > 0$ are colored in red and $\omega_x < 0$ in blue. One finds the classical topological features of the QSVs observed in the uncontrolled flow. Thus, the peculiar $\partial w/\partial x$ layers titled by the mean shear in Figs. 9(i) and 9(l) clearly do not roll-up into coherent vortices. The vast majority of the coherent

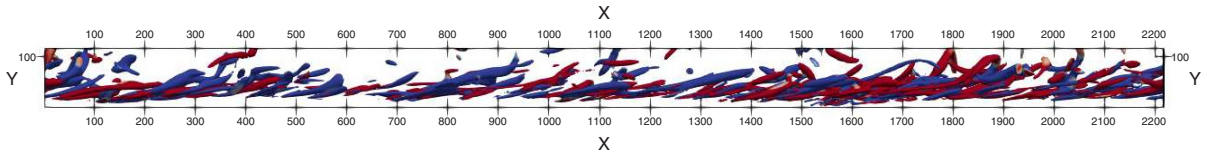

FIG. 11. (Side View) Instantaneous near-wall vortical structures ($\lambda_2 = -0.02$) scaled by the local inner variables for the $A1.25$ case. The regions where $\omega_x > 0$ are colored in red and where $\omega_x < 0$ are colored in blue.

structures reach their maturity well above $y = 20$ (Fig. 11). In Sec. III C, we discussed in detail the disconnection at large amplitudes of the Reynolds stresses transport between low and high buffer layers. The only remaining possibility of communication that remained was the generation of the coherent active eddies emanating from the roll-up of the atypical shear layers of Figs. 9(i) and 9(l). This possibility by now is also discarded.

Last but not least, it is noticeable that the QSVs are systematically organized as packets at $A^* > 0.75$ and have similarities with the transitional-turbulent spots [43]. Packets of vortices, or large-scale motions, containing typically three individual structures, exist in the uncontrolled flow, including at moderate Re [44,45]. At $A^* > 0.75$, on the one hand, the packets are comparatively more common, and on the other hand, they contain a much larger number of individual structures similar to turbulent spots.

IV. CONCLUDING REMARKS

Direct numerical simulations were performed to investigate the effect of transverse wall oscillations in the form of streamwise traveling waves on the Reynolds stresses transport, for the first time to our best knowledge. The angular frequency and the wavelength of the STW were fixed at $\omega^* = 0.16$ and $\kappa^* = 1.66$, and the imposed amplitude was varied nearly by one decade from $A^* = 0.15$ to $A^* = 1.25$. The drag reduction at the largest amplitude reaches 58%. The results were compared with homogeneous spanwise wall oscillations case with imposed period $T_0 = 100$ and amplitude $A_0 = 12$, to identify the proper impact of the STW on the near-wall turbulence.

Forcing in the form of the STW results in substantial decline of all the Reynolds stresses components. The transport terms are in close similarity with HWO when the imposed amplitude of the STW are within the intermediate range $0.30 < A^* < 0.50$. This regime is marked by a strong damping of the wall normal velocity fluctuations on one hand, and some noticeable decline in the velocity-pressure gradient correlations, on the other. The present investigation globally confirms previously published results on HWO.

The situation changes drastically in the large amplitude STW's cases when $A^* > 0.50$. The intercomponent transfer between the Reynolds stresses fade away in the low buffer layer, wherein it is found that $\overline{\Pi_{uu}} \sim \overline{\Pi_{vv}} \sim \overline{\Pi_{ww}} \approx 0$. The annihilation of $\overline{\Pi_{ww}}$ at $y < 10$ is particularly spectacular. It is shown that $\overline{\Pi_{ww}} \approx 0$ in the low buffer layer results in the flattening of the streamwise vorticity intensity near the wall and points at a strong alteration of the active eddies regeneration process. The spanwise component $\overline{ww}$ is autonomously produced by the Stokes strain related terms $\overline{P^1_{ww}} = -2\overline{\langle wu\rangle \partial\widetilde{W}/\partial x}$ and $\overline{P^2_{ww}} = -2\overline{\langle wv\rangle \partial\widetilde{W}/\partial y}$ in the low buffer layer, and the production simply dissipates. Unexpectedly large values of the phase averages $\langle wu\rangle$ are observed at $A^* > 0.75$, but $\overline{P^2_{ww}}$ dominates the $\overline{ww}$ production in the low buffer layer as $\partial\widetilde{W}/\partial y \gg \partial\widetilde{W}/\partial x$.

The buffer layer streaky structures are also strongly altered at large A^*. The most spectacular modification takes place in the $\partial w/\partial x$ shear layers that become strongly inclined in the spanwise direction and alternates between positive and negative values quite coherently. The intensity in these shear layers is related to the major streamwise vorticity production in the low buffer layer, in the uncontrolled and as well as controlled flows. However, there is no topological signature of these shear layers in the active eddies' regeneration process. Thus, the peculiarly different $\partial w/\partial x$

shear layers do not roll-up in the low buffer layer. At $A^* > 0.75$, the quasistreamwise vortices are organized as packets of several vortices typical of transitional turbulent spots.

The low and high buffer layer get disconnected at large forcing amplitudes. Forcing also results in the cutoff of intercomponent energy transfer between different Reynolds stresses components. The low buffer layer becomes autonomous, self-sustained by pure Stokes strain effects. The capital role of the low buffer layer in the uncontrolled flow is by-passed by forcing, resulting in a disconnection with the high buffer layer. This situation is rather uncommon in the near-wall turbulence control.

ACKNOWLEDGMENTS

The simulations of the controlled cases were performed using the GRICAD infrastructure [46], which is supported by Grenoble research communities. The simulations of the uncontrolled case were performed using the Froggy platform of the GRICAD infrastructure [46], which is supported by the Région Auvergne-Rhône-Alpes (GRANT CPER07_13 CIRA) and the Agence Nationale de la Recherche (Equip@Meso project Reference No. ANR-10-EQPX-29-01 of the programme Investissements d'Avenir).

APPENDIX A: COMPUTATIONAL DETAILS

The Navier-Stokes equation scaled by the channel half width h and the centerline velocity U_c together with the continuity equation reads

$$\frac{\partial u_i}{\partial t} + \frac{\partial u_i u_j}{\partial x_j} = -\frac{\partial p}{\partial x_i} + \frac{1}{\mathrm{Re}}\frac{\partial^2 u_i}{\partial x_j^2}, \frac{\partial u_i}{\partial x_i} = 0, \tag{A1}$$

where u_i is the ith velocity component, p is the pressure, and $\mathrm{Re} = hU_c/\nu$ is the Reynolds number (ν being the kinematic viscosity). The computational domain is a rectangular box of size $L_x \times L_y \times L_z$, where L_x, L_y and L_z are the extents of the domain in the streamwise (x), wall-normal (y), and spanwise direction (z), respectively. The computational domain is discretized by a structured mesh using $N_x \times N_y \times N_z$ points. The boundary conditions are the no-slip at the wall and periodic in the streamwise and spanwise directions. The mesh points are uniformly along the streamwise and spanwise directions, while they are refined near the wall in the wall-normal direction through a hyperbolic tangent distribution.

Spatial numerical operators are expressed by using fifth-order explicit optimized (EO) finite differences scheme. EO schemes are derived from the dispersion-relation-preserving (DRP) schemes (see Bauer *et al.* [47] for technical details). In contrast to compact scheme discretization, an explicit scheme requires only the function value at the neighboring points to approximate the derivatives. Hence, the derivative estimations are direct while it necessarily implies a matrix inversion in the compact schemes.

Considering the temporal integration, the solution at the next time (sub)iteration $k+1$ is explicitly obtained by integrating Eq. (A1). The time interval $[t, t+\Delta t]$ is divided into n_k substeps ($t_1 = t, t_2, t_3, ..., t_{n_k} = t + \Delta t$). By applying the fractional step method, the velocity is corrected to become solenoidal at each time iteration. Making use of the conventional Einstein notation for spatial coordinate and velocity components (for which subscripts 1,2,3 refer, respectively, to the spanwise (x), wall-normal (y), and streamwise (z) component), the temporal advancement of Eq. (A1) can be expressed as

$$u^{k+1} = u^k + R_{\mathrm{pmean}} + R_{\mathrm{pfluc}} + R_{\mathrm{adv}} + R_{\mathrm{diff}}, \tag{A2}$$

where

$$R_{\mathrm{pmean}} = -\int_{t_k}^{t_{k+1}} \left(\overline{\frac{\partial p}{\partial x_i}}\right) dt, \; R_{\mathrm{pfluc}} = -\int_{t_k}^{t_{k+1}} \left(\frac{\partial p'}{\partial x_i}\right) dt,$$

$$R_{\text{adv}} = -\int_{t_k}^{t_{k+1}} \left(\frac{\partial u_i u_j}{\partial x_j}\right) dt,\ R_{\text{diff}} = \frac{1}{\text{Re}} \int_{t_k}^{t_{k+1}} \left(\frac{\partial^2 u_i}{\partial x_j^2}\right) dt,$$

$(\partial \overline{p}/\partial x_i)$ and $(\partial p'/\partial x_i)$ stand for the mean and the fluctuating pressure gradient, respectively. R_{pmean} is evaluated through the global flow rate conservation. The advection (R_{adv}) and diffusion (R_{diff}) terms are estimated explicitly from the previous $(k-1)$ and the current (k) fields as

$$R_{\text{adv}} + R_{\text{diff}} = \alpha_k \Delta t \left(-\widehat{\frac{\partial u_i u_j}{\partial x_j}} + \frac{1}{\text{Re}} \widehat{\frac{\partial^2 u_i}{\partial x_j^2}} \right)_k + \beta_k \Delta t \left(-\widehat{\frac{\partial u_i u_j}{\partial x_j}} + \frac{1}{\text{Re}} \widehat{\frac{\partial^2 u_i}{\partial x_j^2}} \right)_{k-1}, \tag{A3}$$

where $\widehat{(.)}$ denotes spatially discretized operators.

The time advancement is performed by a Runge-Kutta third-order (RK3) scheme in which the coefficients involved in the three iteration steps are $\alpha_{1,2,3} = [8/15, 5/12, 3/4]$ and $\beta_{1,2,3} = [0, -17/60, -5/12]$. The quantity R_{pfluc} is evaluated from the pressure at $k+1$. Equation (A3) can be reformulated as

$$u^{k+1} = \widetilde{u^{k+1}} - (\alpha_k + \beta_k)\Delta t \widehat{\nabla p'^{(k+1)}}, \tag{A4}$$

where $\widetilde{u^{k+1}} = u^k + R_{\text{pmean}} + R_{\text{adv}} + R_{\text{diff}}$ is the first estimation of the velocity field based on the terms known at the current time iteration. The quantity $p'^{(k+1)}$ is then calculated by applying the divergence free operator to Eq. (A4), and solving the resulting Poisson equation:

$$\widehat{\nabla^2 p'^{(k+1)}} = \frac{1}{\Delta t(\alpha_k + \beta_k)} \widehat{\nabla \widetilde{u^{k+1}}}. \tag{A5}$$

The Poisson equation for the pressure is solved in the Fourier domain (through FFT decomposition) at each xz plane.

APPENDIX B: VALIDATION AND STATISTICAL CONVERGENCE

There are mainly three particularities of the present DNS: First, the resolution is very fine, with the mesh size in the wall-normal direction Δy being 1/3 of the Kolmogorov scale (η) near the wall while $\Delta y \approx 1.4\eta$ at the centerline. The resolution in the near wall region compares with previous DNS, but it is much finer in the core region here. The mesh size in the streamwise direction is as small as twice the Kolmogorov length at the centerline. The mesh size in the spanwise direction is about η at the centerline. The grid employed in the present study is sufficiently fine to resolve the relevant scales present in the turbulent flow field, and is even finer in the streamwise and spanwise directions compared with many other published DNS studies on channel flows. The second particularity of these DNS is the use of particularly large computational domains: the streamwise and spanwise lengths of the computational domain are $6\pi h$ and $3\pi h$. They are taken particularly large to accommodate multiple wavelengths. The third is the use of fifth-order explicit optimized (EO) finite differences scheme, which resulted in near spectral resolution. The adequacy of the resolution was examined by comparing the profiles of the root-mean-square velocity and vorticity components with the data of Moser and Kim [48] at $\text{Re}_\tau = 180$ in Fig. 12. (For the sake of brevity, Fig. 12 is not included in the manuscript.) As seen in Fig. 12, the profiles of root-mean-square velocity and vorticity components match perfectly with the data of Moser and Kim [48].

In the controlled flow, however, the determination of the stochastic field requires the introduction of the triple decomposition, defined as

$$F = \langle F \rangle + f, \tag{B1}$$

where F is the instantaneous field, $\langle F \rangle$ is the phase-averaged field, and f is the purely stochastic field. The computation of phase-averaged field requires division of the wave cycle into bins of equal widths. We typically chose 200–500 bins, depending on the amplitude of the forcing. To improve the

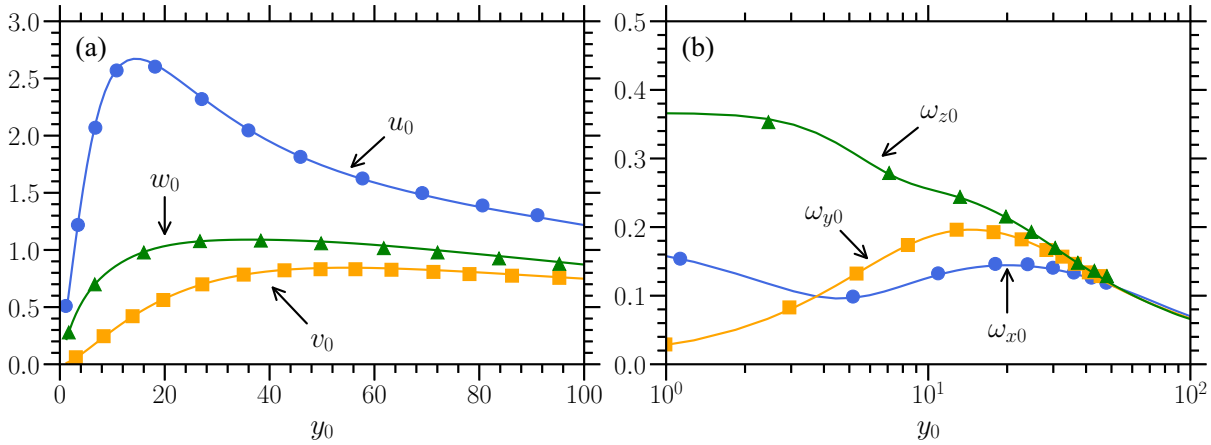

FIG. 12. Comparison of (a) root-mean-square velocity and (b) root-mean-square vorticity components in the streamwise, spanwise, and wall-normal directions with the data of Moser and Kim [47] (in markers).

convergence, we further decreased the time-step to increase the number of variables collected per bin. We tested the convergence of the phase-averaged statistics by computing the ensemble average of the quantities such as Reynolds stresses over 5, 10, 15, 20, etc., cycles. In view of the very high associated costs involved in running the simulation for very long durations, we decided to perform averages over 40 temporal cycles, which is yet very long compared to other studies at even larger Reynolds number. The conclusion that the errors are small is strengthened by the fact that tests with averaging over 20 cycles gave fields very close to those with averaging over all 40 cycles. Despite the fair smoothness observed for all the quantities, the phase-averaged quantities cannot be fully converged because of the presence of the large-scale oscillations in C_f. However, the error is small (less than 1.5%), as illustrated by Fig. 13. To avoid cluttering, only the error margins for the $A1.25$ case are shown for the Reynolds stresses.

APPENDIX C: REYNOLDS STRESSES TRANSPORT EQUATIONS

The Reynolds shear stress transport equations are shortly discussed here. The production, turbulent transport, pressure-velocity gradient, dissipation, and diffusion terms are denoted by $\overline{P_{u_iu_j}}$, $\overline{T_{u_iu_j}}$, $\overline{\Pi_{u_iu_j}}$, $\overline{\epsilon_{u_iu_j}}$, and $\overline{D_{u_iu_j}}$, respectively. There are terms that directly come from the presence of the traveling waves and induced by streamwise gradients of the velocity field U_i. These are discussed in the main text in detail.

The transport equation for the streamwise turbulent intensity $\overline{uu}$ is given by

$$\frac{D\overline{uu}}{Dt} = \overline{P_{uu}} - \overline{T_{uu}} + \overline{\Pi_{uu}} - \overline{\epsilon_{uu}} + \overline{D_{uu}} = 0, \tag{C1}$$

where

$$\overline{P_{uu}} = \underbrace{-2\overline{\langle uu\rangle\frac{\partial\widetilde{U}}{\partial x}}}_{\overline{P^1_{uu}}} \underbrace{-2\overline{\langle uv\rangle\frac{\partial\widetilde{U}}{\partial y}}}_{\overline{P^2_{uu}}} \underbrace{-2\overline{\langle uv\rangle\frac{d\overline{U}}{dy}}}_{\overline{P^3_{uu}}}, \tag{C1a}$$

$$\overline{T_{uu}} = \underbrace{\frac{d\overline{\langle uu\rangle\widetilde{V}}}{dy}}_{\overline{T^1_{uu}}} + \underbrace{\frac{d\overline{\langle uuv\rangle}}{dy}}_{\overline{T^2_{uu}}}, \tag{C1b}$$

$$\overline{\Pi_{uu}} = -2\overline{\left\langle u\frac{\partial p}{\partial x}\right\rangle}, \tag{C1c}$$

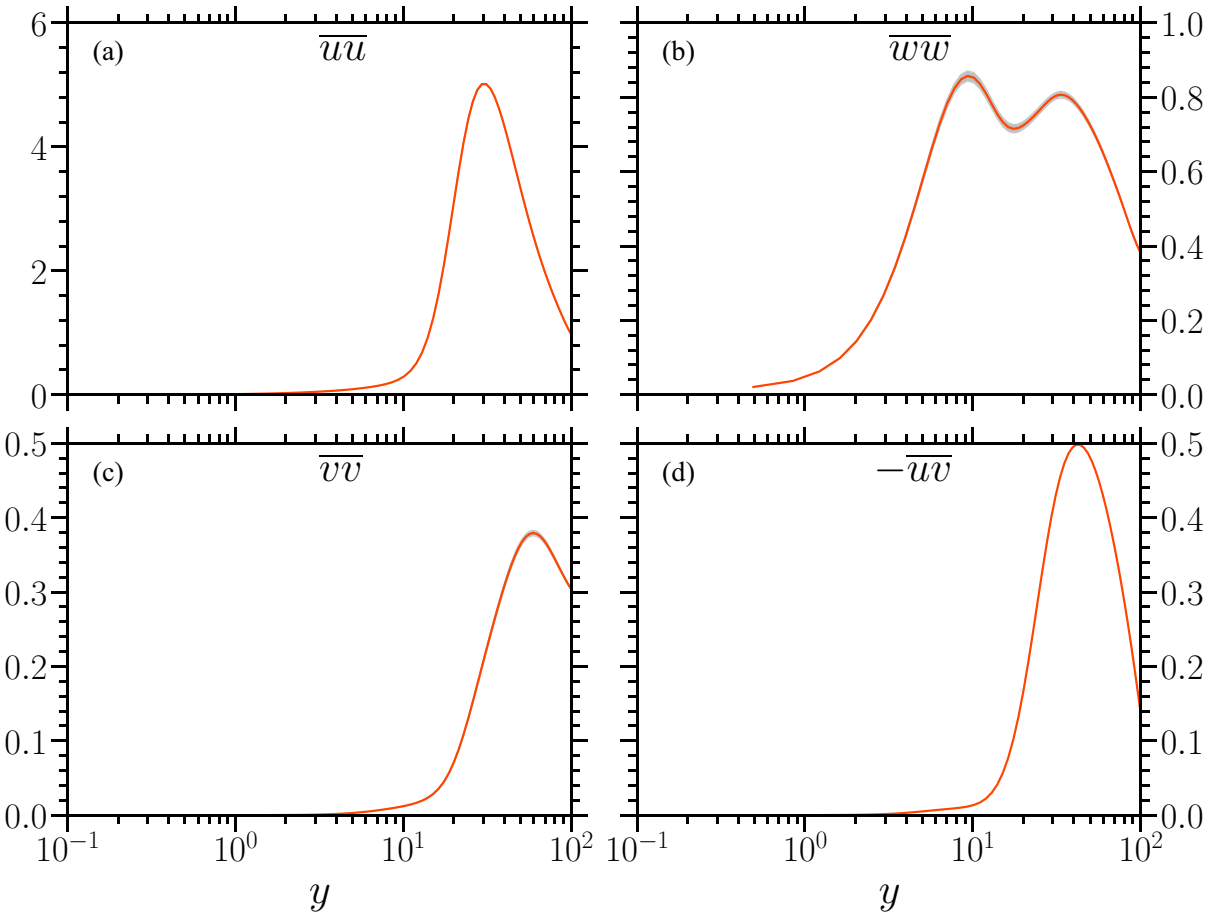

FIG. 13. Reynolds stresses profiles for the $A1.25$ case scaled with the local friction velocity with the corresponding error margins. (a) Streamwise component $\overline{uu}$, (b) spanwise component $\overline{ww}$, (c) wall-normal component $\overline{vv}$, and (d) shear stress $-\overline{uv}$.

$$\overline{\epsilon_{uu}} = 2\left(\overline{\left\langle \frac{\partial u}{\partial x}\frac{\partial u}{\partial x}\right\rangle} + \overline{\left\langle \frac{\partial u}{\partial y}\frac{\partial u}{\partial y}\right\rangle} + \overline{\left\langle \frac{\partial u}{\partial z}\frac{\partial u}{\partial z}\right\rangle}\right), \tag{C1d}$$

and

$$\overline{D_{uu}} = \frac{d^2\overline{\langle uu\rangle}}{dy^2}. \tag{C1e}$$

The transport equation for the wall normal turbulent velocity intensity $\overline{vv}$ is given by

$$\frac{D\overline{vv}}{Dt} = \overline{P_{vv}} - \overline{T_{vv}} + \overline{\Pi_{vv}} - \overline{\epsilon_{vv}} + \overline{D_{vv}} = 0, \tag{C2}$$

where

$$\overline{P_{vv}} = \underbrace{-2\overline{\langle vu\rangle}\frac{\partial \widetilde{V}}{\partial x}}_{\overline{P^1_{vv}}} \underbrace{-2\overline{\langle vv\rangle}\frac{\partial \widetilde{V}}{\partial y}}_{\overline{P^2_{vv}}}, \tag{C2a}$$

$$\overline{T_{vv}} = \underbrace{\frac{d\overline{\langle vv\rangle}\widetilde{V}}{dy}}_{\overline{T^1_{vv}}} + \underbrace{\frac{d\overline{\langle vvv\rangle}}{dy}}_{\overline{T^2_{vv}}}, \tag{C2b}$$

$$\overline{\Pi_{vv}} = -2\overline{\left\langle v\frac{\partial p}{\partial y}\right\rangle}, \tag{C2c}$$

$$\overline{\epsilon_{vv}} = 2\left(\overline{\left\langle \frac{\partial v}{\partial x}\frac{\partial v}{\partial x}\right\rangle} + \overline{\left\langle \frac{\partial v}{\partial y}\frac{\partial v}{\partial y}\right\rangle} + \overline{\left\langle \frac{\partial v}{\partial z}\frac{\partial v}{\partial z}\right\rangle}\right), \tag{C2d}$$

and

$$\overline{D_{vv}} = \frac{d^2\overline{\langle vv\rangle}}{dy^2}. \tag{C2e}$$

The transport equation for the spanwise turbulent velocity $\overline{ww}$ intensity is

$$\frac{D\overline{ww}}{Dt} = \overline{P_{ww}} - \overline{T_{ww}} + \overline{\Pi_{ww}} - \overline{\epsilon_{ww}} + \overline{D_{ww}} = 0, \tag{C3}$$

where

$$\overline{P_{ww}} = \underbrace{-2\overline{\langle wu\rangle\frac{\partial \widetilde{W}}{\partial x}}}_{\overline{P^1_{ww}}}\underbrace{-2\overline{\langle wv\rangle\frac{\partial \widetilde{W}}{\partial y}}}_{\overline{P^2_{ww}}}, \tag{C3a}$$

$$\overline{T_{ww}} = \underbrace{\frac{d\overline{\langle ww\rangle}\widetilde{V}}{dy}}_{\overline{T^1_{ww}}} + \underbrace{\frac{d\overline{\langle wwv\rangle}}{dy}}_{\overline{T^2_{ww}}}, \tag{C3b}$$

$$\overline{\Pi_{ww}} = -2\overline{\left\langle w\frac{\partial p}{\partial z}\right\rangle}, \tag{C3c}$$

$$\overline{\epsilon_{ww}} = 2\left(\overline{\left\langle \frac{\partial w}{\partial x}\frac{\partial w}{\partial x}\right\rangle} + \overline{\left\langle \frac{\partial w}{\partial y}\frac{\partial w}{\partial y}\right\rangle} + \overline{\left\langle \frac{\partial w}{\partial z}\frac{\partial w}{\partial z}\right\rangle}\right), \tag{C3d}$$

and

$$\overline{D_{ww}} = \frac{d^2\overline{\langle ww\rangle}}{dy^2}. \tag{C3e}$$

Finally, the transport equation for the Reynolds shear stress $\overline{uv} < 0$ (not $-\overline{uv} > 0$) is

$$\frac{D\overline{uv}}{Dt} = \overline{P_{uv}} - \overline{T_{uv}} + \overline{\Pi_{uv}} - \overline{\epsilon_{uv}} + \overline{D_{uv}} = 0, \tag{C4}$$

where

$$\overline{P_{uv}} = \underbrace{-\overline{\langle uv\rangle\frac{\partial \widetilde{U}}{\partial x}}}_{\overline{P^1_{uv}}}\underbrace{-\overline{\langle vv\rangle\frac{\partial \widetilde{U}}{\partial y}}}_{\overline{P^2_{uv}}}\underbrace{-\overline{\langle uu\rangle\frac{\partial \widetilde{V}}{\partial x}}}_{\overline{P^3_{uv}}}\underbrace{-\overline{\langle uv\rangle\frac{\partial \widetilde{V}}{\partial y}}}_{\overline{P^4_{uv}}}\underbrace{-\overline{\langle vv\rangle}\frac{d\overline{U}}{dy}}_{\overline{P^5_{uv}}}, \tag{C4a}$$

$$\overline{T_{uv}} = \underbrace{\frac{d\overline{\langle uv\rangle}\widetilde{V}}{dy}}_{\overline{T^1_{uv}}} + \underbrace{\frac{d\overline{\langle uvv\rangle}}{dy}}_{\overline{T^2_{uv}}}, \tag{C4b}$$

$$\overline{\Pi_{uv}} = -\overline{\left\langle u\frac{\partial p}{\partial y}\right\rangle} - \overline{\left\langle v\frac{\partial p}{\partial x}\right\rangle}, \tag{C4c}$$

$$\overline{\epsilon_{uv}} = 2\left(\overline{\left\langle \frac{\partial u}{\partial x}\frac{\partial v}{\partial x}\right\rangle} + \overline{\left\langle \frac{\partial u}{\partial y}\frac{\partial v}{\partial y}\right\rangle} + \overline{\left\langle \frac{\partial u}{\partial z}\frac{\partial v}{\partial z}\right\rangle}\right), \tag{C4d}$$

and

$$\overline{D_{uv}} = \frac{d^2\overline{\langle uv\rangle}}{dy^2}. \tag{C4e}$$

[1] M. Malik, W. Liao, F. Li, and M. Choudhari, DRE-enhanced swept-wing natural laminar flow at high Reynolds numbers, in *Proceedings of the 51st AIAA Aerospace Sciences Meeting* (AIAA, Reston, VA, 2013).

[2] A. Rastegari and R. Akhavan, On the mechanism of turbulent drag reduction with super-hydrophobic surfaces, J. Fluid Mech. **773**, R4 (2015).

[3] M. S. Naim and M. F. Baig, Turbulent drag reduction in Taylor-Couette flows using super-hydrophobic surfaces and liquid-infused surfaces, Phys. Fluids **31**, 095108 (2019).

[4] S. Soleimani and S. Eckels, A review of drag reduction and heat transfer enhancement by riblet surfaces in closed and open channel flow, Int. J. Thermofluids **9**, 100053 (2021).

[5] P. Ricco, M. Skotes, and M. Leschziner, A review of turbulent skin-friction drag reduction by near-wall transverse forcing, Progr. Aerospace Sci. **123**, 100713 (2021).

[6] Y. Huang, L. Wang, and S. Fu, Drag reduction in turbulent channel flows by a spanwise traveling wave of wall blowing and suction, Phys. Fluids **33**, 095111 (2021).

[7] P. Olivucci, D. J. Wise, and P. Ricco, Reduction of turbulent skin-friction drag by passively rotating discs, J. Fluid Mech. **923**, A8 (2021).

[8] X. Q. Cheng, C. W. Wong, Fazle Hussain, W. Schröder, and Y. Zhou, Flat plate drag reduction using plasma-generated streamwise vortices, J. Fluid Mech. **918**, (A24) (2021).

[9] Y. Ji, J. Yao, F. Hussain, and X. Chen, Vorticity transport in turbulent channels under large-scale control via spanwise wall jet forcing, Phys. Fluids **33**, 095112 (2021).

[10] W. J. Jung, N. Mangiavacchi, and R. Akhavan, Suppression of turbulence in wall-bounded flows by high-frequency spanwise wall oscillations, Phys. Fluids A **4**, 1605 (1992).

[11] M. Quadrio, P. Ricco, and C. Viotti, Streamwise-traveling waves of spanwise wall velocity for turbulent drag reduction, J. Fluid Mech. **627**, 161 (2009).

[12] D. Gatti and M. Quadrio, Performance losses of drag-reducing spanwise forcing at moderate values of the Reynolds number, Phys. Fluids **25**, 125109 (2013).

[13] E. Hurst, Q. Yang, and Y. M. Chung, The effect of Reynolds number on turbulent drag reduction by streamwise travelling waves, J. Fluid Mech. **759**, 28 (2014).

[14] D. Gatti and M. Quadrio, Reynolds-number dependence of turbulent skin-friction drag reduction induced by spanwise forcing, J. Fluid Mech. **802**, 553 (2016).

[15] I. Marusic, D. Chandaran, A. Rouhi, M. K. Fu, D. Wine, B. Holloway, D. Chung, and A. J. Smits, An energy-efficient pathway to turbulent drag reduction, Nature Commun. **12**, 5805 (2021).

[16] F. Laadhari, L. Skandaji, and R. Morel, Turbulence reduction in a boundary layer by a local spanwise oscillating surface, Phys. Fluids **6**, 3218 (1994).

[17] K.-S. Choi, Near-wall structure of turbulent boundary layer with spanwise oscillation, Phys. Fluids **14**, 2530 (2002).

[18] G. Karniadakis and K.-S. Choi, Mechanisms on transverse motions in turbulent wall flows, Annu. Rev. Fluid Mech. **35**, 45 (2003).

[19] P. Ricco, Modification of near-wall turbulence due to spanwise oscillations, J. Turbul. **5**, N24 (2004).

[20] C. X. Xu and W. X. Huang, Transient response of Reynolds stress transport to spanwise wall oscillation in a turbulent channel flow, Phys. Fluids **17**, 018101 (2005).

[21] E. Touber and M. A. Leschziner, Near-wall streak modification by spanwise oscillatory wall motion and drag-reduction mechanisms, J. Fluid Mech. **693**, 150 (2012).

[22] P. Ricco, C. Ottonelli, Y. Hasegawa, and M. Quadrio, Changes in turbulent dissipation in a channel flow with oscillating walls, J. Fluid Mech. **700**, 77 (2012).

[23] A. Yakeno, Y. Hasegawa, and N. Kasagi, Modification of quasistreamwise vortical structure in a drag-reduced turbulent channel flow with spanwise wall oscillation, Phys. Fluids **26**, 085109 (2014).
[24] L. Agostini, E. Touber, and M. A. Leschziner, The turbulence vorticity as a window to the physics of friction-drag reduction by oscillatory wall motion, Int. J. Heat Fluid Flow **51**, 3 (2015).
[25] Y. Wenjun, Z. Mengqi, C. Yongdong, and K. Boo Cheong, Phase-space dynamics of near-wall streaks in wall-bounded turbulence with spanwise oscillation, Phys. Fluids **31**, 125113 (2019).
[26] A. Yakeno, Drag reduction and transient growth of a streak in a spanwise wall-oscillatory turbulent channel flow, Phys. Fluids **33**, 065122 (2021).
[27] F. Auteri, A. Baron, M. Belan, G. Campanardi, and M. Quadrio, Experimental assessment of turbulent drag reduction by traveling waves in a turbulent pipe flow, Phys. Fluids **22**, 115103 (2010).
[28] J. Bird, M. Santer, and J. F. Morrison, Experimental control of turbulent boundary layers with in-plane travelling waves, Flow Turb. Comb. **100**, 1015 (2018).
[29] M. Quadrio and P. Ricco, The laminar generalized Stokes layer and turbulent drag reduction, J. Fluid Mech. **667**, 135 (2011).
[30] M. Quadrio and P. Ricco, Critical assessment of turbulent drag reduction through spanwise wall oscillations, J. Fluid Mech. **521**, 251 (2004).
[31] S. Tardu, Near wall dissipation revisited, Int. J. Heat and Fluid Flow **67**, 104 (2017).
[32] S. Tardu and F. Bauer, Fine structure of the production in low to medium Reynolds number wall turbulence, Comput. Fluids **148**, 82 (2017).
[33] S. Tardu, On the topology of wall turbulence in physical space, Phys. Fluids **29**, 020713 (2017).
[34] O. Doche, S. Tardu, J. Schillings, and A. Capogna, Transportation and coherent structures in MHD turbulent channel flow subject to uniform streamwise and spanwise magnetic fields, Phys. Rev. Fluids **6**, 094605 (2021).
[35] L. Agostini, E. Touber, and M. A. Leschziner, Spanwise oscillatory wall motion in channel flow: Drag-reduction mechanisms inferred from DNS-predicted phasewise property variations at $\mathrm{Re}_\tau = 1000$, J. Fluid Mech. **743**, 606 (2014).
[36] A. K. M. F. Hussain and W. C. Reynolds, The mechanics of an organized wave in turbulent shear flow, J. Fluid Mech. **41**, 241 (1970).
[37] T. R. Bewley, P. Moin, and R. Temam, Dns-based predictive control of turbulence: An optimal benchmark for feedback algorithms, J. Fluid Mech. **447**, 179 (2001).
[38] S. Tardu, Active control of near-wall turbulence by local oscillating blowing, J. Fluid Mech. **439**, 217 (2001).
[39] J. Kim, P. Moin, and R. Moser, Turbulence statistics in fully developed channel flow at low Reynolds number, J. Fluid Mech. **177**, 133 (1987).
[40] S. Tardu and O. Doche, Communication between the buffer layer and the wall in a turbulent channel flow, Int. J. Heat and Fluid Flow **82**, 108564 (2020).
[41] J. W. Brooke and T. J. Hanratty, Origin of turbulence producing eddies in a channel flow, Phys. Fluids A **5**, 1011 (1993).
[42] See Supplemental Material at http://link.aps.org/supplemental/10.1103/PhysRevFluids.7.054601 for λ_2 structures of $A1.25$ case.
[43] X. Wu, P. Moin, J. M. Wallace, J. Skarda, A. Lozano-Durán, and J.-P. Hickey, Transitional–turbulent spots and turbulent–turbulent spots in boundary layers, Proc. National Acad. Sci. USA **114**, E5292 (2017).
[44] S. Tardu, Characteristics of single and clusters of bursting events, Exp. Fluids **33**, 640 (2002).
[45] R. J. Adrian, Hairpin vortex organization in wall turbulence, Phys. Fluids **19**, 041301 (2007).
[46] See, https://gricad.univ-grenoble-alpes.fr/.
[47] F. Bauer, S. Tardu, and O. Doche, Efficiency of high accuracy DRP schemes in direct numerical simulations of incompressible turbulent flows, Comput. Fluids **107**, 123 (2015).
[48] R. D. Moser, J. Kim, and N. N. Mansour, Direct numerical simulation of turbulent channel flow up to $\mathrm{Re}_\tau = 590$, Phys. Fluids **11**, 943 (1999).

J. Fluid Mech. (2023), *vol*. 967, A9, doi:10.1017/jfm.2023.478

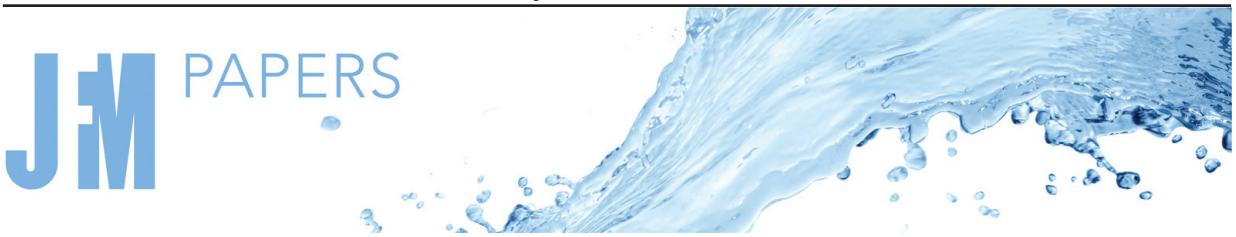

Vorticity transport in a turbulent channel flow subjected to streamwise travelling waves

Mohammad Umair[1],† **and Sedat Tardu**[1]

[1]UMR 5519 Laboratoire des Écoulements Géophysiques et Industriels (LEGI), CNRS, Grenoble-INP, Université Grenoble Alpes, 1209–1211 rue de la piscine, Domaine Universitaire, 38400 Saint-Martin-d'Hères, France

(Received 6 December 2022; revised 30 May 2023; accepted 7 June 2023)

Direct numerical simulations of turbulent channel flow subjected to spanwise wall oscillations in the form of streamwise travelling waves (STW) were performed in an effort to elucidate the mechanism responsible for the observed drag reduction. We imposed large amplitudes to identify the proper effects of STW, while keeping the angular frequency and wavenumber fixed at a particular values. We primarily focus on the vorticity transport mechanism, to better understand the influence of STW actuation on the near-wall turbulence. We identify key terms appearing in the turbulent enstrophy transport equations that are directly linked to the STW actuation. The analysis reveals that the primary effect of the STW forcing is to attenuate the spanwise turbulent enstrophy at the wall, which is linked to the fluctuating wall shear stress. The suppression of the wall-normal turbulent enstrophy is deemed to be subordinate. To strengthen this point, we performed numerical experiments, where the streamwise fluctuating velocity, and consequently the spanwise vorticity, is artificially suppressed next to the wall. The anisotropic invariant maps show striking resemblance for large amplitude STW actuation and artificially forced cases. Detailed analysis of various structural features is provided, which includes the response of the near-wall streaks and shear layers of spanwise fluctuating velocity field. The quasistreamwise vortices, which play a key role in the regeneration mechanism, are shown to be pushed away from the wall, resulting in their weakened signature at the wall.

Key words: drag reduction, turbulence control

1. Introduction

Drag reduction in turbulent flows is a crucial and dynamic field of research that holds substantial practical importance in various industrial sectors. Turbulent flows, characterized by irregular, chaotic fluid motion, often result in elevated levels of frictional resistance, which ultimately translates into increased drag. This leads to elevated

† Email address for correspondence: mohammad.umair@legi.grenoble-inp.fr

energy consumption, causing significant economic and environmental repercussions. As such, mitigating drag in turbulent flows is a vital endeavour for industries, including transportation, aviation and energy production. Until now, various novel techniques have been explored, including the application of various additives, surface coatings and fluid control mechanisms, to optimize and fluid flow and enhance efficiency while simultaneously reducing costs and emissions. Among these, spanwise wall oscillations techniques prove to be one of the most promising approaches towards reducing the skin-friction drag and, undoubtedly, still receives a considerable attention from the drag control community.

Despite the continuous efforts in investigating the various captivating features of spanwise wall oscillations techniques, the mechanism responsible for the observed drag reduction (DR) is still far from being fully understood. The primary focus of most of the earlier investigations, for example of Quadrio & Ricco (2003), Gatti & Quadrio (2013), Hurst, Yang & Chung (2014), Gatti & Quadrio (2016) and Marusic *et al.* (2021), has been to explore the parametric space to find the optimal set of parameters that leads to DR at different Reynolds numbers (Re) and/or to develop scaling laws that predict DR for different actuation scenarios. Studies that primarily target on elucidating the mechanism behind the observed DR are quite rare. The reader is directed to Ricco, Skotes & Leschziner (2021) for a recent review on different wall oscillations techniques.

In the present study we focus on the spanwise wall oscillations in the form of streamwise travelling waves (STW) governed by

$$W_{wall} = A \sin(\kappa x - \omega t), \tag{1.1}$$

where A is the amplitude, $\omega = 2\pi/T$ is the angular frequency and $\kappa = 2\pi/\lambda$ is the wavenumber (T and λ represent the time period and wavelength of the travelling wave, respectively). This type of wall-forcing was first studied numerically by Quadrio, Ricco & Viotti (2009). Throughout the paper x, y and z represent the streamwise, wall-normal and spanwise directions, respectively, and t is time. The corresponding instantaneous velocities in the streamwise, wall-normal and spanwise directions are U, V and W, respectively. Throughout this paper, the terms 'actuation', 'forcing' and 'control' are used interchangeably.

The above forcing results in a streamwise modulated spanwise boundary layer, known as the generalized Stokes layer (GSL) (Quadrio & Ricco 2011). The GSL interacts with the background turbulence to produce either drag reduction or drag increase, depending on the control parameters A, ω and κ. Under the assumption that the thickness of the GSL is much smaller than the channel half-height, Quadrio & Ricco (2011) derived an analytical expression that was found to agree well with the turbulent space-averaged spanwise flow and possess good predictive capabilities for DR margin at low Re. From here on, we will simply be referring to the GSL as the Stokes layer. Most of the scaling laws introduced so far fail at large Re. One such good example that clarifies this issue is the recent pathway introduced by Marusic *et al.* (2021) where they impose STW at small frequency coupled to the large scales that leads to approximately 13 % DR margin at friction Reynolds number $Re_\tau = 12\,800$, while the correlations of Gatti & Quadrio (2016) predict almost little to no DR margin. Predicting DR margins at Re of practical relevance is still an ongoing challenge.

Even though the precise reason behind the turbulence suppression is still unclear, nevertheless, considerable advances have been made towards unravelling the key interactions occurring in the turbulent flow field controlled by spanwise wall oscillations. Most of the early investigations support the idea that the generated Stokes layer perturbs

the near-wall turbulence by distorting and shifting the position of the near-wall low-speed streaks relative to the quasistreamwise vortices (QSVs), thus resulting in the suppression of turbulence intensity and drag reduction (Jung, Mangiavacchi & Akhavan 1992; Akhavan, Jung & Mangiavacchi 1993; Laadhari, Skandaji & Morel 1994). Choi, DeBisschop & Clayton (1998) argued that the action of the Stokes layer generated by the wall motion is to tilt the vorticity vector in the spanwise direction, thus generating a mean negative spanwise vorticity in the viscous sublayer, and hence reduced drag. This view is in line with the study of Dhanak & Si (1999), who used the model proposed by Orlandi & Jiménez (1994), and studied the effect of wall oscillations on the near-wall QSVs. They showed that the effect of wall oscillation is to promote the interaction of the near-wall coherent structures with the wall, leading to their rapid annihilation. The wall oscillation distorts the near-wall low-speed streaks owing to mixing of the momentum associated with the low-speed ejection regions and that associated with the high-speed 'sweep' regions, resulting in a reduction in the rate of momentum convection normal to the wall. This in turn has a direct impact on the Reynolds stress and the skin friction.

Touber & Leschziner (2012) analysed the Reynolds stress budgets in the flows controlled by the homogeneous wall oscillations (HWO). They concluded that the primary cause of the suppression of the near-wall turbulence is the reduction in the wall-normal component of the Reynolds stress tensor. They showed that at the optimum forcing period the organization of the low-speed streaks is severely disrupted owing to the rapid change in the Stokes strain, resulting in their suppression, and hence a significant reduction in skin-friction.

Motivating the connection between the global enstrophy and the turbulent kinetic energy dissipation, Ricco *et al.* (2012) and Ge & Jin (2017) studied the transient response of the global turbulent enstrophy in a turbulent channel flow subjected to HWO. They found that after a sudden implementation of spanwise oscillations, the turbulent enstrophy shows a transient increase, which directly enhances the turbulent dissipation. As a consequence, the turbulent activity is suppressed by the transient increase of the turbulent enstrophy in the initial phase, which drifts the flow towards the low-drag state.

Agostini, Touber & Leschziner (2014, 2015), however, adopted a different approach where they intentionally impose HWO at suboptimal period to allow the flow field to oscillate about a mean low-drag state. They showed that the drag reduction phases extend over a longer proportion of the cycle than the subsequent drag increase phases, and hence display a hysteresis. Agostini *et al.* (2015) observed a strong increase in the spanwise turbulent enstrophy during the drag reduction phase, and identified the Stokes-strain-driven production terms related to vortex tilting and stretching in the regions of high skewness being responsible for the observed effect. They showed that the spanwise tilting of wall-normal turbulent vorticity (that are primarily linked to the near-wall streaks) provoke a strong increase in the skewness near the wall, resulting in reduction in the shear stress. However, a closer look at their plots reveals that the spanwise turbulent enstrophy is annihilated at the drag reduction phases next to the wall – an observation very similar to what we will show in the present study in the case of STW actuation.

Experimental studies on the subject are quite rare owing to the complexity in imposing wall oscillations. Most of the experimental studies were either conducted in a pipe flow configuration or developing boundary layer flow over a flat plate. The results coming from the experimental studies of Laadhari *et al.* (1994), Trujillo, Bogard & Ball (1997), Choi *et al.* (1998), Ricco (2004), Auteri *et al.* (2010) and Kempaiah *et al.* (2020) show good agreement with the numerical investigations presented above. The recent experimental study by Marusic *et al.* (2021) promises net DR even at large Re.

From the review of the state-of-the-art, it is fair to state that a clear and unambiguous explanation of the drag reduction mechanism is still lacking. Most of the advances towards understanding the underlying physical mechanism mentioned above stem from the HWO forcing. In the context of STW, not much has been reported, except for the recent study by Umair, Tardu & Doche (2022) who adopted a similar approach to Touber & Leschziner (2012) and studied the full Reynolds stresses budgets in the flows controlled using STW. In this paper, delving deeper in to the mechanism, we investigate the vorticity transport in a turbulent channel flow with STW actuation. The primary focus is kept on the physical modifications in the near-wall turbulent flow field instigated by the STW actuation. We cover a broad regime of drag reduction margin ranging from approximately 20 %–60 %, with a particular emphasis on the large amplitude STW that yield significantly large drag reduction margins. The idea is to identify the key terms arising in the transport equations of the spanwise, streamwise and wall-normal turbulent enstrophy that significantly alter the near-wall turbulence. By means of a few numerical experiments, we show a striking resemblance in the trajectory of the anisotropy invariants of the large amplitude STW and artificial suppression of turbulent activity. Furthermore, we show the influence of STW on the near-wall quasistreamwise vortical structures, and estimate the DR margin using their drift. Finally, we explain the appearance of organized regular patterns of spanwise fluctuating velocity field observed by Umair *et al.* (2022).

This paper is organized as follows. The computational details and control parameters are described in § 2. The effect of STW control on the transport of turbulent enstrophy is discussed in § 3. In § 4, a detailed discussion on the anisotropy invariant maps of the controlled flow field is provided, and the results from the numerical experiments of artificial suppression of turbulent activity are described. Next, a detailed discussion on the modification of the near-wall flow structures is provided in § 5. Finally, the main findings of this paper are summarized in § 6.

2. Numerical details

In the present study, the DNS data of Umair *et al.* (2022) is used to study the vorticity transport mechanism in a turbulent channel flow subjected to STW. All the simulations were performed at a constant flow rate condition. The schematic diagram in figure 1 shows the domain in the form of a channel with the imposed control. The Reynolds number $Re(= hU_c/\nu)$ was fixed at 4200, where h is the channel half-height, U_c is the centreline velocity of the plane Poiseuille flow and ν is the kinematic viscosity of the fluid. It corresponds to a friction Reynolds number $Re_\tau = hu_\tau/\nu = 180$ for the uncontrolled case (u_τ being the friction velocity). The amplitude (A) of the STW was varied from $0.15U_c$ to $1.25U_c$, while ω and κ were kept fixed at 0.16 and 1.66 in outer units based on h and U_c, respectively. This results in a DR margin of approximately 60 % for the largest amplitude case $A1.25$. The corresponding DR$(= -\Delta C_f/C_{f0})$ margins and the actual (local) friction Reynolds numbers (Re_τ) for all the cases are listed in table 1. Here, C_f is the skin-friction coefficient for the controlled flow and C_{f0} is the skin-friction coefficient for the uncontrolled flow. The skin-friction coefficient is defined as $C_f = 2\overline{\tau_w}/\rho U_b^2$, where $\overline{\tau_w}$ is the wall shear-stress averaged over homogeneous directions x and z, ρ is the density of the fluid and $U_b(= 2U_c/3)$ is the bulk flow velocity. The periodic boundary condition was employed in the streamwise and spanwise directions. The size of the computational domain was selected to accommodate at least six wavelengths, and is $6\pi h \times 2h \times 3\pi h$ long in the streamwise, wall-normal and spanwise directions, respectively. The nodes are uniformly distributed in the streamwise and spanwise directions, while it is stretched in the wall-normal direction using a hyperbolic tangent distribution. The corresponding grid

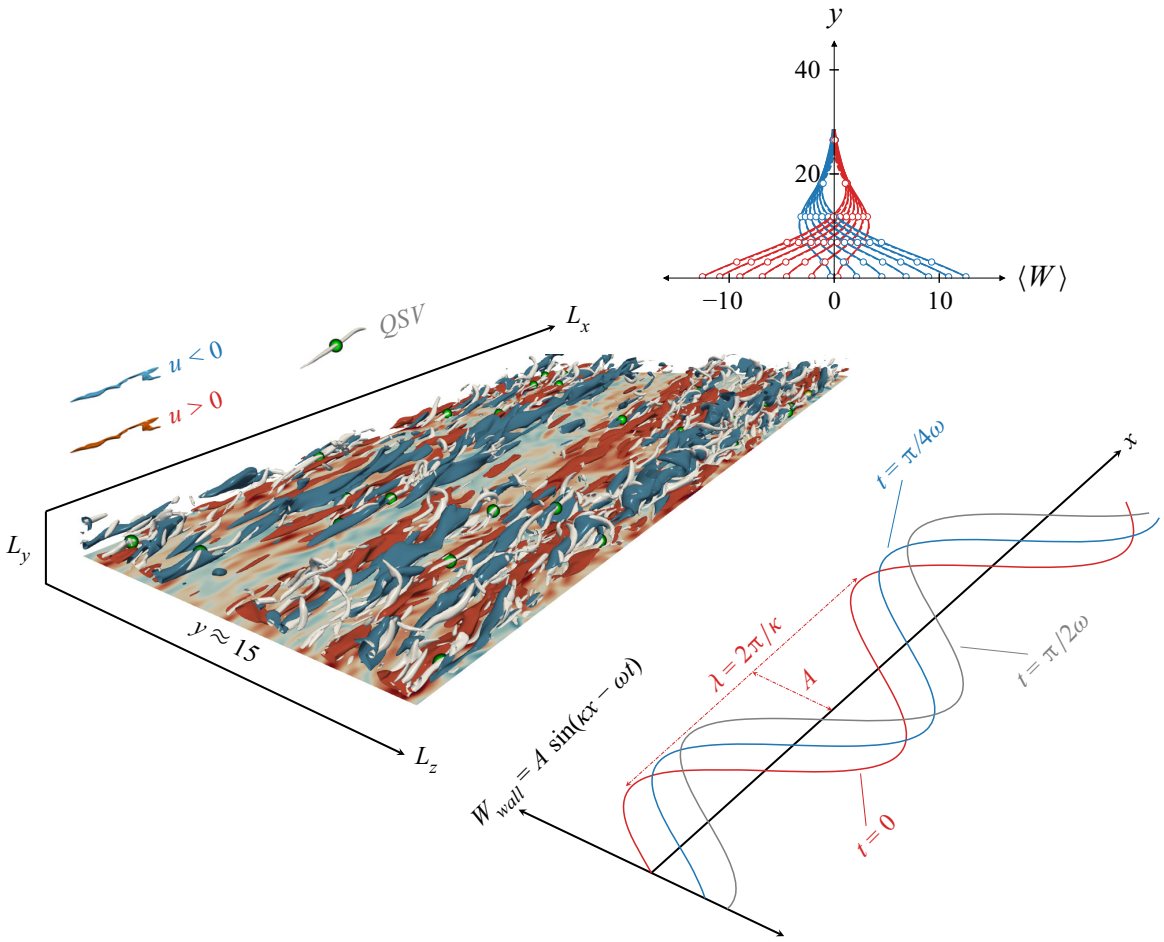

Figure 1. Schematic diagram of the rectangular channel of size $L_x \times L_y \times L_z = 6\pi h \times 2h \times 3\pi h$ in the streamwise, wall-normal and spanwise directions, respectively, subjected to spanwise wall oscillations in the form of STW. The diagram also shows the instantaneous visualizations of the near-wall streaks of streamwise fluctuating velocity field (u), marked with blue ($u < 0$) and red ($u > 0$) contours. The near-wall quasistreamwise vortical structures (QSVs) (identified using $\lambda_2 = -0.02$) that are responsible for the generation of skin-friction are shown in grey colour, with their centres – identified using the eduction scheme of Jeong *et al.* (1997) – marked in green. The diagram also shows the waveform used for the actuation and the corresponding phase-averaged profiles of the spanwise velocity $\langle W \rangle$ for the $A0.50$ case. The phase-averaged profiles collapse well with the laminar solution (represented by dots) derived by Quadrio & Ricco (2011).

resolutions are 8.5, 5 and 0.5–5.5 in wall units based on Re_τ of the uncontrolled flow. The solutions were advanced in time with time steps of 0.04 and 0.008 wall units for the uncontrolled and controlled cases, respectively.

The statistical quantities for the uncontrolled flow were obtained using 50 full three-dimensional (3-D) snapshots of velocity and pressure fields, covering a time window of 37 000 wall units, separated by 770 wall units. The statistical quantities for the controlled cases were obtained by employing the classical triple decomposition of Hussain & Reynolds (1970), where an instantaneous quantity, for example, U is decomposed into a time-invariant mean component ($\overline{U}$), a periodic fluctuating component ($\widetilde{U}$) and a purely stochastic component (u). This decomposition can be expressed as $U = \overline{U} + \widetilde{U} + u = \langle U \rangle + u$, where $\langle \cdot \rangle$ represents the phase-averaged quantity. The phase-averaged quantities were obtained by averaging the corresponding instantaneous quantity over the phase $\xi = x - ct$ of the travelling wave, where $c = \omega/\kappa$ is the wave speed. The initial 20 cycles were discarded to elapse the initial transients, to ensure that the data collected to perform statistical calculations does not lie in the transient phases where the control

Case	Uncontrolled	HWO	$A0.15$	$A0.30$	$A0.50$	$A0.75$	$A0.95$	$A1.25$
A/U_c	—	0.51	0.50	0.30	0.50	0.75	0.95	1.25
$A/u_{\tau 0}$	—	12.0	3.5	7.0	11.7	17.5	22.2	29.2
A/u_τ	—	14.9	4.0	9.0	16.1	25.3	32.7	44.3
DR(%)	—	36	26	42	48	52	54	58
Re_τ	179.8	144.2	156.9	139.0	130.7	124.5	121.9	118.4
Marker								

Table 1. The details of the control parameters, the corresponding DR margins and the actual (local) friction Reynolds number for the controlled cases. The values of angular frequency (ω) and wavenumber (κ) of STW were kept fixed at 0.16 and 1.66 in outer units based on the channel half-height (h) and the centreline velocity (U_c) of the plane Poiseuille flow, respectively.

drives the flow towards the drag reduced state. The data was collected for at least 40 cycles, corresponding to a time window of 12 000 wall units. This resulted in a computing time of approximately 90 000 core hours alone for the STW cases, distributed across 128 processors on the computational clusters of GRICAD, University of Grenoble-Alpes. We carefully compared the phase-averaged profile of the spanwise velocity $\langle W \rangle$ with the laminar solution of Quadrio & Ricco (2011) for all the control cases listed in table 1, and found that we are in the GSL regime. For instance, it is seen at the top of figure 1 that the phase-averaged spanwise velocity profiles $\langle W \rangle$ (represented by lines) collapse well with the laminar solution of Quadrio & Ricco (2011) (represented by dots) for the $A0.50$ case.

The simulations for the artificially forced cases (presented in § 4) were started from an initial turbulent flow field at $Re_\tau = 180$, and the flow was left to develop for at least 3000 wall units before collecting the data to compute statistics to avoid biases in the statistical calculations related to the transient interval. Statistical data for these cases were obtained by averaging 25 full 3-D snapshots of instantaneous velocities and pressure fields, covering a time window of approximately 5000 wall units separated by approximately 200 wall units. Further details about the numerical schemes and the description of the code MULTIFAST used to perform the calculations are provided in Bauer, Tardu & Doche (2015) and Umair *et al.* (2022).

Note that throughout the paper, we consistently used the *local* scaling parameters based on the actual Re_τ of the respective case, for reasons detailed in Umair *et al.* (2022). Wherever necessary, a subscript '0' was put on the quantities to highlight the use of *reference* scaling based on the Re_τ of the uncontrolled reference flow.

3. Turbulent enstrophy transport

3.1. *Spanwise enstrophy transport*

Figure 2 shows the response of turbulent enstrophy for all the cases listed in table 1. In canonical wall-bounded turbulent flows, the spanwise turbulent vorticity ω_z is dominant next to the wall. It is approximately equivalent to the uniform streamwise fluctuating stress τ' up to $y = 3$, i.e. $\omega_z \approx -\partial u/\partial y$. In the large amplitude STW cases, ω_z is entirely annihilated up to $y = 8$, with a negligible turbulent activity at the wall (i.e. $\tau' \approx 0$), and its peak is pushed towards the high buffer layer at $y = 20$. This can be attributed to the strong damping of the near-wall streaks of streamwise fluctuating velocity. This is one of the outstanding effects of STW control compared with the HWO control – the profile of

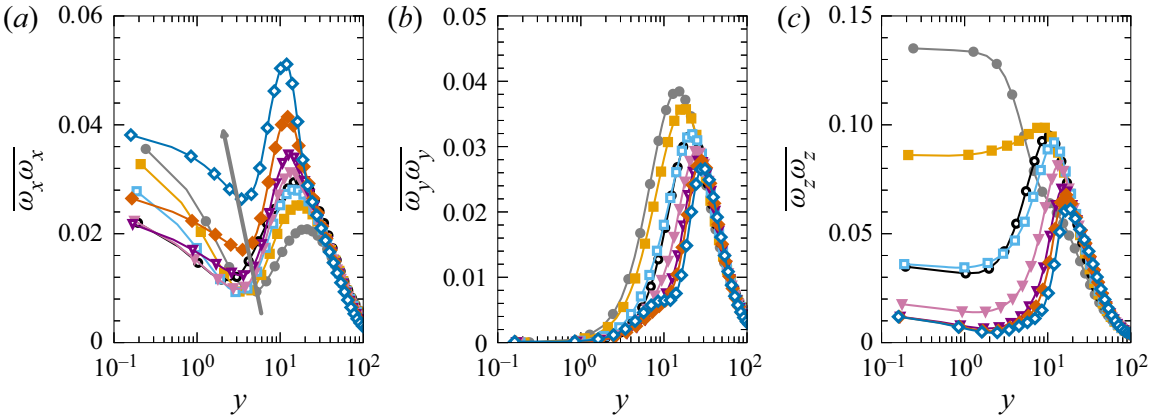

Figure 2. Mean profiles of turbulent enstrophy in each direction for uncontrolled and controlled cases: (*a*) streamwise $\overline{\omega_x\omega_x}$; (*b*) wall-normal $\overline{\omega_y\omega_y}$; and (*c*) spanwise $\overline{\omega_z\omega_z}$. Note that all the profiles are scaled with the local friction velocities of the drag reduced flows. Refer to table 1 for markers corresponding to different cases.

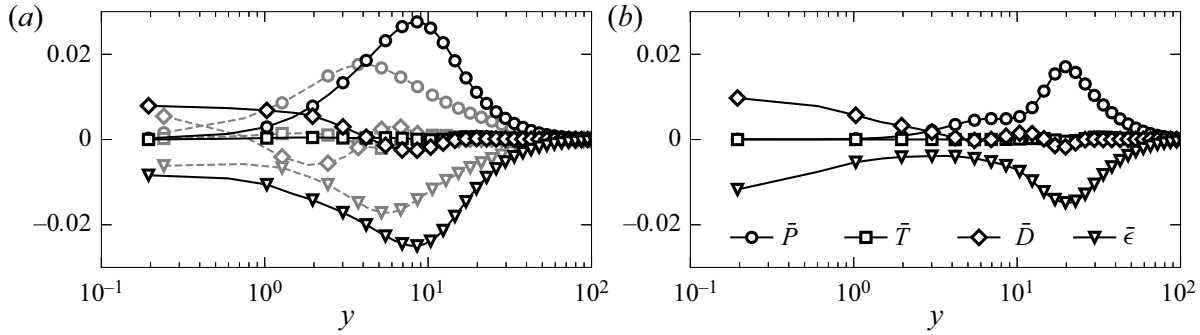

Figure 3. Budget of spanwise turbulent enstrophy transport for (*a*) HWO and (*b*) *A*1.25 cases. The budget for the reference (uncontrolled) canonical case is also included in (*a*) in grey broken lines for comparison. The mean advection term $\overline{A_{\omega_z\omega_z}}$ is negligible, and hence not displayed in the figures to avoid cluttering.

which collapses rather with the small amplitude STW case *A*0.30 (figure 2*c*). In the HWO case $\overline{\omega_z\omega_z}$ is damped in the viscous sublayer with a maximum at approximately $y = 10$.

The production term for the mean spanwise turbulent enstrophy $\overline{\omega_z\omega_z}$ reads

$$\overline{P_{\omega_z\omega_z}} = \underbrace{\overline{2\widetilde{\Omega}_x\left\langle\omega_z\frac{\partial w}{\partial x}\right\rangle}}_{\overline{P^1_{\omega_z\omega_z}}} + \underbrace{\overline{2\widetilde{\Omega}_y\left\langle\omega_z\frac{\partial w}{\partial y}\right\rangle}}_{\overline{P^2_{\omega_z\omega_z}}} + \underbrace{\overline{2\widetilde{\Omega}_z\left\langle\omega_z\frac{\partial w}{\partial z}\right\rangle}}_{\overline{P^3_{\omega_z\omega_z}}} + \underbrace{2\overline{\Omega_z}\,\overline{\omega_z\frac{\partial w}{\partial z}}}_{\overline{P^4_{\omega_z\omega_z}}} + \underbrace{\overline{2\omega_x\omega_z\frac{\partial w}{\partial x}}}_{\overline{P^5_{\omega_z\omega_z}}}$$
$$+ \underbrace{\overline{2\omega_y\omega_z\frac{\partial w}{\partial y}}}_{\overline{P^6_{\omega_z\omega_z}}} + \underbrace{\overline{2\omega_z\omega_z\frac{\partial w}{\partial z}}}_{\overline{P^7_{\omega_z\omega_z}}} + \underbrace{\overline{2\langle\omega_x\omega_z\rangle\frac{\partial\widetilde{W}}{\partial x}}}_{\overline{P^8_{\omega_z\omega_z}}} + \underbrace{\overline{2\langle\omega_y\omega_z\rangle\frac{\partial\widetilde{W}}{\partial y}}}_{\overline{P^9_{\omega_z\omega_z}}}. \tag{3.1}$$

The complete transport equation for each component can be found in Appendix A. The terms with '$\sim$' are purely a consequence of the periodic forcing in the form of spanwise wall oscillations. In the canonical turbulent channel flows, the mean production term $\overline{P_{\omega_z\omega_z}}$ peaks at approximately $y = 4$ within the viscous sublayer, and is roughly in equilibrium with the dissipation, as shown by the profiles in broken lines in figure 3(*a*). The viscous and turbulent diffusion terms are negligible except next to the wall at which they equilibrate mutually as expected. In the controlled cases, however, all the transport terms are shifted

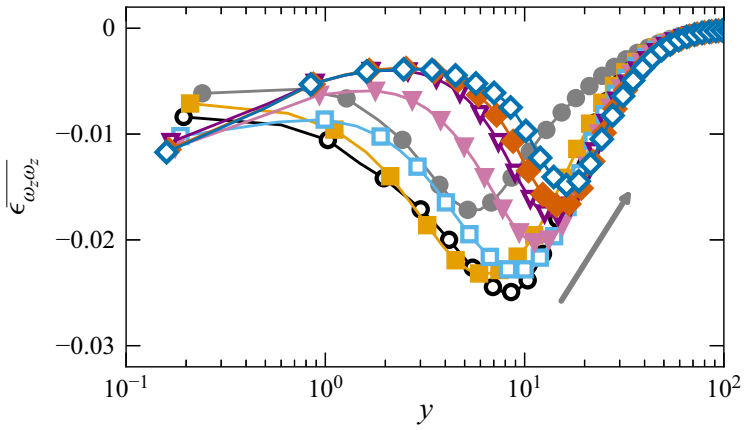

Figure 4. Dissipation term ($\overline{\epsilon_{\omega_z\omega_z}}$) for the spanwise turbulent enstrophy. Refer to table 1 for markers corresponding to different cases.

away from the viscous sublayer. In the HWO and low amplitude STW ($A < 0.50$) cases, the total mean production term peaks at approximately $y = 9$, and it is even further shifted towards the middle of the buffer layer at $y \approx 20$ for the large amplitude STW cases (figure 3*b*). A similar attenuation and shift can also be observed in the dissipation $\overline{\epsilon_{\omega_z\omega_z}}$ (figure 4).

In the canonical turbulent channel flows, the main contribution to the total production of ω_z comes from $\overline{P^4_{\omega_z\omega_z}}$ which emanates from the stretching of the spanwise vorticity interacting with the mean shear $\overline{\Omega_z}$. It peaks at roughly $y = 5$ in the viscous sublayer (figure 5*c*). For the large amplitude STW cases, it is almost annihilated up to $y = 10$ and there is a shift in its peak of approximately 10 wall units. There is a difference in its maximum of approximately 20 % for the A1.25 case compared with the HWO case.

The Stokes straining production terms $\overline{P^1_{\omega_z\omega_z}}$ and $\overline{P^2_{\omega_z\omega_z}}$ act to destroy the production of ω_z (figure 5*a*,*b*). The former originates from the twisting of $\widetilde{\Omega}_x$ by the local $\partial w/\partial x$ gradient, while the latter due to the tilting of $\widetilde{\Omega}_y$ by the local $\partial w/\partial y$ gradient. In the case of HWO, $\overline{P^1_{\omega_z\omega_z}}$ is almost negligible and $\overline{P^2_{\omega_z\omega_z}}$ is obviously absent (as $\partial\widetilde{W}/\partial x = 0$), suggesting that both of these terms are a result of particular effects of STW.

There is another Stokes straining term, denoted by $\overline{P^9_{\omega_z\omega_z}}$, that is significant in both the HWO and STW cases. It results from the tilting of ω_y by the Stokes strain $\partial\widetilde{W}/\partial y$, and is large next to the edge of the viscous sublayer (figure 5*e*). The terms $\overline{P^1_{\omega_z\omega_z}}$ and $\overline{P^9_{\omega_z\omega_z}}$ can be combined to give

$$\overline{P^{1*}_{\omega_z\omega_z}} = \overline{P^1_{\omega_z\omega_z}} + \overline{P^9_{\omega_z\omega_z}} = 2\overline{\frac{\partial\widetilde{W}}{\partial y}\left\langle\omega_z\frac{\partial u}{\partial z}\right\rangle}. \tag{3.2}$$

The resulting term $\overline{P^{1*}_{\omega_z\omega_z}}$ now has a different physical meaning. As $\langle\omega_z\partial u/\partial z\rangle$ represents twisting of ω_x in its transport equation, $\overline{P^{1*}_{\omega_z\omega_z}}$ therefore represents the Stokes straining of $\langle\omega_z\partial u/\partial z\rangle$ by the deterministic streamwise vorticity $\widetilde{\Omega}_x$. Figure 5(*f*) clearly shows that $\overline{P^{1*}_{\omega_z\omega_z}}$ is strongly attenuated in the STW cases of large amplitudes ($A > 0.5$), and its peak is further shifted away towards the buffer layer compared with HWO. The shift in $\overline{P^{1*}_{\omega_z\omega_z}}$ is as large as twice the thickness of the viscous sublayer for *A*1.25 case with respect to the HWO case.

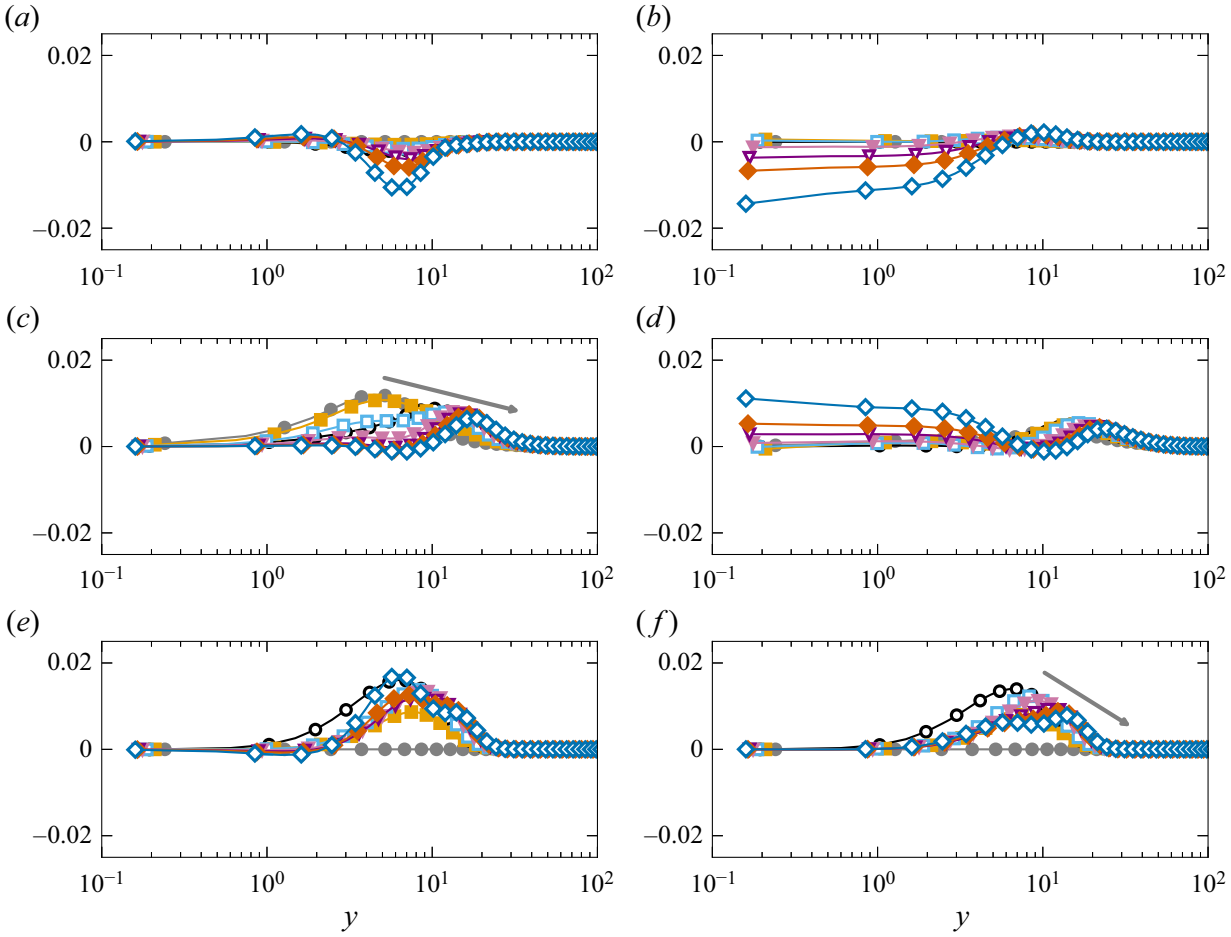

Figure 5. Production terms (*a*) $\overline{P^{1}_{\omega_z\omega_z}}$, (*b*) $\overline{P^{2}_{\omega_z\omega_z}}$, (*c*) $\overline{P^{4}_{\omega_z\omega_z}}$, (*d*) $\overline{P^{6}_{\omega_z\omega_z}}$, (*e*) $\overline{P^{9}_{\omega_z\omega_z}}$ and (*f*) $\overline{P^{1*}_{\omega_z\omega_z}}$. Refer to table 1 for markers corresponding to different cases.

A closer look at figure 6 reveals another peculiar behaviour of the $\overline{\omega_z\omega_z}$ production mechanism next to the wall. The production terms $\overline{P^{2}_{\omega_z\omega_z}}$ and $\overline{P^{6}_{\omega_z\omega_z}}$ cancel each other in the viscous sublayer and low buffer layer up to $y = 10$. Figure 6(*c*) shows how well their phase averages coincide in a somewhat unexpected way at $y = 2$. It is important to note that there is no direct link between $\overline{P^{2}_{\omega_z\omega_z}}$ and $\overline{P^{6}_{\omega_z\omega_z}}$. The former results from Stokes straining, while the latter comes from the local tilting term $\langle\omega_y\partial w/\partial y\rangle$. Next to the wall, $\overline{P^{6}_{\omega_z\omega_z}}$ reduces to the triple correlation $\overline{\omega_x\omega_y\omega_z}$, and can hardly be connected to $\overline{P^{2}_{\omega_z\omega_z}}$. The deterministic $\partial\langle W\rangle/\partial x$ reaches very large values at large imposed amplitudes next to the wall, and correlates almost perfectly with $\langle\omega_z\partial w/\partial y\rangle$ (figure 6*d*).

To summarize, figure 6 recapitulates the major production terms of the $\overline{\omega_z\omega_z}$ transport equations, and figure 7 summarizes its main characteristics. There are finally two terms, namely, $\overline{P^{4}_{\omega_z\omega_z}}$ which is the major term in the uncontrolled flow and $\overline{P^{1*}_{\omega_z\omega_z}}$ which is specific to HWO and STW. All these production terms are the consequences of different mechanisms. Basically, the proper (direct) effect of STW is to reduce the intensity of the total production by Stokes straining, consequently its peak is shifted away from the wall to the buffer layer by approximately 10 wall units for large amplitude STW with respect to the HWO case.

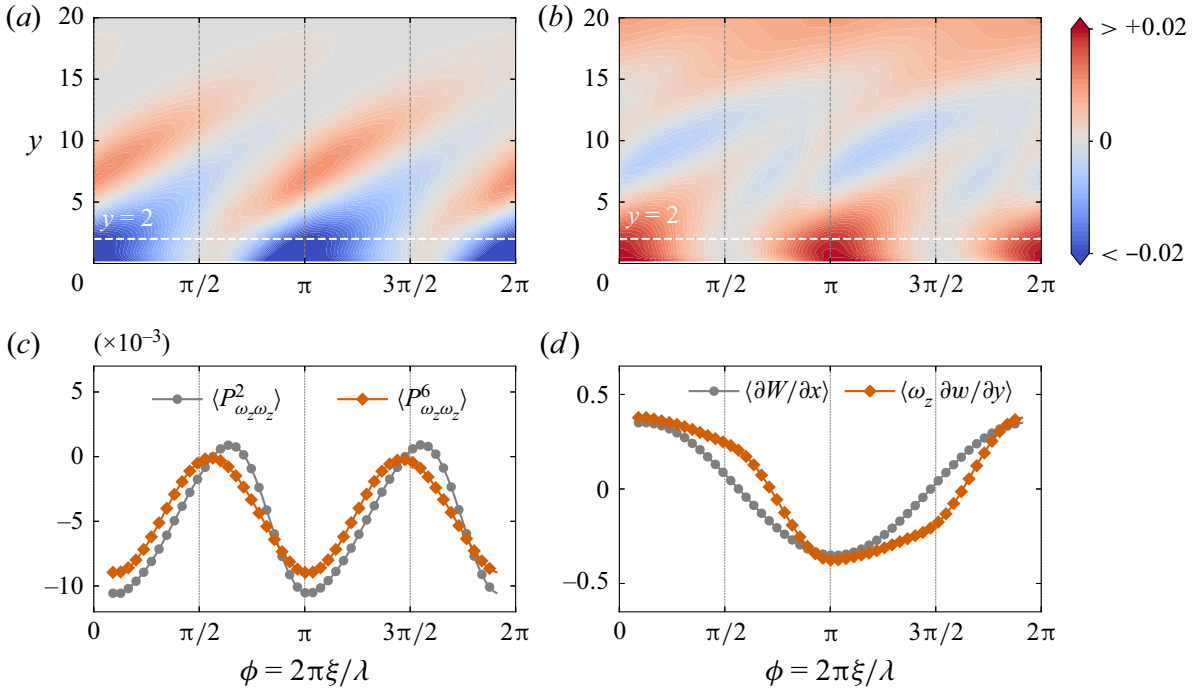

Figure 6. Phase wise variations of (*a*) $\langle P^2_{\omega_z\omega_z}\rangle$, (*b*) $\langle P^6_{\omega_z\omega_z}\rangle$ at different wall-normal locations, (*c*) $\langle P^2_{\omega_z\omega_z}\rangle$ and $\langle P^6_{\omega_z\omega_z}\rangle$ and (*d*) $\langle \partial W/\partial x\rangle$ and $\langle \omega_z \partial w/\partial y\rangle$ for *A*0.95 case at $y = 2$, respectively. The values of $\langle \omega_z \partial w/\partial y\rangle$ are multiplied by a factor of 25.

$$\overline{P^9_{\omega_z\omega_z}} = 2\overline{\langle \omega_y\omega_z\rangle(\partial\widetilde{W}/\partial y)}$$

(Strongly attenuated by STW)

$$+$$

$$\overline{P^1_{\omega_z\omega_z}} = 2\overline{\langle \omega_z\partial w/\partial x\rangle(\partial\widetilde{W}/\partial y)}$$

$$=$$

$$\overline{P^{1*}_{\omega_z\omega_z}} = 2\overline{\langle \omega_z\partial u/\partial z\rangle(\partial\widetilde{W}/\partial y)}$$

(Peak shifted to the middle of the buffer layer)

(Strongly damps $\overline{P^9_{\omega_z\omega_z}}$)

Main production term in the uncontrolled flow

$$\overline{P^4_{\omega_z\omega_z}} = -2\overline{\langle \omega_z\partial w/\partial z\rangle}(\mathrm{d}\overline{U}/\mathrm{d}y)$$

STWs ⟶ Attenuated by 50 % and shift of maximum of about $\Delta y = 10$ with respect of HWO

Figure 7. Summary of main characteristics of the effect of control on the spanwise turbulent enstrophy production process.

3.2. *Streamwise enstrophy transport*

The production term for the streamwise turbulent enstrophy is given as

$$\overline{P_{\omega_x\omega_x}} = \underbrace{2\widetilde{\Omega}_x\left\langle\omega_x\frac{\partial u}{\partial x}\right\rangle}_{\overline{P^1_{\omega_x\omega_x}}} + \underbrace{2\widetilde{\Omega}_y\left\langle\omega_x\frac{\partial u}{\partial y}\right\rangle}_{\overline{P^2_{\omega_x\omega_x}}} + \underbrace{2\widetilde{\Omega}_z\left\langle\omega_x\frac{\partial u}{\partial z}\right\rangle}_{\overline{P^3_{\omega_x\omega_x}}} - \underbrace{2\overline{\omega_x\frac{\partial w}{\partial x}}\frac{\mathrm{d}\overline{U}}{\mathrm{d}y}}_{\overline{P^4_{\omega_x\omega_x}}}$$
$$+ \underbrace{2\overline{\omega_x\omega_x\frac{\partial u}{\partial x}}}_{\overline{P^5_{\omega_x\omega_x}}} + \underbrace{2\overline{\omega_x\omega_y\frac{\partial u}{\partial y}}}_{\overline{P^6_{\omega_x\omega_x}}} + \underbrace{2\overline{\omega_x\omega_z\frac{\partial u}{\partial z}}}_{\overline{P^7_{\omega_x\omega_x}}} + \underbrace{2\overline{\langle\omega_x\omega_x\rangle\frac{\partial\widetilde{U}}{\partial x}}}_{\overline{P^8_{\omega_x\omega_x}}} + \underbrace{2\overline{\langle\omega_x\omega_y\rangle\frac{\partial\widetilde{U}}{\partial y}}}_{\overline{P^9_{\omega_x\omega_x}}}. \qquad (3.3)$$

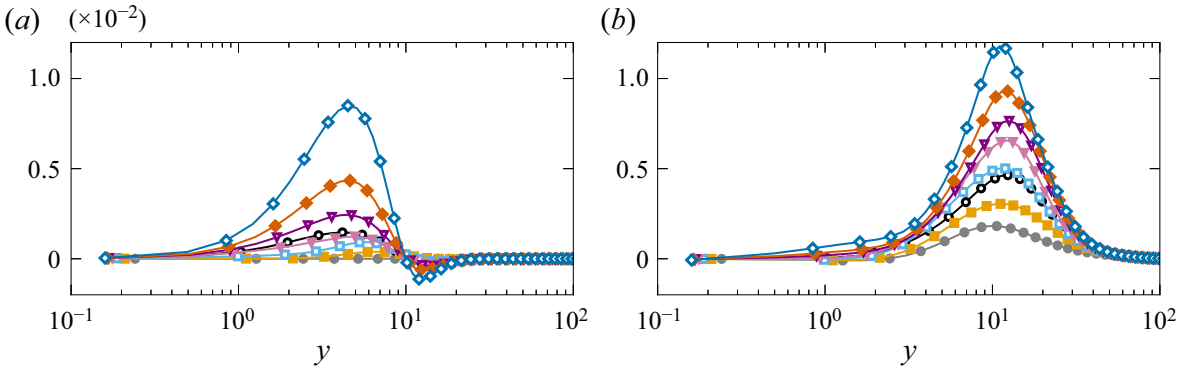

Figure 8. Production terms (*a*) $\overline{P^1_{\omega_x\omega_x}}$ and (*b*) $\overline{P^4_{\omega_x\omega_x}}$. Refer to table 1 for markers corresponding to different cases.

A careful analysis reveals that most of the terms in (3.3) are either negligible or cancel each other. Thus, the total production term $\overline{P_{\omega_x\omega_x}}$ effectively reduces to

$$\overline{P_{\omega_x\omega_x}} \approx \underbrace{2\overline{\widetilde{\Omega}_x\left\langle\omega_x\frac{\partial u}{\partial x}\right\rangle}}_{\overline{P^1_{\omega_x\omega_x}}} \underbrace{-2\overline{\omega_x\frac{\partial w}{\partial x}}\frac{\mathrm{d}\overline{U}}{\mathrm{d}y}}_{\overline{P^4_{\omega_x\omega_x}}}. \tag{3.4}$$

The production term $\overline{P^1_{\omega_x\omega_x}}$ represents the interaction of the Stokes shear $\partial\widetilde{W}/\partial y$ with the stretching of the streamwise vorticity $\langle\omega_x\partial u/\partial x\rangle$. This term is a direct consequence of forcing, and hence is absent in the canonical case. It increases with the amplitude of the STW, reaching large values for the $A1.25$ case, and peaks within the viscous sublayer at $y = 5$ (figure 8*a*). Whereas in the case of HWO, it is negligible compared with the large amplitude STW cases.

The response of the streamwise turbulent enstrophy $\overline{\omega_x\omega_x}$ to the STW forcing is shown in figure 2(*a*). The local minimum and maximum in the profiles of $\overline{\omega_x\omega_x}$ are attributed to the streamwise vortices in the near-wall region (Kim, Moin & Moser 1987). The local minimum increases with the amplitude of the STW, under the effect of Stokes shear $\partial\widetilde{W}/\partial y$ induced production $\overline{P^1_{\omega_x\omega_x}}$ which weakens the signature of the QSVs near the wall under large amplitude STW. Note that there is also a significant undermining of $\overline{\omega_x\omega_x}$ variation in the viscous sublayer for STW cases of $A > 0.50$. For the $A1.25$ case, there is only a slight variation of $\overline{\omega_x\omega_x}$ between the local minimum and the wall, whereas in the case of uncontrolled flow there is an approximately 400 % increase at the same range of wall-normal distance. This is related to the lack of velocity-pressure gradient correlation in the spanwise velocity transport equation in the near-wall region (Umair *et al.* 2022).

For all the cases, the main production of $\overline{\omega_x\omega_x}$ comes from the tilting of ω_y by the mean shear $\mathrm{d}\overline{U}/\mathrm{d}y$ (figure 8*b*). This term, denoted by $\overline{P^4_{\omega_x\omega_x}}$ in (3.3), peaks roughly at $y = 10$–12.5 for all the cases. Note that the profile of $\overline{P^4_{\omega_x\omega_x}}$ in HWO case collapse almost perfectly with the STW case $A0.30$. This strengthens again the observation made by Umair *et al.* (2022) that the direct effects of STW mainly appear at $A > 0.30$.

The turbulent transport (or turbulent diffusion) term in the uncontrolled flow is $\overline{T_{\omega_x\omega_x}} = -\mathrm{d}\overline{\omega_x\omega_x v}/\mathrm{d}y$, and is globally negligible compared with the other terms appearing in the transport equation of $\overline{\omega_x\omega_x}$. However, two additional transport terms emerge directly from the imposed unsteadiness in the STW cases. They are, respectively, given as $\overline{T^1_{\omega_x\omega_x}} = -2\overline{\langle\omega_x u\rangle\partial\widetilde{\Omega}_x/\partial x}$ and $\overline{T^2_{\omega_x\omega_x}} = -2\overline{\langle\omega_x v\rangle\partial\widetilde{\Omega}_x/\partial y}$ (Appendix A). Figure 9(*b*) shows that

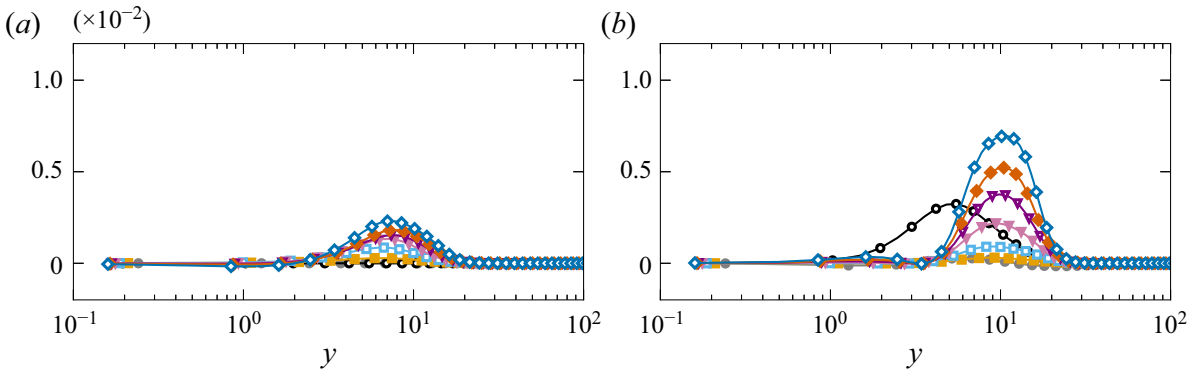

Figure 9. Turbulent transport (or turbulent diffusion) terms (*a*) $\overline{T^1_{\omega_x\omega_x}}$ and (*b*) $\overline{T^2_{\omega_x\omega_x}}$. Refer to table 1 for markers corresponding to different cases.

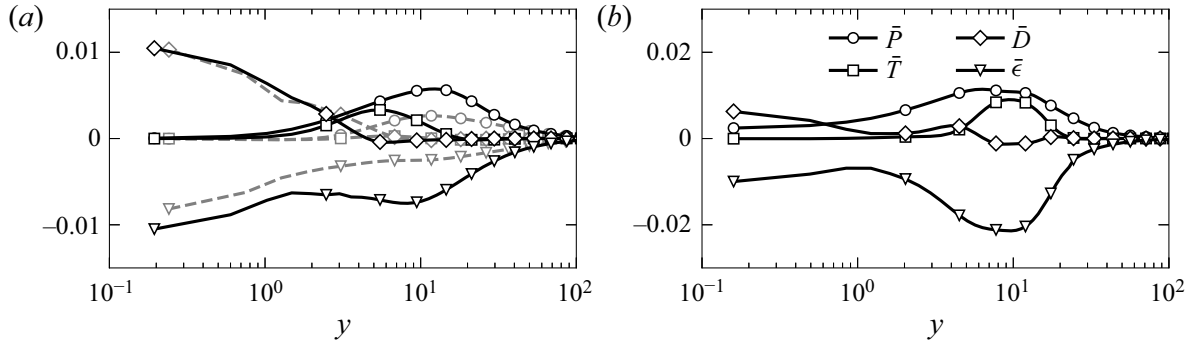

Figure 10. Budget of streamwise turbulent enstrophy transport for (*a*) HWO and (*b*) *A*1.25 cases. The budget for the reference (uncontrolled) canonical case is also included in (*a*) in grey broken lines for comparison. The mean advection term $\overline{A_{\omega_x\omega_x}}$ is negligible, and hence not displayed in the figures to avoid cluttering.

$\overline{T^2_{\omega_x\omega_x}}$ attains large values in the large amplitude STW cases. Recall that the turbulent transport terms correspond to the spatial redistribution of ω_x. These nonlinear terms neither create nor destroy enstrophy, but act to simply redistribute it in space. A movie is attached showing that the production and transport are closely associated next to the wall at approximately $y = 10$. The important point here is that the turbulent transport reaches large values comparable to the production (figure 10*b*). The direct consequence is the setup of excessive dissipation, which is almost twice the production near $y = 10$. As mentioned before, the turbulent transport term is negligible for the uncontrolled case (represented by broken lines in figure 10*a*). In the HWO case, it is relatively smaller, and it is restricted to $y < 10$ (figure 10*a*).

To partially resume, $\overline{\omega_x\omega_x}$ attains large values close to the wall compared with the uncontrolled case. For large amplitude STW, the near-wall variation from the location of local minima and the wall is almost flattened as a consequence of the lack of a velocity-pressure gradient term in the transport equation of spanwise turbulent intensity $\overline{ww}$. The streamwise vorticity layers in the STW cases with large amplitudes are simultaneously produced and transported in space by the turbulent diffusion, but at the same time dissipate quickly and hence do not contribute actively to the formation of the near-wall QSVs.

3.3. *Wall-normal enstrophy transport*

The peculiar behaviour of the $\partial w/\partial x$ and $\partial u/\partial z$ shear layers, constituting ω_y at large amplitude STW, will be discussed in § 5.3 in detail. The maximum of $\overline{\omega_y\omega_y}$ is at $y \approx 10$ in the uncontrolled flow, and is shifted towards $y \approx 20$ in the large amplitude STW

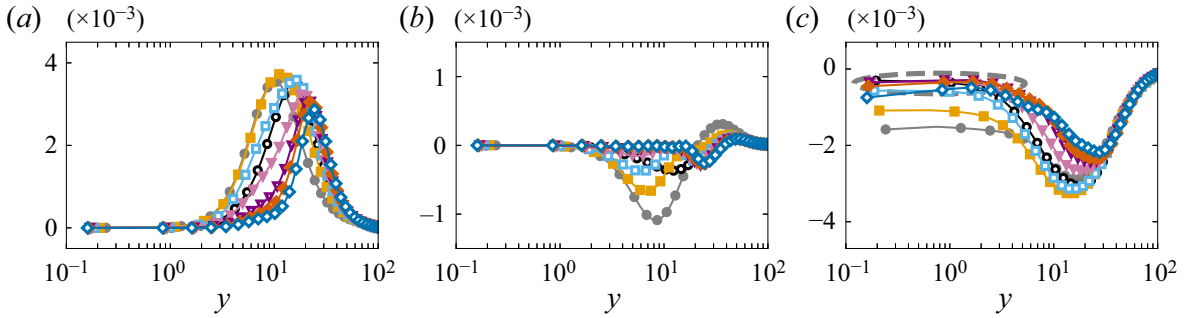

Figure 11. The main transport terms appearing in the transport equation of wall-normal turbulent enstrophy $\overline{\omega_y\omega_y}$: (*a*) the production term $\overline{P^4_{\omega_y\omega_y}}$; (*b*) the turbulent diffusion term $\overline{T^3_{\omega_y\omega_y}}$; and (*c*) the dissipation term $\overline{\epsilon_{\omega_y\omega_y}}$. Refer to table 1 for markers corresponding to different cases.

cases (figure 2*b*). Globally, all the transport terms in the transport equation of $\overline{\omega_y\omega_y}$ are weakened and shifted towards the middle of the buffer layer. This is clearly seen in the dissipation ($\overline{\epsilon_{\omega_y\omega_y}}$) profiles shown in figure 11(*c*). It shows also the suppression of ω_y activity in the viscous sublayer with $\overline{\epsilon_{\omega_y\omega_y}} \approx 0$ at the wall.

Most of the terms appearing in the production term of the wall-normal enstrophy (Appendix A) either vanish or are negligible. Among the first three terms involving the Stokes strain, the only term which differs from zero is $\overline{P^1_{\omega_y\omega_y}}$, but it is also found to be negligible (not shown). Hence, the major production of $\overline{\omega_y\omega_y}$ for the controlled cases still comes from the tilting of the wall-normal turbulent vorticity ω_y by the mean shear, i.e. the term $\overline{P^4_{\omega_y\omega_y}}$, as in the case of the uncontrolled flow. The maximum of the production term $\overline{P^4_{\omega_y\omega_y}}$ is shifted towards $y \approx 20$ in the large amplitude STW cases (figure 11*a*), which explains the shift in the maximum of $\overline{\omega_y\omega_y}$ in figure 2(*b*). The Stokes straining turbulent transport terms $\overline{T^1_{\omega_y\omega_y}} = -2\overline{\langle\omega_y u\rangle\partial\widetilde{\Omega}_y/\partial x}$ and $\overline{T^2_{\omega_y\omega_y}} = -2\overline{\langle\omega_y v\rangle\partial\widetilde{\Omega}_y/\partial y}$ are both nearly zero (not shown). The third turbulent transport term $\overline{T^3_{\omega_y\omega_y}} = -2\,\mathrm{d}\overline{\omega_y\omega_y v}/\mathrm{d}y$ has some importance at $y < 20$ in the uncontrolled flow, but becomes insignificant in the STW cases (figure 11*b*).

4. Reynolds shear stress invariants and similarity with the suppression of the near-wall turbulent activity

Umair *et al.* (2022) showed that both the streamwise and wall-normal turbulent intensities are strongly damped in the large amplitude STW cases, and that the response of the spanwise turbulent intensity is quite peculiar. In § 3 we highlighted the role of production terms appearing directly as a consequence of STW in the spanwise turbulent enstrophy transport in suppressing $\overline{\omega_z\omega_z}$ close to the wall when the imposed amplitude is large enough. Hence, the capital role of the large amplitude STW is to suppress the spanwise vorticity (and therefore streamwise velocity fluctuations) in the near-wall region. To assert this point, we conduct a few numerical experiments where the near-wall streamwise, wall-normal and spanwise velocity fluctuations, u, v, w, respectively, were explicitly damped up to a given wall-normal distance δ. The main idea is to see which cases collapse to the large amplitude STW cases on the anisotropy invariant maps. The effect of suppressing the turbulent activity in the viscous sublayer on the near-wall turbulence regeneration mechanism and drag reduction has already been investigated by Lee & Kim (2002).

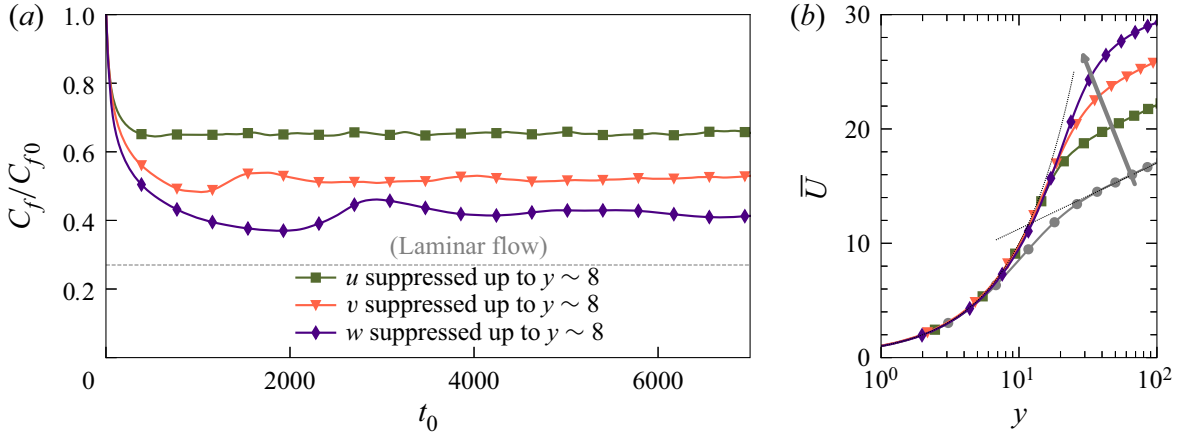

Figure 12. (*a*) Initial response of the skin friction coefficient C_f (normalized by the skin-friction coefficient of the reference uncontrolled flow C_{f0}) and (*b*) mean velocity profiles for the uncontrolled reference case and the artificially forced cases, respectively.

The generic algorithm used for the artificially forced cases is similar to Jiménez & Pinelli (1999), and can be written as

$$\zeta(y, t + \mathrm{d}t) = [\zeta(y, t) + \mathrm{d}t\, R(y)]F(y), \tag{4.1}$$

where ζ is either u, v or w, R is the appropriate right-hand side, and F is the filter function given as

$$F(y) = 0.5\{1 + \tanh[\alpha(y - \delta)]\}, \tag{4.2}$$

such that $F(y) \ll 1$ for $y \ll \delta$. Here, the parameter α controls the steepness of the filter function. For all the numerical experiments, the values of α and δ were kept fixed at 0.25 and 10, respectively, to suppress the fluctuations in the viscous sublayer and low buffer layer effectively up to $y \approx 8$. This was done deliberately to avoid strong damping of the fluctuations near the wall.

The initial response of the skin-friction coefficient and the resulting mean velocity profile are shown in figure 12. In agreement with Lee & Kim (2002), some moderate 30 % of drag reduction was achieved by suppressing u up to $y \approx 8$, while suppressing w up to the same wall-normal distance resulted in a significantly larger drag reduction margin of approximately 60 %. The near-wall mean velocity profile (figure 12*b*) agrees reasonably well with that of the typical drag reduction scenarios, exhibiting a linear behaviour in the viscous sublayer and an upward shift in the region beyond.

Figure 13(*a*) shows response of the turbulent enstrophy profiles resulting from u (or ω_z) suppression in the low buffer layer. Near the wall, ω_z can be approximated as $\omega_z \approx -\partial u/\partial y$, and can be rewritten as $u \approx -y\omega_z(y = 0)$. Therefore, suppressing u is effectively similar to suppressing ω_z near the wall. This is indeed clear by looking at the profile of $\overline{\omega_z\omega_z}$ in figure 13(*a*), where $\overline{\omega_z\omega_z}$ is completely suppressed up to $y \approx 8$. A striking correspondence in the near-wall profile of $\overline{\omega_z\omega_z}$ can be seen with those of the STW controlled cases of $A \geq 0.75$ shown in figure 2(*c*), suggesting that the major effect of the STW is similar to the artificial suppression of the near-wall streaks up to the low buffer layer. Note that unlike STW control, artificial suppression of u close to the wall also leads to the annihilation of $\overline{\omega_y\omega_y}$ up to $y \approx 8$, as in the case of canonical turbulent channel flows ω_y is dominated by $\partial u/\partial z$. In contrast, Umair *et al.* (2022) have shown that in the large amplitude STW controlled cases, triangular wavy patterns of $\partial w/\partial x$ shear layers

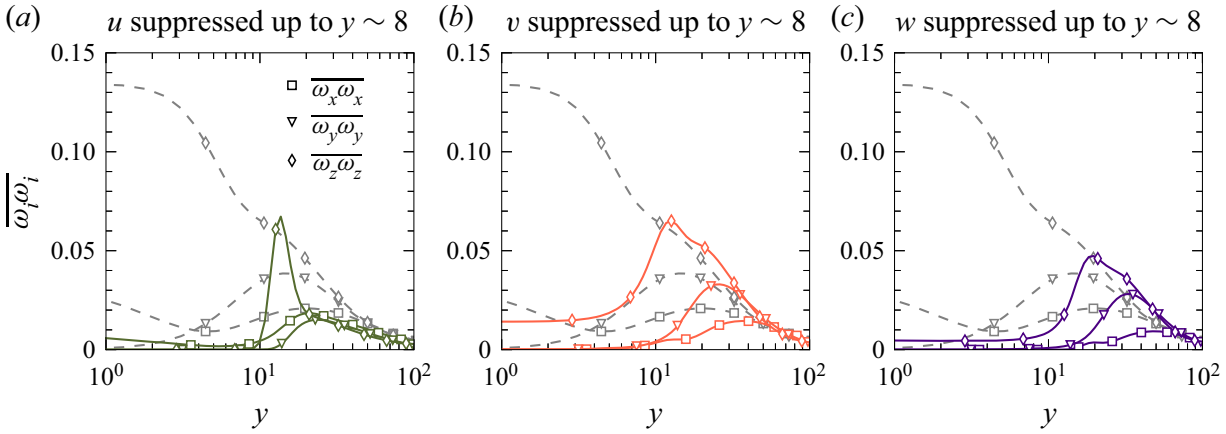

Figure 13. Mean profiles of turbulent enstrophy for (*a*) streamwise fluctuating field (u), (*b*) wall-normal fluctuating field (v) and (*c*) spanwise fluctuating field (w) suppression case, respectively. Note that all the profiles are scaled with the local friction velocities of the forced cases. The dashed lines represent the profiles for the uncontrolled flow.

start to emerge. The contribution of $\partial w/\partial x$ to ω_y thus becomes increasingly significant, reaching approximately 10 times that of $\partial u/\partial z$ very close to the wall (not shown). This is one of the strong signatures of large amplitude STW that are essentially absent in both the HWO control and the canonical turbulent channel flows, and hence point towards strong structural alterations in the near-wall turbulence. These aspects will be discussed in more detail in the subsequent sections. Note that the removal of the spanwise vorticity in the viscous and low buffer layers do not modify the intensity and the peak location of the streamwise vorticity (figure 13*a*). However, the response of the $\overline{\omega_x\omega_x}$ intensity (figure 2*a*) under large amplitude STW is entirely different. The maximum of $\overline{\omega_x\omega_x}$ increases with the imposed amplitude, and there is curiously a negative drift of the streamwise vorticity layers. This is a consequence of the specific response of the near-wall turbulence to the large amplitude STW.

We now return to the next main point of our concern, namely the anisotropy invariants. The wall-bounded turbulent flows are characterized by the presence of organized motions, which reflects a high degree of turbulence anisotropy in the near-wall region. The anisotropy invariant map (AIM) introduced by Lumley & Newman (1977) provides a convenient way to visualize the anisotropy of the turbulent velocity fluctuations through the Reynolds stress anisotropy tensor

$$a_{ij} = \frac{\overline{u_i u_j}}{\overline{u_i u_i}} - \frac{1}{3}\delta_{ij}, \tag{4.3}$$

where, $\overline{u_i u_i}$ is twice the turbulent kinetic energy, and δ_{ij} represents the Kronecker delta (Pope 2000; Busse & Sandham 2012). A plot of the second and third scalar invariants of the tensor a_{ij}, defined as $II = a_{ij}a_{ji}$, and $III = a_{ij}a_{jk}a_{ki}$ (Frohnapfel *et al.* 2007), constitutes the well celebrated Lumley triangle or AIM within which all the realizable turbulent states must lie. The II invariant characterizes the degree of anisotropy, while the III invariant identifies its type. The left-hand and right-hand curve corresponds to the axisymmetric disc-like (straining) and axisymmetric rod-like (expansion) states, and are defined by $II = \pm 3/2(4|III|/3)^{2/3}$. The two-component (2C) state is defined by the straight line $II = 2/9 + 2III$. The three corners of the Lumley triangle or AIM correspond to three different limiting states. The left-hand corner corresponds to the isotropic two-component state, the corner on the right-hand side corresponds to the one-component (1C) axisymmetric state,

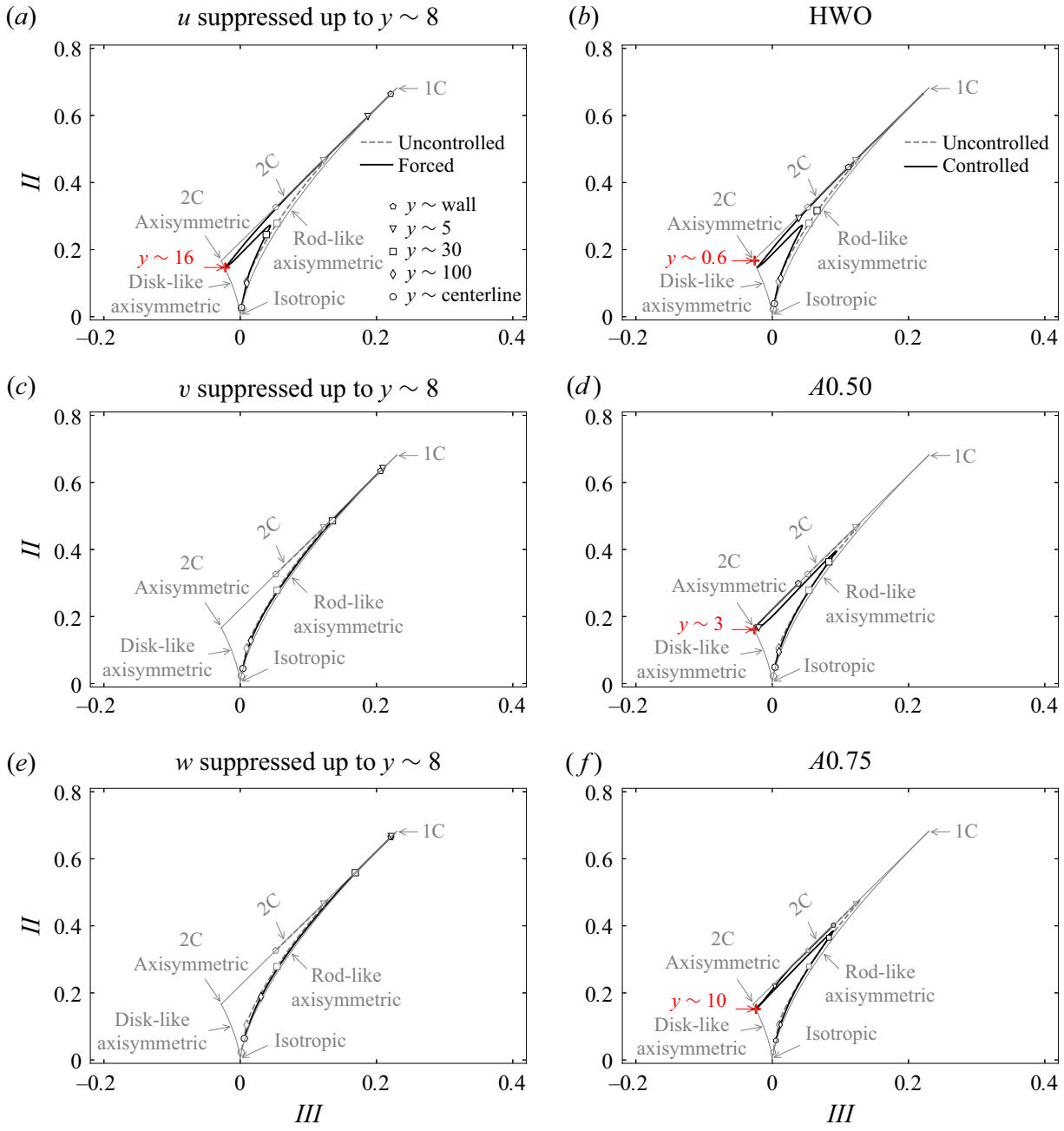

Figure 14. Invariant maps for (*a*,*c*,*e*) forced cases and (*b*,*d*,*f*) controlled cases.

while the bottom most corner of the triangle at $II = III = 0$ corresponds to the isotropic turbulence state.

In the canonical turbulent channel flows, the trajectory of II and III invariants, shown in figure 14 with broken grey lines, lie close to the 2C state next to the wall, as $\overline{vv}$ is much weaker in comparison with $\overline{uu}$ and $\overline{ww}$. Away from the wall, in the viscous sublayer, the anisotropy increases reaching a maximum at $y \approx 8$ with $\overline{uu}$ larger than $\overline{vv}$ and $\overline{ww}$, pushing the trajectory towards the rod-like axisymmetric expansion state, in agreement with Moser, Kim & Mansour (1999). Farther away from this region with increasing distance from the wall, the turbulence becomes more and more isotropic, ultimately acquiring the isotropic state at the centreline.

Figure 14(*a*) shows the AIM for the case where ω_z (or u) is artificially suppressed. The AIMs of STW cases of large amplitudes ($A > 0.5$) are surprisingly similar. Figure 14(*f*) shows, for instance, the AIM for *A*0.75 case. Similar results are obtained for *A*0.95 and

*A*1.25 cases, hence not shown. The AIM trajectories are closely similar in both the large amplitude STW cases and ω_z (or u) suppressed case. In both cases, the trajectories are pushed rapidly from 2C state near the wall towards the disk-like axisymmetric contraction state in the buffer layer. This is mainly due to the annihilation of the near-wall streamwise turbulent intensity ($\overline{uu}$), which is the largest component in canonical turbulent channel flows. It is important to mention that this terminology is strictly related to the shape of the Reynolds stress tensor, which in no way should be confused with the shapes of the turbulent eddies. This point is clarified in detail by Simonsen & Krogstad (2005). The stress tensor has two equal positive and one negative eigenvalue in the disk-like axisymmetric state, which is opposite to the rod-like axisymmetric state. The AIM trajectory approaches the isotropic state transiting through the disk-like axisymmetry from a reduced anisotropy state and catches the trajectory of the canonical turbulent channel flow at $y > 30$.

Umair *et al.* (2022) have shown that the structural modification brought to the wall turbulence by HWO and STW are similar up to $A < 0.50$, and the effects specific to STW appear when the imposed amplitude is increased beyond $A > 0.50$. The AIM analysis provides a nice additional proof, strengthening their arguments. Figure 14(*b*,*d*) shows the AIMs of STW case *A*0.50 and HWO, respectively. Both AIMs are quite similar, but differ from the *A*0.75 case. The trajectory changes rapidly from 2C state at the wall to the 2C axisymmetric state, but then stay relatively away from the isotropic state without touching the disk-like axisymmetric curve.

Frohnapfel *et al.* (2007) considered the drag reduced flow from an anisotropy invariants point of view. Their analyses include the effects of additives, riblets, strong acceleration of boundary layers, and some forced boundary conditions. In their forced cases, they modify the boundary conditions to force near-wall turbulence to tend towards an axisymmetric state by imposing the spanwise fluctuating velocity to follow the wall-normal fluctuations. They obtain a DR of approximately 32 %, and conclude that the anisotropy of the turbulence increases towards the 1C limit in the near-wall region. Curiously, a closer look at their figure 9(*b*) reveals that their forcing also results in a significant suppression of the spanwise fluctuations. Artificial suppression of the wall-normal and spanwise fluctuating velocity field in the viscous and low buffer layers lead indeed to a scenario similar to their suggestion. This is clearly seen in figure 14(*e*) that shows the AIM when w is suppressed up to $y \approx 8$, resulting in DR margin of approximately 60 % in agreement with Lee & Kim (2002). However, in the HWO and STW cases the trend in the AIM trajectory is entirely opposite, with a tendency towards isotropy, especially in STW of amplitude $A > 0.50$. This shows that DR doesn't necessarily lead to increased anisotropy.

5. Effect on near-wall structures

5.1. *Drifts of the near-wall QSVs*

Quasistreamwise vortices are a prominent feature of the near-wall turbulent flow field. The QSVs have been recognized to play a significant role in the regeneration cycle of near-wall turbulence (Hamilton, Kim & Waleffe 1995). They facilitate the exchange of momentum and energy in the near-wall region, and contribute significantly to the generation of Reynolds shear-stress by inducing ejection and sweep events.

Earlier studies have reported a drastic suppression of the near-wall quasistreamwise vortices due to the spanwise wall oscillations control. Yakeno, Hasegawa & Kasagi (2014)

studied the effect of homogeneous spanwise wall oscillations on the structural modifications of QSVs and report that the wall-normal location of the peak population density of QSVs is not affected by the presence of control. Extending their analysis to the STW control, Gallorini, Quadrio & Gatti (2022) also report little to no shift in the position of QSVs. However, their analysis includes only one STW case that produces a DR margin of approximately 36 %. Umair *et al.* (2022), on the other hand, point out that the QSVs reach their full maturity well above $y = 20$ for the large amplitude STW. This point, indeed, needs to be clarified whether there is a shift in the position of the near-wall QSVs because of the imposed control.

To clarify this point, we examine the effect of STW actuation on the near-wall QSVs, focusing on detecting the drift (Δd_s) in QSVs because of the control, if any. We employ the classical eduction scheme proposed by Jeong *et al.* (1997) to detect the near-wall QSVs. First, we detect the vortex cores where the value of $\lambda_2 \leq -0.02$ directly from the 3-D instantaneous velocity fields, where λ_2 being the second-largest eigenvalue of the symmetric and antisymmetric parts of the velocity gradient tensor. Then we identify and count only the structures that have streamwise extent greater than or equal to 150 wall units with inclination and titling angles in the range -30° to $+30^\circ$, respectively. The centre of each individual structure is obtained by locating the point where λ_2 attains its local minimum value within the structure. For all the cases studied here, we analysed an ensemble of at least 50 independent full 3-D instantaneous fields separated by roughly one full-through time unit ($20h/U_c$). Since the criteria we chose to select the relevant QSVs is quite strict, as a consequence only few structures qualify to be considered as relevant candidates. For example, in the uncontrolled case, only approximately 90 structures met the imposed criteria in one snapshot of the instantaneous 3-D field. Figure 15 shows the λ_2 structures for a few of the cases studied here, and figure 16 shows their respective wall-normal distribution of the number of vortices, normalized by the maximum number of vortices.

For the canonical turbulent channel flow, the majority of the mature QSVs are located at $y \approx 24$, which is in agreement with Jeong *et al.* (1997). For the STW cases, however, we observe a systematic drift of QSVs away from the wall (figure 16). The drift is approximately six wall units for the $A0.50$ case, and 10 wall units for the $A1.25$ case. This is in disagreement with Gallorini *et al.* (2022). These authors consider a single DR case with control parameters different from us. The closest case we have to them in terms of DR is $A0.30$ for which we observe a drift of approximately 4.5 wall units, while they report little to no drift. This discrepancy is plausibly coming from the criteria used to select the vortices. There are two points to consider: first, a 'vortex' has to be a 'developed compact object' of sufficient length to exist and be dynamically significant (mature). In the present work, we exclude vortices with streamwise extents shorter than 150 wall units in the same way as in Jeong *et al.* (1997), whereas Gallorini *et al.* (2022) use rather a lower threshold length of 50 wall units, which means in their case a significant number of the detected vortices are immature low buffer layer structures. That indeed results in a twice smaller tilt angle of the structures they detect compared with Jeong *et al.* (1997). Second, in their controlled case they 'opted to discard the same percentage of candidate vortices considered in the reference case, to avoid the assumption that control does not affect the length of QSV', but forcing may affect the related probability density functions, and rejecting the same percentage as in the reference case may induce some bias. Whereas, in the present work, the criteria used to select the mature vortices is unique and consistent for all the cases. The capacity of near-wall QSVs to regenerate new structures is proportional to their intensity and inversely proportional to the square of their distances (d_s) from the wall,

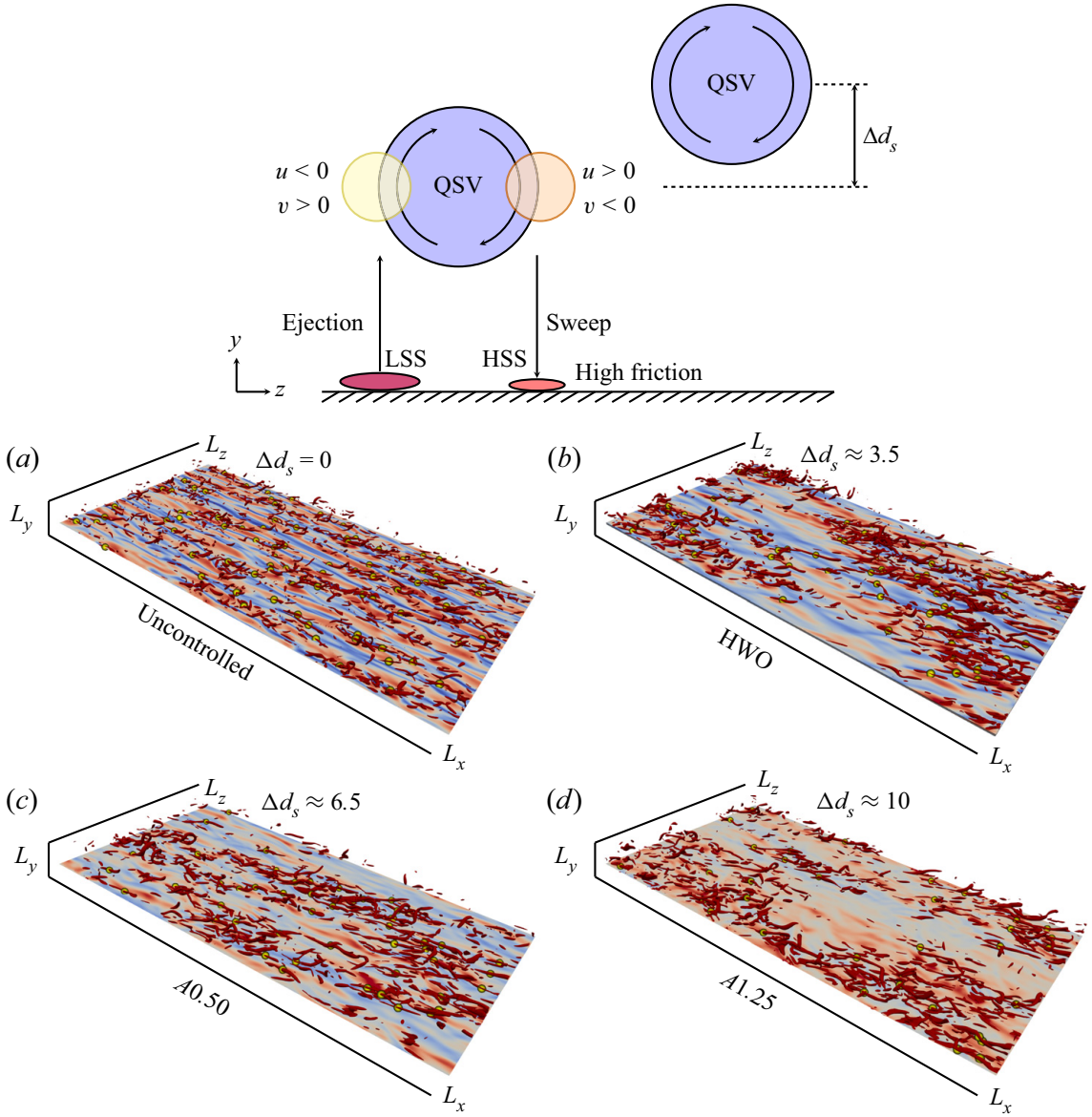

Figure 15. Quasistreamwise vortical structures identified using $\lambda_2 = -0.02$ along with the instantaneous field of streamwise velocity fluctuations u (red, $u > 0$; blue, $u < 0$) on a wall-parallel plane at $y = 15$ for (*a*) uncontrolled, (*b*) HWO, (*c*) *A*0.50 and (*d*) *A*1.25 case, respectively. The centres of the active QSVs educed using the criteria mentioned in § 5.1 are marked with yellow dots. The schematic diagram on the top shows the drift (Δd_s) in the QSVs with respect to the canonical uncontrolled case. (HSS: high-speed streaks; LSS: low-speed streaks.)

as discussed in the following subsection. In the drag reduction scenarios, one would expect an increase in d_s, as observed in the present study. It may, however, happen that d_s remains unaffected, but the intensity of the structures or their population density decreases.

In the subsection below, we estimate the drift directly from the instantaneous visualizations of the near-wall velocity streaks, and show that the drifts estimated from these two independent methods are in close agreement. Moreover, we show that the drift we observe combined with the rest of the results give us a reasonable estimate of the DR margin, thus increasing the quality of these results.

5.2. *Near-wall streaks*

The drift Δd_s of the active streamwise ω_x vorticity layers decreases the drag according to the conceptual model of Jiménez (1994) and also discussed in some detail in Tardu (1995).

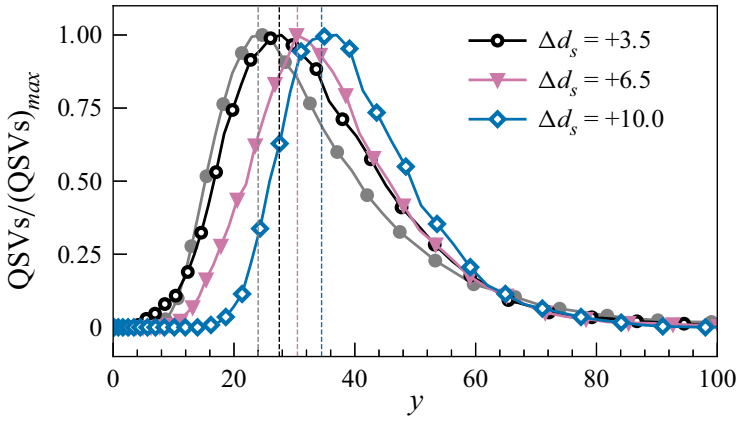

Figure 16. The distribution of QSVs for the uncontrolled, HWO, $A0.50$ and $A1.25$ cases, respectively. The colours and markers in the plot correspond to those presented in figure 2.

By active ω_x layers, we mean those layers from which the Reynolds shear stress producing QSVs emerge. Given the complexity of the wall response to the large amplitude STW discussed before, it is difficult to directly determine the drift. One somewhat qualitative, yet objective, way is to investigate the near-wall streaks in order to estimate the drift. The near-wall streaks in the canonical turbulent wall flows are the footprints of the QSVs, and are at best detected by the $\partial u/\partial z$ shear layers near the wall (Tardu 2022). The $\partial u/\partial z$ shear layers are the thin wall-normal turbulent vorticity ω_y layers separating the low- and high-speed streaks. Figure 17 shows a snapshot of $\partial u/\partial z$ in the uncontrolled, HWO and STW $A1.25$ case, respectively. The near-wall long streaks in the canonical flow are already detectable at the edge of the viscous sublayer with a streak spacing of approximately 80 wall units, in agreement with previously published results (Tardu 2014). The footprints of QSVs are weak at $y = 5$ under HWO, and they are clearly discernible only at $y \approx 12$, with slightly larger spacing of approximately 100 wall units.

On comparing figure 17(o,k), we see that in the case of large amplitude STW ($A1.25$), we have to go even farther in the buffer layer, towards $y \approx 20$, to detect the near-wall streaks of reasonable coherence. Let us suppose that the drift Δd_s in coherent $\partial u/\partial z$ layers can be related to the drift Δd_s of the active streamwise vorticity layers from which Reynolds shear stress producing eddies emanate. Then figure 17 suggests that $\Delta d_s \approx 7$ in the HWO case, because the distribution of $\partial u/\partial z$ shear layers at $y \approx 12$ under HWO becomes comparable to that of the uncontrolled flow at $y = 5$. Similarly, comparing figure 17(l,a) suggests that $\Delta d_s \approx 10$ for STW $A1.25$ case. These observations are in agreement with the previous discussion based on figure 16.

The flow is turbulent in all the controlled cases here, even though the laminar limit is closely approached for the $A1.25$ case. Thus, we have on purpose chosen to use the local wall units to scale the turbulent quantities, the main aim being here is to determine the proper structural modifications. All the quantities scaled by the local inner variables can easily be transformed to the quantities scaled with respect to those based on the friction velocity of the uncontrolled case. Figure 18(a) shows the wall-normal distribution of the streamwise turbulent enstrophy $\overline{\omega_x\omega_{x0}}$ and its main production term, $\overline{P^4_{\omega_x\omega_{x0}}}$ in figure 18(b), both scaled with the wall units based on the friction velocity of the uncontrolled flow. It is seen that $\overline{\omega_x\omega_{x0}}$ decreases systematically in the controlled cases, while the peak location y_0 is not significantly altered and is at approximately 20 wall units.

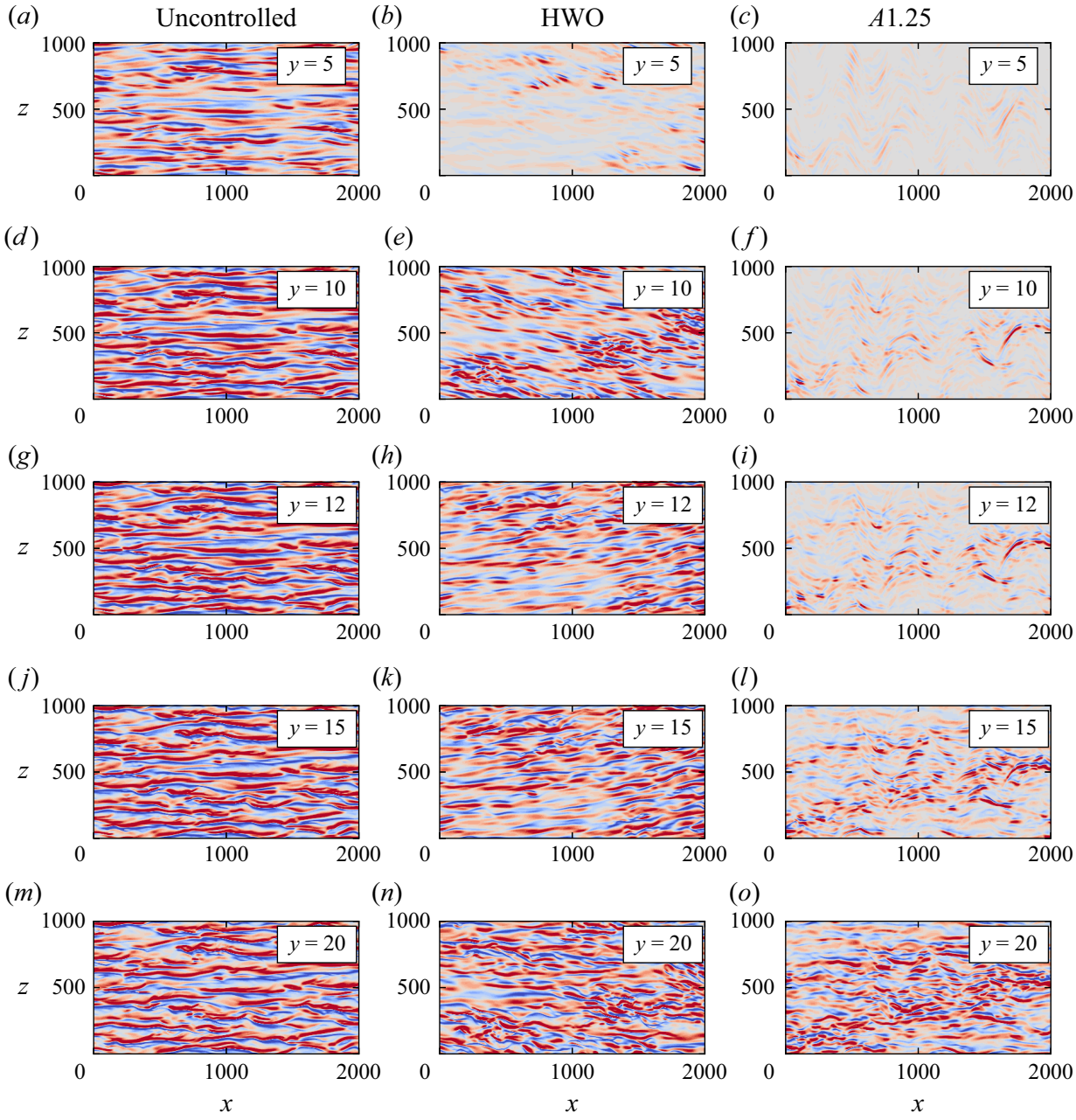

Figure 17. Instantaneous fields of $\partial u/\partial z$ shear layers at $y = 5$, 10, 12, 15 and 20 for the uncontrolled, HWO and $A1.25$ case, respectively. The blue colour represents the region where $\partial u/\partial z < 0$, while the red colour represents the region where $\partial u/\partial z > 0$. The contours are in the range -0.2 to $+0.2$.

Orlandi & Jiménez (1994) relates the location d_s and intensity of the QSVs to the wall shear by

$$\tau_w^* \propto \left(\frac{\Gamma^*}{\nu d_s^{*2}}\right)^{1/2}, \tag{5.1}$$

in dimensional units. In this relation $\Gamma^* = \pi R^{*2}\omega_x^*$ is the mean circulation of the QSVs, d_s^* is the distance to the wall and R is their radius. The qualifier '$*$' here represents quantities in physical dimensional units. This approximate relationship is obtained through a physical argument based on the stagnation flow induced by the QSVs. It gives only a qualitative description of the effect of QSVs on the wall shear, but has the merit to relate intensity and the stand-off distance of the coherent eddies on τ_w. According to (5.1), the rate of

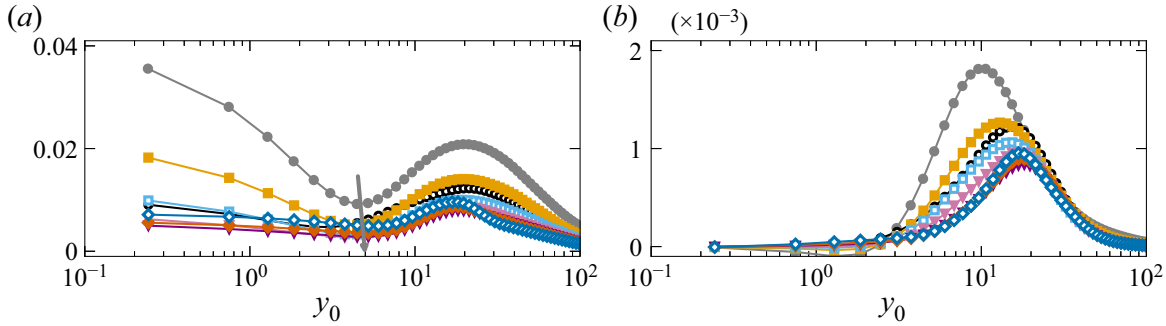

Figure 18. Wall-normal distribution of the (*a*) streamwise turbulent enstrophy $\overline{\omega_x\omega_{x0}}$, and (*b*) its main production term $\overline{P^4_{\omega_x\omega_{x0}}}$, scaled with the wall units based on the friction velocity of the uncontrolled flow. Refer to table 1 for markers corresponding to different cases.

change of $\Delta\tau_{w0}$ can be related to

$$\frac{\Delta\tau_{w0}}{\tau_{w0}} = \frac{1}{2}\frac{\Delta\Gamma_0}{\Gamma_0} - \frac{\Delta d_{s0}}{d_{s0}}, \tag{5.2}$$

when adequately scaled with the wall units based on the friction velocity of the uncontrolled flow.

One of the observations emerging from figure 17 and the λ_2 structures, shown before in figure 15, is that the radius of the QSVs (scaled in local wall units), in a rough sense, remains unaffected in all the controlled cases. Using $R =$ constant and $\overline{\omega_x\omega_{x0}}$ profiles (figure 18*a*), we estimated 42 % of DR for $A0.50$ case from (5.2), which is in close agreement with the value reported in table 1. However, (5.2) gives 80 % of drag reduction at the largest imposed amplitude $A1.25$ case, which is approximately 30 % overestimated. In any case, the $\Delta\Gamma_0/\Gamma_0$ term is found to contribute only 20 % to the DR. Consequently, the drift $\Delta d_{s0}/d_{s0}$ plays a critical role in the drag reduction mechanism investigated here.

Duggleby, Ball & Paul (2007) examined the effect of spanwise wall oscillations on the dynamics of the near-wall turbulent structures in a turbulent pipe flow using Karhunen–Loève decomposition. They argued that the main effect of the Stokes layer generated by spanwise wall oscillations is to push the structures away from the wall into the region of higher mean velocity by creating a zone where turbulent structures cannot form. As a consequence, the structures are advected faster with less time to interact with the roll modes to transfer energy, resulting in their shorter lifetime, and hence damping of the Reynolds shear stress generating bursting events. Our finding strengthens the arguments presented by them and is in full concordance with their interpretation that although drag reduction results in the decorrelation of the near-wall streaks and the QSVs, but it is the lifting of the turbulent structures away from the wall by the Stokes layer induced by the spanwise wall oscillations that results in drag reduction.

5.3. *Shear layers of spanwise fluctuating velocity field*

The spanwise fluctuating velocity field plays a prominent role in the near-wall turbulence. Even though they do not implicitly contribute to the production of turbulent kinetic energy, they are, however, linked to the Reynolds shear stress producing events, and hence intrinsically linked to the characteristics of the near-wall coherent structures (Tardu 2016). The connection between the spanwise fluctuating velocity field and the intense Reynolds shear stress generating events become clear if one considers the classical

hairpin and horseshoe vortex paradigm. The spanwise fluctuating velocity field is nearly zero between the legs of the hairpin vortices, where the intense sweep or ejection events occur. As mentioned previously, the main production of the turbulent streamwise enstrophy comes from the tilting of the wall-normal vorticity by the mean shear, which reduces to $-2\overline{\omega_x(\partial w/\partial x)}(\mathrm{d}\overline{U}/\mathrm{d}y)$. Hence, the $\partial w/\partial x$ shear layers play a crucial role in the generation of ω_x prior to their roll up into QSVs (Brooke & Hanratty 1993; Tardu 2008, 2014, 2016). Hence, as we saw earlier, the suppression of the spanwise velocity fluctuations in the viscous sublayer results in significantly larger drag reduction compared with the suppression of the streamwise or wall-normal velocity fluctuations.

In the canonical turbulent channel flow, the $\partial w/\partial x$ shear layers are spotty and slightly stretched in the spanwise direction, as shown in figure 19(*a*). Using the multiscale approach, Tardu (2022) showed that some of the $\partial w/\partial x$ shear layers may appear as spanwise streaks. As seen in figure 19(*e*), the tilting of these shear layers into identifiable elongated ω_x layers already set up at $y = 10$. The morphology of $\partial w/\partial x$ shear layers under the large amplitude STW is strikingly different. The $\partial w/\partial x > 0$ and $\partial w/\partial x < 0$ are organized into Λ-shaped Christmas-tree-like structures resulting from a direct effect of STW (figure 19*d*). The titled ω_x layers are consequently also Λ-shaped, and they are being elongated into streamwise structures (figure 19*h*). It is necessary to go farther away from the wall towards $y \approx 30$ to identify the elongated streamwise vorticity layers (figure 20*a*,*b*). It is also roughly at this position that the contours of $\omega_x \partial w/\partial x$, related to the major production term $P^4_{\omega_x\omega_x}$, appear as long coherent streaky-like structures (figure 20*c*). The ω_x layers at $y = 10$ for $A0.50$ case are organized more clearly into streamwise elongated structures compared with the $A1.25$ case. They achieve their conventional morphology at $y = 20$, earlier than the $A1.25$ case.

The flow under STW control at large amplitudes develops its own structures in the low buffer layer. In the case of HWO, the $\partial w/\partial x$ shear layers are inclined in the streamwise direction, but do not exhibit Λ-shaped structures that are specific to the STW control. The origin of these structures is tricky to understand. The $\partial w/\partial x$ patterns next to the wall, in the large amplitude STW case, are too regular to be considered as induced by the random turbulence phenomenon. They are indeed related to the large $\partial \widetilde{W}/\partial x$ modulation occurring at the wall. Consider the instantaneous transport equation for the streamwise gradient of the instantaneous spanwise velocity field $(\partial W/\partial x)$ given as

$$\frac{\mathrm{D}}{\mathrm{D}t}\frac{\partial W}{\partial x} = \frac{\partial W}{\partial x}\frac{\partial V}{\partial y} - \frac{\partial V}{\partial x}\frac{\partial W}{\partial y} - \frac{\partial^2 P}{\partial x \partial z} + \nu\nabla^2\frac{\partial W}{\partial x}. \tag{5.3}$$

The complete analysis of $(\mathrm{D}/\mathrm{D}t)(\partial w/\partial x)(\partial w/\partial x)$, which contains 10 terms on the right-hand side (not shown), is complex, especially, because of the local pressure term appearing on the right-hand side of (5.3), and hence, is out of scope of the present investigation. After applying triple decomposition, several other terms appear on the right-hand side of (5.3), among which the term $(\partial \widetilde{W}/\partial x)(\partial v/\partial y)$, which represents the stretching of the Stokes shear $\partial \widetilde{W}/\partial x$ by the local $\partial v/\partial y$, is negligible at $y > 5$, but reaches large values near the wall at $y \approx 0$. Figure 21(*a*,*b*) compares the $(\partial \widetilde{W}/\partial x)(\partial v/\partial y)$ contours with those of $\partial w/\partial x$ layers at $y = 2.5$, respectively. A striking similarity emerges from these two figures. The Stokes shear $\partial \widetilde{W}/\partial x$ induces Λ-shaped $\partial w/\partial x$ next to the wall. The latter are further stretched, intensified and extended to the viscous sublayer. One quick way to estimate the quantitative importance of $(\partial \widetilde{W}/\partial x)(\partial v/\partial y)$ is to compare its r.m.s. value with the r.m.s. of $\partial w/\partial x$. A similar procedure has been conducted, for instance, by Brooke & Hanratty (1993) in the local transport equation $\mathrm{D}\omega_x/\mathrm{D}t$. Figure 21(*d*) shows that the r.m.s. value of $(\partial \widetilde{W}/\partial x)(\partial v/\partial y)$ is as large as 30 % of the r.m.s. of $\partial w/\partial x$ at

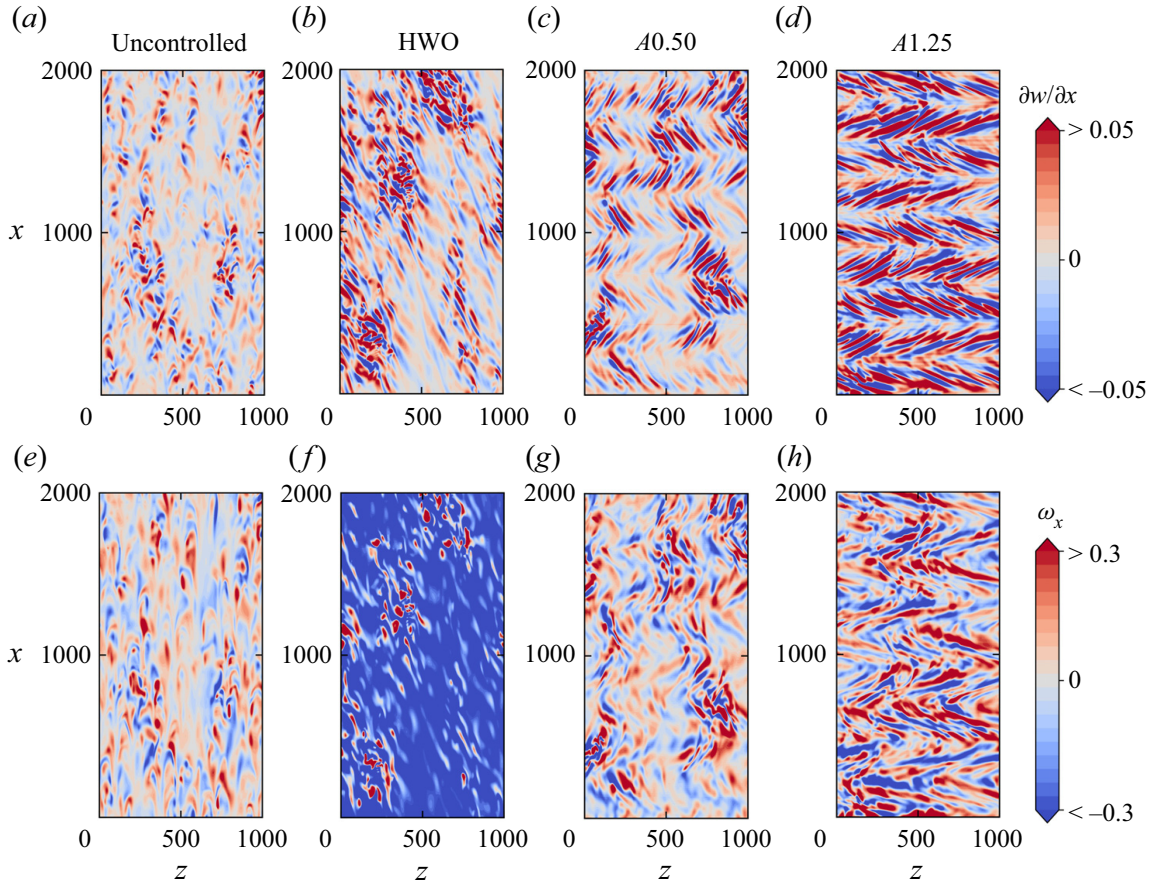

Figure 19. Instantaneous field of $\partial w/\partial x$ shear layers and ω_x layers at $y = 10$ for the uncontrolled, HWO, $A0.50$ and $A1.25$ case, respectively.

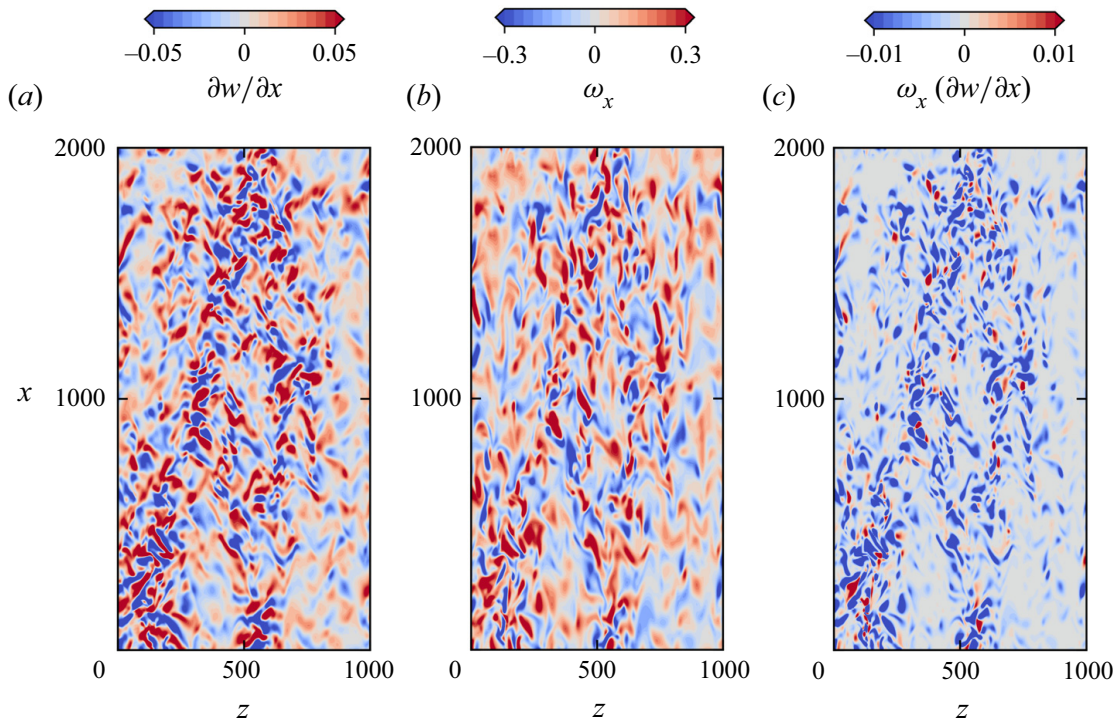

Figure 20. Instantaneous field of (*a*) $\partial w/\partial x$ shear layers, (*b*) ω_x layers and (*c*) $\omega_x \partial w/\partial x$ layers at $y = 30$ for $A1.25$ case.

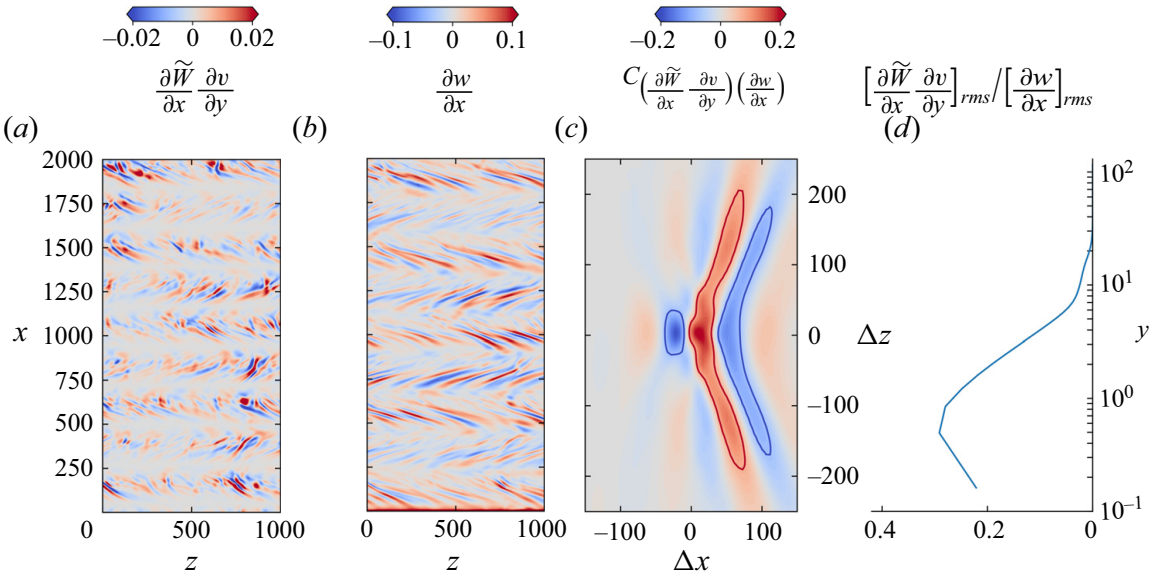

Figure 21. Instantaneous field of (a) $(\partial\widetilde{W}/\partial x)(\partial v/\partial y)$ shear layers, (b) $\partial w/\partial x$ layers, (c) their cross-correlation coefficient at $y = 2.5$ and (d) the wall-normal distribution of the ratio of their root-mean-square (r.m.s.) values for $A1.25$ case.

$y \approx 1$, and progressively disappears towards the edge of the viscous sublayer. Figure 21(c) shows the normalized cross-correlation coefficient C between $(\partial\widetilde{W}/\partial x)(\partial v/\partial y)$ and $\partial w/\partial x$ at $y = 2.5$. We observe specific cross-correlation patterns that are somewhat similar to the patterns observed in the autocorrelations of $(\partial\widetilde{W}/\partial x)(\partial v/\partial y)$ and $\partial w/\partial x$ (not shown). The cross-correlations reach values as large as 0.2, which is far from being negligible.

From the visualizations presented in figure 15, it is clear that the classical topological features of the QSVs are only depicted at $y > 20$ for large amplitude STW. Consequently, the peculiar Λ-shaped $\partial w/\partial x$ shear layers do not roll up into QSVs. Therefore, there is a drift of the active ω_x layers that lead to Reynolds shear-stress producing eddies at large amplitude STW.

6. Conclusions

In this study, we examined the effect of spanwise wall oscillations in the form of STW on the vorticity transport mechanism in a turbulent channel flow at Reynolds number $Re_\tau = 180$. The frequency and wavelength of the imposed travelling wave were kept fixed, and only the amplitude was varied to examine the direct effect arising because of travelling-wave-like wall oscillations. At the largest amplitude studied here, the flow almost reached the relaminarization limit. Such a significant level of drag reduction cannot be achieved in case of HWO.

The wall-normal and spanwise turbulent enstrophy also show a significant reduction in their intensity, the latter almost vanishes in the viscous sublayer for large amplitudes STW. The contribution of the $\partial w/\partial x$ with respect to $\partial u/\partial z$ becomes increasingly important next to the wall for large amplitude STW. However, the attenuation of the wall-normal turbulent enstrophy is of subordinate importance compared with the spanwise turbulent enstrophy. This is also evident from the numerical experiments conducted in § 4, which demonstrates that suppressing the spanwise vorticity near the wall results also in a significant attenuation of ω_y. The streamwise turbulent enstrophy shows a moderate increase in its intensity, and

its near-wall variation is almost flattened as a consequence of a lack of a velocity-pressure gradient term in the transport equation of spanwise turbulent intensity, as explained in Umair *et al.* (2022).

The main production term for the spanwise turbulent enstrophy is shifted in the middle of the buffer layer in large amplitude STW cases. The phasewise plots of the production terms, originating due to forcing, reveal that there is a destruction of the spanwise vorticity by the direct straining through $\partial\widetilde{W}/\partial x$, especially next to the wall. This particular effect is obviously absent in the case of HWO. Globally, STW of large amplitudes attenuates the production by Stokes straining effects and pushes the profiles towards the buffer layer.

For the streamwise turbulent enstrophy, the main production still originates from the tilting of the wall-normal vorticity by the mean shear, as in the case of uncontrolled flow. The location of the peak remains roughly at the same wall-normal location between $y =$ 10–12.5 for all the cases. Two additional turbulent diffusion terms emerge in the transport equation of the streamwise turbulent enstrophy that are directly related to the forcing. The second term attains large values comparable to the total production term in the large amplitude STW cases. However, these terms do not essentially create or destroy the enstrophy, but act to redistribute it in space. This is clearly evident in the movie attached as a supplementary material available at https://doi.org/10.1017/jfm.2023.478. Consequently, the level of dissipation gets enhanced to almost twice of the production at roughly $y = 10$. Hence, the streamwise vorticity layers in the large amplitude STW cases are produced and transported in the space simultaneously, but also get dissipated quickly. As a consequence, these near-wall streamwise vorticity layers do not actively contribute in the regeneration mechanism of near-wall QSVs.

The artificial suppression of the near-wall streamwise fluctuating velocity field results in a significantly large drag reduction margin. A striking correspondence in the near-wall profile of the spanwise turbulent enstrophy can be seen with those of the STW controlled cases of large amplitudes, suggesting that the major effect of the STW is similar to the artificial suppression of the near-wall streaks up to the low buffer layer. This is clearly represented in the AIMs which show a striking resemblance to the large amplitude STW cases. In both cases, the trajectories are pushed rapidly from the 2C state near the wall towards the disk-like axisymmetric contraction state in the buffer layer.

The near-wall QSVs show a systematic drift away from the wall. It was calculated using two procedures: by identifying the location where QSVs are mostly populated, and also by looking at the instantaneous visualizations of the near-wall streaks. Both procedures give roughly the same drift. The observed drift combined with the rest of the results gives a reasonable estimate of the DR margin.

The spanwise fluctuating velocity field which plays a prominent role in the near-wall turbulence shows interesting features. The flow is nearly transitional at the largest imposed amplitude STW, wherein the buffer layer develops its own structures induced by the Stokes straining $\partial\widetilde{W}/\partial x$ and thus becomes entirely uncoupled with the rest of the flow. The $\partial w/\partial x$ shear layers, which are spotty and slightly stretched in the spanwise direction in the case of uncontrolled flow, begin to form coherent Λ-shaped patterns. However, these structures are too regular to be considered induced by the random turbulence phenomenon. The analysis of the instantaneous transport equation of $\partial W/\partial x$ shear layers show that these patterns are directly connected to the Stokes strain $\partial\widetilde{W}/\partial x$. These shear layers, however, do not play any active role in the generation of near-wall QSVs. Such a scenario is rarely observed in wall-bounded turbulence.

Supplementary movie. Supplementary movie is available at https://doi.org/10.1017/jfm.2023.478.

Acknowledgements. The simulations of the controlled cases were performed using the GRICAD infrastructure (https://gricad.univ-grenoble-alpes.fr), which is supported by Grenoble research communities. The simulations of the uncontrolled case were performed using the Froggy platform of the GRICAD infrastructure (https://gricad.univ-grenoble-alpes.fr), which is supported by the Région Auvergne-Rhóne-Alpes (GRANT CPER07_13 CIRA) and the Agence Nationale de la Recherche (Equip@Meso project reference no. ANR-10-EQPX-29-01 of the programme Investissements d'Avenir).

Funding. This research received no specific grant from any funding agency, commercial or not-for-profit sectors.

Declaration of interests. The authors report no conflict of interest.

Data availability statement. The data that support the findings of this study are available upon reasonable request from the corresponding author.

Author ORCIDs.
Mohammad Umair https://orcid.org/0000-0003-0769-9101;
Sedat Tardu https://orcid.org/0000-0003-1312-2085.

Appendix A. Transport equations of mean turbulent enstrophy field

The transport equation for the mean streamwise turbulent enstrophy $\overline{\omega_x\omega_x}$ is given as

$$\left.\begin{aligned}
&\frac{\partial\overline{\omega_x\omega_x}}{\partial t} = \overline{P_{\omega_x\omega_x}} + \overline{A_{\omega_x\omega_x}} + \overline{T_{\omega_x\omega_x}} + \overline{\epsilon_{\omega_x\omega_x}} + \overline{D_{\omega_x\omega_x}},\\
&\text{where}\\
&\overline{P_{\omega_x\omega_x}} = \underbrace{\overline{2\widetilde{\Omega}_x\left\langle\omega_x\frac{\partial u}{\partial x}\right\rangle}}_{\overline{P^1_{\omega_x\omega_x}}} + \underbrace{\overline{2\widetilde{\Omega}_y\left\langle\omega_x\frac{\partial u}{\partial y}\right\rangle}}_{\overline{P^2_{\omega_x\omega_x}}} + \underbrace{\overline{2\widetilde{\Omega}_z\left\langle\omega_x\frac{\partial u}{\partial z}\right\rangle}}_{\overline{P^3_{\omega_x\omega_x}}} - \underbrace{2\frac{\mathrm{d}\overline{U}}{\mathrm{d}y}\overline{\omega_x\frac{\partial w}{\partial x}}}_{\overline{P^4_{\omega_x\omega_x}}}\\
&\qquad + \underbrace{\overline{2\omega_x\omega_x\frac{\partial u}{\partial x}}}_{\overline{P^5_{\omega_x\omega_x}}} + \underbrace{\overline{2\omega_x\omega_y\frac{\partial u}{\partial y}}}_{\overline{P^6_{\omega_x\omega_x}}} + \underbrace{\overline{2\omega_x\omega_z\frac{\partial u}{\partial z}}}_{\overline{P^7_{\omega_x\omega_x}}} + \underbrace{\overline{2\langle\omega_x\omega_x\rangle\frac{\partial\widetilde{U}}{\partial x}}}_{\overline{P^8_{\omega_x\omega_x}}} + \underbrace{\overline{2\langle\omega_x\omega_y\rangle\frac{\partial\widetilde{U}}{\partial y}}}_{\overline{P^9_{\omega_x\omega_x}}},\\
&\overline{A_{\omega_x\omega_x}} = -\underbrace{\overline{\widetilde{U}\frac{\partial\langle\omega_x\omega_x\rangle}{\partial x}}}_{\overline{A^1_{\omega_x\omega_x}}} - \underbrace{\overline{\widetilde{V}\frac{\partial\langle\omega_x\omega_x\rangle}{\partial y}}}_{\overline{A^2_{\omega_x\omega_x}}},\\
&\overline{T_{\omega_x\omega_x}} = -\underbrace{\overline{2\langle\omega_x u\rangle\frac{\partial\widetilde{\Omega}_x}{\partial x}}}_{\overline{T^1_{\omega_x\omega_x}}} - \underbrace{\overline{2\langle\omega_x v\rangle\frac{\partial\widetilde{\Omega}_x}{\partial y}}}_{\overline{T^2_{\omega_x\omega_x}}} - \underbrace{\frac{\mathrm{d}\overline{\omega_x\omega_x v}}{\mathrm{d}y}}_{\overline{T^3_{\omega_x\omega_x}}},\\
&\overline{\epsilon_{\omega_x\omega_x}} = -2\left(\overline{\frac{\partial\omega_x}{\partial x}\frac{\partial\omega_x}{\partial x}} + \overline{\frac{\partial\omega_x}{\partial y}\frac{\partial\omega_x}{\partial y}} + \overline{\frac{\partial\omega_x}{\partial z}\frac{\partial\omega_x}{\partial z}}\right)\text{and}\\
&\overline{D_{\omega_x\omega_x}} = \frac{d^2\overline{\omega_x\omega_x}}{\mathrm{d}y^2}.
\end{aligned}\right\} \quad \text{(A1)}$$

The transport equation for the mean wall-normal turbulent enstrophy $\overline{\omega_y\omega_y}$ is given as

$$\left.\begin{aligned}
&\frac{\partial\overline{\omega_y\omega_y}}{\partial t} = \overline{P_{\omega_y\omega_y}} + \overline{A_{\omega_y\omega_y}} + \overline{T_{\omega_y\omega_y}} + \overline{\epsilon_{\omega_y\omega_y}} + \overline{D_{\omega_y\omega_y}} = 0,\\
&\text{where}\\
&\overline{P_{\omega_y\omega_y}} = \underbrace{\overline{2\widetilde{\Omega}_x\left\langle\omega_y\frac{\partial v}{\partial x}\right\rangle}}_{\overline{P^1_{\omega_y\omega_y}}} + \underbrace{\overline{2\widetilde{\Omega}_y\left\langle\omega_y\frac{\partial v}{\partial y}\right\rangle}}_{\overline{P^2_{\omega_y\omega_y}}} + \underbrace{\overline{2\widetilde{\Omega}_z\left\langle\omega_y\frac{\partial v}{\partial z}\right\rangle}}_{\overline{P^3_{\omega_y\omega_y}}} + \underbrace{\overline{2\overline{\Omega}_z\omega_y\frac{\partial v}{\partial z}}}_{\overline{P^4_{\omega_y\omega_y}}}\\
&\qquad + \underbrace{\overline{2\omega_x\omega_y\frac{\partial v}{\partial x}}}_{\overline{P^5_{\omega_y\omega_y}}} + \underbrace{\overline{2\omega_y\omega_y\frac{\partial v}{\partial y}}}_{\overline{P^6_{\omega_y\omega_y}}} + \underbrace{\overline{2\omega_z\omega_y\frac{\partial v}{\partial z}}}_{\overline{P^7_{\omega_y\omega_y}}}\\
&\qquad + \underbrace{\overline{2\langle\omega_x\omega_y\rangle\frac{\partial\widetilde{V}}{\partial x}}}_{\overline{P^8_{\omega_y\omega_y}}} + \underbrace{\overline{2\langle\omega_y\omega_y\rangle\frac{\partial\widetilde{V}}{\partial y}}}_{\overline{P^9_{\omega_y\omega_y}}},\\
&\overline{A_{\omega_y\omega_y}} = -\underbrace{\overline{\widetilde{U}\frac{\partial\langle\omega_y\omega_y\rangle}{\partial x}}}_{\overline{A^1_{\omega_y\omega_y}}} - \underbrace{\overline{\widetilde{V}\frac{\partial\langle\omega_y\omega_y\rangle}{\partial y}}}_{\overline{A^2_{\omega_y\omega_y}}},\\
&\overline{T_{\omega_y\omega_y}} = \underbrace{\overline{-2\langle\omega_y u\rangle\frac{\partial\widetilde{\Omega}_y}{\partial x}}}_{\overline{T^1_{\omega_y\omega_y}}} - \underbrace{\overline{2\langle\omega_y v\rangle\frac{\partial\widetilde{\Omega}_y}{\partial y}}}_{\overline{T^2_{\omega_y\omega_y}}} - \underbrace{\frac{\mathrm{d}\overline{\omega_y\omega_y v}}{\mathrm{d}y}}_{\overline{T^3_{\omega_y\omega_y}}},\\
&\overline{\epsilon_{\omega_y\omega_y}} = -2\left(\overline{\frac{\partial\omega_y}{\partial x}\frac{\partial\omega_y}{\partial x}} + \overline{\frac{\partial\omega_y}{\partial y}\frac{\partial\omega_y}{\partial y}} + \overline{\frac{\partial\omega_y}{\partial z}\frac{\partial\omega_y}{\partial z}}\right)\text{ and}\\
&\overline{D_{\omega_y\omega_y}} = \frac{d^2\overline{\omega_y\omega_y}}{\mathrm{d}y^2}.
\end{aligned}\right\} \tag{A2}$$

Finally, the transport equation for the mean spanwise turbulent enstrophy $\overline{\omega_z\omega_z}$ is given as

$$\left.\begin{aligned}
&\frac{\partial\overline{\omega_z\omega_z}}{\partial t} = \overline{P_{\omega_z\omega_z}} + \overline{A_{\omega_z\omega_z}} + \overline{T_{\omega_z\omega_z}} + \overline{\epsilon_{\omega_z\omega_z}} + \overline{D_{\omega_z\omega_z}} = 0,\\
&\text{where}\\
&\overline{P_{\omega_z\omega_z}} = \underbrace{\overline{2\widetilde{\Omega}_x\left\langle\omega_z\frac{\partial w}{\partial x}\right\rangle}}_{\overline{P^1_{\omega_z\omega_z}}} + \underbrace{\overline{2\widetilde{\Omega}_y\left\langle\omega_z\frac{\partial w}{\partial y}\right\rangle}}_{\overline{P^2_{\omega_z\omega_z}}} + \underbrace{\overline{2\widetilde{\Omega}_z\left\langle\omega_z\frac{\partial w}{\partial z}\right\rangle}}_{\overline{P^3_{\omega_z\omega_z}}} + \underbrace{2\overline{\Omega_z}\overline{\omega_z\frac{\partial w}{\partial z}}}_{\overline{P^4_{\omega_z\omega_z}}}\\
&\qquad + \underbrace{\overline{2\omega_x\omega_z\frac{\partial w}{\partial x}}}_{\overline{P^5_{\omega_z\omega_z}}} + \underbrace{\overline{2\omega_y\omega_z\frac{\partial w}{\partial y}}}_{\overline{P^6_{\omega_z\omega_z}}} + \underbrace{\overline{2\omega_z\omega_z\frac{\partial w}{\partial z}}}_{\overline{P^7_{\omega_z\omega_z}}}\\
&\qquad + \underbrace{\overline{2\langle\omega_x\omega_z\rangle\frac{\partial\widetilde{W}}{\partial x}}}_{\overline{P^8_{\omega_z\omega_z}}} + \underbrace{\overline{2\langle\omega_y\omega_z\rangle\frac{\partial\widetilde{W}}{\partial y}}}_{\overline{P^9_{\omega_z\omega_z}}},\\
&\overline{A_{\omega_z\omega_z}} = \underbrace{-\overline{\widetilde{U}\frac{\partial\langle\omega_z\omega_z\rangle}{\partial x}}}_{\overline{A^1_{\omega_z\omega_z}}} - \underbrace{\overline{\widetilde{V}\frac{\partial\langle\omega_z\omega_z\rangle}{\partial y}}}_{\overline{A^2_{\omega_z\omega_z}}},\\
&\overline{T_{\omega_z\omega_z}} = \underbrace{-\overline{2\langle\omega_z u\rangle\frac{\partial\widetilde{\Omega}_z}{\partial x}}}_{\overline{T^1_{\omega_z\omega_z}}} - \underbrace{\overline{2\langle\omega_z v\rangle\frac{\partial\widetilde{\Omega}_z}{\partial y}}}_{\overline{T^2_{\omega_z\omega_z}}} - \underbrace{2\overline{\omega_z v}\frac{\mathrm{d}\overline{\Omega_z}}{\mathrm{d}y}}_{\overline{T^3_{\omega_z\omega_z}}} - \underbrace{\frac{\mathrm{d}\overline{\omega_z\omega_z v}}{\mathrm{d}y}}_{\overline{T^4_{\omega_z\omega_z}}},\\
&\overline{\epsilon_{\omega_z\omega_z}} = -2\left(\overline{\frac{\partial\omega_z}{\partial x}\frac{\partial\omega_z}{\partial x}} + \overline{\frac{\partial\omega_z}{\partial y}\frac{\partial\omega_z}{\partial y}} + \overline{\frac{\partial\omega_z}{\partial z}\frac{\partial\omega_z}{\partial z}}\right)\text{and}\\
&\overline{D_{\omega_z\omega_z}} = \frac{\mathrm{d}^2\overline{\omega_z\omega_z}}{\mathrm{d}y^2}.
\end{aligned}\right\} \tag{A3}$$

References

Agostini, L., Touber, E. & Leschziner, M.A. 2014 Spanwise oscillatory wall motion in channel flow: drag-reduction mechanisms inferred from DNS-predicted phase-wise property variations at $Re_\tau = 1000$. *J. Fluid Mech.* **743**, 606–635.

Agostini, L., Touber, E. & Leschziner, M.A. 2015 The turbulence vorticity as a window to the physics of friction-drag reduction by oscillatory wall motion. *Intl J. Heat Fluid Flow* **51**, 3–15.

Akhavan, R., Jung, W.J. & Mangiavacchi, N. 1993 Turbulence control in wall-bounded flows by spanwise ocillations. *Appl. Sci. Res.* **51**, 299–303.

Auteri, F., Baron, A., Belan, M., Campanardi, G. & Quadrio, M. 2010 Experimental assessment of turbulent drag reduction by traveling waves in a turbulent pipe flow. *Phys. Fluids* **22**, 115103.

Bauer, F., Tardu, S. & Doche, O. 2015 Efficiency of high accuracy DRP schemes in direct numerical simulations of incompressible turbulent flows. *Comput. Fluids* **107**, 123–140.

Brooke, J.W. & Hanratty, T.J. 1993 Origin of turbulence–producing eddies in a channel flow. *Phys. Fluids* A **5**, 1011–1022.

BUSSE, A. & SANDHAM, N.D. 2012 Parametric forcing approach to rough-wall turbulent channel flow. *J. Fluid Mech.* **712**, 169–202.
CHOI, K.-S., DEBISSCHOP, J.-R. & CLAYTON, B.R. 1998 Turbulent boundary-layer control by means of spanwise-wall oscillation. *AIAA J.* **36** (7), 1157–1163.
DHANAK, M.R. & SI, C. 1999 On reduction of turbulent wall friction through spanwise wall oscillations. *J. Fluid Mech.* **383**, 175–195.
DUGGLEBY, A., BALL, K.S. & PAUL, M.R. 2007 The effect of spanwise wall oscillation on turbulent pipe flow structures resulting in drag reduction. *Phys. Fluids* **19** (12), 125107.
FROHNAPFEL, B., LAMMERS, P., JOVANOVIĆ, J. & DURST, F. 2007 Interpretation of the mechanism associated with turbulent drag reduction in terms of anisotropy invariants. *J. Fluid Mech.* **577**, 457–466.
GALLORINI, E., QUADRIO, M. & GATTI, D. 2022 Coherent near-wall structures and drag reduction by spanwise forcing. *Phys. Rev. Fluids* **7**, 114602.
GATTI, D. & QUADRIO, M. 2013 Performance losses of drag-reducing spanwise forcing at moderate values of the Reynolds number. *Phys. Fluids* **25**, 125109.
GATTI, D. & QUADRIO, M. 2016 Reynolds-number dependence of turbulent skin-friction drag reduction induced by spanwise forcing. *J. Fluid Mech.* **802**, 553–582.
GE, M. & JIN, G. 2017 Response of turbulent enstrophy to sudden implementation of spanwise wall oscillation in channel flow. *Appl. Math. Mech.* **38**, 1159–1170.
HAMILTON, J.M., KIM, J. & WALEFFE, F. 1995 Regeneration mechanisms of near-wall turbulence structures. *J. Fluid Mech.* **287**, 317–348.
HURST, E., YANG, Q. & CHUNG, Y.M. 2014 The effect of Reynolds number on turbulent drag reduction by streamwise travelling waves. *J. Fluid Mech.* **759**, 28–55.
HUSSAIN, A.K.M.F. & REYNOLDS, W.C. 1970 The mechanics of an organized wave in turbulent shear flow. *J. Fluid Mech.* **41**, 241–258.
JEONG, J., HUSSAIN, F., SCHOPPA, W. & KIM, J. 1997 Coherent structures near the wall in a turbulent channel flow. *J. Fluid Mech.* **332**, 185–214.
JIMÉNEZ, J. 1994 On the structure and control of near wall turbulence. *Phys. Fluids* **6** (2), 944–953.
JIMÉNEZ, J. & PINELLI, A. 1999 The autonomous cycle of near-wall turbulence. *J. Fluid Mech.* **389**, 335–359.
JUNG, W.J., MANGIAVACCHI, N. & AKHAVAN, R. 1992 Suppression of turbulence in wall-bounded flows by high-frequency spanwise wall oscillations. *Phys. Fluids* A **4** (8), 1605–1607.
KEMPAIAH, K.U., SCARANO, F., ELSINGA, G.E., VAN OUDHEUSDEN, B.W. & BERMEL, L. 2020 3-dimensional particle image velocimetry based evaluation of turbulent skin-friction reduction by spanwise wall oscillation. *Phys. Fluids* **32** (8), 085111.
KIM, J., MOIN, P. & MOSER, R. 1987 Turbulence statistics in fully developed channel flow at low Reynolds number. *J. Fluid Mech.* **177**, 133–166.
LAADHARI, F., SKANDAJI, L. & MOREL, R. 1994 Turbulence reduction in a boundary layer by a local spanwise oscillating surface. *Phys. Fluids* **6** (10).
LEE, C. & KIM, J. 2002 Control of the viscous sublayer for drag reduction. *Phys. Fluids* **14** (7), 2523–2529.
LUMLEY, J.L. & NEWMAN, G.R. 1977 The return to isotropy of homogeneous turbulence. *J. Fluid Mech.* **82** (1), 161–178.
MARUSIC, I., CHANDARAN, D., ROUHI, A., FU, M.K., WINE, D., HOLLOWAY, B., CHUNG, D. & SMITS, A.J. 2021 An energy-efficient pathway to turbulent drag reduction. *Nat. Commun.* **12**, 5805.
MOSER, R.D., KIM, J. & MANSOUR, N.N. 1999 Direct numerical simulation of turbulent channel flow up to $Re_\tau = 590$. *Phys. Fluids* **11**, 943–945.
ORLANDI, P. & JIMÉNEZ, J. 1994 On the generation of turbulent wall friction. *Phys. Fluids* **6** (2), 634–641.
POPE, S.B. 2000 *Turbulent Flows*. Cambridge University Press.
QUADRIO, M. & RICCO, P. 2003 Initial response of a turbulent channel flow to spanwise oscillation of the walls. *J. Turbul.* **4**, N7.
QUADRIO, M. & RICCO, P. 2011 The laminar generalized Stokes layer and turbulent drag reduction. *J. Fluid Mech.* **667**, 135–157.
QUADRIO, M., RICCO, P. & VIOTTI, C. 2009 Streamwise-travelling waves of spanwise wall velocity for turbulent drag reduction. *J. Fluid Mech.* **627**, 161–178.
RICCO, P. 2004 Modification of near-wall turbulence due to spanwise oscillations. *J. Turbul.* **5**, N24.
RICCO, P., OTTONELLI, C., HASEGAWA, Y. & QUADRIO, M. 2012 Changes in turbulent dissipation in a channel flow with oscillating walls. *J. Fluid Mech.* **700**, 77–104.
RICCO, P., SKOTES, M. & LESCHZINER, M.A. 2021 A review of turbulent skin-friction drag reduction by near-wall transverse forcing. *Prog. Aerosp. Sci.* **123**, 100713.
SIMONSEN, A.J. & KROGSTAD, P.-Å. 2005 Turbulent stress invariant analysis: clarification of existing terminology. *Phys. Fluids* **17** (8), 088103.

TARDU, S.F. 1995 Coherent structures and riblets. *Appl. Sci. Res.* **54**, 349–385.
TARDU, S.F. 2008 Stochastic synchronization of the near wall turbulence. *Phys. Fluids* **20**, 045105.
TARDU, S. 2014 *Transport and Coherent Structures in Wall Turbulence*. Wiley-ISTE.
TARDU, S. 2016 Concomitance of the local spanwise velocity and production in wall turbulence. *Phys. Fluids* **28** (1).
TARDU, S. 2022 Multiscale analysis of some shear layers in a fully developed turbulent channel flow. *Comput. Fluids* **240**, 105459.
TOUBER, E. & LESCHZINER, M.A. 2012 Near-wall streak modification by spanwise oscillatory wall motion and drag-reduction mechanisms. *J. Fluid Mech.* **693**, 150–200.
TRUJILLO, S.M., BOGARD, D.G. & BALL, K.S. 1997 Turbulent boundary layer drag reduction using an oscillating wall. In *AIAA*, pp. 97–1870.
UMAIR, M., TARDU, S. & DOCHE, O. 2022 Reynolds stresses transport in a turbulent channel flow subjected to streamwise traveling waves. *Phys. Rev. Fluids* **7**, 054601.
YAKENO, A., HASEGAWA, Y. & KASAGI, N. 2014 Modification of quasi-streamwise vortical structure in a drag-reduced turbulent channel flow with spanwise wall oscillation. *Phys. Fluids* **26**, 085109.

Transport des contraintes de Reynolds et de l'enstrophie en turbulence de paroi contrôlée par les ondes progressives longitudinales

Mohammad Umair[†], LEGI, Univ. Grenoble Alpes, CNRS, Grenoble-INP, F-38000 Grenoble, France

Résumé

Des simulations numériques directes ont été réalisées dans un canal pleinement turbulent soumis à des ondes progressives longitudinales (STW) dans le but d'élucider le mécanisme responsable de la réduction de la traînée. De grandes amplitudes ont été imposées pour identifier les effets propres des STW, en maintenant à des valeurs constantes la fréquence angulaire et le nombre d'ondes. Une attention particulière est portée sur le mécanisme de transport de l'énergie et de la vorticité, afin de mieux comprendre l'influence du forçage via les STW sur la turbulence en proche paroi. Les ondes progressives longitudinales de grande amplitude bloquent le transfert d'énergie entre les composantes, ce qui entraîne l'arrêt de la dynamique dans la sous-couche tampon près de la paroi. L'analyse présentée ici suggère que l'effet combiné de la perte de communication entre la haute sous couche tampon et la basse sous couche tampon, combinée avec l'amortissement de la composante verticale des contraintes de Reynolds est associé à l'effet d'ondes progressives et se traduit par des réductions significatives de la traînée. En outre, l'analyse du transport de vorticité révèle que l'effet principal du forçage via les STW est d'atténuer l'enstrophie turbulente transversale, en particulier à la paroi, à travers une diminution importante des fluctuations de la contrainte de cisaillement. Pour renforcer ce dernier point, nous avons réalisé d'autres simulations (des expériences numériques) où les fluctuations de vitesse longitudinale, et par conséquent de la vorticité transversale, ont été artificiellement supprimées en proche paroi. Les invariants de l'anisotropie obtenus à travers le forçage sont fortement similaires à l'écoulement turbulent contrôlé par les STW de grande amplitude. Une analyse détaillée des diverses caractéristiques structurelles est également fournie, notamment la réponse des stries en proche paroi et des couches de cisaillement. Les tourbillons quasi-longitudinaux, qui jouent un rôle clé dans la production de la turbulence pariétale, sont poussés loin de la paroi, ce qui se traduit par un affaiblissement de leur signature dans la sous-couche visqueuse et la basse sous-couche tampon.

Mots clés : Contrôle de la turbulence, Turbulence de paroi, Simulations numériques directes.

1. Introduction

Les écoulements turbulents sont extrêmement intéressants en raison de leur prévalence dans la nature et dans de nombreuses applications industrielles : les exemples les plus courants sont la montée de la fumée de cigarette, les chutes d'eau, le flux sanguin dans les artères et la majeure partie de la recirculation atmosphérique terrestre. Une part importante du frottement à la paroi est générée dans une partie très proche de la paroi, où l'écoulement est principalement turbulent. Dans presque tous les systèmes de transport, la traînée de frottement est une composante majeure de la résistance totale au mouvement, environ 50% pour les avions, 90% pour les véhicules sous-marins et près de 100% pour les écoulements internes dans les tuyaux et les canaux. Cela n'affecte

[†]email pour la correspondance : mohammad.umair@legi.grenoble-inp.fr

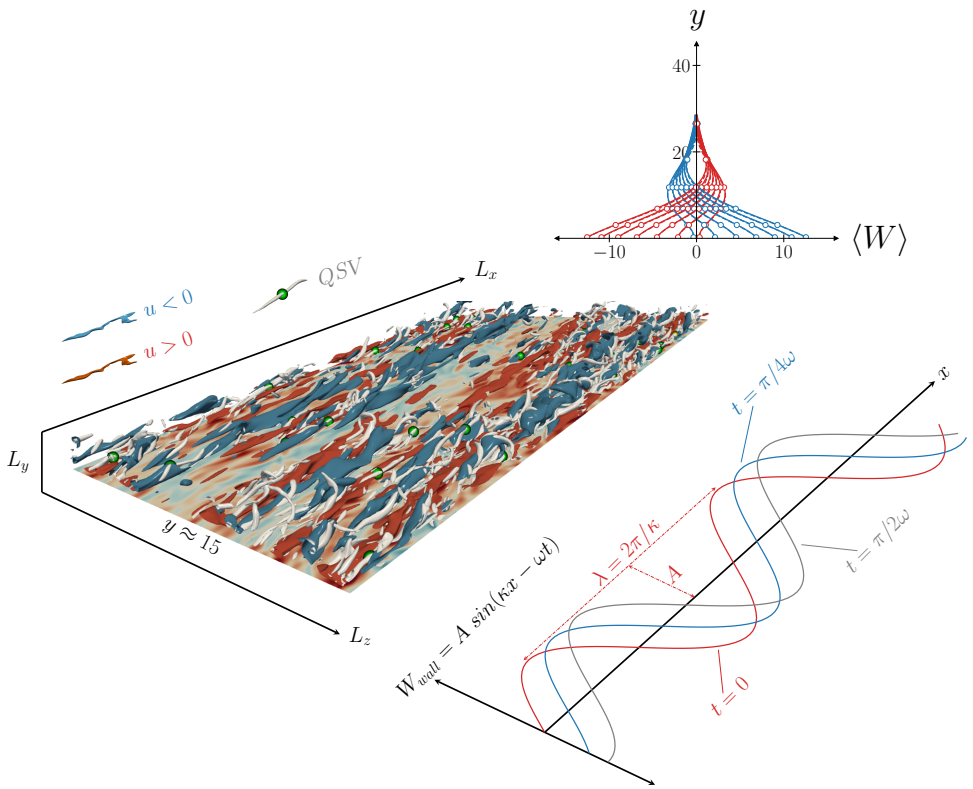

Figure 1: Schéma de principe du canal rectangulaire de taille $L_x \times L_y \times L_z = 6\pi h \times 2h \times 3\pi h$ respectivement dans le sens du courant, de la normale à la paroi et dans la direction transversale, soumis à des oscillations de paroi dans la direction transversale sous la forme d'ondes progressives dans le sens du courant (STW). Le diagramme montre également la forme d'onde utilisée pour l'actionnement et les profils correspondants à moyenne de phase de la vitesse $\langle W \rangle$ dans la direction transversale pour le cas $A0.50$ qui s'effondrent avec la solution laminaire (représentée par des points) dérivée de Quadrio & Ricco [9]. Reproduit d'Umair & Tardu [14] avec la permission de Cambridge University Press (CUP).

pas seulement les performances de ces systèmes, mais a également un impact négatif sur l'environnement, car une quantité importante d'énergie est gaspillée pour surmonter le frottement visqueux, ce qui se traduit par une augmentation de la consommation de carburant et, par conséquent, par une hausse du niveau des émissions de gaz à effet de serre.

De nombreuses techniques de contrôle de la turbulence, certaines pratiquement réalisables et d'autres plus conceptuelles, ont été conçues au cours des dernières décennies pour tenter d'atténuer le frottement visqueux à la paroi. Les techniques de contrôle de la turbulence visant spécifiquement à réduire le frottement pariétal sont généralement classées en deux catégories : passives et actives. Les techniques passives ne nécessitent pas d'énergie et ont tendance à être beaucoup plus réalisables par rapport aux techniques actives, qui, par définition, nécessitent de l'énergie pour leur actionnement. Les techniques de contrôle basées sur les oscillations de paroi dans la direction transversale ont fait l'objet d'une attention considérable en raison de leur capacité à produire des marges de réduction de la traînée (DR) significativement importantes. Dans l'étude ci-présente, nous nous concentrons sur les oscillations de la paroi dans la direction transversale sous la forme d'ondes progressives dans le sens de l'écoulement (STW) régies par

$$W_{\text{wall}} = A \sin(\kappa x - \omega t), \tag{1}$$

où A est l'amplitude, $\omega = 2\pi/T$ est la vitesse angulaire, et $\kappa = 2\pi/\lambda$, is le nombre d'ondes (T et λ représentent respectivement la période de temps et la longueur d'onde de l'onde progressive). Ce type de forçage de

paroi a été étudié pour la première fois numériquement par Quadrio *et al.* [10]. Tout au long de l'article x, y, z représentent respectivement les coordonnées dans le sens de l'écoulement principal, normal à la paroi et transversal, et t est le temps. Les vitesses instantanées correspondantes sont notées respectivement U, V, and W. Le forçage ci-dessus donne lieu à une sous-couche de cisaillement oscillant suivant x, appelée couche de Stokes généralisée (GSL) [9]. Le GSL interagit avec la turbulence pour produire une DR ou une augmentation de la traînée, dépendant des paramètres de contrôle A, ω, et κ. En partant de l'hypothèse que l'épaisseur du GSL est beaucoup plus petite que la demi-hauteur du canal, Quadrio & Ricco [9] ont dérivé une expression analytique qui s'est avérée bien en accord avec l'écoulement turbulent à moyenne spatiale dans la direction transversale et possède de bonnes capacités prédictives pour la marge DR à faible Re. À partir de maintenant, nous nous référerons simplement à la GSL en tant que couche de Stokes. La plupart des lois d'échelle introduites jusqu'à présent échouent à grand Re. Un bon exemple qui clarifie cette question est le travail expérimental conduit par Marusic *et al.* [7] où ils imposent STW à faible fréquence couplée aux grandes échelles qui conduit à environ 13% de marge DR au nombre de Reynolds de frottement Re_τ =12 800, alors que les corrélations de Gatti & Quadrio [2] prédisent presque peu ou pas de marge DR. Prédire les marges DR à Re de manière pratique reste toujours un défi.

La plupart des progrès réalisés dans la compréhension du mécanisme physique sous-jacent mentionné ci-dessus découlent du forçage de l'oscillation de la paroi homogène. Il y a relativement peu de recherches dans le contexte de STW. Dans cette étude, nous étudions le transport des contraintes de Reynolds et d'enstrophie dans un écoulement turbulent contrôlé par STW. L'accent est mis sur les modifications physiques du champ d'écoulement turbulent près de la paroi provoquées les ondes progressives. Nous couvrons un large régime de marge DR allant d'environ 20 à 60%, en mettant particulièrement l'accent sur les STW de grande amplitude qui produisent des réductions de la traînée significativement importantes. L'idée est d'identifier les termes clés qui apparaissent dans les équations de transport des contraintes de Reynolds, ainsi que de l'enstrophie turbulente qui modifient de manière significative la structure turbulente pariétale. Nous montrons une similitude frappante dans la trajectoire des invariants d'anisotropie de la STW de grande amplitude et de la suppression artificielle de l'activité turbulente. En outre, nous analysons également l'influence de la STW sur les structures tourbillonnaires quasi-longitudinales et leur impact à la paroi.

2. Détails des simulations numériques directes

Les simulations numériques directes (DNS) ont été réalisées à débit constant (CFR). Le schéma de la figure 1 montre le domaine sous la forme d'un canal avec le contrôle imposé. Le nombre de Reynolds $Re(= hU_c/\nu)$ a été fixé à 4200, où h est la demi-hauteur du canal, U_c est la vitesse au centre du canal, et ν est la viscosité cinématique du fluide. Le nombre de Reynolds de frottement (nombre de von Karman) est $Re_\tau = hu_\tau/\nu = 180$ pour le cas non contrôlé (u_τ étant la vitesse de frottement). L'amplitude (A) du STW a été varié de $0.15U_c$ to $1.25U_c$, tandis que ω et κ ont été fixés à 0.16 and 1.66 en échelles externes basées sur h et U_c, respectivement. Il en résulte une réduction de la traînée d'environ 60 % pour le cas de la plus grande amplitude $A1.25$. Les marges DR$(= -\Delta C_f/C_{f0})$ correspondantes et les nombres de Reynolds de frottement réels (locaux) (Re$_\tau$) pour tous les cas sont indiqués dans le tableau 1. Ici, C_f est le coefficient de frottement pour l'écoulement contrôlé et C_{f0} est le coefficient de frottement pour l'écoulement non contrôlé. Le coefficient de frottement est défini comme $C_f = 2\overline{\tau_w}/\rho U_b^2$, où $\overline{\tau_w}$ est la contrainte de cisaillement de la paroi moyennée dans les directions homogènes, x et z, ρ est la densité du fluide, et $U_b(= 2U_c/3)$ est la vitesse débitante. Nous utilisons les conditions aux limites périodiques dans les directions longitudinale et transversale. La taille du domaine de calcul a été choisie de

Case	Uncontrolled	HWO	$A0.15$	$A0.30$	$A0.50$	$A0.75$	$A0.95$	$A1.25$
A/U_c	—	0.51	0.15	0.30	0.50	0.75	0.95	1.25
$A/u_{\tau 0}$	—	12.0	3.5	7.0	11.7	17.5	22.2	29.2
A/u_τ	—	14.9	4.0	9.0	16.1	25.3	32.7	44.3
DR(%)	—	36	26	42	48	52	54	58
Re_τ	179.8	144.2	156.9	139.0	130.7	124.5	121.9	118.4

Table 1: Détails des paramètres de contrôle, des marges DR correspondantes et du nombre de Reynolds de frottement réel (local) pour les cas contrôlés. Les valeurs de la fréquence angulaire (ω) et du nombre d'ondes (κ) du STW ont été maintenues à $0,16$ et $1,66$ en unités extérieures basées sur la demie-hauteur du canal (h) et la vitesse de l'axe central (U_c) de l'écoulement de Poiseuille plan, respectivement. Reproduit d'Umair & Tardu [14] avec l'autorisation du CUP.

sorte que le domaine contienne au moins six longueurs d'onde, et elle est de $6\pi h \times 2h \times 3\pi h$ de long dans la direction longitudinale, la direction normale à la paroi et la direction transversale, respectivement. Les nœuds de calcul sont uniformément répartis dans les directions x et z, tandis qu'ils sont étirés dans la direction normale à la paroi à l'aide d'une distribution tangente hyperbolique. Les résolutions de grille correspondantes sont de 8,5, 5 et 0,5-5,5 en unités de paroi basées sur Re_τ de l'écoulement non contrôlé. Les pas de temps dans les simulations sont de 0,04 et 0,008 unités de paroi pour les cas non contrôlés et contrôlés, respectivement.

Les quantités statistiques pour l'écoulement non contrôlé ont été obtenues en utilisant 50 champs instantanés 3D de vitesse et de pression, couvrant une fenêtre temporelle de 37 000, séparées de 770 unités de paroi. Les quantités statistiques pour les cas contrôlés ont été obtenues en utilisant la décomposition triple classique de Hussain & Reynolds [4], où une quantité instantanée, par exemple, U est décomposée en une composante moyenne dans le temps $(\overline{U})$, une composante oscillante périodique $(\widetilde{U})$, et une composante purement stochastique (u). Cette décomposition s'écrit comme $U = \overline{U} + \widetilde{U} + u = \langle U \rangle + u$, où $\langle \cdot \rangle$ représente la quantité moyennée en phase. Les quantités moyennées en phase ont été obtenues en déterminant la moyenne de la quantité instantanée correspondante sur la phase $\xi = x - ct$ de l'onde progressive, où $c = \omega/\kappa$ est la vitesse de phase de l'onde. Les données ont été collectées pendant au moins 40 cycles, ce qui correspond à une fenêtre temporelle de 12 000 unités de paroi. Il en résulte un temps de calcul d'environ 90 000 heures CPU pour les seuls cas STW, réparties entre 128 processeurs sur les grappes de calcul du GRICAD, Université de Grenoble-Alpes. Nous avons soigneusement comparé le profil moyenné en phase de la vitesse dans la direction transversale $\langle W \rangle$ avec la solution laminaire de Quadrio & Ricco [9] pour tous les cas de contrôle répertoriés dans le tableau 1, et avons constaté que nous sommes dans le régime GSL. Par exemple, on voit en haut de la figure 1 que les moyennes de phase $\langle W \rangle$ (représentés par des lignes) correspondent bien à la solution laminaire de Quadrio & Ricco [9] (représentée par des points) pour le cas $A0.50$.

Il convient de noter que tout au long de cette étude, nous avons systématiquement utilisé les paramètres d'échelle *locaux* basés sur la valeur réelle de Re_τ, pour des raisons détaillées dans Umair *et al.* [15]. Chaque fois que cela s'est avéré nécessaire, un indice '0' a été ajouté aux quantités pour souligner l'utilisation d'une mise à l'échelle de *référence* basée sur le Re_τ de l'écoulement de référence non contrôlé.

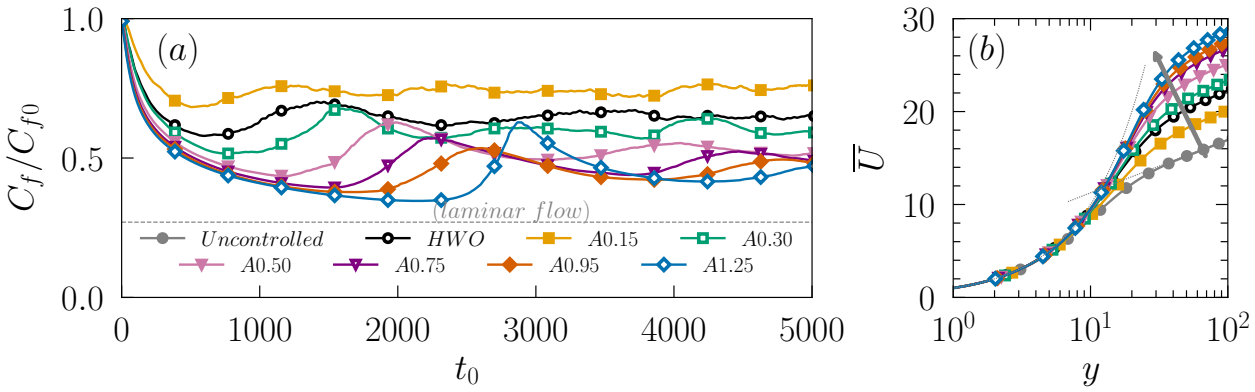

Figure 2: (a) Réponse initiale du coefficient de frottement de la peau normalisé (C_f/C_{f0}) après l'activation de la commande pour différentes amplitudes de forçage. (b) Profils de vitesse moyenne pour les cas non contrôlés et contrôlés. Reproduit d'Umair *et al.* [15] avec l'autorisation de l'American Physical Society (APS).

3. Réponse de l'écoulement moyen et du transport des contraintes de Reynolds

La figure 2(a) montre la réponse initiale de C_f (normalisée par C_{f0}) après l'activation du contrôle. Le coefficient de frottement commence à diminuer fortement, et le taux de décroissance initiale est similaire pour toutes les amplitudes de forçage, à l'exception du cas $A0.15$. Les réponses des cas de grande amplitude sont assez intéressantes, par exemple, l'écoulement n'est pas loin de la limite de relaminarisation vers $t_0 = 2000$ pour le cas $A1.25$, mais revient à l'état turbulent à $t_0 = 3000$. De telles réponses complexes des coefficients de frottement sont également observées dans le contrôle optimal de la turbulence de paroi à des horizons d'optimisation modérés [1].

Figure 2(b) montre l'effet du forçage sur les profils de la vitesse moyenne, mis à l'échelle avec la vitesse de frottement locale et de référence. Conformément aux études précédentes, les profils de la vitesse moyenne montrent un déplacement vers le haut de la partie logarithmique avec un épaississement de la sous-couche visqueuse lorsqu'ils sont mis aux échelles internes in situ. Ce comportement est typique des scénarios de réduction de la traînée, quel que soit le type de contrôle, sauf pour les surfaces super-hydrophobes, au-dessus desquelles la réduction de la traînée entraîne un amincissement de la couche tampon ainsi qu'un déplacement vers le bas de la région logarithmique. L'ampleur du déplacement vers le haut de la partie logarithmique est proportionnelle à la marge DR Gatti & Quadrio [2]. La mise à l'échelle par rapport à la vitesse de frottement de référence met en évidence le fait que l'effet principal du forçage est de réduire considérablement la vitesse dans la sous-couche visqueuse près de la paroi.

Globalement, les profils des composantes de la contrainte de Reynolds se regroupent approximativement pour $A \geq 0.75U_c$ à l'exception de la composante $\overline{ww}$ dans la direction transversale. La composante dans le sens

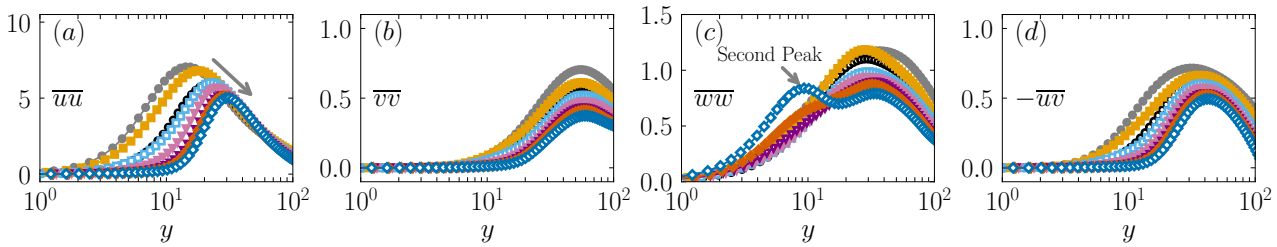

Figure 3: Profils des contraintes de Reynolds pour les cas non contrôlés et contrôlés. Se référer à la figure 1 pour les symboles correspondant aux différents cas. Adapté d'Umair *et al.* [15] avec l'autorisation de l'APS.

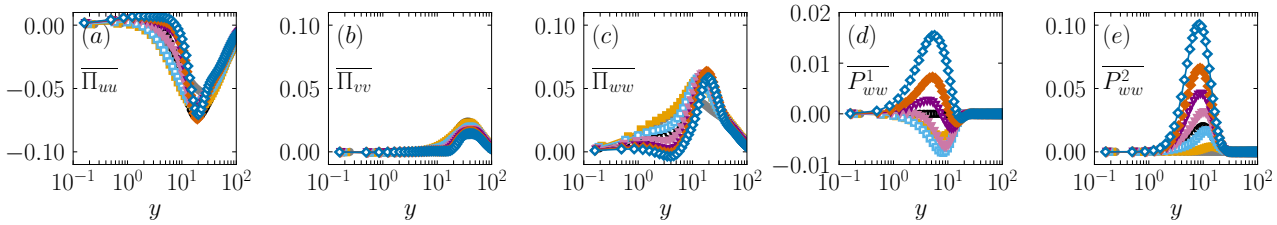

Figure 4: (a, b, c) Terme de gradient de vitesse-pression dans le bilan des contraintes de cisaillement de Reynolds suivant la direction longitudinale, normale à la paroi et dans la direction transversale pour les cas non contrôlés et contrôlés. Se référer à la figure 1 pour les marqueurs correspondant aux différents cas. Adapté d'Umair & Tardu [15] avec l'autorisation de l'APS.

de l'écoulement $\overline{uu}$ est significativement amortie près de la paroi, ce qui reflète une forte réduction de l'intensité des stries de basse et haute vitesse (figure 3a). Les maximums locaux de $\overline{uu}$ et $\overline{uv}$ se déplacent vers la fin de la sous-couche tampon à $y \approx 30$ (figure 3a, d). Le profil de la composante $\overline{ww}$ pour le cas $A1.25$ présente un second maximum local près de la paroi à $y \approx 8$ (figure 3c), nous revenons sur cette caractéristique particulière dans la section suivante. Si l'on ne tient pas compte de l'apparition du second pic dans $\overline{ww}$ pour le cas $A1.25$, les positions normales à la paroi des valeurs maximales de $\overline{vv}$ et $\overline{ww}$ ne sont pas modifiés par le STW.

Dans un écoulement canonique de canal, le terme de production n'apparaît que dans l'équation de transport de $\overline{uu}$. Les deux autres composantes normale et transversale sont alimentées via les termes du gradient vitesse-pression $\Pi_{uu} \rightarrow \Pi_{vv}$ & Π_{ww}. Cependant, dans le cas du contrôle STW, deux termes supplémentaires apparaissent dans l'équation de transport de $\overline{ww}$. Ils sont liés au gradient de Stokes, à la fois dans les directions transversale et normale à la paroi et s'écrivent comme $\overline{P^1_{ww}} = -2\overline{\langle wu \rangle \partial \widetilde{W}/\partial x}$ et $\overline{P^2_{ww}} = -2\overline{\langle wv \rangle \partial \widetilde{W}/\partial y}$. Comme le montre la figure 4(d, e), le dernier terme domine nettement et entraîne donc une production nette positive de $\overline{ww}$ qui culmine à peu près à $y = 8$, ce qui explique également l'apparition du second maximum local dans les profils de $\overline{ww}$ à la même position y. Le transfert inter-composants est significativement affecté par les STW de grande amplitude, et l'effet disparaît dans la région proche paroi (figure 4a - 4c).

4. Effet sur le transport de l'enstrophie

Le comportement le plus spectaculaire se produit dans la réponse de la composante de vorticité turbulente transversale $\overline{\omega_z \omega_z}$. Dans les cas de contrôle STW de grande amplitude, $\overline{\omega_z \omega_z}$ est spectaculairement annihilé jusqu'à $y \approx 8$, avec une activité turbulente entièrement négligeable $(\overline{\tau' \tau'})$ à la paroi. C'est l'un des effets remarquables du contrôle STW par rapport au simple contrôle de l'oscillation homogène de la paroi - dont le profil $\overline{\omega_z \omega_z}$ se confond plutôt avec le cas STW de faible amplitude $A0.30$ (figure 5c). Dans le cas du HWO, $\overline{\omega_z \omega_z}$ est amorti dans la sous-couche visqueuse avec un maximum à $y \approx 10$, alors que le pic de $\overline{\omega_z \omega_z}$ dans le

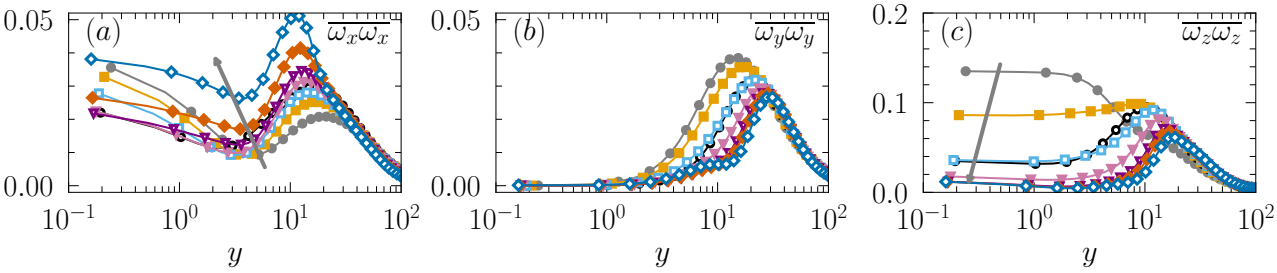

Figure 5: Profils d'enstrophie moyens pour les cas non contrôlés et contrôlés. Se référer à la figure 1 pour les symboles correspondant aux différents cas. Reproduit d'Umair & Tardu [14] avec l'autorisation de CUP.

cas du STW de grande amplitude est poussé vers la haute sous-couche tampon à $y \approx 20$.

La réponse du $\overline{\omega_y\omega_y}$, illustrée sur la figure 5(b) n'est pas surprenante, montrant une diminution de son intensité près de la paroi et un déplacement du maximum local vers la couche externe, tandis que $\overline{\omega_x\omega_x}$ présente un comportement complexe montrant une augmentation près de la paroi à de grandes amplitudes (figure 5a). Une observation particulièrement intéressante est l'aplatissement de son profil proche paroi aux grandes amplitudes. Ce comportement peut s'expliquer en considérant le terme de gradient de vitesse-pression Π_{ww} près de la paroi qui peut être relié au flux de ω_x. A notre connaissance, ce phénomène n'a jamais été observé auparavant. Dans la sous-couche visqueuse, l'intensité turbulente transversale peut être reliée à l'enstrophie longitudinale par $w \approx y\omega_{x,0}$. Ici, l'indice ', 0' fait référence à la paroi. En outre, le gradient de pression $\partial p/\partial z$ à la paroi est égal au flux de ω_x, c'est-à-dire, $\partial p/\partial z_{,0} = \partial\omega_x/\partial y_{,0}$. En combinant les deux relations, on obtient le comportement asymptotique près de la paroi de Π_{ww},

$$\overline{\Pi_{ww}} = -2\overline{\left\langle w\frac{\partial p}{\partial z}\right\rangle} \approx -y\frac{\partial\overline{\langle\omega_x^2\rangle}}{\partial y}\bigg|_{y=0}. \tag{2}$$

L'absence de corrélation $\overline{\Pi_{ww}} \approx 0$ dans les écoulements altérés par des STW de grandes amplitudes impliquerait que $\overline{\langle\omega_x^2\rangle} \approx$ constante en proche paroi selon l'équation 2. On observe en effet un affaiblissement significatif des variations de $\overline{\omega_x^2}$ dans la sous-couche visqueuse dès que $A > 0.50$. Par exemple, à $A = 1.25$, $\overline{\omega_x^2}$ ne varie que de 20% entre la paroi et son minimum local à $y = 3.5$. Cette variation est d'un ordre de grandeur inférieur à celle de l'écoulement non contrôlé, dans lequel $\overline{\omega_x^2}$ diminue de 400% depuis la paroi jusqu'à son minimum local à $y = 5$.

5. Effet sur les structures proches de la paroi

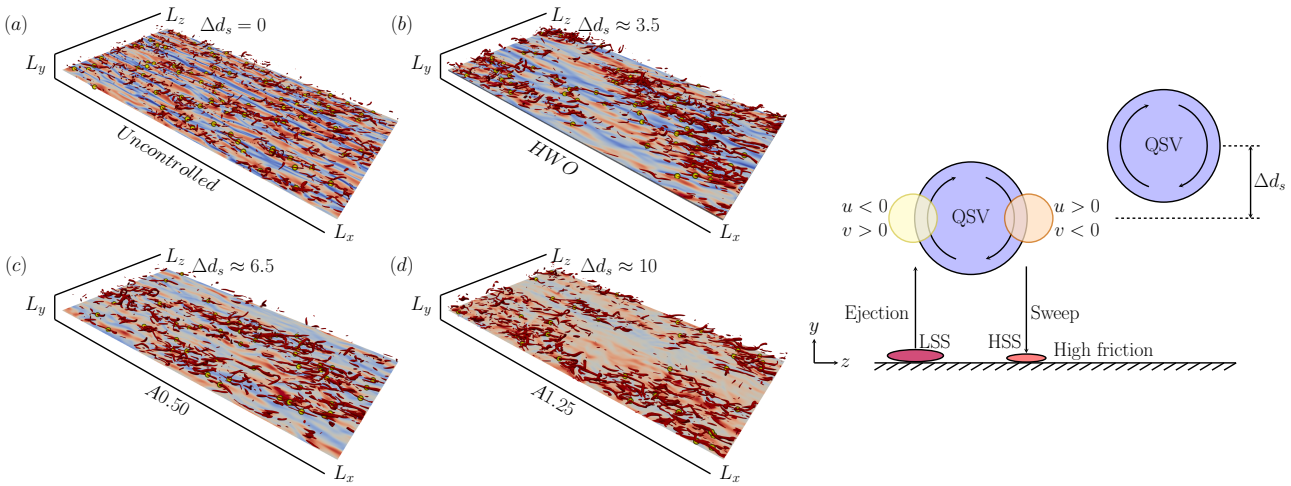

Figure 6: Les tourbillons quasi-longitudinaux (QSVs) identifiées en utilisant le critère $\lambda_2 = -0.02$ appliqué aux champs instantané des fluctuations de vitesse u (rouge : $u > 0$; bleu : $u < 0$) sur un plan parallèle à la paroi à $y = 15$ pour le cas (a) Non contrôlé, (b) HWO, (c) $A0.50$, and (d) $A1.25$, respectivement. Les centres des QSV actifs sont marqués par des points jaunes. Le diagramme du haut montre la dérive (Δd_s) des QSV par rapport au cas canonique non contrôlé. Reproduit d'Umair & Tardu [14] avec l'autorisation du CUP.

Les tourbillons quasi-longitudinaux (QSVs) sont des structures cohérentes qui jouent un rôle fondamental dans le cycle de régénération de la turbulence près de la paroi Hamilton *et al.* [3]. Ils gèrent l'échange de quantité de mouvement et d'énergie et contribuent de manière significative à la génération de la contrainte de cisaillement de Reynolds en provoquant des événements d'éjection et de balayage. Le fluide à faible momentum est transporté loin de la paroi d'un côté de la QSV (éjection), tandis que de l'autre côté, le fluide à fort

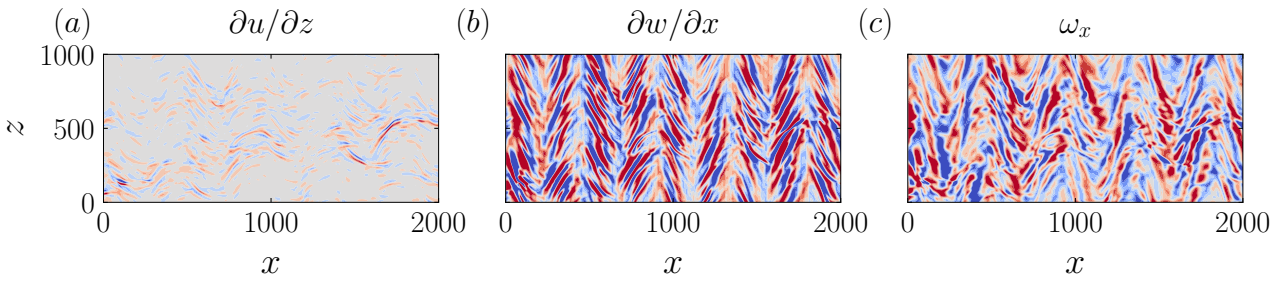

Figure 7: Contours de (a) $\partial u/\partial z$ (entre -0.2 to 0.2), (b) $\partial w/\partial x$ (entre -0.05 to 0.05), and (c) ω_x (entre -0.3 to 0.3) pour le cas $A1.25$ à $y = 10$. La couleur bleue représente les valeurs négatives, tandis que la couleur rouge représente les valeurs positives. Adapté d'Umair & Tardu [14] avec l'autorisation de CUP.

momentum est transporté vers la paroi (balayage). Ces événements d'éjection et de balayage sont les principaux contributeurs à la production d'énergie cinétique turbulente Jeong *et al.* [5].

En écoulement canonique turbulent, la majorité des QSVs matures sont situés à $y \approx 24$, ce qui est en accord avec Jeong *et al.* [5]. Pour les cas STW, cependant, nous observons une dérive systématique de la position des QSVs qui sont repoussés loin de la paroi (figure 6). La dérive (le déplacement des centres des structures) est d'environ 6 unités pariétales pour le cas $A0.50$, et de 10 unités pour le cas $A1.25$. La dérive Δd_s des couches de vorticité actives ω_x diminue la traînée selon le modèle conceptuel de Jiménez [6] comme également discuté en détail par Tardu [12]. Selon un modèle conceptuel simple d'Orlandi & Jiménez [8], le taux de changement de la traînée de $\Delta\tau_{w0}$ peut être lié à

$$\frac{\Delta\tau_{w0}}{\tau_{w0}} = \frac{1}{2}\frac{\Delta\Gamma_0}{\Gamma_0} - \frac{\Delta d_{s0}}{d_{s0}}, \tag{3}$$

lorsqu'il est correctement dimensionné avec les unités internes de frottement de l'écoulement non contrôlé. Cette relation approximative ne donne qu'une description qualitative de l'effet des QSV sur le cisaillement de la paroi, mais a le mérite de relier l'intensité et la distance à la paroi des QSVs à τ_w. Nous avons estimé à 42% de DR pour le cas $A0.50$ à partir de l'équation 3, ce qui est en accord avec la valeur rapportée dans le tableau 1. Cependant, l'équation 3 donne 80% de réduction de traînée au cas $A1.25$ d'amplitude imposée la plus élevée, ce qui est surestimé d'environ 30%. Dans tous les cas, le terme, $\Delta\Gamma_0/\Gamma_0$ ne contribue que pour 20% au DR. Par conséquent, la dérive $\Delta d_{s0}/d_{s0}$ joue un rôle critique dans le mécanisme de réduction de traînée.

L'écoulement sous contrôle STW à grandes amplitudes développe ses propres structures dans la basse sous-couche tampon. Dans l'écoulement turbulent canonique, les couches de cisaillement $\partial w/\partial x$ sont ponctuelles et légèrement étirées dans la direction transversale. En utilisant une approche multi-échelle, Tardu [13] a montré que certaines des couches de cisaillement $\partial w/\partial x$ peuvent apparaître comme des stries dans la direction transversale. Comme le montre la figure 7(b, c), l'inclinaison de ces couches par le cisaillement moyen, résulte en des zones de vorticité longitudinale ω_x allongées à $y = 10$. La morphologie des couches $\partial w/\partial x$ sous la STW de grande amplitude est étonnamment différente. Les zones de $\partial w/\partial x > 0$ et $\partial w/\partial x < 0$ sont organisées en structures de type sapin de Noël en forme de Λ résultant d'un effet direct de STW. Leurs pattes sont inclinées le long de la direction transversale d'environ $\pm\pi/4$ et elles sont inclinées par le cisaillement $d\overline{U}/dy \approx 1$ près de $y = 10$. Les couches étirées ω_x sont par conséquent également en forme de Λ, et elles sont loin d'être allongées en structures alignées dans la direction longitudinale (figure 7c). Dans le cas de HWO, les couches de cisaillement $\partial w/\partial x$ sont inclinées dans le sens du courant, et ne sont strictement pas en forme Λ. L'origine de ces structures est délicate à comprendre. Les patterns $\partial w/\partial x$ proche paroi, dans le cas STW de grande amplitude, sont trop réguliers pour être attribués à un phénomène aléatoire quel qu'il soit. Ils sont en effet une conséquence de la forte modulation imposée, donc déterministe $\partial\widetilde{W}/\partial x$ proche paroi.

6. Conclusions

Nous avons analysé l'effet des oscillations transversales imposées sous forme de STW sur le transport des contraintes de Reynolds et du champ de vorticité à travers les simulations numériques directes à $Re_\tau = 180$. La fréquence et la longueur d'onde de l'onde progressive imposée ont été maintenues fixes à $\omega = 0.16$ et $\kappa = 1.66$ (en unités extérieures), et seule l'amplitude imposée a été modifiée de près d'une décade de $A = 0.15$ à $A = 1.25$ (sur la base de U_c). Les résultats ont été comparés au contrôle à travers des oscillations homogènes de la paroi avec les paramètres optimaux $T_0 = 100$ et une amplitude $A_0 = 12$. L'écoulement est presque relaminarisé à $A = 1.25$ sous STW. Un niveau aussi important de DR ne peut pas être atteint dans le cas d'une oscillation homogène de la paroi.

Le forçage sous forme de STW entraîne une diminution substantielle de toutes les composantes du champ de contraintes de Reynolds. Les termes de transport sont très proches du cas HWO lorsque l'amplitude imposée du STW se situe dans la plage intermédiaire $0.30 < A < 0.50$. Ce régime est marqué par un fort amortissement des fluctuations de la vitesse normale de la paroi, d'une part, et par une diminution notable des corrélations entre la vitesse et le gradient de pression, d'autre part. L'étude ci-présente confirme globalement les résultats précédemment publiés sur le HWO.

La situation change radicalement dans les cas de STW de grande amplitude lorsque $A > 0.50$. Le transfert inter-composantes entre les contraintes de Reynolds s'estompe dans la basse sous-couche tampon, où l'on constate que $\overline{\Pi_{uu}} \sim \overline{\Pi_{vv}} \sim \overline{\Pi_{ww}} \approx 0$. L'annihilation de $\overline{\Pi_{ww}}$ à $y < 10$ est particulièrement spectaculaire. Il est montré que $\overline{\Pi_{ww}} \approx 0$ dans la couche tampon basse entraîne l'aplatissement de l'intensité de vorticité longitudinale près de la paroi et indique une forte altération du processus de régénération des tourbillons actifs. La composante $\overline{ww}$ est produite de manière autonome par les termes liés à la déformation de Stokes et elle dissipe rapidement dans la basse sous-couche tampon.

Il y a une réduction significative des intensités des enstrophies normale à la paroi et transversale, cette dernière s'annulant presque dans la sous-couche visqueuse pour les grandes amplitudes STW. La contribution de $\partial w/\partial x$ par rapport à $\partial u/\partial z$ déviant de plus en plus importante près de la paroi pour les STW de grande amplitude. Cependant, l'atténuation de l'enstrophie turbulente normale à la paroi est d'une importance secondaire par rapport à l'enstrophie turbulente transversale.

Les QSV sont repoussés vers la couche externe. La dérive de la position normale à la paroi des QSV, combinée au reste des résultats, donne une estimation raisonnable de la marge DR.

Le champ de vitesse fluctuant transversal, qui joue un rôle important dans la turbulence près de la paroi, présente des caractéristiques intéressantes. L'écoulement est presque transitoire à la plus grande amplitude imposée STW, où la couche tampon développe ses propres structures induites par la déformation de Stokes $\partial\widetilde{W}/\partial x$ et devient ainsi entièrement découplée du reste de l'écoulement. Les couches de cisaillement $\partial w/\partial x$ qui sont ponctuelles et légèrement étirées dans la direction transversale dans le cas d'un écoulement incontrôlé, commencent à former des motifs cohérents en forme de Λ. Cependant, ces structures sont trop régulières pour être considérées comme induites par un phénomène aléatoire. L'analyse de l'équation de transport instantané des couches de cisaillement $\partial W/\partial x$ montre que ces patterns sont directement liés à la déformation de Stokes $\partial\widetilde{W}/\partial x$. Ces couches de cisaillement ne jouent cependant aucun rôle actif dans la génération de QSVs près de la paroi. Un tel scénario n'a jamais été observé en turbulence de paroi auparavant.

7. Perspectives

Bien que le travail présenté ici contribue à notre compréhension du DR par ondes progressives, des efforts supplémentaires sont nécessaires pour obtenir des informations plus approfondies sur le mécanisme sous-jacent. Il est évident, d'après notre discussion, que la plupart de nos connaissances sur les écoulements contrôlés à travers STW sont dérivées d'études numériques, peu d'investigations expérimentales ayant été menées jusqu'à présent. Notamment, les travaux récents expérimentaux de Marusic *et al.* [7] ont donné des résultats prometteurs, suggérant la possibilité d'obtenir un gain positif net de DR (quoique faible) même à des nombres de Reynolds élevés. Comme l'ont noté Ricco *et al.* [11], l'établissement d'une relation entre la contrainte de cisaillement et les paramètres d'actionnement basés sur les équations de transport est crucial. Une telle relation permettra d'optimiser les stratégies de contrôle avec plus de précision et d'efficacité.

Un autre défi à relever consiste à trouver des moyens pour mettre en pratique des techniques de contrôle basées sur les oscillations des parois. En effet, la mise en œuvre d'un dispositif de contrôle expérimental pour la R&D basé sur les ondes progressives implique généralement l'utilisation de systèmes d'actionnement actifs ou et/ou de matériaux intelligents. Cependant, il serait très intéressant d'explorer la possibilité de concevoir une technique passive capable d'imiter le comportement des ondes progressives sans apport d'énergie externe. Une telle technique présenterait des avantages en termes de simplicité, de rentabilité et de durabilité à long terme. Le développement des méthodes passives nécessiterait des solutions techniques innovantes. Il s'agit d'une voie passionnante pour la recherche future, qui pourrait ouvrir de nouvelles possibilités en termes d'applications industrielles.

Bibliography

[1] Thomas R. Bewley, Parviz Moin, and Roger Temam. "DNS-based predictive control of turbulence: an optimal benchmark for feedback algorithms". In: *J. Fluid Mech.* 447 (2001), pp. 179–225.

[2] Davide Gatti and Maurizio Quadrio. "Reynolds-number dependence of turbulent skin-friction drag reduction induced by spanwise forcing". In: *J. Fluid Mech.* 802 (2016), pp. 553–582.

[3] J.M. Hamilton, John Kim, and F. Waleffe. "Regeneration mechanisms of near-wall turbulence structures". In: *J. Fluid Mech.* 287 (1995), pp. 317–348.

[4] A.K.M.F. Hussain and W.C. Reynolds. "The mechanics of an organized wave in turbulent shear flow". In: *J. Fluid Mech.* 41 (2 Apr. 1970), pp. 241–258.

[5] J. Jeong et al. "Coherent structures near the wall in a turbulent channel flow". In: *Journal of Fluid Mechanics* 332 (1997), pp. 185–214.

[6] Javier Jiménez. "On the structure and control of near wall turbulence". In: *Physics of Fluids* 6.2 (1994), pp. 944–953. DOI: 10.1063/1.868327. eprint: https://doi.org/10.1063/1.868327. URL: https://doi.org/10.1063/1.868327.

[7] Ivan Marusic et al. "An energy-efficient pathway to turbulent drag reduction". In: *Nature Communications* 12.5805 (2021).

[8] Paolo Orlandi and Javier Jiménez. "On the generation of turbulent wall friction". In: *Physics of Fluids* 6.2 (1994), pp. 634–641. DOI: 10.1063/1.868303.

[9] Maurizio Quadrio and Pierre Ricco. "The laminar generalized Stokes layer and turbulent drag reduction". In: *J. Fluid Mech.* 667 (2011), pp. 135–157.

[10] Maurizio Quadrio, Pierre Ricco, and Claudio Viotti. "Streamwise-travelling waves of spanwise wall velocity for turbulent drag reduction". In: *J. Fluid Mech.* 627 (2009), pp. 161–178.

[11] Pierre Ricco, Martin Skotes, and Michael Leschziner. "A review of turbulent skin-friction drag reduction by near-wall transverse forcing". In: *Progress in Aerospace Sciences* 123.100713 (2021).

[12] S.F. Tardu. "Coherent structures and riblets". In: *Appl. Sci. Res.* 54 (1995), pp. 349–385. DOI: 10.1007/BF00863518.

[13] Sedat Tardu. "Multiscale analysis of some shear layers in a fully developed turbulent channel flow". In: *Computers & Fluids* 240 (2022), p. 105459. ISSN: 0045-7930. DOI: https://doi.org/10.1016/j.compfluid.2022.105459. URL: https://www.sciencedirect.com/science/article/pii/S0045793022001104.

[14] Mohammad Umair and Sedat Tardu. "Vorticity transport in a turbulent channel flow subjected to streamwise travelling waves". In: *J. Fluid Mech.* 967 (2023), A9. DOI: 10.1017/jfm.2023.478.

[15] Mohammad Umair, Sedat Tardu, and Olivier Doche. "Reynolds stresses transport in a turbulent channel flow subjected to streamwise traveling waves". In: *Phys. Rev. Fluids* 7 (5 2022), p. 054601. DOI: 10.1103/PhysRevFluids.7.054601. URL: https://link.aps.org/doi/10.1103/PhysRevFluids.7.054601.